Novus Scientia 2026

23. Medzinárodná vedecká konferencia doktorandov strojníckych fakúlt technických univerzít a vysokých škôl

Novus Scientia 2026

Zborník príspevkov z XXIII. Medzinárodnej vedeckej konferencie doktorandov strojníckych fakúlt technických univerzít a vysokých škôl

29.01.2026

Strojnícka fakulta

Technická univerzita v Košiciach

Zameranie konferencie:

- Automatizácia, mechatronika a robotika
- Technologické a materiálové inžinierstvo
- Manažment, priemyselné a digitálne inžinierstvo
- Konštrukčné a procesné inžinierstvo
- Špeciálne inžinierske procesológie

Vedecký a organizačný výbor konferencie

Patronát konferencie

Dr.h.c. mult. prof. Ing. Jozef Živčák, DrSc., MPH, akademik UčSS
Technická univerzita v Košiciach, Slovensko

Garant konferencie

prof. Ing. Ján Slota, PhD.
Technická univerzita v Košiciach, Slovensko

Vedecký výbor konferencie

prof. Ing. Jozef Bocko, CSc., Technická univerzita v Košiciach, Slovensko

Dr.h.c. mult.prof. Ing. Miroslav Badida, PhD., Technická univerzita v Košiciach, Slovensko

prof. Ing. Michal Kelemen, PhD., Technická univerzita v Košiciach, Slovensko

prof. Ing. et Ing. Peter Trebuňa, PhD., Technická univerzita v Košiciach, Slovensko

prof. Ing. Emil Spišák, CSc., Technická univerzita v Košiciach, Slovensko

prof. Ing. Tomáš Brestovič, PhD., Technická univerzita v Košiciach, Slovensko

prof. Ing. Ján Kráľ, PhD., Technická univerzita v Košiciach, Slovensko

prof. Ing. Peter Frankovský, PhD., Technická univerzita v Košiciach, Slovensko

prof. Ing. Marek Kočiško, PhD., Technická univerzita v Košiciach, Slovensko

prof. Ing. Michal Holubčík, PhD., Žilinská univerzita v Žiline, Slovensko

prof. Ing. Marcela Pokusová, PhD., Slovenská technická univerzita v Bratislave, Slovensko

prof. Ing. Peter Šugár, CSc., Slovenská technická univerzita v Bratislave, Slovensko

doc. Ing. Jaroslav Katolický, Ph.D., Vysoké učení technické Brno, Česká republika

doc. Ing. Miroslav Mahdal, Ph.D., VŠB Technická univerzita Ostrava, Česká republika

prof. Ing. Tomáš Jirout, Ph.D., ČVUT Praha, Česká republika

doc. Ing. Petr Lepšík, Ph.D., Technická univerzita v Liberci, Česká republika

doc. Ing. Václav Vaněk, Ph.D., Západočeská univerzita v Plzni, Česká republika

prof. dr. hab. inž. Andrzej Burghardt, Politechnika Rzeszowska, Poľsko

Dr inż. Tomasz Jachowicz, Politechnika Lubelska, Poľsko

Dr inż. Jacek Rysiński, Uniwersytet Bielsko – Bialski, Poľsko

Členovia odbornej komisie

prof. Ing. Jozef Kuľka, PhD.

doc. Ing. Miriam Pekarčíková, PhD.

prof. Ing. Miroslav Pástor, PhD.

prof. Ing. Michal Kelemen, PhD.

doc. Ing. Ľudmila Dulebová, PhD.

doc. Ing. Teodor Tóth, PhD.

Organizačný výbor konferencie

prof. Ing. Ján Slota, PhD.

Ing. Jaroslav Melko

Ing. Erika Dubňanská

Ing. Martina Hančinová

Ing. Barbara Schürger

Ing. Veronika Sedláková

Ing. Katarína Dudová

Recenzovaný zborník z vedeckej konferencie

Príspevky v zborníku z vedeckej konferencie boli recenzované recenzentmi prostredníctvom anonymného recenzného konania.

Novus Scientia 2026

Zborník príspevkov z XXIII. Medzinárodnej vedeckej konferencie doktorandov strojníckych fakúlt technických univerzít a vysokých škôl

Názov:	Novus Scientia 2026
Editor:	© prof. Ing. Ján Slota, PhD.
	© Ing. Erika Dubňanská
	© Ing. Martina Hančinová
	© Ing. Barbara Schürger
Vydavateľ:	Technická univerzita v Košiciach,
	Strojnícka fakulta,
	Letná 1/9, 042 00 Košice-Sever
Rok:	2026
Náklad:	75 výtlačkov
Rozsah:	374 strán
Miesto konania:	Strojnícka fakulta, Technická univerzita v Košiciach
Dátum konania:	29.01.2026

ISBN 978-80-553-5042-4

OBSAH

Autorský kolektív a názov príspevku	Strany
ALI T., ŽIVČÁK J., ŠIŠKOVÁ S.: Biomechanical factors in the pathophysiology and clinical features of Wilkie syndrome	8 – 12
BADIDOVÁ M., SOBOTOVÁ L.: Research on non-exhaust ultrafine particles generated by car driving	13 – 20
BENDA M. M., SPIŠÁK E., MULIDRÁN P.: Experimental analysis of the influence of layer order in double-layer blanking of electrical steel sheets with variable strength properties	21 – 27
BÖSZÖRMÉNYI P., SCHNITZER M., HUDÁK R., ŽIVČÁK J., ŠEVČÍK T.: Patient-Specific Surgical Guide for Ulna Reconstruction Using CT-Based Digital Planning and Additive Manufacturing	28 – 33
BRADA L., MIKOVÁ Ľ., PRADA E.: Design of educational tool for PID motor control	34 – 40
BRNA J., SUKOP M.: Design and Evaluation of a Cross-Platform Communication Architecture for Industrial Data Exchange	41 – 45
BUBER M., TOMÁŠ M.: Analysis of the cup-wall thickness change during deep drawing of a bearing housing	46 – 52
BUČKO M., DIŽO J., SAMAŠ V., SLUŠŇÁK P.: Design of a Double-Axle Bogie for Regional Rail Vehicles	53 – 58
CICHÝ M., DUPLÁKOVÁ D.: Current State and Potential Applications of Real-Time Data for Predictive Assessment of Ergonomic Risks in Industry	59 – 64
ČAJKOVÁ J., TREBUŇOVÁ M., BAČENKOVÁ D.: MSC Senescence in Prolonged Biocompatibility Evaluation of Biomaterials	65 – 70
ČURMA P., MILENOVSKÝ P., LÁZÁR M.: Development of an Apparatus for Recycling Metal Hydride Alloys	71 – 76
DIVOKOVÁ V., HUDÁK R., DIVOK M.: Application potential of physiologically beneficial vibrations in traumatological practice	77 – 83
DOMINIK F., SLOTA J., VRABEĽ M., KUŠNÍR J., PILÁT P.: Automation of VRFB component production using a custom-made vacuum fixture	84 – 89
DUBŇANSKÁ E., HANČINOVÁ M., SCHÜRGER B., HUŇADY R.: Numerical Modelling and Simulation of the Buildability of a 3D-Printed Component Using Grasshopper Plug-in	90 – 94
DUDOVÁ K., BEDNARČÍKOVÁ L., ŽIVČÁK J.: Quantitative and Visual Assessment of Burn Scars Using 3D Scanning	95 – 100
DZURŇÁK P., MANTIČ M.: Image classification using convolutional neural network in container spreader control process	101 – 105
EIBEN V., KRÁLIKOVÁ R., LUMNITZER E.: Advancing Technical Research through Thermal Imaging: Educational Perspectives and Case Studies	106 – 114
GREGA M., BREZINOVÁ J.: Influence of chemical composition, inclusions and microcracks on the mechanical properties of G24Mn6 type steel	115 – 122
HANČINOVÁ M., DUBŇANSKÁ E., SCHÜRGER B., HUŇADY R., MACHALLA M.: Finite Element Simulation of Tensile Test of Silicone Material	123 – 129

IVANECKÝ J., KUĽKA J., VIROSTKO M.: Analysis of accuracy of additive technology models	130 – 135
KAPRAĽ V., GAJDOŠ I., KRASINSKYI V., LIOSIS CH.: Analysis of the Hopper Shape in the Extruder Feeding Section	136 – 142
KEREKEŠ S., SCHÜRGER B., DELYOVÁ I., FRANKOVSKÝ P.: Kinematic Design and Functional Principle of a Kinetic Sculpture Mechanism	143 – 147
KOKARDA V.: Comparison of EDX and LIBS analytical methods in evaluating technical cleanliness in industrial applications	148 – 158
KORDOŠOVÁ M., TÓTH T., BEDNARČÍKOVÁ L., MICHALÍKOVÁ M.: Digitization of custom orthotic insole manufacturing	159 – 164
KUŠNÍR J., DEMKO M., BRINDZA J., VRABEĽ M., DOMINIK F.: Experimental data acquisition from a milling fixture	165 – 172
LEŠČINSKÝ M., KOVÁČ J.: Extension of an Open-Source Control System for Bimanual Robotic Manipulation Using CyberGlove Data Gloves	173 – 179
LEVICKÁ S., PRAŽÁK D., SEDLÁK V., NAJMANOVÁ E., PLUHÁČEK F.: International metrological comparison of ocular tonometers for optometry purposes	180 – 184
MAJERČÁK O., ŠARGA P., RÁKAY R.: Detection of compressed air leakage using compressor energy consumption analysis	185 – 191
MALAKHOV D., KELEMENOVÁ T.: Overview of calibration methods for measuring microscopes	192 – 199
MÁLIK M., JÁNOŠ R.: Communication Layer Compatibility in Cross-Generation ROS Systems	200 – 205
MAŚLANKA M., PYTKA D., WALUSZEK M.: Sound Generator Selection for Musical Tesla Coils	206 – 210
MELKO J., JÁNOŠ R., MLINARČEK D., BRNA J.: Methodology of Design and Simulation Verification of the Air Force TUKE Pneumatic Drive	211 – 216
MINALE Y. F., GAJDOŠ I., SZABO T., POLYÁKNÉ KOVÁCS A., MAROSSY K., ÁDÁMNÉ MAJOR A.: Segmental Dynamics and Thermo-Mechanical Response of PVC/TPU Blends Plasticized with a Bio-Based Plasticizer	217 – 221
NOVOTNÝ Š., PALKO M.: Design of engine modifications and construction for an experimental vehicle	222 – 227
ONDERČO P., RYBÁŘ J., LEJA J., ĎURIŠ S.: Construction of timetables in urban public transport from a metrological perspective	228 – 232
PAĽOVÁ K., KELEMENOVÁ T.: The Surface Roughness Standards	233 – 238
PILÁT P., VARGA J., SEMJON J., DOMINIK F, TAKÁČ K.: IMU-Based experimental verification of the stability of a specialized robotic locomotion system for pipeline environments	239 – 246
PORUBČANOVÁ D., ZÁBAVSKÝ T., BALÁŽIKOVÁ M.: Assessment of the impact of noise on mental stress	247 – 251
ROMANČÍK J., VAGAŠ M., MAJERČÁK O.: Integration of Shape-Memory Alloy Actuator into a Scissor-Mechanism Gripper Design	252 – 256
RUDA F., SPIŠÁK E.: Influence of Rolling Mill Parameters on the Mechanical and Surface Properties of Thin Galvanized Sheets	257 – 262

RUSIŇÁK D., VIRGALA I.: A Data-Driven Forward Kinematics Model for a Tendon-Driven Continuum Robot Using MLP-Based Regression	263 – 268
SAMAŠ V., BUČKO M., GERLICI J., SLUŠŇÁK P.: Design and Testing of a Device for Measuring Flywheel Brake Rotation to Enhance Static Friction Coefficient Evaluation	269 – 275
SAVKOVÁ N., ŠTEFANOVIČ B., IVANČOVÁ E., SCHNITZER M., ŽIVČÁK J.: Advancing Early Cleft Care: The Role of Intraoral Scanning (IOS) in Neonatal Patients — A Case Report and Literature Review	276 – 285
SEDLÁKOVÁ V., HUDÁK R., TÓTH T., HAKULIN D.: Overview of the Effects of Vibrations on Stem Cells	286 – 290
SCHÜRGER B., FRANKOVSKÝ P., HANČINOVÁ M., DUBŇANSKÁ E., KEREKEŠ S.: Metamaterials for Smart and Sustainable Cities	291 – 297
STARINSKÝ G., RYBÁŘ J., ONDERČO P., BENČAT A., GERNESCHOVÁ J., SMETÁNKA A.: The use of digital calibration certificates in healthcare	298 – 301
SUKOPOVÁ D., FIĽO M., KÁDÁROVÁ J., LEŠČINSKÁ L.: Trends in the Use of Artificial Intelligence in Enterprises in Slovakia and the EU and Their Relationship to Performance Indicators	302 – 304
SZÁSZI D., KRÁĽ J.: Use of simulation methods in production machines using virtual and augmented reality	305 – 310
ŠIŠKA R., SLOTA J.: Analysis of the Effect of Surface Treatment of Shearing Tools on the Accuracy and Quality of Roll-Bonded Sheet Cutting	311 – 315
ŠIŠKOVÁ S., ŽIVČÁK J., ALI T., VINCZE L., DEÁKOVÁ D., ŠČIPÁKOVÁ M.: Abdominopelvic Vascular Compression Syndromes: Pathophysiological Mechanisms and Connective Tissue Links	316 – 321
ŠPURO P., CZAN A., SAJGALIK M., DRBUL M., MARKOVIC J., SCOTKA A.: Effect of Laser Shock Peening on Additively Manufactured Components	322 – 327
ŠTEFČÁK P., GAJDOŠ I., SOBASZEK Ł., MINALE Y. F.: Definition and application of process tools for rib structure design in Large-scale additive manufacturing	328 – 332
TOMKOVÁ V., SLOTA J.: Manufacturing possibilities of steel sheets with organic coatings, their testing and damage in practice	333 – 340
VARJÚ E., KOVÁČ J.: Implementation of Realistic Physical Interactions for Maintenance Tools in Unity3D	341 – 348
VIĽCHA J., FERKO J., ŽIVČÁK J.: Follicular cyst removal and stabilization with 3D planned splint - case report	349 – 353
VIROSTKO M., MANTIČ M., MALÁKOVÁ S., IVANECKÝ J.: Generative Design for Spur Gear Optimization	354 – 358
WALUSZEK M., MAŚLANKA M., PYTKA D.: Real-Time Machine Vision Inspection of Embedded Inserts on a Belt Feeder	359 – 364
YEROMINA M., DUPLÁK J., MIKULÁŠKO S.: Assessment of the productivity of a robotic dental production cell design using simulation tool	365 – 371

TECHNICAL UNIVERSITY OF KOŠICE
Faculty of Mechanical Engineering

Biomechanical factors in the pathophysiology and clinical features of Wilkie syndrome

Talal Ali[1, 2,*], Jozef Živčák[1], Silvia Šišková[1, 3]

[1] Technical University of Košice, Faculty of Mechanical Engineering, Department of Biomedical Engineering, Letná 1/9 | 042 00 Košice-Sever, Slovakia
[2] National Institute of Cardiovascular Diseases, Pod Krásnou hôrkou 1/7185, 833 48 Bratislava; dr.talal.ali8@gmail.com
[3] Asociácia Vaskulárnych Kompresívnych Syndrómov a Ehlers-Danlos, o.z., Balkánska 110/108, 851 10 Bratislava, Slovakia, silvia.siskova@student.tuke.sk
* Correspondence: dr.talal.ali8@gmail.com

Abstract: Wilkie syndrome, also known as Superior Mesenteric Artery Syndrome (SMAS), is a rare vascular compression disorder caused by the mechanical obstruction of the third portion of the duodenum between the abdominal aorta and the superior mesenteric artery (SMA). This review examines the specific biomechanical factors driving the pathophysiology of SMAS, including the critical reduction of the aortomesenteric angle and distance, the depletion of the retroperitoneal fat pad, and the influence of spinal deformities such as lumbar lordosis and scoliosis. Furthermore, it highlights the emerging clinical association between SMAS and heritable connective tissue disorders, specifically Ehlers-Danlos Syndrome (EDS) and Hypermobility Spectrum Disorders (HSD). In these patients, ligamentous laxity and visceroptosis contribute to altered anatomical relationships, predisposing them to vascular compression. A thorough understanding of these biomechanical principles is vital for timely diagnosis and effective management.

Keywords: Wilkie syndrome; Superior Mesenteric Artery Syndrome; biomechanics; aortomesenteric angle; Ehlers-Danlos syndrome; visceroptosis

1. Introduction

Wilkie syndrome, clinically designated as Superior Mesenteric Artery Syndrome (SMAS), is a rare but serious form of upper gastrointestinal obstruction caused by the compression of the third portion of the duodenum. First described comprehensively by Sir David Wilkie in 1927, the condition involves a mechanical entrapment of the duodenum within the "nutcracker" formed by the abdominal aorta (AA) posteriorly and the superior mesenteric artery (SMA) anteriorly [1], [2].

While historically associated almost exclusively with rapid weight loss and the loss of the mesenteric fat pad, recent research has elucidated a more complex biomechanical etiology. Anatomical variations, spinal deformities, and heritable connective tissue disorders (HCTD) such as Ehlers-Danlos Syndrome (EDS) and Hypermobility Spectrum Disorders (HSD) play significant roles in its pathogenesis [3], [4], [5], [6]. The clinical presentation typically follows a triad of postprandial epigastric pain, bilious emesis, and progressive weight loss, establishing a pathophysiological feedback loop where malnutrition further diminishes the protective retroperitoneal fat., creating a self-perpetuating cycle of malnutrition that further exacerbates the biomechanical compression [2], [7]. This review analyzes the quantitative biomechanical factors and pathophysiological mechanisms underlying this syndrome.

2. Biomechanical pathophysiology

The pathophysiology of Wilkie syndrome is fundamentally a problem of geometry and mechanics within the retroperitoneal space. The third (horizontal) part of the duodenum passes between the aorta and the SMA at the level of the L3 vertebra. In healthy individuals, this passage is maintained by a cushion of retroperitoneal adipose tissue and the natural angle of the SMA takeoff [2], [7].

2.1. Quantitative Biomechanics: Angles and Distances

The diagnosis of SMAS relies on specific radiographic measurements obtained via Computed Tomography Angiography (CTA) and upper GI barium swallow study [8], [9].
Aortomesenteric Angle (AMA): In a healthy population, the SMA originates from the aorta at an angle between 20° and 70°. In patients with Wilkie syndrome, this angle is critically reduced, typically falling below 20° [8], [10]. Figure.1
Aortomesenteric Distance (AMD): The normal distance between the aorta and the SMA at the level of the duodenum ranges from 10 to 28 mm. In SMAS, this distance is pathologically narrowed to less than 10 mm, resulting in the mechanical sequestration of the duodenal lumen, thereby impeding the bolus transition[8], [10].Figure.2

While the diagnostic thresholds of an AMA < 20 and AMD < 10 are widely accepted, a critical analysis of current literature suggests these metrics should not be interpreted in isolation. Ozkurt et al. [10] demonstrated that while these measurements correlate with BMI, they do not always correlate with symptom severity. In the context of heritable connective tissue disorders (HCTD), patients may present with 'borderline' measurements (e.g., an angle of 22 - 25) yet suffer from severe obstruction due to the dynamic nature of visceroptosis. This suggests that static CT imaging—often performed in the supine position—may underestimate the degree of compression occurring when the patient is upright or symptomatic."

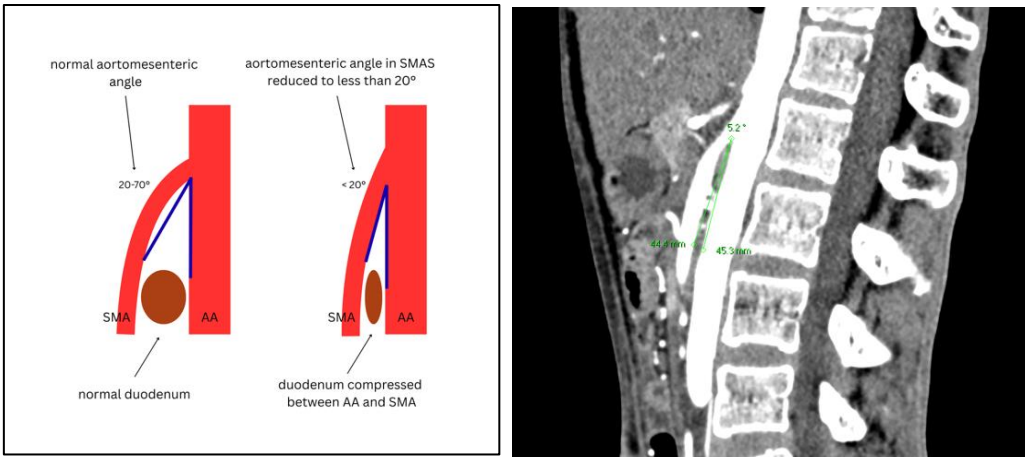

Figure 1. Comparison of normal vs. SMAS aortomesenteric angles; CT in sagittal view showing a reduced aortomesenteric angle in SMAS patient (own source)
AA - abdominal aorta, SMA - superior mesenteric artery

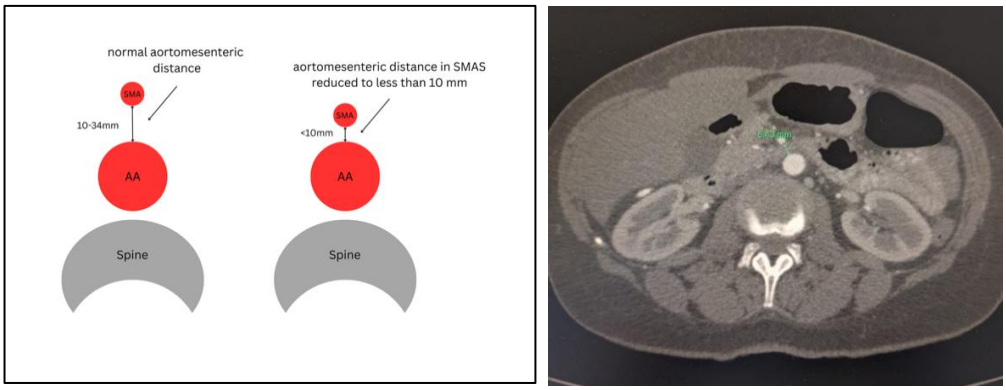

Figure 2. Comparison of normal vs. SMAS aortomesenteric distance; CT in axial view showing a reduced aortomesenteric distance in SMAS patient (own source)
AA - abdominal aorta, SMA - superior mesenteric artery

2.2. Dynamic Biomechanics

Upper GI barium swallow study represents an equally important diagnostic tool in Wilkie syndrome because it captures duodenal obstruction dynamically and in real time. During fluoroscopy, diluted barium is swallowed and its passage through the stomach and duodenum is continuously observed, typically demonstrating dilatation of the first and second parts of the duodenum and an abrupt cut-off in the third part, often with antiperistaltic "to-and-from" movement proximal to the obstruction [8], [9]. Positional maneuvers (supine, prone, left lateral decubitus, knee-elbow) can be performed during the examination, allowing direct visualization of how changes in posture widen the aortomesenteric angle, improve emptying, or relieve the obstruction, which provides functional confirmation of the biomechanical nature of the compression [9].

2.3. The Role of the Retroperitoneal Fat Pad

The most common biomechanical trigger for SMAS is the depletion of the mesenteric fat pad that normally elevates the SMA away from the aorta [1]. Rapid and severe weight loss, due to eating disorders, catabolic states (e.g., burns, trauma), or malignancy, reduces this adipose cushion, causing the SMA to collapse posteriorly toward the spine. This creates a vicious cycle: compression causes vomiting and inability to eat, leading to further weight loss and tightening of the vascular clamp [2].

2.4. Spinal and Anatomical Factors

Biomechanical compression is frequently exacerbated by skeletal abnormalities. Exaggerated anterior curvature (lordosis) of the lumbar spine pushes the aorta and vertebral column anteriorly, narrowing the space available for the duodenum [8]. SMAS is a recognized complication of scoliosis surgery. Corrective lengthening of the spine can increase longitudinal tension on the mesentery, biomechanically stretching the SMA and narrowing the aortomesenteric angle [2]. Finally, some anatomical variations, such as a low origin of the SMA or a high insertion of the Ligament of Treitz (suspensory ligament of the duodenum) can anatomically elevate the duodenum into the apex of the aortomesenteric angle, predisposing the patient to obstruction [2], [8].

3. The Connective Tissue Disorder Connection

An increasing body of literature supports a strong association between Wilkie syndrome and heritable connective tissue disorders, particularly Ehlers-Danlos Syndrome (EDS) and Hypermobility Spectrum Disorders (HSD) [3], [4], [5], [6]. The biomechanical link in these patients is distinct from simple weight loss. The primary mechanism is visceroptosis (ptosis of the abdominal organs) caused by generalized ligamentous laxity and collagen defects [8], [11]. The Ligament of Treitz and other mesenteric supports may be

lax, allowing the duodenum to descend or hang loosely. The visceral geometry is altered. As abdominal organs droop (enteroptosis), they exert traction on the mesentery, pulling the SMA taut and narrowing the angle regardless of the patient's BMI [11]. Finally, patients with EDS frequently present with multiple vascular compressions (e.g., co-occurring Nutcracker Syndrome) due to this generalized tissue fragility and vascular mobility [3], [4], [5], [6].

4. Clinical Features

The clinical presentation of Wilkie syndrome is a direct consequence of the biomechanical obstruction. The classic triad consists of postprandial epigastric pain (often severe and cramping), bilious vomiting, and weight loss. Patients often report "early satiety" or a sensation of food "getting stuck" [1], [7]. A hallmark clinical feature is the relief of symptoms with specific changes in posture. The knee-chest position or lying in the left lateral decubitus position can biomechanically open the aortomesenteric angle by allowing gravity to pull the SMA and visceral fat pad anteriorly, temporarily relieving the obstruction. Conversely, the supine position often exacerbates symptoms [2], [9]. While acute cases may present with complete obstruction and electrolyte imbalance, chronic cases (common in EDS) present with long-standing, vague abdominal pain and "failure to thrive," often leading to misdiagnosis as functional dyspepsia or psychogenic eating disorders [7], [8].

5. Proposed Clinical Management Algorithm

To improve diagnostic accuracy and therapeutic outcomes, a structured approach is required. This algorithm emphasizes the distinction between simple malnutrition-induced SMAS and the complex biomechanical factors seen in HCTD/EDS patients.

Step 1: Clinical and Phenotypic Screening

Symptom Review: Evaluate for the "Wilkie Triad" (postprandial pain, bilious vomiting, weight loss).

Positional Relief: Document if symptoms improve in the left lateral decubitus or knee-chest position (pathognomonic for SMAS).

Phenotypic Assessment: Screen for generalized ligamentous laxity using the Beighton Score. Patients with EDS/HSD may present with visceroptosis-driven compression even without significant weight loss.

Step 2: Multimodal Imaging (The "Critical" Gap)

Radiological findings must be correlated with clinical symptoms, as static measurements can be misleading.

CTA/MRA (Supine): Measure the Aortomesenteric Angle (AMA) and Distance (AMD).

Critical Note: A "normal" angle (>25^\circ) on a supine CT does not rule out SMAS in hypermobile patients whose anatomy shifts upon standing (orthostatic visceroptosis).

Dynamic Barium Swallow: The gold standard for functional confirmation. Look for:

Dilatation of the proximal duodenum.

Abrupt "cutoff" at the third portion.

"To-and-fro" antiperistalsis (chyme struggling to pass the vascular clamp).

Step 3: Therapeutic Hierarchy

Management should follow a stepwise progression from conservative to surgical intervention.

6. Conclusions

Wilkie syndrome is not merely a consequence of weight loss, but a multi-factorial biomechanical failure. The traditional 'nutcracker' mechanism is often exacerbated by skeletal variables (lordosis) or the ligamentous laxity inherent in Ehlers-Danlos Syndrome. Future clinical practice should adopt a position-dependent diagnostic approach, particularly in hypermobile populations, to ensure that transient mechanical obstructions are not overlooked by static imaging.

While the literature consistently cites an AMA <20 as diagnostic, this review highlights a critical "grey zone." In patients with Ehlers-Danlos Syndrome, the pathophysiology is driven by visceroptosis (the "mesenteric sink" effect). As abdominal organs descend, they exert downward traction on the SMA, narrowing the angle dynamically. Consequently, these patients may fail conservative nutritional therapy because the underlying issue is ligamentous laxity rather than a simple loss of adipose tissue. Clinicians must maintain a high index of suspicion in "thin but stable" hypermobile patients who do not fit the classic rapid-weight-loss profile.

Wilkie syndrome remains a diagnosis of "mechanical exclusion." By understanding the quantitative biomechanics—specifically the interaction between the SMA, the aorta, and the suspensory ligament of Treitz—clinicians can move beyond symptomatic management toward targeted anatomical correction. The emerging link with Ehlers-Danlos Syndrome necessitates a paradigm shift in how we interpret "normal" vascular angles in hypermobile populations.

Acknowledgments: This paper was written with the financial support from the KEGA granting agency within the project solutions No. 050TUKE-4/2022 and No. 021TUKE-4/2022, and with financial support from the APVV granting agency within the project solutions No. APVV-20-0068 and No. SK-CZ-RD-21-0056.

Conflicts of Interest: The authors declare no conflict of interest.

References

1. Sir David Percival Dalbreck Wilkie, "Chronic duodenal ileus," *American Journal of Medical Sciences*, vol. 173, pp. 643–649, 1927.
2. T. Welsch, M. W. Büchler, and P. Kienle, "Recalling superior mesenteric artery syndrome," *Dig Surg*, vol. 24, no. 3, pp. 149–156, Jun. 2007, doi: 10.1159/000102097.
3. W. Sandmann, T. Scholbach, and K. Verginis, "Surgical treatment of abdominal compression syndromes: The significance of hypermobility-related disorders," *Am J Med Genet C Semin Med Genet*, vol. 187, no. 4, pp. 570–578, Dec. 2021, doi: 10.1002/ajmg.c.31949.
4. Spanish Society of Vascular Compresion Syndromes, "Spanish Society of Vascular Compresion Syndromes," *Angiologia*, vol. 77, no. 2, pp. 142–144, Mar. 2025, doi: 10.20960/angiologia.00742.
5. S. Šišková, J. Živčák, R. Gil Sánchez, and T. Ali, "The Biomechanisms and Links between Abdomino-Pelvic Vascular Compression Syndromes and Symptomatic Joint Hypermobility Syndromes," *Novus Scientia 2024*, pp. 369–374, 2024, [Online]. Available: http://www.sjf.tuke.sk/NovusScientia/index.html
6. Lukáš Vincze, Silvia Šišková, Jozef Živčák, and Talal Ali, "Abdomino-Pelvic Vascular Compression Syndromes in the Abdominal Cavity," in *13. Slovenská konferencia o zriedkavých chorobách*, Nov. 2024.
7. T. Ali, J. Tomka, I. Bakirli, and I. Bakirov, "Surgical Treatment of Wilkie's Syndrome by Vascular Transposition," *Cureus*, Apr. 2022, doi: 10.7759/cureus.24251.
8. M. D'Oria *et al.*, "International Union of angiology consensus document on vascular compression syndromes," *International Angiology*, vol. 42, no. 4, pp. 282–309, Aug. 2023, doi: 10.23736/S0392-9590.23.05100-3.
9. J. R. Hines, R. M. Gore, and G. H. Ballantyne, "Superior Mesenteric Artery Syndrome. Diagnostic Criteria and Therapeutic Approaches," *The American Journal of Surgery*, vol. 148, pp. 630–632, 1984.
10. H. Ozkurt, M. M. Cenker, N. Bas, S. M. Erturk, and M. Basak, "Measurement of the distance and angle between the aorta and superior mesenteric artery: Normal values in different BMI categories," *Surgical and Radiologic Anatomy*, vol. 29, no. 7, pp. 595–599, Oct. 2007, doi: 10.1007/s00276-007-0238-9.
11. S. Kucera and S. Sullivan, "Visceroptosis and the Ehlers-Danlos Syndrome," *Cureus*, Nov. 2017, doi: 10.7759/cureus.1828.

TECHNICAL UNIVERSITY OF KOŠICE
Faculty of Mechanical Engineering

Research on non-exhaust ultrafine particles generated by car driving

Miroslava Badidová [1], Lýdia Sobotová [1,*]

[1] Technical University of Kosice, Faculty of Mechanical Engineering; miroslava.badidova@student.tuke.sk; lydia.sobotova@tuke.sk
* Correspondence: miroslava.badidova@student.tuke.sk; Tel.: +421 55 602 2716

Abstract: Industrialization, transport, urbanization, agriculture, fires, desert dust and poor waste management have intensified health risks and environmental pollution. Due to rapid urbanization and motorization in many cities, transport (especially road transport) is a growing and major source of air pollutants. In OECD countries, road transport accounts for around 50 % of the cost of air pollution (OECD, 2014). In addition to general air pollutants, transport also releases CO_2 and short-lived climate pollutants (SLCPs) such as black carbon particles and methane, contributing to short- and long-term climate change and the deterioration of local air quality.

Keywords: transport; particulate emissions; wear of tires; brakes; roads

1. Introduction

The dust and aerosol particles (PM) are considered one of the major risk factors for adverse health effects and premature deaths worldwide. Human exposure to PM (especially the fine fraction) is associated with worsening allergies, respiratory, cardiovascular, eye problems and even cerebrovascular diseases. Particles may be directly emitted into the environment as primary aerosols or formed in the atmosphere through gas-to-particle conversion processes, i.e., as secondary aerosols transported by wind and produced by photochemical processes.

This paper synthesizes the current state of knowledge on the nature, causes, and consequences of emitted and ambient solid aerosol particles originating from tyre wear, brake wear, road surface abrasion, and road dust resuspension. It also simulates how emissions of solid aerosol particles from non-exhaust sources will evolve in the coming years and identifies existing technological and policy measures to mitigate these emissions and immissions.

2. Classification of Particulate Matter (PM)

The despite all implemented and ongoing measures, pollution remains a major global problem, as the transport sector is expected to experience an increase in emissions in the coming years. Companies and policymakers face growing pressure to reduce the impact of their logistics activities and achieve more environmentally sustainable transport.

As part of the Zero Pollution Action Plan within the European Green Deal, the European Commission has set a target to reduce the number of premature deaths caused by fine particles ($PM_{2.5}$) by at least 55 % by 2030 compared to 2005 levels. To achieve this, the EC aims to align air quality standards with the recommendations of the World Health Organization (WHO), which are stricter than current EU limits.

Despite reductions in emissions from various sources, in 2021 up to 97 % of EU urban residents were exposed to $PM_{2.5}$ levels exceeding the WHO annual limit (5 μg/m^3). For

PM_{10}, 71 % of residents were exposed to values above the WHO annual limit (15 μg/m³). [1, 2]

Particulate Matter (PM) is a mixture of microscopic solid and liquid particles dispersed in the air. These particles may originate:

- **from natural sources** – e.g., dust, pollen, sea salt,
- **from human activities** – e.g., fuel combustion, transport, industrial processes, tyre and brake wear.

PM particles are hazardous because they can be inhaled and, depending on their size, penetrate deep into the lungs or even enter the bloodstream, negatively affecting human health and the environment.

PM is most often divided according to the **aerodynamic diameter of the particles**:

- **PM_{10}** – particles ≤ 10 μm; penetrate the upper respiratory tract; include road dust, pollen, ash.
- **$PM_{2.5}$** – particles ≤ 2.5 μm; penetrate deep into the lungs and may enter the bloodstream; contain soot, heavy metals, organic compounds; most harmful to health.
- **PM_1** – particles ≤ 1 μm; may reach alveoli and pass into the blood.
- **Ultrafine particles (UFP)** – diameter < 0.1 μm (100 nanometres); They are difficult to measure, but they are extremely harmful.

2.1. Micro-particles in Transport

During driving, both road surfaces and tyres wear down, generating wear particles. The greatest abrasion occurs in winter when studded tyres—introduced in the 1970s to reduce asphalt wear—are used. Despite this, approximately 100,000 tons of asphalt were worn away annually and had to be replaced. In addition to the economic cost of asphalt replacement, tyre and road wear produce fine PM10 particles that negatively affect health.

Figure 1 shows a simplified representation of the dispersion of particles from tyre wear.

Figure 1. PM particle exposure scenarios in urban environments.

After tyre- and road-wear particles are generated, they may be dispersed into the air, remain on the road surface, accumulate nearby, or be transported to waterways, degrading environmental quality. Rain washes some particles into storm water drains and ditches, where they can settle into soil or sediments or continue toward rivers, lakes, and seas. When roads are wet or frozen, particles adhere to the surface and are later dried and re- suspended by traffic turbulence.

The topic of nanoparticles generated by tyre wear has recently gained significant attention due to uncertainties (both realistic and perceived) and is examined across several areas [2–5]:

- Physicochemical properties and risks: Tyre wear particles (TWP) form heterogeneous mixtures with road wear particles (TRWP) of varying shapes, sizes, surface areas, and chemical composition; their risk properties remain largely undetermined.

- "What enters is not what comes out": Nanomaterials embedded in tyre treads are not released as pure nanomaterials (MNMs) but as components of micro- and nanoparticles containing both original and chemically altered substances, including nucleation particles [2].
- Different exposure characteristics: Released TWP can affect humans and ecosystems directly near roads or be transported to distant terrestrial and aquatic environments.
- Different roles and responsibilities: Stakeholders include automobile, rubber, and tyre manufacturers, drivers, road maintenance workers and their employers, road authorities, as well as local, national, and international bodies; roles are not clearly or legally defined.
- Different risk management strategies: From innovative tyre designs and road engineering to socio-economic measures influencing driver behavior (e.g., reducing aggressive driving), speed limits, and restrictions on heavy vehicles such as SUVs [2].

TWP (Tyre Wear Particles) refers to particles that are not contaminated by road wear, which is the most likely form to arise in laboratory experiments (e.g. in a road simulator). The term TWP is also used when referring to the release of particles from tires in general [2 - 5].

TRWP (Tyre and Road Wear Particles) refers to agglomerates or aggregates of TWP with road wear particles. This is the most likely form to occur in the environment and is used in practical risk assessment [2 - 5].

In cities, road traffic is a significant source of PM emissions. Particulate matter (PM) emissions from vehicles come from, Figure 2:

- exhaust emissions – incomplete combustion of fuel and lubricant evaporation (Figure 3),
- non-exhaust emissions – tyre wear, brake wear, road abrasion (Figure. 2),
- road dust resuspension.

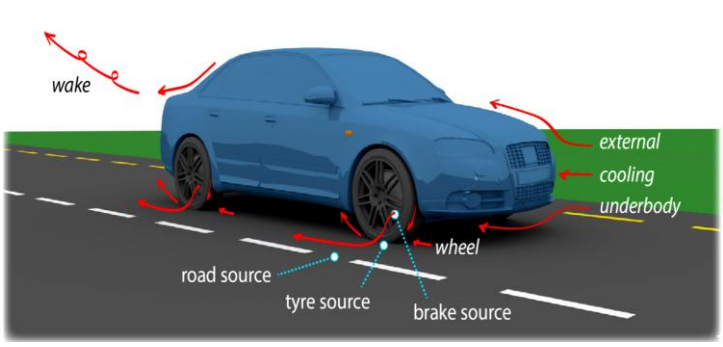

Figure 2. Risk scenario of exposure to PM particles in transport, which affect the transfer of pollution from sources of brakes, tires and roads to the wider environment.

In recent decades, the application of strict emission limits for exhaust gases has led to technologies that have almost completely eliminated PM in exhaust gases through the use of solid-phase filters, zero-emission vehicles such as battery electric vehicles (BEVs), and hydrogen fuel cell vehicles.

However, this has caused an increase in the proportion of non-exhausted PM.

Another factor affecting the formation of particles is:

- the growing popularity of heavier SUVs, causing more tyre and brake wear,
- rapid growth of electric vehicles increases the share of non-exhaust PM,
- although EVs eliminate exhaust emissions, their higher weight increases tyre wear, producing more PM_{10}.

2.2. Tire tread wear

When we drive, tires wear out and form small particles that mainly consist of rubber (natural and synthetic) and fillers, adjusting oils and reinforcing materials. Tire wear is recognized worldwide as the single largest source of micro plastics.

In the EU, tire wear is estimated at around 500,000 tons per year and e.g. in Sweden it is around 11,000 tons/year, which is approximately the same as the weight of 1.1 million passenger car tires. Tire particles take a long time to decompose, which means that they can have a negative impact on nature well into the future, as they lie in soil, water or sediment.

2.3. Brakes produce finer particles

Tires and even more brakes wear out per kilometer in an urban area, where intersections, roundabouts, and heavy traffic cause more acceleration, braking, and cornering. The use of a car, its brakes, produces particles that are generally smaller than other wear particles and that contain relatively high amounts of metals from brake discs and brake pads.

It is believed that the wear of brakes during driving in vehicles produces nanoparticles. Recent studies have shown that non-exhaust emissions are comparable to those of diesel engines and that the relative contribution of brake emissions to the overall vehicle emissions is increasing due to improvements in exhaust emission reduction technologies [5,14].

Micro plastic emissions from brake pads vary depending on their structure. According to research, low-alloy steel brake pads emit much higher emissions than non-steel or semi-metallic pads [15,16]. The properties of the abrasive layer formed on the brake surface play an important role. [8, 9, 15].

3. Measurement and Discussion of Non-Exhaust Particles PM

Measuring non-exhaust particles PM is still a scientific challenge, mainly due to the difficulties in collecting samples in dynamic and contaminated environments.

To obtain realistic data, measurements must be made directly on vehicles, but the precise determination of the source of particles is complicated - the brake system is located close to the tires and isolating individual components without affecting the test conditions is difficult.

Nevertheless, regulations and manufacturers require specific tests to identify particles from tires and brakes.

Recently, the EU proposed limits for brake emissions within the Euro 7 framework, based on Global Technical Regulation No. 24 (GTR 24).

GTR 24 standardizes the procedures for measuring emissions from braking of light commercial vehicles, defining the conditions of the test cycle (WLTP-Brake: Worldwide Harmonized Light Vehicles Test Procedure) using brake dynamometers. Another complication in the case of tires is that particle production is highly dependent on the interaction with asphalt, which introduces additional uncertainty. As a result, emission factors vary considerably even under seemingly similar operating conditions.

When analyzing road dust samples, it can be observed that most fractions are between 50 and 200 μm.

In the methodology of emission assessment, it is important to design and process test samples by choosing the sampling location, the method of taking test samples, so as not to contaminate the collected materials. It is necessary to use separation methods (drying, multiple separation, flotation - the use of deionized water to remove biological compounds, drying, heating the test samples to 35°C during the test period (time - dust 24 hours, soil 72 hours).

Figure 3 and Figure 4 show representative spectra of micro plastics from soil and road dust samples.

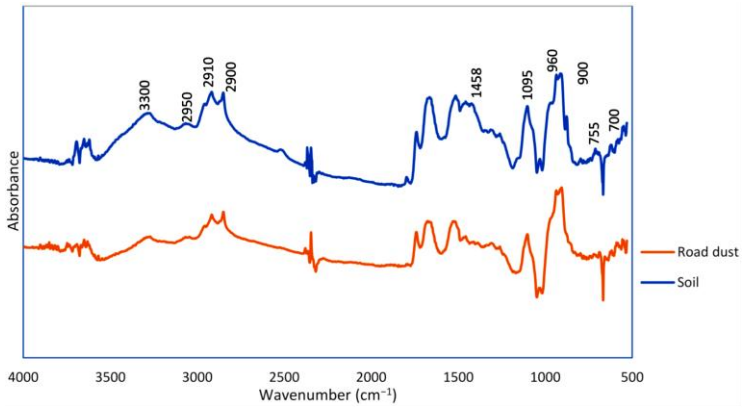

Figure 3. FTIR spectra of black fragments detected in soil and road dust samples [7].

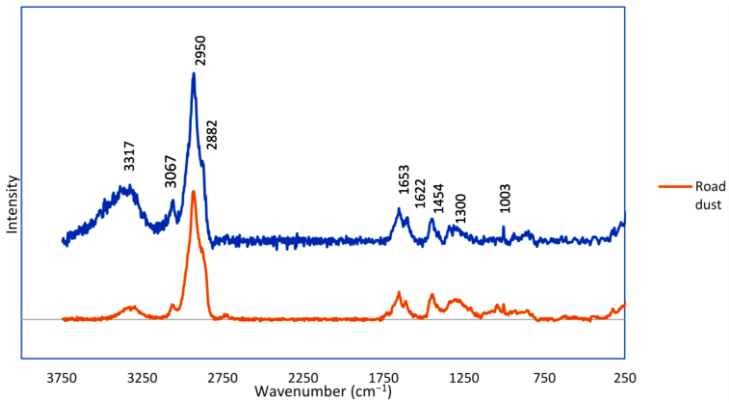

Figure 4. Typical Raman spectra of black fragments from soil and road dust samples [8].

Urban air pollution, particularly fine particulate matter ($PM_{2.5}$ and PM_{10}), poses health risks, including damage to the ocular surface.

The majority of particles belonged to the $PM_{2.5}$ fraction (1 – 2.5 μm), whereas PM_{10}-sized particles (2.5 – 10 μm) were less represented, and PM_1 particles (≤1 μm) were only occasionally observed, data are shown in Table 1. Morphometric descriptors calculated in ZEISS ZEN showed a broad variability in projected area and Feret diameters, with median (± SD) values across subjects of 3.2 ± 1.4 μm² for area, 1.4 ± 0.6 μm for minimum Feret diameter, and 2.3 ± 0.8 μm for maximum Feret diameter. Circularity values ranged from 0.55 to 0.95 (median = 0.78), indicating that most particles were moderately rounded, although some irregular and elongated shapes were also observed.

Table 1. Morphometric distribution of tear-borne particles detected by SEM.

Size Category	Mean Particle Count ± SD	Relative Proportion (%)
PM1 (≤1 μm)	2.7 ± 1.5	13%
PM2.5 (1–2.5 μm)	10.3 ± 4.2	52%
PM10 (2.5–10 μm)	7.0 ± 3.6	35%

Summary of the number and relative proportions of particles identified in tear samples from three individuals (n = 63 total particles; 14, 19, and 30 particles respectively per subject). Particles were classified according to their equivalent circle diameter (ECD) into three size categories: PM_1 (≤ 1 μm), $PM_{2.5}$ (1 – 2.5 μm), and PM_{10} (2.5 – 10 μm). Values are expressed as mean particle count ◎} standard deviation (SD) across the three subjects, together with their corresponding relative proportions (%).

Overall, these results indicate that the particulate matter recovered from the tear samples was predominantly composed of fine particles within the PM2.5 range, with variable

morphology and a limited presence of coarse (PM10) or ultrafine (PM1) fractions. In the Figure 5, a collection of representative images. Particles were identified as carbon rich aglo merates, metallic debris (primarily Fe, Si, and Al), and fibrous fragments, consistent with urban atmospheric particulate. In contrast, tears sampled from the washed control eyes showed no detectable particulate matter under the same conditions. [12]

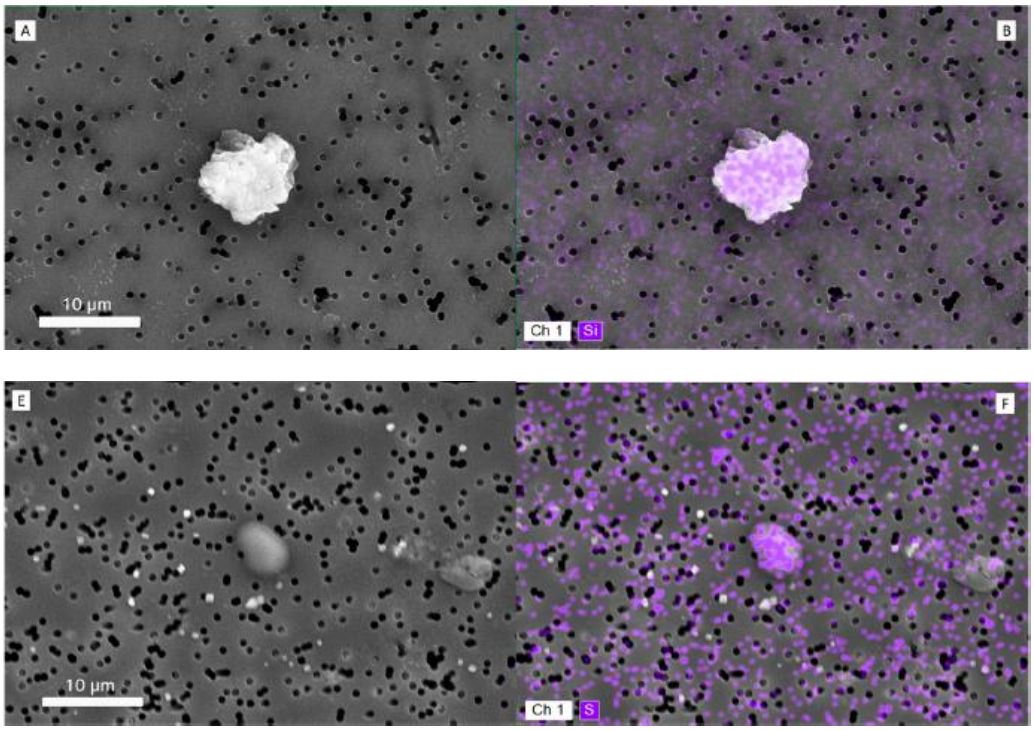

Figure 5. Representative images of particulate matters deposited onto filter and their characterization. (A) Scanning Electron Microscopy (SEM) image of a PM_{10} particle from a tear sample (subject #10). (B) Corresponding Energy-Dispersive X-ray Spectroscopy (EDS) elemental map showing a silica-based composition of the same particle. (E) SEM image of a PM_5 particle with sulphur-rich composition, typical of atmospheric particulate matter. (F) EDS elemental map of the particle in (E), confirming sulphur as the major constituent.

SEM analysis of tear samples revealed the consistent presence of airborne-like micro particles embedded within the tear matrix, contrasting with the absence of detectable material in rinsed control eyes. This observation suggests that the tear film is directly exposed to and capable of transiently retaining environmental particulate matter. These findings support the hypothesis that the tear film may function as a short-term reservoir for airborne particles, although further investigation is required to characterize deposition dynamics, residence time, and the correlation with ambient exposure levels.

Road dust loading is a road property which in general corresponds to a steady-state condition between a complex combination of production, loss and redistribution processes.

Production processes are mainly due to traffic intensity (i.e. wear and exhaust particle generation), atmospheric deposition, dust sources on the roadside, road shoulder, sanding/salting in countries with a lot of snowfall, the presence of additional fugitive sources (building and maintenance activities), and the deposition of pollen and other organic materials. Loss processes are mainly the resuspension itself – traffic or windinduced – drainage, and road cleaning. Redistribution processes are particle crushing, aggregating and migration. Most of the aforementioned processes are heavily affected by road surface conditions, such as age, state, composition, texture, porosity and moisture.

Road dust emissions also depend on the amount of material deposited on the road. An example of road emissions measurements in Bratislava is shown in Fig. 6, Fig. 7 and Fig. 8. The measurements were carried out in cooperation with TSI Aachen, Germany.

Figure 6. Bratislava cross-road.

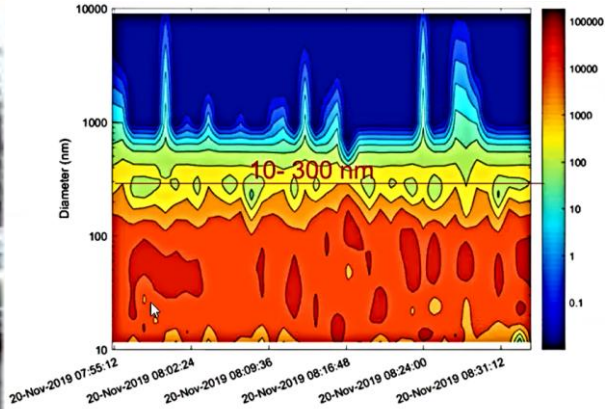

Figure 7. Measured UFP from cross-road.

4. Conclusions

The study analyzed environmental examples for the presence of micro particle fractions. A huge amount of black fragments (91% from soil and road dust) was found in all samples, both FTIR and Raman spectra confirm the presence of the most characteristic functional groups and additives used in tires. A higher amount of micro plastics particles were found in road dust samples than in soil. This may be due to the direct effect of braking, which causes a greater accumulation of samples at the emission source than over a short distance in soil. In the case of soils, the fraction below 50 μm is the most common. When analyzing road dust samples, it can be observed that most fractions are between 50 and 200 μm.

Moreover, it was difficult to analyze the smallest particles below 10 μm, which are the most harmful from a health perspective. The main problems of micro particle analysis include the lack of standardization and a reference unit of the results obtained, which would allow comparison of the obtained results between researchers.

Ocular surface alterations and conjunctival hyperemia were significantly associated with air pollution exposure, while subjective symptoms showed weaker trends. The detection of particulate matter in human tear fluid supports the use of the ocular surface as a sensitive, non-invasive tool for biomonitoring. These findings highlight its potential role in early warning systems for pollution-related health effects, with implications for public health surveillance and urban planning.

Acknowledgments: The contribution was prepared as a part of the grant project of the Ministry of Education of the Slovak Republic - UNIVNET No. 0201/0082/19 - University and Industrial Research and Education Platform of the Recycling Company and the grant project KEGA 032TUKE- 4/2025 Implementation of the results of scientific research activities into the processing of a modern university textbook "Solid aerosols - fine and ultrafine particles in the environment".

Conflicts of Interest: “The authors declare no conflict of interest. The funders had no role in the design of the study; in the collection, analyses, or interpretation of data; in the writing of the manuscript, or in the decision to publish the results”.

References

1. Worek, J, ; Badura, X. ; Białas, A. ; Chwiej, J., et al: Pollution from Transport: Detection of Tyre Particles in Environmental Samples, *Energies* 2022, 15 p.
2. Broekhuizen,P. ; Säämänen, ;Schuurbiers, D. ; Isigonis, P. ; Jensen, K., A., ; Kühnel, D. ; Le Blansch, K.: Tyre wear nanoparticles as test for a nano risk governance framework, *Environmental Science*, 10, 2022, pp. 1- 17

3. Starzomska,A.; Strużewska,J.: A six-year measurement-based analysis of traffic-related particulate matter pollution in urban areas: the case of Warsaw, Poland (2016-2021), *Archives of Environmental Protection*, Vol. 50 no. 2 pp. 75–84, PL ISSN 2083-4772,
4. Fussell,J.C.; Franklin,M. ; Green,D.C. ; Gustafsson,M. et al: A Review of Road Traffic-Derived Non-Exhaust Particles: Emissions, Physicochemical Characteristics, Health Risks, and Mitigation Measures, *Environ. Sci. Technol*. 2022, 56, pp. 6813−6835
5. Sabelström, H. ; Boberg, P.V. ; Engholm, H. ; Genberg Safont, J., G. ; Larsson, H, ; and Latvala, S.: Air & Environment, Arkitektkopia AB, Bromma, Schwede ,2023., pp.1-94, ISBN 978-91-620-1309-7.
6. Song, S,: Transport Emissions & Social Cost Assessment: Methodology Guide, WRI.org.,China, p. 110, ISBN 978-1-56973-908-2
7. Kole, J., P.; Löhr, A.J.; van Belleghem, F.G.A.J.; Ragas, A.M.J.Wear and Tear of Tyres: A Stealthy Source of Microplastics in the Environment. Int. J. Environ. Res. Public Health 2017, 14, 1265.
8. Grigoratos, T.; Brake, M., G. :Wear Particle Emissions: A Review. Environ. Sci. Pollut. Res. 2015, 22, pp. 2491–2504.
9. Eriksson, M.; Bergman, F.; Jacobson, S.: On the Nature of Tribological Contact in Automotive Brakes; Elsevier: Amsterdam, The Netherlands, 2002; Volume 252.
10. Sanders, P.G.; Xu, N.; Dalka, T.M.; Maricq, M.M. Airborne BrakeWear Debris: Size Distributions, Composition, and a Comparison of Dynamometer and Vehicle Tests. Environ. Sci. Technol. 2003, 37, pp. 4060–4069.
11. Zhang, M.; Hang Yin, H. ; Jianwei Tan, J. ; Xin Wang, X, ; Zhengjun Yang, Z, ; Hao, L. ; Du, T. ; Niu. ; Ge., Y: A comprehensive review of tyre wear particles: Formation, measurements, properties, and influencing factors Atmospheric Environment 297
12. Battistini ,R. ; ,Di Geronimo,N..; Porru,E. et al: Real-Life Assessment of Multi-Pollutant Exposure and Its Impact on the Ocular Surface: The Bike-Eye Pilot Study on Urban Cyclists in Bologna. *Environmental research and Public Health*, 22, 2025, pp.1-15.

TECHNICAL UNIVERSITY OF KOŠICE
Faculty of Mechanical Engineering

Experimental analysis of the influence of layer order in double-layer blanking of electrical steel sheets with variable strength properties

Martin Matej Benda [1,*], Emil Spišák [1], Peter Mulidrán [1]

[1] Technical University of Košice, Faculty of Mechanical Engineering, Košice, Slovakia
[*] Correspondence: martin.matej.benda@tuke.sk, Department of Mechanical Engineering Technologies and Materials, Technical University of Košice, Letná 9, 042 00 Košice, Slovakia

Abstract: Blanking of the double layer configuration is new innovation of the blanking process, whose purpose is to increase productivity of the production, especially for the rotor and stator iron core sheets. While this innovation doubles the productivity, quality of the produced blanks is worse than conventional blanking, which calls for research on optimization of the process. One of viable options is blanking of layers with different strength properties, specifically usage of same material for each layer but from opposite sides of tolerance field of its strength properties. Experiment follows this idea by conducting blanking operations in two of the possible layer configurations. After observation of the dishing deformation and sheared edge of the inner diameter on the samples, it was found out this innovation of the process may be beneficial, especially for configuration where the material with better strength properties is positioned as top layer and material with weaker strength properties is positioned as bottom layer. Biggest advantage was absence of deformation on the bottom layer that is normally observed on the plastic shear zone of samples produced by conventional double layer blanking which allows for production of more stable blanks.

Keywords: double-layer, blanking, punching, sheared edge, dishing

1. Introduction

Iron cores of the rotors and stators used as the drive units in the electrical vehicles are generally made by vertical stacking of great amounts of individual layers of electrical steel sheets [1]. These steel sheets can be produced by several technologies but based on the comprehensive research of Paltanea et. al., blanking is preferred method because of the required production volumes. This technology is capable of much higher production output, which is critical as it is a bottleneck of the electric motor production [2,3].

Even though the blanking technology provides the highest productivity, there are still limits to the output of a single press. To push these limitations, the double-layer configuration blanking was introduced. In this type of blanking there are two sheets of the material blanked at the single position with one stroke of the press. These steel sheets are placed on each other designated as the top layer and the bottom layer. For each of these layers the deformation induced by the blanking process is different from conventional process, and each of the deformations for the respective layers are different from each other. This is the result of partial replacement of the geometry of the tool in the process by the material itself. For the top layer, the die is replaced by the bottom layer and for the bottom layer, the punch is replaced by the top layer. These replacements are fluidly deforming during the process which means that the cutting forces are distributed differently. Deformation process of the double layer blanking simulated in Simufact Forming software can be seen in Figure 1 [4].

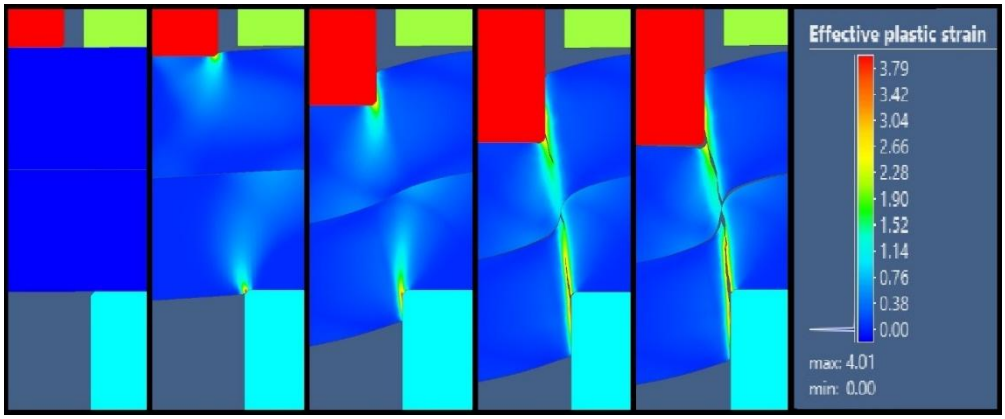

Figure 1. Double layer blanking process (contact with punch/elastic phase/plastic phase/fracture initiation/break) [4].

One of the possible optimizations of this process may be based on using materials with slight difference in the material properties for each respective layer.

2. Double-layer blanking of layers with variable strength properties

While the double-layer is based on blanking of two layers of steel sheets which are made of the same material, it is not a rule for them to have perfectly equal material properties. Material supplier can't make two batches of material with perfectly aligned properties, instead, the material is produced in certain tolerance ranges with nominal value and main strength properties which are measured after production and these parameters are included in the cover letter that the buyer receives with the material delivery.

Thanks to this there is possibility to choose two different batches of material produced with the strength properties from the opposite limits of the tolerance range and put them into the double-layer configuration.

Two possible variations of the configuration can be created:

- Stronger punch- Material from the upper limit of the strength tolerance range is placed in configuration as the top layer. Material from the bottom limit of the tolerance is placed as bottom layer.
- Stronger matrix- Material from the bottom limit of the strength tolerance range is placed in configuration as the top layer while the material from the upper limit of the tolerance is placed as bottom layer.

Position of the stronger material layer will influence the results of these experiments more because of its higher material strength and lower ductility. Variant where the stronger layer is positioned as the top layer should have:

- Smaller rollover zone thanks to the higher strength of the material which places resistance to deformation.
- Smaller plastic shear zone due to the decreased ductility.
- Higher fracture zone as the fracture will be initiated earlier because of the lower plasticity.

Variant where the stronger layer is placed as bottom layer is expected to have worse quality of the sheared edge, potentially, the dishing of the part may be lower in comparison because of the stronger layer acting partly as the counterpunch.

3. Materials and methods

3.1. Materials used in experiment

Two types of thin electrical steel sheets with 0.5 mm thickness were used in the experiment. Most important differences of these materials are their different mechanical properties. Material ,,H´´ is characterized by its high silicone content, high material

strength and low ductility. Material „S´´ is characterized by its lower silicone content, lower material strength but higher ductility.

Chemical composition of these materials is shown in Table 1 and Table 2. Mechanical properties were acquired by uniaxial tensile test on five samples per material on standardized specimens. Important mechanical properties in the rolling direction are shown in Table 3.

Table 1. Chemical composition of electrical steel sheet H (weight %).

Fe	C	Si	Mn	P	S	Cu	Al
94.13	< 0.002	2.806	0.267	0.038	< 0.002	0.037	2.422
Cr	Mo	Ni	V	Ti	Nb	Co	
0.027	0.069	0.035	0.019	0.004	0.048	0.099	

Table 2. Chemical composition of electrical steel sheet S (weight %).

Fe	C	Si	Mn	P	S	Cu	Al
98.29	< 0.002	0.744	0.329	0.071	0.004	0.036	0.182
Cr	Mo	Ni	V	Ti	Nb	Co	
0.033	0.037	0.034	0.012	< 0.002	0.031	0.086	

Table 3. Mechanical properties of electrical steel sheet S and H.

	$R_{p0.2}$ [MPa]	R_m [MPa]	A_g [%]	A_t [%]	A80 [%]
Material H	406 ±5.3	516 ±5.8	13.8 ±1.76	19.2 ±0.9	19.1 ±0.9
Material S	321 ± 2.5	434 ±2.6	23.4 ±3.3	35.6 ±0.5	35.6 ±0.5

3.2. Experimental setup and equipment

Experiment was conducted with the progressive experimental blanking tool. Diameters of the punches are Ø25.003 mm and Ø15.039 mm. Diameters of the dies were Ø25.013 mm and Ø15.049 mm. Shear gap of the tool was 0.01 mm and nominal blanked thickness t_n was 1 mm because each of the two layers is 0.5 mm. Simplified sketch of this experimental tool with the dimensions can be seen on Figure 2.

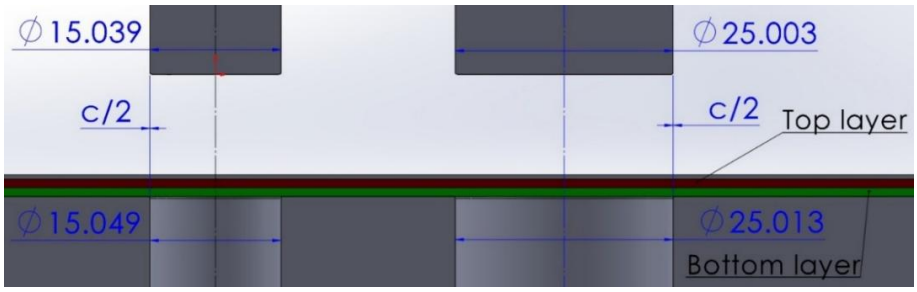

Figure 2. Layout of the double layer configuration (top layer is red and bottom layer is green).

Produced blanks are of the toroid shape as it is possible to use this shape in the Epstein Frame device for research into the influence of deformation on the electromagnetic properties of the blanks.

Hydraulic press with the nominal force of 200kN was used for this experiment.

Sheets were blanked in two configurations:

- Configuration A- Stronger material H was used as the top layer, while the weaker material S was used as the bottom layer.
- Configuration B- Weaker material S was used as the top layer while the stronger material H was used as the bottom layer.

4. Experiment results and analysis

Based on the previous methodology from the double layer blanking experiments [5], two main measurements were done on the blanks produced by current experiment:

1. Measurement of the dishing operation of the top and bottom layers.
2. Observation of the inner sheared edge produced by the punching operation under the microscope.

Observations and measurements were compared to the results of previous experiment where material S was used in both layers of the configuration.

4.1. Dishing deformation

Four types of blanks were produced by the experiment and each sample was measured at 4 points with the calibrated caliper. From these four measurements per blank average value was calculated. The deformation is equal to difference between the measurement and the nominal thickness value t_n of the metal sheet. Downside of this measurement is that its value can be influenced by the burr on the blanks. Measurements of the dishing along with measurements from previous experiment with layers of same material properties are in Table 4.

Table 4. Dishing values of samples.

Configuration	Layer	Average measurement (mm)	Dishing increment t_i (mm)	Layer dishing deviation (mm)
S+S	Top = S	1.26 ±0.04	0.76	0.04
	Bottom - S	1.22 ±0.02	0.72	
S+H	Top = S	1.62 ±0.05	1.12	0.29
	Bottom = H	1.33 ±0.04	0.83	
H+S	Top = H	1.24 ±0.04	0.74	0.07
	Bottom = S	1.31 ±0.03	0.81	

Measurements have shown less dishing deformation for the configuration where top layer consists of material with higher strength and bottom layer with lower strength in comparison to the opposite configuration. Even though this configuration was superior, it still had slightly bigger dishing than the configuration consisting of both layers with weaker strength material properties.

4.2. Sheared edge

Inner sheared edge of the blanks produced by the punching operation were observed under the Keyence microscope after they were cast in resin and ground to the middle.

Results of previous experiment of configuration S+S where both layers have same strength properties is on Figure 3 and Figure 4. Material of these layers have lower mechanical strength properties in comparison to material H [5].

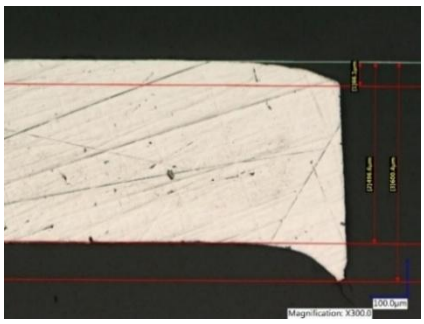

Figure 3. Top layer S+S configuration [5].

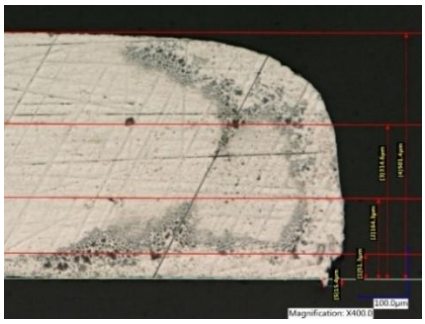

Figure 4. Bottom layer S+S configuration [5].

While the top layer has a big burr, it has small rollover area and big ration of plastic shear zone. Bottom layer has minimal burr but the rollover zone takes big parts of the shear edge at the expense of the plastic shear zone [5].

Sheared edge of blanks produced from S+H configuration where material with lower material strength is positioned as top layer can be seen on Figure 5. Material with higher strength positioned as bottom layer can be seen on Figure 6.

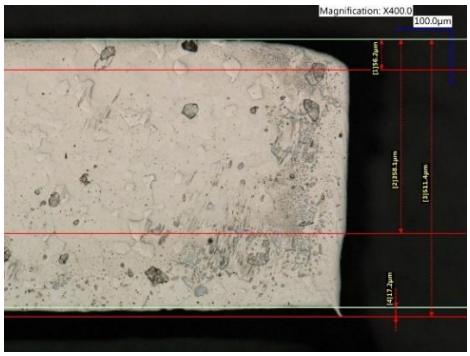

Figure 5. Top layer S.

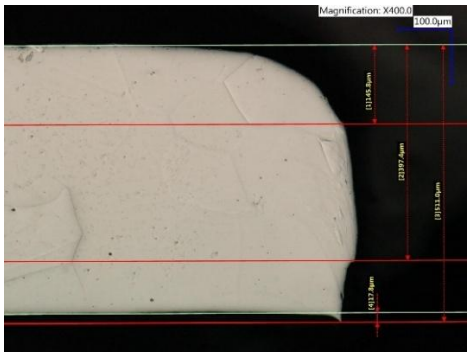

Figure 6. Bottom layer H.

Top layer was material of the weaker material strength and the quality of its shear edge is good. Rollover area is small, zone of the plastic shear is 60.38% and the burr is small.

Bottom layer was material with the higher material strength and the quality is worse than the top layer, its shape is similar to the double layer blanking with configuration of both layers with same strength properties. Rollover area and its radius is big, plastic shear zone is lower, 50.32% and the burr is small.

Sheared edge of blanks produced from H+S configuration, where the top layer is material H with higher strength properties can be seen on Figure 7, and sheared edge of material S with lower strength properties can be seen on Figure 8.

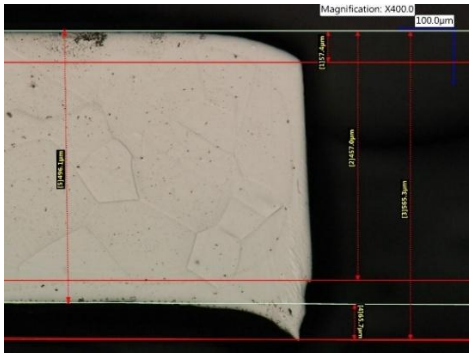

Figure 7. Top layer H.

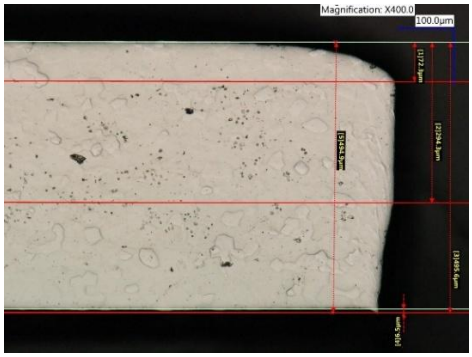

Figure 8. Bottom layer S.

Top layer was material H which has better material strength and it produced sheared edge of a good quality like the sheared edge produced by blanking of the two layers with same material strength. Rollover is small, plastic shear zone is biggest of the samples as it is 79.92% of the nominal thickness value. Burr is big because the material was bend over the bottom layer.

Bottom layer was material with lower material strength and its sheared edge is of good quality. Rollover is small and its plastic shear zone is straight but short as it makes just 44.4% of the nominal thickness of material. Fracture zone is bigger, 38.96% of the nominal thickness of the material. Bottom layer sample had nearly non-existent burr.

Values of the measured rollover area, plastic shear zone, breakage zone and the burr along with percentage calculated based on the nominal thickness of the material which was 0.5mm, can be seen in table 5. Values for the configuration of layers with same material properties were used from the previous experiment and article.

Table 5. The proportion of the individual shear-edge zones and their percentage shares [5].

Configuration	S+S				S+H				H+S			
Layer	Top S		Bottom S		Top S		Bottom H		Top H		Bottom S	
Unit	(μm)	(%)	(μm)	(%)	(μm)	(%)	(μm)	(%)	(μm)	(%)	(μm)	(%)
Rollover	66.1	13.22	186.8	37.36	56.2	11.24	145.8	29.16	57.4	11.48	72.3	14.46
Plastic zone	430.5	86.1	263.3	52.66	301.9	60.38	251.6	50.32	399.6	79.92	222	44.4
Breakage zone	17.1	3.4	66.7	13.34	136.1	27.22	95.8	19.16	108.3	21.66	194.8	38.96
Burr	37.7	7.54	15.4	3.08	17.2	3.44	17.8	3.56	65.7	13.14	6.5	1.3
Edge lenght	600.4	120.1	516.8	103.4	511.4	102.3	511	102.2	565.3	103.4	495.6	99.1
Rollover Radius	667.3		390.8		223		225.4		356.8		405.5	

5. Conclusions

After carefully examining the data regarding the dishing, results geometry and dimensions of the inner sheared edge produced by the punch, we came to the following conclusions:

- Dishing
    - Deformation, which we predicted better in the case of the configuration where the stronger material would be used as the lower layer was worst of the three observed options. Top layer experienced much higher dishing, and dishing deviation between the layers was nearly 0.3mm.
    - Dishing of the configuration where the stronger material acted as the top layer was nearly as good as the dishing observed on the configuration with both layers of same strength parameters, with the dishing deviation just 0.07mm.
- Shape of the sheared zone was different for each option. When compared to the conventional double layer blanking, each of the configurations had its own improvements.
    - Configuration with the weaker material in the place of the top layer had its burr greatly reduced. Plastic deformation zone was decreased while the breakage zone increased. Bottom layer stayed similar with biggest difference in the breakage zone which saw 15% increase.
    - Configuration with the stronger material in the place of the top layer had slightly reduced quality because of the smaller zone of the plastic shear and increased zone of breakage. This is probably result of the decreased ductility between the materials compared. Bottom layer saw the biggest improvement as it was not deformed like the bottom layer of the conventional double layer blanking. Its shape was like the shape of the top layer with just slightly worse quality regarding the zones. When compared to each other, rollover zone difference was just 3%, plastic deformation zone had a bigger difference of 35%. Breakage zone was larger by 17% and the bottom layer had no burr.

Configuration where stronger material is used as top layer and weaker material as the bottom layer proven itself to be superior to the configuration where weaker material is used as the top layer and stronger material as the bottom layer.

To confirm success of this innovation, more experiments need to be conducted, specifically experiments where layers would consists of the same material but from opposite tolerance ranges for the strength properties of the material.

Acknowledgments: Funded by the EU NextGenerationEU through the Recovery and Resilience Plan for Slovakia under the project No. 09I03-03-V05-00015. This work was supported by the project APVV-21-0418.

Conflicts of Interest: The authors declare no conflict of interest.

References

1. Xia C., Wang H., Wu Y., Wang H., 2020. "Joining of the Laminated Electrical Steels in Motor Manufacturing: A Review. " Materials. Vol. 13, no.20.
2. Paltanea G., Manescu V., Antonia A., Nemoianu I. V., Gavrila H. 2024. "Mechanical and Magnetic Properties in Non-Oriented Electrical Steels with Different Cutting Technology: A Review. " Materials. Vol. 17, no. 6.
3. Mahmouditabar, F., Baker, N., 2023. "A review on the effect of electrical steel manufacturing processes on the performance of electric machines. " Energies. Vol. 16, page 24.
4. Benda M.M., Spišák E., 2025. "Experimental analysis of blanking technology for electrical steel in double layer configuration. " In: Novus Scientia 2025 : Zborník príspevkov z 22. Medzinárodnej vedeckej konferencie doktorandov strojníckych fakúlt technických univerzít a vysokých škôl. - Košice (Slovensko) : Technická univerzita v Košiciach s. 21-26 [online, print]. - ISBN 978-80-553-4828-5.
5. Benda, M.M., Spišák, E., Mulidrán, P., & Kaščák, Ľ. (2025). "Influence of Double Layer Configuration on the Quality of the Sheared Edge of Blanks Produced from Soft Electrical Steel. " *Acta Mechanica Slovaca*, *29*(3), 42-47. doi: 10.21496/ams.2025.024

TECHNICAL UNIVERSITY OF KOŠICE
Faculty of Mechanical Engineering

Patient-Specific Surgical Guide for Ulna Reconstruction Using CT-Based Digital Planning and Additive Manufacturing

Peter Böszörményi [1,*], Marek Schnitzer, Radovan Hudák [1], Jozef Živčák [2] and Tomáš Ševčík [3]

[1] Biomedical Engineering s.r.o./Technical University of Košice, Faculty of mechanical Engineering
[2] Technical university of Košice, Faculty of mechanical Engineering
[3] AGEL University Hospital, Clinic of Musculoskeletal and Sports Medicine
* Correspondence: peter.boszormenyi@student.tuke.sk

Abstract: Post-traumatic deformities of the ulnar diaphysis represent a challenging clinical condition, particularly when precise correction of bone alignment is required. Conventional surgical techniques rely largely on intraoperative estimation, which may lead to limited accuracy and variability in outcomes. This contribution presents a patient-specific digital workflow combining computed tomography imaging, three-dimensional modelling, computer-aided design, and additive manufacturing for corrective osteotomy of the ulnar shaft. Virtual planning was based on mirrored contralateral anatomy and enabled accurate definition of the osteotomy plane and correction parameters. A patient-specific surgical guide was designed and manufactured to ensure precise intraoperative transfer of the virtual plan. The osteotomy was stabilized using a standard straight fixation plate for the ulna. The presented workflow enabled accurate execution of the planned correction and restoration of anatomical alignment. The results demonstrate the potential of patient-specific surgical guides to improve precision and reproducibility in corrective ulnar osteotomy.

Keywords: patient-specific surgical guide; ulnar diaphysis; corrective osteotomy; additive manufacturing; biomedical engineering

1. Introduction

Deformities of the ulnar diaphysis resulting from trauma, malunion, or growth disturbances can significantly impair forearm function and biomechanics. Inaccurate alignment of the ulna may affect load transmission, forearm rotation, and the stability of the distal radioulnar joint. Corrective osteotomy remains the treatment of choice in symptomatic cases; however, achieving precise correction using conventional techniques can be technically demanding. [3]

Traditional osteotomy planning is often performed intraoperatively, relying on two-dimensional imaging and surgical experience. This approach may lead to variability in correction accuracy, prolonged operative time, and suboptimal anatomical restoration. Advances in medical imaging, three-dimensional modelling, and additive manufacturing have enabled the development of patient-specific solutions that support detailed preoperative planning and accurate intraoperative execution. [1, 2, 4, 7]

Patient-specific surgical guides have emerged as a promising tool for improving the precision of corrective osteotomies. By transferring the virtual surgical plan directly to the operative field, these guides can reduce intraoperative uncertainty and enhance reproducibility. The aim of this contribution is to present a technical case study describing the application of a patient-specific surgical guide for corrective osteotomy of the ulnar diaphysis using a CT-based digital workflow. [1, 3]

2. Materials and Methods

Computed tomography imaging of both forearms was performed using a high-resolution clinical CT scanner with thin-slice acquisition to ensure accurate visualization of cortical and trabecular bone structures. DICOM datasets were imported into medical image processing software, where segmentation of the affected ulna and the contralateral healthy ulna was performed. The healthy ulna was mirrored along the sagittal plane and registered to the affected bone to identify angular deviation, rotational malalignment, and longitudinal discrepancies.

Virtual surgical planning was carried out based on comparison with the mirrored contralateral anatomy. The optimal osteotomy plane and correction parameters were defined to restore the anatomical axis and length of the ulnar diaphysis. A patient-specific surgical guide was subsequently designed to fit the surface geometry of the ulna and to guide the osteotomy according to the virtual plan.

The surgical guide was manufactured using additive manufacturing technology Selective laser sintering from a medical-grade polymer Polyamide PA2200 suitable for sterilization. The entire process of preparation, design, manufacturing, and clinical application of the patient-specific guide was reviewed and approved by the institutional Ethics Committee. The committee evaluated the technological workflow, potential surgical risks, and procedures ensuring adequate patient information. Written informed consent was obtained from the patient, and anonymized clinical and imaging data were used for research and publication purposes in compliance with the General Data Protection Regulation.

The corrective osteotomy was performed using the patient-specific guide to ensure accurate execution of the planned cut. Fixation was achieved using a standard straight osteosynthetic plate designed for ulnar shaft stabilization.

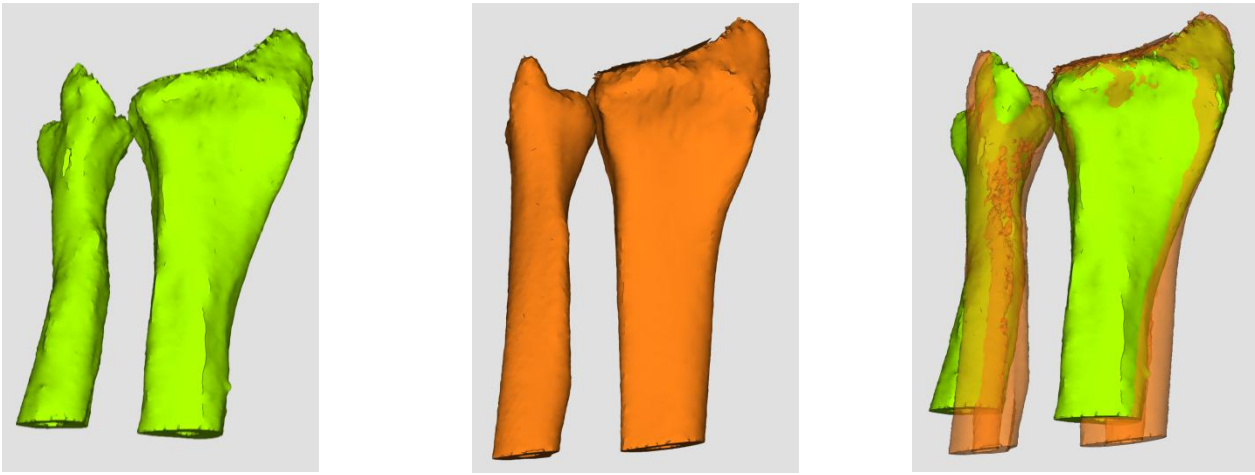

(**a**) (**b**) (**c**)

Figure 1. (**a**) Three-dimensional CT-based surface model of the affected ulna and radius showing post-traumatic deformity of the ulnar diaphysis. (**b**) Three-dimensional CT-based surface model of the contralateral healthy ulna and radius used as a reference for anatomical comparison and virtual planning. (**c**) Three-dimensional overlay of the affected ulna and radius with the mirrored contralateral healthy models, illustrating anatomical deviations and serving as a basis for virtual planning of corrective osteotomy.

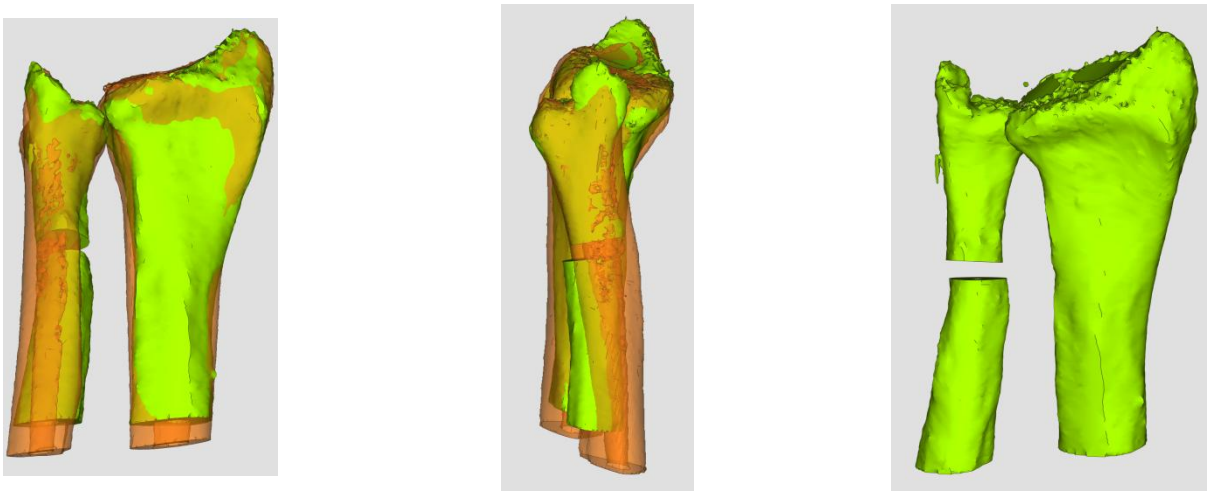

(**a**) (**b**) (**c**)

Figure 2. (**a**) Three-dimensional overlay illustrating repositioning of the resected proximal ulnar segment according to the mirrored contralateral healthy anatomy. (**b**) Three-dimensional overlay illustrating repositioning of the resected proximal ulnar segment according to the mirrored contralateral healthy anatomy from side view. (**c**) Three-dimensional model of the ulna after virtual osteotomy, demonstrating separation of bone segments and simulated anatomical correction.

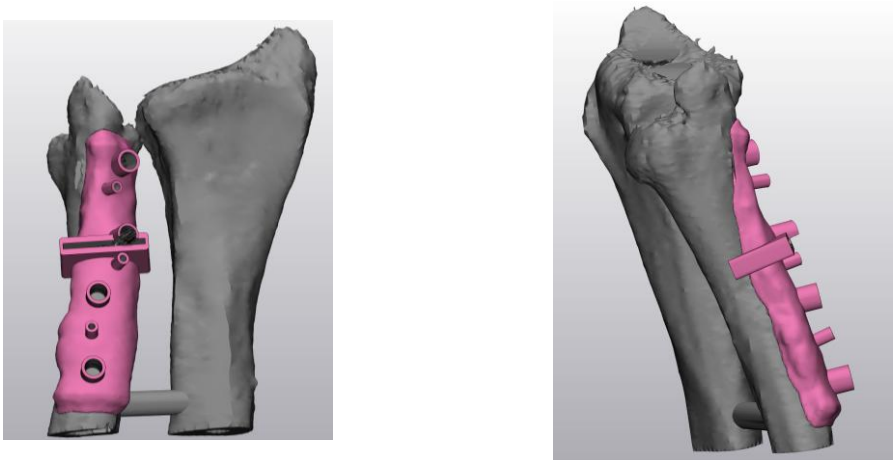

(**a**) (**b**)

Figure 3. (**a**) Three-dimensional visualization of the patient-specific surgical guide positioned on the ulnar diaphysis, demonstrating its fit and alignment relative to the planned osteotomy site. (**b**) Three-dimensional visualization of the patient-specific surgical guide from side view.

3. Results

3.1. Anatomical Reconstruction and Virtual Planning Accuracy

CT-based segmentation and three-dimensional reconstruction enabled precise visualization of the ulnar diaphyseal deformity. Comparison with the mirrored contralateral ulna allowed accurate identification of angular and rotational deviations. Virtual correction resulted in restoration of the anatomical axis and length of the ulna with minimal deviation from the reference anatomy.

3.2. Surgical Guide Performance and Osteotomy Execution

The patient-specific surgical guide demonstrated stable and reproducible positioning on the ulnar surface. Its geometry ensured accurate transfer of the planned osteotomy plane to the surgical field. The guide enabled controlled execution of the osteotomy according to the predefined correction parameters and minimized intraoperative variability.

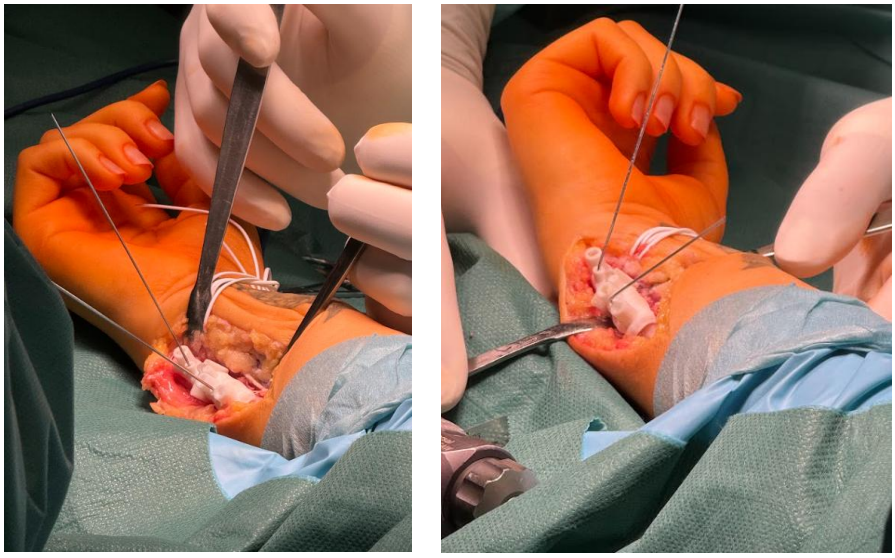

(**a**) (**b**)

Figure 4. (**a**) Intraoperative view demonstrating placement and fixation of the patient-specific surgical guide on the ulnar diaphysis prior to osteotomy.; (**b**) Intraoperative visualization of the guided osteotomy being performed through the patient-specific surgical guide to ensure accurate execution of the planned bone cut.

3.3. Fixation and Early Clinical Outcome

The corrected ulnar segment was successfully stabilized using a standard straight fixation plate. Postoperative imaging confirmed satisfactory alignment of the ulnar diaphysis and correct positioning of the fixation hardware. No intraoperative or early postoperative complications related to guide usage or fixation stability were observed. The achieved correction created favorable conditions for subsequent rehabilitation and functional recovery.

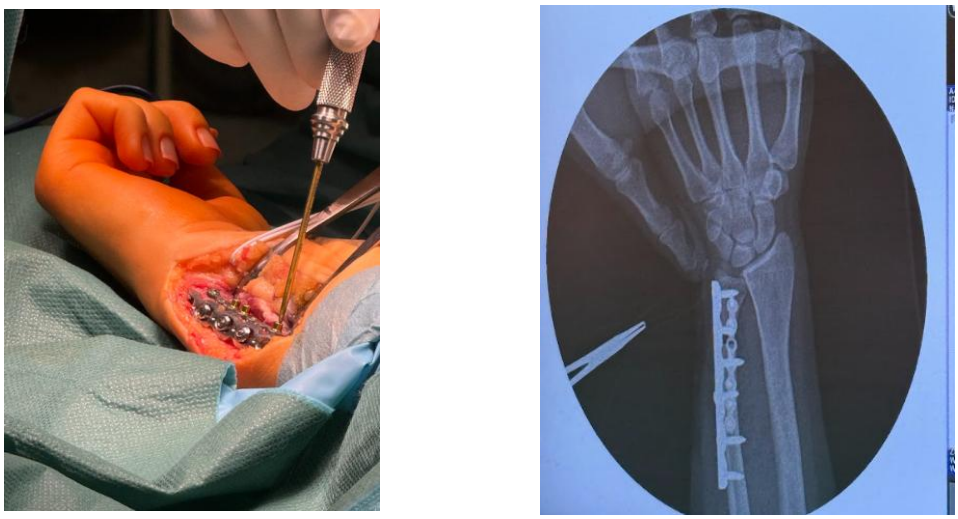

(**a**) (**b**)

Figure 5. (**a**) Intraoperative view demonstrating definitive fixation of the corrected ulnar diaphysis with a standard straight plate following guided osteotomy; (**b**) Postoperative radiographic image confirming correct alignment of the ulnar diaphysis and stable fixation using a standard straight osteosynthetic plate.

4. Discussion

The presented case study demonstrates the feasibility of integrating digital surgical planning with additive manufacturing for the correction of post-traumatic ulnar deformities. The use of CT-based three-dimensional modelling enabled accurate visualization of the deformity and allowed the creation of a mirrored anatomical reference from the contralateral forearm. [3, 5]

Patient-specific surgical guides provide a reliable method for transferring the virtual surgical plan into the operating room. Compared to conventional freehand osteotomy techniques, this approach reduces the reliance on intraoperative estimation and may improve the precision and reproducibility of the procedure.[4, 6]

In addition, the integration of digital planning tools and additive manufacturing technologies represents an important step toward personalized orthopaedic surgery. Such workflows allow surgeons to better understand complex anatomical deformities and to plan corrective procedures more precisely.

Future research should focus on evaluating the clinical outcomes and surgical accuracy of patient-specific guides in larger patient cohorts and across different anatomical regions.

Despite the promising results, several limitations of this study should be acknowledged. First, the presented work represents a single-patient case study, which limits the generalizability of the findings. Further validation on a larger cohort of patients would be necessary to statistically confirm the clinical benefits of patient-specific surgical guides for corrective osteotomy of the ulna.

Another limitation is the dependence of the workflow on high-quality CT imaging and precise segmentation, which may influence the accuracy of the resulting 3D models and surgical guides. Additionally, the process requires access to specialized software and additive manufacturing technologies, which may not yet be routinely available in all clinical environments.

5. Conclusions

Patient-specific surgical guides represent an effective tool for improving the precision of corrective osteotomy of the ulnar diaphysis. The integration of biomedical engineering methods, virtual planning, and additive manufacturing enables accurate transfer of the surgical plan into clinical practice. The presented workflow supports the broader adoption of personalized solutions in orthopedic surgery.

Acknowledgments: This work was supported by the KEGA project No. 012UPJŠ-4/2023, implemented within the framework of the Technical University of Košice. The authors would like to acknowledge Biomedical Engineering for providing certified medical manufacturing of the patient-specific surgical guide. Clinical testing and evaluation were conducted in cooperation with the Technical University of Košice.

Conflicts of Interest: The authors declare no conflicts of interest related to this work.

References

1. WONG, Kwok Chuen. 3D-printed patient-specific applications in orthopedics. Orthopedic Research and Reviews. 2016, 8, 57–66. DOI: 10.2147/ORR.S99614
2. MARTELLI, Nicolas; SERRANO, Carole; VAN DEN BRINK, Hélène; et al. Advantages and disadvantages of 3-dimensional printing in surgery: A systematic review. Surgery. 2016, 159(6), 1485–1500. DOI: 10.1016/j.surg.2015.12.017.
3. KUNZ, Manuela; MA, Burton; RUDAN, John F.; ELLIS, Randy E.; PICHORA, David R. Image-guided ulna osteotomy using patient-specific instrument guides. The Journal of Hand Surgery (American Volume). 2013, 38(8), 1618–1624. DOI: 10.1016/j.jhsa.2013.05.018.
4. MITSOURAS, Dimitrios; LI, Adam C.; IGLIORE, Adam B.; et al. Medical 3D printing for the radiologist. Radiographics. 2015, 35(7), 1965–1988. DOI: 10.1148/rg.2015140320.

5. YANG, Li; SHANG, Xiao-Wei; FAN, Jia-Nan; et al. Application of 3D printing in the surgical planning of orthopedic surgery: A review. Journal of Orthopaedic Surgery and Research. 2017, 12(1), 1–8. DOI: 10.1186/s13018-017-0614-3.
6. MATSUMOTO, Justin S.; MORRIS, Jeremy M.; ROHREN, Edward M.; et al. Three-dimensional physical modeling: Applications and experience at Mayo Clinic. Radiographics. 2015, 35(7), 1989–2006. DOI: 10.1148/rg.2015140325.
7. TACK, Pieter; VICTOR, Jan; GEMMEL, Filip; ANNEMANS, Lieven. 3D-printing techniques in a medical setting: A systematic literature review. BioMedical Engineering OnLine. 2016, 15(1), 115. DOI: 10.1186/s12938-016-0236-4.

TECHNICAL UNIVERSITY OF KOŠICE
Faculty of Mechanical Engineering

Design of educational tool for PID motor control

Leo Brada [1,*], Ľubica Miková [1] and Erik Prada [1]

[1] Technical University of Košice, Faculty of Mechanical Engineering, Department of Industrial Automation and Mechatronics, Park Komenského 8, 042 00 Košice; leo.brada@tuke.sk; lubica.mikova@tuke.sk; erik.prada@tuke.sk
* Correspondence: leo.brada@tuke.sk

Abstract: The article presents the design and experimental evaluation of a low-cost educational tool for teaching PID control using a real-world mechatronic system. The proposed platform is based on a DC motor with an integrated encoder, controlled by an Arduino Uno microcontroller and an H-bridge driver. The system enables real-time monitoring and visualization of motor speed and controller behavior using the Arduino IDE Serial Monitor and Serial Plotter. A PI controller was implemented and experimentally evaluated under different operating conditions, including variable load scenarios. The results demonstrate stable and accurate speed regulation with little deviation. Due to its simple design, low cost, and use of widely available components, the developed tool effectively bridges the gap between theoretical control concepts and practical implementation, making it well-suited for control systems.

Keywords: PID control; DC motor control; Arduino; educational tool.

1. Introduction

As industry and technology advance, the demand for engineers and technicians who master complex electromechanical systems rises. One of the great challenges of mechanical engineering education is bridging the gap between theoretical concepts and real-world implementations. Control theory and the modeling of mechatronic systems are essential concepts in mechanical engineering, forming the foundation for a wide range of applications, from robotics and automation to power electronics and the automotive industry. Feedback mechanisms, such as encoders, are necessary to make a dynamic system that behaves in a desired way. The use of the Proportional–Integral–Derivative (PID) controller is the dominant method used for control theory because of its simplicity, robustness, and effectiveness. The PID controller continuously adjusts the input to a system based on the error between the desired output and the actual output. To achieve stable and accurate control, the combination of present (proportional K_p), accumulated past (integral K_i), and predictive future (derivative K_d) weighted errors is used [1, 11].

$$C_{(s)} = K_p + K_i \frac{1}{s} + K_d s \tag{1}$$

Despite its simplicity, the effectiveness of a PID controller in practice depends highly on proper tuning of its parameters. This fact is a double-edged sword because in the university scenario, it is very simple to modify the gains of the PID controller to achieve different results. But in real-world scenarios, it is crucial to calculate and precisely set the gains to get optimal results. This tuning is carried out by using optimization-based approaches, for example, the pole placement method, Ziegler and Nichols, and Naslin's method [2]. The pole placement method is a model-based method in which closed-loop poles are assigned to achieve a specific dynamic response. The location of the poles determines stability, settling time, damping, and oscillatory behavior. Selecting them allows shaping the system's performance with high precision. Desired pole positions are defined

based on performance requirements. Then, the formulation of the closed-loop characteristic equation combined with the PID controller is performed. By equating this equation with the characteristic polynomial, the PID parameters are calculated [3]. Naslin's method is a heuristic tuning technique for calculating PID parameters on the desired closed-loop dynamic behavior of a system. It is based on the assumption that the target characteristic polynomial has coefficients that follow a predefined ratio, ensuring a stable system response. The maximum allowable overshoot is selected, corresponding to a constant αused in subsequent calculations [4]. Lastly Ziegler-Nichols method is based on manual modification of proportional gain until the system reaches sustained oscillations, from which the ultimate gain and oscillation period are measured. These values are then used in predefined formulas to calculate PID gains. The main advantage of using this method is that it doesn't require an accurate mathematical model of the system but it can often lead to aggressive tuning with significant overshoot [5].

Traditional methods relying on written calculations can be abstract for students who lack hands-on experimentation and direct observation. Using simulation software such as MATLAB [12] is a great improvement because changes in the PID controller are instantaneously visible, and modification of parameters is straightforward. The problem of abstractness arises because students don't see real systems, but only the mathematical expression of the system. For this reason, a physical tool would be a great addition to the educational process because students could get a hands-on experience with the mechanical system and its control [6]. Simplicity of design and low cost were essential to ensure easy replication. Controlling the speed and position of a DC motor is one of the most common methods for teaching PID control using real-world systems.

2. Methodology

To achieve a simple, effective, and low-cost solution, the components were selected based on their suitability for the application and availability. The DC motors chosen were Rk-370CA-18260 from the company Mabuchi Motor. The parameters of the motor, based on its datasheet [8], are:

- Operating voltage: 12 V;
- Max torque: 3,52 mNm;
- Speed under load: 8500 RPM;
- Output under load: 2.35W.

The motors were chosen based on the encoders on the units, their availability during the project's development, and their suitable parameters. The selected components were first individually tested to verify their functionality, then connected into a circuit to confirm proper communication and overall system operation. The motors, along with their encoders, are connected to the Arduino Uno platform. This platform was chosen as the best-suited due to its ease of use and robustness [7]. The circuit was designed in Fritzing [9] as shown in Figure 1. The Rk-370CA-18260 motors are controlled using the H-bridge, specifically the L298N model. L298N was selected because it can control two motors independently and protects a low-power Arduino controller from high load on pins and EMF (electromagnetic force) voltage spikes. The H-bridge requires a separate power supply that is adjustable. The power supply chosen was Diametral R124R50E. The Arduino remains connected to the PC continuously to display the specified values as graphs. Buttons were added to the system to allow dynamic, separate speed adjustments for both motors. PWM (Pulse Width Modulation) is used to control motor speed. The first motor is operated with three buttons that set fixed PWM levels of 0, 50, and 100. The second motor is controlled by two buttons that increase or decrease the PWM value by 1. The first motor operates at fixed setpoints for PID speed control testing, while the second motor serves as a variable load. The wiring diagram is shown in Figure 1.

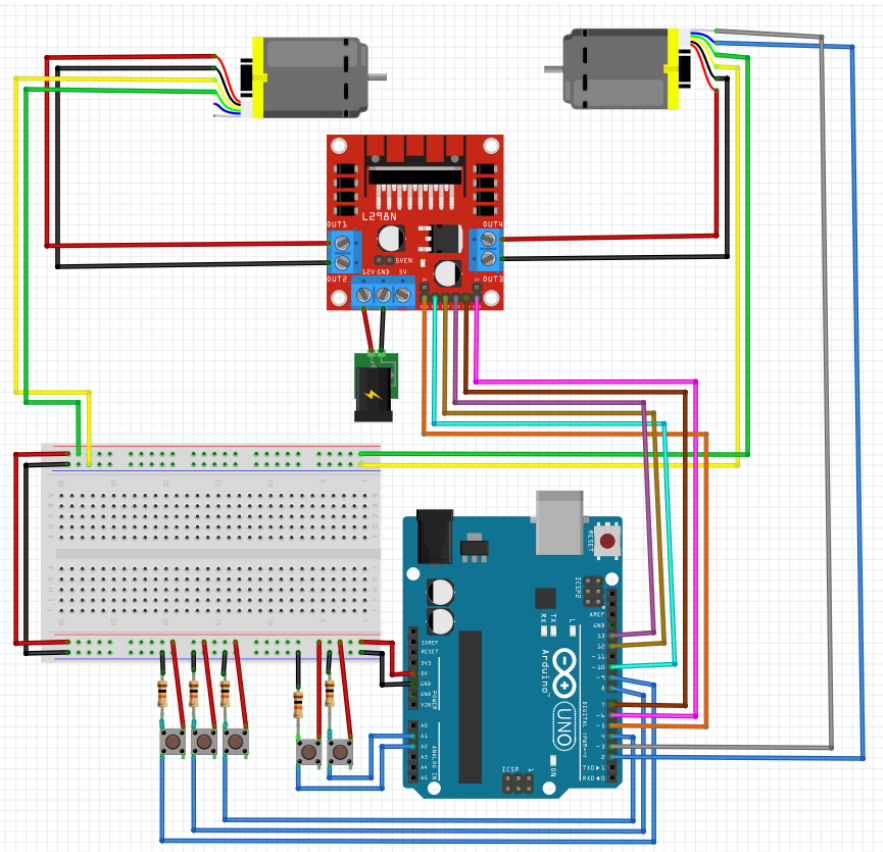

Figure 1. Wiring diagram of the educational tool.

The educational tool was programmed using Arduino IDE. The sequence of operations within the program is presented in the accompanying scheme in Figure 2. The program begins by setting the initial parameters, defining which Arduino pins will function as inputs and which as outputs. Then the system reads the input value of the buttons controlling the speed of the motors. After the input reading, the velocity of the main motor is computed with the encoder data and filtered with a noise filter. A low-pass filter with a passband of 25 Hz was selected. The mathematical notation of the filter is:

$$v_f = 0.854 * v_{fp} + 0.0728 * v + 0.0728 * v_p, \quad (2)$$

where v_f is the filtered angular velocity value, v_{fp} is the previous angular velocity filtered value, v is the velocity value without filtering, and v_p is the previous velocity value without filtering [10].

Smoothed out velocity measurement was then used to calculate the PID controller. For this tool, only the proportional and integral control was implemented. The output of the calculation is then used to control the motor speed. Lastly, the current and desired speeds of the first motor are plotted in the Serial Plotter, along with the current speed of the second motor.

Regarding data processing and sampling, the control loop operates with a dynamic sampling period calculated using the micros() function. The elapsed time is measured between consecutive speed calculations to ensure the velocity estimation remains accurate despite variations in execution time. The typical sampling frequency observed during operation is approximately 150–200 Hz, which is well above the Nyquist frequency required for the motor's mechanical time constant. The velocity was calculated by monitoring the change in encoder pulses relative to elapsed time.

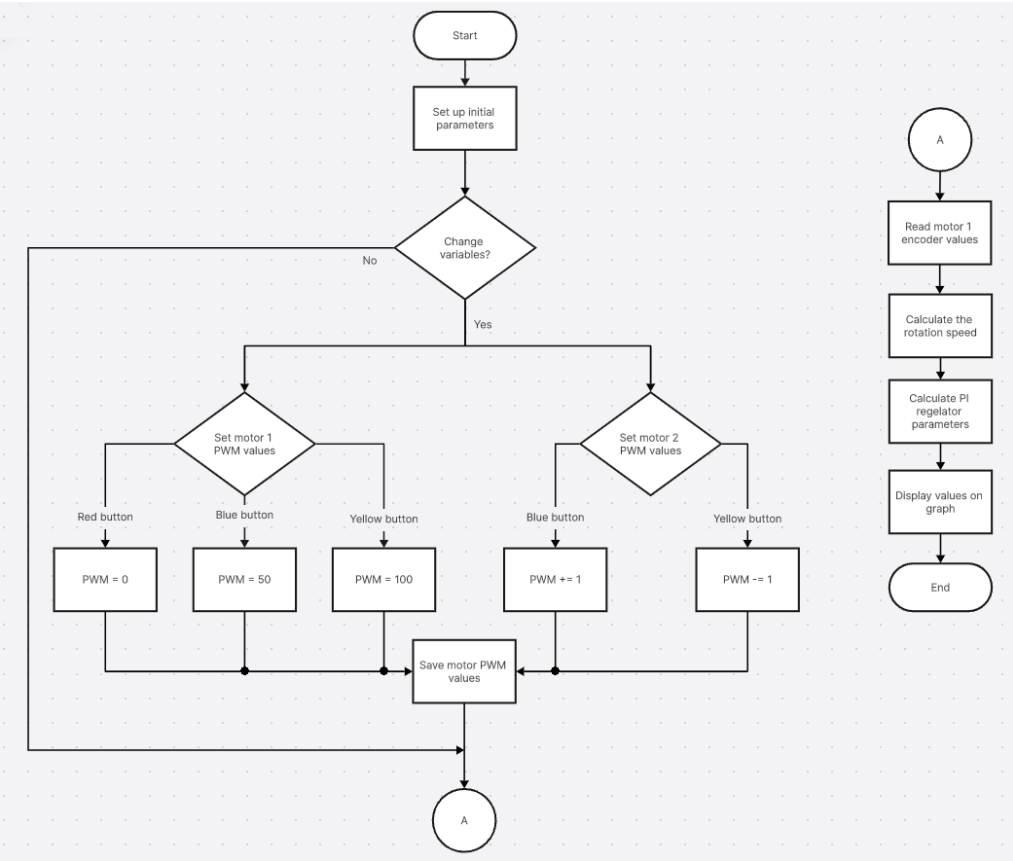

Figure 2. Flowchart of the educational tool control algorithm.

All components were housed in a plastic junction box for easier manipulation and overall compactness. The junction box was chosen because it was easy to mount motors on it, as it is made of plastic and has drill holes in it for the connection of components. The motors are mounted on top of the container using custom 3D-printed brackets. The motors face each other and are connected with a flexible coupler. In addition to the motors, two banana sockets are included to allow them to be powered externally using an adjustable power supply. During testing, two additional banana sockets were added for the motor encoder, but they are not necessary because the encoders are connected directly to the Arduino board. The control buttons for the motors are located on the front side of the container. They are also placed in 3D-printed sockets. On the back side of the container, there is a visible Arduino Uno power connector.

Figure 3. Complete educational tool.

3. Results

The performance of the educational system was evaluated through real-time monitoring and analysis using Arduino IDE Serial Monitor and Serial Plotter. These tools enabled continuous observation of the motor speed response, controller behavior, and system stability during operation. For the experimental evaluation, the PID controller was configured as a PI regulator, with the proportional gain set to $K_p = 5$ and the integral gain set to $K_i = 10$. These values were selected to achieve a balance between response speed and stability. There were two reasons for choosing to leave out the derivative gain. First, when regulating motor speed, the system can be characterized as a first-order system, which is inherently stable and thus well-suited for PI control without the need for additional damping. Second, derivative gain has the potential to amplify high-frequency artifacts from encoders. Since the system already utilizes a low-pass filter, the lag introduced by this filtering negates the benefits of the derivative gain and introduces unstable PWM output.

The results show that the regulated speed of the primary DC motor closely followed the desired setpoint. The measured motor speed remained ±0.13 RPM while the desired setpoint was set to 100 RPM. When set to 50 RPM, the measured speed is ± 1 RPM. When the load motor operated at a speed closely matching that of the main motor, the PI controller successfully regulated the main motor speed, with the deviation from the no-load condition remaining within ±1.5 RPM in both cases. The powering of the main motor on the 100 RPM setpoint was also analyzed, and the maximum oscillation was measured at 110.54 RPM. The system response observed in the Serial Monitor confirms smooth convergence to the desired speed without excessive oscillations or instability. For educational purposes, the value of proportional and integrational gains can easily be modified to test other possible configurations. Figures 4, 5, and 6 show a Serial monitor in different scenarios.

Figure 4. Main motor speed set to 100 RPM.

Figure 5. Main motor speed set to 50 RPM.

Figure 6. Main motor speed set to 0 RPM.

4. Conclusions

This article presented the design, implementation, and experimental evaluation of a low-cost educational tool for teaching PID control. The purpose of this educational tool is to bridge the gap between theoretical and practical experience of controlling a DC motor with a PID controller. By combining real-time hardware interaction with intuitive software visualization through the Arduino IDE, the developed system enables students to directly observe the change of controller parameters. The experimental results demonstrate that the implemented PI controller achieved stable and accurate speed regulation across multiple operating conditions. The controller maintained the desired speed with minimal deviations of ±1.5 RPM with load and ±1 RPM without load. The simplicity of the hardware design, the use of widely available components, and overall low cost make the system easy to replicate and suitable for the study of motion control. Furthermore, the ability to modify controller gains in real time provides a valuable platform for experimentation and a deeper understanding of PID tuning methods. In the future, the created educational tool can be improved by utilizing Simulink in combination with Arduino to create a more complex system with simple data collection.

While the developed tool provides an effective platform for basic DC motor speed control, there are certain limitations to be addressed. The use of L298N H-bridge introduces a voltage drop and thermal losses, which may cause problems during longer use sessions. Also, the reliance on Arduino C++ coding is a limitation, because to change the PID regulator parameters or modify the motor's behavior, the code needs to be rewritten.

The use of a flexible coupler can also pose a problem due to occasional slips from the motors.

Future iterations of this educational tool will incorporate MATLAB and Simulink integration, enabling the transition from embedded C++ coding to a Model-Based Design approach. Moreover, the independent speed measurement can be integrated to provide feedback, allowing for better verification of the controller's accuracy.

Acknowledgments: This article was created thanks to the project support: KEGA 016TUKE-4/2025 Development of progressive methods for the design of mechatronic systems and their implementation into the industrial mechatronics study program, VEGA 1/0409/25 Nonconventioanl and soft robotic structures.

References

1. Chen, J. (2024). The application of PID control in DC motor control systems. *Appl Comput Eng*, *81*, pp. 164-170.
2. Ľubica Miková ... [et al.]. Mechatronika sústav, 1. vyd. Košice : TU, 2018. 149 s. (Edícia študijnej literatúry). - ISBN 978-80-553-2912-3 (brož.).
3. Wang, Q. G., Zhang, Z., Astrom, K. J., Zhang, Y., & Zhang, Y. (2008). Guaranteed dominant pole placement with PID controllers. IFAC Proceedings Volumes, 41(2), pp. 5842-5845.
4. Paulusová, J., & Dúbravská, M. (2012). Application of design of PID controller for continuous systems. Humusoft. Cz, 1, 2-7.
5. Patel, V. V. (2020). Ziegler-nichols tuning method: Understanding the pid controller. Resonance, 25(10), pp. 1385-1397.
6. Cabré, T. P., Vela, A. S., Ribes, M. T., Blanc, J. M., Pablo, J. R., & Sancho, F. C. (2021). Didactic platform for DC motor speed and position control in Z-plane. ISA transactions, 118, pp. 116-132.
7. Chaouch, S., Hasni, M., Boutaghane, A., Babes, B., Mezaache, M., Slimane, S., & Djenaihi, M. (2018, October). DC-motor control using arduino-uno board for wire-feed system. In 2018 international conference on electrical sciences and technologies in Maghreb (CISTEM) pp. 1-6. IEEE.
8. RK-370CA-18260 Datasheet, Available online: https://www.casa.co.nz/motors/dc/pmdc/RK-370CA-MABUCHI-Data_1p.pdf (accessed on 10 December 2025).
9. Ribeiro, R. P., Pereira, P., & Gama, J. (2016). Sequential anomalies: a study in the railway industry. Machine Learning, 105(1), pp. 127-153.
10. Knörig, A., Wettach, R., & Cohen, J. (2009, February). Fritzing: a tool for advancing electronic prototyping for designers. In Proceedings of the 3rd international conference on tangible and embedded interaction pp. 351-358.
11. Munoz-Vazquez, A. J. (2025). Intuition and importance of feedback control through laboratory experiences. arXiv preprint arXiv:2501.15742.
12. Hammoodi, S. J., Flayyih, K. S., & Hamad, A. R. (2020). Design and implementation speed control system of DC motor based on PID control and matlab simulink. International Journal of Power Electronics and Drive Systems, 11(1), pp. 127-134.

TECHNICAL UNIVERSITY OF KOŠICE
Faculty of Mechanical Engineering

Design and Evaluation of a Cross-Platform Communication Architecture for Industrial Data Exchange

Jakub Brna [1,*], Marek Sukop [1]

[1] Technical University of Košice, Department of Production Technology and Robotics, Park Komenského 8, 042 00 Košice; jakub.brna@tuke.sk; marek.sukop@tuke.sk
* Correspondence: jakub.brna@tuke.sk

Abstract: This paper presents a prototype system for real-time video transmission between heterogeneous computing platforms, specifically a Windows-based workstation and an industrial computer running Ubuntu Linux. A USB camera connected to the Windows system serves as the image source, while video data are transmitted over a local network using the ZeroMQ (ZMQ) messaging framework and processed with OpenCV. The primary objective of this work is to establish a stable and reproducible baseline for future vision-based industrial applications. The proposed solution focuses on reliable image transfer, qualitative latency evaluation, and practical implementation aspects. Experimental results demonstrate that continuous video streaming can be achieved with near-real-time performance, while maintaining sufficient image quality for visual inspection and preliminary analysis. Particular attention is given to color fidelity and cross-platform differences in image handling, which were identified as important practical challenges. Latency was measured in milliseconds and evaluated qualitatively using graphical representations. The presented system represents an initial milestone toward more advanced applications, such as real-time tracking and feature extraction, leveraging the computational capabilities of industrial Linux-based hardware.

Keywords: ZeroMQ, video streaming, industrial computer, computer vision, Windows–Linux communication

1. Introduction

The integration of vision-based sensing into industrial and research environments increasingly relies on heterogeneous computing architectures, where different operating systems and hardware platforms must cooperate in real time. In practice, it is common to encounter scenarios where data acquisition is performed on a general-purpose workstation running Microsoft Windows, while subsequent processing, analysis, and control tasks are delegated to an industrial computer operating under Linux. This separation is often motivated by hardware compatibility, availability of drivers, or the need to exploit the computational robustness and long-term stability of industrial Linux-based systems.

A key challenge in such distributed architectures is the reliable and low-latency transfer of image data. Camera streams represent high-bandwidth, time-sensitive information, and any degradation in transmission quality—such as increased latency, jitter, frame loss, or color distortion—can significantly reduce the usefulness of the acquired data for downstream tasks. These tasks may include object detection, feature extraction, motion tracking, or higher-level perception algorithms that depend on consistent visual input.

This paper presents a practical study focused on the design and evaluation of a prototype communication pipeline for real-time video transmission between a Windows-based system and an industrial computer running Ubuntu Linux. The communication is implemented using the ZeroMQ (ZMQ) messaging framework, selected for its lightweight design, high throughput, and suitability for distributed systems. A USB camera

connected to the Windows machine serves as the image source, while the Linux system acts as the receiver and visualization endpoint.

The primary motivation of this work is to establish a stable and reproducible baseline for future research involving real-time visual data processing on industrial hardware. Particular attention is given to transmission quality, qualitative latency behavior, and practical implementation issues encountered during development. The presented solution is intended as an initial milestone toward more advanced applications, such as real-time tracking of points, objects, or positions, where the industrial computer provides the main computational capacity. [1-3]

2. Materials and Methods

2.1. System Architecture

The proposed system consists of two physically separate computing units connected via a local network:

- A **Windows-based workstation**, responsible for camera access and image acquisition.
- An **industrial computer running Ubuntu Linux**, responsible for receiving, decoding, and displaying the video stream.

The USB camera is directly connected to the Windows machine. Captured frames are processed using the OpenCV library and transmitted over the network using a ZMQ-based publisher–subscriber communication pattern. The Linux system subscribes to the video stream, reconstructs the frames, and displays them in real time. [1-2]

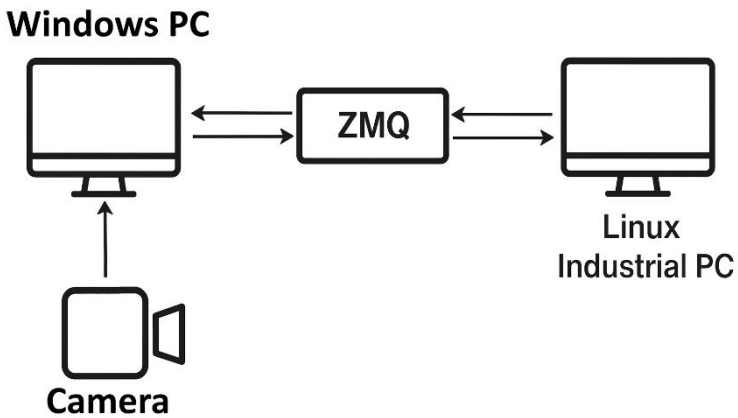

Figure 1. Block diagram.

2.2. Hardware and Software Components

The camera used in this study is a standard USB 2.0 webcam capable of VGA and HD resolutions. During experiments, multiple operating points were evaluated, including resolutions of 640×480 and 1280×720, with frame rates up to the maximum supported by the device under given lighting conditions.

On the software side, the following components were employed:

- **OpenCV** for camera access, frame capture, and image handling.
- **ZeroMQ** (ZMQ) for message-oriented communication between systems.
- **Python 3** as the implementation language on both platforms.

The choice of ZeroMQ (ZMQ) was motivated by its simplicity, cross-platform support, and ability to handle high-frequency message streams without the overhead of heavier middleware solutions. Compared to broker-based communication systems such as MQTT or RabbitMQ, ZeroMQ operates without requiring a dedicated message broker, which simplifies deployment in experimental environments. In addition, its efficient socket-based architecture enables low-latency data transmission, making it suitable for real-time transfer of high-frequency image frames between heterogeneous systems. [1]

2.3. Video Transmission Pipeline

On the Windows side, frames are captured from the camera using OpenCV's VideoCapture interface. To maintain compatibility and minimize preprocessing overhead, frames are kept in RGB/BGR format as provided by the camera driver. Each frame is then compressed using cv2.imencode(), allowing flexible adjustment of compression parameters while preserving color fidelity as much as possible.

The encoded frame data are transmitted as binary payloads via a ZMQ PUB socket. On the Linux side, a corresponding SUB socket receives the data stream, decodes each frame using OpenCV, and displays it in a dedicated visualization window.

Both sender and receiver include graphical user interface elements that allow the user to terminate execution gracefully via an on-screen STOP control. This feature was introduced to support repeated experimental runs and controlled testing without reliance on terminal-based interruption. [2,3]

2.4. Latency Measurement Approach

Latency was evaluated qualitatively by embedding timing information into the transmitted data and measuring the elapsed time between frame capture on the Windows system and frame display on the Linux system. Measurements were performed in milliseconds.

Rather than focusing on absolute numerical values in this paper, the emphasis is placed on the observed latency behavior and its stability over time. The detailed numerical results are visualized using dedicated graphs. [4,5]

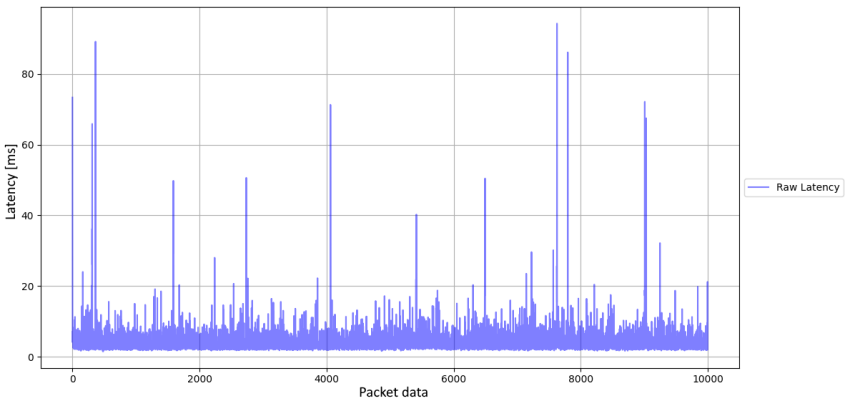

Figure 2. Graph of raw latency.

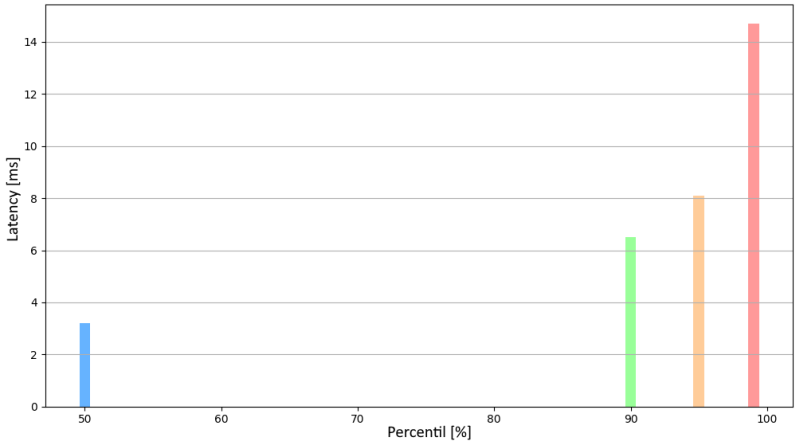

Figure 3. Graph of latency percentil.

2.5. Practical and Technical Challenges

Several practical issues were encountered during development. These included camera driver behavior under Windows, differences in default color handling between local preview and transmitted video, and platform-specific limitations related to graphical user interfaces. In particular, color fidelity required careful handling to avoid unintended grayscale or desaturated output after transmission and decoding.

Additionally, ensuring smooth frame delivery without excessive buffering proved essential for maintaining acceptable responsiveness, especially when operating near the camera's maximum frame rate.

3. Results

The experimental setup enabled continuous video streaming from the Windows-based camera system to the Linux industrial computer without critical interruptions. At both tested resolutions (640×480 and 1280×720), frames were successfully reconstructed and displayed in real time, with higher resolutions increasing bandwidth demands but remaining usable within the local network.

Qualitative evaluation showed that scene structure and motion were preserved sufficiently for visual inspection and preliminary analysis. Minor compression artifacts and reduced color saturation were observed on the Linux receiver compared to the local Windows preview, indicating the influence of encoding and cross-platform color handling.

Latency measurements, expressed in milliseconds, confirmed near-real-time behavior with moderate variability typical for user-space network communication. Quantitative analysis of the recorded latency values shows that the median latency was approximately 3 ms. The 90th percentile reached about 6.5 ms, while the 95th percentile was around 8 ms. Occasional spikes were observed in the latency distribution, with rare peaks approaching approximately 90 ms, as illustrated in Figure 2. The percentile-based overview shown in Figure 3 further confirms that the majority of transmitted frames experience low latency, indicating stable real-time transmission under the tested conditions.

Overall, the results demonstrate that the proposed ZMQ-based pipeline is stable and suitable as a baseline for further development of real-time industrial vision applications.

4. Discussion

The experimental results demonstrate that ZMQ provides a viable foundation for real-time video streaming between heterogeneous operating systems in a laboratory or industrial setting. The achieved transmission quality was sufficient for visual inspection and preliminary testing, confirming that the chosen architecture can support further development toward more complex vision-based tasks.

Latency measurements indicate that frame transfer delays remain within a range suitable for non-safety-critical real-time applications. While individual latency values vary depending on network conditions and encoding parameters, the overall behavior suggests that the system can be tuned for improved performance if required.

A noteworthy outcome of this work is the identification of color processing as a non-trivial aspect of cross-platform video streaming. Even when raw frames appear correct on the source system, differences in encoding, compression, or decoding stages can introduce perceptual artifacts. Addressing these issues early is crucial, as color integrity directly affects the reliability of subsequent computer vision algorithms.

From a broader perspective, the presented prototype highlights the importance of systematic testing and incremental validation. By first focusing on stable image transfer and qualitative latency evaluation, a solid foundation is established for future extensions involving real-time feature detection, tracking, and data fusion on the industrial computer.

5. Conclusions

This paper presented a prototype system for real-time video transmission between a Windows-based camera node and a Linux-based industrial computer using ZeroMQ and OpenCV. The work demonstrates that such a heterogeneous setup can achieve stable image transfer with acceptable latency characteristics, making it suitable as a baseline for further research and development.

The conducted experiments represent an initial milestone toward building a robust testing environment for vision-based industrial applications. Beyond basic image streaming, the system is designed to support future extensions involving real-time extraction of positions, points of interest, and other visual features, leveraging the computational capabilities of industrial hardware.

Future work will focus on systematic latency optimization, quantitative performance evaluation under varying network loads, and integration of real-time vision algorithms. The insights gained from addressing practical issues such as color fidelity and cross-platform compatibility will inform the design of more advanced and reliable industrial vision systems.

Acknowledgments: This research was funded by Slovak Grant Agency - project VEGA 1/0294/24 - Research and development of a multi-robotic system with distributed intelligence in the cloud and project KEGA 043TUKE-4/2024 - Creating promising educational tools for the field of additive manufacturing with the implementation of progressive virtual reality elements.

Conflicts of Interest: The authors declare no conflicts of interest.

References

1. Hintjens, P.; Bex, T. ZeroMQ: Messaging for Many Applications. *IEEE Internet Computing* 2013, *17*, 76–80..
2. Bradski, G.; Kaehler, A. OpenCV and Computer Vision. In *Learning OpenCV: Computer Vision with the OpenCV Library*, 2nd ed.; O'Reilly Media: Sebastopol, CA, USA, 2016; pp. 1–28.
3. Szeliski, R. *Computer Vision: Algorithms and Applications*, 2nd ed.; Springer: London, UK, 2022; pp. 15–42.
4. Koubaa, A.; Qureshi, B. Real-Time Video Streaming over Heterogeneous Networks for Industrial Applications. *Int. J. Adv. Robot. Syst.* 2020, *17*, 1–12.
5. Novák, P.; Hruboš, M.; Kováč, M. Low-Latency Image Transmission in Distributed Vision Systems. In *Proceedings of the International Conference on Applied Electronics*, Pilsen, Czech Republic, 6–7 September 2021; University of West Bohemia: Pilsen, Czech Republic, 2021; pp. 89–94.

TECHNICAL UNIVERSITY OF KOŠICE
Faculty of Mechanical Engineering

Analysis of the cup-wall thickness change during deep drawing of a bearing housing

Marek Buber [1,*], Miroslav Tomáš [1]

[1] Department of Automotive Production, Faculty of Mechanical Engineering, Technical University of Košice, Mäsiarska 74, 040 01 Košice; miroslav.tomas@tuke.sk
* Correspondence: marek.buber@tuke.sk, Tel. +421 55 602 3519

Abstract: The paper investigates the thickness changes in the cup wall during multi-stage deep drawing of a bearing housing under production-experiment conditions. The paper presents the methodology used to evaluate both material formability and wall-thickness variation. As the experimental material, a drawing-quality cold-rolled steel sheet KOHAL 240 was used. Finally, the study discusses the experimental results concerning material formability and the measured wall-thickness distributions of the cups produced within the production experiment, together with their graphical representation. Thickness was measured manually by micrometer with point contact tips and by modern method based on contactless scanning by GOM Scan1 and Zeiss Scanport device. Results of thickness in each draw showed good agreement in the course and the values of thickness with a small deviation when compared to manually measured ones.

Keywords: deep drawing, bearing-housing, thickness change, scanning

1. Introduction

Among sheet-metal forming operations, deep drawing represents one of the most complex deformation process in terms of the mechanical deformation modes involved, particularly when considering its anisotropic character. The complexity of the deep-drawing process is further intensified by the fact that, throughout the real operation — from the blank to the final cup — different mechanical deformation modes act on the same regions of the material. Thus, mentioned results in localized deformation in specific regions of the cup wall. [1].

In real deep-drawing operations, the uniformity of the final cup-wall thickness is influenced by the fact that different stress and strain modes are active in various regions of the wall throughout the drawing process. Consequently, the wall thickness of the drawn cup exhibits variations along the cup curvilinear when compared with the initial sheet thickness: $a \geq a_0$ when deep-drawing (tangential stress) prevails (flange) or $a \leq a_0$ when single- or bi- axial stretching prevails (radii, cup wall); where a_0 is initial sheet thickness and a is actual sheet thickness. [2]

The situation regarding wall-thickness evolution during cup drawing is further complicated by the fact that real sheet metals are not isotropic materials; instead, they exhibit anisotropy in their mechanical and plastic properties. As a result, the deep-drawing process itself becomes anisotropic, which manifests as a directional dependence of the cup-wall thickness relative to the sheet-rolling direction [1,2].

Nowadays advanced measurement instruments and techniques to ensure product quality assurance are implemented in factories. By employing specialized tools such as 3D scanners and dedicated post-processing software, physical parts can be accurately converted into digital CAD models [3,4]. Through the application of triangulation principles that transform 2D digital images into spatial coordinates, photogrammetric algorithms

can accurately reconstruct an object's surface as a dimensionally faithful 3D digital model [5].

The aim of the article is to compare thickness change measurement in three stage deep drawing process when evaluated by manual measuring using micrometer and by modern scanning method and its evaluation in specialized software.

2. Materials and methodology of experiment

Research of the wall thickness changes was carried out on a bearing housing stamped part, the production process for which was designed in our Institute and whose was produced by CHEMES, a. s. Humenne. The technological production process consists of three drawing operations (Fig. 1) and two subsequent calibration operations (not included in the research). In the first drawing, a cylindrical cup with a flat bottom is drawn. Then reverse drawing is performed in the second draw when the flange and rim are formed. In the third draw, cup cylinder is reduced while the flange and rim are calibrated. [6]

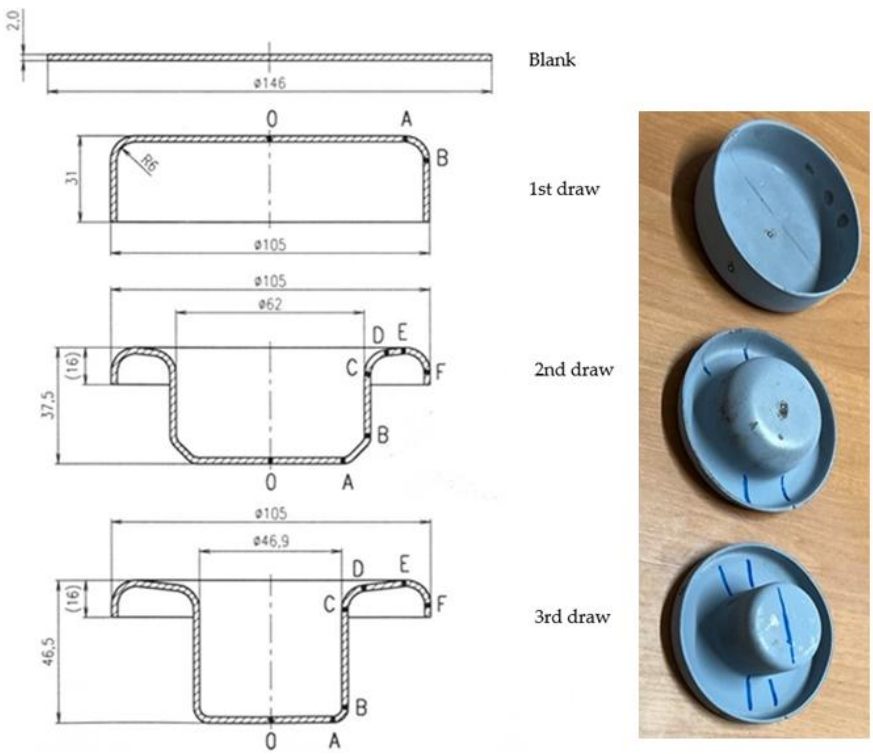

Figure 1. The technological process of bearing housing production step by step.

The production of blanks for research was carried out on tools under conditions corresponding to the actual conditions of bearing housing blank production. Plastic foil made of linear polyethylene (lPE) JK 283 815 100 710, thickness 0.015 mm, trade name Mikroten (SK), was used as a lubricant.

As part of a production experiment, KOHAL 240 cold-rolled deep-drawn steel sheet with a nominal thickness of a_0 = 2.0 mm was examined. The material formability of the examined sheet was evaluated by following tests: mechanical properties by ISO 6892-1), normal anisotropy by ISO 10113, strain-hardening exponent by ISO 10250. Deep drawing test according to Schmidt determined limit drawing ratio m_m = 0.462.

Table 1. Chemical composition of KOHAL 240 [wt %].

C	Mn	Si	P	S	Al	Cu	Ni	Cr	O_2	N_2
0.054	0.19	0.02	0.014	0.016	0.053	0.031	0.014	0.021	0.0166	0.0045

Table 2. Mechanical properties and anisotropy parameters of KOHAL 240.

	Smer	$RP_{0,2}$ [MPa]	Rm [MPa]	A80 [%]	$PR_{P0,2}$ [%]	PR_m [%]	PA80 [%]	r	r_m	Δr	n	n_m	Δn
KOHAL 240	0°	156	300	45.8				1.71			0.243		
	45°	171	314	40.4	10	5	-12.0	1.03	1.37	0.68	0.237	0.241	0.007
	90°	158	301	46.5	2	0	1.5	1.71			0.247		

2.1. Measuring by micrometer

When measuring changes in wall thickness in individual drawing operations, a micrometer with point contact tips with an accuracy of 0.01 mm clamped in a stand was used as a measuring device. The thickness of the individual stamped part was measured in the areas as indicated in Fig. 1 for each draw. The imaginary cutting plane through the center of the stamped part, along which the thickness measurements were taken, was oriented at 0°, 45°, and 90° relative to the rolling direction. To facilitate access to the measured locations, the part was cut with a hacksaw at a distance of 5 mm from the imaginary cutting plane. The position of the points at which the wall thickness of the part was measured was determined by a scale - a flexible ruler with 1 mm divisions, which was used to mark the measured points with a marker at 3 mm intervals in the specified directions. The starting point of the ruler was identical to the center of the part.

2.2. Scanning by optical scanner GOM Scan1

The wall thickness of the parts was assessed using a non-contact optical 3D scanning method. For this purpose, a GOM Scan 1 structured-light scanner with a measuring volume of MV 400 was used (Fig. 2). Scanner was mounted on Scanport arm. Three-dimensional surface models were subsequently generated in ZEISS Inspect Pro software. According to the instrument specification and ISO 10360 performance criteria, the system provides a dimensional accuracy of 0.02 mm and can capture approximately 6 million points within a scanning field of 400 × 250 mm.

Prior to scanning, the samples were mounted on a motorized rotary table and positioned at the optimal working distance from the scanner. To ensure correct spatial alignment and sufficient overlap between consecutively captured frames, retro-reflective reference markers were applied to the surface of each cup. For complete geometric coverage, 20 scans were acquired from both the inner and outer surfaces in angles between scanner and rotary table of 20° and 70°. The rotary table rotating in 36° increments between individual scans.

Figure 2. Scanning with GOM Scan 1 scanner setup with rotary table and SCANport.

3. Results and discussion

Based on the mechanical properties, the values of the new deep drawing criteria, and the limit drawing ratio, it can be concluded that KOHAL 240 sheet metal is a typical deep-drawing steel sheet of the EDDQ-S grade. The anisotropy of the strain-hardening exponent Δn is almost zero (0.007). The strain hardening coefficient r shows a high degree of anisotropy with a minimum in the 45° direction and a maximum in the 0° and 90° directions against the rolling direction. The 45° direction against the rolling direction is also the most unfavorable for the yield strength, tensile strength, and elongation.

Based on the analysis of thickness variation as a function of the curvilinear coordinate, derived from measurements of wall thickness changes in stamped parts after the 1st, 2nd, and the 3rd drawing operations in the 0°, 45°, and 90° directions relative to the rolling direction, it can be concluded that the maximum reduction in wall thickness occurred consistently in the 45° direction for all drawing stages. This direction corresponds to the least favorable mechanical properties and the lowest value of the normal anisotropy coefficient. The wall thickness variation curves for the stamped parts in this direction for the individual drawing operations are presented in Fig. 3, 4, and 5.

The course of the wall thickness of the stamped part from the first draw, where the drawing coefficient $m_1 = 0.719$, shows a course typical for cylindrical cups with a flat bottom when deep-drawn from a flange. In Fig. 3, 4 and 5, there are 3 lines, shown in the graph: the blue one represents initial thickness (2mm), green one represents the measurement in the Zeiss inspect program and the red one represents the manual measurement with a micrometer. **The thickness values measured in Zeiss Inspect will be evaluated and the deviation from the values measured manually with a micrometer will be shown.**

In Fig. 3 there is no change in thickness in the area from 0 to A (bottom of the cup). In area A-B (radius between the bottom and the cup wall), there is a change in the thickness, with the minimum value of 1.88±0,01 mm. The difference in measurements using the scanner and the micrometer was more pronounced at the edge of the part, where the difference is 0.08 mm.

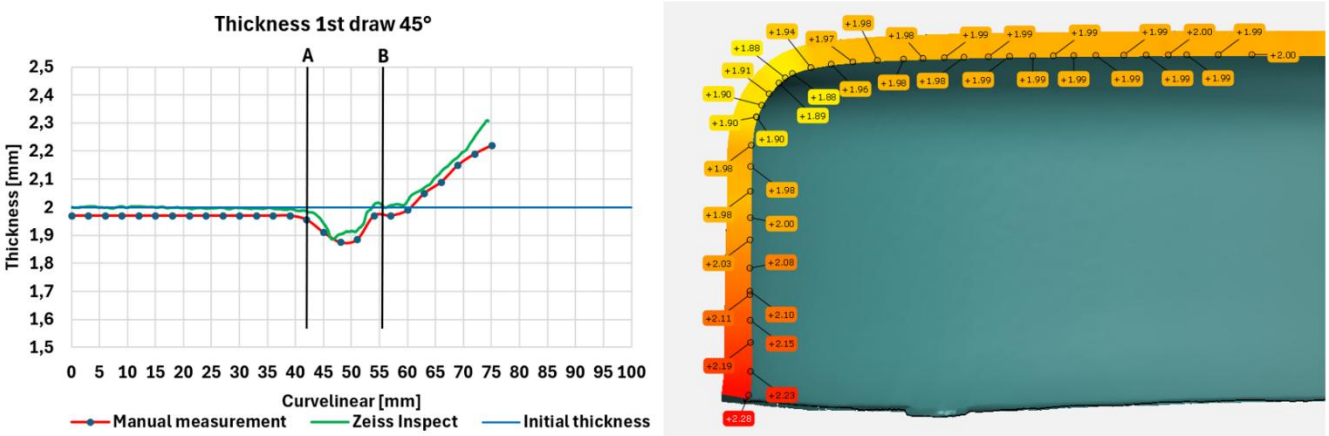

Figure 3. The wall thickness change of the bearing housing part in the 1st draw.

During the second draw, the stamped part is drawn in reverse direction, creating a flange and a rim. Different parts of the stamped part undergo varying degrees of thinning and strengthening. Along with the thickness change curves, several local maxima of thickness can be observed in individual parts of the stamped part. On Fig 4 in the interval 0-A (bottom of the part), the material thickness changed from the original 2 mm (blank) to 1.85±0,01 mm on average. In the interval A-B (radius between the bottom and the wall of the part), the most significant change in thickness occurs with a value of 1.73±0,01 mm. In the area B-C (wall of the part), the material thickness is 1.78mm on average. In the area

C-D (transition between the wall of the part and the flange), the material thickness rises up to a value of 2.09±0,01 mm. In this area, there is also a more significant difference between the values measured by both measurement methods, with differences of 0.07 mm. In the area D-E (flange), the material thickness was 2.093±0,01 mm. In the area E-F (rim), the material thickness was 2.23±0,01 mm.

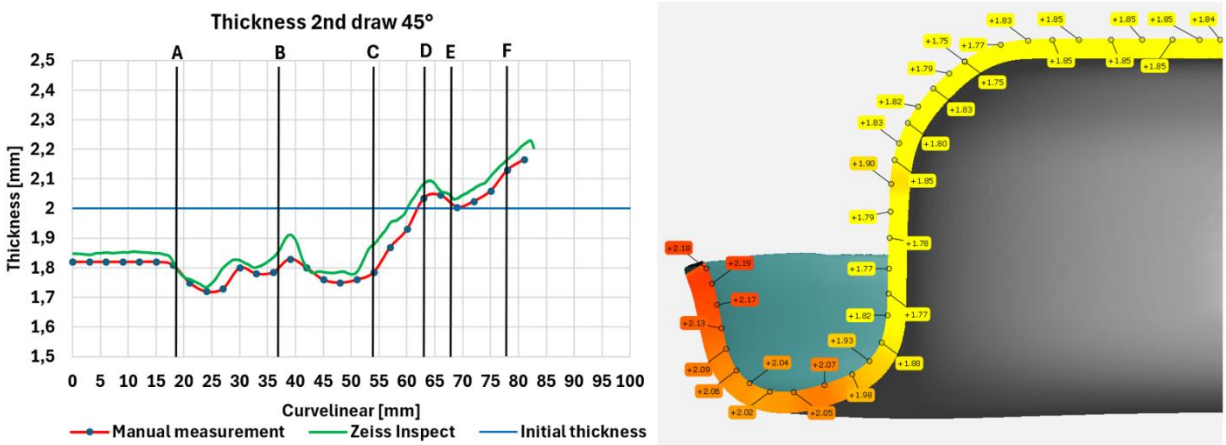

Figure 4. The wall thickness change of the bearing housing part in the 2nd draw.

In the third draw (Fig.5), when the cup is reduced and the flange calibrated, the course of the thickness change does not change significantly. In area 0-A (bottom of the part), there was no change in thickness compared to the previous drawing stage. In area A-B (radius between the bottom and the wall of the part), there was a change in thickness compared to the previous drawing stage, on average by 0.18±0,01 mm. The largest difference between the measurements with the scanner and the micrometer is also observed in this area. In the area B-C (wall of the part), there was a decrease in thickness by 0.09 mm on average due to a change in the height of the cylindrical wall of the part. In the area C-D (transition between the wall of the part and the flange), already in this third drawing stage, there is a decrease in thickness due to a change in the height of the part. In the area D-E (flange) and the area E-F (rim), there are no significant changes in thickness. Thickness measurements across the entire cross-section do not show significant deviations except for area D-E where measurement using a scanner showed a higher thickness of 0.08 mm.

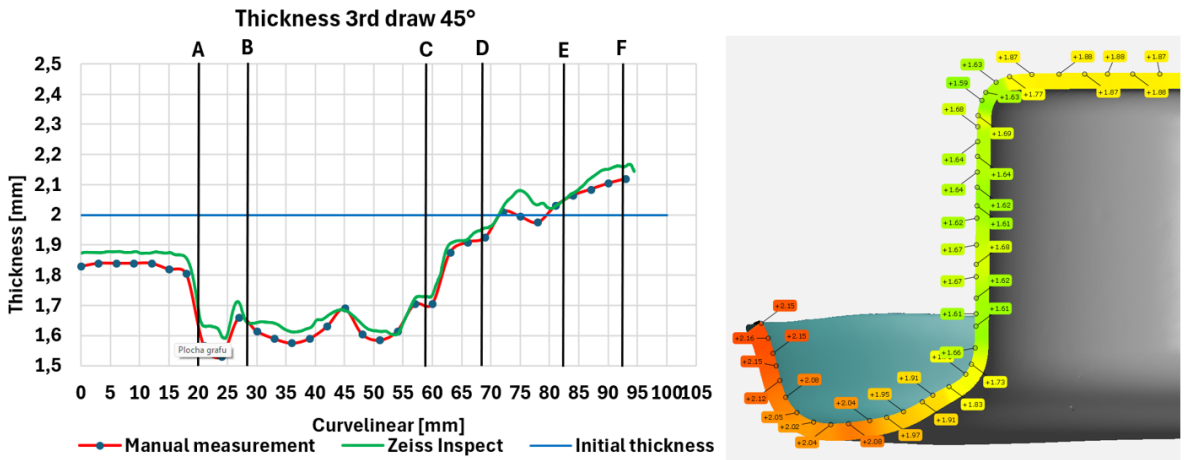

Figure 5. The wall thickness change of the bearing housing part in the 3rd draw.

By comparing the accuracy of contact micrometer measurements and non-contact scanner measurements, it is possible to state a higher accuracy of thickness measurements by contact micrometer in the range of ±0.005. However, the accuracy of determining the

position of the thickness measurement relative to the center of the stamped part must be considered, with an accuracy of ±0.5 mm. At the same time, non-contact measurement using the SCANport device allows you to measure the thickness of the yield with the accuracy of the position of the measured point (the place of thickness measurement) from 0.0005 to 0.035 due to the triangulation of the point cloud when converted to .stl format. The accuracy of the scanner measurement also depends on the measuring volume, which is given by the number of scanned points.

4. Conclusions

Based on the experimental research conducted, the following conclusions can be drawn:

1. The change in the wall thickness in the first drawing stage is typical for cylindrical parts with a flat bottom deep-drawn from a flange. The greatest thinning was measured at the bottom to wall radius.
2. The change in the wall thickness in the second stage (reverse drawing) shows several local minima: 1st local minimum at the transition from the bottom to the cylindrical wall (critical point of the housing), 2nd local minimum in the cylindrical wall of the part (its position corresponds to the maximum thinning of the thickness from the first stage – in this part of the housing, the inheritance of thickness changes from the first stage of drawing is evident), 3rd local minimum at the flange to rim radius.
3. The course of the thickness change in the third draw is analogous to the course of the change in the thickness change in the second draw but shifts to lower values. The minimum thickness was found at the bottom to wall radius of the housing (critical point of the part).
4. The directional dependence of thickness changes correlates with the normal anisotropy coefficient – the most unfavorable direction on the part in terms of thickness changes is the direction of the significant minimum value of the normal anisotropy coefficient.

Measuring material thickness using a 3D scanner offers more comprehensive and surface-representative data compared to a micrometer, as it enables analysis of the entire object rather than only local measurement points. A significant advantage is the non-contact nature of the measurement, which eliminates the risk of material deformation and increases accuracy, especially for thin-walled or soft samples. Through 3D scanning, it is possible to obtain a detailed thickness distribution map and to identify local deviations, inhomogeneities, and manufacturing defects that point-based micrometer measurements may fail to detect. In addition, a 3D scanner allows digital data archiving, repeated analyses, and integration into CAD/CAE systems, thereby substantially improving the efficiency of quality control and research processes.

Acknowledgments: This work was supported by the projects: VEGA 1/0238/23 "Implementation of CAx systems and virtual engineering techniques in the redesign of car-body parts for deformation zones"; VEGA 1/0609/25 "Research and development of methodologies for the assessment of strains of sheet metal and manufacturability of the car components in a virtual environment"; and KEGA 024TUKE-4/2025 "Hybrid education of students for the current needs of the automotive industry".

References

1. Pollák, L.: Anizotropia a hlbokoťažnosť oceľových plechov. ALFA, Bratislava, 1978.
2. Pollák, L.: Normal anisotropy as a deep-drawability criterion of steel sheets. International Sheet Metal Review, spring 1999, Mack-Brooks Publishing Ltd., Hatfield, England, p. 84.
3. Valerga Puerta, A. P., Jimenez-Rodriguez, R. A., Fernandez-Vidal, S., & Fernandez Vidal, S. R. : Photogrammetry as an engineering design tool. In C. Alexandru, C. Jaliu, & M. Comşit (Eds.), Product Design. IntechOpen. 2020. https://doi.org/10.5772/intechopen.92998
4. Ghobakhloo, M.: Industry 4.0, digitization, and opportunities for sustainability. Journal of Cleaner Production, Vol. 252, p. 119869, 2020, doi: 10.1016/j.jclepro.2019.119869.

5. Valença, J.; Júlio, E. N. B. S. and Araújo, H. J.: Applications of photogrammetry to structural assessment. In: Experimental Techniques, Vol. 36, No. 5, 2010, pp. 71–81, 2012, doi: 10.1111/j.1747-1567.2011.00731.x
6. Tomáš, M.: Príspevok k štúdiu procesov plastického pretvorenia pri ťahaní zložitých rotačne symetrických tvarov výťažkov. Dizertačná práca, KTaM SjF TU Košice, 2000

TECHNICAL UNIVERSITY OF KOŠICE
Faculty of Mechanical Engineering

Design of a Double-Axle Bogie for Regional Rail Vehicles

Martin Bučko [1,*], Ján Dižo [1], Vladimír Samaš [1], Patrik Slušňák [1]

[1] University of Žilina, Faculty of Mechanical Engineering, Department of Transport and Handling Machines, Univerzitná 8215/1, 010 26 Žilina, Slovakia; martin.bucko@fstroj.uniza.sk; jan.dizo@fstroj.uniza.sk; vladimir.samas@fstroj.uniza.sk; patrik.slusnak@fstroj.uniza.sk
* Correspondence: martin.bucko@fstroj.uniza.sk

Abstract: Rail transport is an integral part of transport infrastructure and is therefore considered one of the leaders in sustainable mobility, mainly due to its low environmental impact. It offers ecological and economic advantages over other modes of transport, as it can transport both people and various types of goods over short and very long distances. In order to ensure the environmentally friendly, comfortable, and safe transport of people and goods by rail, it is necessary to have rolling stock with good running characteristics. Currently, there is a growing need for innovative solutions in various transport sectors that increase efficiency, comfort, reliability, and environmental sustainability, and therefore it is necessary to create innovative rail vehicles for passenger transport. These vehicles are equipped with different types of bogies, which have different running characteristics. Since the dynamic and running characteristics of rail vehicles depend on a large extent on the design of the bogie, increased attention is required when designing rail vehicle bogies. The bogie of a rail vehicle essentially always represents a certain compromise between suitable characteristics when running on the track. This article focuses on the design and creation of an innovative double-axle bogie for passenger rail vehicles. The proposed design will reflect the latest requirements for safety, comfort, and environmental sustainability in rail transport. The aim of the project is to create an operationally efficient bogie that will be suitable for implementation in new as well as modernized regional and suburban trains. Its design features an internal steel frame that includes a primary and secondary suspension system. The next phase will involve the development of a technical design for the new bogie concept and the creation of a 3D model in Autodesk Inventor software.

Keywords: rail vehicles, a double-axle bogie, a bogie frame

1. Introduction

Rail transport is rightly considered a leader in sustainable mobility, primarily due to its environmental friendliness. In a period of rapid technological development and constant change in the transport industry, it is very important to seek innovative solutions that will contribute to increasing the efficiency, reliability, and environmental sustainability of transport systems. Although rail transport is perceived as an environmentally friendly alternative, its popularity among passengers is mainly due to its high level of comfort, safety, relatively dense network of connections, and speed of transport [17].

One of the main priorities of modern development in rail transport is the design of vehicles that can meet increasingly stringent requirements for performance, passenger comfort, and environmental protection. Public interest in rail transport also raises expectations regarding the safety and comfort of vehicles. However, a major challenge remains the fact that the rolling stock is outdated in many countries and often exceeds its technical service life. To reduce costs, transport operators are therefore resorting to modernizing older vehicles, which prolongs their operation but generally fails to meet the environmental and technological standards of new rail vehicles.

This approach is not correct, and the best option for maintaining and increasing passenger interest in rail transport is to build new, modern, safe, and comfortable low-floor vehicles.

This objective is met by regional units, which are capable to run on local lines. These vehicles represent an innovative response to the demands of the modern railway industry. Their design of a bogie allows for more flexible and efficient use of the railway network, improves passenger comfort, and reduces the negative impact on the environment.

2. A rail vehicle bogie

The bogie bears all loads from the vehicle body and is also a key element in wheel-rail interaction. The bogie itself consists of a frame, wheels, axles, suspension components, and traction and braking units, which are exposed to static and dynamic loads. For this reason, the bogie structure must be sufficiently strong, but at the same time flexible, so that it meets the requirements of technical standards, in particular the EN 13749 standard [1, 7].

Currently, the main goal is to achieve the largest possible low-floor section of the vehicle, which is, however, limited by the wheelbase and the distance between the chassis pivot pins. The vehicle must be able to safely and reliably negotiate the small-radius curves characteristic of local tracks, which requires minimizing the difference between the wheelbase and the distance between the pivot pins — ideally to the point where they are equal. This requirement calls for an innovative design that must also take into account the competitive market environment and the strict technical standards of the TSI for modern rail vehicles, in particular the TSI LOC&PAS and TSI PRM.

Bogie weight optimization is a key factor not only from a technical but also from an economic point of view. Given that most components have already reached the limit of possible weight reduction, there is only limited scope for further reducing the structural weight of the bogie. One of the few components that still offers potential for weight optimization is the bogie frame.

In this context, the use of an internal bogie frame appears to be a promising solution. However, such a bogie frame brings complications, especially in the area of axle placement—which is exposed to the greatest bending moment—and also due to the significantly limited design space inside the frame. This space must accommodate all the necessary structural elements, which is particularly challenging in a drive bogie, where drive mechanisms must also be integrated.

When designing the bogie frame, it is also necessary to comply with the requirements of UIC 515 and ISO 5725 [5, 6], which ensure the reliability and safety of the vehicle's mechanical parts.

Despite these technical complications, the potential for weight savings and improved functionality of the internal chassis frame remains attractive to manufacturers. This approach is being implemented by several global manufacturers of rail vehicles.

3. A bogie frame

A bogie frame is the basic and load-bearing part of the rail vehicle bogie. It carries and guides the body of a rail vehicle. In freight vehicles, this is usually done by means of a pivot pin, in others by means of secondary suspension and a device for transmitting braking and traction forces. The bogie frame must be capable to transmit forces in all directions. Bogie frames can be produced as a welded structure, consisting of sheet metal stampings, or as a structure produced by casting. An additional equipment such as a braking system, a traction motor, cabling, and others may be attached or suspended from the bogie frame. The frame must be securely attached to the vehicle body that the entire bogie can be lifted together with the rail vehicle body, for example after derailment. Due to the importance of the bogie frame for the safety of the rail vehicle, high demands are placed on the frame [1-3].

Bogie frames can be divided as follows:

- external frames;
- internal frames;
- closed frames;
- semi-closed frames;
- open frames;
- flexible frames.

4. A suspension system

Nowadays, a two-stage suspension system is commonly used. A two-stage suspension consists of a primary suspension, which is located between the bogie frame and the axle bearings, and a secondary suspension, which is located between the bogie and the vehicle body. The parts of the vehicle that are not suspended are called unspring masses. These include the wheels, axle bearings, and approximately a half the weight of the primary suspension. In order to minimize the dynamic stress caused by these unspring masses, their weight must be reduced as much as possible. When the suspension is implemented using coil springs, hydraulic vibration dampers are parallelly connected to them.

The suspension of both the traction vehicle and the wagon must meet the following basic requirements:

- driving safety;
- driving comfort of the vehicle;
- maintaining the height of the buffers above the top of the rail;
- elimination of the effects of track irregularities;
- an optimal natural frequency of vibrations.

4.1. A primary suspension

A primary suspension plays particularly an important role. It largely determines the vehicle's driving performance and thus has a direct impact on driving stability, cornering control, derailment safety, and driving comfort [2].

The design of the bogie frame serves to transfer longitudinal and lateral forces between the bearing housing. It has a significant influence on the vehicle's running characteristics. The wheel set guidance must allow for lateral suspension through its lateral flexibility and must reduce the quasi-static effects of the track curve through its play, while also transmitting longitudinal forces between the wheel set and the bogie frame [4, 8]. The accuracy of the wheel set guidance is also very important, preferably without any play, as under certain conditions on a straight track, the wheel set may develop a wavy motion, which can lead to unstable running. The properties of an essential importance for assessment of the primary suspension and bearing box guidance design should be mentioned, namely the long-term stability of mechanical elements, which can be problematic with rubber blocks, maintenance requirements, and simplicity of design [18, 20].

4.2. A secondary suspension

This type of suspension ensures a vertical and lateral suspension of the body relative to the bogie frame and it transmits the vertical and lateral forces between the body frame. Above all, it ensures a smooth run and largely determines the overall level of ride comfort for passengers.

Currently, an air suspension system is the preferred option. The advantage of this type of suspension is its adjustability, and by changing the air pressure in the spring, it can ensured that the height of the air bellows does not change during static load changes.

This means that the vertical stiffness of the air suspension is not limited by the requirement to maintain the height of the bumpers within the permitted range of values. This results to the fact that this type of a suspension system can be very soft, which is particularly important for rail vehicles that are lightweight and have very different static loads, for example during the course of a day. Such vehicles include urban public transport rail vehicles (metro vehicles), regional units, double-decker carriages, etc. The use of air suspension allows for a simple bogie frame design [19, 20].

5. A bogie frame design

The bogie frame is the main load-bearing element of the vehicle, which other bogie parts are subsequently attached to. The considered frame has an internal structure, which was chosen primarily to reduce the overall weight [12]. From a structural point of view, the bogie is made of steel with guaranteed weldability and the increased yield strength S355J2 [13]. The frame consists of rectangular profiles with a wall thickness of 15 mm. The common parameter will be the wheelbase of 2000 mm.

Two bogie frame designs were created (Fig. 1). The material thickness is the same, but the structure is different. One design is an open H-shaped frame, where this bogie frame design is used in practice, more often in the form of an outer frame, while the second design is experimental in the shape of the letter I [14].

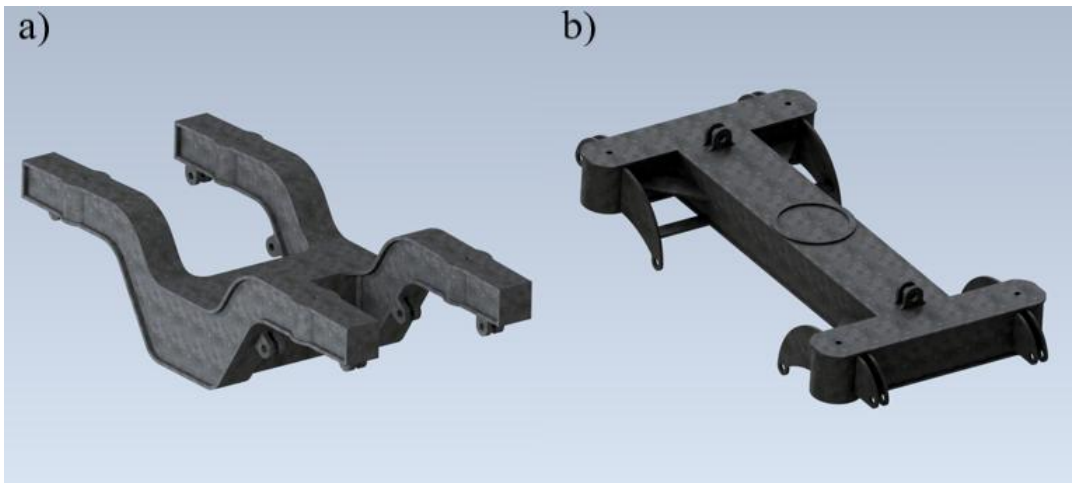

Figure 1. Open internal bogie frame design (**a**) and experimental bogie frame design (**b**).

The advantage of the proposed innovative bogie frames over commonly used bogie frames in regional rail vehicles is their internal structure, which is lightweight, resulting in lower dynamic forces between the wheel- rail contact and smaller installation dimensions, which are key for regional vehicles [9, 10]. It is also possible to use disc or block brakes on the bogie. It is also possible to use various types of secondary suspension without major interference with the bogie frame design.

The following figure shows an example of its possible mounting with important components such as a wheelset, axle bearings, a primary suspension in a form od coil springs, shock absorbers in the primary suspension, lemniscate guidance and a secondary suspension in the form of an air spring, which is the ideal solution for this type of bogie, or in a form of a coil spring [15]. This configuration is only for visualization purposes and the functionality of such an assembly has not been verified.

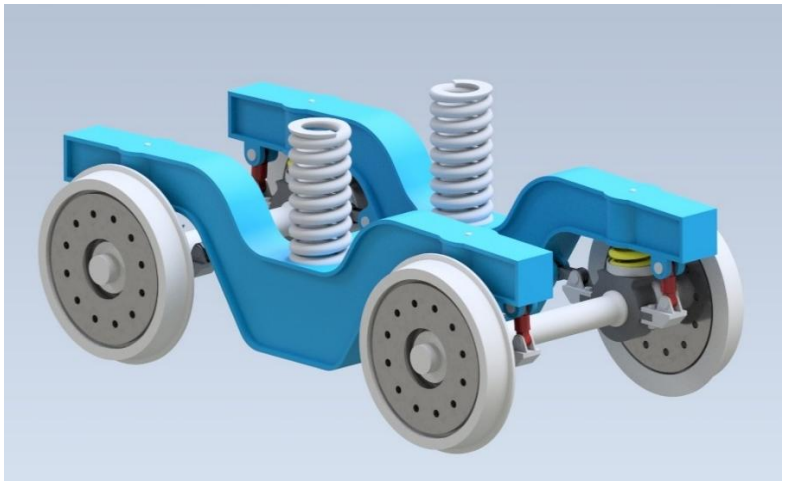

Figure 2. An open internal bogie frame with implemented components.

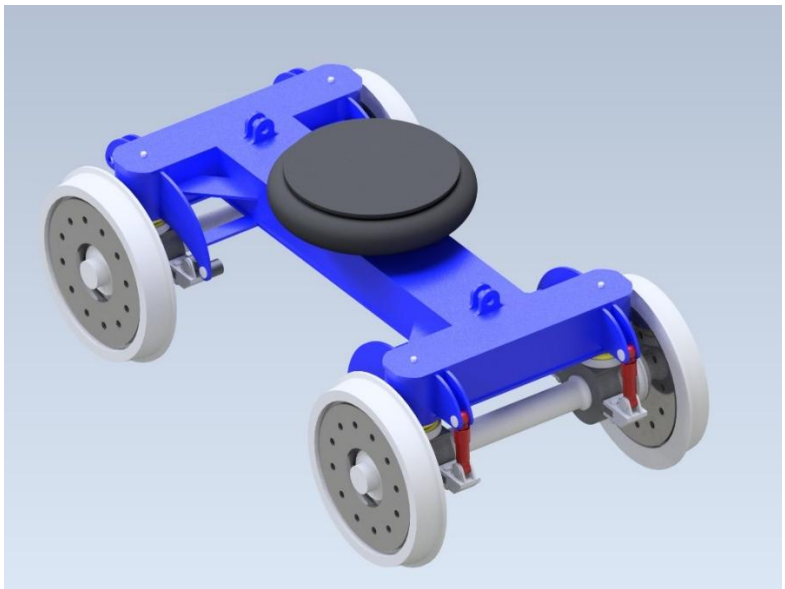

Figure 3. An experimental frame with implemented components.

6. Conclusion

This paper has addressed the design of an innovative double-axle bogie intended for modern passenger rail vehicles, with a particular emphasis on regional and suburban applications.

The bogie design inherently represents a compromise between competing requirements, such as low-floor vehicle concepts, curve negotiation capability on local lines, structural strength, weight minimization, and compliance with TSI and relevant EN and ISO standards. The adoption of an internal steel frame made of S355J2 material is a promising solution, despite the associated design constraints related to axle placement, limited internal space, and integration of suspension and auxiliary components.

Two alternative frame concepts—an open H-shaped frame and an experimental I-shaped frame—were proposed. While both concepts share identical material properties and wheelbase parameters, their differing structural layouts provide a basis for future comparative evaluation in terms of stiffness, a mass distribution and manufacturability. The integration of a two-stage suspension system, with particular emphasis on air-based secondary suspension, reflects the current practice in passenger rail vehicles and supports high levels of ride comfort.

The results presented in this study form the basis for further research steps. These steps will be supplemented by FEM analysis and a possible modification of the frame design. Furthermore, other components on the bogie will be optimized to ensure the functionality of the bogie as a whole.

Acknowledgments: This research was also supported by the Slovak Research and Development Agency of the Ministry of Education, Science, Research and Sport of the Slovak Republic VEGA 1/0308/24 "Research of dynamic properties of rail vehicles mechanical systems with flexible components when running on a track. This publication was supported by the Cultural and Educational Grant Agency of the Ministry of Education of the Slovak Republic in the project KEGA 031ŽU-4/2023: Development of key competencies of the graduate of the study program Vehicles and Engines. This publication was supported by the UNIZA grant project No. 21144: A design of an innovative double-axle traction bogie of a rail vehicle for passenger transport.

References

1. HELLER, P., 2009. Rail vehicles II. University of West Bohemia, Pilsen. ISBN 978-80-7043-641-7
2. HELLER, P., 2011. Rail vehicles III. University of West Bohemia, Pilsen. ISBN 978-80-261-0028-7
3. LATA, M., 2004. Rail vehicle design II. University of Pardubice. ISBN 80-7194-696-6.
4. KALINČÁK, D., 2008. Rail vehicles I. University of Žilina. ISBN 978-80-8070-864-1
5. UIC 515-4:1993 "Passenger rolling stock – Trailer bogies – Running gear – Bogie frame structure strength tests", Union Internationale des Chemins de Fer, 1993.
6. ISO 5725-1:2023 "Accuracy (trueness and precision) of measurement methods and results — Part 1: General principles and definitions", International Organization for Standardization, 2023.
7. EN 13749:2021 + A1:2023, Railway applications — Wheelsets and bogies — Method of specifying the structural requirements of bogie frames, CEN, 2021/2023
8. GAŠPARÍK, J., GRENČÍK, J., MEŠKO, P., ZITRICKÝ, V., ĽUPTÁK, V., 2016. Mechanics in rail transport. University of Žilina. ISBN 978-80-554-1274-0
9. PEIBIN, J., LIANG, L., JINGYU, Z., WANMING, Z., 2024. Experimental and numerical study on bogie hunting motion of metro vehicles induced by wheel concave wear, DOI: 10.1080/00423114.2024.2362942
10. WEI, L., YINGJIE, Q., ZEFENG, W., MAORU, CH., HENGYU, W., XIAOXIAO, CH., XIONGFEI, Z., JIANFENG, S., 2024. Coupling effect of track irregularity and wheel–rail contact conicity on carbody swaying of a metro vehicle: an experimental investigation, DOI: 10.1080/00423114.2024.2362947
11. ZHENG, B., WEI, L., ZHENG, J., ZHANG, D., 2024. Experimental and Numerical Investigation of Bogie Hunting Instability for Railway Vehicles Based on Multiple Sensors, DOI: 10.3390/s24124027
12. MALOCH, M., CORNAK, S., 2020. Aspects of tandem bogie axles from perspective of state-space modeling, DOI: 10.22616/ERDev.2020.19.TF350
13. BO, P., XINGWEN, W., ZIHAO, CH., WEI, W., NINGRUI, Y., YANG, L., JUNZUO, L., CAIYING, M., MAORU, CH., 2025. Fatigue failure mechanism of a metro bogie frame and its Mitigation method, DOI: 10.1016/j.engfailanal.2025.109511
14. WANG, T., SUN, W., GONG, D., ZHOU, K., LIU, Z., ZHANG, Z., ZHOU, J., 2024. An efficient modelling approach to obtain dynamic properties of equipment coupled to the bogie of vehicle, DOI: 10.1080/00423114.2024.2330445
15. SINGH, S. K., VISHWAKARMA, A., SINGH, S. R., RACHERLA, V., 2023. Effect of suspension parameters on dynamics of a metro coach: A parametric study, DOI: 10.1007/s12206-023-0503-9
16. MATEJ, J., ORLINSKI, P., 2023. New possibilities to reduce wheel and rail wear in the operation of metro wagons on curved track with small curve radii without considering propulsion and braking systems, DOI: 10.17531/ein.2023.1.15
17. GIOSSI, R. L., PERSSON, R., STICHEL, S., 2025. Innovative Two-Axle Vehicle with Improved Ride Comfort via Blended Active Vibration Control, DOI: 10.1007/978-981-97-7525-5_9
18. ISACCHI, G., RIPAMONTI, F., 2024. On the implementation of hydraulic-interconnected-suspensions at the primary suspension stage of high-speed rail vehicles, DOI: 10.1177/09544097241257550
19. PARK, J., YANG, H., 2023. Design of a lateral active suspension controller for railway vehicles: a focus on ride comfort and perturbations, DOI: 10.1007/s12206-023-1017-1
20. SINGH, S. K., VISHWAKARMA, A., SINGH, S. R., RACHERLA, V., 2023. Effect of suspension parameters on dynamics of a metro coach: A parametric study, DOI: 10.1007/s12206-023-0503-9

TECHNICAL UNIVERSITY OF KOŠICE
Faculty of Mechanical Engineering

Current State and Potential Applications of Real-Time Data for Predictive Assessment of Ergonomic Risks in Industry

Matej Cichý [1,*] and Darina Dupláková [1]

[1] Technical University of Kosice, Faculty of Manufacturing Technologies with a seat in Presov, Bayerova 1, 080 01 Presov; Email: matej.cichy@tuke.sk, darina.duplakova@tuke.sk.
* Correspondence: matej.cichy@tuke.sk

Abstract: Ergonomic risks are a significant factor in modern industry, affecting occupational safety, employee health and the long-term sustainability of production processes. Traditional methods of ergonomic assessment are based mainly on visual observation or ex-post analysis, which limits their use in dynamic production conditions. However, current technological trends are bringing new possibilities for the use of real-time data from camera and sensor systems, which enable continuous monitoring of workers' movement patterns and immediate assessment of risky postures. The aim of this article is to present an overview of existing technologies and tools for monitoring ergonomics, compare their capabilities and limitations, and identify the potential of real-time data processing for predictive assessment of ergonomic risks. The focus is mainly on modern computer vision methods based on the detection of key points of the human body (pose estimation), which represent a promising alternative to IMU sensors and traditional commercial solutions. The article also proposes a concept of an adaptive model that enables dynamic tracking of worker movement, real-time calculation of ergonomic indicators, and identification of potential risks before they arise. The proposed approach shows that the combination of available RGB cameras, computer vision algorithms, and ergonomic metrics can provide an affordable, contactless, and easily scalable solution, especially for small and medium-sized manufacturing companies.

Keywords: ergonomic risks, real-time analysis, computer vision, industrial ergonomics, predictive assessment

1. Introduction

Given the increasing demands on the dynamics of the manufacturing industry, manufacturing companies are increasingly faced with the need to monitor and manage ergonomic risks in real time. Despite technological advances, a large part of industrial work remains manual, physically demanding and significantly influenced by the individual movement patterns of workers. Long-term strain, inappropriate working positions and frequent bending or lifting of materials are factors that contribute to musculoskeletal disorders and reduce overall productivity.

Traditional ergonomic assessments such as RULA, REBA, OWAS, and NIOSH have been in use for decades, but their practical application is largely static and limited to ex-post analysis of individual work tasks. This leads to insufficient feedback and a weaker ability of companies to respond to changing conditions in real time. Modern production environments require flexibility, rapid adaptation of work tasks and continuous monitoring of worker load. Available commercial camera and digital solutions are advanced tools, but they usually operate as closed platforms, often with high licensing costs or the need for wearable sensors. This can limit implementation, especially in small and medium-sized enterprises. Another problem with current approaches is their limited adaptability. Many solutions require repeated sensor setup, workspace calibration, or specific lighting

and spatial conditions. This reduces their usability in real-world operations, where work positions, tasks and workplace layout are constantly changing. Therefore, there is a growing demand for systems that can not only collect data, but also automatically adapt to the context of the work activity. [1]

Digital tools based on computer vision, which do not require physical contact with employees, therefore represent a promising direction for development. In particular, pose estimation algorithms allow the position of body segments to be tracked without the need for IMU sensors, which significantly increases worker comfort and reduces implementation costs. The rapid development of Industry 4.0 technologies also enables the linking of visual data with intelligent analytical tools. This gives manufacturing companies the opportunity to use real-time data not only for retrospective evaluation, but also for predictive assessment of ergonomic risks. In combination with the trend towards human-centric manufacturing, there is an increasing emphasis on the need for systems that can respond flexibly to the variability of work tasks, individual differences between workers and changing conditions in the workplace. In this context, an approach based on camera systems and computer vision algorithms appears to be particularly promising. These offer the possibility of evaluating workers' movement patterns in a non-invasive, more affordable and continuous manner. They create space for the development of intelligent tools that can provide immediate feedback while collecting data for long-term modelling of ergonomic risks. This approach opens up new possibilities for predictive occupational safety management and improved ergonomics in production processes. [2–4]

2. Materials and Methods

As part of the analysis of the issue, a systematic review of available technologies designed to monitor the physical activity of workers in industrial environments was first conducted. The analysis included classic ergonomic assessments (RULA, REBA, OWAS, NISOH) and technical approaches such as commercial camera solutions (Kinetica, Viact, Protex), wearable IMU platforms (Xsens, WearHealth), and open-source computer vision algorithms such as MediaPipe, MoveNet, and OpenPose. The analysis of evaluation methods (RULA, REBA, OWAS, NIOSH) did not focus on comparing their technologies, but on assessing their suitability for automated processing using individual technical solutions. The aim of this step was to identify the advantages of individual approaches, their limitations when used in real production conditions, and to evaluate their applicability in continuous real-time measurement. [1,5,6]

Following this analysis, a comparison was made of selected open-source algorithms for human position detection, which represent the most promising group of solutions suitable for contactless ergonomic data collection. Attention was focused primarily on the MediaPipe Pose, Teachable Machine and MoveNet models, which are known for their high processing speed and ability to reliably identify key points of the human body while maintaining low hardware requirements. Their performance parameters were compared, including detection accuracy, stability when changing lighting or spatial conditions, video processing speed, and overall computing power requirements. This comparison made it possible to determine which algorithms are suitable for real-time applications without the need for specialised computing units.[7]

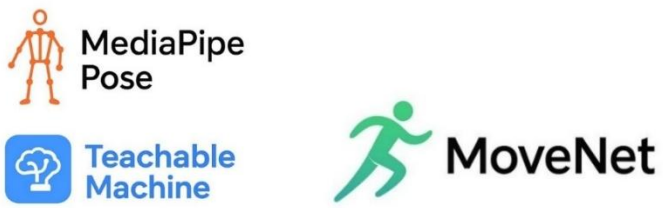

Figure 1. Pose Estimation Framework Logos Overview.

Based on an analysis of available solutions and a comparison of technologies, principles were identified that are key to the future development of real-time ergonomic systems in industry. The findings indicate that camera-based approaches using computer vision algorithms represent a promising alternative to wearable sensors, particularly in terms of easy implementation, lower operating costs and the possibility of continuous scanning without compromising worker comfort. However, for their successful use, it is necessary to ensure reliable detection of key points, stable calculations of angular parameters, and appropriate linking to ergonomic metrics that can be automated. At the same time, it has been demonstrated that evaluation metrics such as RULA and REBA are most suitable for implementation in computer vision systems from an automation perspective, as their input requirements correspond to the type of data obtained from human position estimation algorithms. Challenges that need to be addressed in the future have also been identified, such as the sensitivity of models to changes in lighting conditions, limited accuracy in complex movements, and the need to consider the context of the work task when interpreting results. These findings provide a framework for directing further research in the field of real-time ergonomic assessment, indicating which technologies have potential and what conditions must be met for their effective deployment in manufacturing companies. [8–10]

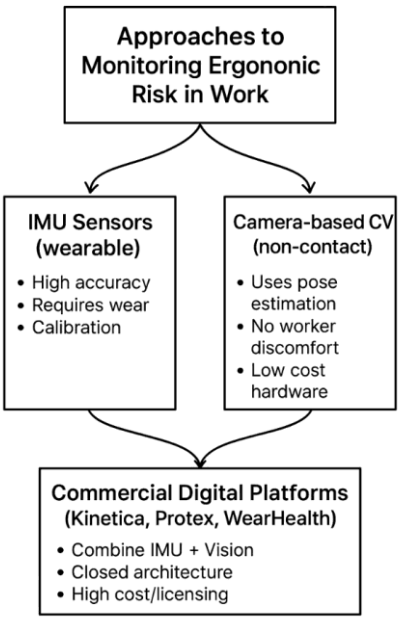

Figure 2. Schematic comparison of ergonomics monitoring approaches.

3. Results

Based on the analysis of available solutions and comparison of technologies, principles were identified that are key to the future development of real-time ergonomic systems in industry. The findings indicate that camera-based approaches using computer vision algorithms represent a promising alternative to wearable sensors, particularly in terms of easy implementation, lower operating costs and the possibility of continuous monitoring without compromising worker comfort. However, for their successful use, it is necessary to ensure reliable detection of key points, stable calculations of angular parameters, and appropriate linking to ergonomic metrics that can be automated. At the same time, it has been demonstrated that evaluation metrics such as RULA and REBA are most suitable for implementation in computer vision systems from an automation perspective, as their input requirements correspond to the type of data obtained from human position estimation algorithms. Challenges that need to be addressed in the future have

also been identified, such as the sensitivity of models to changes in lighting conditions, limited accuracy in complex movements, and the need to consider the context of the work task when interpreting results. These findings provide a framework for directing further research in the field of real-time ergonomic assessment, indicating which technologies have potential and what conditions must be met for their effective deployment in manufacturing companies.

4. Discussion

An analysis of available technologies for monitoring ergonomic risks in industrial environments has revealed a number of strengths that indicate the potential of modern digital tools for future use. The most significant advantages include contactless camera scanning, which eliminates the need for wearable sensors and thus does not compromise worker comfort. Equally important is the high speed of detection of key body points in models such as MediaPipe, Teachable Machine or MoveNet, while these algorithms maintain low hardware requirements and enable real-time data processing. Of the ergonomic methods, RULA and REBA have proven to be the most suitable for automation using computer vision, as they work with clearly defined angular criteria. The OWAS method has proven to be suitable in situations where high detection accuracy cannot be ensured, as it works with the categorisation of body positions. The limitations identified include factors that need to be considered when implementing these technologies in a real production environment. The most significant problem is the sensitivity of camera solutions to lighting conditions, which can negatively affect detection reliability. Limited accuracy is also possible with fast or obscured movements, which cause the loss or inaccurate rendering of key points. A cost comparison identified that commercial wearable systems require high investment not only in procurement but also in maintenance and calibration. At the same time, in order to correctly evaluate ergonomic results, it is necessary to know the nature of the specific work task, as some technologies are unable to distinguish between natural work movements and genuinely risky positions. This may limit their universal use.

Summary of strengths and limitations in the current state of real-time ergonomic data assessment in industrial production:

- Camera solutions offer contactless data collection without the need for wearable devices.
- Algorithms such as MediaPipe, Teachable Machine, or MoveNet provide high detection speeds with low hardware requirements.
- The traditional RULA and REBA methods are suitable for automation thanks to clearly defined angular criteria.
- OWAS is applicable in environments with lower detection accuracy;
- The sensitivity of camera systems to lighting conditions is a limitation in practical applications.
- Fast or obscured movements reduce detection accuracy.
- Commercial wearable systems are expensive to purchase and maintain.
- Interpretation of results often requires knowledge of the specific work context.

Table 1. Comparison of Technologies for Real-Time Ergonomic Assessment.

Technology	Detection Accuracy	Processing Speed	Hardware Requirements	Suitability for Industrial Environments	Compatibility with RULA/REBA
IMU systems (Xsens, Noraxon)	Very high	High	Wearable sensors, calibration required	Medium (worker discomfort, attachment needed)	High
Commercial camera systems (Kinetica, Protex)	High	High	Professional cameras, licensed software	High but expensive	High
Computer vision – MediaPipe	Medium to high	Very high	Standard RGB camera, CPU/GPU	High (low cost, easy setup)	Very good
Computer vision – MoveNet	High	Very high	Standard RGB camera, low computational load	Very high	Very good
Teachable Machine (pose model)	Medium	High	Minimum requirements	Medium (simplified keypoints)	Limited
Manual methods (RULA/REBA)	Depends on evaluator	Low	None	Low for real-time use	N/A

5. Conclusions

A comparative analysis of current approaches to monitoring ergonomic risks in industrial environments shows that camera-based solutions supported by pose estimation algorithms represent a promising direction for real-time assessment. Although wearable IMU systems remain the most accurate option, their practical use is limited by worker discomfort, the need for calibration, and high operating costs. Commercial platforms provide robust functionality but rely on closed architectures and costly licensing models, limiting their flexibility of use, especially for small and medium-sized enterprises. The evaluation further showed that open-source computer vision models such as MediaPipe and MoveNet offer a favourable balance between accuracy, speed and hardware simplicity. Their ability to extract key body points in real time makes them suitable for automated ergonomic scoring, especially when combined with methods such as RULA or REBA. Nevertheless, several challenges remain, including sensitivity to environmental conditions, reduced performance during occlusion or rapid movements, and the need to incorporate context information about specific work tasks.

Overall, the findings emphasise that future developments in real-time ergonomic risk monitoring should focus on improving the robustness of computer vision-based models, improving integration with standardised ergonomic metrics, and creating modular solutions that can be easily deployed in different industrial environments. Such advances can make ergonomic risk assessment accessible, continuous, and practical, thereby promoting safer and more productive manufacturing environments.

Acknowledgments: This work was supported by research grant VEGA 1/0302/25 and also was supported by research grant KEGA 014TUKE-4/2024.

Conflicts of Interest: The authors declare no conflict of interest

References

1. Ciccarelli, M.; Papetti, A.; Germani, M. Empowering Industry 5.0: Automated Sensor-Based Ergonomic Risk Assessment. *International Journal on Interactive Design and Manufacturing* 2025, doi:10.1007/s12008-025-02412-5.
2. Arbealez Garces, G. Development of an IMU-Based Ergonomics Assessment Tool for Virtual Reality. 2025, doi:10.20870/IJVR.2020...3316.
3. Koca, R.; Koca, Y.B. Anatomy-Based Assessment of Spinal Posture Using IMU Sensors and Machine Learning. *Sensors* 2025, *25*, 5963, doi:10.3390/s25195963.
4. Li, Z.; Zhang, R.; Lee, C.H.; Lee, Y.C. An Evaluation of Posture Recognition Based on Intelligent Rapid Entire Body Assessment System for Determining Musculoskeletal Disorders. *Sensors (Switzerland)* 2020, *20*, 1–21, doi:10.3390/s20164414.
5. Wu, Z.; Hoang, D.; Lin, S.-Y.; Xie, Y.; Chen, L.; Lin, Y.-Y.; Wang, Z.; Fan, W. MM-Hand: 3D-Aware Multi-Modal Guided Hand Generative Network for 3D Hand Pose Synthesis. 2020.
6. Battini, D.; Berti, N.; Finco, S.; Guidolin, M.; Reggiani, M.; Tagliapietra, L. WEM-Platform: A Real-Time Platform for Full-Body Ergonomic Assessment and Feedback in Manufacturing and Logistics Systems. *Comput Ind Eng* 2022, *164*, doi:10.1016/j.cie.2021.107881.
7. Guo, Z.; Zhou, D.; Hao, A.; Wang, Y.; Wu, H.; Zhou, Q.; Yu, D.; Zeng, S. An Evaluation Method Using Virtual Reality to Optimize Ergonomic Design in Manual Assembly and Maintenance Scenarios. *International Journal of Advanced Manufacturing Technology* 2022, *121*, 5049–5065, doi:10.1007/s00170-022-09657-4.
8. Iyer, H.; Macwan, N.; Guo, S.; Jeong, H. Computer-Vision-Enabled Worker Video Analysis for Motion Amount Quantification. 2025.
9. Mortensen, J.; Trkov, M.; Merryweather, A. Improved Ergonomic Risk Factor Assessment Using Opensim and Inertial Measurement Units. In Proceedings of the Proceedings - 2018 IEEE/ACM International Conference on Connected Health: Applications, Systems and Engineering Technologies, CHASE 2018; Institute of Electrical and Electronics Engineers Inc., 2018; pp. 27–28.
10. Govaerts, R.; De Bock, S.; Provyn, S.; Vanderborght, B.; Roelands, B.; Meeusen, R.; De Pauw, K. The Impact of an Active and Passive Industrial Back Exoskeleton on Functional Performance. *Ergonomics* 2024, *67*, 597–618, doi:10.1080/00140139.2023.2236817.

TECHNICAL UNIVERSITY OF KOŠICE
Faculty of Mechanical Engineering

MSC Senescence in Prolonged Biocompatibility Evaluation of Biomaterials

Jana Čajková [1,*], Marianna Trebuňová [1] and Darina Bačenková [1]

[1] Technical University of Košice, Košice, Slovakia;
* Correspondence: jana.cajkova@tuke.sk

Abstract: Mesenchymal stem cells (MSCs) are widely employed in the biocompatibility evaluation of biomaterials due to their regenerative potential, immunomodulatory properties, and relevance to bone and connective tissue engineering. While short-term in vitro assays provide essential information on cytotoxicity and early cell–material interactions, prolonged culture conditions are increasingly used to better reflect long-term implantation scenarios. Under such conditions, cellular senescence emerges as a critical but often underestimated biological response that can substantially influence experimental outcomes and their interpretation. This review addresses the role of MSC senescence in long-term biocompatibility testing of biomaterials, with emphasis on their molecular hallmarks, functional consequences, and methodological implications. Key senescence-associated features, including irreversible cell cycle arrest, altered differentiation capacity, metabolic reprogramming, and the development of a senescence-associated secretory phenotype, are discussed in the context of sustained cell–material interactions. Particular attention is given to the use of senescence detection strategies, notably β-galactosidase activity assays, as practical tools for monitoring senescence onset during extended in vitro evaluations. The review highlights how biomaterial composition, degradation behavior, surface chemistry, and mechanical properties may modulate senescence-related pathways in MSCs, thereby affecting the perceived biocompatibility of materials.

Keywords: mesenchymal stem cells; cellular senescence; biomaterials; biocompatibility

1. Introduction

In the context of in vitro cultivation for biomaterial analysis, cellular senescence represents a critical biological response that can arise during prolonged cell–material interaction and significantly influence the interpretation of biocompatibility outcomes [1]. When mesenchymal stem cells or other primary cells are cultured on or in contact with biomaterials for extended periods, they are exposed not only to replicative stress associated with serial cell divisions but also to material-induced stimuli, including surface chemistry, topography, stiffness, degradation products, and the release of ions or low-molecular-weight compounds [2]. These factors can cumulatively activate stress-response pathways that promote the transition of cells into a senescent state, independent of acute cytotoxic effects [3] [4].

To reliably identify senescence under such cultivation conditions, senescence-associated β-galactosidase (SA-β-gal) activity assays are among the most widely used and practical analytical tools [5]. β-Galactosidase activity in senescent cells reflects increased lysosomal content and elevated expression of lysosomal hydrolases, which become detectable at suboptimal pH conditions (typically pH ~6.0). Commercial β-galactosidase activity kits exploit this characteristic by providing chromogenic or fluorogenic substrates that are cleaved by β-galactosidase specifically in senescent cells, resulting in a measurable color-

imetric or fluorescent signal. In adherent cultures on biomaterials, these assays allow direct visualization and semi-quantitative assessment of senescent cells at the cell–material interface without requiring cell detachment or extensive sample processing [5] [3].

2. Mesenchymal stem cells

Mesenchymal stem cells (MSCs) are multipotent stromal cells commonly used in in vitro biocompatibility testing due to their high sensitivity to environmental cues and their direct relevance to regenerative medicine and tissue engineering [2]. MSCs can be isolated from various adult tissues, including bone marrow, adipose tissue, and umbilical cord, and are characterized by their capacity for self-renewal, adherence to standard culture surfaces, and differentiation into mesodermal lineages such as osteoblasts, chondrocytes, and adipocytes (Figure 1.). These properties make MSCs particularly suitable for evaluating biomaterials intended for bone, cartilage, and soft tissue applications [6] [7].

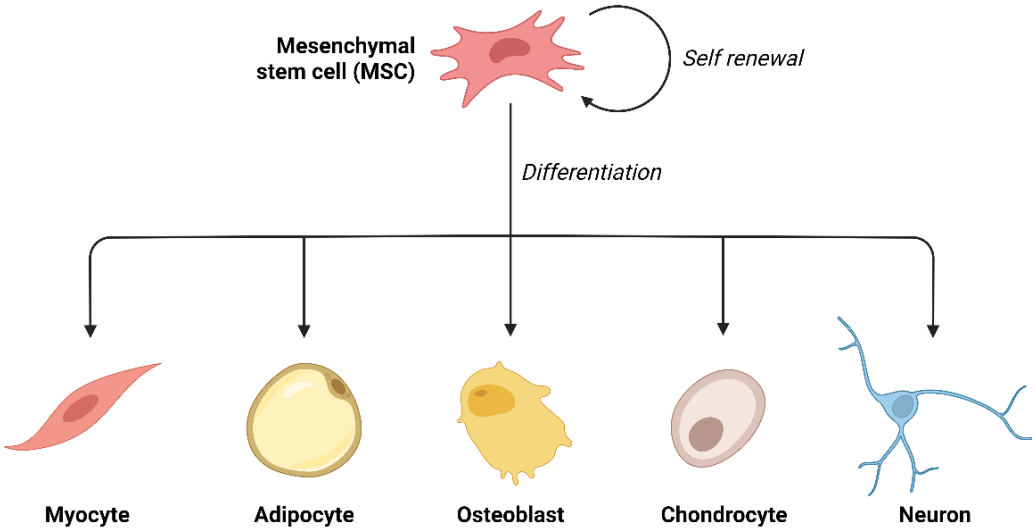

Figure 1. Differentiation potential of mesenchymal stem cells (MSCs). At the top, an MSC is shown with the ability to self-renew or differentiate. Arrows point downward to the various specialized cell types MSCs can become myocytes (muscle cells), adipocytes (fat cells), osteoblasts (bone cells), chondrocytes (cartilage cells), and neurons (nerve cells).

In biocompatibility testing, MSCs are valued because they respond dynamically to material-related parameters, including surface chemistry, roughness, stiffness, degradation behavior, and released by-products. Unlike immortalized cell lines, MSCs reflect physiologically relevant cellular responses, allowing more accurate assessment of how materials influence cell adhesion, proliferation, morphology, metabolic activity, and lineage commitment [8] [9]. As a result, MSC-based assays provide insight not only into cytotoxicity but also into the functional compatibility of biomaterials.

Importantly, MSCs are highly responsive to long-term culture conditions, making them a sensitive model for prolonged biocompatibility evaluation. Changes in MSCs behavior—such as reduced proliferation, altered morphology, impaired differentiation, or induction of cellular senescence—can indicate chronic material-induced stress that may not be detected in short-term assays. Therefore, MSCs are increasingly used to assess long-term cell–material interactions, supporting a more comprehensive understanding of biomaterial performance beyond simple cell survival [10].

Authors Koobatian et al. investigated how senescence affects the proliferation and smooth muscle differentiation of MSCs derived from bone marrow (BM-MSCs) and hair

follicles (HF-MSCs). They found that HF-MSCs are less prone to culture-induced senescence than BM-MSCs. Additionally, the study showed that HF-MSCs and BM-MSCs respond differently to mechanical cues, indicating that MSCs from distinct tissue sources may activate different pathways under the same conditions. These findings suggest that tissue engineering strategies should consider the MSC source, donor age, and culture duration to achieve optimal regenerative outcomes [11].

3. Cellular senescence

Cellular senescence is a stable and essentially irreversible state of cell cycle arrest that occurs in response to a variety of intrinsic and extrinsic stressors, while cells remain metabolically active and viable. Originally described as a consequence of replicative exhaustion due to telomere shortening, senescence is now recognized as a multifaceted biological program that can also be triggered prematurely by DNA damage, oxidative stress, oncogene activation, mitochondrial dysfunction, epigenetic alterations, and sustained environmental cues [12] [13].

During cellular senescence, cells undergo pronounced and characteristic morphological changes that reflect underlying alterations in cytoskeletal organization, chromatin structure, and intracellular metabolism [4]. One of the most consistently observed features is a marked increase in cell size, accompanied by a flattened and irregular morphology (Figure 2.). Senescent cells typically exhibit an expanded cytoplasmic area and reduced thickness, which contrasts with the smaller, spindle-shaped or polygonal morphology of proliferating cells. This enlargement is largely attributable to sustained metabolic activity in the absence of cell division, leading to the accumulation of cytoplasmic components and organelles [1] [14].

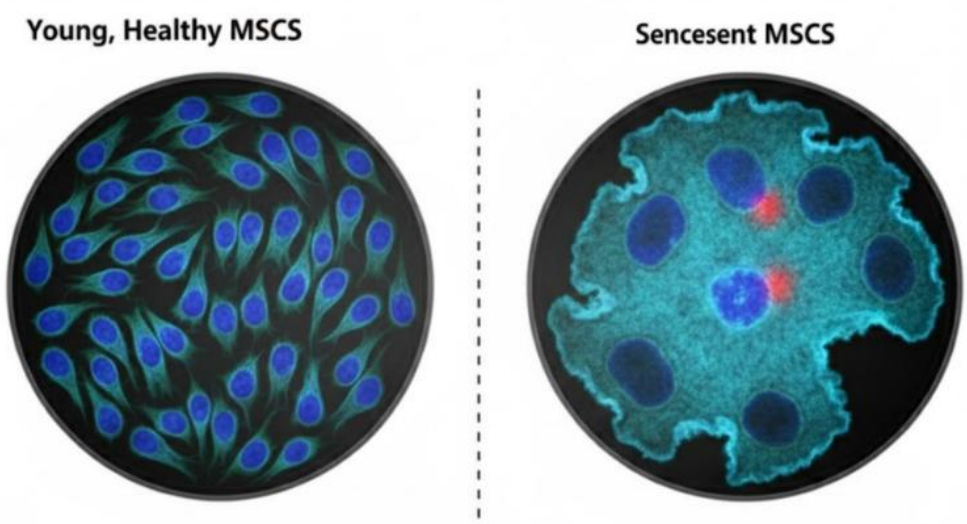

Figure 2. The ilustration compares young, healthy mesenchymal stem cells (MSCs) with senescent MSCs. Healthy MSCs appear elongated, spindle-shaped, and uniformly organized, with smaller, regular nuclei, reflecting active proliferation and intact cytoskeletal structure. In contrast, senescent MSCs are enlarged, flattened, and irregularly shaped, with expanded cytoplasm and larger, distorted nuclei, indicative of cytoskeletal reorganization and genomic stress. The comparison highlights the pronounced morphological changes that accompany MSC senescence during prolonged cultivation.

Senescence is an intrinsic cellular program that evolved as a protective mechanism [15] [16]. Under normal physiological conditions, it serves several beneficial functions.

During development, transient senescence contributes to tissue patterning and morphogenesis. In adult tissues, senescence acts as a tumor-suppressive safeguard, preventing the proliferation of cells that have accumulated excessive DNA damage, telomere shortening, or oncogenic stress [17]. In wound healing and tissue remodeling, short-lived senescent cells can promote repair through the controlled secretion of growth factors and cytokines, after which they are typically cleared by the immune system [4] [18].

4. Impact of Biomaterials on MSC Senescence

The interaction between MSCs and the biomaterials on which they are cultured plays a pivotal role in determining the onset and progression of cellular senescence during prolonged in vitro expansion [19]. Biomaterials are not merely passive substrates; their physicochemical properties—including composition, stiffness, topography, and surface chemistry—can profoundly influence MSCs behavior, proliferation, and maintenance of stemness. In tissue engineering, understanding how these factors modulate senescence is critical for designing scaffolds that support long-term cellular functionality [20].

Biomaterial composition is a key determinant of MSCs fate. Naturally derived matrices, such as collagen, hyaluronic acid, and chitosan, often provide bioactive motifs that mimic the native extracellular matrix (ECM), thereby preserving cell adhesion, proliferation, and differentiation potential [21] [22]. In contrast, purely synthetic polymers lacking bioactive signals may fail to provide the necessary cues to maintain MSCs "youth," leading to accelerated replicative senescence [23] [5]. Studies have demonstrated that hybrid scaffolds combining natural and synthetic components—such as nano-hydroxyapatite/chitosan/PLGA composites—can reduce the expression of senescence while maintaining stem cell proliferation over extended passages [24] [25] [26].

Substrate stiffness is a critical mechanical cue that influences MSCs morphology, cytoskeletal organization, and mechanotransduction pathways. Soft substrates that approximate the elasticity of native tissue have been shown to mitigate stress-induced senescence, whereas overly rigid surfaces can promote cytoskeletal tension, DNA damage, and premature growth arrest. MSCs sense and respond to these mechanical cues through integrin-mediated adhesion complexes and downstream signaling pathways, which ultimately impact the balance between proliferation and senescence [27] [28].

The topographical features of scaffolds, including nanoscale roughness, porosity, and fiber alignment, also modulate senescence. Nanostructured surfaces can enhance cell-matrix interactions, promote cytoskeletal organization, and facilitate nutrient exchange, thereby delaying the onset of senescence. Surfaces with irregular or non-physiological topographies may induce cellular stress and contribute to early senescence, particularly under long-term culture conditions [29].

Evaluating senescence on candidate biomaterials is therefore essential for scaffold optimization. Techniques such as SA-β-galactosidase activity assays, expression analysis of cyclin-dependent kinase inhibitors, and morphological assessment of MSCs provide complementary insights into how scaffold properties influence cellular aging. Incorporating these assessments early in biomaterial development can guide the design of substrates that support long-term MSC functionality, enhancing the translational potential of tissue-engineered constructs [30] [31].

5. Conclusions

Cellular senescence represents a major limitation in the long-term expansion and functional application of MSCs for tissue engineering and regenerative medicine. The onset of senescence compromises proliferation, differentiation potential, and the overall regenerative capacity of MSCs, thereby influencing the outcomes of biomaterials-based therapies [17]. Biomimetic scaffolds that recapitulate key biochemical, mechanical, and topographical features of the native extracellular matrix can preserve MSC stemness, delay senescence, and maintain functional potential even during prolonged culture [32] [33].

The differential responses of MSCs derived from various tissue sources to both intrinsic and extrinsic cues underscore the importance of tailoring biomaterials and culture conditions to cell origin, donor age, and intended application. Incorporating comprehensive senescence assessment—including SA-β-gal activity, molecular markers, and functional assays—into biomaterials evaluation allows for the rational design of scaffolds that support long-term cell viability and regenerative efficacy [34] [35].

Given the critical impact of cellular senescence on MSCs functionality, it is increasingly recognized that senescence evaluation should be incorporated into standard biocompatibility testing. Routine assessment of senescence—using assays such as SA-β-gal activity, expression of cell cycle inhibitors, and morphological analysis—can provide a more biologically relevant measure of scaffold performance over prolonged culture periods [22]. Integrating these assessments into conventional workflows allows researchers to detect early signs of functional decline, compare materials more reproducibly, and make informed decisions on scaffold design.

In the context of MSC longevity within 3D systems, these three abbreviations represent the primary drivers of cellular aging and environmental stress. SIPS, or Stress-Induced Premature Senescence, differs from natural aging as it is an accelerated state of cell cycle arrest triggered by external stressors such as sub-optimal scaffold stiffness or chemical toxicity within a bioreactor [36]. This process is often fueled by ROS, or Reactive Oxygen Species, which are highly reactive molecules that accumulate during cellular metabolism and cause oxidative damage to DNA and proteins. Once these cells are compromised, they develop a SASP, or Senescence-Associated Secretory Phenotype, transforming into "pro-inflammatory factories" that secrete cytokines like IL-6 to negatively influence the surrounding ECM and neighboring healthy cells [37] [17].

To counteract these degenerative pathways, bioreactors provide critical advantages over static cultures by ensuring efficient mass transfer, which prevents the localized buildup of ROS and metabolic waste. By maintaining precise control over O2 tension and delivering constant nutrient perfusion, these systems minimize the environmental triggers of SIPS, while the application of controlled mechanical shear stress helps maintain MSC multipotency and delays the onset of SASP [38] [22].

Acknowledgments: This research was funded by grant number: **KEGA 018TUKE-4/2023** by Cultural and Educational Grant Agency MŠVVaŠ SR; and **VEGA 1/0403/25** by Scientific Grant Agency.

Conflicts of Interest: "The authors declare no conflict of interest."

References

1. D. Muñoz-Espín a M. Serrano, "Cellular senescence: from physiology to pathology", *Nat. Rev. Mol. Cell Biol.*, roč. 15, č. 7, s. 482–496, 2014.
2. M. Trebuňová *et al.*, "Evaluation of biocompatibility of PLA/PHB/TPS polymer scaffolds with different additives of ATBC and OLA plasticizers", *J. Funct. Biomater.*, roč. 14, č. 8, s. 412, 2023.
3. A. Hernandez-Segura, J. Nehme, a M. Demaria, "Hallmarks of cellular senescence", *Trends Cell Biol.*, roč. 28, č. 6, s. 436–453, 2018.
4. A. Calcinotto, J. Kohli, E. Zagato, L. Pellegrini, M. Demaria, a A. Alimonti, "Cellular senescence: aging, cancer, and injury", *Physiol. Rev.*, roč. 99, č. 2, s. 1047–1078, 2019.
5. K. Itahana, J. Campisi, a G. P. Dimri, "Methods to detect biomarkers of cellular senescence: the senescence-associated β-galactosidase assay", *Biol. Aging Methods Protoc.*, s. 21–31, 2007.
6. M. Trebuňová, J. Demeterová, D. Bačenková, V. Rajťuková, a J. Živčák, "Surface biocompatibility of porous titanium structures with stem cells", roč. 53, č. 1, 2023, doi: https://doi.org/10.14311/CTJ.2023.1.03.
7. S. D. Sandhaanam, G. Pathalam, S. Dorairaj, a V. Savariar, "Mesenchymal stem cells (MSC): identification, proliferation and differentiation", 2013.
8. Y.-K. Wang a C. S. Chen, "Cell adhesion and mechanical stimulation in the regulation of mesenchymal stem cell differentiation", *J. Cell. Mol. Med.*, roč. 17, č. 7, s. 823–832, júl. 2013, doi: 10.1111/jcmm.12061.
9. X.-Y. He, H.-M. Yu, S. Lin, a Y.-Z. Li, "Advances in the application of mesenchymal stem cells, exosomes, biomimetic materials, and 3D printing in osteoporosis treatment", *Cell. Mol. Biol. Lett.*, roč. 26, č. 1, s. 47, nov. 2021, doi: 10.1186/s11658-021-00291-8.
10. D. Bačenková *et al.*, "In vitro model of human trophoblast in early placentation", *Biomedicines*, roč. 10, č. 4, s. 904, 2022.

11. M. T. Koobatian, M.-S. Liang, D. D. Swartz, a S. T. Andreadis, "Differential Effects of Culture Senescence and Mechanical Stimulation on the Proliferation and Leiomyogenic Differentiation of MSC from Different Sources: Implications for Engineering Vascular Grafts", *Tissue Eng. Part A*, roč. 21, č. 7–8, s. 1364–1375, apr. 2015, doi: 10.1089/ten.tea.2014.0535.
12. A. Kowald, J. F. Passos, a T. B. Kirkwood, "On the evolution of cellular senescence", *Aging Cell*, roč. 19, č. 12, s. e13270, 2020.
13. R. Kumari a P. Jat, "Mechanisms of cellular senescence: cell cycle arrest and senescence associated secretory phenotype", *Front. Cell Dev. Biol.*, roč. 9, s. 645593, 2021.
14. W. Wei a S. Ji, "Cellular senescence: Molecular mechanisms and pathogenicity", *J. Cell. Physiol.*, roč. 233, č. 12, s. 9121–9135, 2018.
15. M. Piechota *et al.*, "Is senescence-associated β-galactosidase a marker of neuronal senescence?", *Oncotarget*, roč. 7, č. 49, s. 81099, 2016.
16. R. I. Martínez-Zamudio, H. K. Dewald, T. Vasilopoulos, L. Gittens-Williams, P. Fitzgerald-Bocarsly, a U. Herbig, "Senescence-associated β-galactosidase reveals the abundance of senescent CD8+ T cells in aging humans", *Aging Cell*, roč. 20, č. 5, s. e13344, 2021.
17. N. N. Hooten a M. K. Evans, "Techniques to induce and quantify cellular senescence", *J. Vis. Exp. JoVE*, č. 123, s. 55533, 2017.
18. D. Bandyopadhyay, C. Gatza, L. A. Donehower, a E. E. Medrano, "Analysis of Cellular Senescence in Culture In Vivo: The Senescence-Associated β-Galactosidase Assay", *Curr. Protoc. Cell Biol.*, roč. 27, č. 1, s. 18–9, 2005.
19. D. E. Rodríguez-Fuentes, L. E. Fernández-Garza, J. A. Samia-Meza, S. A. Barrera-Barrera, A. I. Caplan, a H. A. Barrera-Saldaña, "Mesenchymal Stem Cells Current Clinical Applications: A Systematic Review", *Arch. Med. Res.*, roč. 52, č. 1, s. 93–101, jan. 2021, doi: 10.1016/j.arcmed.2020.08.006.
20. D. F. Williams, "The plasticity of biocompatibility", *Biomaterials*, roč. 296, s. 122077, 2023.
21. F. Rosso, A. Giordano, M. Barbarisi, a A. Barbarisi, "From cell–ECM interactions to tissue engineering", *J. Cell. Physiol.*, roč. 199, č. 2, s. 174–180, 2004.
22. J. Cajkova, M. Trebunova, a D. Bacenkova, "Organoids as models for tissue engineering and biomedical applications", *Organoids Models Tissue Eng. Biomed. Appl.*, roč. 11, č. 3, doi: https://doi.org/10.22306/atec.v11i3.276.
23. Y. Zhang, R. Judeh, S. Aravind, H. Zreiqat, a Z. Lu, "Mesenchymal Stem Cell Senescence and Biomaterial-Based Next-Generation Rejuvenation Strategy", *Tissue Eng. Part B Rev.*, sep. 2025, doi: 10.1177/19373341251372962.
24. W. Liu, Y.-Y. Yang, a Z.-J. Shi, "Post-translational modifications in the oral microenvironment: Stem cell regulation from periodontal regeneration to oral cancer therapy", *World J. Stem Cells*, roč. 17, č. 11, s. 112702, 2025.
25. H. Wei, J. Cui, K. Lin, J. Xie, a X. Wang, "Recent advances in smart stimuli-responsive biomaterials for bone therapeutics and regeneration", *Bone Res.*, roč. 10, č. 1, s. 17, 2022.
26. F. Danhier, E. Ansorena, J. M. Silva, R. Coco, A. Le Breton, a V. Préat, "PLGA-based nanoparticles: an overview of biomedical applications", *J. Controlled Release*, roč. 161, č. 2, s. 505–522, 2012.
27. Y. Wu *et al.*, "The combined effect of substrate stiffness and surface topography on chondrogenic differentiation of mesenchymal stem cells", *Tissue Eng. Part A*, roč. 23, č. 1–2, s. 43–54, 2017.
28. D. Bačenková, M. Trebuňová, a J. Čajková, "Enhancing biomaterial performance: the advantages and applications of Collagen coating", *Enhancing Biomater. Perform. Advant. Appl. Collagen Coat.*, roč. 11, č. 1, s. 25–30, doi: https://doi.org/10.22306/atec.v11i1.269.
29. D. Bačenková, J. Demeterová, E. Dosedla, P. Gašparová, a M. Trebuňová, "The use of alginate in the cultivation of mesenchymal cells in biomedical engineering", *Acta Technol.*, roč. 10, č. 2, 2024, doi: https://doi.org/10.22306/atec.v10i2.198.
30. M. Zinner, I. Lukonin, a P. Liberali, "Design principles of tissue organisation: How single cells coordinate across scales", *Curr. Opin. Cell Biol.*, roč. 67, s. 37–45, 2020.
31. J. Čajková *et al.*, "Influence of Oligomeric Lactic Acid and Structural Design on Biodegradation and Absorption of PLA-PHB Blends for Tissue Engineering", *Polymers*, roč. 16, č. 21, s. 2969, 2024.
32. M. Trebuňová, J. Demeterová, D. Bačenková, V. Rajťuková, a J. Živčák, "Surface biocompatibility of porous titanium structures with stem cells", *Clin. Technol.*, roč. 53, č. 1, 6 2023, doi: https://doi.org/10.14311/CTJ.2023.1.03.
33. M. Trebuňová, D. Bačenková, a J. Čajková, "Hydrogels as bioactive scaffolds in biomedical engineering", *Hydrogels Bioact. Scaffolds Biomed. Eng.*, roč. 11, č. 2, doi: https://doi.org/10.22306/atec.v11i2.272.
34. X. Su, T. Wang, a S. Guo, "Applications of 3D printed bone tissue engineering scaffolds in the stem cell field", *Regen. Ther.*, roč. 16, s. 63–72, 2021.
35. M. Modrák, M. Trebuňová, A. F. Balogová, R. Hudák, a J. Živčák, "Biodegradable Materials for Tissue Engineering: Development, Classification and Current Applications", *J. Funct. Biomater.*, roč. 14, č. 3, 2023, doi: 10.3390/jfb14030159.
36. L. Freed, G. Vunjak-Novakovic, a R. Langer, "Cultivation of cell-polymer cartilage implants in bioreactors", *J. Cell. Biochem.*, roč. 51, č. 3, s. 257–264, 1993.
37. D. Bačenková *et al.*, "Analysis of Same Selected Immunomodulatory Properties of Chorionic Mesenchymal Stem Cells", *Appl. Sci.*, roč. 10, č. 24, 2020, doi: 10.3390/app10249040.
38. J. L. Kirkland a T. Tchkonia, "Cellular senescence: a translational perspective", *EBioMedicine*, roč. 21, s. 21–28, 2017.

TECHNICAL UNIVERSITY OF KOŠICE
Faculty of Mechanical Engineering

Development of an Apparatus for Recycling Metal Hydride Alloys

Peter Čurma [1,*], Peter Milenovský [1] and Marián Lázár [1]

[1] Department of Energy Engineering, Faculty of Mechanical Engineering, Technical University of Košice, 04200 Košice, Slovakia; peter.curma@tuke.sk; peter.milenovsky@tuke.sk; marian.lazar@tuke.sk
* Correspondence: peter.curma@tuke.sk; Tel.: +421 911 078 466

Abstract: The present paper focuses on the recycling of metal hydride alloys through a melting process performed using a newly developed prototype device. Particular attention is devoted to the analysis of induction heating parameters that significantly influence the efficiency of metal hydride alloy melting. The principles of induction heating, its effects on the properties of the molten metal hydride alloys, and potential approaches to the optimisation of the recycling process are examined in detail. In addition, the paper presents the structural design of the induction heating system, including the crucible. The configuration and functional design of the oscillator module, power supply module, and water-cooling module employed for precise control of the melting process are described comprehensively.

Keywords: metal hydride alloy, recycling, melting

1. Introduction

Metal hydride alloys play an increasingly important role in modern engineering applications, particularly in fields related to hydrogen storage, clean energy systems, and advanced materials research. Their chemical behavior is complex, as these alloys can participate in nucleophilic, electrophilic, and radical reactions depending on the nature of the hydride bond and surrounding reactants. This reactivity, combined with extremely high melting points—typically above 1,300 °C—creates demanding conditions for their processing. When such materials must be melted or recycled, traditional thermal technologies often struggle to maintain purity, temperature stability, or sufficient heating efficiency [1].

For these reasons, induction heating has emerged as one of the most practical approaches for handling metal hydrides. Unlike surface-based heating methods, induction generates heat directly within the material through electromagnetic induction, which significantly enhances process efficiency. This direct transfer of energy reduces heat losses, minimizes unwanted temperature gradients, and allows for precise heating control—advantages that are particularly relevant for sensitive hydride materials [2] and [3].

The study summarized and expanded here focuses on the design and development of a prototype induction heating system dedicated to the recycling of metal hydride alloys before melting. The research analyzes the physical principles that guide the heating process, outlines the structural design of a three-module heating device, and discusses important operational challenges such as heat penetration, crucible compatibility, and thermal regulation. The ultimate goal is to present a functional technological solution capable of melting hydride alloys efficiently while maintaining material purity and preventing degradation.

The recycled material in this study is the commercial hydrogen storage alloy Hydralloy C5, which is an AB_2-type Ti–Zr-based intermetallic alloy with added elements such as V, Cr, Mn, and Ni. Because of the presence of highly reactive elements (especially Ti and

Zr), the alloy is prone to oxidation at high temperatures, which necessitates strict control of the crucible compatibility and atmosphere cleanliness during the melting process.

2. Fundamentals of Induction Heating and Their Relevance to Hydrides

Induction heating relies on electromagnetic principles where alternating current in a coil generates a changing magnetic field, inducing currents inside conductive materials placed nearby. In the described device, the induction coil serves as the primary winding of an air-core transformer, while the metal charge acts as the secondary [4]. Heat generation occurs due to two main mechanisms:

1. Eddy current heating

These currents form loops within the alloy, and because the material has a measurable electrical resistance, the circulating currents convert electrical energy into thermal energy. The magnitude of this heating depends on resistivity, magnetic coupling, and frequency. Since metal hydrides often have a fine microstructure with increased resistance, eddy-current heating becomes the dominant heating mechanism for most of them.

2. Hysteresis heating

This effect is present only in ferromagnetic materials. During each cycle of magnetization and demagnetization, energy is dissipated, contributing to heat generation. The magnitude of this effect depends on the area of the hysteresis loop and the operating frequency. For paramagnetic crucible materials—such as tungsten—this loss is negligible, which helps reduce unwanted heating of the crucible walls [5].

3. Skin depth and its importance

A critical concept in induction heating is skin depth, the distance below the material's surface where current density remains significant. Skin depth decreases with increasing frequency, causing currents to concentrate near the surface. For thick materials such as metal hydride charges, using lower frequencies helps deliver heat more uniformly throughout the material.

However, practical constraints sometimes require the use of higher frequencies—especially when rapid heating or controlled surface melting is desired. The relationship between frequency, material conductivity, and magnetic permeability must therefore be carefully considered when designing induction systems [6].

4. Crucible Selection and Material Challenges

Melting metal hydrides presents several difficulties beyond reaching extremely high temperatures. Their structure tends to increase electrical resistance, making uniform heating harder to achieve. Additionally, hydrides may react with crucible materials at elevated temperatures. To avoid such complications, the researchers selected a tungsten crucible, which offers several advantages:

- exceptional thermal resistance and mechanical stability,
- chemical inertness, preventing undesirable reactions,
- resistance to deformation under extreme temperatures,
- paramagnetic behavior, reducing magnetic energy losses.

The crucible's dimensions and geometry were optimized to support uniform heat distribution and stable electromagnetic coupling inside the induction coil (see Figure 1) [3].

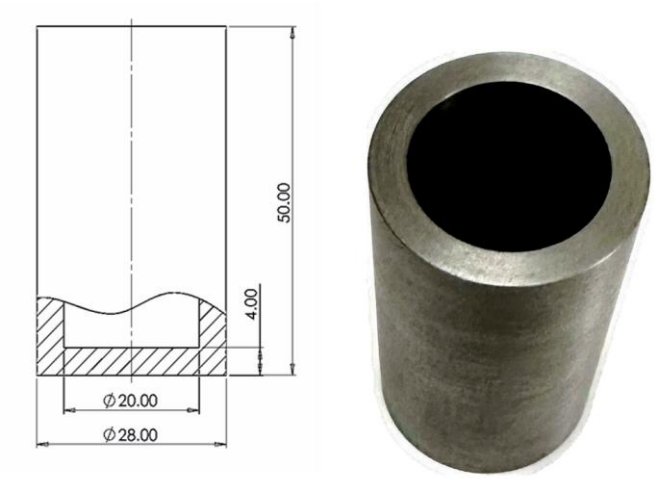

Figure 1. Tungsten crucible.

5. Adhesion and protective coatings

A significant issue in melting hydride alloys is the tendency of molten material to adhere to crucible walls. Mechanical adhesion occurs when the melt infiltrates microscopic pores in sintered tungsten, while chemical adhesion may arise from high-temperature reactions or diffusion processes. Uncontrolled wetting can damage both the crucible and the quality of the melt.

To prevent these problems, a thin boron nitride (BN) coating is typically applied to the crucible interior. BN is chemically inert, thermally stable, and forms a non-reactive barrier between the molten metal and crucible surface. When applied as a spray or slurry and subsequently heat-treated at temperatures between 500 and 800 °C, the coating provides reliable protection without contaminating the melt.

In addition to BN, yttrium oxide (Y_2O_3) is also widely used as a high-performance crucible coating for reactive metal processing. Y_2O_3 exhibits exceptional resistance to chemical attack, minimal wetting by molten metals and hydrides, and excellent stability at temperatures exceeding 2000 °C. Its dense microstructure prevents infiltration of the melt, while its thermodynamic inertness minimizes interfacial reactions. As a result, Y_2O_3 coatings—applied by spraying, slurry deposition, or plasma coating—serve as an effective alternative or complementary barrier to BN, particularly in environments where stronger chemical resistance or higher thermal durability is required [7].

For processing Hydralloy C5, the choice of the protective coating reflects the high reactivity of Ti–Zr-based alloys. Y_2O_3 is preferred because it has thermodynamic stability and relatively low wettability by reactive melts under fully melting conditions. Bilayer Y_2O_3 coatings are expected to have higher chemical resistance compared to BN to highly reactive hydride alloys above the liquidus temperature.

6. Design and Construction of the Prototype Heating System

All experiments are conducted under a continuous flow of high-purity argon directed to the melting zone. Prior to heating, the working area is flushed with argon to reduce the presence of oxygen and moisture in the immediate vicinity of the crucible. To improve safety, manage heat, and simplify operation, the induction heating apparatus was constructed as a three-module system. Each module contributes to a different functional aspect of the overall device.

Module 1 – Oscillator and Induction Coil

The heart of the system is a Zero Voltage Switching (ZVS) oscillator (see Figure 2), chosen for its efficiency and relative simplicity. It operates as a resonant converter that

naturally minimizes switching losses [8]. Powered by a DC supply, the oscillator produces a sinusoidal current in the primary coil, which in turn induces currents within the crucible and charge.

The primary coil is made from a thin-walled copper tube that allows coolant circulation during operation. With a solenoid-shaped geometry and seven turns, it was engineered to provide adequate magnetic field strength and coupling efficiency. A thermistor is attached to monitor the coil's surface temperature, preventing overheating [9] and [10].

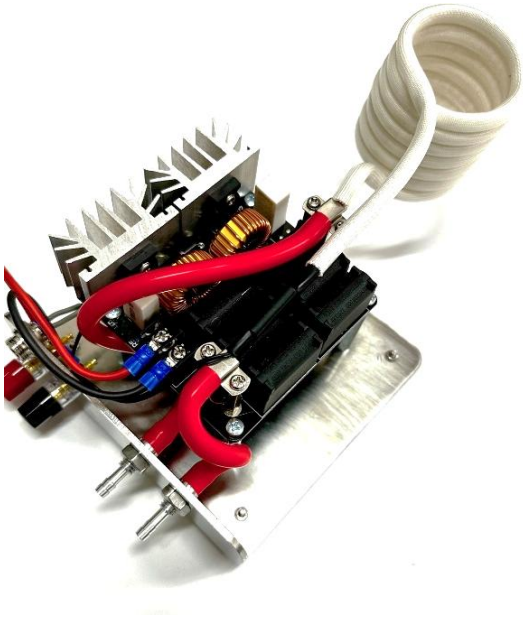

Figure 2. Oscillator and induction coil.

Module 2 – Power Supply

The second module contains a robust 48 V, 21 A DC power supply, equipped with forced-air cooling and protective components such as fuses and an emergency disconnect switch (see Figure 3). Because induction heating can produce high currents and rapid load changes, stable power regulation is essential. Real-time voltage indicators ensure that the operator can monitor the system's behavior during operation.

Figure 3. Power supply.

Module 3 – Cooling System

Effective thermal management is critical for preventing damage to the coil and electronic components. Module 3 (see Figure 4) uses an active water-cooling system consisting of:

- a forced-air cooled heat exchanger,
- a circulation pump,
- temperature-controlled fan activation,
- a coolant based on diluted ethylene glycol.

The system automatically activates cooling once the coil temperature exceeds 40 °C and continues until it drops to a safe threshold. This integrated thermal protection ensures stable operation even under prolonged heating.

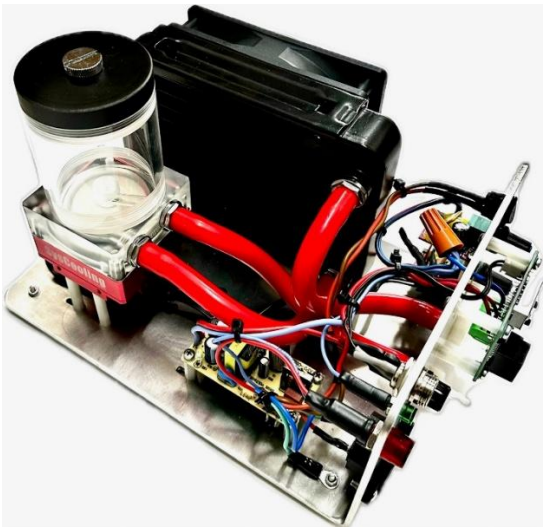

Figure 4. Cooling system.

7. Thermal Behavior and Operational Considerations

The recycling process is based on complete melting of the alloy above its liquidus temperature, followed by a holding period to allow proper homogenization of the melt. The objective is not merely hydrogen removal, but full metallurgical regeneration of the material. After solidification, the alloy is crushed and milled to obtain an appropriate particle size and restore the active surface required for subsequent hydrogen absorption.

Induction heating behaves differently depending on material temperature, coil design, and operating frequency. At high temperatures, the electrical conductivity and magnetic permeability of the heated alloy change significantly, affecting skin depth and heat distribution. As the alloy gets hotter, skin depth increases, allowing heat to penetrate more deeply. This can be beneficial for homogenizing the melt but must be controlled to avoid overheating or uneven melting.

The device must also handle heat-related hazards such as thermal expansion, potential crucible deformation, and the risk of alloy-crucible interaction. Monitoring systems—such as thermocouples placed inside the charge—enable accurate evaluation of the temperature profile throughout the melting process.

The study also highlights that induction furnaces typically rely on frequencies in the tens to hundreds of kilohertz, because lower frequencies may cause excessive heating in the coil itself. Balancing reactance and resistive losses is therefore essential for optimizing both energy transfer and system longevity [11].

8. Conclusions

The research presented in the original article and expanded here demonstrates that induction heating offers a highly effective approach to melting and recycling metal hydride alloys. By analyzing the electromagnetic principles involved and addressing the complex behavior of hydride materials, the study provides valuable insights into how induction heating can be tailored for specialized metallurgical processes. The modular device constructed for this purpose illustrates how thoughtful engineering—spanning oscillator design, power management, crucible selection, and cooling strategies—can produce a reliable and efficient system capable of operating under harsh thermal conditions.

The use of tungsten crucibles, combined with protective Y_2O_3 coatings, provides a robust and chemically stable environment for melting hydrides, minimizing contamination risks and extending equipment life. Furthermore, the detailed consideration of skin depth, frequency selection, and thermal regulation ensures that the heating process remains controlled, efficient, and adaptable for various alloy types.

Overall, the prototype system not only fulfills its intended purpose for laboratory-scale recycling but also represents a platform for future industrial innovations. With further advancements such as enhanced automation, higher-power oscillators, or improved monitoring systems, induction-based melting technologies could become even more versatile and capable. This study contributes meaningfully to that development, offering a strong foundation for continued research and practical engineering progress.

Acknowledgments: This work was supported by the Slovak Research and Development Agency under the Contract No. APVV-23-0266 and No. APVV-21-0274, by internal grant IVG-25-01, by the VEGA granting agency within the Project No. 1/0224/23 and Project No. 1/0587/25 and by the KEGA granting agency within the Project No. 031TUKE-4/2025.

Conflicts of Interest: "The authors declare no conflict of interest."

References

1. Evans, M. 2.6: Metal Hydrides. Available online: https://chem.libretexts.org/Bookshelves/Inorganic_Chemistry/Organometallic_Chemistry_(Evans)/02%3A_Organometallic_Ligands/2.06%3A_Metal_Hydrides.
2. Pickering, L. et al. Induction melted AB 2 -type metal hydrides for hydrogen storage and compression applications. *Materials Today: Proceedings* **2018**, *4*, 10470-10478. DOI: https://doi.org/10.1016/j.matpr.2017.12.378.
3. Nacar, S. et al. Induction heated metal hydride tube for hydrogen storage system. *Pamukkale University Journal of Engineering Sciences* **2022**, *28*, 676-680. DOI: https://doi.org/10.5505/pajes.2021.97692.
4. Lucia, O. et al. Induction Heating Technology and Its Applications: Past Developments, Current Technology, and Future Challenges. *IEEE Transactions on Industrial Electronics* **2024,** *5*, 2509-2520. DOI: https://doi.org/10.1109/TIE.2013.2281162.
5. Fashu, S. et al. A review on crucibles for induction melting of titanium alloys. *Materials & Design* **2020**, *186*, 108295. DOI: https://doi.org/10.1016/j.matdes.2019.108295.
6. De Vaux, S. R. et al (2017). Influence of skin depth on convective heat transfer in induction heating. *Magnetohydrodynamic*s **2017**, *4*, 611-618 DOI: https://doi.org/10.22364/mhd.53.4.3.
7. Rudolph, S. Boron Nitride Release Coatings. In: WHITELEY, Peter R. (ed.). *Aluminium Cast House Technology*. Hoboken, NJ, USA: John Wiley & Sons, 2013, pp. 163-170. ISBN 9781118806364. DOI: https://doi.org/10.1002/9781118806364.ch16.
8. AMAZON. ZVS Driver 1000W ZVS Induction Heating Module Low Voltage Induction Heating Board Module Tesla Coil Heating Power Supply Module 12V-48V Flyback Driver Heater DIY. Available online: https://www.amazon.com/induction-Heating-Voltage-Induction-Flyback/dp/B0BMF638YT.
9. Zin, R. M. et al. Zero voltage switching driver and flyback transformer for generation of atmospheric pressure plasma jet. *AIP Conference Proceedings* **2017**, 1883, 020023, DOI: https://doi.org/10.1063/1.5002041.
10. Park, S. M. et al. Optimal Design of High-Frequency Induction Heating Apparatus for Wafer Cleaning Equipment Using Superheated Steam. *Energies* **2020**, *13*, 6196. DOI: https://doi.org/10.3390/en13236196.
11. Truong, Ch.T. et al. Improved ZVS Criterion for Series Resonant Converters. *IEEE Access* **2024**, *12*, 5333-5344. DOI: https://doi.org/10.1109/ACCESS.2024.3350437.
Barman, B. et al. Parameter Determination of a Multi-layered Induction Heating Coil: Analytical, Simulation and Experimental Studies. *Journal of The Institution of Engineers*: *Series B*, **2024**, *105*, 1299-1317. DOI: https://doi.org/10.1007/s40031-024-01000-7.

TECHNICAL UNIVERSITY OF KOŠICE
Faculty of Mechanical Engineering

Application potential of physiologically beneficial vibrations in traumatological practice

Viktória Divoková [1,*], Radovan Hudák [1] and Maroš Divok [2]

[1] Department of biomedical engineering and measurement Faculty of mechanical engineering Technical university of Košice, viktoria.divokova@student.tuke.sk; radovan.hudak@tuke.sk
[2] Department of aviation engineering, Faculty of Aeronautics, Technical university of Košice, maros.divok@tuke.sk
* Correspondence: viktoria.divokova@student.tuke.sk

Abstract: Vibration-based mechanical stimulation represents a dynamically developing physiotherapeutic modality with considerable potential for application within traumatological treatment and rehabilitation [7,8]. This article provides a comprehensive review of current scientific literature focusing on the physiological mechanisms, clinical effects, and therapeutic potential of vibration-based mechanical stimulation in traumatological practice and rehabilitation. Physiologically beneficial vibrations modulate neuromuscular activation, influence regional microcirculation, and stimulate cellular mechanotransduction pathways, thereby contributing to structural and functional recovery of the musculoskeletal system following traumatic injury [1,4,11] . A synthesis of current scientific evidence demonstrates that vibration stimuli increase reflexive activation of motor units, strengthen muscle–tendon functional interactions, improve local perfusion, and induce adaptive changes in bone tissue consistent with remodeling processes [3,5,10]. Despite these promising findings, existing literature displays substantial heterogeneity in methodological parameters—including frequency, amplitude, duration, and mode of vibration transmission—which complicates inter-study comparability and hinders the establishment of standardized therapeutic guidelines [9,14]. Current knowledge indicates clear therapeutic benefits of vibration stimulation in trauma rehabilitation; however, optimized clinical implementation requires further controlled investigations aimed at defining precise stimulation parameters, safety thresholds, and diagnostic-specific indications[6,12].

Keywords: whole-body vibration; vibration therapy; traumatology; rehabilitation; neuromuscular activation; mechanotransduction; microcirculation; bone remodeling; musculoskeletal injuries; proprioception; balance; fracture healing

1. Introduction

Mechanical vibrations, defined as periodic oscillatory stimuli characterized by specific frequency and amplitude, are transmitted to the human body either indirectly via contact surfaces or directly through localized mechanical applicators [4]. Their integration into rehabilitation medicine originated as an experimental approach intended to enhance neuromuscular function and influence the condition of skeletal, muscular, and neural structures [1,2]. Today, physiologically beneficial vibration stimulation—applied as whole-body vibration (WBV) or localized vibration—is the subject of intensive research within physiatry, orthopedics, and traumatology [7,10]. Clinical and experimental studies investigate its potential to enhance musculoskeletal functional capacity, stimulate reparative and regenerative processes, and optimize neuromuscular activation in patients recovering from trauma or surgical intervention [6,11]. The aim of this article is to analyze the mechanisms of action, clinical outcomes, and practical implications of physiologically beneficial vibration stimulation as an adjunct modality in trauma rehabilitation. The growing interest in vibration-based interventions reflects their unique ability to induce

mechanical loading without imposing excessive strain on compromised tissues [5,15]. This characteristic is particularly relevant in early rehabilitation phases, where conventional strengthening approaches may be contraindicated [9,20]. Consequently, vibration stimulation is increasingly viewed as a complementary therapeutic modality capable of supporting efficient restoration of function following traumatic musculoskeletal injuries [12].

2. Mechanisms of physiological response to vibration

Physiologically beneficial vibration acts as a controlled mechanical stimulus that activates neuromuscular reflex pathways, enhances regional microcirculation, and initiates cellular mechanotransduction mechanisms. These processes collectively promote adaptive responses in muscle, connective tissue, and bone, supporting structural integrity and functional recovery following traumatic injury or immobilization [1,4,11].

2.1 Neuromuscular stimulation

Vibration stimuli act as repeated mechanical inputs that activate proprioceptive sensory structures, predominantly muscle spindles and mechanoreceptors located in tendon and fascial networks [1,4]. Their stimulation increases afferent signaling in Ia and II fibers, which convey information on rapid changes in muscle length and tension [1,2,21]. The resulting modulation of spinal segmental circuits induces activation of α-motoneurons, generating rhythmic reflexive muscle contractions—known as the tonic vibration reflex—without the need for high external loads [4].

This mechanism enhances muscle tension, improves recruitment efficiency of motor units, and promotes coordination among synergistic and stabilizing muscle groups [10]. The neuromuscular response elicited by vibration stimuli resembles adaptations observed during low-load strength training, yet with substantially reduced mechanical stress imposed on joints and soft tissues [9]. Additionally, vibration-induced neuromotor adaptation facilitates more efficient signal integration between peripheral structures and the central nervous system, contributing to functional recovery following trauma, immobilization, or neuromuscular disuse [3,14].

The intensity of neuromuscular activation depends on the interaction between frequency, amplitude, and exposure duration [10]. These relationships are well documented using electromyographic (EMG) measurements [13]. Table 1 summarizes representative data demonstrating the differential effects of vibration parameters on muscle activation patterns.

Table 1. EMG activation at different WBV frequencies and amplitudes

Conditions: semi-squat (static/dynamic), WBV frequencies 0, 30, 40 Hz; amplitudes 0, 2, 4 mm.

Mode	Frequency (Hz)	Amplitude (mm)	Muscles with significant ↑ EMG	Key conclusion
No vibration	0	0	–	Reference EMG activation level during static and dynamic semi-squat.
WBV – SSS/DSS	30	2	VL, BF	Increased EMG vs. 0 Hz; DSS elicits higher activation than SSS.
WBV – SSS/DSS	30	4	VM, VL, BF	EMG significantly higher at 4 mm than at 0 or 2 mm; strong amplitude effect.
WBV – SSS/DSS	40	2	VL, BF	Increased EMG vs. 0 Hz; difference between 30 and 40 Hz is modest.

WBV – SSS/DSS	40	4	GS (DSS)	40 Hz / 4 mm markedly increases gastrocnemius EMG; amplitude more influential than frequency shift.

WBV – whole-body vibration, EMG – electromyography, SSS – static semi-squat, DSS – dynamic semi-squat, VL – vastus lateralis muscle, VM – vastus medialis muscle, RF – rectus femoris muscle, BF – biceps femoris muscle, GS – gastrocnemius muscle, Hz – hertz, mm – millimeter.

Main interpretation: In this neuromuscular model, amplitude exerts a stronger influence on muscle activation than the small frequency difference between 30 and 40 Hz. Frequencies within the 30–40 Hz range significantly enhance activation of RF, VM, VL, BF, and GS compared to non-vibration conditions [10].

2.2 Vascular and perfusion effects

Vibration-induced mechanical loading influences hemodynamics by modifying vascular tone, enhancing the action of the muscle pump, and inducing micro-level compression–decompression cycles within soft tissues [7,8]. These mechanisms facilitate increased flow velocity in arterial and venous circuits, improved capillary perfusion, and enhanced delivery of oxygen and nutrients [8].

Clinical observations demonstrate that vibration exposure promotes restoration of vascular reactivity, characterized by improved responsiveness of arterioles to metabolic and neural regulatory stimuli [7,19]. Additionally, increased cardiac output and systemic perfusion contribute to accelerated transport of metabolites, enhanced removal of by-products of anaerobic metabolism, and improved conditions for tissue repair [8,19].

In trauma rehabilitation, these effects are especially valuable. Improved microcirculation supports faster healing, reduces susceptibility to ischemic secondary damage, and enhances regeneration of both soft tissue and bone [6]. Vibration therapy may thus serve as an important adjunctive modality in regions with compromised perfusion due to immobilization, surgical manipulation, or high-impact contusive injuries [7].

2.3 Mechanotransduction and bone response

Mechanical vibrations initiate deformation forces that activate cellular mechanotransduction pathways responsible for converting mechanical signals into biochemical responses [11]. This process governs adaptive remodeling in bones, tendons, ligaments, and muscles [5]. Vibrations induce strain within the cellular matrix, activate mechanosensitive receptors, alter ion fluxes, and trigger intracellular cascades that regulate tissue regeneration [11,12].

In bone tissue, vibration stimulates osteoblastic activity while concurrently reducing osteoclastic resorption, promoting a net anabolic effect [5]. This is particularly beneficial during post-injury immobilization, when physiological loading is limited and bone loss is prevalent [6,18]. Similarly, vibration applied to tendons and ligaments enhances fibroblast activity, promotes collagen synthesis, and improves the organization and biomechanical resilience of connective tissues [11].

Mechanotransduction therefore represents a central physiological mechanism through which vibration therapy supports structural recovery and facilitates the adaptive remodeling required for functional restoration following trauma [12].

3. Clinical results and therapeutic implications of vibration stimulation

Clinical and experimental findings demonstrate that vibration stimulation improves neuromuscular activation, postural stability, and sensorimotor control, while also facilitating tissue regeneration and bone remodeling. These effects contribute to reduced pain, improved functional outcomes, and accelerated recovery, supporting the integration of vibration therapy as an adjunct modality in trauma rehabilitation [3,6,14].

3.1 Functional effects on muscle activity and stability

Evidence from controlled clinical trials suggests that vibration stimulation can positively influence neuromuscular function by enhancing intermuscular coordination, facilitating motor unit recruitment, and improving dynamic as well as postural stability [10,14]. Such adaptations may support more efficient performance of repetitive motor tasks, attenuation of fatigue, and accelerated restoration of motor control processes compromised by injury or immobilization [9,16]. In rehabilitation contexts, these effects are associated with earlier recovery of functional movement patterns and greater overall stability, particularly during the early phases of intervention [17,20,23].

3.2 Tissue-Level Effects in Musculoskeletal Injury

Mechanical vibration accelerates regeneration in injured tissues by enhancing collagen fiber reorganization, improving tendon and ligament strength, and restoring elasticity in the musculotendinous system [11]. Clinical observations report decreased pain, improved range of motion, and faster restoration of functional properties following muscle or tendon injuries [6]. In joint-related trauma, vibration stimulation supports relaxation of periarticular muscle tension and contributes to normalization of movement patterns.

The differential effects of vibration frequency on cartilage, bone, and function have been demonstrated in preclinical studies. Table 2 summarizes findings from an experimental rabbit model evaluating WBV frequencies from 5 to 40 Hz [3,13].

Table 2. Effects of different WBV frequencies in knee OA – ACLT rabbit model

WBV 40 min/day, 5 days/week, 8 weeks; amplitude 2–4 mm.

Group	Frequency (Hz)	Amplitude	Effect on cartilage	Effect on subchondral bone	Functional effect
Control	–	–	Progressive degeneration; poor histology	Impaired trabecular structure	Poor limb loading
5 Hz	5	2–4 mm	No significant change	Minimal effect	No functional improvement
10 Hz	10	2–4 mm	Reduced cartilage resorption; improved morphology	Improved trabecular structure	Decreased pain; improved symmetry
20 Hz	20	2–4 mm	Most beneficial effect; best histological outcomes	Enhanced bone turnover	Most significant functional improvement
30 Hz	30	2–4 mm	Undesirable deterioration of cartilage	Prevention of bone loss but poor functional results	Increased asymmetry
40 Hz	40	2–4 mm	Similar to 30 Hz; worsening of cartilage	Increased turnover but detrimental to cartilage	Worse pain and load distribution

3.3 Bone regeneration after injury and immobilization

Vibration stimulation appears particularly promising for post-fracture management and prevention of immobilization-induced osteopenia. Physiological measurements show increased markers of bone turnover and improved microarchitectural restoration. By supporting balanced activity between bone formation and resorption, vibration exposure may serve as a valuable adjunct in bone healing protocols [6, 22].

3.4 Effects on balance and proprioception

Patients with proprioceptive deficits following lower-limb trauma benefit from vibration stimulation, exhibiting improved postural control, shorter reaction times, and enhanced stability during dynamic tasks. This is especially important in patients recovering from long-term immobilization or surgical reconstruction of stabilizing structures [9].

4. Interpretation, limitations, and research prospects

Current evidence suggests that vibration stimulation can effectively support musculoskeletal recovery in trauma rehabilitation, particularly in early phases when traditional high-load exercises are contraindicated. Nevertheless, the clinical translation of these findings is limited by substantial heterogeneity in stimulation parameters, application protocols, and study designs. The absence of standardized therapeutic guidelines and limited long-term outcome data underscore the necessity for further well-controlled clinical studies to define optimal dosing strategies, safety limits, and injury-specific indications for vibration therapy [12,14].

4.1 Interpretation in the context of trauma rehabilitation

Synthesis of available evidence indicates that vibration stimulation effectively supports restoration of musculoskeletal function across a broad spectrum of traumatic conditions [6,10]. Its benefits are most pronounced where neuromuscular activation is required without imposing excessive mechanical load—precisely the scenario typical of early rehabilitation phases. Tissue-level improvements in perfusion, collagen organization, and bone remodeling further underscore its therapeutic potential [9].

4.2 Limitations and need for standardization

Despite promising outcomes, current research is limited by significant heterogeneity in study design. Inconsistent frequencies, amplitudes, application methods, and exposure durations complicate comparison and preclude universally applicable clinical guidelines [14]. Furthermore, robust long-term randomized controlled trials in traumatology remain scarce.

To implement vibration therapy reliably in practice, standardized protocols must be developed and validated for specific injury types and patient categories [12].

4.3 Prospects for further research

Future studies should aim to:

- define isolated and synergistic effects of vibration parameters,
- evaluate long-term impacts on bone and soft tissue healing across diverse injury models,
- establish therapeutic protocols with clearly delineated stimulation parameters,
- identify safety thresholds for vulnerable patient groups.

Such research will provide the foundation for integrating vibration therapy into routine traumatological rehabilitation [7].

5. Discussion

A comprehensive analysis of current literature suggests that controlled vibration stimulation constitutes a promising adjunct for restoring musculoskeletal function following trauma. Its physiological effects—enhanced neuromuscular activation, improved microcirculation, and facilitation of sensorimotor recovery—align well with therapeutic objectives in early and mid rehabilitation phases. Importantly, vibration provides a means of delivering mechanical stimulation in patients for whom conventional high-load exercise is contraindicated[12].

Methodological inconsistencies, however, remain the primary barrier to clinical standardization. Variability in vibration parameters across studies limits comparability

and precludes definitive conclusions regarding optimal therapeutic dosing. Furthermore, safety considerations underline the necessity for controlled application, as excessive or inappropriate stimulation may compromise healing tissues or exacerbate functional deficits [23].

Overall, the evidence supports the view that vibration therapy is an effective yet insufficiently standardized modality requiring[10].

6. Conclusion

Vibration stimulation represents a compelling complementary intervention within trauma rehabilitation, capable of supporting recovery of muscle function, enhancing proprioception, and reducing the risk of atrophy during immobilization or reduced loading [6,10,14]. Its effectiveness is underpinned by combined neuromuscular, circulatory, and tissue-regenerative mechanisms, positioning it as a valuable asset within comprehensive rehabilitation frameworks [21,15,17]..

However, clinical integration requires:

- standardized protocols specifying frequency, amplitude, duration, and application technique;
- well-designed controlled trials targeting specific injury categories;
- evaluation of long-term outcomes and identification of optimal stimulation parameters.

While current evidence supports its therapeutic potential, widespread clinical implementation of vibration stimulation necessitates consistent, high-quality scientific validation and the establishment of clear therapeutic guidelines [12].

Acknowledgments: The paper was written with support of the project VEGA/1/0387/22Development and testing systems for controlled stimulation of cell growth in bioreactor environment using computer vision.

References

1. Burke D, Hagbarth KE, Lofstedt L, Wallin BG. The responses of human muscle spindle endings to vibration of non-contracting muscles. *Journal of Physiology*. 1976;261(3):673–693.
2. Fromm C, Noth J. Reflex responses of gamma motoneurones to vibration in man. *Journal of Physiology*. 1976.
3. Wang J, et al. Effect of low-magnitude different-frequency whole-body vibration on subchondral trabecular bone microarchitecture, cartilage degradation, bone/cartilage turnover and joint pain in rabbits with knee osteoarthritis. *BMC Musculoskeletal Disorders*. 2017;18:1579.
4. Person R. Tonic vibration reflex of human limb muscles. *Human Movement Science*. 1992.
5. Lau E, Al-Dujaili S, Guenther A, et al. Effect of low-magnitude, high-frequency vibration on osteocytes: inhibition of osteoclast formation via soluble factors. *Bone*. 2010.
6. Wang J, et al. The effect of whole-body vibration on fracture healing: a systematic review. 2017.
7. Games KE, Sefton JM, Wilson AE. Whole-body vibration and blood flow and muscle oxygenation: a review. 2015.
8. Mahbub MH, Hiroshige K, Harada N. Acute effects of whole-body vibration on peripheral blood flow: evidence from clinical studies. *International Journal of Environmental Research and Public Health*. 2020;17(3):1069.
9. Seixas A, et al. Whole-body vibration for individuals with reconstructed anterior cruciate ligament: a systematic review of knee function, EMG activity, balance, and strength outcomes. 2020.
10. Wang Z, et al. Effect of whole-body vibration on neuromuscular activation and performance outcomes: systematic review and meta-analysis. *PLOS ONE*. 2022.
11. Steppe L, et al. Influence of low-magnitude high-frequency vibration on bone biology and regeneration: mechanistic pathways and clinical implications. *Frontiers in Bioengineering and Biotechnology*. 2020.
12. Jing D, et al. Effect of low-level mechanical vibration on osteogenesis and osseointegration in osseous defects. *Scientific Reports*. 2015;5:17134.
13. Wang JB, et al. Effects of low-magnitude whole-body vibration on knee osteoarthritis in rabbits. 2017.
14. Tariq N, et al. Effect of whole-body vibration on balance and proprioception: synthesis of current evidence and methodological considerations. 2023.
15. Steppe L, van Loon J, Hemmersbach R, Vico L, Clément-Lacroix P, Rittweger J. Influence of Low-Magnitude High-Frequency Vibration on Bone Cells and Bone Regeneration. Front Bioeng Biotechnol. 2020;8:595139. doi:10.3389/fbioe.2020.595139. Verified link: https://doi.org/10.3389/fbioe.2020.595139

16. Mahbub MH, Hiroshige K, Harada N. Acute Effects of Whole-Body Vibration on Peripheral Blood Flow, Vibrotactile Perception and Balance in Older Adults. Int J Environ Res Public Health. 2020;17(3):1069. doi:10.3390/ijerph17031069. Verified link: https://doi.org/10.3390/ijerph17031069
17. Seixas A, Sa-Caputo D, Sousa-Goncalves CR, et al. Whole-Body Vibration for Individuals with Reconstructed Anterior Cruciate Ligament: A Systematic Review. Biomed Res Int. 2020;2020:7362069. doi:10.1155/2020/7362069. Verified link: https://doi.org/10.1155/2020/7362069
18. Qiu J, Ong MTY, Leong HT, He X, Fu SC, Yung PSH. Effects of Whole-Body Vibration Therapy on Quadriceps Function in Patients With Anterior Cruciate Ligament Reconstruction: A Systematic Review. Sports Health. 2022;14(2):216-226. doi:10.1177/19417381211004937. Verified link: https://doi.org/10.1177/19417381211004937
19. Wang Z, Wei Z, Li X, Lai Z, Wang L. Effect of whole-body vibration on neuromuscular activation and explosive power of lower limb: A systematic review and meta-analysis. PLoS One. 2022;17(12):e0278637. doi:10.1371/journal.pone.0278637. Verified link: https://doi.org/10.1371/journal.pone.0278637
20. Tariq N, Khan Z, Veqar Z. Effect of Whole-Body Vibration on Balance or Proprioception in Nonspecific Chronic Low Back Pain: A Systematic Review. J Chiropr Med. 2023;22(4):284-293. doi:10.1016/j.jcm.2023.04.006. Verified link: https://doi.org/10.1016/j.jcm.2023.04.006
21. Zafar T, Zaki S, Alam MF, Sharma S, Babkair RA, Nuhmani S, Pandita S. Effect of Whole-Body Vibration Exercise on Pain, Disability, Balance, Proprioception, Functional Performance and Quality of Life in People with Non-Specific Chronic Low Back Pain: A Systematic Review and Meta-Analysis. J Clin Med. 2024;13(6):1639. doi:10.3390/jcm13061639. Verified link: https://doi.org/10.3390/jcm13061639
22. Simon AB, Bajaj P, Samson J, Harris RA. The Clinical Utility of Whole Body Vibration: A Review of the Different Types and Dosing for Application in Metabolic Diseases. J Clin Med. 2024;13(17):5249. doi:10.3390/jcm13175249. Verified link: https://doi.org/10.3390/jcm13175249
23. Li Q, Wang X, Gao Y, et al. Therapeutic effects of whole-body vibration on postmenopausal women with osteoporosis: a systematic review and meta-analysis. Braz J Med Biol Res. 2024;57:e13996. doi:10.1590/1414-431X2024e13996. Verified link: https://doi.org/10.1590/1414-431X2024e13996

TECHNICAL UNIVERSITY OF KOŠICE
Faculty of Mechanical Engineering

Automation of VRFB component production using a custom-made vacuum fixture

Filip Dominik [1,*], Ján Slota [2], Marek Vrabeľ [1], Ján Kušnír [1], Patrik Pilát [1]

[1] Prototyping and Inovation centre, Faculty of Mechanical Engineering Technical University of Kosice, Slovak republic; filip.dominik@tuke.sk; marek.vrabel@tuke.sk; jan.kusnir@tuke.sk; patrik.pilat@tuke.sk
[2] Department of Technology, Materials and Computer Supported Production, Faculty of Mechanical Engineering, Technical University of Kosice, Slovak republic; jan.slota@tuke.sk
* Correspondence: filip.dominik@tuke.com

Abstract: This paper presents a custom-made vacuum fixture developed for the automated machining of plastic and aluminum components used in Vanadium Redox Flow Batteries (VRFBs). Due to the thin-walled geometry and high flatness requirements of key reactor components, conventional mechanical clamping methods often lead to deformation and insufficient accuracy. The proposed vacuum fixture utilizes an internal channel network and low-hardness EPDM foam seals to achieve uniform clamping forces and deformation-free machining. Additional features such as mechanical stops, coolant evacuation channels, and integration with a zero-point clamping system improve repeatability and reduce setup times. In practical operation, the solution reduced total manufacturing time by approximately 40% compared to conventional clamping. An economic evaluation shows that while injection molding is optimal for high-volume components, vacuum-fixture-based machining represents the most cost-effective solution for distribution plates at expected production volumes, offering rapid investment payback and high process flexibility.

Keywords: custom-made vacuum fixture, manufacturing, vanadium redox flow battery, reactor

1. Introduction

The automation of the manufacturing process of complex systems such as Vanadium Redox Flow Batteries (VRFBs) often relies on automating the production of individual subsystems, ranging from assembly operations and mechanical parts to battery reactor components. The achievable level of automation is primarily influenced by economic indicators, including the number of required parts, expected production volumes, manufacturing repeatability, and process scalability. In the context of VRFB component manufacturing, it is therefore essential to select machining and workholding solutions that are not only precise and reliable, but also economically viable and adaptable to varying production volumes.

2. VRFB System Overview and Machined Components

A VRFB is a type of flow battery that utilizes vanadium-based electrolytes in different oxidation states. A typical VRFB system is shown in Fig. 1, while the core element of such energy storage systems is the electrochemical reactor, that is illustrated in Fig. 2.

The reactor design follows a sandwich-type architecture and consists of a series of electrochemical cells stacked together. For reliable operation, electrical insulation, chemical resistance, and hydraulic stability must be ensured. Components responsible for positioning the electrochemically active elements therefore require high electrical non-conductivity and excellent flatness in order to guarantee proper sealing performance.

These components mainly consist of thin plastic half-frames and distribution plates that form the structural skeleton of the reactor. They maintain the position of the electrochemically active elements, define electrolyte flow paths, and are typically manufactured from non-conductive polymer materials such as PVC or PP [2].

To achieve the required dimensional accuracy and flatness, the use of a custom-designed vacuum fixture proved to be a suitable manufacturing solution. From an economic standpoint, vacuum-based machining is particularly advantageous for distribution plates, whereas high-volume components such as half-frames are more efficiently produced using injection molding.

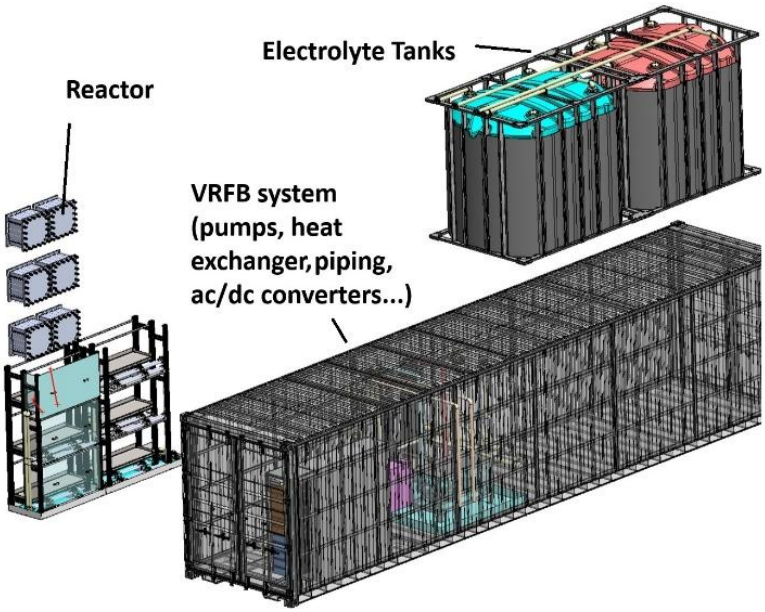

Figure 1. VRFB system.

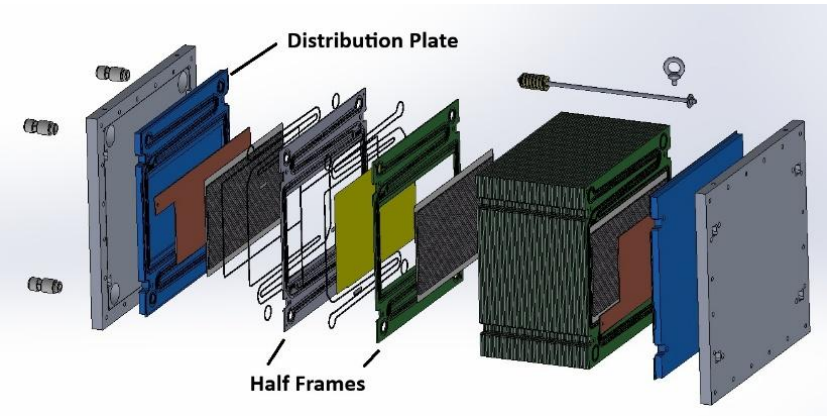

Figure 2. Electrochemical reactor – exploded view.

3. Vacuum Fixture, principle and advantages

During the machining of plastic and in some cases aluminum components, one of the primary challenges is achieving rigid and precise clamping without inducing deformation of the workpiece. Plastic parts are often relatively soft, geometrically complex, or thin-walled, making them susceptible to indentation, bending, or vibration when conventional mechanical clamping methods (jaws, clamps, vises) are used [1].

A vacuum fixture provides an effective solution by utilizing negative pressure to clamp the workpiece uniformly across its entire contact surface. This approach significantly reduces localized stresses and minimizes the risk of deformation during machining operations [7].

The main advantages of vacuum fixtures include:

- Deformation-free clamping - uniform pressure distribution across the entire workpiece surface.
- Fast and simple setup - the workpiece is positioned on the fixture and auto matically secured once the vacuum circuit is activated.
- Improved machining accuracy - stable clamping prevents workpiece move ment, resulting in higher dimensional repeatability [4].
- Capability to machine complex geometries and thin-walled components vacuum clamping can be adapted to various shapes and sizes [6].
- Reduced risk of surface damage - particularly important for plastic components, where mechanical clamps may leave marks or cause defects [1].

Typical applications include machining of plastic covers, panels, thin-walled structures, post-processing of 3D-printed parts, prototypes, and small-batch production using plastics (e.g., PVC, PP, PE, POM, PC) as well as aluminum.

3.1. Fixture Design and Technical Implementation

The developed vacuum fixture incorporates an internal network of channels that connect the vacuum circuit to the fixture surface. These channels terminate at the clamping surface and are equipped with fine filter screens that prevent chips and contaminants from entering the vacuum system. This design reduces the risk of clogging and vacuum loss during workpiece exchange [5].

Machined grooves on the fixture surface accommodate a sealing element, typically an EPDM foam seal with a circular cross-section. The sealing material must exhibit sufficient elasticity: under compression, it deforms elastically, fills the groove volume, and ensures airtight sealing around the entire perimeter of the workpiece.

Rubber foams such as EPDM are particularly suitable for this application due to their high flexibility, elasticity, and deformability. These materials can absorb mechanical energy and return elastically to their original shape after deformation. As a result, even thin or mechanically weak workpieces remain flat and are not deformed by the sealing pressure [3].

For comparison, the hardness of the EPDM foam seal used in this application is approximately 15 Shore A, indicating a very soft sealing material. In contrast, conventional sealing materials often exhibit significantly higher hardness values, such as 40 Shore A for silicone seals or 70–80 Shore A for harder elastomers like FKM.

The use of a soft, low-hardness seal is advantageous when clamping thin plastic components, as it compensates for minor surface irregularities and prevents localized pressure peaks that could otherwise lead to deformation or surface damage.

The position of the grooves and seals is always customized for the specific workpiece geometry, maximizing the effective vacuum area. This is particularly important for large and thin components, where conventional mechanical clamping typically concentrates forces at the edges, potentially causing concave deformation or uneven clamping, as commonly observed when thin plates are clamped in a vise.

The combined use of vacuum clamping, sealing grooves, and elastic EPDM seals is therefore essential for:

- uniform distribution of clamping forces,
- minimization of deformation risks for thin components,
- reliable machining of complex geometries,
- preservation of surface quality and dimensional accuracy.

3.2. Integration into Production and Hybrid Clamping Concept

In addition to the vacuum system, the fixture is equipped with mechanical stops and additional mechanical clamps. These elements ensure precise and repeatable positioning of the workpiece during serial production, which is particularly important when frequent workpiece changes are required. Mechanical stops significantly reduce handling and setup times, and when combined with vacuum clamping and optional mechanical locking, they allow more aggressive machining without the risk of workpiece displacement resulting in increased productivity.

The fixture was designed to accommodate multiple workpiece types, including both plastic and aluminum plates, thereby maximizing its utilization across different stages of battery reactor manufacturing.

An additional critical feature is the integrated coolant evacuation system used during machining operations such as through-hole drilling. When high-speed milling cutters or drills with internal coolant supply are used, blind holes may be created in the fixture beneath the workpiece. Pressurized coolant can accumulate in these cavities. Without proper evacuation, the pressure difference between the coolant (up to approximately 30 bar) and the vacuum system (approximately −1 bar) could compromise the vacuum seal, potentially leading to vacuum loss and workpiece pull-out.

To prevent this, the fixture contains additional evacuation channels that divert excess coolant away from the vacuum zone, ensuring stable clamping even during machining operations with internal coolant delivery.

To further enhance flexibility and reduce downtime, the fixture is integrated with a zero-point clamping system. This enables rapid fixture changes without the need for repeated alignment, which is particularly advantageous when switching between different workpiece types or production setups.

In practical operation, this approach resulted in an approximately 40% reduction in total manufacturing time, including handling and machining, compared to conventional mechanical clamping methods such as jaws, clamps, or vises. Manufactured vacuum fixture is shown at Figure 3.

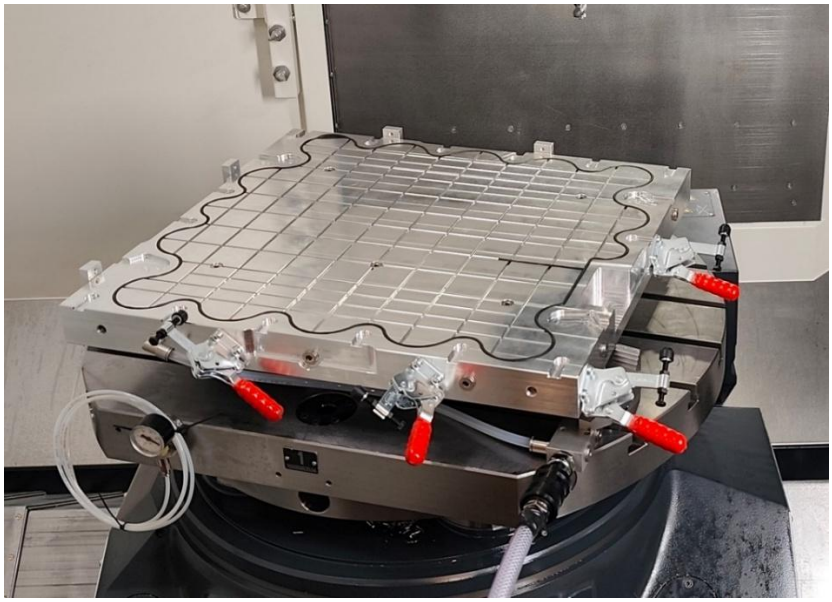

Figure 3. Custom-made vacuum fixture.

4. Economic Evaluation of Manufacturing Technologies

An economic comparison was conducted for two types of VRFB components: half-frames and distribution plates. For half-frames, an injection molding tool was manufactured, resulting in a significant reduction in production costs. The original machining cost

was approximately €116 per part, whereas after implementation of injection molding, the cost decreased to approximately €8.5 per part.

The investment cost of the injection mold was €340,000, corresponding to a break-even point of approximately 3334 produced parts. Given the production volumes anticipated for this project, injection molding represents the most economically advantageous solution for this component type.

A different situation applies to distribution plates. Manufacturing without a dedicated fixture was compared to production using the custom vacuum fixture, which significantly reduces machining time and labor costs. The vacuum fixture reaches its break-even point after approximately 150 produced parts, which is well within the planned production volumes.

In contrast, comparison with a potential injection molding solution showed that mold payback would occur at approximately 10858 parts, a quantity far exceeding the expected demand for this component. As a result, manufacturing an injection mold for distribution plates would not be economically justified.

These findings indicate that injection molding is the most efficient manufacturing method for half-frames, while vacuum fixture-based machining represents the optimal economic solution for distribution plates, offering the shortest investment payback and the lowest operating costs for realistically expected production volumes.

This project consists of the production of 550 reactors, where the resulting number of half frames is 44000 and 1100 distribution plates. A detailed quantitative comparison is presented in Figure 4.

component		Half-Frame			Distribution Plate		
number of components per reactor		80			2		
number of expected parts		44000			1100		
production technology		no fixture	vaccum vixture	injection molding	no fixture	vaccum vixture	injection molding
OPEX	material [€/pcs.]	-	6	0,5	35	35	3
	cena výroby [€/pcs.]	-	110	8	120	60	25
	time of production [min/part]	-	60	1	120	45	3
CAPEX		-	9000	340000	0	9000	380000
break-even point [number of components]		-	-	3333,333333	-	150	10857,14286
saved at project [€]		-	-	4148000	-	57000	-341500

Figure 4. Economic table of comparison (OPEX operating expenses, CAPEX capital expenses).

5. Conclusion

The conducted analysis confirms that the selected custom-made vacuum fixture represents the most suitable solution for manufacturing distribution plates within the VRFB system. Its implementation significantly reduces machining time, lowers operating costs, and achieves rapid economic payback even at relatively low production volumes.

Comparison with alternative manufacturing technologies demonstrates that investment in an injection molding tool would be economically inefficient for this component given the expected production quantities, whereas the vacuum fixture provides an optimal balance between cost efficiency, process flexibility, and high-precision manufacturing. The economic evaluation therefore clearly confirms the suitability and effectiveness of the proposed solution.

Acknowledgments: This work was supported by the grant project APVV SK-PL-25-0118. The authors also gratefully acknowledge support for the experimental work provided under grant KEGA 035TUKE-4/2026.

References

1. H.-C. Möhring, D. Biermann, F. Bleicher, S. Melkote, G. Kappmeyer, Fixtures and workpiece clamping systems in machining, CIRP Annals, Volume 74, Issue 2, 2025, Pages 945-969, DOI: 10.1016/j.cirp.2025.04.096
2. F.Dominik; J.Slota. Redoxné batérie: pohľad na cenovo dostupnú energiu budúcnosti, Transfer inovácií 2024, 50, Pages 53-56

3. P. S. Ravishankar, et al., Morphological, Mechanical and Thermal Properties of Rubber Foams, Materials, 2022, Article ID PMC10004622. Available online: https://pmc.ncbi.nlm.nih.gov/articles/PMC10004622/
4. iBAG North America, 6 Advantages of Vacuum Chucks – Vacuum Workholding Systems, iBAG North America, 2025. Available online: https://www.ibagnorthamerica.com/blog/advantages-of-vacuum-chucks
5. AccTek CNC, What Is a Vacuum Worktable: A Comprehensive Guide, AccTek CNC, 2023. Available online: https://acctekcnc.com/what-is-a-vacuum-worktable
6. Haibo Liu, et al., Fixturing Technology and System for Thin-Walled Parts Machining, Frontiers of Mechanical Engineering, Volume 17, Issue 4, 2022, Pages 55–70, ISSN 2095-0189, https://doi.org/10.1007/s11465-022-0711-5
7. Anebon, Milling Workholding Strategies Showdown: Vacuum vs. Mechanical Clamping for Uninterrupted Deep Pocket Machining, Anebon, 2025. Available online: https://www.anebon.com/news/milling-workholding-strategies-showdown-vacuum-vs-mechanical-clamping-for-uninterrupted-deep-pocket-machining

TECHNICAL UNIVERSITY OF KOŠICE
Faculty of Mechanical Engineering

Numerical Modelling and Simulation of the Buildability of a 3D-Printed Component Using Grasshopper Plug-in

Erika Dubňanská [1,*], Martina Hančinová [1], Barbara Schürger [1] and Róbert Huňady [1]

[1] Department of Applied Mechanics and Mechanical Engineering, Faculty of Mechanical Engineering, Technical University of Košice, Letná 1/9, 042 00 Košice-Sever, Slovakia; erika.dubnanska@tuke.sk; martina.hancinova@tuke.sk; barbara.schurger@tuke.sk
* Correspondence: erika.dubnanska@tuke.sk

Abstract: Extrusion-based 3D concrete printing requires reliable prediction of buildability, i.e., the ability of a fresh, layer-wise structure to retain its shape under self-weight without premature structural instability, such as elastic buckling or plastic collapse. Finite element analysis (FEA) is therefore adopted to quantify the structural response during deposition. In this paper, a pre-processing workflow implemented in Grasshopper using the VoxelPrint plug-in was employed to generate a finite element (FE) model. Abaqus/Standard was used as the solver with stepwise element activation to represent the deposition sequence. The analysed component was a cylindrical wall of fresh-state concrete under self-weight loading. Material behaviour was described using a time-dependent constitutive model based on the Mohr–Coulomb criterion.

Keywords: 3D concrete printing; buildability; VoxelPrint; early-age concrete; time-dependent material model

1. Introduction

Buildability is one of the main criteria in extrusion-based 3D concrete printing and describes the ability of the fresh, progressively deposited structure to retain its geometry during printing. It characterises the capacity of the extruded filament and the growing layer-wise body to sustain self-weight and the additional loading from subsequently deposited layers without excessive deformation or loss of stability. Buildability is typically assessed through the limiting build height, often expressed as the maximum number of layers that can be deposited before the onset of structural instability, such as elastic buckling or plastic collapse. Insufficient buildability results in reduced dimensional accuracy and an increased risk of failure due to structural instability during printing [1,2].

Finite-element analyses (FEA) enable prediction of the evolving structural response during deposition and help identify conditions leading to premature failure. Wolfs and Suiker [3] investigated failure of extrusion-based 3D-printed walls by elastic buckling and plastic collapse using a parametric model with closed-form expressions. The model showed very good agreement with the finite-element simulations and 3D printing experiments across different wall geometries and curing rates, and it captured the transition from buckling to plastic collapse as material properties evolved. Wolfs et al. [4] developed a finite-element model to describe the early-age mechanical behaviour of fresh concrete after deposition using a time-dependent Mohr–Coulomb failure criterion with a linear stress–strain response up to failure. The model was calibrated using uniaxial compression and direct shear tests and validated against printing experiments, accurately predicting the observed failure mode despite some quantitative deviations. Vantyghem et al. [5] conducted a comparative study based on the work of Wolfs et al. [4] and introduced the

Grasshopper plug-in VoxelPrint for generating voxel-discretised FE models of 3D concrete printing. They examined the influence of voxel size and the number of computational steps, and reported close agreement with Wolfs et al.

VoxelPrint is a plug-in for the Grasshopper visual programming environment integrated into Rhinoceros 3D. The plug-in discretises the geometry using voxelisation, enabling FE mesh generation via a direct voxel-to-element mapping and sequential element activation to represent the deposition sequence in the numerical simulation, without requiring contact constraints between segments. The workflow relies on a sequence of interconnected components in the Grasshopper environment to build the numerical model and generate the Abaqus input file (.inp) [5,6].

2. Numerical Modelling

2.1 Numerical Model Generation

A numerical model of a cylindrical wall representing an extrusion-based 3D-printed structure was generated using the Grasshopper plug-in VoxelPrint. The model geometry was defined by a mean radius of 180 mm, a thickness of 16 mm, and a layer height of 8 mm.

The basic VoxelPrint workflow comprises five interconnected components – two core (*BrepToVoxel*, *VoxelToAbaqus*) and three auxiliary (*Material*, *PrintSettings*, *VoxelPreview*). The setup defines voxel geometry, material properties, and print parameters required for generating the Abaqus input file.

Figure shows interconnections among VoxelPrint components forming the workflow adopted for numerical modelling.

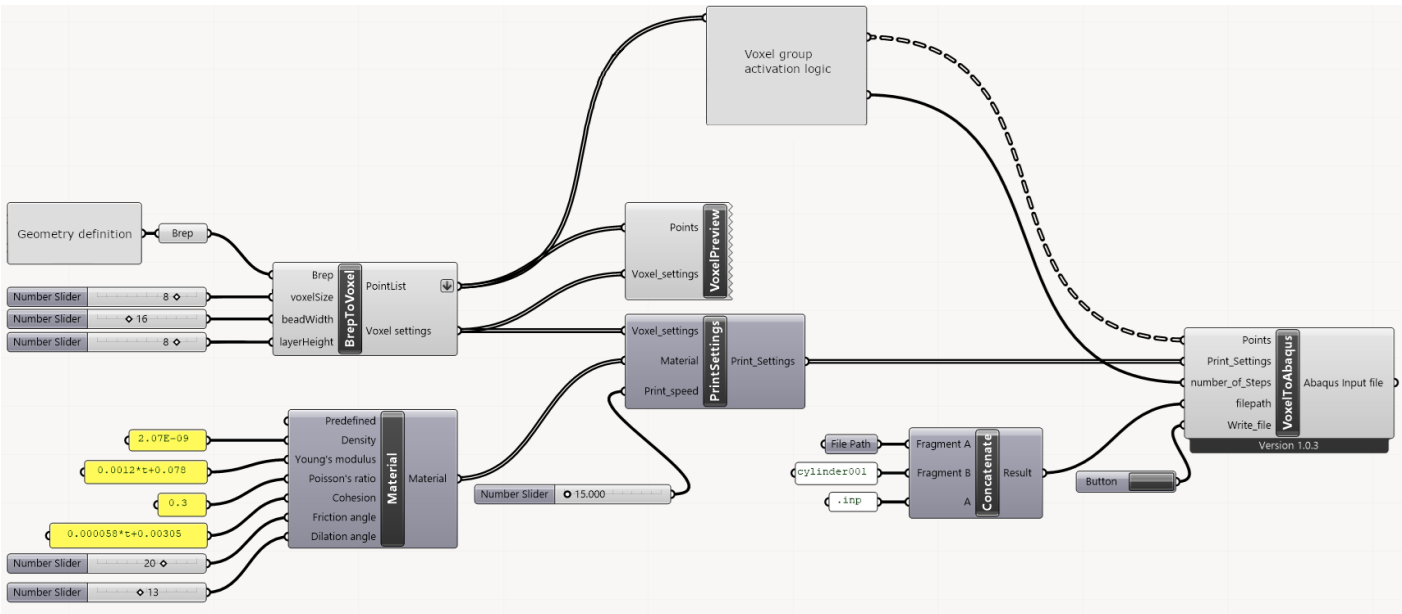

Figure 1. Interconnections among the VoxelPrint components.

Using the BrepToVoxel component, the geometry was discretised into three-dimensional cubic elements (voxels). The voxel distribution follows the decomposed printing path and is primarily governed by the deposited bead width and the voxel size (spatial discretisation). A voxel size of 8 mm was used in this study.

The finite-element discretisation generated using VoxelPrint is shown in Figure.

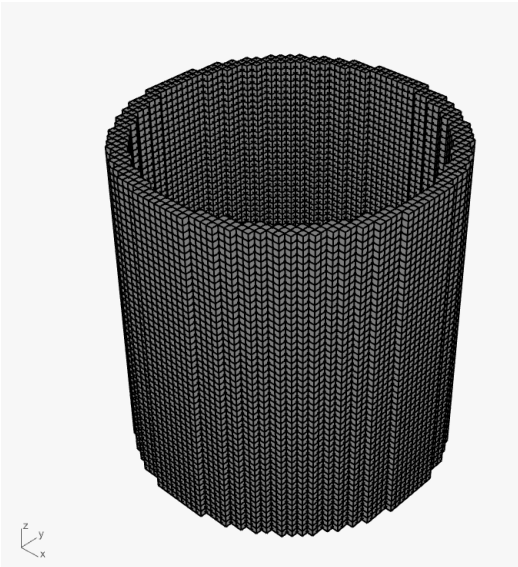

Figure 2. Finite-element discretisation of the cylindrical wall.

2.2 Mohr-Coulomb criterion and material properties

The numerical model was based on a time-dependent Mohr–Coulomb failure criterion and linear stress–strain behaviour up to failure. In its expanded form to include the time-dependent development of material properties, it is given by:

$$\tau_y = C(t) + \sigma_n \tan\big(\varphi(t)\big), \tag{1}$$

where τ_y is the shear yield stress, σ_n– normal stress, C– cohesion between particles, φ- the angle of internal friction caused by the frictional resistance and interlocking between internal particles. Both C and φ may be time-dependent [4].

The material used was fresh concrete, with time-dependent material properties adopted from Wolfs et al. [4]. The authors of the referenced study determined the Mohr–Coulomb parameters for this material as functions of concrete age based on the results of direct shear tests. The cohesion is given by the function:

$$C(t) = 0.000058t + 0.00305, \tag{2}$$

where C is the cohesion [MPa], t– concrete age [min] [4].

Experimental results did not indicate an obvious proportion between material age and the internal friction angle; therefore, a constant value of the internal friction angle, $\varphi = 20°$, was adopted.

Then, equation (1) can be written as [4]:

$$\tau_y(t) = (0.000058t + 0.00305) + \sigma_n \tan(20°). \tag{3}$$

Based on compression test results, the time-dependent stiffness and deformation behaviour were established. The Young's modulus as a function of concrete age was determined at 5% strain and is given by:

$$E(t) = 0.0012t + 0.078, \tag{4}$$

where E is Young's modulus [MPa] and t– concrete age [min] [4,5].

The material constants were density $\rho = 2070$ kg.m^{-3}, Poisson's ratio $\nu = 0.3$ and dilation angle $\psi = 13°$. [4,5].

3. Numerical Simulation

The numerical simulations were performed in Abaqus/Standard using a Static, General procedure. The geometry was discretised using three-dimensional solid elements (C3D8) with a characteristic element size equal to the voxel size (8 mm). The resulting FE mesh consisted of approximately 14 200 elements, which were partitioned into element sets containing a prescribed number of elements to enable stepwise activation and represent progressive material deposition during the printing process.

In the initial step, all elements were deactivated, and in subsequent steps, element sets were activated stepwise along the toolpath using Model Change (ADD with strain). Self-weight was applied as a gravitational body load, and the base surface of the first deposited layer was fully constrained.

Geometrical nonlinearity was included to capture large displacements and stability effects. Failure was assumed to occur upon the onset of yielding within the structure, indicated by the development of plastic strain. Plastic strain was therefore used as the primary response quantity to assess buildability. Thermal effects, interlayer bonding imperfections, and post-yield viscous behaviour were not considered in the numerical model.

4. Results

The numerical simulation captures the progressive development of plastic deformation and the emergence of the failure mechanism within the printed cylindrical wall. Plastic strain (PE) was evaluated to identify the onset and evolution of yielding within the structure. Figure presents the evolution of maximum principal plastic strain in the 3D-printed cylindrical wall, illustrating how plastic deformation initiates in the upper part of the wall and progressively localises in the region of maximum curvature of the wall as instability develops. The figure shows the failure mechanism, with the color scale modified for visualization purposes. The results correspond to selected representative increments within the final printing step, captured during the deposition of the last layer at which collapse occurred.

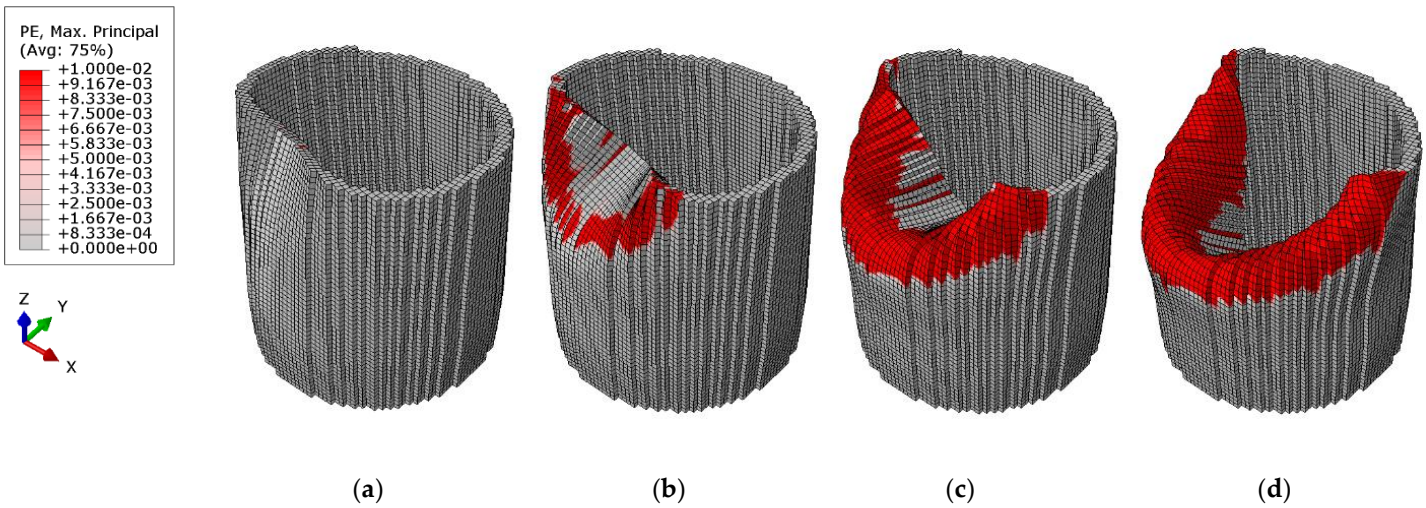

Figure 3. Numerical results of PE, Max. Principal in 3D-printed cylindrical wall for increments: (**a**) 35; (**b**) 45; (**c**) 80; (**d**) 300).

The failure was initiated during the deposition of the 49th layer, after 48 layers had been fully activated. This corresponds to a critical build height of 392 mm. At the onset of failure, the maximum principal plastic strain reached 0.6828, indicating localisation of plastic deformation in the upper region of the wall. The lower part of the wall remained predominantly elastic.

5. Conclusions

This study investigated the early-age buildability of an extrusion-printed cylindrical concrete wall using finite element simulation. The numerical model was generated in Grasshopper using the VoxelPrint pre-processing workflow, and the analyses were performed in Abaqus/Standard with stepwise element activation along the printing path to represent progressive deposition under self-weight.

Plastic strains developed predominantly in the upper part of the wall and localised in the region of maximum lateral deflection, whereas the lower part remained essentially elastic. The observed failure mechanism is therefore interpreted as elastic–plastic buckling of the upper wall region driven by self-weight. The buildability limit of the analysed configuration was reached at a critical build height of 392 mm.

Acknowledgments: This work was supported by the Slovak Research and Development Agency under the project APVV-23-0461, and by the Ministry of Education, Research, Development and Youth of the Slovak Republic under the project VEGA No. 1/0342/24 and KEGA 005TUKE-4/2024.

Conflicts of Interest: The authors declare no conflict of interest.

References

1. Li, Z.; et al. Fresh and Hardened Properties of Extrusion-Based 3D-Printed Cementitious Materials: A Review. *Sustainability* **2020**, *12(14)*.
2. Malaeb, Z.; et al. 3D Concrete Printing: Machine and Mix Design. *International Journal of Civil Engineering and Technology* **2015**, *6 (6)*, 14-22.
3. Wolfs, R. J. M.; Suiker, A. S. J. Structural Failure During Extrusion-Based 3D Printing Processes. *The International Journal of Advanced Manufacturing Technology* **2019**, 104, 565–584.
4. Wolfs, R. J. M.; Bos, F. P.; Salet, T. A. M. Early Age Mechanical Behaviour of 3D Printed Concrete: Numerical Modelling and Experimental Testing. *Cement and Concrete Research* **2018**, 106, 103–116.
5. Vantyghem, G.; Ooms, T.; de Corte, W. VoxelPrint: A Grasshopper Plug-In For Voxel-Based Numerical Simulation of Concrete Printing. *Automation in Construction* **2021**, 122, 103469.
6. Vantyghem, G.; Ooms, T.; de Corte, W. FEM modelling techniques for simulation of 3D concrete printing. *Computational Physics* **2020**.

TECHNICAL UNIVERSITY OF KOŠICE
Faculty of Mechanical Engineering

Quantitative and Visual Assessment of Burn Scars Using 3D Scanning

Katarína Dudová [1,*], Lucia Bednarčíková [1] and Jozef Živčák [1]

[1] Technical University of Košice, Faculty of Mechanical Engineering, Department of Biomedical Engineering and Measurement, Letná 1/9, 04200, Košice, Slovakia
* Correspondence: katarina.dudova@tuke.sk

Abstract: Objective assessment of burn scars is important for clinical documentation and evaluation of treatment outcomes. Conventional two-dimensional methods are limited in their ability to capture complex surface geometry, whereas three-dimensional (3D) scanning enables non-contact quantitative and visual assessment of scar morphology. This study compared two 3D scanning systems-a professional structured-light scanner (Artec Eva) and a portable infrared structured-light scanner (Revopoint Miraco)-for burn scar assessment across anatomically diverse regions. Five patients with scars located on the arm, shoulder, chest, and thigh were included. Three-dimensional surface models were generated using both scanners, and scar surface area, maximum length, and maximum width were measured. Qualitative visual comparison of the reconstructed models was also performed. Surface area measurements showed close agreement between scanners, with absolute differences ranging from 16.6 to 670.0 mm² and no systematic directional trend. Linear measurements of length and width demonstrated even smaller differences, remaining within a few millimeters across all cases. Visual assessment revealed differences in color representation, with Miraco reconstructions displaying more vivid scar appearance; however, these differences did not affect quantitative results. Overall, both scanning systems provided consistent measurements across different anatomical locations, supporting their use for objective burn scar documentation and future personalized treatment applications.

Keywords: burn scars, 3D scanning, surface area

1. Introduction

Objective measurement of scar characteristics is crucial in clinical burn care to evaluate healing, plan treatment, and monitor progression over time. Traditional two-dimensional (2D) methods (e.g., ruler measurements and photography) are limited by geometric distortions and cannot fully represent the complex 3D geometry of human skin surfaces. These limitations can result in inaccurate area estimation and hinder longitudinal assessment of irregular scars [1,2].

Three-dimensional imaging technologies, such as stereophotogrammetry and structured light scanning, provide non-contact surface reconstructions that can overcome these limitations. These approaches have been shown to yield reliable surface measurements and capture detailed morphology in studies of scar and wound assessment [3-5]. For example, 3D stereophotogrammetry was demonstrated as a valid technique for measuring scar volume and surface area with high repeatability [3]. Similarly, dedicated wound scanners have shown strong agreement with clinical measurement techniques in quantifying wound and scar dimensions [6].

Objective imaging tools improve upon subjective clinical scar scales, such as the Vancouver Scar Scale or Patient and Observer Scar Assessment Scale (POSAS), by reducing observer variability and providing quantifiable endpoints [7]. Digital 3D methods have

also been utilized in other wound contexts, including chronic ulcer and surgical sites, indicating broad applicability of these techniques for surface characterization [8,9].

However, direct comparative studies of different 3D scanning systems for burn scar assessment remain limited. Most research focuses on either validating a single device or describing a specific imaging methodology, without systematic evaluation across devices on clinical patient data. Furthermore, the impact of anatomical region — with its associated curvature and surface variation — on measurement agreement between devices is not well characterized.

In this study, we evaluated surface area and linear dimensions of burn scars obtained from two distinct 3D scanning systems across five patients with scars on different anatomical locations. We also conducted qualitative visual evaluations of the 3D reconstructions to explore differences in surface detail representation.

2. Materials and Methods

To obtain data, ethical approval was first secured, and informed consent was obtained from each patient. This study was approved by the Ethics Committee of AGEL Hospital Košice-Šaca (Slovakia) under the number 17-2023.

This study utilized two types of three-dimensional documentation of the same burn scar, acquired using different 3D scanning technologies. The objective was to compare the quality and usability of a professional and a portable 3D scanning system for quantitative and visual assessment of burn scars.

A high-precision 3D model of the scar was acquired using the Artec Eva scanner (Artec 3D, Luxembourg). This professional handheld device employs structured-light projection and is widely used in medical and scientific applications requiring high geometric accuracy. The scan provided detailed surface reconstruction suitable for quantitative analysis of scar surface area, as well as visual assessment of surface morphology. Owing to its established accuracy, this dataset was used as a reference for comparative evaluation.

A second 3D model of the same scar was obtained using the Revopoint Miraco scanner (Revopoint 3D, China), a compact and portable device utilizing infrared structured light technology. The scanner's lightweight design and ease of use make it suitable for simplified and cost-effective scanning scenarios. The resulting 3D model provided sufficient resolution for visual inspection and basic quantitative measurements, although fine surface details were less consistently represented compared to the professional scanning system.

All scans were performed with the patient in a stable seated position to minimize motion artifacts. Both scanning devices were operated according to the manufacturers' recommendations, maintaining a consistent scanning distance and coverage of the scarred region. Each scan was completed within a single session to ensure comparable acquisition conditions. Following acquisition, the raw scan data were processed using the proprietary software provided by each manufacturer. Processing steps included alignment of individual frames, noise reduction, and reconstruction of the final surface mesh.

2.1. Data Processing and Surface Segmentation

The processed 3D models from both scanning systems were exported as polygonal mesh files in *.obj* format, including the associated texture information. The meshes were subsequently imported into the freeware software Meshmixer (Autodesk Inc., San Rafael, CA) for segmentation of the scarred areas.

All segmentation procedures were performed by a single operator to ensure methodological consistency across datasets obtained from both scanners. The segmentation workflow comprised the following steps:

- removal of residual scanning artifacts and mesh imperfections,
- manual delineation of the burn scar using surface selection tools,
- separation of the segmented scar region into an independent mesh object,

- calculation of scar surface area (mm²) using Meshmixer's integrated measurement tools (Figure 1).

Figure 1. Segmentation and measurement of scarred area.

2.2. Linear Measurements

Maximum scar length and maximum scar width were measured directly from the three-dimensional surface models exported in .obj format. All linear measurements were performed using Artec Studio software (Artec 3D, Luxembourg), which provides tools for distance and dimensional analysis on polygonal mesh models.

For each patient, .obj files generated by both scanning systems were imported into Artec Studio. Maximum scar length was defined as the longest visible axis of the scar, while maximum width was measured along the perpendicular axis (Figure 2). To minimize variability related to measurement technique, all measurements were performed by a single operator following a standardized protocol and using the same software environment for both scanners.

Figure 2. Linear measurement of scar dimensions (length and width).

2.3. Visual Assessment

In addition to quantitative analysis, a qualitative visual comparison of the 3D reconstructions was performed. Corresponding models obtained from both scanners were visually inspected to assess surface smoothness, boundary delineation, and local texture representation. This visual assessment was descriptive in nature and aimed to identify qualitative differences in scar appearance between the two scanning systems.

3. Results

3.1. Surface Area Measurements

Surface area measurements obtained from the two 3D scanning systems are summarized in Table 1. Across all five patients, both scanners produced surface area values within comparable ranges, despite substantial differences in scar size between individuals.

Surface area measured using the Artec Eva scanner ranged from 3927.48 to 25 892.20 mm², while values obtained using the Revopoint Miraco scanner ranged from 3910.88 to 25 222.20 mm². Absolute differences in measured surface area between the two systems varied from 16.60 to 670.00 mm².

The smallest difference was observed in Patient 5, where surface area values differed by only 16.60 mm², indicating very close agreement between scanners for smaller scars. The largest difference was observed in Patient 3 670.00 mm², corresponding to the largest scar in the dataset. When considered relative to the total scar size, this difference remained low and did not exceed approximately 3%.

Across the dataset, both positive and negative differences were observed, with no consistent tendency toward higher or lower surface area values for either scanning system. These findings indicate that both scanners provide comparable surface area measurements across scars of varying size and anatomical location.

Table 1. Surface Area Measurements.

Patient	Surface area Artec Eva (mm²)	Surface area Revopoint Miraco (mm²)	Difference in measured surface area (mm²)
Patient 1	5002.16	4932.94	69.22
Patient 2	9464.6	9770.55	305.95
Patient 3	25892.2	25222.2	670
Patient 4	10219.9	10486.6	266.7
Patient 5	3927.48	3910.88	16.6

3.2. Linear Measurements: Length and Width

Maximum scar length and width measurements obtained from both 3D scanning systems are summarized in Table 2. Across all five patients, linear dimensions measured using the Artec Eva and Revopoint Miraco scanners showed close agreement.

Maximum scar length measured with the Artec Eva scanner ranged from 43.32 to 229.88 mm, while corresponding measurements obtained using the Revopoint Miraco scanner ranged from 46.05 to 226.42 mm. Absolute differences in length measurements between the two systems ranged from 0.86 to 3.46 mm.

Similarly, maximum scar width values ranged from 54.58 to 263.44 mm for Artec Eva and from 56.93 to 266.68 mm for Revopoint Miraco. Differences in width measurements varied between 1.78 and 3.83 mm across patients.

No consistent directional trend was observed in either length or width measurements, as both scanners alternately produced slightly higher or lower values depending on the individual case. Compared to surface area measurements, variability between scanners was lower for linear dimensions, indicating high consistency in capturing global scar geometry.

Table 2. Linear Measurements: Length and Width.

Patient	Artec Eva (mm)		Revopoint Miraco (mm)		Difference in linear measurements (mm)	
	length	width	length	width	length	width
Patient 1	43.32	112.93	46.05	115.85	2.73	2.92
Patient 2	124.37	145.88	123.16	142.05	1.21	3.83
Patient 3	144.2	263.44	143.34	266.68	0..86	3.24
Patient 4	229.88	76.37	226.42	74.59	3.46	1.78
Patient 5	87.6	54.58	88.69	56.93	1.09	2.35

3.3. Visual comparison of 3D Reconstruction

Visual inspection of the 3D reconstructions showed that both scanning systems successfully captured the scar regions across all anatomical locations. The scars were clearly identifiable on the reconstructed surfaces in all cases.

A noticeable difference between the two systems was observed in the colour representation of the textured models. In the Miraco reconstructions (Figure 3), the scar regions appeared with more pronounced and vivid colour contrast compared to the surrounding tissue. In contrast, the Artec models generally exhibited more subdued colour tones, resulting in a less visually accentuated scar appearance.

In addition to colour differences, minor variations in surface smoothness and local texture representation were observed between the scanners. However, these visual differences did not correspond to substantial discrepancies in quantitative measurements of surface area or linear dimensions.

Overall, both scanners provided visually interpretable 3D models suitable for qualitative assessment of burn scars, with differences primarily related to visualization characteristics rather than measurable geometric parameters.

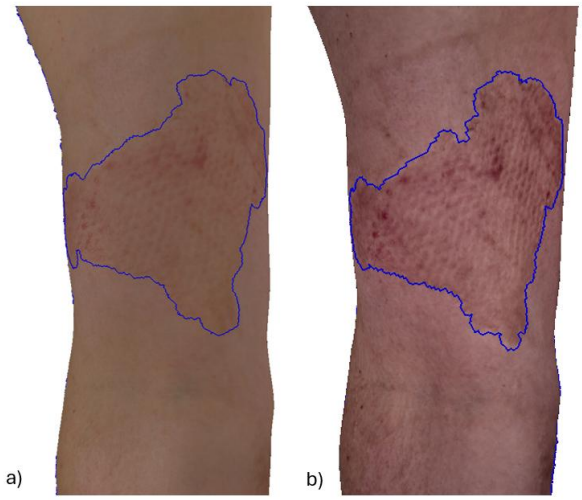

Figure 3. Visual comparison of 3D Reconstruction, a) Artec Eva, b) Revopoint Miraco.

4. Discussion

This study compared two 3D scanning systems for quantitative and visual assessment of burn scars located on anatomically diverse regions. Both scanners provided comparable measurements of scar surface area as well as linear dimensions, indicating consistent capture of global scar geometry.

Differences in surface area between systems were small and showed no systematic directional trend. Linear measurements of length and width exhibited even closer agreement, suggesting that variability between scanners is primarily related to surface reconstruction and segmentation rather than overall dimensional accuracy.

Visual inspection revealed differences in the appearance of textured models, particularly in colour representation. Scar regions appeared more vividly coloured in Miraco reconstructions, whereas Artec models showed more muted tones. These visual differences did not correspond to substantial differences in quantitative measurements.

The main limitation of this study is the small sample size; however, inclusion of scars from multiple anatomical locations supports the applicability of both scanning systems across surfaces with varying curvature. Importantly, accurate 3D scanning and reliable scar segmentation are essential not only for objective clinical documentation but also for the future development and research of 3D-printed, patient-specific compression garments for burn treatment. Overall, the results indicate that both professional and portable 3D scanners can be used for objective burn scar documentation.

Acknowledgments: This research was supported by national project APVV-22-0340- Development and testing of orthoses to support burn treatment using 3D scanning and additive manufacturing, granted by the Cultural and Education Grant Agency of the Slovak Ministry of Education and by national project KEGA 054TUKE-4/2025 - Use of CAx systems in prosthetic and orthotic practice.

Conflicts of Interest: The authors declare no conflict of interest.

References

1. Goutos, I.; Ogawa, R. Strategies for the assessment and treatment of hypertrophic scars and keloids—A review. Scars Burns Heal. 2017, 3, 1–10.
2. Atiyeh, B.S.; Dibo, S.A. Surgical and non-surgical management of scars: An updated review. *Burns Trauma* 2018, 6, 1–19.
3. Stekelenburg, C.M.; Jaspers, M.E.H.; Niessen, F.B.; Knol, D.L.; van der Wal, M.B.A.; de Vet, H.C.W.; van Zuijlen, P.P.M. A clinometric analysis of 3D stereophotogrammetry for measuring scar volume and surface morphology. *J. Clin. Epidemiol.* 2015, 68, 782–787.
4. Zuijlen, P.P.M.; Angeles, A.P.; Kreis, R.W.; Bos, K.E.; Middelkoop, E. Three-dimensional digital stereophotogrammetry: A reliable and valid technique for measuring scar surface area. *Plast. Reconstr. Surg.* 2013, 132, 1025–1035.
5. Jin, J.; Li, H.; Chen, Z.; Sheng, J.; Liu, T.; Ma, B.; Zhu, S.; Xia, Z. A 3D wound scanner: A novel, effective, reliable, and convenient tool for measuring scar area. *Burns* 2018, 44, 1930–1939.
6. Choo, A.M.H.; Martin, R.; Fryer, L.; et al. Scar assessment tools: How do they compare? *Front. Surg.* 2021, 8, 643098.
7. Draaijers, L.J.; Tempelman, F.R.H.; Botman, Y.A.M.; Kreis, R.W.; Middelkoop, E.; van Zuijlen, P.P.M. The Patient and Observer Scar Assessment Scale: A reliable and feasible tool for scar evaluation. *Plast. Reconstr. Surg.* 2004, 113, 1960–1965.
8. Liu, Y.; Dang, C.; Li, H.; Wang, Z. Clinical application of three-dimensional imaging techniques in wound assessment: A review. *Int. Wound J.* 2021, 18, 676–692.
9. Bağcıer, O.; Şimşek, G.G.; Güneş, A.; et al. Advanced three-dimensional imaging techniques for dermatologic surface analysis. *Dermatol. Surg.* 2020, 46, 1021–1029.

TECHNICAL UNIVERSITY OF KOŠICE
Faculty of Mechanical Engineering

Image classification using convolutional neural network in container spreader control process

Pavol Dzurňák [1,*], Martin Mantič [1]

[1] Faculty of Mechanical Engineering, Technical university of Košice, Slovakia; dzurnak@tuke.sk; martin.mantic@tuke.sk
* Correspondence: dzurnak@tuke.sk; Tel.: +421 55 602 7654

Abstract: Automation of container handling represents a significant challenge in modern logistics and port systems. A critical step in this process is the reliable identification and localization of containers during the operation of a container spreader. This article focuses on the application of convolutional neural networks (CNNs) to the task of image classification within the control process of a spreader in a container terminal model. The proposed solution is based on the ResNet-50 architecture and is integrated into an object detection framework using YOLOv5, enabling real time image processing. Experimental results confirm that the combination of detection and classification achieves high accuracy and robustness even when trained on a limited amount of data.

Keywords: convolutional neural network, image classification, container spreader, ResNet-50, YOLOv5, transfer learning, computer vision

1. Introduction

Container transport forms the backbone of the global logistics chain, and its efficiency directly affects the speed and cost of goods transportation. Container handling in ports and container terminals is often based on manual or semi-automated control, which is prone to human error and limited reaction times. With the advancement of the Industry 4.0 paradigm, there is an increasing demand for autonomous systems capable of independent decision-making based on sensory data. One of the key challenges in implementing real time control of a container terminal model is the reliable recognition of containers in camera imagery and their discrimination from other objects present in the scene. Traditional image processing methods, such as color thresholding or edge detection, prove insufficient under real-world operating conditions. Deep neural networks, and convolutional neural networks in particular, offer a substantially higher level of robustness and accuracy [1].

Several prior studies have addressed related problems in automated container handling using deep learning and computer vision. Lee [7] proposed a deep learning–assisted system for real-time container corner casting recognition using a recurrent neural network with LSTM units combined with GoogLeNet features, achieving an average detection accuracy exceeding 98% under diverse real-world conditions. Wang [8] applied convolutional neural networks to the recognition and positioning of container lock holes for intelligent handling terminals, demonstrating the feasibility of CNN-based approaches for precise spatial localization tasks in container manipulation. More recently, Nguyen Thi Phuong et al. [9] employed the YOLO-NAS architecture for automated container damage detection, achieving a mean average precision (mAP) of 91.2% in real-time inspection scenarios at port facilities. While these works address specific subtasks of container handling — corner casting detection, lock hole positioning, and damage inspection — the integra-

tion of a two-stage pipeline combining fast object detection with dedicated image classification for container spreader control remains underexplored. The present work aims to fill this gap by proposing a YOLOv5 + ResNet-50 pipeline specifically designed for real time container identification in a bridge crane model environment.

2. Convolutional neural networks and ResNet-50 architecture

Convolutional neural networks constitute a fundamental deep learning tool for image data processing. Their principal advantage lies in the ability to automatically extract relevant features without the need for manually designed descriptors [2]. CNNs employ convolutional filters, pooling layers, and nonlinear activation functions to hierarchically model visual structures.

The ResNet (Residual Network) architecture, described for example in [1], addresses the problem of accuracy degradation in very deep networks through the introduction of residual (skip) connections. ResNet-50 consists of 50 layers and enables effective training of deep models without suffering from vanishing gradients. Owing to these properties, it is well suited for industrial applications where high accuracy and model stability are required.

Within the control process of a bridge crane model, ResNet-50 is employed as a classification model, leveraging the principle of transfer learning. Pretrained weights from the ImageNet dataset serve as the foundation, while only the final fully connected layer is trained and adapted to the target classes. The objective is to recognize containers (Fig. 1) within the terminal environment in order to guide the spreader toward container grasping as efficiently as possible.

Figure 1. Container Stacking Strategy in the Container Terminal Model.

3. Coupling Image Classification with Object Detection Based on the YOLOv5 Framework

Standalone classification of the entire image is insufficient for bridge crane control, as the camera captures a complex scene containing multiple objects. For this reason, a combined detection / classification approach is implemented. Object detection within the image is performed using the YOLOv5 (You Only Look Once) model, which ranks among the fastest detection algorithms and is well suited for real time applications [3].

The system pipeline is structured as follows:

1. The camera captures the image of the spreader's working area (Fig. 2)
2. YOLOv5 detects objects in the scene and generates bounding boxes.
3. The cropped regions are subsequently provided as input to the ResNet-50 classification model.

The classification output determines whether the detected object corresponds to a container or to a different type of object.

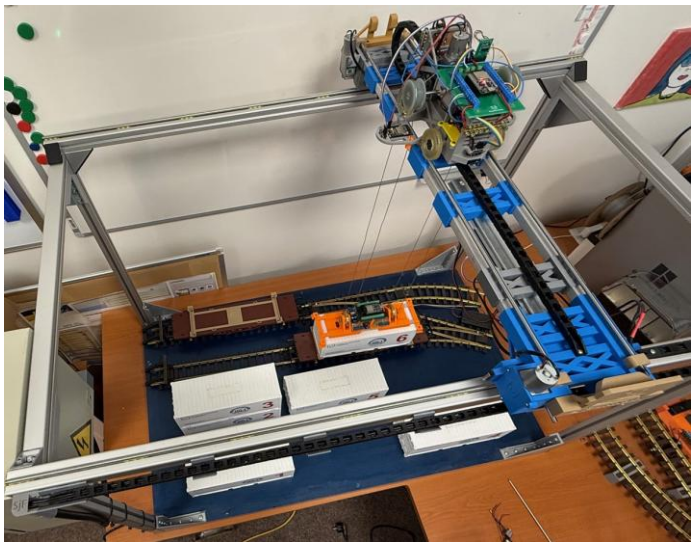

Figure 2. Perspective View of the Container Terminal Model.

4. Dataset Composition, Model Training, and Experimental Results

The dataset used in this project consists of a combination of the public CIFAR-10 dataset and a custom-defined container class. The CIFAR-10 dataset was selected as the base because it provides a diverse set of 60,000 labeled images across 10 general object categories, enabling the classifier to develop robust low-level and mid-level feature representations before specializing for the target container class. This strategy leverages the known effectiveness of multi-class pretraining for improving generalization in fine-grained classification tasks [4]. The custom container class comprised 120 manually annotated images captured from the terminal model camera under varying lighting conditions and viewing angles. After applying data augmentation — including rotations (±15°), scaling (0.8–1.2×), brightness jittering (±20%), horizontal flipping, and perspective transformations — the container class was expanded to approximately 840 samples. The final combined subset of CIFAR-10 dataset contained 6800 images. An 80/10/10 split was applied, resulting in 5440 training images, 680 validation images, and 680 test images. The test set was held out entirely during training and used solely for final evaluation.

Training was performed using the Adam optimizer [5] with an initial learning rate of 1×10^{-3} and a batch size of 64, in conjunction with the cross-entropy loss function. Training was conducted for 50 epochs with early stopping (patience = 5) based on validation loss. The experimental results (Fig. 3) demonstrate that the model converges reliably. On the held-out test set, the ResNet-50 classifier achieved an overall accuracy of 94.2%, with the container class reaching a precision of 0.96, recall of 0.94, and F1-score of 0.95. When integrated with YOLOv5 detection (confidence threshold 0.85), the end-to-end pipeline achieved a container detection mAP@0.5 of 0.93 and a combined classification F1-score of 0.94.

Table 1. Comparison of classification approaches on the container test set.

Method	Precision	Recall	F1-score
Color Thresholding	0.68	0.56	0.61
ResNet-50 (standalone)	0.91	0.84	0.87
MobileNetV2 + YOLOv5	0.92	0.87	0.89
ResNet-50 + YOLOv5 (proposed)	**0.96**	**0.94**	**0.95**

For comparison, Table 1 presents baseline results obtained using alternative approaches on the same test set: a standalone ResNet-50 classifier without YOLO detection achieved an F1-score of 0.87 for the container class, while a color-based thresholding method achieved only 0.61. A MobileNetV2 classifier combined with YOLOv5 reached an F1-score of 0.89, confirming the advantage of the deeper ResNet-50 backbone in this application.

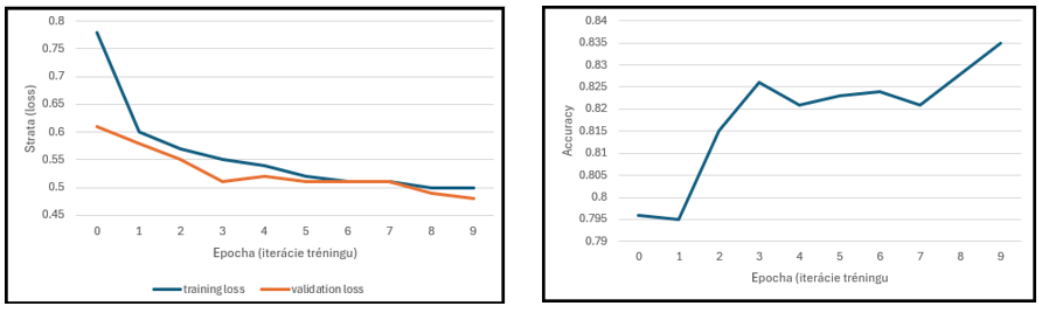

(**a**) Loss. (**b**) Accuracy.

Figure 3. Visualization of Training Progress – Loss and Accuracy. During training, both loss and accuracy were monitored on the training and validation datasets. The plots show a consistent decrease in loss, while accuracy steadily increases until reaching a plateau, indicating effective learning behavior without pronounced signs of overfitting.

To achieve higher accuracy, object detection using YOLOv5 was incorporated into the system. YOLOv5 is a state-of-the-art deep learning algorithm designed for real time object detection. It belongs to the You Only Look Once (YOLO) family of models, whose defining characteristic is the ability to perform object detection in a single forward pass through the neural network, resulting in very high image processing speed. YOLOv5 is implemented as a single stage detection system that directly predicts, from the input image:

- the coordinates of bounding boxes,
- the object class, and
- a confidence score.

The system implementation was realized in real time within a web-based interface using the Flask framework, with the confidence threshold set to 0.85 in order to minimize false positive detections.

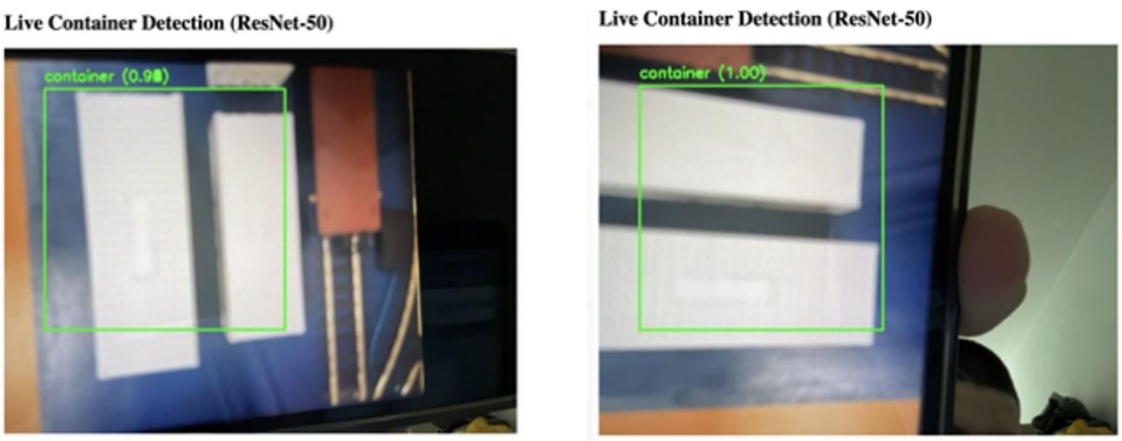

Figure 4. Examples of object detection in real time using YOLOv5.

5. Discussion

The implemented solution employs an ESP32-CAM microcontroller as the image acquisition sensor, an ESP32 WROOM S3 for controlling the crane and spreader motors, and an NVIDIA Jetson Nano for performing the image recognition tasks. The selected infrastructure satisfies two fundamental requirements for the implementation of bridge crane control, namely real time operation and cost effective deployment.

Communication between the individual components of the infrastructure is realized via Wi-Fi 6 (IEEE 802.11ax), with a transmission speed of up to 1 Gbps. The use of the specified hardware platform provides a high degree of scalability and enables future extensions, such as container distance estimation and trajectory prediction.

6. Conclusions

This article presents a practical application of convolutional neural networks in the control process of a container crane model. The combination of object detection using YOLOv5 and classification based on ResNet-50 provides a robust solution suitable for real industrial operating conditions. The output of the classification model is directly usable within the crane control algorithm. Once the presence of a container is confirmed, the system can automatically adjust the position of the spreader along the X and Y axes and initiate the container grasping process.

The project results confirm that deep learning represents a promising tool for the automation of logistics processes. In future system designs, it will be necessary to also address cybersecurity considerations, particularly with respect to the requirements of the NIS2 Directive (EU) 2022/2555 and the Cyber Resilience Act (CRA), Regulation (EU) 2024/2847 [6], which are specifically targeted at IoT devices.

Acknowledgments: This article was elaborated in the framework of the Grant Projects KEGA 044TUKE-4/2024.

References

1. K. He, X. Zhang, S. Ren, J. Sun, *Deep Residual Learning for Image Recognition*, Proceedings of the IEEE Conference on Computer Vision and Pattern Recognition (CVPR), 2016, pp. 770–778.
2. Y. LeCun, Y. Bengio, G. Hinton, *Deep Learning*, Nature, vol. 521, no. 7553, 2015, pp. 436–444.
3. J. Redmon et al., *You Only Look Once: Unified, Real-Time Object Detection*, CVPR, 2016.
4. A. Krizhevsky, I. Sutskever, G. E. Hinton, *ImageNet Classification with Deep Convolutional Neural Networks*, NIPS, 2012.
5. Diederik P. Kingma, Jimmy Ba, *Adam: A Method for Stochastic Optimization*, https://doi.org/10.48550/arXiv.1412.6980, 2017.
6. European Parliament & Council. (2024). Regulation (EU) 2024/2847 of the European Parliament and of the Council of 23 October 2024 on horizontal cybersecurity requirements for products with digital elements (Cyber Resilience Act). *Official Journal of the European Union* L, 2024/2847, 20.11.2024
7. J. Lee, Deep Learning–Assisted Real-Time Container Corner Casting Recognition, International Journal of Distributed Sensor Networks, vol. 15, no. 1, 2019. https://doi.org/10.1177/1550147718824462
8. X. Wang, Recognition and Positioning of Container Lock Holes for Intelligent Handling Terminal Based on Convolutional Neural Network, Traitement du Signal, vol. 38, no. 2, 2021, pp. 467–472. https://doi.org/10.18280/ts.380226
9. T. N. T. Phuong, G. S. Cho, I. Chatterjee, Automating Container Damage Detection with the YOLO-NAS Deep Learning Model, Science Progress, vol. 108, no. 1, 2025. https://doi.org/10.1177/00368504251314084

TECHNICAL UNIVERSITY OF KOŠICE
Faculty of Mechanical Engineering

Advancing Technical Research through Thermal Imaging: Educational Perspectives and Case Studies

Valéria Eiben [1,*], Ružena Králiková [1], Ervin Lumnitzer [1]

[1] Technical University of Kosice; valeria.eiben@student.tuke.sk; ruzena.kralikova@tuke.sk; ervin.lumnitzer@tuke.sk
* Correspondence: Ing. Valeria Eiben, Lomonosovova 36, 040 01 Kosice, valeria.eiben@student.tuke.sk; Tel.: +421 905 357 097

Abstract: Thermal imaging, also known as infrared thermography, has become an essential diagnostic and analytical tool across engineering, environmental science, materials research, and biomedical fields. Its ability to non-invasively visualize temperature gradients and thermal phenomena uniquely suited to studying dynamic physical processes that cannot be easily observed by conventional instrumentation. This article examines the scientific underpinnings of thermal imaging, its expanding role in technical research, and its emerging significance in education. Through selected case studies, we highlight how thermal imaging enhances problem-solving, fosters experiential learning, and supports innovation in modern research environments.

Keywords: thermal imaging; education; infrared camera.

1. Introduction

As technological developments continue to accelerate, modern education particularly within technical and engineering disciplines faces increasing pressure to adopt innovative teaching methods that connect theoretical foundations with practical skills. While traditional didactic instruction remains essential, it often lacks the capacity to fully develop the hands-on competencies and diagnostic reasoning demanded in contemporary industrial environments. In response, educators are integrating advanced diagnostic technologies into the learning process, with thermographic infrared (IR) imaging emerging as one of the most promising tools [1]. Thermography, or thermal imaging, is a non-contact technique used to visualize temperature distributions on surfaces by detecting the infrared radiation emitted by objects. Any object above absolute zero emits IR radiation, which can be captured and converted into a visual representation through a thermographic camera [2]. These thermal images, or thermograms, reveal temperature anomalies, heat transfer patterns, and energy losses, making thermography invaluable across mechanical engineering, electrical diagnostics, materials science, and building inspection. The fundamental principle underlying thermography is rooted in Planck's law of blackbody radiation, which describes how objects emit electromagnetic radiation as a function of their temperature. Thermographic cameras contain highly sensitive detectors capable of identifying minute temperature variations with considerable precision. Unlike conventional temperature measurement instruments, thermal imaging provides a spatially resolved temperature map, enabling real-time observation of dynamic processes without direct contact or disruption. The integration of thermographic sensors into unmanned aerial vehicles (UAVs) has further transformed data acquisition in scientific and technical applications. Numerous studies demonstrate the growing significance of thermal UAVs as scalable, intelligent platforms for environmental monitoring, resource management, and technical

diagnostics [2]. With continuing advancements in sensor resolution, AI-enhanced analytics, and autonomous flight control, thermal drones are becoming indispensable tools in multidisciplinary research and applied science [3].

Within educational contexts, thermography introduces a valuable shift toward experiential and inquiry-based learning. By making invisible thermal phenomena visible, students gain deeper understanding of concepts such as heat transfer, thermal conductivity, frictional heating, and energy efficiency. Moreover, thermographic experiments promote interdisciplinary thinking by connecting principles from physics, engineering, environmental science, and digital technologies. This paper examines the educational potential of thermographic imaging in technical instruction, emphasizing its capacity to enhance student engagement, strengthen diagnostic reasoning, and better prepare learners for real-world engineering challenges [4].

2. Educational Applications

Thermal imaging has become a powerful tool in technical education, particularly in mechanical engineering, because it allows abstract concepts of heat transfer to be visualized in a clear and engaging way. For example, when students study conduction, convection, and radiation, thermal cameras provide real-time images of temperature distribution, making these processes visible rather than purely theoretical. This direct visualization helps learners grasp the dynamics of energy transfer more intuitively and supports deeper understanding of fundamental principles. In laboratory settings, thermal imaging serves as an effective teaching aid. It enables students to analyze the thermal behavior of different materials, evaluate insulation efficiency, and assess the performance of mechanical systems under varying conditions. By comparing conventional and environmentally friendly materials, students can directly observe differences in thermal conductivity or heat retention, which reinforces both theoretical knowledge and practical skills [5].

Another important aspect is interactive learning. Thermal cameras allow students to actively participate in experiments by observing how temperature changes across surfaces or components. This hands-on experience increases engagement, stimulates curiosity, and encourages critical thinking. Instead of relying solely on numerical data, learners can interpret visual patterns and connect them with engineering concepts, which enhances comprehension and retention. Thermal imaging plays a crucial role in safety training. In technical education, students often work with machines, electrical systems, or experimental setups where overheating can pose risks [5]. By using thermal cameras, instructors can demonstrate how to identify hot spots, faulty connections, or components under stress. This not only improves safety awareness but also prepares students for real-world engineering practice, where preventive diagnostics are essential. We can assume these benefits into next points:

- Visualization of heat transfer: Using thermal cameras to demonstrate conduction, convection, and radiation in real time;
- Laboratory teaching tool: Enhances understanding of material properties, insulation efficiency, and mechanical system performance;
- Interactive learning: Students can directly observe temperature distribution in experiments, improving engagement and comprehension;
- Safety training: Identifying overheating components in machines or electrical systems during practical courses [5].

3. Research Applications

Thermal imaging has proven to be an invaluable tool in research across mechanical engineering, particularly when investigating environmentally friendly materials. One of its most significant applications lies in material characterization. By analyzing thermal conductivity, emissivity, and degradation patterns, researchers can better understand how eco-friendly composites behave under different thermal loads. This knowledge is essential for designing sustainable materials that maintain mechanical performance while reducing environmental impact. Another important area is structural health monitoring. Thermal imaging enables the detection of defects, cracks, or delamination in mechanical structures by identifying irregular thermal signatures. Such non-invasive diagnostics are crucial for ensuring the reliability and safety of components, especially when working with new bio-based or recycled materials whose long-term performance must be carefully validated. Thermal imaging also plays a central role in energy efficiency studies. It allows researchers to evaluate insulation properties, quantify heat losses in mechanical systems, and compare the performance of sustainable materials against conventional alternatives. This application is particularly relevant in the context of climate change, as it supports the development of energy-efficient technologies and contributes to reducing carbon footprints in industrial processes. Finally, thermal imaging is widely used in non-destructive testing (NDT). Infrared thermography provides a means of assessing mechanical components without causing damage, making it ideal for testing prototypes, monitoring wear, and validating new material solutions. This approach not only saves resources but also accelerates the research cycle by enabling repeated testing under different conditions. Together, these applications highlight the versatility of thermal imaging as both a diagnostic and developmental tool. Its integration into mechanical engineering research supports the advancement of sustainable materials and technologies, bridging the gap between laboratory innovation and practical implementation. The main research areas are primarily focused on:

- Material characterization: Studying thermal conductivity, emissivity, and degradation of eco-friendly composites;
- Structural health monitoring: Detecting defects, cracks, or delamination in mecha**ni**cal structures via thermal signatures;
- Energy efficiency studies: Evaluating insulation, heat losses in mechanical systems, and performance of sustainable materials;
- Non-destructive testing (NDT): Applying infrared thermography to assess mechanical components without damaging them [5].

Thermal imaging also plays a central role in energy efficiency studies. Building and mechanical system audits frequently employ infrared cameras to identify heat losses, evaluate insulation performance, and optimize energy consumption. Several works have integrated thermal imaging with UAV platforms and advanced image processing, enabling large-scale diagnostics of industrial and residential infrastructure [2,3,4,5]. Such applications highlight the contribution of thermography to sustainability goals by reducing carbon footprints and improving energy management. The integration of thermal imaging into mechanical engineering supports the transition toward sustainable technologies. It bridges the gap between material science, smart innovations, and industrial practice, making it a versatile tool for both academic and applied engineering contexts oriented to:

- Eco-friendly materials: Comparing thermal behavior of biodegradable polymers vs. conventional composites;
- Smart materials: Using thermal imaging to study self-healing or adaptive materials;
- Industrial applications: Monitoring machinery, engines, and manufacturing processes for sustainability and efficiency.

4. Methodological Considerations

Methodological Considerations in thermal Imaging consists from these steps:

4.1. Calibration and accuracy

Proper calibration is essential to ensure reliable measurements. Thermal cameras must be adjusted to account for reference temperatures and emissivity values of the observed materials. Without calibration, recorded data may be misleading, especially when comparing different materials or conducting long-term monitoring. Accuracy also depends on sensor quality, lens characteristics, and the stability of environmental conditions during measurement.

4.2. Data processing and image analysis (software tools, false-color mapping)

Raw thermal images often require post-processing to extract meaningful information. Software tools enable false-color mapping, temperature profiling, and quantitative analysis of heat distribution. Advanced image analysis can highlight subtle variations that are not visible to the naked eye, supporting both educational demonstrations and research applications. In mechanical engineering, such processing is crucial for evaluating insulation efficiency, detecting defects, or comparing eco-friendly materials with conventional alter-natives.

4.3. Limitations of thermal imaging

Emissivity variations, environmental conditions, resolution constraints. Despite its advantages, thermal im-aging has inherent constraints. Emissivity variations between materials can affect accuracy, as surfaces with low emissivity may appear cooler than they are. Environmental conditions such as ambient temperature, humidity, or airflow can distort readings. Resolution limitations of thermal cameras may restrict the detection of fine details, particularly in micro-scale material studies. Researchers must therefore interpret results carefully and, when possible, combine thermal imaging with complementary [6,7].

5. Practical experiment

The test of this paper is indoors. The main contents of the test are indoor air temperature, outdoor air temperature and the surface temperature of the envelope structure. The main equipment and instruments used are IR FLUKE infrared thermal imager. The testing time is in the afternoon. During the testing period, the weather is cloudy and the temperature varies obviously day and night. It belongs to the typical winter climate. During the test, the distance between the infrared thermal imager and the target is 1.5 m, and the shooting line of sight is parallel to the surface normal of the target. In addition, the hot box method is used as the standard data to compare the effectiveness and superiority of this method. Figure 1 is the flow chart of experiment. After choosing a reasonable environment, the test of this example is carried out. Firstly, the infrared thermal imager is used to take pictures and process images; secondly, the air tightness of the wall is checked; then, the thermal defect area is judged, and the reasonable detection area is selected after eliminating the thermal defect area. Finally, the data obtained are processed by using correction method is used to detect and correct, and after re-processing, the corrected data are obtained [7].

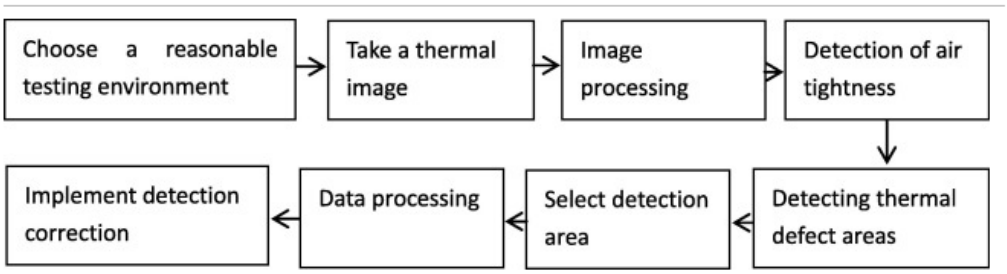

Figure 1. Test flow chart.

After capturing images with an infrared thermal imager, the recorded data must be processed to obtain meaningful results. Thermal images are typically displayed in pseudo color form, as shown in Figure 2.

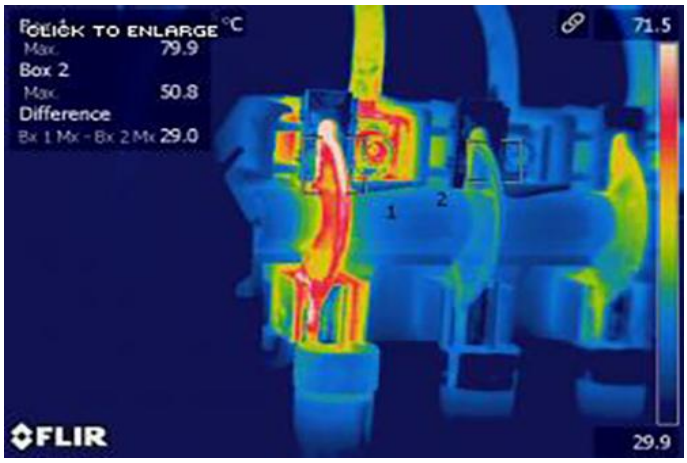

Figure 2. Thermographic Electrical Inspection.

However, the practical information lies in the one-dimensional temperature values of individual pixels, while the three-dimensional pseudo color representation is less suitable for precise extraction of temperature data. Once a suitable detection environment is selected, thermal images of the object are collected with the infrared imager. Through image processing, can be evaluated and thermal defect areas identified. A reasonable detection area is then chosen, and the relevant temperature information is extracted.

To minimize errors in calculating the heat transfer coefficient from raw infrared data, a temperature correction method is introduced. This approach adjusts the values obtained from thermal images using environmental radiation data measured by the hot box method. In this study, the hot box method yielded a heat transfer coefficient of U = 0.732, which was used to correct the infrared measurements [8].

The thermal transmittance U is calculated as:

$$U = \frac{Q}{\mathrm{A} \cdot \Delta \mathrm{T}} \tag{1}$$

Where:

U = thermal transmittance (W/(m²·K))

Q = steady-state heat flow rate through the sample (W)

A = surface area of the specimen (m²)

ΔT = temperature difference between the hot and cold sides (K)

The experiment also included quantitative comparisons of the results obtained using the infrared (IR) method and the hot box method, as shown in Table 1.

Table 1. Comparison of heat transfer coefficient measurement results.

Measurement method	Heat transfer coefficient U [W·m⁻²·K⁻¹]	Difference from hot box	Relative deviation [%]
Infrared Thermography (IR)	0,756	+ 0,024	3,28 %
Hot box method	0,732	0	0 %

Explanation

- The IR method yielded a U-value of 0.756 $W \cdot m^{-2} \cdot K^{-1}$.
- The hot box method (reference method) yielded a U-value of 0.732 $W \cdot m^{-2} \cdot K^{-1}$.
- The absolute difference between the methods is 0.024 $W \cdot m^{-2} \cdot K^{-1}$.
- The relative deviation is approximately 3.28%, indicating good agreement between the two methods.

The measurement results show that the heat transfer coefficients obtained by infrared thermography are very close to those obtained by the hot-box reference method. The relative deviation between the methods is approximately 3.28%, confirming that the infrared method can be a suitable tool for the rapid diagnosis of the thermal properties of building structures [9].

The proposed detection method is therefore considered feasible, and the corrected temperature values substantially reduce the measurement error compared to the use of unadjusted infrared data. The thermal transmittance (U-value) was calculated according to ISO 8990 using the relation (1) [8,9,10,11].

5.1. Analysis of the Results

Based on the analysis of thermographic images, surface temperature values for the analyzed structure were obtained. Using this data and the temperature difference between the indoor and outdoor environments, the heat transfer coefficient was then calculated. A comparison of the results showed that the value obtained using the infrared method was very close to the value determined by the hot box reference method. Infrared thermography provided a value of approximately U = 0.756 $W \cdot m^{-2} \cdot K^{-1}$, while the hot box method determined a value of U = 0.732 $W \cdot m^{-2} \cdot K^{-1}$. The difference between these values is approximately 0.024 $W \cdot m^{-2} \cdot K^{-1}$, which corresponds to a relative deviation of approximately 3.3%. Such a deviation is relatively small and indicates good agreement between the two methods. The results thus confirm that infrared thermography can be an effective tool for the rapid diagnosis of the thermal properties of building structures. The main advantages of the infrared method are its non-invasive nature, the speed of measurement, and the ability to identify thermal defects over a large area without the need for physical intervention in the structure. On the other hand, it is important to emphasize that the accuracy of this method depends on several factors, particularly the correct setting of the

material's emissivity, climatic conditions, and the quality of thermographic data processing [10,11].

5.2. Measurement uncertainties and potential sources of error

When measuring using infrared thermography, several sources of uncertainty may arise that can affect the accuracy of the results:

- Surface emissivity: one of the most important factors is the correct setting of surface emissivity. Different materials have different abilities to emit infrared radiation, and an incorrect emissivity setting can lead to significant errors in determining surface temperature.
- Reflected infrared radiation: surfaces with higher reflectivity can reflect infrared radiation from the surroundings, which can cause a distortion in the measured temperature. This effect is particularly pronounced on shiny or metallic surfaces.
- Environmental influences: measurement accuracy can also be affected by ambient temperature, airflow, humidity, or solar radiation. These factors can influence the surface temperature of the measured object and thus the resulting calculation of the heat transfer coefficient.
- Measurement geometry: the angle of view and the distance between the camera and the object can affect measurement accuracy. At larger angles, the measured values may be distorted; therefore, it is important to keep the camera as close as possible to the perpendicular direction to the object's surface.
- Thermal camera resolution: measurement accuracy also depends on the technical parameters of the camera used, such as thermal sensitivity (NETD) or the spatial resolution of the sensor.
- Processing of thermographic data: errors can also occur during the processing of thermographic images, for example, when an inappropriate area is selected for analysis or when pseudo color thermograms are misinterpreted [11].

6. Discussion

The future development of thermal imaging in technical education and mechanical engineering research is strongly connected with digitalization, artificial intelligence, and new modes of experimental work. AI-assisted thermal image analysis for predictive research and maintenance. In research, artificial intelligence offers new possibilities for processing large datasets of thermal images. Machine learning algorithms can identify subtle temperature anomalies, classify defect patterns, and predict material degradation over time. This enables researchers to move beyond descriptive analysis toward predictive modeling, supporting both fundamental studies of eco-friendly materials and applied research in mechanical systems. Integration with digital twins for experimental validation. Digital twins provide virtual replicas of mechanical systems that can incorporate real-time thermal data. In research, this integration allows scientists to simulate heat transfer, evaluate material performance, and test design modifications under controlled conditions. Thermal imaging thus becomes a validation tool, linking experimental measurements with computational models. This approach enhances reproducibility, accelerates innovation, and supports interdisciplinary collaboration in sustainable engineering. Thermal imaging also supports the expansion of remote and blended learning. Virtual laboratories can provide students with access to recorded or live thermal imaging experiments, enabling them to analyze heat distribution, insulation performance, or material degradation

from a distance. These platforms make technical education more inclusive, allowing international collaboration and ensuring that students without access to specialized equipment can still gain practical experience. IR thermography can also be embedded into remote experimental platforms, enabling researchers to share datasets, conduct joint experiments, and analyse results across borders. Virtual laboratories with thermal imaging demonstrations allow international teams to collaborate without physical presence, making research more inclusive and resource-efficient. This is particularly relevant for projects focused on sustainability, where global cooperation is essential.

7. Conclusions

Thermal imaging has become a transformative instrument in technical research, enabling detailed examination of thermal processes across engineering, environmental science, renewable energy, and biomedical disciplines. Its capacity to deliver real-time, non-contact thermal information supports technological innovation and enhances diagnostic accuracy. As its integration into research laboratories and educational environments continues to expand, thermal imaging is expected to assume an increasingly central role in advancing scientific inquiry and technological development.

The future of thermal imaging in technical education and research is closely connected to ongoing digitalization and the advancement of intelligent data-processing methods. A particularly promising direction is AI-assisted thermal image analysis for predictive maintenance. By applying machine-learning algorithms to extensive datasets of thermal images, it becomes possible to automatically identify anomalies, forecast component failures, and optimize maintenance strategies. This approach contributes to reduced operational downtime, improved safety, and more sustainable functioning of mechanical systems.

Another significant development is the integration of thermal imaging with digital twins. Digital twins—virtual representations of physical systems—can incorporate real-time thermal data to simulate heat transfer, material behaviour, and overall system performance. These models enable researchers to test various scenarios, visualize thermal effects, and assess design modifications without the need for physical prototypes. Such integration strengthens experiential research and effectively bridges the gap between theoretical knowledge and practical application.

Finally, thermal imaging creates new opportunities for remote experimentation through virtual laboratories. Online platforms allow users to access thermal imaging demonstrations, analyze recorded experiments, and review thermal data from a distance. These virtual environments enhance the inclusivity of technical education, support international collaboration, and provide learners with opportunities to develop practical competencies beyond traditional laboratory settings.

Acknowledgments: This work was supported by the Cultural and Educational Grant Agency of the Ministry of Education, Science, Research, and Sport of the Slovak Republic under project KEGA No. 038TUKE-4/2024 titled *"Increasing the applicability of graduates on the labour market by implementing practice requirements into the teaching process of the environmental engineering study program"*.

Conflicts of Interest: "The authors declare no conflict of interest."

References

1. Theoretical principles of thermography Available online: http://joe-c.de/pages/projekte/thermografie.php. https://op.europa.eu/en/publication-detail/-/publication/815a1969-f74c-11e7-b8f5-01aa75ed71a1/language-en
2. Thermal Imaging Used in Building Thermal Evaluation. Available from: https://www.researchgate.net/publication/379204609_Thermal_Imaging_Used_in_Building_Thermal_Evaluation [accessed Dec 10 2025].
3. Liang, S.L.. Building energy efficiency analysis and diagnosis using integrated image processing and thermal imaging technologies. Traitement du Signal, 2024, Volume 41, No. 3, pp. 1387-1395. https://doi.org/10.18280/ts.410327
4. Cai, W.; Wen, X.; Wang, S.; Wang, L.. A real-time detection method of building energy efficiency based on image processing. Journal of Visual Communication and Image Representation, 2019, Volume 60, pp. 295-304.

5. Niranjan, S.K. Proceedings of the International Conference on Smart Technologies in Computing Electrical and Electronics (IC-STCEE 2020), October 9-10, 2020.
6. Manullang, M.C.T.; Lin, Y.-H.; Lai, S.-J.; Chou, N.-K. Implementation of Thermal Camera for Non-Contact Physiological Measurement: A Systematic Review, Sensors, 2021, pp. 21.
7. Silva, G. P.; Batista, P. I. B.; Póvoas, Y. V. The usage of infrared thermography to study thermal performance of walls: a bibliographic review, In Revista ALCONPAT 2019, pp. 117 - 129.
8. Brynda, P. Úvod do teorie termovizního měření, Praha: České vysoké učení technické, pp. 1-7, 2010.
9. Proszak-Miąsik, D. Use of thermal imaging in construction, In IAPGOS, 2019, pp. 12–15.
10. Liu, L.; Ouyang, W.; Wang, X.; Fieguth, P.; Chen, J. Deep learning for generic object detection: a survey. International Journal of Computer Vision, 2023, pp. 261–318.
11. Nguyen, T. X. B. K.; Chahl, J. A review of modern thermal imaging sensor technology and applications for autonomous aerial navigation, J. Imag., 2021, Volume 7, pp. 217.

TECHNICAL UNIVERSITY OF KOŠICE
Faculty of Mechanical Engineering

Influence of chemical composition, inclusions and microcracks on the mechanical properties of G24Mn6 type steel

Marek Grega [1,*], Janette Brezinová [1]

[1] Technical University of Košice, Faculty of Mechanical Engineering, Department of Technology and Materials engineering, Košice, Slovakia
* Correspondence: - marek.grega@student.tuke.sk, janette.brezinova@tuke.sk

Abstract: This study investigates the relationship between the chemical composition and mechanical properties of G24Mn6 cast steel. Analysis of 13 experimental melts focused on the effects of extreme elemental variations, particularly carbon (C) and manganese (Mn), on notch toughness (KV) at -40°C. Results indicated no significant correlation between C or Mn changing representation and toughness within the narrow range tested. However, substantial variability in KV was observed (up to 29 J within a single melt), which was attributed to material inhomogeneity and non-metallic inclusions averaging 25 µm. A 376 µm microcrack associated with inclusions was identified, significantly reducing KV values to 27 J at -40°C. The findings confirm that while heat treatment determines baseline properties, localized discontinuities and inclusion are the primary cause of mechanical deviations

Keywords: Steel microstructure; microcracks; inclusions in metal; mechanical properties, casting

1. Introduction

The requirements for the quality mechanical parameters of G24Mn6 steel castings impose significant limitations on their industrial application, primarily due to their specific chemical composition and mechanical properties. This steel grade is commonly used in machinery, railroad, automotive industries, and transportation applications and it is essential that the material exhibits both good machinability and weldability [1].

The mechanical properties of hardened steels are highly dependent on the type and amount of basic and alloying elements. Proper optimization of elements such as C, Cu, Ni, Mo, Cr, Mn, Al, Ti and V, combined with appropriate processing, allows the design of steels with excellent strength, toughness and ductility [2-7].However, excessive or poorly balanced alloying can lead to adverse effects, which highlights the importance of precise control of composition and processing. Despite significant research on the influence of chemical elements on the mechanical properties of steel, gaps remain in the understanding of the combined effects of multiple alloying elements and the optimization of heat treatment processes for these steels [7-10].

The main specification of chemical element at additives is change the mechanical and technological properties of steel materials in both positive and negative ways. Cast steel G24Mn6 is specific in that, out of the entire group of steels described in the EN 10293 standard [11], it is one of 30 types of steel that must meet the requirements for a notched toughness of at least 27 Joules at -20°C, a tensile strength of at least 700 MPa, and at the same time has a limited range for carbon to 0.05% and for manganese only 0.3%. The balance and interaction of chemical elements, together with processing parameters such as heat treatment are essential for optimizing the performance of high-strength steels[12]. Based on the analyses, it was shown that, increasing the Cu and Ni content can significantly increase the yield strength and tensile strength while maintaining acceptable

toughness. Molybdenum and niobium additions are known to refine martensitic microstructures, improve tempering resistance, and increase both strength and toughness. However, excessive or poorly balanced alloying can lead to reduced ductility, increased brittleness, or other adverse effects. [13-15]. While analyzing a dataset of 134 melts, significant local extremes in mechanical property behavior were found even when chemical elements did not change. [16] This led to a detailed investigation of the emergence of such anomalies.

The presence of microcracks, metallic and non-metallic inclusions in steels of the G24Mn6 type and similar high-manganese steels leads to a deterioration in the mechanical properties of castings. Microcracks are mainly caused by segregation of elements, rapid cooling, stress concentrations and the presence of inclusions, which act as initiation points for crack propagation. Inclusions, especially oxides, sulfides and complex compounds (e.g. MnS, Al2O3, CaO), reduce the toughness, fatigue life and fracture toughness of steel. Larger and more numerous inclusions have a more significant negative effect on strength and fracture toughness [17, 18].

The paper presents the results of research aimed at determining the presence of metallic and non-metallic inclusions in G24Mn6 steel, which cause the occurrence of microcracks and thus negatively affect the results of mechanical properties.

2. Materials and Methods

The research was based on data collected over 20 months of casting production, followed by 13 experimental melts with specific chemical compositions. The investigated G24Mn6 steel was produced in induction furnaces with a maximum capacity of 2 ton. Castings were formed using sand–bentonite molds and poured with a manually operated ladle with a standard bottom outlet. Following casting, the components were knocked out from the molds, the gating and feeding systems were removed, and the castings were normalized, sandblasted, visually inspected, and repaired by welding as required. Subsequently, heat treatment—consisting of quenching in a continuous hardening line with polymer cooling followed by tempering in a continuous gas furnace with electronic temperature control. Subsequently, chemical analyses of individual melts were performed, as well as their mechanical properties. Using correlation analyses, the most optimal chemical ratio of individual elements was determined for a balanced achievement of the mechanical properties of this type of steel.

In the previous findings [16] on a test sample of 134 melts, the basic effects of chemical elements that most affect the tensile strength, elasticity and notch toughness of steel were determined using advanced statistical methods. Elements such as copper, carbon, chromium, nickel and molybdenum had the most significant effect on mechanical values. Elements such as manganese, silicon, phosphorus, sulfur and aluminum had a low or negligible effect. It should be noted that the research was carried out only on steel grade G24Mn6 for norm EN 10293:2005, which means that the limits of the composition of individual elements of this steel are precisely determined.

Based on the results, the most optimal chemical composition of individual basic and alloying elements in steel was determined, resulting in the most accurate achievement of optimal mechanical values, as shown in Table 1. For an optimal balance between strength and toughness, we optimizing chemical elements with goal minimize the contents of chromium (Cr) and copper (Cu), maintain molybdenum (Mo) below 0.02 wt %, set carbon (C) around 0.23 wt %, and keep manganese (Mn) near the lower end of its range (approximately 1.5 wt %). A slight increase in nickel (Ni) content (by about 0.15 wt %) is advisable to compensate for the reduction in low-temperature toughness. Within the prescribed compositional limits of this steel grade, adjustments to the alloying elements Cr, Cu, and C al-low fine-tuning of the final mechanical response. Increasing the concentrations of these elements results in higher yield strength (Re) and tensile strength (Rm), but simultaneously leads to a reduction in impact toughness (K_V at −20 °C).

The mechanical properties of G24Mn6 steel are primarily determined by the efficiency of its heat treatment and quenching. Therefore, normalizing and quenching were carried out in a continuous quenching line with polymer cooling, followed by tempering in a continuous gas furnace with electronic temperature control. The normalizing and quenching furnaces are verified in accordance with DIN 17052-1 [19], ensuring temperature uniformity for all investigated melts.

In this investigation, 13 individual batches with specific chemical property were subjected to a notch toughness test at a lower temperature of -20°C and -40°C. The tensile test was conducted in accordance with EN ISO 6892-1 [20], while the Charpy impact test for evaluating impact toughness was carried out following EN ISO 148-1:2016 [21]. The difference between the notch toughness results in the two temperature ranges was analyzed, as well as the influence of the main elements (carbon and manganese) on the tensile test results. Subsequently, a metallographic analysis was performed to determine the grain size, the proportion of individual phases, as well as the presence of non-metallic impurities. The type of metallographic phase, the proportion of these phases, the presence of inclusions in the metal and the grain size were evaluated according to ASTM 112-24 [22]. The samples were prepared by gradual polishing and subsequent etching with Nital etchant.

3. Results

This section may be divided by subheadings. It should provide a concise and precise description of the experimental results, their interpretation, as well as the experimental conclusions that can be drawn.

3.1. Chemical analyses

Samples for chemical analysis were evaluated using the optical emission spectrometry (OES) method, performed on specimens taken from a single representative casting. The measurements were carried out with a SPECTRO Analytical Instruments GmbH (Kleve, DE) spectrometer. The chemical composition of individual heats is summarized in Table 1. The ranges of the analyzed individual chemical elements in G24Mn6 steel with highlighted local extrema, main range and average are shown in the graph in Figure 1.

Table 1. The main statistical parameters for selected chemical elements.

	Parameter	**C [wt.%]**	**Mn [wt.%]**	**Si [wt.%]**	**Ni [wt.%]**	**Mo [wt.%]**
Limits according to norm EN 10293:2005	Maximal	0.27	1.5	0.6	0.4	0.12
	Minimal	0.2	1.8	0.0	0.0	0.0
Results from special dataset	average	0.19	1.77	0.43	0.12	0.01
	median	0.18	1.76	0.42	0.12	0.01
	minimal	0.15	1.45	0.39	0.10	0.01
	maximal	0.29	2.00	0.47	0.15	0.02

The observed samples of individual melts were selected so that the carbon content was just outside (0.19 and 0.29) the prescribed limits of 0.2-0.27 wt.%, which is also visible in the average value and median from the analyzed data. The manganese content in these melts was also shifted beyond (1.45 and 2.00) the required limits of 1.5 to 1.8 wt.%. The other evaluated elements were within the prescribed limits.

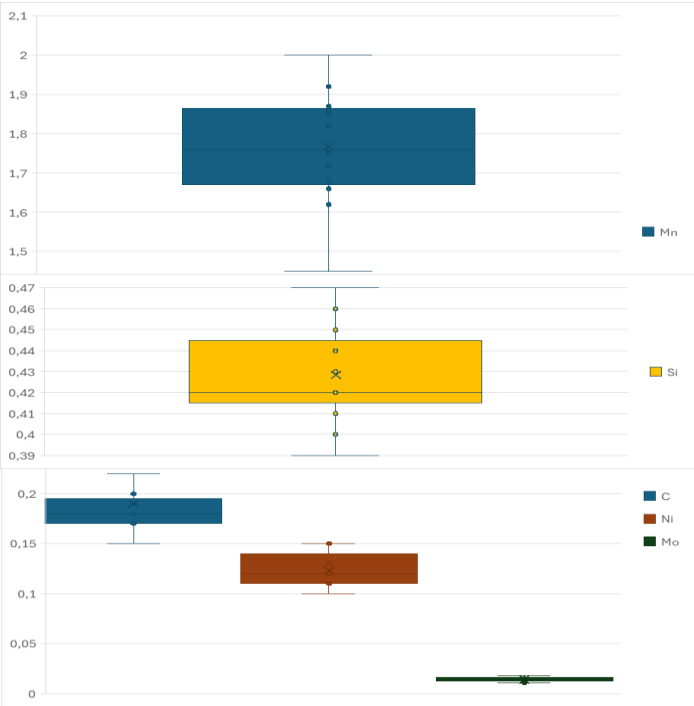

Figure 1. Analyzed individual chemical elements in G24Mn6 steel.

3.2. Tests of selected mechanical properties

At the same time, specimens for mechanical testing were extracted from the same casting. The impact toughness results meet the required limit for G24Mn6 steel in the +QT1 condition, defined as Kv (−20 and -40°C) ≥ 27 Joules. Mechanical test results for all analyzed batches are presented in Table 2.

Table 2. The main statistical parameters for mechanical properties.

	Tensile test			Charpy impact test -20°C	Charpy impact test -40°C	Difference -20°C and -40°C
parameter	**Re [MPa]**	**Rm [MPa]**	**A [%]**	**Kv [J]**	**Kv [J]**	**Kv [J]**
Limit [1]	Min. 550	700-800	Min. 12	Min. 27	-	-
average	555	714	16.15	52	36,8	15.7
median	561	716	17.00	53	36,5	16.5
minimal	518	689	13.00	31	22	9
maximal	591	740	18.00	74	48	26
standard deviation	23.7	18.6	1.65	10.3	5.8	4.5
Max. variation in one melt	-	-	-	29	18	37

[1] Limit for mechanical properties according of EN 10293:2005.

From the obtained data for individual melts, a statistical analysis was created, shown in Table 2. From the available data, it can be concluded that the variability of the results in the tensile test is within the expected range and the influence of individual elements, mainly carbon (C) and manganese (Mn), is as expected. By achieving the prescribed composition of the steel, the mechanical values of the tensile tests are also achieved. Any deviation, mainly in the elements carbon and manganese, causes local extremes in the tensile tests, especially at the yield point (Re).

In the results of the Charpy notched toughness, in the case of the observed steel G24Mn6, there is a significant difference in the values between the individual samples.

The average Kv value at -20 °C is 52 Joules and the standard deviation is 10.4 Joules. The maximum difference in one melt is up to 29 Joules.

The average Kv value at -40 °C is 36.8 Joules and the standard deviation is only 5.8 Joules. The maximum difference at -40°C in one melt is 18 Joules. In the case of the difference between the minimum and maximum value at both temperature ranges, it is up to 37 Joules. At the same time, anomalies are observed, when for the same melt (A23), the dispersion is 2 Joules at -20°C and up to 18 Joules at -40°C.

At the same time, it can be stated that those melts that have the smallest dispersion in the notched toughness Kv have their tensile test results comply with the prescribed values in all examined parameters (Re, Rm, A).

3.3. Metallographic analysis

Samples from all 13 batches were subjected to metallographic analysis. A summary of the results of metallographic analysis is given in Table 3. Figure 2 shows the most common impurities found on the prepared samples.

Table 3. The metallographic results.

phase	proportion	Grain size	Inclusions	
			dimension	proportion
Bainite/martensite, tempered martensite	100%	G10-G12	5-85 μm	0,5-1,5%

The microstructure consists predominantly of fine tempered martensite or bainite, characterized by a dark-etching, acicular or lath-like morphology typical for quenched and tempered steel. The fine features suggest a fully transformation and subsequently tempered structure.

The microstructure exhibits a very fine-grained tempered structure. Precise prior-austenite grain size determination is challenging from this structures. However, based on the overall fineness of the transformed constituents and comparison with the 50 μm scale bar, the effective grain size is estimated to be approximately ASTM G10-12. This indicates an average effective grain diameter in the range of 6-11 μm.

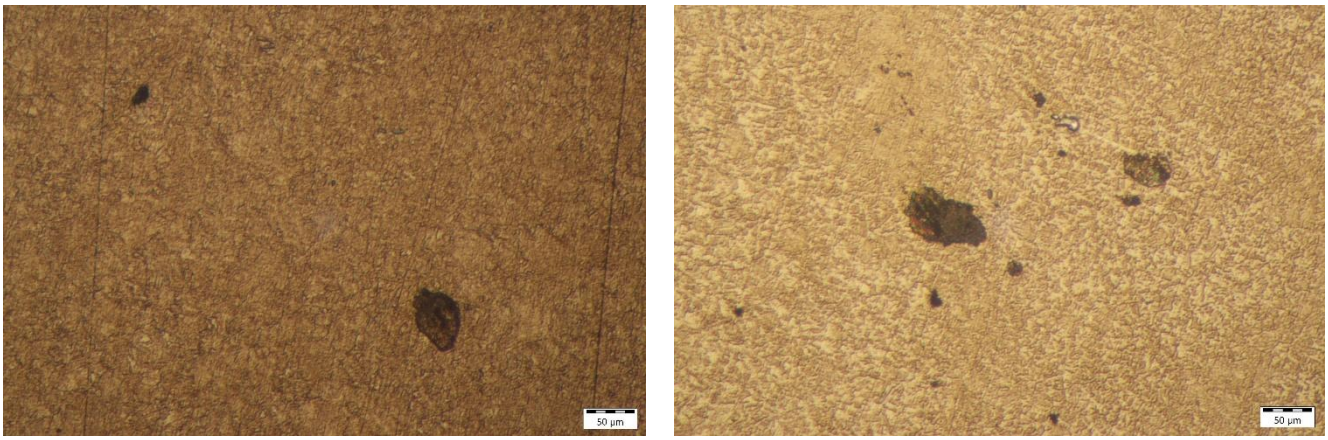

(**a**) (**b**)

Figure 2. (**a**) Microstructure of steel sample A26 with non-metallic inclusions . (**b**) Microstructure of steel sample A24 with non-metallic inclusions and oxides with metallic luster.

The attached photographs show typical metallographic structures of the investigated steel G24Mn6. Since the samples for this analysis were made directly from castings, the photographs show the typical presence of non-metallic inclusions in the steel. The size of the inclusions in the steel is on average 25 μm. Some inclusions have hints of metallic or

colored reflections, which may indicate their complex nature with a predominance of silicates and oxide inclusions. The proportion of these inclusions in the steel is in the ratio of 0.5-1.5%.

On one of the samples, a microcrack was identified during metallographic analysis, as shown in Figure 3. The microcrack in the image is visible as a distinct, irregular crack, extending to three different sides and having a longest measured length of 376 μm. This microcrack is associated with several dark inclusions along its path. In addition, smaller, scattered dark spots, probably non-metallic inclusions or tiny pores, are also present in the photo.

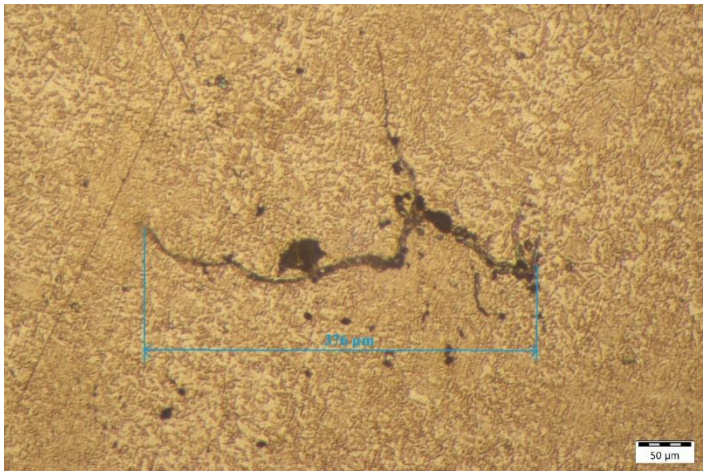

Figure 3. Microstructure of steel sample A29 with non-metallic inclusions and microcracks.

4. Discussion

The investigation of 13 batches from G24Mn6 steel melts involved subjecting samples to extreme compositions exceeding prescribed limits for key elements Carbon (C) and Manganese (Mn). The primary objective was to determine the influence of these compositional variations on the mechanical properties, specifically Charpy V-notch toughness (K_V) at a reduced temperature -40°C.

Across the observed sample set, the results did not establish a significant correlation between variations in the percentage of Carbon or Manganese and the evaluated mechanical properties. This finding is likely attributable to the relatively narrow range of compositional variation present within the studied melts. Similarly, no change in the observed martensitic grain size was confirmed following changes in the carbon percentage.

Regarding alloying elements, nickel (Ni) was the only element that was found to have a slightly positive effect on the yield strength (Re). Due to its low content in G24Mn6 steels, nickel contributed minimally to the increase in both toughness and strength values, with more significant benefits generally expected at higher concentration levels. No experiments were performed with other alloying chemical elements (Cr, Mo, V, Cu,...) with extreme values within the limits of G24Mn6 steel, and therefore their effect on mechanical values was not evaluated.

Microstructural analysis, performed using the comparative method outlined in ASTM E112 , revealed an extremely fine microstructure across all samples, characterized by indistinguishable original austenitic grain boundaries. Grains consistently adhered to an estimated size of G11 according to the ASTM standard, with numerous structures falling within the G10-G12 range, confirming a highly refined grain structure. The predominant phase of the microstructure in all samples is tempered martensite or bainite, formed mainly by fine needles, which is typical for tempered hardened steel.

A significant degree of inter-melt variability was observed when comparing the average Charpy notch toughness values between the test temperatures of -20°C and -40°C.

The minimum observed difference in average toughness K_V between the two temperatures was 9 Joules, while the maximum difference reached 26 Joules in two separate cases. It is necessary to emphasize, that 27 Joules also represents the minimum permissible value for the Charpy impact toughness test at -20°C.

Furthermore, substantial intra-melt variability was established, even at a single testing temperature -20°C. The difference between the highest and lowest measured K_V values across the entire set was 48 Joules. In one specific melt A28 a 29 Joules difference in notch toughness was recorded between individual samples at -20°C, decreasing to 12 Joules at -40°C. Such inconsistent and widely divergent results are primarily attributed to material inhomogeneity, or the presence of non-metallic inclusions, or microcracks in probe.

The presence of non-metallic inclusions in proximity to or directly within the microcrack path facilitates crack growth and propagation. Correspondingly, sample A29, where a microcrack was observed with 376 μm length, exhibited one of the lowest measured Charpy notch toughness values of 27 Joules at -40°C. The average toughness difference between 20°C and 40°C for this specific sample was 21 Joules. It is the occurrence of such discontinuities in uniform samples that can affect inconsistent results of mechanical values, especially in the case of notch toughness tests at reduced temperature.

5. Conclusions

The mechanical properties of G24Mn6 steel are primarily determined by the effectiveness of its heat treatment and hardening, as demonstrated by previous research studies. Within the prescribed compositional limits of this steel G24Mn6, adjustments to the alloying elements that Cr, Cu, and Ni allow fine-tuning of the final mechanical properties. A slight increasing the concentrations of these elements results in higher yield strength (Re) and tensile strength (Rm), but at the same time, in the case of carbon, it can contribute to reduction in impact toughness (K_V at −20 °C).

Within the analyzed data set, several melts showed similar chemical compositions but different mechanical properties. At the same time, different chemical compositions at local extremes have very similar mechanical values. These variations in individual mechanical properties, especially in the Charpy impact toughness test, were confirmed to demonstrate the presence of non-metallic inclusions (e.g. SiO_2) as well as other inclusions with metallic luster (e.g. Fe2O3). These inclusions disrupting the microstructural heterogeneity also cause the formation of microcracks and these have a negative impact on the evaluation of mechanical properties of materials. Such effects need to be taken into account in future analyses and production management to ensure consistent mechanical performance of G24Mn6 steel components.

Acknowledgments: The Slovak Research and Development Agency, the VEGA Scientific Grant Agency "Possibilities of applying laser additive technologies in the restoration of functional surfaces" (VEGA 1/0597/23), the Cultural and Educational Grant Agency KEGA "Hybrid education of students for the current needs of the automotive industry" (KEGA 024TUKE-4/2025), "Innovative approaches to the restoration of functional surfaces by laser surface treatment" (APVV-20-0303), Visegrad Fund fellowship No. 62510252 - Development of cooperation in the field of research of renovation technologies and increasing the service life of functional surfaces of products and "Integrity of protective multilayers under high-temperature exposure conditions" (APVV-24-0381)

Conflicts of Interest: The authors declare no conflict of interest.

References

1. Safe-Metal. Alloy Data Sheet. G24Mn6, from https://www.safe-metal.com/wp-content/uploads/2021/02/Alloy-Data-Sheet-G24Mn6.pdf, (01.12.2025).
2. Coppard, R., Coulon, P., Koyama, Y., & Endo, M. Impact of Carbon Macrosegregation on the Mechanical Properties of Low-Alloy Steel Forgings. *Volume 6B: Materials and Fabrication*, 2019.

3. Hebda, M., Dębecka, H., & Kazior, J. Influence of silicon addition on the mechanical properties and corrosion resistance of low-alloy steel. *Bulletin of Materials Science* **2015**, *38*, 1687-1692.
4. Sun, M., Jiang, Z., Li, Y., Chen, C., S., Ji, Y., Wang, J., & Liu, H. Effect of Sulfur Content on the Inclusion and Mechanical Properties in Ce-Mg Treated Resulfurized SCr420H Steel. *Metals*, 2022.
5. Goritskiy, V., Shneyderov, G., & Vorob'ev, S. Influence of Chemical Composition and Structure on Characteristics of Cold Resistance and Impact Strength of Low-Carbon Steel. *Metallurgist* **2023**, *66*, 1539-1551.
6. He, Q., Liu, Y., Zhu, C., Xie, X., Zhu, R., & Li, G. Effect of Phosphorus Content on Magnetic and Mechanical Properties of Non-Oriented Electrical Steel. *Materials* **2022**, *15*.
7. Xia, T., Y., Zhang, Y., Li, J., & Xu, H. Effect of Mo and Cr on the Microstructure and Properties of Low-Alloy Wear-Resistant Steels. *Materials* **2024**, *17*.
8. Wu, X., Xiao, P., Wu, S., Yan, C., X., Liu, Z., Chen, W., Zhu, L., & Zhang, Q. Effect of Molybdenum on the Impact Toughness of Heat-Affected Zone in High-Strength Low-Alloy Steel. *Materials* **2021**, *14*.
9. Liu, W., Zhao, H., Wang, B., & Tian, Y. Impact of Mo/Ni alloying on microstructural modulation and low-temperature toughness of high-strength low-alloy steel. *Journal of Iron and Steel Research International* **2023**, 1-17.
10. Zhu, Z., Liang, Y., & Zou, J. Modeling and Composition Design of Low-Alloy Steel's Mechanical Properties Based on Neural Networks and Genetic Algorithms. *Materials* **2020**, 13.
11. EN 10293. Steel castings for general engineering uses. CEN-CENELEC Management Centre. Brussels, Belgium, 2005.
12. Sun, B., Da Silva, K., Wu, Y., Y., Chen, H., Scott, C., Ponge, D., & Raabe, D. Physical metallurgy of medium-Mn advanced high-strength steels. *International Materials Reviews* **2023**, *68*, 786-824.
13. Kostina, M., Blinov, V., Kalinin, G., Fomina, O., & Mushnikova, S. Structure and mechanical properties of high strength austenitic Mn–Ni–Cu–V–C dispersion ally hardened steel. *Voprosy Materialovedeniya*, 2022.
14. Furuhara, T., Zhang, Y., Sato, M., Miyamoto, G., Enoki, M., Ohtani, H., Uesugi, T., & Numakura, H. Sublattice alloy design of high-strength steels: Application of clustering and nanoscale precipitation of interstitial and substitutional solutes. *Scripta Materialia*, 2022.
15. Jiao, Z., Luan, J., Miller, M., & Liu, C. Precipitation mechanism and mechanical properties of an ultra-high strength steel hardened by nanoscale NiAl and Cu particles. *Acta Materialia* **2015**, 97, 58-67.
16. Grega, M., Brezinová, J. INFLUENCING THE MECHANICAL PROPERTIES OF G24MN6 STEEL BY USING ALLOYING ELEMENTS IN THE PRODUCTION OF CASTINGS USED IN THE RAILWAY INDUSTRY. *Transfer Inovácií* **2026**, *52*.
17. Kalandyk, B., & Zapała, R. Comparison of Microstructure and Mechanical Properties of Cast Steel Carried out on Cast-on Samples and Samples Cast Separately. *Archives of Foundry Engineering*, 2023. https://doi.org/10.24425/afe.2021.136102.
18. Kalandyk, B., Zapała, R., Sobula, S., & Tęcza, G.. The Effect of CaSiAl Modification on the Non-metallic Inclusions and Mechanical Properties of Low-carbon Microalloyed Cast Steel. *Archives of Foundry Engineering*, 2023. https://doi.org/10.24425/afe.2018.125190.
19. DIN 17052-1. Heat treatment furnaces - Part 1: Requirements for temperature uniformity. DIN German Institute for Standardization. Berlin, Germany, 2013.
20. 6892-1. Metallic materials — Tensile testing — Part 1: Method of test at room temperature. ISO International Organization for Standardization. Geneve, Switzerland, 2019.
21. ISO 148-1, Metallic materials — Charpy pendulum impact test Part 1: Test method. ISO International Organization for Standardization. Geneve, Switzerland, 2016.
22. ASTM E112-24. Standard Test Methods for Determining Average Grain Size. ASTM International, West Conshohocken, PA, USA, 2024.

TECHNICAL UNIVERSITY OF KOŠICE
Faculty of Mechanical Engineering

Finite Element Simulation of Tensile Test of Silicone Material

Martina Hančinová [1,*], Erika Dubňanská [1], Barbara Schürger [1], Róbert Huňady [1] and Matyáš Machalla [2]

[1] Department of Applied Mechanics and Mechanical Engineering, Faculty of Mechanical Engineering, Technical University of Košice, Letná 9/B, 042 00 Košice, Slovakia; martina.hancinova@tuke.sk; erika.dubnanska@tuke.sk; barbara.schurger@tuke.sk; robert.hunady@tuke.sk
[2] Department of Robotics, Faculty of Mechanical Engineering, VŠB - Technical University of Ostrava, 17. listopadu 2172/15, 708 00 Ostrava-Poruba, Czech Republic; matyas.machalla@vsb.cz
* Correspondence: martina.hancinova@tuke.sk

Abstract: Silicone elastomers are widely used in engineering and biomedical applications due to their high deformability, near-incompressibility, and stable mechanical response under large strains. Accurate numerical representation of their mechanical behaviour is therefore essential for reliable finite element simulations. This study presents a combined experimental–numerical investigation of a silicone elastomer subjected to uniaxial tensile loading. Tensile tests were performed at a loading rate of 50 mm/min, and the experimental stress–strain data were post-processed to isolate the quasi-linear deformation regime prior to material failure. The resulting averaged stress–strain response was used to identify effective elastic properties. A three-dimensional finite element model of the tensile test was developed in Abaqus using a compressible Neo-Hookean, Ogden and Arruda-Boyce hyperelastic formulations. The numerical response obtained under displacement-controlled loading was compared with the experimental data. The results demonstrate that, despite the inherently nonlinear nature of elastomers, the selected hyperelastic models are capable of reproducing the quasi-linear tensile response of the investigated silicone material over the considered strain range. The proposed modelling strategy provides a simple and robust framework suitable for rapid material calibration and preliminary numerical analyses.

Keywords: silicone elastomer; uniaxial tensile test; hyperelasticity; finite element method; Abaqus

1. Introduction

Silicone elastomers represent an important class of polymeric materials characterized by high elasticity, large allowable deformations, and near-incompressible behaviour, often expressed by a Poisson's ratio close to 0.5 [1-3]. These properties make them attractive for applications ranging from soft robotics and flexible electronics [4] to medical and pharmaceutical supplies [5]. In many of these applications, components are subjected to large mechanical strains, which necessitates reliable experimental characterization and appropriate constitutive modelling, often initiated through uniaxial tensile testing.

From a mechanical standpoint, elastomers exhibit a nonlinear stress–strain response, particularly at large deformations, which is commonly described using hyperelastic constitutive models [6–9]. Classical formulations such as the Neo-Hookean, Mooney–Rivlin, and Ogden models are widely reported in the literature for representing the mechanical behaviour of rubber-like materials [6,7,9]. It is generally recognized that the applicability of a given hyperelastic model depends on the deformation mode and the strain range considered, as demonstrated in several comparative studies focusing on rubber-like materials under mechanical loading [6–9]. For moderate strain regimes and when the objective is an initial description of the global tensile response, simplified hyperelastic models are commonly adopted as a first approximation, offering advantages in terms of straightforward parameter identification [8–10].

In finite element simulations, the behaviour of hyperelastic materials is commonly described using strain energy density functions implemented in commercial software such as Abaqus. The strain energy density functions together with material constants for models selected for this work are shown in Table 1.

Table 1. Strain energy density functions and material parameters of selected hyperelastic models.

Model	Strain Energy Density Function	Material Constants
Neo-Hooke	$W = C_{10}\left(\bar{I}_1 - 3\right)$	C_{10}
Ogden	$W = \sum_{i=1}^{N} \frac{2\mu_i}{\alpha_i^2}\left(\bar{\lambda}_1^{\alpha_i} + \bar{\lambda}_2^{\alpha_i} + \bar{\lambda}_3^{\alpha_i} - 3\right)$	μ_i , α_i
Arruda-Boyce	$W = \mu \sum_{i=1}^{5} \frac{C_i}{\lambda_m^{2i-2}}\left(\bar{I}_1^i - 3^i\right)$	μ , λ_m

Where $\bar{I}_1$ - first invariant of the deviatoric strain, $\bar{\lambda}_i = J^{-1/3}\lambda_i$, λ_i are the principal stretches and J is the volume ratio. For the Arruda-Boyce model (also known as the eight-chain model) are $C_1 = 1/2$, $C_2 = 1/20$, $C_3 = 11/1050$, $C_4 = 19/7050$ and $C_5 = 519/673750$ [10].

In practical testing of silicone elastomers, uniaxial tensile tests are commonly used to characterize the hyperelastic response of the material. The present study investigates the numerical reproduction of uniaxial tensile behaviour of a silicone elastomer based on experimentally obtained stress–strain data.

2. Materials and Methods

2.1. Experimental Tensile Testing

The geometry of the tensile test specimen was defined in accordance with ČSN ISO 37 (62 1436) [11], which specifies the determination of tensile properties (Figure 1a). The manufactured silicone elastomer specimens used in the experiments are shown in Figure 1b.

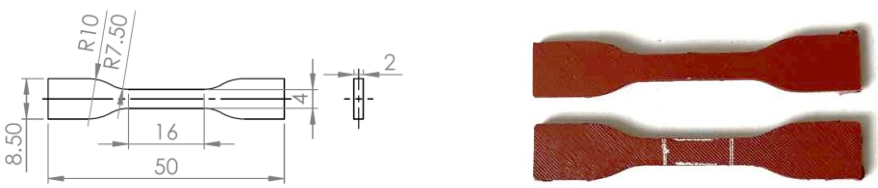

(**a**) (**b**)

Figure 1. Tensile test specimen geometry defined according to ČSN ISO 37 (62 1436): (**a**) schematic representation with nominal dimensions, (**b**) manufactured silicone elastomer specimens used in the experimental tests.

Uniaxial tensile tests were performed on silicone elastomer specimens using a computerized electronic universal testing machine (Kason WDW-5). The specimens were loaded under displacement control at a crosshead velocity of 50 mm/min, and the tests were carried out at room temperature.

Axial displacement was measured using a video extensometer system (Figure 2 a), enabling non-contact strain measurement directly on the specimen surface. The measurement principle is based on tracking the relative motion of two reference points marked on the specimen and aligned with the tensile axis, as illustrated in Figure 2 b. During each

test, a high-resolution grayscale video of the deforming specimen was recorded. The recorded video data were subsequently processed and evaluated in the MATLAB environment using a digital image correlation (DIC) algorithm.

Engineering stress and engineering strain were determined from the measured force and displacement using the initial cross-sectional area and gauge length of the specimens. The use of a contactless optical measurement technique allowed accurate strain evaluation without influencing the mechanical response of the highly deformable silicone material, particularly at larger strains.

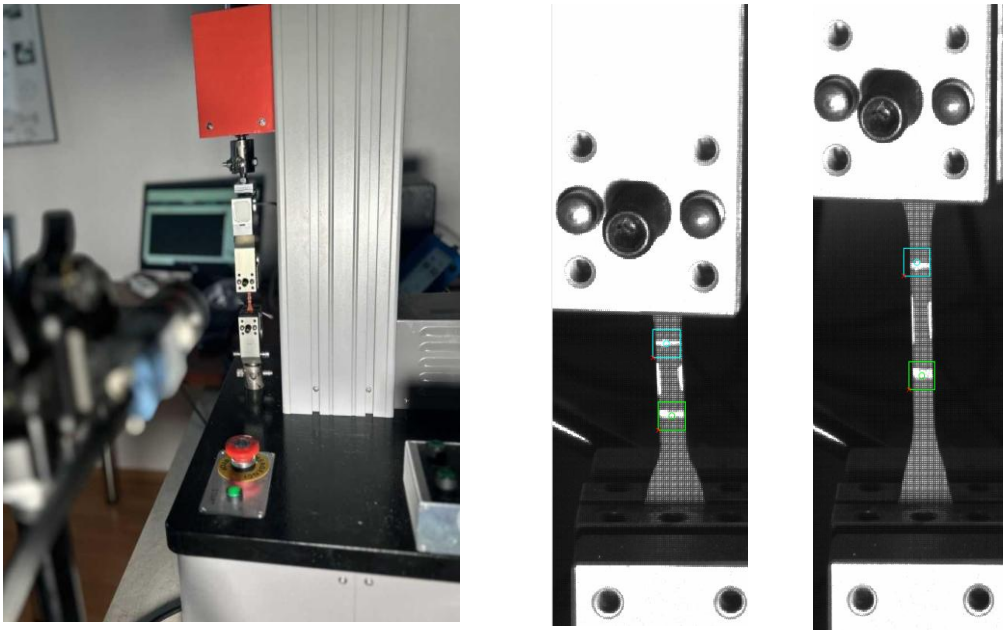

Figure 2. Measurement of specimen deformation using a video extensometer.

2.2. Data Processing

As shown in Figure 3, the experimental stress–strain curves were processed to remove the initial transient region associated with specimen seating and the final region corresponding to material failure. For the purposes of constitutive modelling, only the remaining stable quasi-linear portion of each stress–strain curve was retained for further analysis.

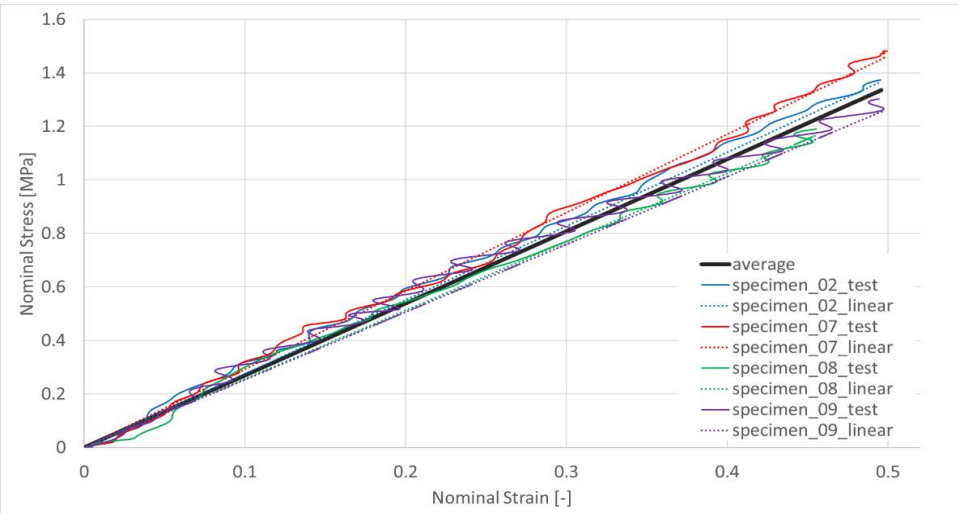

Figure 3. Stress–strain curves obtained from uniaxial tensile tests at a loading rate of 50 mm/min.

The extracted quasi-linear segments were approximated using linear regression implemented in MATLAB, and an averaged representative stress–strain response was subsequently constructed. The effective Young's modulus, determined directly from the slope of the averaged representative stress–strain curve is 2.695 MPa.

2.3. Finite Element Model

A three-dimensional finite element model of the tensile test specimen was developed using Abaqus/Standard. The specimen geometry was created in SolidWorks and subsequently imported into Abaqus for numerical analysis. The geometry corresponded to the nominal specimen dimensions used in the experimental tests. Figure 4 shows a specimen with partitioned domains and marked measurement area, boundary conditions, and finite element mesh.

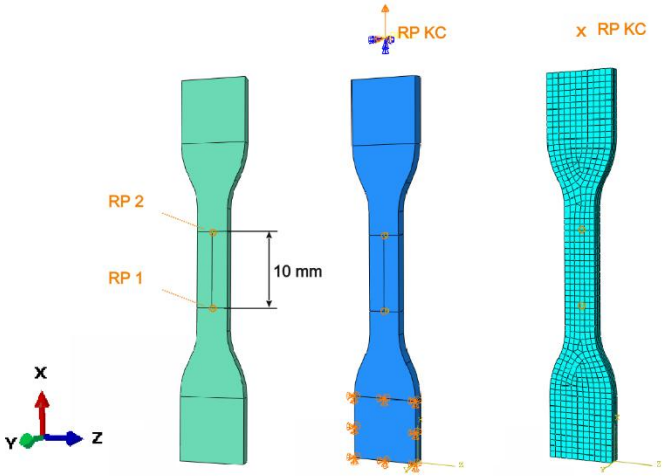

Figure 4. Finite element model of the tensile specimen, including reference points, boundary condition definition and finite element mesh.

Due to the near-incompressible nature of the material, hybrid solid elements (C3D8H) were employed to avoid volumetric locking and to ensure numerical stability of the numerical solution.

2.4. Boundary Conditions and Loading

The numerical tensile test was simulated under displacement-controlled loading conditions. The lower end of the specimen was fully fixed using a partition. At the opposite end, axial displacement was prescribed using a kinematic coupling between the reference point and the upper partition, ensuring uniform axial deformation. To prevent rotation, the translations in the y and z axes on the upper partition were locked.

The applied displacement was selected to correspond to the maximum strain observed in the experimental tests. Reaction forces and axial displacements were recorded as history outputs from reference points and used to evaluate the global stress–strain response of the numerical model.

3. Results

The numerical response of the silicone elastomer specimen obtained using the Ogden model is illustrated in Figure 5 in terms of von Mises stress distribution and axial displacement at the final loading step. All models predict a similar global deformation mode, characterized by uniform axial elongation of the gauge section and stress concentration in the reduced cross-sectional area of the specimen.

A quantitative comparison between the experimentally obtained averaged stress–strain response and the numerical predictions is presented in Figure 6. Over the investigated nominal strain range up to approximately 0.5, noticeable differences in the predictive capability of the individual constitutive models can be observed.

The finite element simulation was performed using the material parameters $C_{10} = 0.538$ MPa for the Neo-Hooke, $\mu_i = 0.935$ MPa, $\alpha_i = 3.818$ for the Ogden model. For the Arruda Boyce model, the parameters $\mu = 0.325$ MPa and $\lambda_m = 1.035$ were adopted.

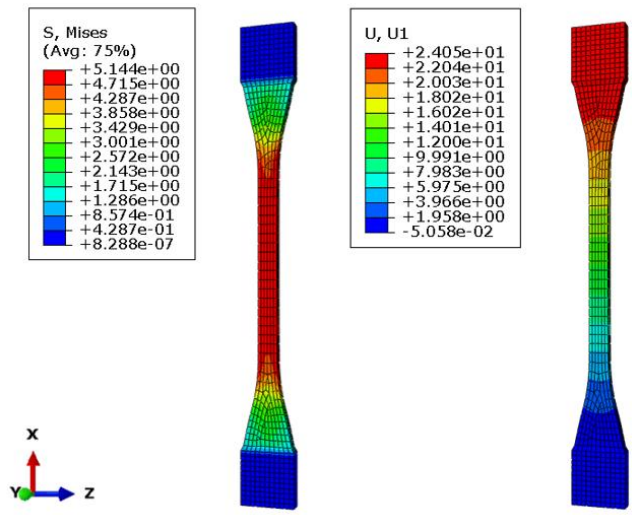

(**a**) (**b**)

Figure 5. Numerical results of the uniaxial tensile simulation of the silicone elastomer specimen obtained using the Ogden hyperelastic model. The deformed configuration is shown together with the contour plots of (**a**) von Mises stress distribution and (**b**) axial displacement U_1 at the final loading step.

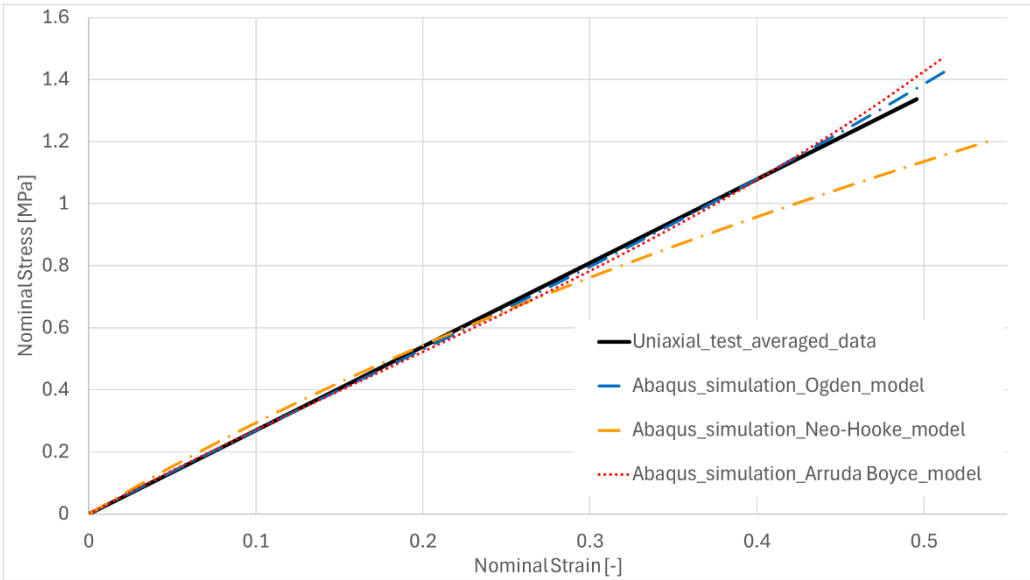

Figure 6. Comparison of experimental averaged stress–strain curve and numerical simulation result.

The Neo-Hookean model provides a good agreement with the experimental response in the low to intermediate strain region, accurately capturing the initial stiffness and the overall quasi-linear trend of the tensile behaviour. This is reflected by a coefficient of determination of $R^2 = 0.953$ indicating that even a simplified hyperelastic formulation can adequately describe the global response within the considered deformation regime.

Improved agreement over a broader strain range is obtained with the Ogden and Arruda–Boyce models, which yield significantly higher coefficients of determination ($R^2 = 0.999$ and $R^2 = 0.997$, respectively). The Ogden model most closely reproduces the curvature of the experimental stress–strain curve at higher strains, while the Arruda–Boyce formulation predicts a progressively stiffer response, leading to a slight overestimation of tensile stress in the upper part of the investigated strain range.

Overall, the comparison confirms that although all three hyperelastic models can reproduce the general tensile behaviour of the silicone elastomer, the predictive accuracy is strongly influenced by the selected constitutive formulation and the strain range of interest.

4. Discussion

The presented results confirm that the experimentally observed tensile response of the investigated silicone elastomer exhibits a linear character over a considerable portion of the deformation range. This feature allows the material behaviour to be approximated using simplified hyperelastic formulations when the analysis is restricted to moderate strains.

Among the considered constitutive models, the Neo-Hookean formulation provides the simplest representation and enables straightforward parameter identification based on the effective Young's modulus. Its good agreement with experimental data in the low to intermediate strain regime indicates that this model is suitable for applications focused on global stiffness estimation and preliminary numerical analyses.

More advanced hyperelastic models, such as the Ogden and Arruda–Boyce formulations, introduce additional material parameters that allow the nonlinear stiffening behaviour at higher strains to be captured more accurately. This is reflected in the improved agreement of the Ogden model with experimental data over the full investigated strain range. However, this increased accuracy comes at the cost of higher model complexity and more demanding parameter calibration.

The Arruda–Boyce model, which is physically motivated by polymer chain network mechanics, predicts a stronger stiffening response at large deformations. While this behaviour may be relevant for extreme strain applications, it leads to an overestimation of the tensile stress for the quasi-linear regime considered in this study.

5. Conclusions

This study presented a combined experimental and numerical investigation of the uniaxial tensile behaviour of a silicone elastomer. Experimental tensile tests conducted at a loading rate of 50 mm/min were processed to extract a representative quasi-linear stress–strain response, which served as the basis for constitutive model calibration.

Finite element simulations of the tensile test were performed using three hyperelastic material models: Neo-Hookean, Ogden, and Arruda–Boyce. A direct comparison between experimental data and numerical predictions demonstrated that all considered models are capable of reproducing the general tensile behaviour of the material within the investigated strain range.

The Neo-Hookean model provided a satisfactory approximation of the experimental response in the low to intermediate strain regime, capturing the effective tensile stiffness with minimal model complexity. The Ogden model showed improved agreement at

higher strains, while the Arruda–Boyce formulation predicted a stiffer response, leading to stress overestimation in the quasi-linear regime.

Future work could aim to extend the present study by incorporating strain-rate-dependent tensile data and compressive loading conditions. In addition, time-dependent experiments, such as stress relaxation tests, may be included to better describe the viscous contribution to the material response and to support the development of viscoelastic material models.

Acknowledgments: This work was supported by the Slovak Research and Development Agency under the grant project VEGA 1/0152/24, KEGA 039TUKE-4/2024 and by European Union under the REFRESH–Research Excellence for REgion Sustainability and High-tech Industries project number CZ.10.03.01/00/22_003/0000048 via the Operational Programme Just Transition and by the EU NextGenerationEU through the Recovery and Resilience Plan for Slovakia under the project No. 09I03-03-V05-00015.

Conflicts of Interest: "The authors declare no conflict of interest."

References

1. Gokhale, M. N.: Hyperelastic Material Modelling of Silicone Rubber. *International Journal of Science and Research (IJSR)* **2023**, Volume 12, pp. 2069 – 2073.
2. Francesconi, L. et al.: Variable Poisson's ratio materials for globally stable static and dynamic compression resistance. *Extreme Mechanics Letters* **2019**, Volume 26, pp. 1-7
3. Nedoluha, R. et al.: Errors matter when measuring Poisson's ratio of nearly incompressible elastomers. *Soft Matter.* **2025,** Volume 21(34), pp. 6689-6696.
4. Du, Y.; Mefford, O. T.: Effects of uniaxial tensile strain on the release of small molecules from silicone rubber. *Journal of Applied Polymer Science* **2024**, Volume 141 (4).
5. Chruściel, J.J.: Most Important Biomedical and Pharmaceutical Applications of Silicones. *Materials* **2025**, 18, 2561.
6. Marckmann, G.; Veronn, E.: Comparison Of Hyperelastic Models For Rubber-like Materials. *Rubber Chemistry and Technology* **2006,** 79(5).
7. He, H. et al.: A comparative study of 85 hyperelastic constitutive models for both unfilled rubber and highly filled rubber nanocomposite material. *Nano Material Science* **2022**, Volume 4, pp. 64-82.
8. Khaniki, H. B. et al.: Hyperelastic structures: A review on the mechanics and biomechanics. *International Journal of Non-Linear Mechanics* ***2023*,** Volume 148.
9. Park, S.-J.: Comparative Study on Hyperelastic Constitutive Models for the Static and Dynamic Behavior of Resilient Mounts. *Materials* **2025**, Volume 18.
10. Dassault Systems: Fitting of rubber test data. https://help.3ds.com/2024x/english/dsdoc/SIMA3DXBMKRefMap/simabmk-c-rubberfit.htm?contextscope=cloud&id=2fef455fcc574b2885763873e7e472cb
11. ČSN ISO 37 (62 1436) - Rubber, vulcanised or thermoplastic elastomer

TECHNICAL UNIVERSITY OF KOŠICE
Faculty of Mechanical Engineering

Analysis of accuracy of additive technology models

Ján Ivanecký [1,*], Jozef Kuľka [1], Matúš Virostko [1]

[1] Faculty of mechanical engineering, Technical University of Košice; jan.ivanecky@tuke.sk; jozef.kulka@tuke.sk; matus.virostko@tuke.sk
* Correspondence: jan.ivanecky@tuke.sk

Abstract: Additive Manufacturing using Fused Deposition Modeling (FDM) technology is widely employed for its accessibility and cost-effectiveness, primarily in prototyping. A key challenge for its application in mechanical engineering remains the achievement of the required dimensional and geometric accuracy simultaneously with printing speed. The objective of this work is to quantify and analyze the dimensional deviations of cylindrical samples printed using the FDM method from PLA material. Experimental data were obtained by measuring the diameters, heights, and holes of a series of samples using a digital caliper, surface roughness gauge. The determined dimensional deviations indicate the influence of anisotropy and thermal processing of the material on the final shape. The results provide valuable information for the calibration of 3D printers with the aim of improving the production accuracy of components with rotational symmetry. The result of the experimental verification showed that the Bambu Lab printer is more susceptible to incorrect setting of printing parameters and to achieve higher accuracy it is necessary to adjust them.

Keywords: additive manufacturing; FDM; dimensional accuracy

1. Introduction

Additive Manufacturing represents a substantial shift in the design and production process, with FDM technology being among the most widespread. FDM consists of layering molten thermoplastic material, which enables the creation of complex geometric shapes. Despite its advantages (speed, low cost, wide range of materials), the main challenge for full-scale industrial deployment is dimensional accuracy and repeatability [1, 2].

The accuracy of components manufactured using FDM technology is influenced by numerous factors, including layer height, printing speed, nozzle temperature, build plate temperature, the type of drives and guides, and particularly material properties, especially material shrinkage during cooling. These factors lead to significant deviations from nominal dimensions, particularly in samples with circular and cylindrical geometries, where undesirable ellipticity or loss of roundness may manifest.

For such samples, a decisive factor is also the quality of the 3D model format, which determines the degree of roundness, as well as the software settings that govern the object's polygonization (Figure 1). This term denotes the phenomenon where a circle is not perfect but approaches the shape of a polygon, being formed by segments of short straight lines [3].

Figure 1. Detail of polygonization effect.

The aim of the presented study is to analyze the dimensional and geometric accuracy of a set of cylindrical samples manufactured using FDM technology from PLA material under defined printing conditions. The work will focus on quantifying the average absolute and relative error and on evaluating the influence of print orientation on the resulting dimensions.

2. Materials and Methods

To perform the dimensional accuracy analysis of the printed samples, it was necessary to determine the input parameters and select them in such a way that it would be possible to determine which printing settings are most suitable for achieving the highest possible dimensional accuracy.

2.1 Material selection for printing

For the reason that PLA (Polylactic Acid) is the most commonly used material for general printing and the creation of simple prototypes, we have also selected this material for testing. The goal will be to determine whether this material is suitable for precise printing. We chose two different colours to printing to distinguish the samples. For the filaments we selected, the recommended printing settings are a nozzle temperature from 210° to 240°C and a build plate temperature from 50°C to 60°C.

For printing, we chose values of 215°C for the nozzle and 55°C for the build plate.

2.2 Additive printers selection

For the purpose of the analysis, we selected two brands of 3D printers for printing the samples, whose printing capabilities we will compare.

First chosen printer was PRUSA i3 MK3S with nozzle diameter 0,40 mm.

Second chosen printer was Bambu Lab X1C with nozzle diameter 0,40 mm.

2.3 Sample selection

We designed samples of a circular shape for printing. We used two types of samples: one type was a classic cylinder with a diameter of 30 mm without a hole (Figure 2 a)), and the second type included a hole with a diameter of 12 mm running through the entire part (Figure 2 b)). The part with the hole was designed because we want to verify whether the hole positively or negatively influences the shape stability during the cooling of the part. Thermoplastics expand when heated and contract as they cool. The geometry of a ring (a

circular part with a hole) creates unique thermal dynamics. As the outer layers cool, they shrink toward the center. However, the inner "perimeters" around the hole also shrink along their circumference. This often pulls the inner wall of the hole inward, resulting in a diameter that is significantly smaller than intended. This is particularly prevalent in high-shrinkage materials like ABS or Nylon.

The reason for selecting circular samples was to verify the influence of polygonization (Fig. 1) on the circular shape of the sample and to determine which printer, as well as which software slicer, achieves the lowest degree of circle segmentation.

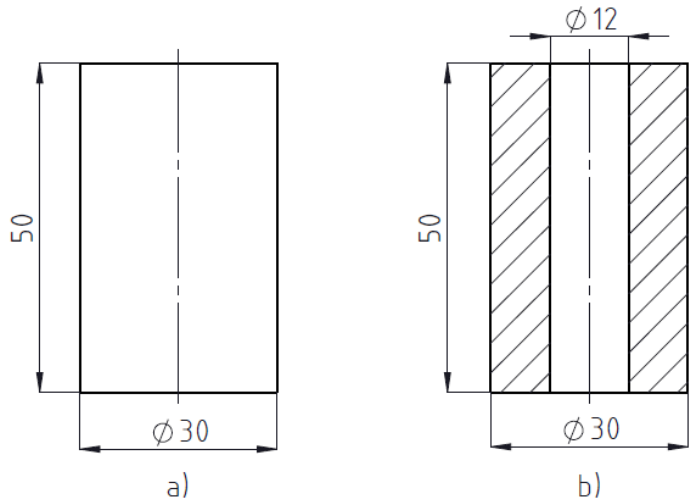

Figure 2. Design of samples: (**a**) 1st sample without hole; (**b**) 2nd sample with hole.

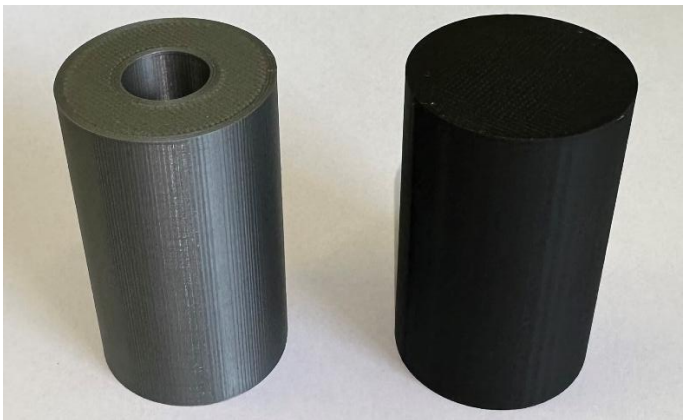

Figure 3. Printed samples.

We printed together eight of samples (Tab. 1). Every sample has different printing parameters.

Table 1. Amount of samples.

Printer	Sample without hole	Sample with hole
Prusa MK3S	2	2
Bambu Lab X1C	2	2

2.4. Printing parameters

Parts created in SolidWorks must be converted to the .stl format so that the slicer for 3D printing can process them and subsequently generate the G-code that will control the printer. The accuracy of the .stl file generation is important, and therefore, we chose 2 different settings. One was the standard setting that the software commonly offers, and the second was the highest quality achievable using custom settings.

Than was necessary to chose layer height, speed of printing. Also was needed to record temperature and humidity so thar we prevent deviations in these values from influencing the overall result.

Table 2. Printing parameters.

Number	Printer	Layer Height	Temperature	Humidity
1	Prusa	0,15 mm	24,90°C	34%
2	Prusa	0,10 mm	26,90°C	33%
3	Bambu Lab	0,15 mm	24,40°C	30%
4	Bambu Lab	0,10 mm	24,70°C	32%

3. Results

We obtained data through experimental measurement of samples which define the printing accuracy (Table 3, Table 4) and will help us in the correct selection of printing parameters for the optimal setup of print files.

3.1. Priciples of measurement

On the printed samples, we experimentally measured their length, surface roughness, and diameter. We measured the diameter on each sample a total of four times.

The method by which the diameters were measured involved selecting the upper and lower halves of the component for measurement purposes. In each half, we measured the diameter and then rotated the component by 90° and measured it again in the same section. This measurement provided us with an indication of whether the component has an approximately circular shape or if it significantly deviates.

The length dimension was measured along the component's axis on a universal length measuring machine.

The surface roughness was measured three times on each component, and subsequently, the mean value was calculated as the representative roughness value.

3.1.1. Measuring devices

1. Universal Length Measuring Instrument VEB Carl Zeiss Jena – accuracy of measuring is 0,0001 mm. Used for length of samples.
2. Digital caliper Mitutoyo 0-200 mm – accuracy of measuring is 0,01 mm. Used for measuring a diameters of samples.
3. Mitutoyo Surftest SJ410 – ISO 1997 – accuracy of measuring is 80 μm. Used for measuring roughness.

3.2. Measured values

Table 3. Measured values grey samples (Prusa printer).

Grey sample	Length [mm]	ØUpper half [mm]		ØLower half [mm]		Roughness
With hole 1	50.0930	0°	29,80	0°	29,83	Ra 0,279
		90°	29,93	90°	29,82	
Without hole 1	50.0590	0°	29,82	0°	29,86	Ra 0,366
		90°	29,84	90°	29,89	
With hole 2	50.0950	0°	29,85	0°	29,86	Ra 0,667
		90°	29,84	90°	29,86	
Without hole 2	50.0050	0°	29,85	0°	29,72	Ra 0,317
		90°	29,75	90°	29,81	

Table 4. Measured values black samples (Bambu lab printer).

Black sample	Length [mm]	ØUpper half [mm]		ØLower half [mm]		Roughness
With hole 1	50.0235	0°	29,88	0°	29,86	Ra 0,381
		90°	29,90	90°	29,84	
Without hole 1	50.0010	0°	29,80	0°	29,82	Ra 0,294
		90°	29,86	90°	29,85	
With hole 2	49,9375	0°	29,94	0°	29,95	Ra 0,847
		90°	29,95	90°	29,97	
Without hole 2	49,9920	0°	29,91	0°	29,94	Ra 0,379
		90°	29,95	90°	30,00	

4. Discussion

After evaluating the results, we gained insight that for not every type of printer will it be beneficial to exchange overall printing time for accuracy by changing certain parameters, because the result will be practically the same.

4.1. Accuracy of Prusa printer

The measured data (Table 3.) show that for the Prusa printer, it is not necessary to reduce the printing speed or the layer height to achieve higher print accuracy, as these changes were not reflected in the final quality.

The height of the component was nearly constant for every sample, and the component's diameter also did not change significantly. However, the diameter never reached the specified 30 mm and was consistently smaller than this dimension by one to two tenths of a millimetre.

The quality of the print file (.stl) also did not significantly affect either the diameter or the roughness of the sample.

Further quality improvement is likely constrained by the printer's mechanical design and accuracy, not by software settings.

4.2. Accuracy of Bambu Lab printer

With this printer, we already see the influence of higher print file quality and a smaller layer height.

At a larger layer height, the accuracy when measuring the diameter was consistent with the accuracy of the previous printer. However, when the quality of the .stl file was increased and the layer height was reduced, a noticeable difference in print accuracy occurred, such that an exact diameter of 30.00 mm was achieved on one sample (Table 4.).

In other cases, the deviation from the nominal dimension ranged in hundredths of a millimeter and never exceeded one tenth of a millimeter. Better surface roughness of the component was not achieved; for this parameter, software adjustments had no influence.

Regarding the component height, a larger deviation from the nominal length can be observed in the sample with a hole [4], which may indicate the influence of the hole on the overall height. However, on a solid area, the deviation was only in thousandths of a millimeter.

We can conclude that with this type of setting and a printer that does not fall into the category of industrial printers, it is possible to print highly accurate components for prototyping.

Acknowledgments: This particle could be realized with support of KEGA 037TUKE-4/2024 of Creation of interactive tool for increasing of students' skills and competences in teaching of study subjects relating to elaboration of drawing documentation.

References

1. SINGH, Rupinder; GARG, Harish K. Fused deposition modeling–a state of art review and future applications. Reference Module in Materials Science and Materials Engineering, 2016, 1-20.
2. HALEEM, Abid; JAVAID, Mohd. 3D printed medical parts with different materials using additive manufacturing. Clinical Epidemiology and Global Health, 2020, 8.1: 215-223.
3. DEY, Arup; YODO, Nita. A systematic survey of FDM process parameter optimization and their influence on part characteristics. Journal of Manufacturing and Materials Processing, 2019, 3.3: 64.
4. VOLPATO, Neri; AGUIOMAR FOGGIATTO, José; CORADINI SCHWARZ, Daniel. The influence of support base on FDM accuracy in Z. Rapid prototyping journal, 2014, 20.3: 182-191.
5. GADELMAWLA, Elamir S., et al. Roughness parameters. Journal of materials processing Technology, 2002, 123.1: 133-145.
6. PALOVÁ, Katarína; KELEMENOVÁ, Tatiana; KELEMEN, Michal. Measuring procedures for evaluating the surface roughness of machined parts. Applied sciences, 2023, 13.16: 9385.

TECHNICAL UNIVERSITY OF KOŠICE
Faculty of Mechanical Engineering

Analysis of the Hopper Shape in the Extruder Feeding Section

Viliam Kapraľ [1,*], Ivan Gajdoš [1], Volodymyr Krasinskyi [2] and Christos Liosis [3]

[1] Slovakia, Technical University of Košice, Department of Technology, Materials and Computer Supported Production, Mäsiarska 74,040 01 Košice; viliam.kapral@tuke.sk; ivan.gajdos@tuke.sk
[2] Poland, Łukasiewicz Research Network – Institute of Polymer Materials, Marii Skłodowskiej-Curie 55, Toruń; volodymyr.krasinskyi@impib.lukasiewicz.gov.pl
[3] Greece, University of Thessaly, Department of Civil Engineering, Pedion Areos, GR-38334,Volos; liosischristos@uniwa.gr
* Correspondence: viliam.kapral@tuke.sk

Abstract: The geometric configuration of the hoppers feeding section plays a crucial role in determining the flow efficiency of granular polymer composites in extrusion processes. This analysis focuses on the discharge behavior of polybutylene succinate (PBS) reinforced with carbon nanotubes (CNTs), and evaluates how inlet geometry influences material throughput. Two hopper designs with identical global dimensions but differing inlet shapes (oval and rectangular with a rounded edge) were examined through Discrete Element Method (DEM) simulations and validated by experimental measurements using three pellet sizes. Results consistently showed that smaller particles discharge faster and that the rectangular inlet achieved higher throughput and shorter discharge times under identical conditions. The flow remained stable across all configurations with no signs of clogging, highlighting the role of geometrical optimization in enhancing mass flow. The data used in this evaluation originate from work conducted within the framework of the PROMATAI project, which investigated processing performance under varying material and design parameters. These findings underscore the significance of simulation based design in developing efficient feeding systems for biodegradable polymer composites and provide a foundation for further applied research in extrusion technology.

Keywords: Polybutylene Succinate, Carbon Nanotubes, Hopper Design, Discrete Element Method

1. Introduction

Biodegradable polymers have become a key focus in materials engineering due to the environmental persistence of conventional plastics. Polybutylene succinate (PBS) is one of the most widely studied candidates because it combines mechanical strength, thermal stability, and full biodegradability. Its properties can be further improved through nanoscale reinforcement with carbon nanotubes (CNTs), which are among the most effective additives. Even low CNT loadings significantly modify the crystallinity and structural behavior of PBS resulting in enhanced mechanical and thermal performance. CNT reinforced PBS composites therefore represent a promising class of materials for applications that require improved functional properties. [1] Since the processing behaviour of PBS/CNT composites strongly depends on the efficiency of granular feeding, an appropriate hopper design becomes essential for ensuring stable throughput during extrusion.

The flow behaviour of granular materials in hoppers is of great interest to many industries that involve the handling of bulk materials. The scale of hoppers varies from millilitres to thousands of litres depending on the desired hopper capacity, and the handled materials may range from cohesive particles to free flow particles. [2] Although most hoppers are simple in geometric configurations, the discharge flow dynamics can be complicated due to the influence of various factors related to the geometry of the hopper and the

characteristics of the flow media. Hopper design is critical because inappropriate design can result in poor operation performance and even equipment or functionality issues. [3] Since the flow characteristics of the granular material is of vital importance for the operational stability and structural integrity of these units, a deeper knowledge and understanding of the mechanical behavior within a hopper is necessary for the best possible design and operation. Nevertheless, a general approach for designing a hopper is not available. [4]

Particle discharge is one of the key physical processes governing the macroscopic flow behavior in hoppers. Factors affecting the discharge rate include hopper geometry and particle properties such as friction coefficient, shape, and size. [5] The Discrete Element Method (DEM) simulates the movement of granular materials by calculating the motion of individual particles based on Newton's second law, considering only contact interactions between neighboring particles. The resulting linear and rotational motions are determined by the summation of forces and moments acting at each contact. [6] Recent DEM studies have shown that particle flow behavior is strongly influenced by local arching, stress redistribution, and contact force chains within the granular assembly. These works demonstrate that DEM can accurately capture microstructural mechanisms, enabling detailed predictions of discharge rates and flow patterns across different hopper configurations. Furthermore, small variations in particle or wall properties can significantly affect clogging probability and mass flow discharge. [7] Predicting granular flow, however, remains challenging due to the strong coupling between particle–particle and particle–wall interactions. The discharge behavior is highly sensitive to parameters such as friction, particle shape, and surface roughness, as well as to local stress conditions. Even small changes in these factors can lead to marked differences in flow regimes, stress propagation, and overall discharge behavior. [8] To ensure the credibility of the numerical findings the simulated discharge behavior must be verified through controlled experimental measurements allowing a direct assessment of the agreement between modeled and real systems. Therefore, the objective of this study is to analyse how two hopper inlet geometries affect the discharge rate and flow stability of PBS/CNT pellets. The evaluation combines DEM simulations with experimental validation to identify geometric features that enhance feeding efficiency in extrusion processes.

2. Materials and Methods

2.1. Material Definitions for Hopper Feeding Analysis

Materials used in this study included the PBS/CNT composite prepared for testing, which served as the base material for evaluating the different hopper geometries. The polymer matrix consisted of polybutylene succinate (PBS) supplied by PTT MCC Biochem Company Limited (Bangkok, Thailand) under the trade name BioPBS™ FZ91PM. The nanofiller consisted of multi walled carbon nanotubes (CNT) supplied by Nanografi Nanotechnology (Ankara, Turkey) under the product code NG01IM0101 used at a concentration of 0.5 wt%. Higher CNT loadings were not considered as they typically increase melt viscosity and promote agglomeration, which complicates processing and reduces the functional performance of the composite. The PBS/CNT composite was prepared by melt compounding using a corotating twinscrew extruder BTSK 20/40D (Bühler, Germany). The extruded composite material was pelletized using a TS-40 pelletizer to produce pellets of 2×3 mm, 3×3 mm, and 5×3 mm. The measured PBS/CNT parameters are reported in Table 1. These pellet sizes were subsequently used in the DEM simulations and in the experimental measurements.

Table 1. Mechanical properties of PBS/CNT 0.5 wt % material.

Properties	Value
Density [g/cm³]	1.27
Melting Point [°C]	114
Tensile Modulus [MPa]	575 – 620
Stress at Break [MPa]	30 – 32
Strain at Break [%]	125 – 208
Surface Tension [mN/m]	52

2.2. Geometry of the Hopper Feeding Section

Both CAD designed hopper variants were developed with identical global dimensions to enable a controlled comparison of their flow performance. Each hopper has a total height of 450 mm, an inlet width equal to the screw diameter of 45 mm and a wall inclination angle of 70°. Keeping these geometric parameters constant ensures that any differences observed in the material discharge behaviour can be attributed solely to the geometry of the feeding opening.

The variants differ exclusively in the shape of the inlet region, which defines the local geometry of the hopper walls. In the first design, shown in Figure 1a, the feeding opening has an oval profile with a length of 67.5 mm, corresponding to 1.5 times the inlet width, and an effective area of 3046 mm². In the second design, illustrated in Figure 1b, the opening is rectangular with one rounded shorter edge. The opening length remains identical at 67.5 mm, while the total area is larger, reaching 3355 mm². These two geometries were selected to examine how the cross sectional shape of the feeding opening influences the overall discharge characteristics under otherwise identical hopper conditions.

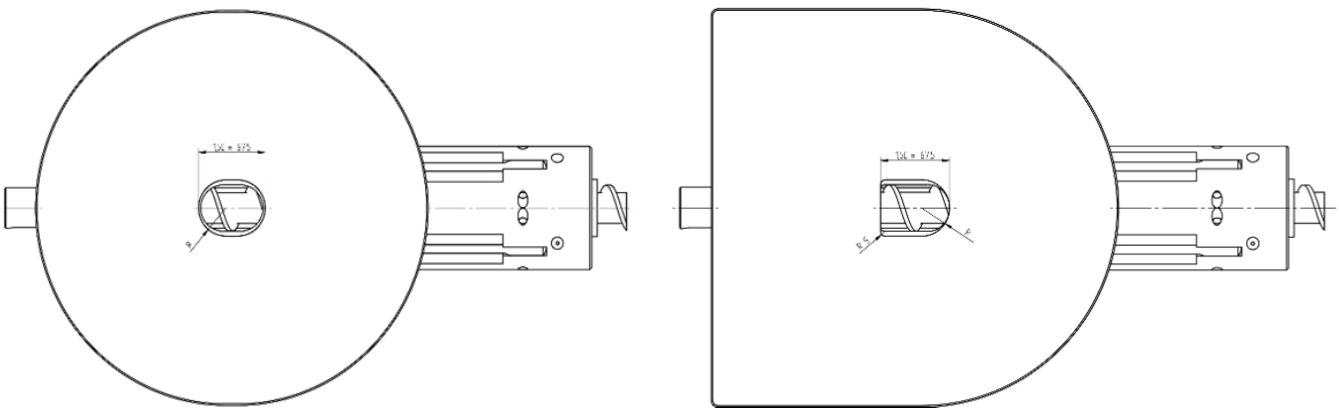

(**a**) (**b**)

Figure 1. Top view CAD models of the two hopper variants (**a**) hopper with an oval shape, (**b**) hopper with a rectangular shape featuring one rounded shorter edge.

2.3. Discrete Element Method Simulation of Hopper Geometries

For each hopper variant three separate simulations were performed differing in the radius of the spherical particles $r_1 = 0.002414$ m, $r_2 = 0.001717$ m, and $r_3 = 0.001311$ m. These values do not represent the actual dimensions of the pellets (5×3 mm, 3×3 mm, and 2×3 mm), but their spherical equivalents. Since the DEM model operates with spherical particles it was necessary to transform the irregular shape of the pellets into a spherical form with a comparable volume. This approximation ensured the numerical stability of the model and enabled consistent comparison of the individual variants. The geometry of the

hoppers was divided into three parts: the filling plane through which the hopper was filled (the upper inlet), the hopper body, and the measuring plane, which closed the geometry during filling to prevent free particle discharge. At the moment the simulation was started the measuring plane served as a detection plane determining the number of discharged particles and the time required to empty the entire hopper volume. The remaining parameters used in the simulation are presented in Table 2.

Table 2. Parameters used in the DEM simulation

Parameter	Value
Poisson´s ratio	0.46
Rolling friction coefficient	0.8
Coefficient of restitution	0.5
Filling time [s]	4
Input mass rate [kg/s]	4
Gravity [m·s^{-2}]	9.81
Iteration step [s]	10^{-5}

In the first hopper variant with an oval inlet, the filling with pellets lasted 4 s. After the hopper was filled, the particle exit phase began, which for all particle sizes r_1, r_2, and r_3 lasted between 4 and 7.75 s. After a short initial fluctuation, the flow stabilized and remained practically constant until the hopper was completely emptied. The particles with the largest radius r_1 required the most time to empty the entire hopper volume through the measuring plane namely 3.75 s with a total of 53 875 particles passing through the measuring plane. For particles with radius r_2 the exit time was 3.50 s and the number of particles was 149 717. The hopper volume was emptied the fastest by the particles with radius r_3, in 3.35 s, with a total of 336 348 particles. Figure 2 provides a graphical representation of the discharge behavior for the hopper with an oval inlet, showing both the number particle count passing measuring plane and the particle flow rate for all three pellet radii.

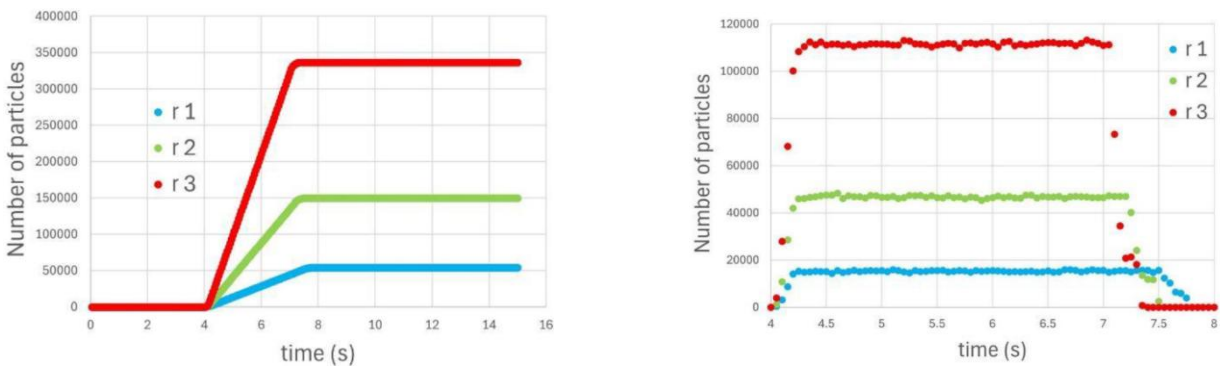

(**a**) (**b**)

Figure 2. Particle discharge characteristics (**a**) Total number of particles passing through the measuring plane for the hopper with oval inlet, (**b**) Number of particle rate for the hopper with a oval inlet.

For the second hopper configuration, the inlet was rectangular with one rounded shorter edge, the initial filling of the hopper volume proceeded similarly to the first variant however the geometry allowed more particles to be inserted into the hopper. The interval for emptying the hopper volume ranged from 4 to 7.5 s, which was the time required to empty 4 kg of material. For particles with radius r_1 the exit time was 3.50 s and the number of particles passing through the measuring plane was 53 924. The exit time for 149 653 particles with radius r_2 was 3.20 s. As in the first variant, the smallest particles

with radius r_3 required the shortest time to exit the hopper, namely 3.05 s, and the number of particles leaving the hopper volume was 336 015. Figure 3 illustrates the discharge behaviour for the hopper with a rectangular inlet with one rounded shorter edge, again showing the number particle count passing measuring plane and the particle flow rate.

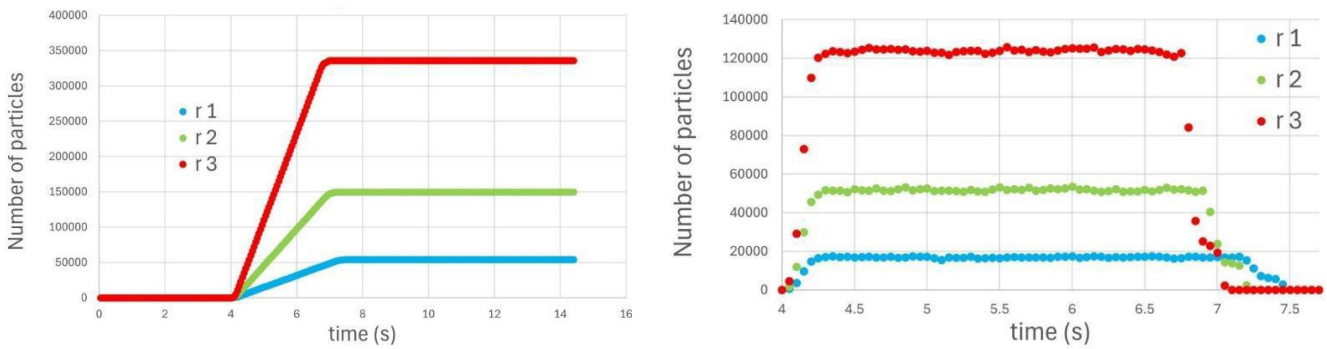

(**a**) (**b**)

Figure 3. Particle discharge characteristics (**a**) Total number of particles passing through the measuring plane for the hopper with a rectangular shape featuring one rounded shorter edge, (**b**) Number of particle rate for the hopper with a rectangular shape featuring one rounded shorter edge.

A comparison of the two simulated variants shows that the dominant factor influencing the emptying process is the particle size, as also reflected in Table 3, which clearly illustrates the progressively shorter discharge times for smaller radii. Smaller radii consistently led to a faster exit from the hopper volume and a higher number of particles passing through the measuring plane. The difference between the geometries manifested mainly in the amount of material that could be inserted into the hopper. The second geometry allowed for a larger number of particles to be loaded, while still maintaining a stable flow behaviour for all examined radii.

Table 3. Exit time for two inlet geometries at three pellet sizes [s].

Inlet geometry	Exit time at r_1	Exit time at r_2	Exit time at r_3
Oval inlet	3.75	3.50	3.35
Rectangular inlet (rounded edge)	3.50	3.20	3.05

2.4. Experimental Comparison of Hopper Geometries

For the purposes of the experiment, it was necessary to print prototype hoppers, which were manufactured on a Fortus 400mc 3D printer. Due to the limited size of the printing area, it was necessary to change the original hopper height from 450 mm to 350 mm. After printing the individual models, it was necessary to adjust the internal surfaces of the hoppers by sanding to ensure identical surface roughness (Ra ≈ 0.2 μm) for both variants. Subsequently, a supporting structure was produced onto which the individual hoppers were mounted in order to minimize measurement deviation during the experiments. The opening and closing of the hopper were carried out using a pneumatic piston, which ensured a reproducible opening and closing speed throughout all tests. The throughput of both hopper variants was measured for all tested pellet sizes (2×3 mm, 3×3 mm, and 5×3 mm). For each combination, the experiment was repeated 10 times, resulting in a total of 60 measurements. The measurements were conducted in the laboratory of the Institute of Polymeric Materials (Instytut Materiałów Polimerowych, Poland).

The results of the experiment presented in Table 4 show that the hopper with the rectangular inlet featuring a rounded shorter edge achieves higher throughput than the hopper with the oval inlet, and this applies to all tested pellet sizes. For the 2×3 mm pellets,

an increase in throughput of 525 kg/h was recorded, corresponding to 13.3%. For the 3×3 mm pellets, the difference was 487 kg/h, i.e., 13.4%. The most pronounced effect was observed for the largest pellets, 5×3 mm, where the throughput increased by 620 kg/h, which corresponds to 16.2%. These results confirm that the enlarged area and modified shape of the discharge opening reduce the flow resistance of the granulate and enable a higher mass flow under identical boundary conditions.

Table 4. Measured throughput capacity for different inlet geometries [kg/h].

Pellet size [mm]	Oval inlet	Rectangular inlet (rounded edge)
2×3	3948	4473
3×3	3633	4120
5×3	3830	4450

Note: All values were measured with an uncertainty of ±25.

Table 5 summarizes the average discharge time of the material for the individual combinations of outlet geometry and pellet size. In all cases, a shorter discharge time was achieved with the rectangular outlet with a rounded shorter edge, which is consistent with the higher throughput presented in Table 4. For pellets of 2×2 mm, the discharge time was shorter by 0.43 s, which represents a 13.35% difference compared to the oval outlet. For the 3×3 mm size, the difference was 0.41 s, corresponding to 11.55%. The largest difference was observed for the 5×3 mm pellets, where the discharge time was shorter by 0.51 s, which corresponds to a 15.74% difference. The experimental results indicate that an appropriate modification of the outlet shape can significantly reduce the hopper discharge time without a negative impact on flow stability.

Table 5. Discharge time for two inlet geometries for three pellet sizes [s].

Pellet size [mm]	Oval inlet	Rectangular inlet (rounded edge)
2×3	3.65	3.22
3×3	3.96	3.55
5×3	3.75	3.24

3. Discussion

A comparison of the DEM simulation results with the experimental measurements shows a consistent trend in the discharge behaviour of pelletized material for both inlet geometries as summarized in Table 6. In all evaluated cases, the discharge time increased with increasing pellet size, which was captured in the simulation as well as in the experiment.

For the oval inlet, the DEM simulation consistently predicted shorter discharge times than the experiment. The deviations were 0.30 s for 2×3 mm pellets (3.35 s vs. 3.65 s), 0.46 s for 3×3 mm pellets (3.50 s vs. 3.96 s), and 0.00 s for 5×3 mm pellets (3.75 s vs. 3.75 s). Despite this offset, the model correctly reproduced the relative differences among pellet sizes. For the rectangular inlet with a rounded edge, the agreement was significantly better for the 2×3 mm pellets. The differences between simulation and experiment were smaller 0.17 s for pellets (3.05 s vs. 3.22 s), 0.35 s for 3×3 mm pellets (3.20 s vs. 3.55 s), and 0.26 s for 5×3 mm pellets (3.50 s vs. 3.24 s). These results indicate that the DEM model captured the discharge behaviour more accurately in this geometry, likely due to the more uniform outflow enabled by the enlarged effective opening.

Overall, the comparison confirms that the DEM simulation reliably reproduces the qualitative behavior of the pellet discharge process and provides quantitatively acceptable predictions. The model demonstrated sufficient accuracy to distinguish the influence of

pellet size and inlet geometry on discharge time. The rectangular inlet consistently enabled faster discharge in both the simulation and the experimental setup, which validates its suitability for applications requiring higher material throughput.

Table 6. Discharge time comparison between DEM simulation and experiment [s].

Pellet size [mm]	Oval inlet		Rectangular inlet (rounded edge)	
	Simulation time	Experiment time	Simulation time	Experiment time
2×3	3.35	3.65	3.05	3.22
3×3	3.50	3.96	3.20	3.55
5×3	3.75	3.75	3.50	3.24

Acknowledgments: This research was funded by the European Union's programme for research and innovation Horizon Europe under the Marie Skłodowska-Curie Action grant agreement No 101129698–PROMATAI– Horizon–MSCA–2022–SE–01. Views and opinions expressed are however those of the author(s) only and do not necessarily reflect those of the European Union or European Research Executive Agency (REA). Neither the European Union nor the granting authority can be held responsible for them.

References

1. MODYFIKACJA POLIMERÓW STAN I PERSPEKTYWY W ROKU 2025, MWCNT-Reinforced Biopbs for Sustainable Application, Krasinskyi, V., Bajer, K., Krasinska, O., Sarris, I., Dulebová, Ľ., Ganusauskaité, A., Manduľak, D., TEMPO s.c., Wroclaw, 2025, pp. 92-94, ISBN 978-83-86520-27-5
2. Jihoe, K., Dong-Woo, R., Investigation of discharge characteristics of rod-shaped particles in a hopper: Experimental and numerical studies using polygonal/polyhedral DEM, Advanced Powder Technology, Elsevier B.V., 2020, Volume 31, pp. 4207-4221, ISSN 0921-8831
3. Lai, Z., Xia, Y., Chen, Q., Discrete element modeling of granular hopper flow of irregular-shaped deformable particles, Advanced Powder Technology, Elsevier B.V., 2023, Volume 34, ISSN 0921-8831
4. Höhner, D., Wirtz, S., Scherer, V., A numerical study on the influence of particle shape on hopper discharge within the polyhedral and multi-sphere discrete element method, Powder Technology, Elsevier B.V., 2012, Volume 226, pp. 16-28, ISSN 0032-5910
5. Fan, J., Wang,H., Luu, L., Philippe, P., Wang, L., Wei, Z., Yu, J., Numerical study of granular discharge flows through centred and off-centred rectangular hoppers using discrete element simulations, Powder Technology, Elsevier B.V., 2023, Volume 429, ISSN 0032-5910
6. K. Tanaka, M. Nishida, T. Kunimochi, T. Takagi, Numerical and experimental studies for the impact of projectiles on granular materials, Handbook of Powder Technology, 1st ed, A. Levy, H. Kalman, Elsevier Science, Amsterdam, New York, 2001, Volume 10, pp. 263-270, ISBN 9780444502353
7. R. Balevičius, R. Kačianauskas, Z. Mróz, I. Sielamowicz, Analysis and DEM simulation of granular material flow patterns in hopper models of different shapes, Advanced Powder Technology, Elsevier B.V., 2011, Volume 22, pp. 226-235, ISSN 0921-8831
8. Bovo, E., Sorgato, M., Lucchetta, G., An image-based approach for the mass flow measurement of plastic granules as an alternative solution to loss-in-weight feeding systems, Powder Technology, Elsevier B.V., 2023, Volume 430, ISSN 0032-5910

TECHNICAL UNIVERSITY OF KOŠICE
Faculty of Mechanical Engineering

Kinematic Design and Functional Principle of a Kinetic Sculpture Mechanism

Samuel Kerekeš [1,*], Barbara Schürger [1], Ingrid Delyová [1] and Peter Frankovský [1]

[1] Technical University of Košice, Faculty of Mechanical Engineering, Department of Applied Mechanics and Mechanical Engineering, Letná 1/9, 042 00 Košice, Slovakia; samuel.kerekes@tuke.sk; peter.frankovsky@tuke.sk; barbara.schurger@tuke.sk; ingrid.delyova@tuke.sk
* Correspondence: samuel.kerekes@tuke.sk

Abstract: This paper presents the kinematic design and operating principle of a novel kinetic sculpture that transforms two distinct images using a multilayer rotational mechanism with mechanical stop-time control. The system consists of 38 individual layers, each equipped with a custom-developed bearing, paired stop elements, and a mechanical locking interface. During rotation, the layers collectively align to form a complete image, which subsequently disappears and is replaced by a second image through vertical displacement of the central shaft. The transformation is achieved without the need for electronic synchronization, relying solely on precise geometric positioning of stops within each layer. The research describes the development of the bearing element, including material selection and surface hardening to meet load and wear requirements. The results demonstrate the potential of this mechanism for artistic installations, public spaces, and educational exhibits, combining mechanical engineering with visual art.

Keywords: kinetic mechanism; multilayer geometry; transformation design; mechanical stops

1. Introduction

Kinetic artworks combine visual aesthetics with mechanical motion, creating dynamic installations capable of changing shape and meaning over time. Unlike digital displays, mechanically driven sculptures are tangible systems whose visual transformation is achieved through real physical movement. The presented mechanism represents an innovative method for transforming two different images into each other, using a rotational multilayer arrangement.

The novelty of this design lies in its purely mechanical synchronization. Transformation is achieved using 38 rotating layers with fixed stops that define two unique geometric positions for the formation of images without electronic control or sensory feedback.

2. Mechanical Design of the Transformation System

The sculpture functions as a multilayer mechanical device in which two images are created through controlled motion of a central shaft. The mechanism contains 38 rigid layers, each with a nitrided bearing hub and two stop positions. Motion is transferred by 38 welded Hardox fingers, which rotate or lift the layers depending on the active actuator. Contact between the fingers and mechanical stops determines each layer's position and forms the image without any electronic synchronization. The structural arrangement of the mechanism is illustrated in Figure 1.

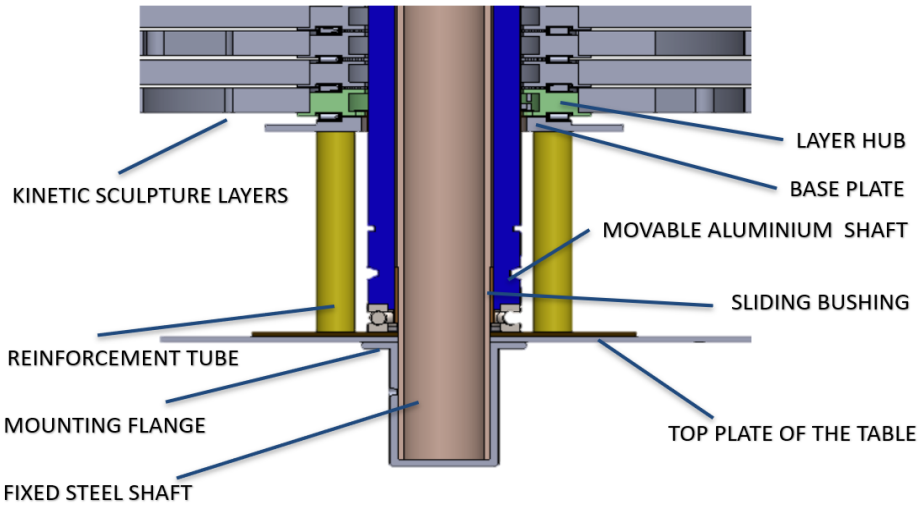

Figure 1. Bottom sectional view of the kinetic sculpture mechanism.

2.1. Development of Layer Bearing Hubs

Each of the 38 layers includes a custom hub optimized for repeated point contact loading from the motion fingers. Early prototypes made from conventional steel showed indentation and jamming due to insufficient hardness [1,2,3,4]. Vickers hardness testing confirmed inadequate durability. After optimization, gas nitriding was selected, producing a wear-resistant surface that allows long-term cyclic rotation without deformation, as demonstrated in Figure 2.

Figure 2. Comparison of the hub before and after nitriding treatment.

2.2. Shaft and Hardened Fingers

All layers are driven by a single aluminium shaft with a continuous T-slot. Inside the slot are 38 welded Hardox fingers, each transferring rotational and lifting motion directly into an individual layer. The hardness of Hardox prevents surface deformation when contacting stop pins, ensuring accurate alignment of both image positions.

2.3. Geometry of Stop Pins and CNC Machining of Angular Positions

Each layer contains two stop pins:

1. the lower stop is identical across all layers and defines the position for Image A,
2. the upper stop is rotated by a defined angular offset and defines Image B.

During CNC machining, a special fixture allowed milling of both positions on the same component. First, the layer was machined at 0° (Image A). Then the layer was rotated by ±30° or kept at 0°, and the second geometry was milled at 180°, producing the shape for Image B. The distribution of these angular offsets across layers creates the mechanical transformation effect without electronic control.

3. Kinematic Operating Principle

The transformation mechanism operates through a combination of rotational positioning and controlled axial displacement of the central shaft. Each motion phase corresponds to the formation of one of two distinct image states. The interaction between hardened fingers and mechanically indexed stop pins ensures repeatability of alignment, eliminating the need for digital or sensory feedback. The rotation and lifting movements are actuated through a lever-based system driven by two independent motors, as illustrated in Figure 3 [8,14].

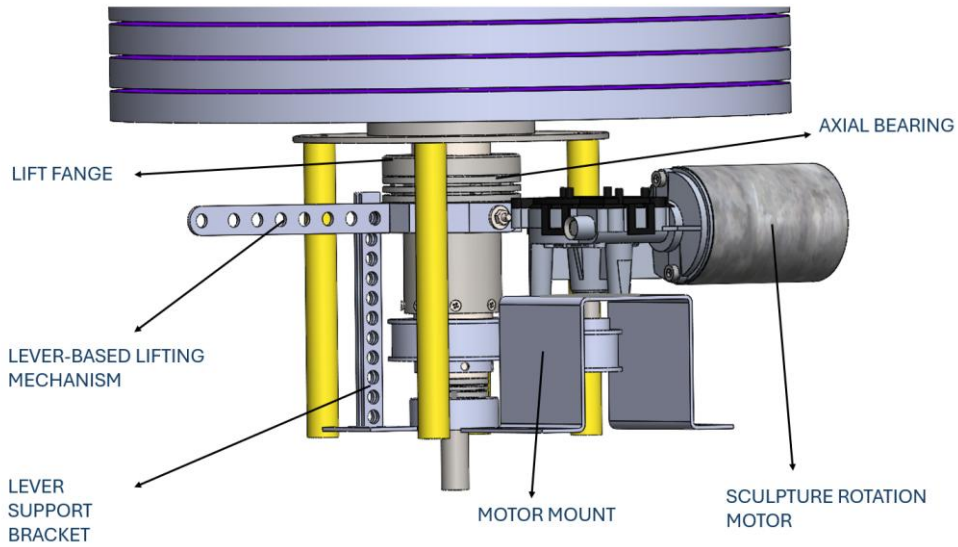

Figure 3. Actuation system of the kinetic sculpture mechanism.

3.1. Formation of Image A (Rotation Mode)

The rotation motor drives the central shaft, forcing all 38 Hardox fingers to push the layers against their identical lower stops. When all layers reach this synchronized indexed position, the geometry of Image A is formed. The accuracy of this state depends exclusively on the rotational stop angles and the surface hardness of the contact zones, ensuring stable and repeatable transformation during each cycle.

3.2. Transformation into Image B (Lift Mode)

When the lifting actuator is engaged, the shaft moves vertically upward, causing the fingers to disengage from the lower stops and progressively press against the mechanically indexed upper stops. Due to the angular offsets machined into each layer, all elements simultaneously realign into the second geometric configuration. Once all fingers reach full contact with the upper stops, Image B is formed, while Image A fully disappears. The transformation between these two visual states is demonstrated in Figure 4.

Figure 4. Real transformation between two visual states of the kinetic sculpture.

3.3. Mechanical Design of the Transformation System

The transformation sequence requires no electronic timing. Instead, image formation is governed by:

- the **rotation position** of the shaft,
- the **axial stroke height** at which stop engagement changes,
- the **hardness and stiffness** of the stop–finger interfaces.

Because the stop contact determines the final orientation, the mechanism inherently corrects minor backlash or mechanical imperfections, functioning as a self-aligning system.

3.4. Mechanical Design of the Transformation System

The use of nitrided hubs and hardened fingers ensures that stop angles remain constant even after prolonged usage. Unlike software-based systems prone to calibration drift, this mechanism achieves long-term stability through surface hardness and rigid constraints. The expected result is high repeatability of image transformation over thousands of cycles, making the mechanism suitable for continuous public operation [10].

4. Discussion

The long-term reliability of the kinetic mechanism is determined by several interacting design factors, including the precision of the stop geometry, the surface durability of the bearing hubs, and the stability of motion transfer through the hardened Hardox fingers. The optimization of the hub material through gas nitriding proved essential, as the increased surface hardness significantly reduced local deformation at the mechanical stop interfaces. This ensures that the stop angle remains consistent over time, directly stabilizing the geometry of the generated images. Because the sculpture relies entirely on mechanical synchronization, even minor wear or dimensional deviation would immediately affect the visual quality of the transformed image. Long-term operational testing confirmed that the combination of nitrided surfaces, welded Hardox actuator fingers, and rigid layer construction allows the system to withstand thousands of transformation cycles without recalibration or adjustment. This robustness makes the mechanism highly suitable for public installations where continuous operation is expected and maintenance interventions must be minimized. The dual-actuator system—comprising the rotation drive and the lifting drive—has also demonstrated high functional reliability, enabling two distinct image positions to be formed purely through controlled mechanical contact. The absence of electronic sensors or feedback devices reduces system complexity and eli-

minates potential failure points, resulting in a stable and predictable operating mechanism whose accuracy is defined solely by material selection and machining quality. Future development may focus on monitoring long-term micro-abrasion under extreme usage conditions or exploring additional structural optimizations for outdoor environments. Nevertheless, the current results clearly demonstrate that the chosen mechanical concept provides high repeatability, durability, and operational stability, making it an effective solution for kinetic art and presentation systems based on purely mechanical synchronization.

5. Conclusions

The kinetic mechanism demonstrates that transformation between two images can be achieved entirely mechanically, using only dual-motion shaft actuation and stop geometry. Hardened surfaces ensure durability and precision without electronic control. By integrating mechanical engineering with visual art, the system provides a robust solution for public installations, museum exhibits, and architectural applications.

Acknowledgments: The work was supported by the grant project KEGA 039TUKE-4/2024 and VEGA 1/0152/24.

Conflicts of Interest: The authors declare no conflict of interest

References

1. Zhou, Z.; Li, C.; Huang, X.; et al. Nitriding behavior of alloy steels and its effect on mechanical properties. *Surface & Coatings Technology* 2022, 437, 128136. https://doi.org/10.1016/j.surfcoat.2022.128136
2. Kumar, S.; Sharma, A. Tribological performance of nitrided steel components. *Journal of Tribology and Materials* 2023, 29(2), 55–62.
3. Budynas, R.; Nisbett, K. *Shigley's Mechanical Engineering Design*, 11th ed.; McGraw-Hill: New York, USA, 2020.
4. Liu, R.; Shi, M.; Dong, H. Evaluation of surface hardness of nitrided steels using Vickers method. *Materials & Design* 2021, 204, 109634.
5. Sophia, R.; Koc, M. Effect of precision nitriding on wear properties of bearing components. *Tribology International* 2024, 197, 108–122.
6. Hutchings, I.; Shipway, P. *Tribology: Friction and Wear of Engineering Materials*, 2nd ed.; Butterworth-Heinemann: Oxford, UK, 2017.
7. Meredith, T.; Walker, D. Fatigue and wear reduction in kinematic joints via surface hardening treatments. *International Journal of Mechanical Sciences* 2020, 184, 105842.
8. Amer Motors. *AMER MP80 Servo Motor Datasheet.* [Online] (accessed 2025-01-15). Available at: https://www.amer-motors.com/products/mp-series-motors/
9. SPIŠÁK, E – GREŠKOVIČ, F – MAŇKOVÁ, I a kol.: STROJÁRSKE TECHNOLÓGIE. 1. vydanie. Košice: SjF TU, 2011. ISBN 978-80-553-0820.
10. BOCKO, Jozef; DELYOVÁ, Ingrid; FRANKOVSKÝ, Peter. Kinematika. 1. vydanie. Košice: Technická univerzita v Košiciach, 2012. ISBN 978-80-553-1205-7.
11. KURUC, Ján a KURUC, Marcel. Časti a mechanizmy strojov. 1. vydanie. Košice: Technická univerzita v Košiciach, 2015. ISBN 978-80-553-2015-2.
12. LEINVEBER, Jiří a Pavel VÁVRA. Strojnické tabulky. 6. vydanie. Úvaly: ALBRA, 2017. ISBN 978-80-7361 111-8.
13. ŠIMŠÍK, Dušan et al. Základy automatizácie. 1. vydanie. Košice: Technická univerzita v Košiciach, 2019. ISBN 978-80-553-3372-4.
14. KOVÁČ, Miroslav. Technológia obrábania: Frézovanie. 2. vydanie. Košice: Technická univerzita v Košiciach, 2015. ISBN 978-80-553-2015-2.
15. MALÁKOVÁ, Silvia a Daniela KEPEŇ HARACHOVÁ. Konštruovanie strojov – Prevody. 1. vydanie. Košice: Technická univerzita v Košiciach, 2023. ISBN 978-80-553-4448-5.

TECHNICAL UNIVERSITY OF KOŠICE
Faculty of Mechanical Engineering

Comparison of EDX and LIBS analytical methods in evaluating technical cleanliness in industrial applications

Vladimír Kokarda [1,*]

[1] Department of Technology, Materials and Computer-Aided Technologies, Faculty of Mechanical Engineering, Technical University of Košice, Mäsiarska 74, 040 01 Košice, Slovakia; vladimir.kokarda@gmail.com
* Correspondence: vladimir.kokarda@gmail.com; Tel.: 0910890179

Abstract: Technical cleanliness has become a decisive quality factor in modern industrial manufacturing, especially in the automotive and precision engineering sectors. Increasing functional integration, miniaturization, and tighter tolerances significantly increase the sensitivity of components and systems to particulate contamination. As a result, reliable detection, classification, and evaluation of particles are essential to prevent functional failures and ensure long-term product reliability. The updated VDA 19 and VDA 19.2 standards address these challenges by strengthening requirements for particle analysis, material determination, reproducibility, and documentation of cleanliness results. This paper discusses the implications of the updated VDA requirements on analytical methods used in technical cleanliness inspection and presents a detailed comparison of Laser-Induced Breakdown Spectroscopy (LIBS) and Energy Dispersive X-ray Spectroscopy (EDX). Both technologies are evaluated with regard to their analytical capabilities, automation potential, and suitability within the VDA cleanliness framework. LIBS is characterized as a fast and highly automatable spectroscopic method that enables rapid material classification of particles and supports inline or near-line process monitoring. Its high throughput and sensitivity to light elements make it particularly suitable for screening applications and production-oriented cleanliness control. In contrast, EDX, typically integrated with scanning electron microscopy (SEM), is identified as the reference method according to VDA 19.2. It offers superior spatial resolution, detailed particle morphology evaluation, and quantitative elemental analysis required for laboratory-based validation and root cause investigations. The comparison demonstrates that LIBS and EDX are complementary rather than competing technologies. Their combined use supports an efficient and robust technical cleanliness strategy that meets the increased demands of the updated VDA standards while balancing process efficiency and analytical depth.

Keywords: Technical Cleanliness; Particle Contamination; Cleanliness Inspection; LIBS (Laser-Induced Breakdown Spectroscopy); EDX (Energy Dispersive X-ray Spectroscopy); SEM/EDX

1. Introduction

Technical cleanliness has become a critical quality factor in modern industrial manufacturing, particularly in sectors such as automotive, electronics, and precision engineering. Microscopic contaminants on component surfaces or within assemblies can lead to functional failures, reduced service life, and increased warranty costs. As products become more complex and tolerances tighter, the ability to reliably detect, identify, and evaluate contamination is more important than ever.

In response to these increasing demands, an updated version of the VDA standard for technical cleanliness has been released. This update reflects technological progress in

analytical methods and emphasizes improved accuracy, reproducibility, and traceability of cleanliness evaluations. Manufacturers and suppliers are therefore required to reassess not only their production and cleaning processes, but also the analytical technologies used for contamination analysis.

This article focuses on two advanced analytical methods widely discussed in the context of technical cleanliness: Laser-Induced Breakdown Spectroscopy (LIBS) and Energy Dispersive X-ray Spectroscopy (EDX). Their principles, advantages, limitations, and suitability for industrial cleanliness analysis are compared with respect to the updated VDA/ISO standard requirements.

2. Materials and Methods

2.1. Application of the technical cleanliness method in industry

Technical cleanliness is an area of quality focused on controlling and minimizing solid contaminants (particles) on the surface of components, in liquids, or in closed systems. It is particularly important where even microscopic contaminants can cause malfunctions, wear, or equipment failure. Even a microscopic particle can cause serious failure in critical applications – that is why technical cleanliness is an integral part of quality in the automotive, engineering, electrical engineering, and medical industries.

Why technical cleanliness is important, insufficient cleanliness can lead to:

- seizing of moving parts
- clogging of valves, nozzles, and channels
- leaks in hydraulics and pneumatics
- shortened component life
- failure of safety systems

In modern industry, tolerances are becoming smaller, and therefore cleanliness requirements are becoming significantly stricter.

2.2. VDA 19 / ISO 16232 Standard and Its Impact on Technical Cleanliness

Standard defines procedures for sampling, extraction, analysis, and evaluation of particulate contamination on technical components. The standard precisely defines the particle extraction process and the time required for analysis, either optical analysis using a light microscope or EDX chemical analysis using SEM.

1. Cleaning processes:

- wet cleaning (ultrasound, spraying)
- vacuum and dry cleaning
- multi-stage cleaning

2. Inspection and measurement:

- particle extraction (rinsing, ultrasound)
- filtration
- microscopic analysis with optical microscope
- gravimetry
- particle material analysis with EDX technology or LIBS technology

These standards highlight the growing importance of analytical methods that not only detect particles but also provide rapid and reliable characterization of materials. As a result, spectroscopic techniques such as LIBS and EDX are gaining increasing attention in industrial applications. Using these methods, we can obtain information about the source of contamination and thus improve (optimize the production process).

2.3. LIBS Technology in Technical Cleanliness Analysis

Laser-Induced Breakdown Spectroscopy (LIBS) is an optical emission spectroscopy technique based on the interaction of a focused laser pulse with the sample surface. The laser generates a micro-plasma, and the emitted light is analysed to determine the elemental composition of the material. Ater the laser pulse hits the sample, a very small amount of material is vaporized and rapidly heated to temperatures exceeding 10,000 °C, resulting in the formation of plasma. The resulting plasma contains excited atoms and ions from which electrons have been knocked out of their outer electron shells by laser radiation. After the laser pulse ends, the plasma gradually cools down, and the electrons return to lower energy levels. During these transitions, electromagnetic radiation is emitted at wavelengths characteristic of individual chemical elements. The result is an emission spectrum consisting of a large number of spectral lines, with each element identifiable by its specific emission lines. The laser pulses used typically have a wavelength ranging between 331 and 1064 nm, The laser pulse vaporizes the material and generates plasma. Depending on the system, the observed wavelength range lies between 400 and 800nanometers. Pure metals generally emit a strong signal. The strength of the signal mainly depends on the point of vaporization of the material. So, the more material is vaporized by the laser pulse, the stronger is the signal. Because elements each have a specific spectrum, metals and inorganic materials can be clearly identified by means of spectrum databank. See figure 1.

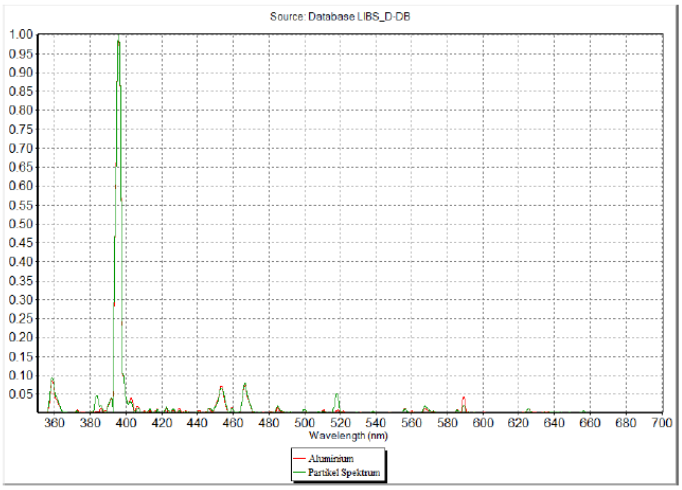

Figure 1. LIBS spectra -comparison of aluminum (green) with particle spectrum (red) (Adapted from *Inspection of Technical Cleanliness* (VDA, 2025, p.315).

The emitted radiation is captured by optical fiber and then analysed by a spectrometer. The intensity of the individual spectral lines is proportional to the concentration of the respective element in the sample. Advanced mathematical and statistical algorithms are used to process the measured data, enabling the identification of the sample composition and the quantitative determination of the content of individual elements.

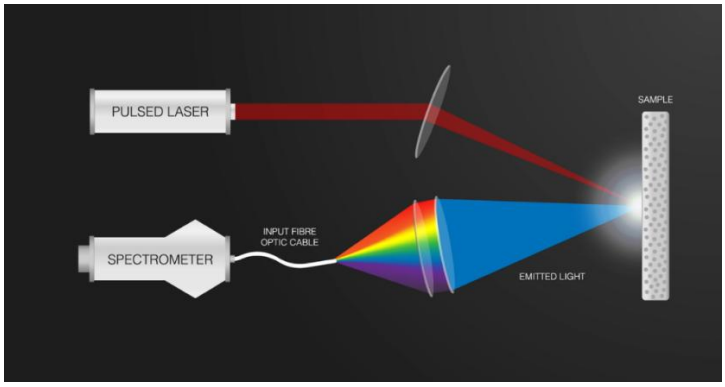

Figure 2. This is a figure. Schemes follow the same formatting [Online]. (Available: https://hha.hitachi-hightech.com/en/blogs-events/blogs/2018/01/03/what-is-libs/).

Key advantages of LIBS include:

- Very fast analysis times (milliseconds per measurement)
- Minimal or no sample preparation
- Capability for inline and automated inspection
- High sensitivity to light elements (e.g. aluminum, magnesium)

In the context of technical cleanliness, LIBS is particularly suitable for rapid identification of metallic particles and for sorting particles according to material type. Its speed and automation potential make it attractive for high-volume industrial environments and process monitoring.

Limitations include lower spatial resolution compared to electron microscopy and limited capability to provide detailed morphological information about particles.

2.4. EDX Technology in Technical Cleanliness Analysis

Energy-dispersive X-ray spectroscopy (EDX) is widely applied in combination with scanning electron microscopy (SEM) for technical cleanliness analysis. When the focused electron beam interacts with the sample, characteristic X-ray radiation is generated, enabling elemental analysis of individual particles. This technique provides elemental information and therefore allows particle characterization that goes beyond optical classification, which is limited to morphological features in light-optical analysis (see Figure 3).

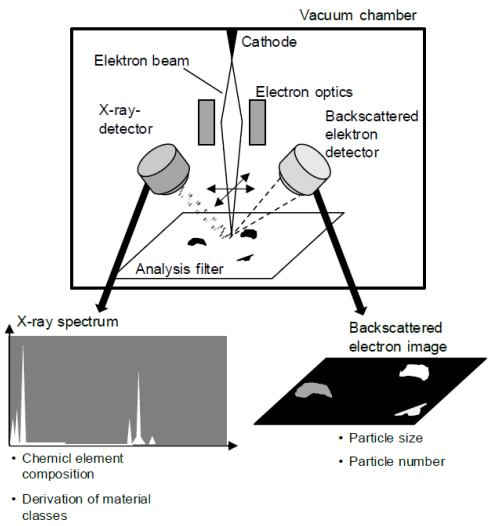

Figure 3. Schematic principle of SEM/EDX (Adapted from *Inspection of Technical Cleanliness* (VDA, 2025, p.276).

Particle detection and imaging in SEM are based on material contrast. This contrast arises from differences in detector signal intensity caused by the material-dependent yield of backscattered electrons originating from the chemical elements present in both the particles and the filter background.

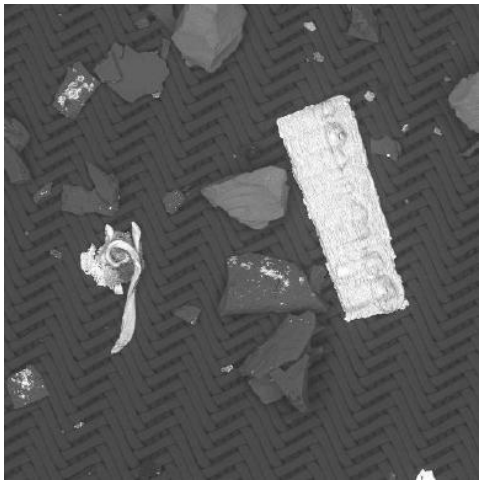

Figure 4. Dark filter substrate with various particles appearing brighter than the background (Adapted from *Inspection of Technical Cleanliness* (VDA, 2025, p.277).

For image regions identified as particles, an EDX spectrum is acquired. The energy positions of the characteristic peaks in the X-ray spectrum are specific to the chemical elements from which they originate (see Figure 7). Evaluation of these spectral lines enables qualitative and semi-quantitative determination of the elemental composition.

However, spectral interpretation may be affected by peak overlaps, statistical noise, or short acquisition times, which can lead to misinterpretation. Therefore, whenever possible, the evaluation should be restricted to relevant elements only.

To obtain an accurate representation of the elemental composition of a detected particle, the electron beam should not be confined to a single point during EDX analysis. Instead, it should scan a representative area covering as much of the particle surface as possible (see Figure 5). For smaller particles, the relative contribution of the filter background to the measured signal increases; therefore, for very small particles, point-based EDX analysis may be more appropriate.

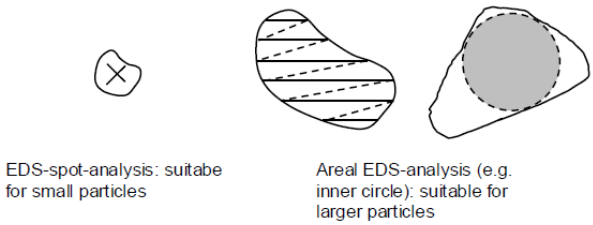

Figure 5. Particle area used for EDX analysis (Adapted from *Inspection of Technical Cleanliness* (VDA, 2025, p. 278).

The results of EDX analysis allow reliable conclusions to be drawn regarding the chemical (elemental) composition of detected particles. For automated particle classification, appropriate material definitions and reference components must be implemented within the SEM/EDX system.

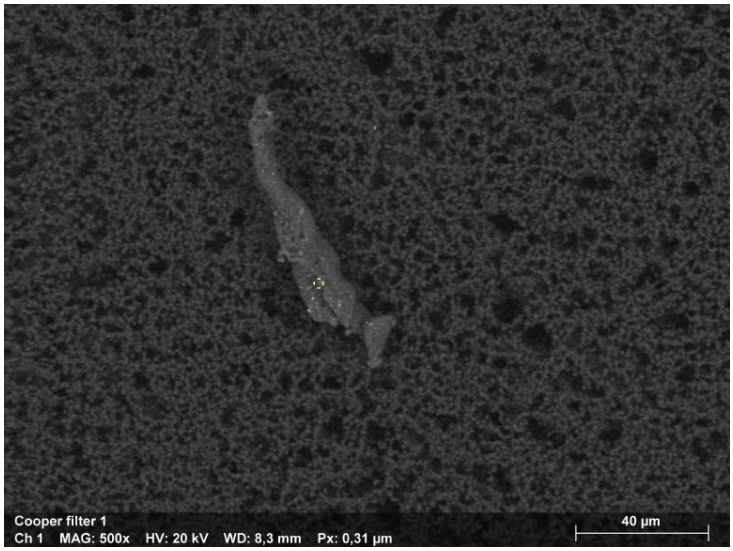

Figure 6. Example of a particle detected on a filter membrane.

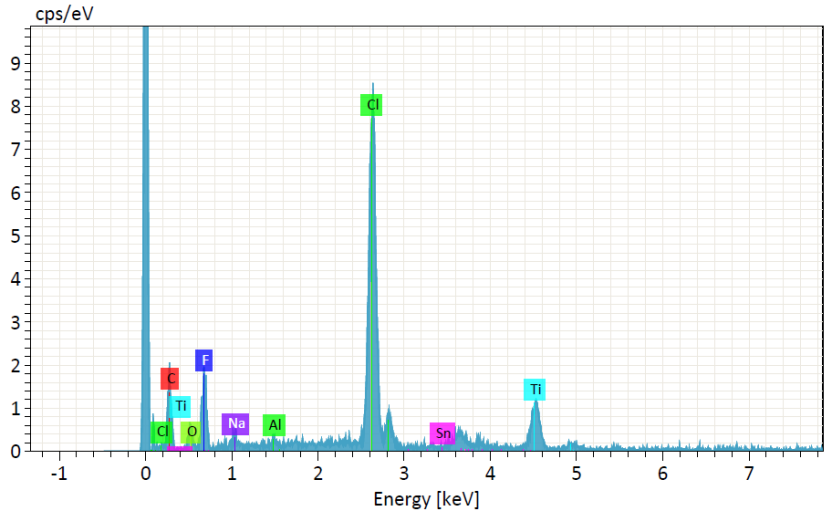

Figure 7. Example of an EDX spectrum obtained from a particle.

Key advantages of EDX include:

- High spatial resolution and precise particle localization
- Detailed elemental composition analysis
- Excellent correlation between particle morphology and material type
- Well-established method in cleanliness laboratories

EDX is particularly valuable for root cause analysis and detailed investigation of critical contaminants. It provides comprehensive information required for failure analysis and documentation in accordance with VDA standards.

Limitations

Despite its advantages, EDX analysis involves relatively long measurement times, higher system complexity, and limited suitability for inline or high-throughput inspection applications.

3. Results

3.1. Comparison parameters of EDX and LIBS methods in technical cleanliness

3.1.1. Particle Detection and Identification Capability

One of the fundamental requirements of VDA 19 and ISO 16232 is the reliable detection and identification of contaminant particles, particularly metallic particles that may

critically affect component functionality. SEM/EDX allows precise localization of individual particles on the filter and subsequent elemental identification based on characteristic X-ray lines. This capability is crucial for distinguishing metallic, oxide, and non-metallic particles.

LIBS identifies particles through emission spectral lines generated by laser-induced plasma. While LIBS enables rapid detection of a wide range of elements, precise localization of individual particles can be limited for fine or complexly shaped particles, especially in cases of high background signals or heterogeneous substrates.

3.1.2. Scope and Accuracy of Elemental Analysis

EDX provides qualitative and semi-quantitative analysis of particle composition, with high identification accuracy, particularly for elements with medium to high atomic numbers. This method is well-established for detecting metals and their alloys, which is critical in the context of technical cleanliness.

LIBS can detect nearly all chemical elements, including light elements such as lithium, boron, or carbon, which are challenging for EDX. However, its quantitative accuracy strongly depends on calibration, sample matrix, and plasma stability, which may reduce comparability between measurements.

3.1.3. Spatial Resolution and Minimum Particle Size

Spatial resolution is a key parameter for assessing fine particles, which are often the most critical according to VDA 19. SEM/EDX achieves very high spatial resolution, enabling the analysis of particles down to the micrometer scale or smaller, depending on measurement conditions.

LIBS is limited by the laser spot size and thermal effects on the surrounding area. The typical analyzed area ranges from tens of micrometers, which can result in signal overlap from multiple particles or the substrate. Consequently, LIBS is less suitable for very small or densely distributed particles.

The LIBS analytical beam is formed by a focused pulsed laser, typically ranging from approximately 20 to 100 μm in diameter depending on optics and system settings. Interaction with the sample causes material ablation and plasma formation, analyzing both the surface and a thin subsurface layer. As a result, the minimum particle size that can be reliably analyzed with LIBS is generally on the order of tens of micrometers. Smaller particles produce signals mixed with the substrate, negatively affecting identification and quantification accuracy.

In contrast, EDX uses the electron beam in a scanning electron microscope (SEM), which can have a beam diameter as small as a few nanometers. Although the actual electron interaction volume is larger (typically hundreds of nanometers to a few micrometers depending on electron energy and material composition), EDX allows analysis of significantly smaller particles than LIBS. In practice, particles around 1 μm can be reliably analyzed, and in optimal conditions, even smaller particles, especially those with higher atomic numbers.

Figure X illustrates a multilayer material composed of several layers of different materials, each a few micrometers thick. Analysis with LIBS shows that the laser spot is several times larger than the individual layers, making it impossible to determine their precise chemical composition, whereas EDX can resolve the elemental composition of each layer.

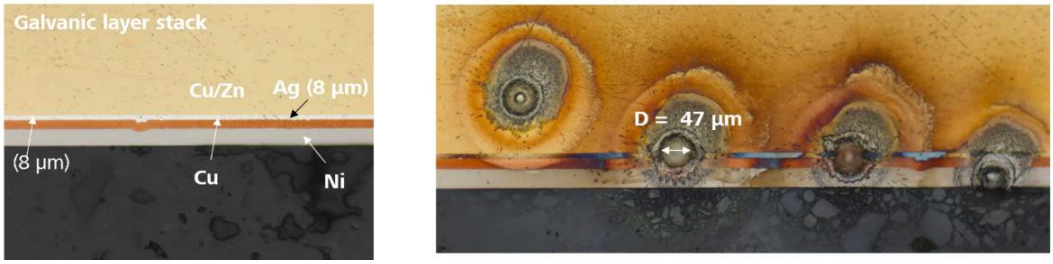

Figure 8. Comparison of LIBS and EDX in terms of analytical beam size and minimum detectable particle size.

3.1.4. Analysis Speed and Measurement Throughput

From an industrial application perspective, analysis speed and overall measurement throughput are critical factors. SEM/EDX analysis is time-consuming, particularly when performing detailed elemental analysis of a large number of particles. This limitation reduces its applicability for high-volume or inline measurements.

In contrast, LIBS provides significantly shorter measurement times, as spectra are generated within microseconds and do not require a vacuum environment. Consequently, LIBS offers potential for high-throughput measurements and rapid screening analyses in technical cleanliness processes.

3.1.5. Influence of Substrate and Background on Measurement Results

In SEM/EDX, signals originating from the substrate—especially the filter membrane—can significantly affect the analysis of small particles. This effect can be partially mitigated by optimizing acquisition parameters and selecting appropriate filter materials.

LIBS is more strongly influenced by the substrate, since the laser pulse often interacts with both the particle and the underlying material. This can lead to the mixing of spectral lines from the particle and substrate, complicating unambiguous interpretation of results.

3.1.6. Automation, Reproducibility, and Practical Usability

Automated particle analysis is a primary goal of modern technical cleanliness systems. SEM/EDX systems offer a high degree of automation in particle detection and classification; however, this comes at the cost of significant investment, operational complexity, and the need for skilled personnel.

LIBS systems are easier to integrate into manufacturing environments and require less operator expertise. Reproducibility, however, depends on laser source stability, optical configuration, and the quality of calibration models.

3.1.7. Compliance with VDA 19 and ISO 16232 Standards

SEM/EDX is currently considered the reference analytical method for extended particle analysis in technical cleanliness and is indirectly supported by the methodological recommendations of VDA 19 and ISO 16232.

LIBS is not yet explicitly established as a standard analytical method in these norms; however, its characteristics make it suitable as a complementary or screening technology, particularly where speed and approximate elemental information are prioritized.

3.1.8. Destructive Nature of LIBS Compared to EDX

An important aspect when comparing analytical methods for technical cleanliness is the degree of measurement destructiveness. Laser-Induced Breakdown Spectroscopy (LIBS) is generally classified as a micro-destructive technique. The interaction of a high-energy laser pulse with the particle or surface induces local material ablation and plasma

formation, resulting in partial or complete destruction of the analyzed particle. Consequently, repeated measurements on the same particle are not possible, and subsequent morphological or compositional analyses cannot be performed.

In contrast, Energy Dispersive X-ray Spectroscopy (EDX), performed under standard scanning electron microscopy (SEM) conditions, is considered non-destructive for particle analysis in the context of technical cleanliness. Electron beam interaction does not significantly alter particle geometry or composition, allowing repeated measurements, detailed morphological evaluation, and correlation between particle shape and elemental composition. This non-destructive nature is particularly important for root cause analysis and documentation in accordance with VDA 19.2 requirements.

From a practical perspective, the micro-destructive nature of LIBS is acceptable—and often advantageous—in screening and process monitoring applications, where high throughput and rapid material classification are prioritized over particle preservation. However, for reference measurements, failure analysis, and traceable documentation, EDX remains the preferred method due to its non-destructive character and analytical depth.

Table 1. Comparison of LIBS and EDX According to VDA 19.2.

VDA-relevant Criterion	LIBS – Typical Range / Assessment	EDX (SEM/EDX) – Typical Range / Assessment
Measurement principle (VDA)	Optical emission spectroscopy (laser-induced plasma)	X-ray spectroscopy based on electron beam interaction
Analysis time per particle	~1–50 ms	~1–10 s
Minimum detectable particle size	≥ 20–50 µm	≥ 1–2 µm
Throughput (particles per hour)	>10,000	<500
Use in root cause analysis	Limited	Fully suitable
Reproducibility of results	Good	Very high
Material classification capability (VDA 19.2)	Good (metallic / non-metallic / alloy group)	Excellent (precise alloy identification)
Particle morphology evaluation	Not suitable	Fully suitable (SEM imaging)
Quantitative elemental analysis	Semi-quantitative	Quantitative
Automation potential (cleanliness inspection)	High (automated / inline systems)	Low
Sample preparation effort	None or minimal	Required (vacuum, sample mounting)
Suitability as VDA reference method	NO	YES

4. Discussion

The comparative analysis of SEM/EDX and LIBS in the context of technical cleanliness, following VDA 19 and ISO 16232 standards, clearly demonstrates that SEM/EDX currently represents the most methodologically robust approach for evaluating contaminant particles. Its high spatial resolution, precise particle localization, and reliable elemental identification ensure reproducibility and traceability of results, which are essential for normative assessments of technical cleanliness.

In contrast, LIBS, while offering potential for rapid and high-throughput elemental analysis, is limited within the current regulatory framework by lower spatial resolution

and increased sensitivity to substrate effects. These limitations can lead to ambiguous interpretation of results, particularly for fine or isolated particles that pose the highest functional risk. Therefore, LIBS cannot currently be considered a full substitute for established reference methods.

Overall, these findings support the conclusion that SEM/EDX remains the preferred analytical technique for detailed and standards-compliant technical cleanliness assessment, whereas LIBS is most appropriate as a complementary tool for preliminary or process-supporting applications.

5. Conclusions

The comparison of SEM/EDX and LIBS highlights their respective strengths and limitations, directly influencing their industrial applicability. The choice of method should be guided by the specific requirements of the application, the nature of contamination, and the objectives of technical cleanliness evaluation.

SEM/EDX proves to be a highly reliable tool for detailed particle analysis, particularly regarding precise localization, high spatial resolution, and robust elemental identification of metallic and oxide particles. Its established role in technical cleanliness, supported by methodological recommendations of VDA 19 and ISO 16232, makes it the reference method for in-depth analysis, documentation, and critical investigations such as root cause analysis. Its main limitations are longer analysis times, higher system complexity, and limited suitability for high-throughput or inline applications.

LIBS shows considerable potential for rapid elemental analysis and high-throughput measurement. Its capability to detect a wide range of elements, including light elements, represents an advantage over EDX. However, limited spatial resolution, higher substrate sensitivity, and dependence on calibration models constrain its use for detailed analysis of fine or isolated particles. Within the current regulatory framework, LIBS is best regarded as a complementary or screening technology, effectively supporting early-stage technical cleanliness assessment.

In conclusion, SEM/EDX and LIBS should not be viewed as direct alternatives but as complementary approaches. An optimal technical cleanliness assessment strategy may combine both methods: LIBS for rapid preliminary identification of contamination and SEM/EDX for subsequent detailed and standards-compliant analysis of critical particles. Such an approach effectively balances speed, accuracy, and regulatory compliance in modern industrial processes.

References

1. VDA. (2015). *VDA 19.1: Inspection of Technical Cleanliness, Volume 19, Part 1: Particulate contamination of functionally relevant automotive components* (2nd rev. ed.). VDA.
2. International Organization for Standardization. (2018). *ISO 16232: Road vehicles – Cleanliness of components and systems*. ISO.
3. ZVEI. (2018). *Technical cleanliness in electrical engineering: Dirt is simply matter in the wrong place* (2nd ed.). ZVEI.
4. Hitachi High-Tech. (2018, January 3). What is LIBS? *Hitachi High-Tech Blog*. https://hha.hitachi-hightech.com/en/blogs-events/blogs/2018/01/03/what-is-libs/
5. Cremers, D. A., & Radziemski, L. J. (2006). *Handbook of laser-induced breakdown spectroscopy*. Wiley & Sons.
6. Miziolek, W. A., Palleschi, V., & Schechter, I. (2008). *Laser-induced breakdown spectroscopy (LIBS)* (1st ed.). Cambridge University Press.
7. Hahn, D. W., & Omenetto, N. (2012). Laser-induced breakdown spectroscopy (LIBS), part II. *Applied Spectroscopy, 66*, 347–365. https://doi.org/10.1366/11-06535

8. Jolivet, L., Leprince, M., Moncayo, S., Sorbier, L., Lienemann, C.-P., & Motto-Ros, V. (2019, January). Review of the recent advances and applications of LIBS-based imaging. *Spectrochimica Acta Part B: Atomic Spectroscopy*. https://doi.org/10.1016/j.sab.2019.01.001
9. VDA. (2025, July). *VDA 19 Part 1: Inspection of technical cleanliness, Volume 19, Part 1: Particulate contamination of functionally relevant automotive components* (3rd rev. ed.). VDA.

TECHNICAL UNIVERSITY OF KOŠICE
Faculty of Mechanical Engineering

Digitization of custom orthotic insole manufacturing

Magdaléna Kordošová [1,*], Teodor Tóth [2], Lucia Bednarčíková [2], Monika Michalíková [2]

[1] PROTETIKA, a.s., Bojnická 10, 823 65 Bratislava, Slovakia; m.kordosova@protetika.sk
[2] Department of Biomedical Engineering and Measurement, Institute of Special Engineering Processes, Faculty of Mechanical Engineering, Technical University of Košice, Letná, 9, 04001 Košice, Slovakia; teodor.toth@tuke.sk; lucia.bednarcikova@tuke.sk; monika.michalikova@tuke.sk
* Correspondence: m.kordosova@protetika.sk

Abstract: Proprioceptive (sensorimotor) insoles play a significant role in correcting foot posture and improving gait by stimulating specific muscles and proprioceptors. The foot is essential for support, balance, and coordinated movement, and structural or neurological impairments can lead to biomechanical dysfunctions. Sensorimotor insoles apply small wedge-shaped elements or protrusions that exert targeted pressure, triggering reflexive muscle responses to correct joint positions and muscle imbalances over time. The production of these insoles is a complex process involving 3D foot scanning, CAD modeling, and CAM-based manufacturing using CNC milling or 3D printing. Digital workflows ensure accurate capture of foot geometry, precise customization, and the ability to adjust shape, arch support, and heel corrections before production. Multi-axis CNC systems—ranging from 3-axis to 7-axis machines—enable shaping from simple flat designs to complex 3D anatomical forms. Selection of materials, such as EVA, PU, or specialized orthopedic resins, is guided by the user's needs and chosen manufacturing method. Integrated CAD/CAM processes reduce human error, streamline production, and allow simulations of pressure distribution and functional performance. Digital models can be archived and reused, facilitating repeat production without new measurements. This centralized and coordinated approach enhances collaboration between orthopedists, technicians, and manufacturers, ensuring reproducible, patient-specific, and clinically effective insoles for both orthopedic and neurological applications.

Keywords: insoles; proprioception; milling

1. Introduction

Proprioceptive orthoses play an important role in affecting the foot. Through targeted stimulation of certain muscles, muscle imbalances are changed, which results in long-term and permanent correction of incorrect posture and functional abnormalities.

Proprioception itself is important in terms of coordination of movements, maintaining balance, control of the strength and range of body movement, protection against injury, ensuring the automation of motor skills / e.g. walking, etc.

A sensorimotor orthosis is an orthosis whose task is to stimulate the tendons of the long and short muscles of the leg. This stimulation is achieved by creating pressure in the right places. The central nervous system responds to this pressure by tensing and relaxing the muscles. When this orthosis is worn for a long time (regularly for at least 3 months), the position of the joints changes and muscle imbalances are corrected.

By activating proprioceptors in the foot, it is assumed that the tone of hypertonic muscles will be reduced and the gait will be modified. [1] Sensorimotor insoles are applied to people who have demonstrated pathological foot position or posture. The most common indication for treatment was various foot deformities such as pathological talipes planovalgus, internal and external rotational gait, initial and complex talipes equinus, or imbalance with a pathological effect on the statics and dynamics of the body. With regular

check-ups and an optimal course of treatment, a decrease in sensorimotor dysfunction, postural weakness, and abnormal statics of the leg should occur during the first year of treatment. [2]

Several studies have explored the idea of whether sensorimotor insoles can be as effective and efficient as orthoses. These insoles also work by changing the proprioceptive chain, i.e. by stimulating certain points on the feet and subsequently changing the walking strategy [3].

The basic element of a sensorimotor insole is a wedge-shaped element or protrusion. These are small pads with a typical thickness of 1-5 mm, which exert targeted pressure on the desired part of the foot. The applied pressure triggers reflexes, which causes muscle contraction. [4] They are made with the desired stiffness, shape and location. The protrusions are located in the area of the midfoot, toes, heel and longitudinally along the sides of the foot.

The toe bones maintain contact between the toes during walking, reducing heel displacement and relieving tension in the toe flexors. Retrocapital bones around the midfoot influence lower limb rotation, with lateral elements correcting inversion and medial elements correcting eversion; insufficient height is compensated by additional lateral or medial supports along the arch. Heel spurs provide mechanical support to the calcaneus, positioned posteriorly in high arches and anteriorly in flat feet, while spine curvature should be monitored, as excessive use may deepen lumbar lordosis, particularly in children.

2. Materials and Methods

Proprioceptive insoles are made individually for each patient. They are adapted in shape, size, material and function based on the specific needs of the person. The production of shoe insoles is a complex process that is created in cooperation between a doctor and an orthopedic technician. It includes examination, taking measurements, determining the geometry of the insole, selection of materials, production and quality testing (Figure 1). All these processes have changed and improved with the gradual development of technology and medicine.

Acquisition of measurement data

Examinations are performed both with and without weight. In the non-weight-bearing assessment (sitting or supine), foot symmetry, swelling, and pressure areas are observed, comparing with the unaffected foot. Deformities of the toes are checked, and the range of motion of the thumb base and ankle joints is measured (plantar/dorsi-flexion, pronation, supination). Sensitivity is assessed via palpation along the fibula, hindfoot, midfoot, and forefoot using varying pressure. [6]

During the weight-bearing examination (standing), lateral view assesses head position, knee flexion/hyperextension, spinal curvature (lumbar/cervical), and calf/thigh muscle strength. Focus is on pelvic tilt, which may relate to arch deformation. Frontal view evaluates shoulder, scapula, and pelvis alignment, as well as varus/valgus of knees and heels. [6]

From the posterior view, heel position and deviation are assessed using two axes: base of calcaneus to Achilles insertion, and mid-Achilles to mid-calf. An angle ≥5° indicates valgus (pronation, foot outward), ≤5° indicates varus (supination, foot inward) (Figure 3) [7].

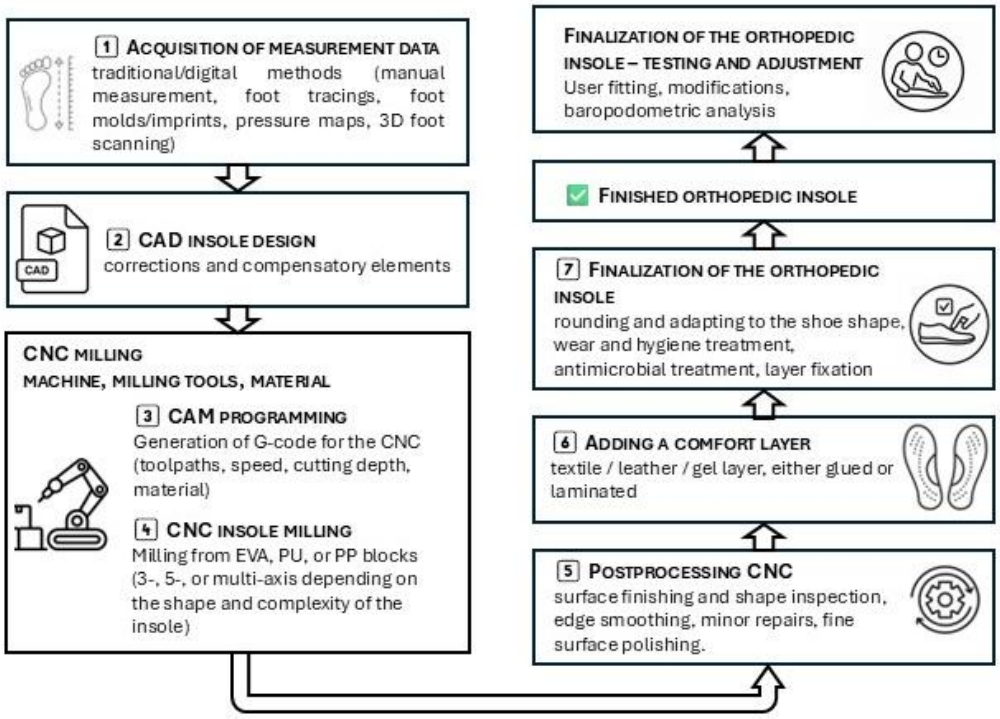

Figure 1. Process of Manufacturing Orthopedic Insoles.

Measurements of the foot can be 2D or 3D. Classic 2D methods include:

- plantograph – a rubber membrane with ink captures a footprint; the technician traces the foot on a grid.
- podoscope – a transparent platform with a tilted mirror visualizes pressure areas; images are captured and processed by software.

Modern 3D methods use:

- pressure platforms – provide real-time analysis of foot pressure.
- 3D scanners – create accurate visualizations of the foot in an optimal clinical position, allowing detailed measurement of length, width, arch height, lateral edge, and instep.

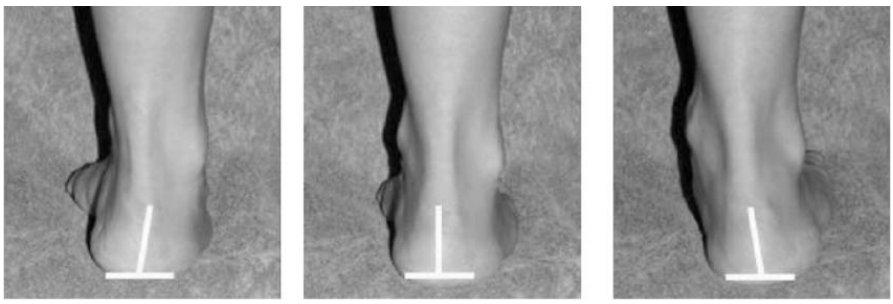

-2	-1	0	+1	+2
More than 5 degrees (5°) inverted (varus)	Between the vertical and five degrees (5°) inverted (varus)	Vertical	Between the vertical and five degrees (5°) everted (valgus)	More than five degree (5°) everted (valgus)

Figure 2. Illustration of varus and valgus alignment [8].

CAD insole design

The basic design of the insole should fulfill the required function through its geometry, i.e. ensure even pressure distribution, relieve overloaded areas and support the arches

of the foot. It is possible to apply sensorimotor elements such as pads or wedges to the insole, and further shape it according to requirements.

Modern 3D software designed for the production of insoles is one of the more innovative ways of designing them. Measured data from a plantogram or 2D scanner is used to obtain the anatomical shape of the foot and reference points, where the length and width of the insole should be guided by the size of the shoe. The advantages of CAD systems designed for insole design are the ability to choose combinations of materials, insert pre-set compensation elements with adjustable height and size, or manually adjust the format by drawing protrusions directly on the insole for detailed achievement of the design of a custom-made insole.

Table 1. Comparison of the most commonly used software for orthopedic insole manufacturing.

SW	Benefits	Disadvantages
Pedcad	-database with different insole shapes that can be individually adapted to the patient's needs based on measured data -modeling functions - Imports data from the Rothballer scanner	- high acquisition costs - contains a database of only 6 basic inserts, additional packages must be purchased
LutraCAD	- technical support - updates - 100 pairs of inserts - 2x2 hours of online course - help with online installation	**-** Pay-per-design system - After 100 pairs of inserts, refills are charged at a fee of -3€/per pair - Dependence on the supplier - online installation
EasyCAD Insole	**-**Libraries with 9 different insert template models - Automatic modeling functions - Hand drawing tools -3D element library management -Automatic correction of minimum and maximum thickness -Automatic tool for creating custom templates -Direct import from 2D-3D scanners	**-** higher procurement costs - despite Slovak representation, more complicated communication

In the Insole Designer 3.8 software (Figure 4) for individual modeling of Proprio orthoses, there is a set of functionalities with correction options for individual pads, including a manual scaling module and a reading function for any measuring device, as well as a data printing module and a 3D module.

CNC milling

The quality of a manufactured orthopedic insole depends on the technological parameters of the production equipment (number of axes, workpiece clamping, etc.), the tools used (flat-end mills, ball-end mills, roughing tools, etc.), the choice of CAM software (depending on the machine's compatibility), and the production parameters (cutting speeds, toolpaths, etc.).

In practice, it is possible to use specialized machines designed specifically for orthopedic manufacturing; however, these are often limited by the capabilities of their CAM software. Alternatively, universal CNC machining centers and robotic arms can be used—these can be adapted for a broader production portfolio (trunk orthoses, limb models, shoe insoles, etc.) but require more complex programming.

In practice, the most used systems are 3-, 5-, and multi-axis robotic arms. In 3-axis systems, only linear tool movement is used; in 5-axis systems, the tool can also tilt and rotate; and in 7-axis systems, both the tool and the workpiece can be manipulated (Figure 5).

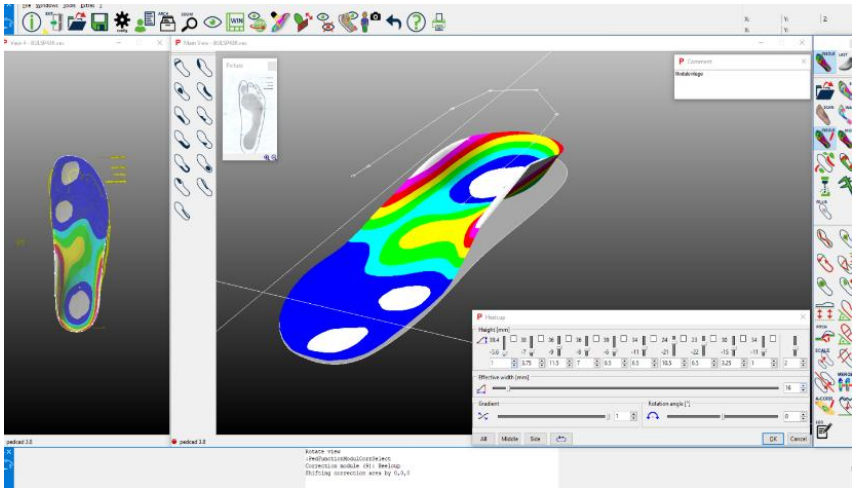

Figure 3. Insole Designer 3.8 SW from Pedcad for the production of proprioceptive orthoses.

The difference between multi-axis robotic arms is shown in Table 2.

Table 2. Difference between 3-axis, 5-axis and 7-axis arms in orthopedic insole manufacturing.

CNS device	Movement Capabilities / Shape Complexity	Materials	Postprocessing	Insoles examples
3-axis	Movement in X, Y, Z (vertical and horizontal), suitable for simple shapes	EVA, PU, PE, polypropylen	Grinding, polishing, thickness inspection	Simple flat orthopedic insoles, sport insoles with mild arch shaping
5-axis	Movement in X, Y, Z + two rotational movements (tilt and rotation), enables shaping of angled surfaces and slopes	EVA, PU, PP, polymer composites	Grinding, polishing, thickness calibration	Insoles with precise heel and midfoot coverage, insoles with mild support profiles, diabetic foot insoles
7-axis	Full rotation and tilting, milling of undercuts and complex 3D shapes	EVA, PU, PP, polymer composites, special orthopedic resins	Grinding, polishing, smoothing, calibration, lamination	Insoles with complex 3D anatomy, sports insoles with dynamic supports, fully customized insoles with extreme correction, pediatric insoles for deformities

The selection of adequate materials for the production of proprioceptive insoles is based not only on the functionality of the insole, but also on the type of user, their comfort, the suitability of the material for a given method of their production and the economic point of view.

The choice of material largely depends on the choice of production technology. In CNC milling, the insoles are made of ethylene vinyl acetate (EVA) - foam of different hardness depending on the patient. Ethylene vinyl acetate (EVA) is an elastomer polymer that is a lightweight, yet durable and elastic material. Its advantages at low density are shock absorption, and at higher density it is resistant to creasing, cracking or tearing. The standard proprio insole for an adult or. for a patient with pain is 35Sh.

3. Conclusion

The use of an integrated digital process in CAD/CAM manufacturing of proprioceptive and orthopedic insoles offers substantial advantages over traditional methods. All stages – from 3D foot scanning to final production – are interconnected and coordinated,

ensuring a streamlined workflow. Precise 3D scanning increases production accuracy by 30–50 % and eliminates errors associated with manual measurements or mold-based shaping. The insoles precisely replicate the anatomical foot geometry, which is crucial for effective proprioceptor stimulation, while CNC milling guarantees high reproducibility.

Shape adjustments, heel corrections, or modifications of insole stiffness can be performed directly in the digital model, and the CAM software immediately generates toolpaths for the CNC machine, reducing production time from 3–5 hours using traditional methods to 1–2 hours, while increasing overall process efficiency. The digital workflow also enables pre-production verification of insole functionality through load simulations and pressure distribution analyses, minimizing the risk of defective products.

Additionally, digital models can be archived and reused, simplifying repeat production for the same patient without repeated measurements. Centralized digital production allows different insole types to be manufactured on a single multi-purpose CNC machine or 3D printer by simply loading the appropriate CAD/CAM program, reducing investment costs, minimizing manual labor, and improving economic efficiency. Coordinated collaboration between the orthopedist, technician, and production team is facilitated by a shared digital model, ensuring consistency, reproducibility, and high-quality outcomes across all products.

Acknowledgments: This work was supported by the projects 025TUKE-4/2025 "Implementation of measurement systems of human physiological parameters in the educational process in the biomedical engineering program" and 054TUKE-4/2025 "Use of CAx systems in prosthetic and orthotic practice".

Conflicts of Interest: The authors declare no conflict of interest. The funders had no role in the design of the study; in the collection, analyses, or interpretation of data; in the writing of the manuscript, or in the decision to publish the results".

References

1. Mabuchi, A. et al.: The biomechanical effect of the sensomotor insole on a pediatric intoeing gait. ISRN ortho-pedics vol. 2012 396718. 10 Oct. 2012, doi:10.5402/2012/396718 Dostupné z https://www.hindawi.com/journals/isrn/2012/396718/
2. Herberger, U. Woltring, S.: Sensorimotor foot bedding – care for children via network. In: SENSORIMO-TOR FUNCTION [online]. 2012. 5-7 s., https://www.springer-berlin.de/en/downloads.html
3. Neto, P. H. et al.: Postural insoles on gait in children with cerebral palsy: Randomized controlled double-blind clinical trial. In: Journal of bodywork and movement therapies vol. 21,4. [online]. 2017, https://www.sciencedirect.com/science/article/abs/pii/S1360859217300281#bbib10
4. Ludwig, O. et al.: The influence of insoles with a peroneal pressure point on the electromyographic activity of tibialis anterior and peroneus longus during gait. In: Journal of Foot and Ankle Research 9. [online]. 2016. doi: 10.1186/s13047-016-0162-5, https://jfootankleres.biomedcentral.com/articles/10.1186/s13047-016-0162-5
5. Novaped sensoCAD by schein: Sensomotoric insole concept for holistic and active care. [online]. Remscheid, Germany: Schein orthopädie service KG. [cit. 22-12-19], https://www.schein.de/en/produkte/einlagen.html?seite=novaped_sensocad
6. Grabinski, J.: Senzomotorické vložky: Príručka pre úspešné vybavenie. In: Springer Active AG. 2016. 8. vyd.
7. Kothekar, V.: Biomechanical Assessment of Foot and Ankle. In: Physiopedia, [online]. 2023. [cit. 23-01-11] Dostupné z https://www.physio-pedia.com/Biomechanical_Assessment_of_Foot_and_Ankle
8. Oleksy, Ł., Mika, A., Łukomska-Górny A., et al. (2010). Intrarater reliability of the Foot Posture Index (FPI-6) applied as a tool in foot assessment in children and adolescents. Med Rehabil, 14(4), 18-28.

TECHNICAL UNIVERSITY OF KOŠICE
Faculty of Mechanical Engineering

Experimental data acquisition from a milling fixture

Ján Kušnír [1,*], Michal Demko [1], Jozef Brindza [1], Marek Vrabeľ [1] and Filip Dominik [1]

[1] Prototyping and Innovation Centre, Faculty of Mechanical Engineering, Technical University of Kosice, Slovak Republic; jozef.brindza@tuke.sk (J.B.); michal.demko@tuke.sk (M.D.); marek.vrabel@tuke.sk (M.V.) ; filip.dominikl@tuke.sk (F.D.)
* Correspondence: jan.kusnir@tuke.sk; Tel.: +421 55 602 3371

Abstract: Milling of thin-walled components is challenging in terms of process stability and surface quality because the local stiffness of the wall changes during material removal and the system becomes sensitive to dynamic phenomena, including self-excited vibrations (chatter). The objective of this work was to experimentally verify the feasibility and comparability of data acquired from three sources: (i) internal CNC machine signals, (ii) the SCHUNK iTENDO² smart toolholder, and (iii) an external 6-axis IMU sensor, which in the pilot phase was mounted directly on the workpiece (with a planned relocation to the fixture). Measurements were conducted during side milling of a representative thin wall made of Al 6061-T6 on a DMG MORI ecoMill 50 machine. Because the individual data sources have different time bases, event-based segmentation (idle, air-cut, entry, steady cut, exit) was applied, primarily derived from machine signals. As a robust frequency marker within the limited IMU bandwidth, the tooth passing frequency (TPF) was selected, as it can be predicted from spindle speed and the number of tool teeth. It was observed that, during steady cutting, both the IMU and iTENDO² exhibit similar dominant frequency bands, including the region around TPF and selected harmonic/modal components; the spectral similarity and coherence support the conclusion that the IMU is suitable for monitoring process events and dynamic changes in thin-walled milling.

Keywords: thin-wall milling; process monitoring; IMU; iTENDO²; CNC internal data; tooth passing frequency; spectral analysis;

1. Introduction

Milling of thin-walled components is technologically demanding mainly due to low stiffness and changing boundary conditions during material removal. Even under relatively stable cutting conditions, the local stiffness of the wall changes with thickness and the length of the free span, which increases sensitivity to process dynamics and raises the risk of self-excited vibrations (chatter). In practice, this manifests as deteriorated surface quality, increased tool wear, and reduced dimensional accuracy [1–3].

In industrial practice, monitoring of milling processes is implemented through several approaches: (i) machine/controller signals (e.g., spindle and axis-related signals), (ii) smart toolholders and instrumented tooling, and (iii) external or retrofit sensors (typically accelerometers/IMUs). These data sources differ in information content, bandwidth, susceptibility to noise, and—critically—in their time synchronization capabilities and practical deployability on production machines [4–6].

The aim of this work is to experimentally verify whether data from the machine, a smart toolholder, and an IMU (mounted on the workpiece in the pilot phase and intended to be integrated into the fixture in the final setup) are feasible, relevant, and comparable for thin-wall milling monitoring. Emphasis is placed on acquisition architecture, process segmentation, and spectral quality metrics as prerequisites for subsequent process modeling and robust instability detection, consistent with multi-sensor monitoring and chatter-detection practice reported in the literature [6–8].

2. Materials and Methods

2.1. Test workpiece and geometry simplification

Thin-walled industrial parts (e.g., in aerospace) feature complex topology, local stiffness variations, and typically undergo multiple operations. For pilot validation of acquisition and data quality, reproducing the full part is not necessary; what matters is capturing the dominant phenomena associated with low stiffness and regenerative instability. Therefore, a representative thin wall was used as an elementary model, enabling controlled variation of thickness and progressive weakening of the wall during the experiment.

The workpiece contained multiple thin-wall features; for this contribution, three walls with systematically varied thickness were used. In the pilot phase, IMU integration into the fixture was replaced by mounting directly on the workpiece, enabling rapid iteration of the solution (mechanical integration, sensor protection, wiring, chip evacuation) while preserving the ability to measure vibration response induced by cutting (Figure).

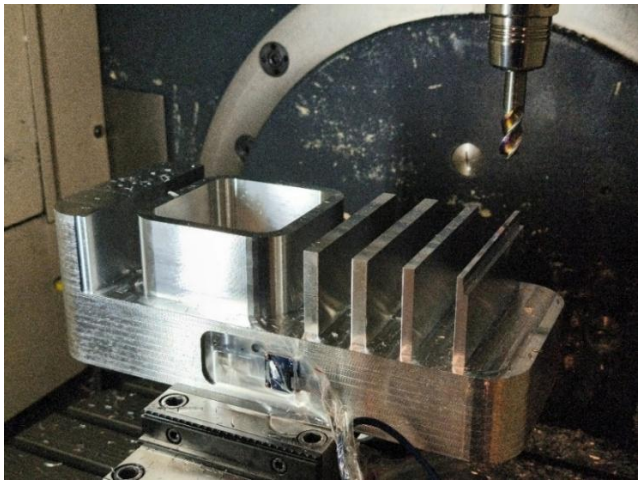

Figure 1. Workpiece placed in a machine with an IMU sensor mounted. Wall geometry: height 55mm, length 130mm, width of the cutting segment 7mm.

2.2. Machine tool, cutter, material

Experiments were performed on a 5-axis CNC machining center DMG MORI ecoMill 50. The machine configuration supports spindle speeds up to approximately 12,000 rpm. Workpiece material: aluminum alloy 6061-T6.

A solid carbide end mill GARANT Master Alu PickPocket, HPC, DLC, order number 202014 16 (⌀16 mm), was used [9].

Relevant tool parameters (per datasheet):

- cutting diameter: D_C = 16 mm,
- number of teeth: Z = 3
- helix angle: 42°, unequal tooth spacing (unequal spacing)
- cutting length: L_C = 31 mm,
- overall length: L = 108 mm,
- shank diameter: D_S = 16 mm,
- corner rounding: r_v = 0.32 mm,
- coating: DLC

2.3. Measurement chains and data sources

2.3.1. IMU sensor (external retrofit)

A 6-axis IMU ISM330IS (3-axis accelerometer + 3-axis gyroscope) was used, with selectable full-scale ranges up to ±16 g and ±2000 dps [10].

Measurement configuration in the experiment:

- accelerometer: ±16 g (acceleration)
- gyroscope: ±2000 dps (degrees per second)
- output data rate: f_S = 1667 Hz (accelerometer and gyroscope)

Sensitivities for the selected ranges (datasheet):

- accelerometer at ±16 g: 0.488 mg/LSB (accelerometer sensitivity)
- gyroscope at ±2000 dps: 70 mdps/LSB (gyroscope sensitivity)

In the pilot phase, the IMU was mounted directly on the workpiece near the thin wall. Data were acquired using a Raspberry Pi (local logging/streaming), with recording triggered from a laptop over Wi-Fi. Part of the signals were continuously visualized in MATLAB (Figure).

2.3.2. Smart toolholder iTENDO²

As a second source of process vibrations, the smart toolholder **SCHUNK iTENDO²** was used. It employs an acceleration sensor located close to the cutting zone and supports wireless transmission and data logging (in the basic setup via a tablet). In the experiment, iTENDO² was paired with the supplied tablet, which served for recording "RAW" toolholder data [11].

2.3.3. Internal CNC machine data

Internal CNC data were used mainly to identify process states and provide time orientation between asynchronous sources. Typical signals include:

- spindle speed, spindle load/current or estimated spindle power,
- axis servo currents/loads and potentially torque/control deviation,
- actual vs commanded feed rates, and rapid traverse activation,
- program/state signals (operation start, block changes, M-codes).

In this study, these machine signals were treated primarily as an "event log" for segmenting the process into non-cutting and cutting intervals.

2.4. Experimental plan and cutting conditions

Machining was performed as side milling along a defined wall segment. To compare repeatability and the effect of progressive wall weakening, multiple runs were executed on multiple walls; during the experiment, wall thickness and radial width of cut a_e and feed per tooth f_z were varied while keeping axial depth of cut a_p constant (Table 1).

Table 1. Summary of machining runs (overview).

Run ID	Wall	Thickness before → after [mm]	a_e [mm]	a_p [mm]	f_z [mm/tooth]	V_c [1] [m/min]	f_{TPF} [Hz]
W1-1	1	7.0 → 5.5	1.5	5	0.03 (A)	393	400
W1-2	1	5.5 → 4.5	1.0	5	0.04 (B)	393	400
W1-3	1	4.5 → 4.0	0.5	5	0.05 (C)	393	400
W2-1	2	7.0 → 5.5	1.5	5	0.04 (B)	393	400
W2-2	2	5.5 → 4.5	1.0	5	0.05 (C)	393	400
W2-3	2	4.5 → 4.0	0.5	5	0.03 (A)	393	400
W3-1	3	7.0 → 5.5	1.5	5	0.05 (C)	393	400
W3-2	3	5.5 → 4.5	1.0	5	0.03 (A)	393	400
W3-3	3	4.5 → 4.0	0.5	5	0.04 (B)	393	400

[1] Vc is reduced due to the actual diameter of the cutter.

2.5. Frequency marker selection: Tooth Passing Frequency (TPF)

A key element of the methodology is the tooth passing frequency (TPF), representing the fundamental excitation frequency associated with tooth engagements:

$$f_{TPF} = \frac{n \cdot z}{60}$$

where $n$is spindle speed [rpm] and $z$is the number of teeth.

In the experiment, spindle speed was approximately $n = 8000$rpm and the tool had $z = 3$, hence:

$$f_{TPF} = \frac{8000 \cdot 3}{60} = 400 \text{ Hz}$$

TPF was selected also with respect to IMU bandwidth limitations at the chosen sampling rate. For $f_s = 1667$Hz, the Nyquist frequency is:

$$f_N = \frac{f_s}{2} = 833.5 \text{ Hz}$$

which enables tracking not only $f_{TPF} \approx 400$Hz but also the second harmonic $2f_{TPF} \approx 800$Hz without aliasing. Although thin-walled milling may exhibit phenomena above 1 kHz, this study deliberately relies on a robust, physically interpretable marker within the measurable band that is also predictable and useful for coarse alignment of asynchronous data streams.

Figure 2. Experiment setup from left: CNC control system, notebook connected to RPi, iTendo tablet.

3. Results

3.1. Macroscopic observations on the workpiece

After machining, vibration-related tool marks ("chatter marks") were observed on the walls, with varying severity across runs and walls. It was observed that, for smaller wall thickness (after material removal) and certain combinations of a_e and f_z, visual evidence of vibration became more pronounced, supporting the assumption of increasing dynamic sensitivity as the wall is weakened (Figure).

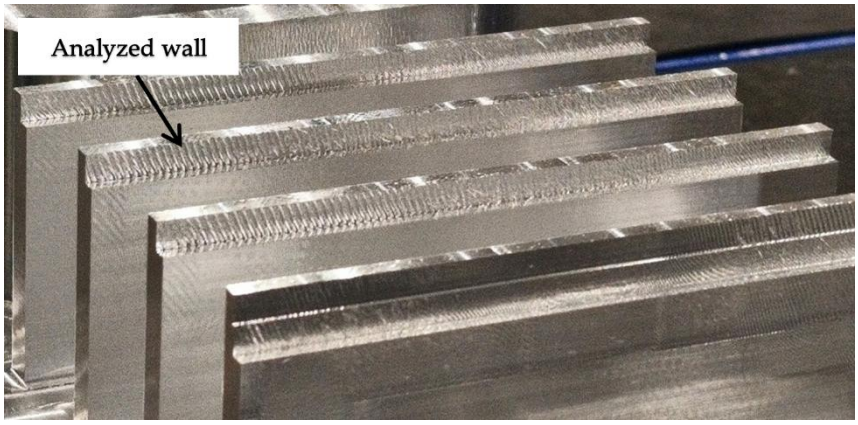

Figure 3. Photo of walls with visible chatter marks. The analyzed wall is marked with an arrow.

3.2. Event-based segmentation and use of machine data

Because IMU, CNC, and iTENDO² can have different time bases and different latencies, an event-based approach was used with the states:

- idle (machine running without cutting or before the operation),
- air-cut (motion without engagement),
- entry (tool engagement),
- steady cut (steady-state cutting),
- exit (tool leaving the material).

It was observed that machine data clearly reflect spindle activation, axis motion, changes in load, and rapid traverse activation/deactivation (Figure). These events were used to define state boundaries, which were then transferred to IMU and iTENDO² signals (i.e., the same time windows were evaluated in a comparable way).

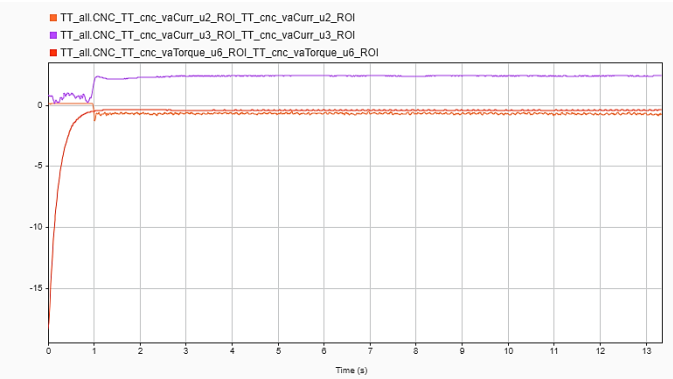

Figure 4. example of machine signals (e.g., axis current and spindle torque).

3.3. Comparison of time-domain signals: IMU vs iTENDO²

In the time domain, transitioning into steady cut was accompanied by an increase in vibration energy in both measurement chains, while absolute amplitudes are not directly comparable (different mechanical coupling, transfer function, and internal scaling). Practically, it was observed that, for segmentation purposes (idle vs cutting) and identification of dominant excitations, the IMU signal is informative and consistently responds to cutting events (Figure).

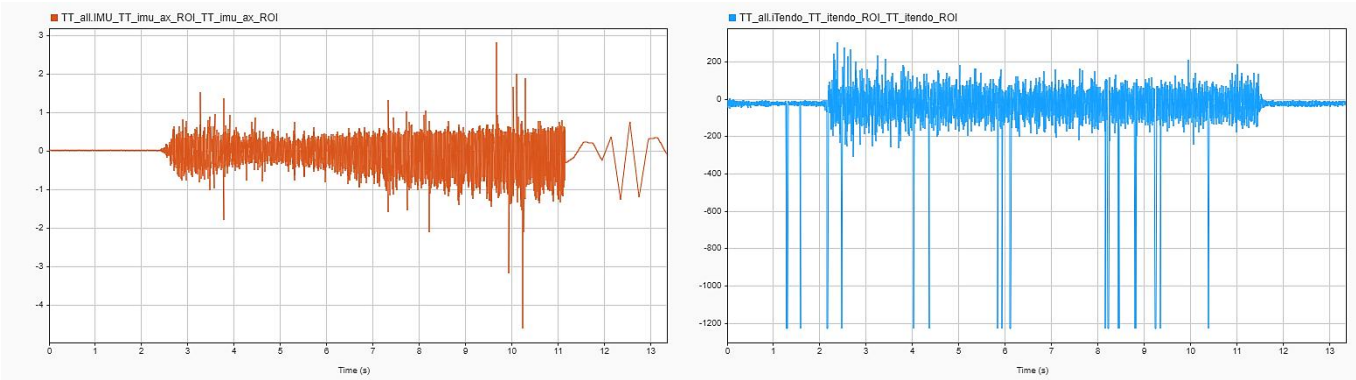

Figure 5. time trace of a selected IMU channel (orange) and iTENDO² signal (blue).

3.4. Spectral analysis: TPF and dominant bands

To verify similarity without relying on absolute amplitude, spectral similarity (dominant peaks) between idle and steady cut was evaluated. Frequency analysis showed that, in steady cutting, peaks appear in the expected TPF region (~400 Hz) as well as in selected harmonic/modal bands.

In an illustrative case, the following was observed:

- increased spectral energy around **~400 Hz (TPF)** compared to idle (Figure)

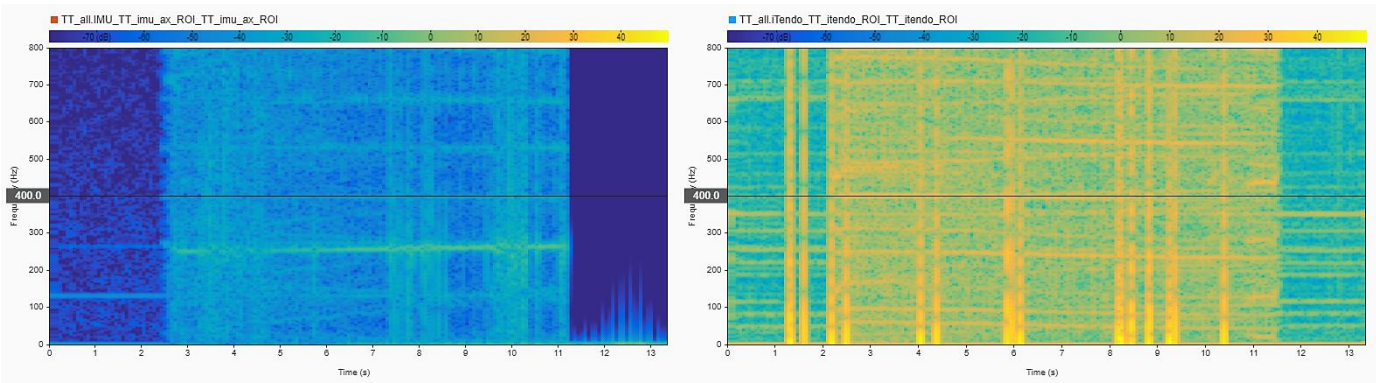

Figure 6. spectrogram with the ~400 Hz band highlighted.

- a more dominant band around **~250 Hz** (Figure)

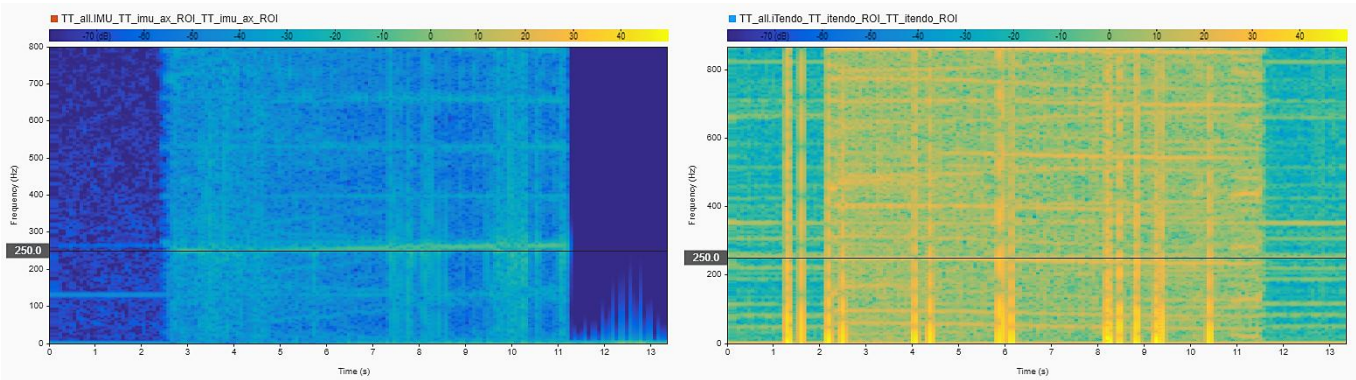

Figure 7. spectrogram with the ~250 Hz band highlighted.

- a weaker but consistent peak around **~545 Hz** (Figure)

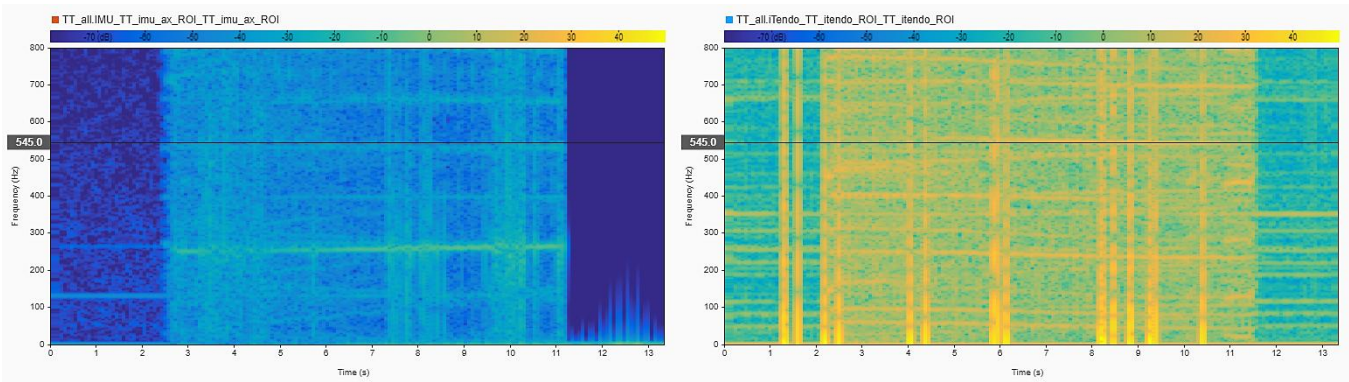

Figure 8. spectrogram with the ~545 Hz band highlighted.

- an additional modal contribution in the lower band around **~155 Hz** (in some runs).

3.5. Coherence between IMU and iTENDO²

To quantify the relationship between the measurements, magnitude-squared coherence was computed between the IMU channel with the highest energy and the corresponding iTENDO² channel. It was observed that coherence increases around dominant process bands (especially near TPF and in bands with pronounced peaks), indicating that both sensors capture a common process source (cutting excitation), albeit through different transfer functions.

Additionally, normalized PSD (e.g., dividing by total energy or by bandpower in a defined band) was compared to reduce the influence of differing amplitudes and emphasize spectral-shape similarity in relevant bands.

4. Discussion

The results confirm the feasibility of robust IMU data acquisition in a machining environment and the usefulness of event-based segmentation compatible with asynchronous data sources. Detection of TPF provides a physically interpretable reference for verifying the measurement chain (sensor, transmission, processing) and also provides an "anchor" for comparisons across runs.

The fact that, besides TPF, a more dominant mode around ~250 Hz and another contribution around ~545 Hz were observed is consistent with the interpretation that the thin-walled system has its own modal frequencies that are excited by cutting and may dominate over purely tooth-periodic excitation. Practically, this means that even if TPF is well predictable, the decisive influence on vibration intensity can be the proximity of excitation to a natural frequency of the wall or the interaction between tooth excitation and modal response (including modulation/harmonics and transmission through the clamping system).

Mounting the IMU on the workpiece proved sensitive to the local response of the wall, which is advantageous for capturing thin-wall dynamics and potentially detecting the onset of instability. In contrast, the planned IMU placement in the fixture is promising for robustness and long-term integration but will likely measure a more "global" response of the clamping structure. This implies the need to optimize sensor location, axis orientation, and mechanical vibration transmission within the fixture.

Regarding whether a single IMU at a single location can reliably capture the same information for multiple walls at different distances: the results suggest that an IMU can capture common process excitations (e.g., TPF and cutting-related bands), but localization of "which wall" will be limited by structural transmission, damping, and overlap of modal responses. For spatial discrimination between walls, a multi-sensor setup or an experimental strategy with clearly time-separated cuts and calibration of transfer functions will likely be required.

Recommended next steps include:

- repeating the experiment using the prepared pocket and/or thinner post-machined walls,
- evaluating all runs and comparing them against parameters (a_e, f_z, thickness),
- analyzing multiple IMU components (ax, ay, az; potentially gyro) to exploit directional information,
- extending metrics to include trend effects (drift) and repeatability checks of sensor mounting.

5. Conclusions

It was observed that combining CNC internal data, the iTENDO² smart toolholder, and an external IMU provides a practically usable acquisition architecture for pilot monitoring of thin-wall milling. Event-based segmentation enabled consistent comparison of asynchronous data sources. In the spectral domain, both IMU and iTENDO² exhibited similar dominant process bands (including the TPF region and selected harmonic/modal components), and coherence supported the conclusion of a shared excitation source. These findings provide a foundation for expanding the experiment and developing robust detection of dynamic instability under thin-wall machining conditions.

Acknowledgments: This work was supported by the Slovak Research and Development Agency projects APVV SK-BG-23-0020 "Intelligent Quality Systems for Flawless Production of Critical Machined Parts" and APVV SK-HU-24-0036 "Industry 4.0 based control of machining process in cutting of difficult-to-cut materials."

Conflicts of Interest: The authors declare no conflict of interest.

References

1. Li F, Liu J, Feng Z (2025) Chatter suppression in milling thin-walled structural components using spindle speed regulation and sinusoidal variable speed methods. Journal of the Brazilian Society of Mechanical Sciences and Engineering 47:. https://doi.org/10.1007/s40430-025-05950-x
2. Sun Y, Zheng M, Jiang S, et al (2023) A State-of-the-Art Review on Chatter Stability in Machining Thin−Walled Parts. Machines 11:. https://doi.org/10.3390/MACHINES11030359
3. Wu G, Li G, Pan W, et al (2021) A state-of-art review on chatter and geometric errors in thin-wall machining processes. J Manuf Process 68:
4. Li H, Chen Y (2014) Machining Process Monitoring. Handbook of Manufacturing Engineering and Technology 1–33. https://doi.org/10.1007/978-1-4471-4976-7_6-1
5. Wang WK, Wan M, Zhang WH, Yang Y (2022) Chatter detection methods in the machining processes: A review. J Manuf Process 77:240–259. https://doi.org/10.1016/J.JMAPRO.2022.03.018
6. Teti R, Mourtzis D, D'Addona DM, Caggiano A (2022) Process monitoring of machining. CIRP Annals 71:529–552. https://doi.org/10.1016/J.CIRP.2022.05.009
7. Navarro-Devia JH, Chen Y, Dao DV, Li H (2023) Chatter detection in milling processes—a review on signal processing and condition classification. The International Journal of Advanced Manufacturing Technology 2023 125:9 125:. https://doi.org/10.1007/S00170-023-10969-2
8. Mostaghimi H, Park CI, Kang G, et al (2021) Reconstruction of cutting forces through fusion of accelerometer and spindle current signals. J Manuf Process 68:990–1003. https://doi.org/10.1016/J.JMAPRO.2021.06.007
9. Data sheet GARANT Master Alu PickPocket solid carbide roughing end mill HPC, DLC, ⌀ e8 DC: 16mm Order data. https://www.hoffmann-group.com/GB/en/hom/p/202014-16. Accessed 29 Jan 2026
10. ISM330IS 6-axis IM. https://www.st.com/resource/en/datasheet/ism330is.pdf. Accessed 29 Jan 2026
11. iTENDO² Sensory toolholder, components and accessories - Tool clamping – SCHUNK. https://schunk.com/de/en/tool-clamping-technology/toolholders/tendo-hydraulic-expansion-chuck/itendo2/c/PGR_6468. Accessed 29 Jan 2026

TECHNICAL UNIVERSITY OF KOŠICE
Faculty of Mechanical Engineering

Extension of an Open-Source Control System for Bimanual Robotic Manipulation Using CyberGlove Data Gloves

Matúš Leščinský [1,*], Juraj Kováč [1]

[1] Technical University of Kosice, Faculty of Mechanical Engineering, Department Industrial and Digital Engineering, Park Komenskeho 9, 042 00 Kosice, Slovakia; matus.lescinsky@tuke.sk; juraj.kovac@tuke.sk
* Correspondence: matus.lescinsky@tuke.sk

Abstract: This paper addresses the integration of virtual reality and robotic systems with a focus on hand motion transfer using data gloves. In the initial system configuration, a single CyberGlove II data glove was used to control one robotic hand, enabling basic grasping experiments but limiting the system to single-hand operation. The presented work extends this architecture to a dual-hand configuration by integrating two data gloves and enabling simultaneous control of two robotic hands. The system consists of a virtual reality interface, motion tracking components, robotic hands, and custom-developed control software implemented in C++. Experimental verification confirms stable real-time operation of both robotic hands and independent yet synchronized motion control. Visual feedback from the CyberGlove control environment demonstrates correct sensor mapping, calibration, and servo actuation for both manipulators. The proposed approach introduces a modular open-source control architecture that enables reliable dual-hand robotic manipulation using wearable motion capture devices. The proposed dual-hand system significantly enhances the applicability of virtual reality–based robotic control, particularly in industrial training, teleoperation, and advanced human–robot interaction scenarios.

Keywords: virtual reality; robotics; data glove; dual-hand control; human–robot interaction

1. Introduction

The integration of virtual and physical systems represents an important trend in modern industrial automation, robotics, and human–machine interaction. Advances in virtual reality technologies, motion sensing, and real-time data processing have enabled new forms of intuitive control of robotic systems. These technologies allow operators to interact with complex robotic devices using natural human movements, which significantly improves usability and reduces the learning time required for system operation.

Data gloves represent one of the most widely used wearable technologies for capturing human hand motion. By measuring finger joint movements and hand posture, these devices enable direct mapping of human hand kinematics to robotic manipulators or virtual models. Such interfaces are frequently used in teleoperation systems, robotic manipulation, rehabilitation technologies, and virtual training environments [1-4].

Several studies have demonstrated that glove-based interfaces can significantly improve the intuitiveness of robotic control systems and allow operators to perform complex manipulation tasks using natural hand gestures. These approaches are particularly relevant in applications requiring precise manipulation, such as telemanipulation, collaborative robotics, and human–robot interaction in industrial environments.

Despite the increasing use of data gloves in robotic control applications, many existing systems are limited to single-hand operation or rely on proprietary hardware and software architectures that restrict system flexibility and extensibility. In practical industrial scenarios, however, many manipulation tasks require coordinated bimanual operation,

which significantly increases the complexity of both hardware configuration and software control architecture.

The work presented in this paper builds upon a previously developed robotic control system based on a CyberGlove II data glove. The original system allowed control of a single robotic hand and enabled basic motion transfer experiments within a virtual reality environment [5]. However, the system architecture was limited to single-hand operation and did not support simultaneous control of both robotic manipulators.

The main objective of this research is to extend the original control architecture to support synchronized dual-hand robotic control using two CyberGlove II data gloves. The proposed solution introduces a modular software architecture that separates sensor acquisition, calibration, and servo control logic for each robotic hand. This approach enables stable real-time operation and independent yet synchronized control of both robotic manipulators.

The main contribution of this work lies in the implementation and experimental verification of a dual-hand robotic control system capable of real-time bimanual manipulation. The proposed system significantly expands the capabilities of the original solution and demonstrates the potential of modular virtual reality–based control architectures for advanced human–robot interaction applications.

2. Materials and Methods

This section describes the original system configuration, the extended dual-hand architecture, and the key software and hardware components used in the experimental implementation. Particular emphasis is placed on sensor processing, calibration procedures, and control logic necessary for stable operation.

2.1. Original System Configuration (Single-Hand Control)

Based on the limitations identified in the Introduction, the following subsection describes the technical configuration of the original single-hand control system.

In the original system configuration, robotic control was implemented using a single CyberGlove II data glove. The software interface enabled data acquisition, sensor calibration, and servo control exclusively for the right robotic hand. The experimental setup allowed basic grasping tests and verification of hand motion transfer [5]; however, the left robotic hand was not functionally implemented. Although a left-hand acquisition module was present in the software interface, it remained inactive, without implemented sensor mapping, calibration routines, or servo control.

Figure 1 presents the CyberGlove 2 RoboticHand software interface in its initial state for the left robotic hand. Although the interface already contains modules for left-hand data acquisition, calibration, and servo control, no sensor values or actuator responses are active at this stage. This configuration represents the original system state, in which the left robotic hand was not yet functionally implemented.

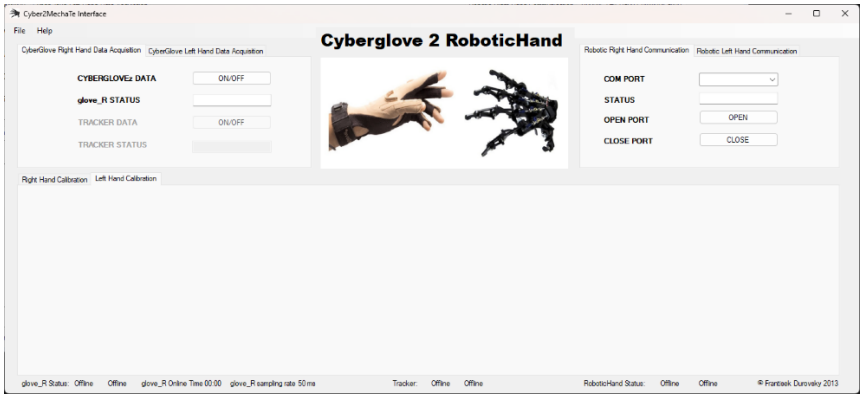

Figure 1. Original system state for the left robotic hand prior to activation.

2.2. Extended System Configuration (Dual-Hand Control)

The system was extended to support dual-hand robotic control by integrating two CyberGlove II data gloves, one assigned to each robotic hand. The software architecture was modified to process parallel data streams from both gloves and to ensure real-time synchronization of sensor data and servo commands. Independent calibration procedures were implemented for the left and right robotic hands, enabling stable and accurate motion mapping.

The extended configuration allows simultaneous and independent control of both robotic manipulators, significantly expanding the system's functional capabilities.

2.3. Sensor Processing, Servo Control, and Calibration

To enable accurate and stable control of the robotic hands, several configuration and programming steps were required. The CyberGlove II data gloves provide multiple sensor signals corresponding to finger joint movements. These sensor values were acquired in real time and processed within the control software to ensure reliable motion transfer.

Each finger was mapped to the corresponding servo motors of the robotic hand. For every servo actuator, individual parameters were defined, including minimum and maximum motion limits, offset values, and sensitivity coefficients. This allowed adaptation of the robotic hand kinematics to the anatomical differences of the human operator's hand.

Calibration procedures were implemented separately for each robotic hand. During calibration, sensor offsets were adjusted and scaling factors were applied to achieve a linear and intuitive correspondence between glove movements and servo positions. Sensitivity tuning was required to avoid excessive servo response, mechanical stress, or unstable motion, particularly during grasping tasks.

In addition, feedback mechanisms were integrated to monitor the status of data acquisition, communication with servo controllers, and system responsiveness. Visual feedback within the CyberGlove control interface enabled real-time verification of sensor activity, servo positions, and overall system state, contributing to stable and repeatable operation.

2.4. Correction of Hand Assignment and Control Logic

In the initial software implementation, only one robotic hand was programmed and experimentally verified. However, the control logic and data structures were incorrectly labeled as a left-hand module, despite being physically connected to and controlling the right robotic hand. This inconsistency originated in the early stage of control software development and contributed to functional limitations of the original system configuration, while also significantly restricting its further extensibility.

To ensure correct dual-hand functionality, it was necessary to redesign the hand assignment logic within the control software. The data acquisition, calibration, and servo control modules were explicitly separated into right-hand and left-hand components. Corresponding sensor mappings, communication channels, and servo identifiers were reassigned to accurately reflect the physical configuration of the robotic hands.

In addition to the software modifications, hardware-level adjustments were also required. An additional control chip was integrated into the system, and the Bluetooth wireless communication architecture was reconfigured to enable parallel and independent communication with both robotic hands. This modification effectively enabled the connection of a second robotic hand and ensured reliable data transmission for dual-hand operation.

This combined software and hardware correction represented a crucial step toward achieving stable and independent control of both robotic hands, as it eliminated ambiguities in hand identification and ensured consistent and synchronized data flow between the virtual interface and the physical robotic system.

The extension of the control system required modifications in the original source code written in C++. The existing software architecture was restructured to enable modular separation of control logic for each robotic hand.

Separate software modules were implemented for sensor acquisition, calibration routines, and servo control for both the left and right robotic hands. Each module processes data from its corresponding CyberGlove device and generates servo control signals for the assigned robotic manipulator.

Device communication was implemented using independent Bluetooth communication channels. Each robotic hand is initialized through a dedicated communication port and controlled through separate device handlers in the software.

This modular implementation enables independent calibration and motion mapping for each hand while maintaining synchronized operation of the entire system.

To improve system robustness, the control software was extended with automatic detection of connected devices and automatic assignment of communication ports. This mechanism enables reliable identification of the left and right robotic hands and ensures correct initialization of communication channels during system startup.

2.5. Software Architecture and Open-Source Framework

The control software used in this work is based on an open-source framework originally developed for CyberGlove-based robotic control experiments. The framework provides modular components for sensor acquisition, calibration, and servo actuation.

The open-source architecture allows modification of individual modules and integration of additional hardware components without altering the entire system structure. In this work, the existing software framework was extended to support dual-hand operation.

The modular architecture enabled separation of core functional blocks, including data acquisition modules, calibration procedures, and servo control routines. This structure significantly simplified the extension of the original single-hand implementation to a dual-hand configuration.

3. Results

This section presents the experimental verification of the robotic control system, starting with the original single-hand operation and followed by the functional evaluation of the extended dual-hand configuration.

3.1. Verification of Original Single-Hand Operation

Experimental tests conducted in the original system configuration confirmed correct motion transfer and grasping functionality for the right robotic hand. The left robotic hand remained non-operational, as no control logic or calibration was implemented for this manipulator in the initial setup.

During system extension, an inconsistency in the original software architecture was identified, where the functional right-hand control was implemented under a left-hand module designation. Resolving this issue required restructuring the control logic and separating right- and left-hand data paths, which enabled reliable dual-hand operation.

3.2. Functional Verification of Dual-Hand Operation

After extending the system architecture, experimental verification demonstrated full functionality of both robotic hands. Each robotic hand responded accurately to the movements of the corresponding data glove in real time. The dual-hand configuration enabled synchronized bimanual manipulation and stable grasping of test objects.

Visual evidence from the CyberGlove control software confirms correct sensor activation, calibration, and servo response for both robotic hands (Figure 2).

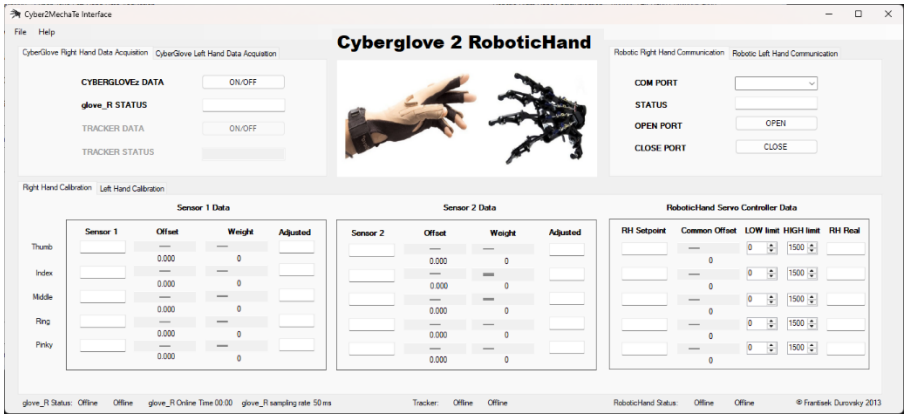

Figure 2. Extended system configuration – simultaneous control of both robotic hands.

The successful implementation of dual-hand control required explicit separation of software logic for the right and left robotic hands. Independent communication routines, device handlers, and status monitoring mechanisms were implemented for each hand. The control software includes separate port management, device initialization, and error-handling procedures for both manipulators, ensuring reliable and parallel operation.

Figure 3 and 4 illustrate selected elements of the control software interface, including independent communication routines and automatic device detection used for the control of the right and left robotic hands.

```
7978:                 this->textBox_LH_Status->Text = String::Empty;        //Clear Status Textbox
7979:                         //try{
7980:                                 //if(!this->serialPort_LHand->IsOpen){                                                    //is port is not open
7981:                                 //      this->serialPort_LHand->PortName = this->comboBox_LH_ComPort->Text;          //Load COM Port name
7982:                                 //      this->serialPort_LHand->BaudRate = 9600;                                          //Communication Baudrat
7983:                                 //      this->serialPort_LHand->Open();                                                          //Open Port
7984:                                 //      this->textBox_LH_Status->Text = "Open";                                           //Status textbox
7985:                                 //      this->textBox_LH_Status->ForeColor::set(System::Drawing::Color::Green);
7986:                                 //      this->label_LH_Status->Text = "Online";
7987:                                 //      this->label_LH_Status->ForeColor = System::Drawing::Color::Green;
7988:         //                      }
7989:
7990:
7991:                                  this->textBox_LH_Status->Text = String::Empty;        //Clear Status Textbox
7992:                 if (device_L_open == 0){
7993:                         try{
7994:                                 List<DeviceListItem^>^ connectedDevices = Usc::getConnectedDevices();
7995:
7996:                                         device_L = gcnew Usc(connectedDevices[this->comboBox_LH_ComPort->SelectedIndex]); // Connect to the device.
7997:                                         device_L_open = 1;
7998:
7999:                                         this->textBox_LH_Status->Text = "Open";                                           //Status textbox
```

Figure 3. Excerpt of the C++ control software illustrating independent communication routines for robotic hand control.

```
7901:private: void findPorts(void)
7902:                 {
7903:                 ////find available COM ports
7904:                 //array <Object^>^objectArray = SerialPort::GetPortNames();
7905:                 ////add string array to combobox
7906:                 //this->comboBox_RH_ComPort->Items->AddRange(objectArray);
7907:                 //this->comboBox_LH_ComPort->Items->AddRange(objectArray);
7908:                         try{
7909:                                         List<DeviceListItem^>^ connectedDevices = Usc::getConnectedDevices();
7910:                                 for each (DeviceListItem^ dli in connectedDevices)
7911:                                         {
7912:                         this->comboBox_LH_ComPort->Items->Add(dli->ToString());
7913:                                         this->comboBox_RH_ComPort->Items->Add(dli->ToString());
7914:                                         }
7915:                                 }
7916:                         catch (System::Exception ^e)
7917:                         {
7918:
7919:                         }
7920: }
```

Figure 4. Control software interface illustrating automatic detection of connected devices, automatic port assignment, and reliable identification of the left and right robotic hands.

The implementation of independent calibration, sensitivity adjustment, and servo parameterization for each robotic hand proved to be essential for achieving stable dual-hand operation. The system configuration allows flexible adaptation to different operators and robotic hardware without structural changes to the control architecture.

4. Discussion

The transition from a single-hand to a dual-hand robotic control architecture represents a significant functional improvement. While the original system demonstrated the feasibility of virtual reality–based hand control, it was limited to basic manipulation tasks. The extended dual-hand configuration enables more complex interaction scenarios and better reflects real industrial requirements, where bimanual manipulation is often essential. The proposed system extends existing glove-based teleoperation approaches by enabling stable real-time bimanual robotic manipulation within a modular virtual reality control architecture.

The proposed solution enhances the potential applicability of the system in teleoperation, operator training, and advanced human–robot interaction. Future work will focus on further improving system robustness, integrating additional sensory feedback, and extending the experimental evaluation.

Although the experimental verification confirmed stable operation of the system, the current implementation was tested primarily in a laboratory environment with a limited set of manipulation tasks. Future research will focus on evaluating the system in more complex industrial scenarios and extending the experimental validation to a wider range of robotic manipulators.

Correct identification and separation of control logic for individual robotic hands proved to be essential for system scalability. The resolution of hand assignment inconsistencies significantly improved system robustness and enabled further extensions toward bimanual and multi-joint robotic control.

5. Conclusions

This paper presented an extended virtual reality–based robotic control system that enables simultaneous control of two robotic hands using dual data gloves. Compared to the original single-hand implementation, the proposed solution significantly increases system functionality and applicability. Experimental verification confirms stable real-time operation and effective bimanual control, highlighting the potential of the system for advanced industrial and research applications.

The proposed dual-hand control system represents a modular platform that can be further extended in several research and industrial directions. One potential area of development is the expansion of the motion tracking system from the hand level to the forearm and upper limb. Integrating additional sensors would enable more complex kinematic modeling and coordinated arm movements.

Another promising direction is the extension of the control architecture to a full robotic arm or an industrial robotic manipulator. The existing data acquisition and mapping principles can be adapted to control multiple joints, enabling intuitive programming of industrial robots through natural human motion.

From an industrial perspective, such a system could be applied in operator training, remote manipulation, and flexible assembly tasks. Virtual reality–based control combined with real-time robotic feedback provides a powerful tool for reducing programming time, improving ergonomics, and enhancing human–robot collaboration in Industry 4.0 environments.

Acknowledgments: This article was created by the implementation of the grant project APVV-17-0258 “Digital engineering elements application in innovation and optimization of production flows”, APVV19-0418 “Intelligent solutions to enhance business innovation capability in the process of transforming them into smart businesses”, VEGA 1/0508/22 „Innovative and digital technologies in manufacturing and logistics processes and system“, VEGA 1/0383/25 “Optimizing the activities of manufacturing enterprises and their digitization using advanced virtual means and tools”, KEGA 020TUKE-4/2023 “Systematic development of the competence profile of students of industrial and digital engineering in the process of higher education”, KEGA 003TUKE-4/2024 “Innovation of the

profile of industrial engineering graduates in the context of required knowledge and specific capabilities for research and implementation of intelligent systems of the future".

Conflicts of Interest: The authors declare no conflict of interest.

References

1. Dipietro, L.; Sabatini, A.M.; Dario, P. A survey of glove-based systems and their applications. **IEEE Trans. Syst. Man Cybern. C** 2008, 38, 461–482.
2. Lin, J.; Wu, Y.; Huang, T.S. Modeling the constraints of human hand motion in robotic manipulation. **IEEE Robot. Autom. Lett. 2017**, 2, 110–117.
3. Kim, H.; Lee, J.; Bae, J. A wearable hand motion capture device using flexible sensors for human–robot interaction. **Sensors** 2019, 19, 2205.
4. Glauser, O.; Wu, Y.; Hilliges, O. A data glove with low-cost sensors for real-time hand tracking. **IEEE Access** 2020, 8, 200896–200907.
5. Kováč, J.; Rudy, V.; Malega, P. Prepojenie robotizovaných systémov s dátovou rukavicou CyberGlove II. In **Proceedings of the Conference**, Západočeská univerzita v Plzni, Plzeň, Czech Republic, 2021. Available online: http://hdl.handle.net/11025/46405 (accessed on 12 December 2025).

TECHNICAL UNIVERSITY OF KOŠICE
Faculty of Mechanical Engineering

International metrological comparison of ocular tonometers for optometry purposes

Stela Levická [1,*], Dominik Pražák [2], Václav Sedlák [2], Eliška Najmanová [1] and František Pluháček [1]

[1] Department of Optics, Faculty of Science, Palacký University, 17. listopadu 12, 771 46 Olomouc, Czech Republic; levicka.stela@gmail.com; eliska.najmanova@upol.cz; frantisek.pluhacek@upol.cz
[2] Unit of Primary Metrology of Pressure, Vacuum and Low Mass Flow, Czech Metrology Institute, Okružní 31, 638 00 Brno, Czech Republic; dominik.prazak@cmi.gov.cz; vaclav.sedlak@cmi.gov.cz
* Correspondence: levicka.stela@gmail.com; Tel.: +421 944 444 740

Abstract: This conference paper focuses on the international metrological comparison of non-contact ocular tonometers used in optometry and ophthalmology. The aim of the study was to evaluate the accuracy and reliability of tonometers in measuring intraocular pressure. Standardized metrological procedures and equipment were used for the comparison between the Czech Republic and Slovakia, ensuring the consistency of results and identifying potential discrepancies between the devices. The findings reveal measured differences in intraocular pressure readings, which directly affect the quality of diagnostics and patient care. Based on these results, recommendations are proposed to improve metrological standards and tonometer calibration within the framework of international collaboration to ensure metrological traceability of intraocular pressure in practice.

Keywords: Intraocular pressure, Metrological comparison, Metrological traceability, Ocular tonometers

1. Introduction

Currently, several types of standards are used for the metrological calibration of non-contact tonometers, such as silicone eyes, flapper, and electronic eye. Each of these standards is often limited to specific types of devices or manufacturers, or has other specifications and constraints. These limitations have led to the need to develop a universal metrological tool for calibrating tonometers that would ensure reliable and comparable results across different devices. [1] Within the framework of research projects, a new eye model has been developed [2], offering several innovations, including independence from specific manufacturers and types of tonometers, which allows for broader application in the fields of optometry and ophthalmology. The aim of this conference paper is to present the results of an international metrological comparison of non-contact tonometers designed for optometric purposes. In this comparison, tonometers from multiple brands (see Table 1, Table 2 and Table 3) were tested using the newly developed eye model as the metrological standard. Measurements were conducted at several institutions in the Czech Republic and Slovakia, with all tested devices meeting the clinical test requirements according to the ČSN EN ISO 8612:2009 standard [3]. This conference paper provides an overview of the comparison process, the measurement methodology, and an analysis of the results, which are crucial for ensuring high accuracy and reliability in intraocular pressure measurements in practice.

Non-contact ocular tonometers measure intraocular pressure [4] using an air puff that flattens the cornea, with the time of this flattening being measured to calculate the pressure. Intraocular pressure is an important factor for the diagnosis of eye conditions and the potential development of glaucoma [5]. The issue with this measurement technique is that it is not physically linked to the SI base units [6] but relies on the biological

variability of patients, which can affect the accuracy of the measured results. Currently, various metrological standards are used to calibrate these devices in order to ensure that the results are reliable within the field of medical metrology. Metrological comparisons are conducted across countries and different devices, one of which is presented in this conference paper.

2. Materials and Methods

The aim of the materials for the international metrological comparison of non-contact tonometers is to verify the reliability, accuracy, and comparability of intraocular pressure measurements across various devices and countries, taking into account the relevant metrological traceability.

- **Selection of Standards and Devices**

Several metrological standards are used in the international comparison of non-contact tonometers, such as silicone eyes, flapper, and electronic eye, each of which has specific limitations and is often restricted to particular types of devices or manufacturers. These limitations led to the development of a universal eye model, which introduces several innovations, such as independence from specific manufacturers and device types, applicability across a wide range of measurement ranges, consideration of other ophthalmological parameters, and metrological traceability to the SI base unit system [6]. This eye model was chosen as the primary metrological standard for this comparison because it allows broader use in the fields of optometry and ophthalmology. The devices were selected with consideration for their availability, ensuring that the results would be applicable to a variety of non-contact tonometers.

- **Measurement Protocol**

The measurement process was conducted in accordance with the guidelines set by the metrological institute, taking into account the requirements defined by the standard ČSN EN ISO 8612:2009 [3], which outlines procedures for the clinical testing of non-contact tonometers as part of medical metrology. The ability of the tonometers to measure intraocular pressure using a puff of air that applanates the cornea was assessed. The time required for this applanation (applanation time) is used to calculate intraocular pressure, with the devices recording this time to derive pressure values.

- **Use of the Tested/Developed Eye Model**

The tested eye model, serving as the universal metrological standard, was used for the calibration of all tested tonometers. This eye model was designed to overcome the limitations of traditional calibration standards by offering a more flexible and consistent reference for various types of non-contact tonometers. The model's design ensures its independence from specific manufacturers and types of tonometers, allowing it to be used in a broader range of clinical and research environments, while also ensuring direct physical (metrological) traceability. [7]

The eye model was employed to simulate the conditions of the human eye during the calibration and testing of tonometers, ensuring that the measurements reflected real-world conditions. Each non-contact tonometer was tested multiple times using the eye model to verify its accuracy and reliability in measuring intraocular pressure.

- **Data Collection and Analysis**

Data were collected from each non-contact tonometer according to the aforementioned measurement protocol. The results of all tonometers were compared with the reference device used for metrological control at the Czech Metrology Institute. This comparison enabled the evaluation of the performance of each non-contact tonometer and the identification of any discrepancies or deviations in their measurements.

The data were analyzed to identify potential sources of error, including the influence of biological variability among patients, which can affect the accuracy of measurements with non-contact tonometers. This analysis is crucial for understanding the reliability of these devices in real clinical practice and ensuring the comparability of results across

different devices and locations. [7] The results are presented in the following chapter (Chapter 3 – Results).

3. Results

The used model eye was tested on the following types of ocular tonometers. Note: The measurements were carried out under laboratory conditions with constant temperature, pressure, and humidity, and all parameters for metrological comparison were met.

Table 1. Calibration using a model eye on the Nidek NT2000 ocular tonometer /CZ – Czech Metrological Institute, Regional Inspectorate Most/. Source: Own processing.

Ref. Pressure	Measured Intraocular Pressure Values (mmHg)										Evaluation (mmHg)	
Calibration Type: model eye	Tonometer type: Non-contact tonometer NIDEK NT2000/CZ/											
(mmHg)	1	2	3	4	5	6	7	8	9	10	Ø	SD
10.00	11	11	12	10	11	11	11	11	11	11	11.0	0.4
15.00	15	15	16	15	14	15	15	15	16	15	15.1	0.5
20.00	20	20	20	21	21	20	20	20	20	20	20.2	0.4
25.00	25	26	26	26	26	25	26	25	25	26	25.6	0.5
30.00	30	31	31	32	32	31	31	32	32	32	31.4	0.7
35.00	36	36	37	37	37	38	37	37	37	36	36.8	0.6
40.00	43	43	42	42	45	45	43	43	43	43	43.2	1.0

The Nidek NT2000 tonometer /CZ/ demonstrates overall very stable eye pressure measurements, with average deviations being relatively low, especially at lower pressure values. For a pressure of 10 mmHg, the average value is 11.0 mmHg with a deviation of only 0.4 mmHg, which is excellent. At higher values (e.g., 40 mmHg), the deviation increases to 1.0 mmHg, which may be influenced by the higher pressures, and ensuring accuracy at these values can be more challenging. Overall, this tonometer can be considered highly accurate, with minor deviations that may increase at higher pressures. In further studies, it is necessary to consider additional influencing measurement parameters, according to [8].

Table 2. Calibration using a model eye on the Nidek NT2000 ocular tonometer /SK – Glaucoma Clinic, Ružinov Hospital, Bratislava/. Source: Own processing.

Ref. Pressure	Measured Intraocular Pressure Values (mmHg)										Evaluation (mmHg)	
Calibration Type: model eye	Tonometer type: Non-contact tonometer NIDEK NT2000/SK/											
(mmHg)	1	2	3	4	5	6	7	8	9	10	Ø	SD
10.00	12	12	11	11	12	11	11	11	12	11	11.4	0.5
15.00	15	16	16	16	15	16	15	15	15	16	15.5	0.5
20.00	20	21	21	21	21	21	21	21	20	21	20.8	0.4
25.00	25	26	26	27	27	26	27	26	26	26	26.2	0.6
30.00	32	32	32	32	32	31	32	32	31	31	31.7	0.5
35.00	37	37	36	36	37	38	37	38	36	37	36.9	0.7
40.00	42	42	42	42	44	44	43	43	43	42	42.7	0.8

The Nidek NT2000 tonometer /SK/ shows similarly stable results, with the average deviation typically around 0.5 mmHg in most cases. Even at higher pressures, such as 40 mmHg, the deviations remain acceptably low (maximally 0.8 mmHg). Measurements at lower pressure values (10 and 15) mmHg demonstrate that the tonometer is reliable

and has low variability, making this device suitable for a wide range of intraocular pressures. This tonometer is also well-calibrated and provides consistent results. In further studies, it is necessary to consider additional influencing measurement parameters, according to [8].

Table 3. Calibration using a model eye on the Nidek TONOREF III ocular tonometer /CZ - Faculty of Science, Palacký University, Olomouc/. Supplementary measurement on the school ocular tonometer. Source: Own processing.

Ref. Pressure	Measured Intraocular Pressure Values (mmHg)										Evaluation (mmHg)	
Calibration Type: model eye			Tonometer type: Non-contact tonometer NIDEK TONOREF III /CZ/									
(mmHg)	1	2	3	4	5	6	7	8	9	10	Ø	SD
10.00	12	11	11	10	11	10	11	10	11	11	10.8	0.6
15.00	16	15	16	15	15	16	15	15	16	15	15.4	0.5
20.00	21	21	21	21	21	20	20	21	21	20	20.7	0.5
25.00	26	26	26	26	26	26	26	26	25	26	25.6	0.3
30.00	30	30	31	31	31	31	31	31	31	31	30.8	0.4
35.00	36	36	36	36	36	36	36	37	37	36	36.2	0.4
40.00	42	41	41	42	43	42	43	42	43	43	42.2	0.7

The results from the school's Nidek TONOREF III tonometer are also very stable, especially at lower pressures. The average deviation for a pressure of 10 mmHg is 0.6 mmHg, which is again a very good result. At higher pressures (35–40) mmHg, the average deviation (0.4–0.7) mmHg is also a very acceptable value. This tonometer shows solid performance at various pressure levels and is reliable when compared to other devices. This device was used solely for supplementary metrological comparison purposes as part of the School's optical tonometer at the Department of Optics, Faculty of Science, Palacký University Olomouc. No clinical testing for calibration was performed on this device, but its results met the requirements of the metrological control.

4. Discussion

The results of the metrological comparison of non-contact ocular tonometers highlight the importance of standardization to ensure accurate and reliable measurements. This highlights the need for more universal calibration models that can work across different devices and pressure ranges. Although biological variability, such as corneal thickness, may influence measurements, it is essential to improve metrological tools and conduct regular international comparisons to ensure high-quality glaucoma and ocular disease diagnosis. Standardization is crucial to reduce variations and improve diagnostic accuracy, especially as tonometry technology evolves. The Nidek NT2000 (both devices) and Nidek TONOREF III devices performed well in controlled tests, but further studies are needed to assess long-term reliability across diverse patient populations and conditions. Continual international comparisons and improvements are key to maintaining high-quality, consistent eye pressure measurements for glaucoma diagnosis [9].

5. Conclusions

The results of the metrological comparison are presented in this paper, providing an overview of the performance of multiple non-contact tonometers tested using the developed eye model. The methodology and results demonstrate the importance of using reliable metrological standards to ensure accurate and consistent intraocular pressure measurements, which are crucial for the diagnosis and management of eye conditions such as glaucoma. By comparing devices across different countries and types of devices, this

study aims to promote the development of universal standards that can be applied globally in the field of optometry and ophthalmology. This international comparison also emphasizes the need for continued innovation in metrological tools for calibrating non-contact tonometers, ensuring that these devices provide reliable and comparable results across different clinical settings.

Acknowledgments: The authors would like to thank the Faculty of Science at Palacký University Olomouc and the Czech Metrology Institute for their support in preparing this conference paper, as well as for the partial funding provided through the Institutional Grant from the Ministry of Industry and Trade of the Czech Republic. Thanks are also extended to all those involved in the international comparison of ocular tonometers.

Conflicts of Interest: "The authors declare that there are no conflicts of interest regarding this conference paper. The sources of funding did not influence the study design, data collection, analysis, or interpretation, nor the writing of the manuscript or the decision to publish the results."

References

1. Rybář, J.; Suchý, V.; Ďuriš, S.; Pavlásek, P.; Grosinger, P.; Hučko, B.; Ferková, S. L.; Sekáč, J.; Chytil, M. Metodika kalibrací bezkontaktních očních tonometrů. In *Metrológia a skúšobníctvo*. Roč. 25, č. 1 (2020), s. 8-13. /Methodology for the calibration of non-contact ocular tonometers. In *Metrology and Testing*. Vol. 25, No. 1 (2020), pp. 8–13/. ISSN 1335-2768.
2. Rybář, J.; Leja, J.; Dunaj, Š.; Smetánka, A. and Onderčo, P. New design solution of reference device with model eye. In *10th International scientific conference on advances in mechanical engineering*: Selected peer-reviewed full text papers from the 10th International scientific conference on advances in mechanical engineering (ISCAME 2024). 1. vydanie /1st edition/. Zurich, Švajčiarsko: Trans Tech Publications, 2025, S. /PP./ 81 - 86. ISSN 1662-0356. In the database: SCOPUS: 2-s2.0-105008444446.
3. *ISO 8612:2009. Ophthalmic Instruments – Tonometers.* Prague: Office for Technical Standardization, Metrology and State Testing, 2009. 28 pages.
4. Rybář, J.; Ďuriš, S.; Pavlásek, P.; Šrenkel, P. and Chytil, M. Měření nitroočního tlaku v oftalmologické praxi. In *Metrológia a skúšobníctvo*. Roč. 23, č. 1 (2018), s. 8-12. /Measurement of Intraocular Pressure in Ophthalmic Practice. In *Metrology and Testing*. Vol. 23, No. 1 (2018), pp. 8–12/. ISSN 1335-2768.
5. Morrison, J. C. and Pollack, I. P. *Glaucoma: science and practice.* [s.l.]: Thieme, 2003. 530 s. /530 pgs./.
6. Smetánka, A.; Rybář, J.; Onderčo, P.; Leja, J. and Gerneschová, J. What is metrological traceability and what role does physics play? In *27th Conference of Slovak Physicists: Proceedings*. 1. vydanie /1st edition/. Košice: Slovak Physical Society, 2024, S. 65 - 66. ISBN 978-80-89855-26-1. In the database: SCOPUS: 2-s2.0-85214019262.
7. Kelemenová, T. and Dovica, M. *Kalibrácia meradiel*. 1. vydanie. Košice: Technická univerzita v Košiciach, Strojnícka fakulta. Edícia vedeckej a odbornej literatúry, 2016. 232 s. *Calibration of Measuring Instruments*. 1st edition. Košice: Technical University of Košice, Faculty of Mechanical Engineering. Scientific and Professional Literature Series, 2016. 232 pp./. ISBN 978-80-553-3069-3.
8. Rybář, J.; Hučko, B.; Ďuriš, S.; Pavlásek, P.; Chytil, M.; Furdová, A. and Veselý, P. Factors affecting measurements of IOP using non-contact eye tonometer. In *Strojnícky časopis = Journal of Mechanical engineering*. Roč. 70, č. 2 (2020), s. 133-140 /Vol. 70, No. 2 (2020), pp. 133–140/. ISSN 0039-2472 (2020). In the database: SCOPUS: 2-s2.0-85099079234.
9. Tham, YC.; Li, X.; Wong TY.; et al. Global prevalence of glaucoma and projections of glaucoma burden through 2040: a systematic review and meta-analysis. *Ophthalmology*. 2014; 121: 2081–2090. DOI: 10.1016/j.ophtha.2014.05.013.

TECHNICAL UNIVERSITY OF KOŠICE
Faculty of Mechanical Engineering

Detection of compressed air leakage using compressor energy consumption analysis

Ondrej Majerčák [1,*], Patrik Šarga [1], Róbert Rákay [1]

[1] Technical University of Kosice, Faculty of Mechanical Engineering, Department of Industrial Automation and Mechatronics;
* Correspondence: ondrej.majercak@tuke.sk

Abstract: This paper presents a method for detecting compressed air leakage based on the analysis of compressor energy consumption. The proposed approach utilizes a digital power meter Finder to measure real-time electrical parameters of two identical piston compressors—one operating under normal conditions and the other with an artificial air receiver leakage. Measurement data were transmitted via ESP32 to the Node-RED platform for processing, visualization, and duty cycle analysis. The results demonstrated a significant increase in compressor operating time and energy consumption in the presence of leakage, confirming the method's effectiveness for early fault detection. The proposed solution offers a low-cost and non-invasive alternative for predictive maintenance of pneumatic systems, enabling continuous monitoring of compressor performance through energy-based indicators.

Keywords: Node-RED; esp32; compressed air system; consumption analysis; air leakage

1. Introduction

Compressed air is one of the most widely used forms of energy in industrial applications, yet its generation is energy-intensive. It is estimated that as much as 20–40 % of the produced energy is lost due to leaks in the compressed-air system, causing unnecessary economic losses and environmental burden [1]. Therefore, effective leak detection is a key element of maintenance and energy-efficiency optimization [2].

This article presents an implemented experimental method for detecting compressed-air leaks through analysis of the compressor's electrical-energy consumption. A Finder sensor was used to measure the real current consumption of the compressor, recording data during one hour of operation. Measurements were carried out on two compressors — a functional one (without leakage) and a faulty one (with a leak in the air receiver). The collected data were processed using an ESP32 microcontroller, which transmitted them in real time to the Node-RED platform. Here, the compressor's duty cycle — the ratio of on-time to off-time — was analyzed. An increased switching frequency of the compressor was interpreted as an indicator of a potential compressed-air leak. This approach enables non-intrusive and cost-effective monitoring of the pneumatic system's condition without the need for complex sensor assemblies [3].

The aim of this study is to verify the effectiveness of analyzing the compressor's electrical-energy consumption as an indicator of compressed-air leakage and to propose a method that could be implemented within predictive maintenance in industrial environments.

2. Materials and Methods

The measurements were carried out using two ABAC JUNIOR 30 piston compressors, which served as the source of compressed air for the pneumatic circuit. This type of

compressor has a rated power of 0.19 kW, a maximum output pressure of 8 bar, and an air-receiver volume of 6 liters [4]. During the experiment, two identical compressors were used — the first in fully functional condition and the second with an artificially created leak in the air receiver in the form of a hole approximately 1 mm in diameter (the size of a pin). In this way, it was possible to observe changes in electrical consumption and the compressor's duty cycle depending on the presence of a compressed-air leak. To measure electrical consumption, a Finder 7M.24.8.230.0210 digital measuring instrument was used, designed for monitoring voltage, current, and power of single-phase devices. The device is equipped with an RS485 communication interface supporting the Modbus RTU protocol, which enabled reliable transmission of measured data to the control system. Output data from the measuring device were read by an ESP32 microcontroller, which ensured their transmission to the Node-RED software platform via a local network [5,6].

In the Node-RED environment, real-time processing, filtering, and visualization of the compressor-current data were carried out. The measured data were subsequently stored and evaluated according to the compressor's switching time intervals. The obtained information was used to analyze the compressor's duty cycle, which represented a key parameter for detecting increased energy consumption and identifying compressed-air leaks [7].

The electrical-energy consumption was determined from instantaneous values of voltage, current, and on-time according to the equation [8]:

$$E = U \cdot I \cdot t \tag{1}$$

where:

- E – electrical-energy consumption [Wh],
- U – voltage value [V],
- I – current value [A],
- t – compressor on-time [h].

3. Experiment

The experiment consisted of creating a wireless measurement workstation for detecting compressed-air leaks through the analysis of the compressor's electrical-current consumption. The measurement was carried out using industrial components, microcontrollers, and the Node-RED software environment, which provided real-time data acquisition, processing, and evaluation.

3.1. Experimental Workstation

The experimental workstation consisted of an interconnected pneumatic and electronic system. The pneumatic circuit included a rodless actuator, a 5/3 directional control valve, throttle valves, a digital air-pressure sensor, and a compressed-air source — the compressor. The entire pneumatic process was designed to withdraw air from the system at regular intervals, simulating real operating conditions with the possibility of leakage. The control system was a Siemens Logo! PLC, which handled actuator movement and communication with the Node-RED platform. The PLC was connected to Node-RED through a network variable that enabled bidirectional data exchange between the physical device and the digital control environment.

3.2. *Communication and Measurement System*

The compressor's power supply was routed through a Finder measurement device, which made it possible to monitor the instantaneous current of the compressor and communicate via the RS485 interface. The transmitted data were received by an ESP32 microcontroller, which subsequently published them to Node-RED using the MQTT protocol.

In Node-RED, a visualization was created that enabled manual initiation of the measurement through a Start button. The control sequence and data communication process are illustrated in Figure 1.

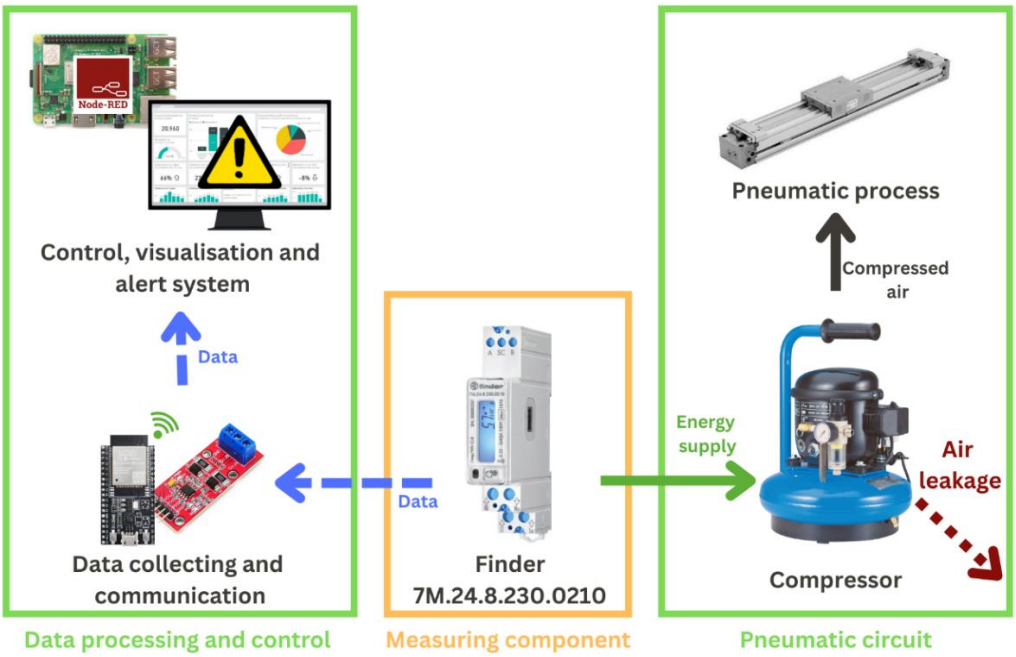

Figure 1. Communication flow between Finder, ESP32, Node-RED and Pneumatic circuit.

3.3. Control Program

A simple control program was implemented in the Node-RED environment, generating 15-second pulses (Pulse 15s). This signal was sent to the Siemens Logo! PLC and triggered the actuator movement from one end position to the other. The piston movement was accompanied by visual signaling of its position, allowing real-time monitoring of each cycle.

The program in Siemens Logo! (Figure 2) consisted of:

- two outputs for the two end positions of the actuator,
- one logical negation used for switching control,
- visual indication of the current position.

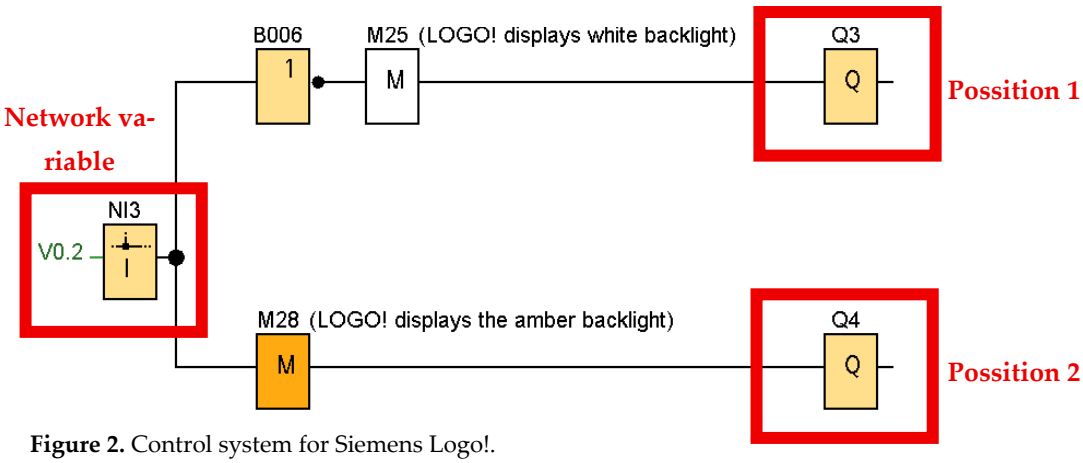

Figure 2. Control system for Siemens Logo!.

The main input was a network variable from Node-RED, which activated the measurement cycle every 15 seconds. This interval was chosen to simulate periodic load in an

industrial application and to allow observation of the compressor's response under different system conditions. An example of the Node-RED visualization with actuator control and MQTT data monitoring is shown in Figure 3.

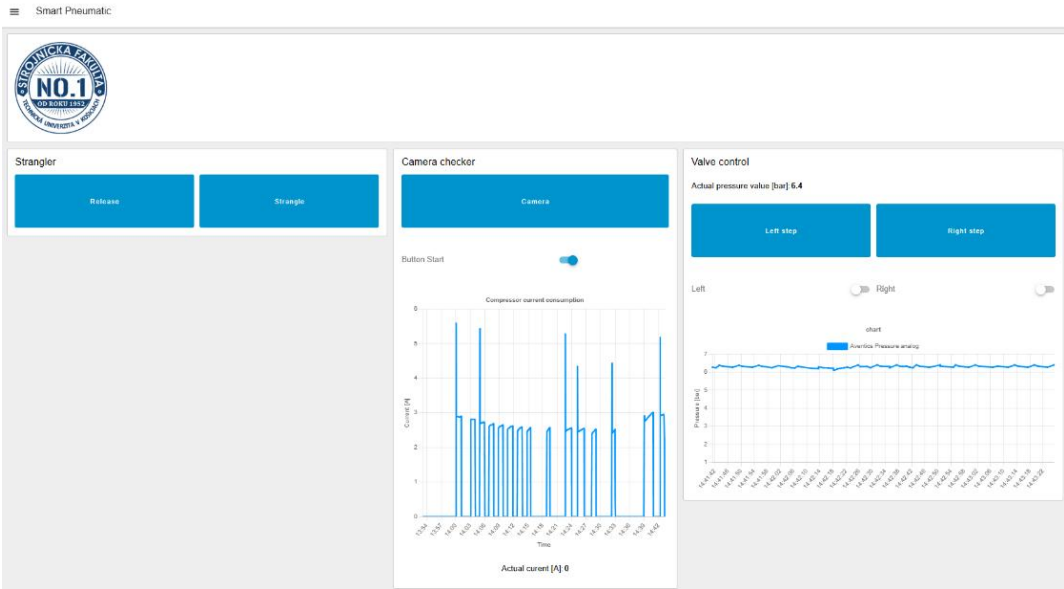

Figure 3. Node-RED dashboard and control logic.

3.4. Data Acquisition and Processing

Data reading from the Finder component was carried out in Node-RED through the MQTT in node. Since the component transmitted multiple data variables, a filtering function was created to work exclusively with the compressor-current values. In addition, a protective function was implemented to handle cases of incorrect data format or transmission errors — in such situations, the system did not record values into the database (Figure 4).

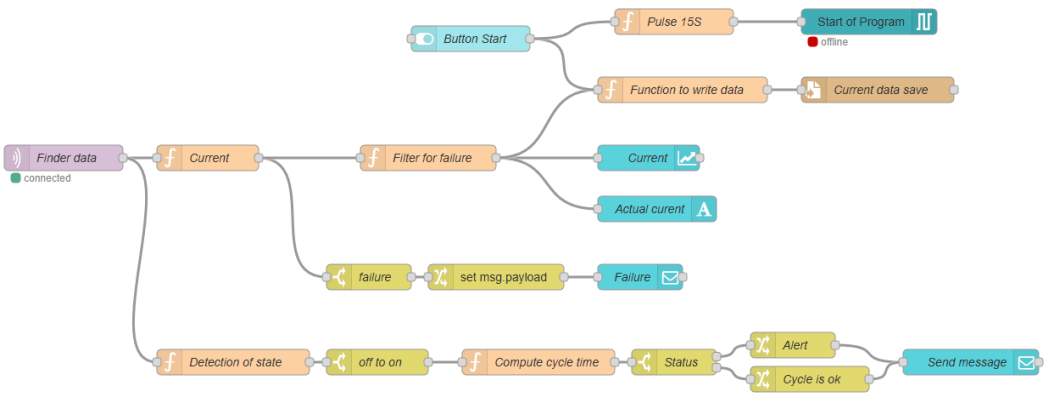

Figure 4. Node-RED flow.

Data were recorded only if:

- the measurement was active,
- the incoming data were in the correct format,
- the value was not equal to 999 (an indicator of communication failure).

3.5. Measurement Procedure

The experiment was conducted in two phases:

- Measurement with a fully functional compressor without leakage — duration: 1 hour,
- Measurement with a compressor with leakage — a small leak (hole) was created in the air receiver, causing a drop in pressure,
- At the beginning of each measurement, the compressor was pressurized to 6.5 bar. During the experiment, instantaneous current consumption and compressor switching times were monitored.

3.6. Measurement Conclusion

The data were evaluated directly in the Node-RED environment. Based on the measured values, the compressor's duty cycle was calculated — the ratio of time the compressor was running to the total measurement time. An increase in this duty cycle compared to reference values indicated a probable compressed-air leak. A logical branch was subsequently implemented in Node-RED for automatic evaluation — when the duty cycle exceeded the limit, the system generated an alert indicating potential damage or leakage in the pneumatic circuit.

4. Results

The results of our study confirm the importance and necessity of addressing compressed-air leak detection in industrial systems. Based on the conducted measurements, graphically illustrated in Figure 5, it can be observed that analyzing the compressor's electrical-energy consumption is an effective and reliable method for detecting leaks in systems with stable operating cycles [9]. Our experiment confirmed the hypothesis that an increased compressor duty cycle indicates the presence of a compressed-air leak. Evaluation of the switching times showed that the fully functional compressor without leakage had a total operating time of 468.3 s, whereas the compressor with leakage operated for 874.9 s within the same pneumatic cycle. This difference clearly indicates an increased need for pressure compensation in the system due to the leak [10, 11].

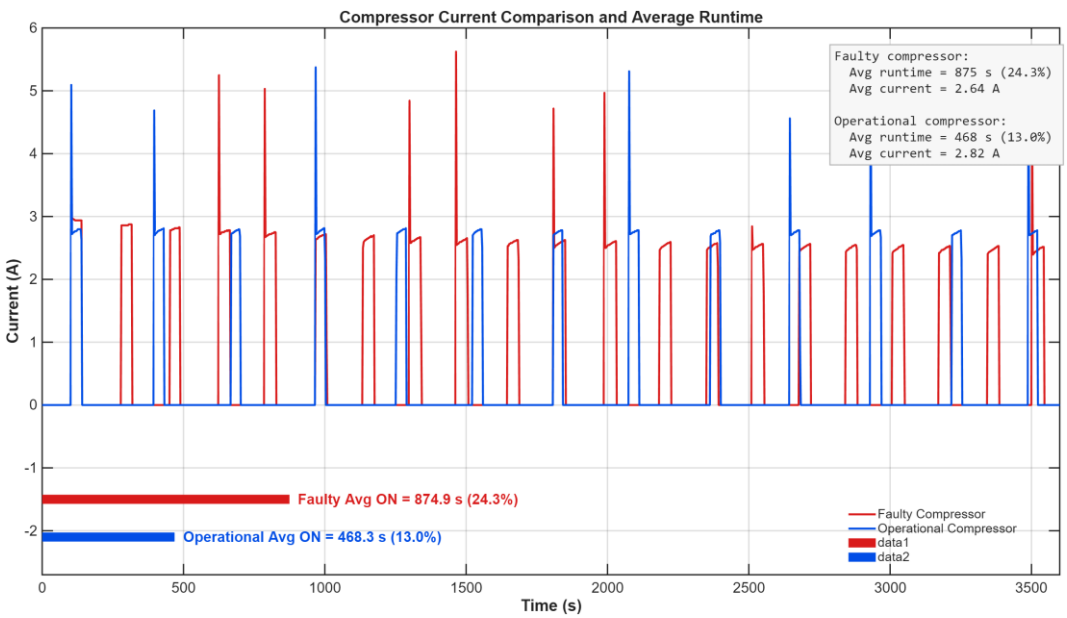

Figure 5. Compressor current comparison and average runtime.

Figure 5 shows the electrical-current profiles for both compressors. The average current values differ slightly — the difference is approximately 0.22 A, which does not significantly affect the conclusions of the experiment. This discrepancy can be attributed to variations in compressor load during the measurements.

From the perspective of energy consumption, it was found that:

- the functional compressor consumed 0.027 kWh during one hour,
- the compressor with a leak consumed 0.050 kWh.

At the current electricity price of 0.217 EUR·kWh^{-1}, operating the functional compressor costs 0.58 EUR per hour, while the compressor with a leak reaches 1.09 EUR per hour [12]. Even with a relatively small air leak, this represents nearly double the energy consumption, which over an eight-hour workday corresponds to a difference of more than 4 EUR daily. These results confirm that even minor air leaks can lead to significant financial losses and unnecessary energy inefficiency. The results also demonstrate the suitability of the proposed methodology for predictive maintenance of pneumatic systems, where real-time analysis of the compressor duty cycle can timely identify emerging faults or air leaks.

5. Discussion

The experiment results showed that analyzing the compressor's electrical-energy consumption represents a simple and reliable method for detecting compressed-air leaks. The observed difference in operating time between the functional and faulty compressor was significant, confirming that even small leaks have a noticeable impact on operating time and system energy demand. Compared to traditional leak-detection methods, which require specialized sensors or intervention in the pneumatic circuit, the proposed method is less invasive and cost-effective. It was also confirmed that monitoring the duty cycle can serve as a basis for predictive maintenance in compressed-air systems. However, it should be noted that the measurements were conducted under laboratory conditions with constant load, which may yield different results in real industrial operation. Further research should therefore focus on long-term monitoring in actual production processes, across various compressor types, and under variable load conditions. Expanding the experiment to analyze a larger dataset could allow the development of a compressor behavior model, which, using artificial intelligence algorithms, could automatically detect anomalies and predict the occurrence of leaks. Ultimately, this could lead to the creation of an intelligent energy-management system that reduces energy losses, increases maintenance efficiency, and contributes to sustainable operation of industrial equipment.

Acknowledgments: This work has been funded by the EU NextGenerationEU through the Recovery and Resilience Plan for Slovakia under the project No. 09I03-03-V05-00015.

Conflicts of Interest: The authors declare no conflict of interest.

References

1. Desmet, A. and Delore, M. Leak detection in compressed air systems using unsupervised anomaly detection techniques. Proceedings of the Annual Conference of the PHM Society 2017. https://doi.org/10.36001/phmconf.2017.v9i1.2401.
2. Borg, M.; Refalo, P.; Francalanza, E. Failure Detection Techniques on the Demand Side of Smart and Sustainable Compressed Air Systems: A Systematic Review. Energies 2023. https://doi.org/10.3390/en16073188
3. Eret, P.; Meskell, C. Microphone Arrays as a Leakage Detection Tool in Industrial Compressed Air Systems, Advances in Acoustics and Vibration. 2012. https://doi.org/10.1155/2012/689379
4. ABAC Junior 30 – Bezhlukový kompresor. [Online]. Available: https://www.abac.sk/sk/dielenske-piestove-kompresory-detail/2797/abac-junior-30-bezhlun-kompresor-30-l-min-0-19-kw-8-bar. (accessed on 11th December 2024).
5. Finder 7M Series Smart Energy Meters. [Online]. (accessed on 11th December 2025). Available: https://www.finder-net.com/en/uk/series/7m-series-smart-energy-meters/type/type-7m-24-single-phase-bi-directional-energy-meters-with-backlit-lcd-display/.
6. Galajdová, A; Rákay, R. Long range IoT communication. MM Science Journal. 2021. doi: 10.17973/MMSJ.2021_10_2021038.
7. F. A. Hussein, M. T. Yaseen, and M. O. Mustafa, "The Future of Intelligent Industrial Systems: PLC, Node-RED, and IoT/IIoT," AUIQ Technical Engineering Science, vol. 2, no. 2, Article 5, 2025. DOI: https://doi.org/10.70645/3078-3437.1034.
8. Vagas, M; Majercak, O. Analysis and Graphical Evaluation of Pressure Changes in Pneumatic Circuits for Industrial Applications. Measurement Science Review 2025. https://doi.org/10.2478/msr-2025-0026.
9. Mallia, J.; Francalanza, E.; Xuereb, P.; Refalo, P. Intelligent Approaches for Anomaly Detection in Compressed Air Systems: A Systematic Review. Machines 2023. https://doi.org/10.3390/machines11070750

10. Chatterjee, A; Ahmed, B. S. IoT anomaly detection methods and applications: A survey. Internet of Things. 2022. https://doi.org/10.1016/j.iot.2022.100568.
11. Majercak, O; Romancik, J. and Vagas, M. IoT Approach Implementation Based on Flexible and Robust Node-RED Platform for Workplace Digitisation Increasing. 21st International Conference on Mechatronics - Mechatronika (ME), Brno, Czech Republic, 2024. doi: 10.1109/ME61309.2024.10789749.
12. Regulatory Office for Network Industries (ÚRSO), "Kalkulačka cien elektriny 2025," [Online]. Available: https://data.urso.gov.sk/CISRES/Agenda.nsf/KalkulackaElektrinaNewWeb2023. (accessed on 11th December 2025).

TECHNICAL UNIVERSITY OF KOŠICE
Faculty of Mechanical Engineering

Overview of calibration methods for measuring microscopes

Dmytro Malakhov [1,*], Tatiana Kelemenová [1]

[1] Faculty of Mechanical Engineering, Technical University of Kosice, Letna 9, 04200 Kosice, Slovakia; tatiana.kelemenova@tuke.sk (T.K.)
* Correspondence: dmytro.malakhov@tuke.sk

Abstract: This paper provides an overview of calibration methods for optical measuring microscopes and the reference standards required for reliable dimensional metrology. The study highlights the absence of a dedicated ISO standard for such microscopes and examines the applicability of ISO 10360-7, originally developed for coordinate measuring machines (CMMs) equipped with imaging probing systems. Both composite and component approaches defined in ISO 10360-7 are analyzed, with emphasis on their advantages, limitations, and practical implementation. Furthermore, the role of calibration artefacts—including linescales, gauge blocks, precision squares, and circular standards discussed in the context of ensuring traceability, accuracy, and comparability of measurements. The paper concludes with a reflection on the necessity for harmonized calibration methodologies and the potential benefits of universal reference standards in advancing optical coordinate metrology.

Keywords: Optical measuring microscope; Calibration; ISO 10360-7; Coordinate measuring machine (CMM); Reference standards

1. Introduction

Optical measuring microscopes are widely used in industry and research due to their non-contact operation, high measurement speed, and ability to automate inspection tasks. They are essential in precision engineering, quality control, and micro-manufacturing, where delicate or very small components cannot be reliably measured with tactile systems. Their versatility and ease of use make them a common tool for microscale dimensional inspection [1].

However, calibration and verification of these instruments remain challenging. Unlike tactile CMMs, for which mature procedures and international standards exist, no universally accepted or dedicated ISO standard fully addresses the calibration of optical measuring microscopes. Laboratories and manufacturers often rely on internal methods, custom artefacts, or adaptations of procedures developed for vision systems or CMMs. Several recent studies propose calibration strategies to help address this gap [2].

A relevant guideline is ISO 10360-7:2011, which defines acceptance and verification procedures for CMMs with imaging probing systems. Although originally intended for CMMs rather than standalone optical microscopes, it provides useful principles for evaluating imaging-based measurement errors, especially for 2D measurements from image projections. Nonetheless, the terminology and some test methods originate from tactile CMM standards, limiting direct applicability to many microscope configurations.

Recent work further highlights approaches to improve traceability in optical measurement systems (e.g., Y. Yin et al., 2012) and to develop microscope-specific reference artefacts (Martínez et al., 2022) [3]. Overall, there is a clear need for more harmonized and refined calibration procedures. Establishing standardized methodologies would improve comparability across laboratories and strengthen traceability to SI units, thereby increasing confidence in optical measurement results.

2. Methodology of ISO 10360-7 standard

The ISO 10360 series represent the key international framework for verifying the performance of coordinate measuring machines (CMMs). Each part defines standardised procedures for evaluating CMM accuracy with various probing systems. ISO 10360-7, introduced in 2011, focuses specifically on CMMs equipped with imaging probing systems, which differ from tactile probes by relying on optical two-dimensional projections rather than physical contact [4]. Its scope covers Cartesian CMMs operating in discrete point probing mode — a category largely represented by vision or video measuring machines widely used in industrial quality control, electronics, and precision engineering. Prior to the publication of this standard, no harmonised procedure existed for acceptance and verification testing of such systems, resulting in inconsistencies between manufacturers and laboratories, as illustrated in **Figure 1** [5,6].

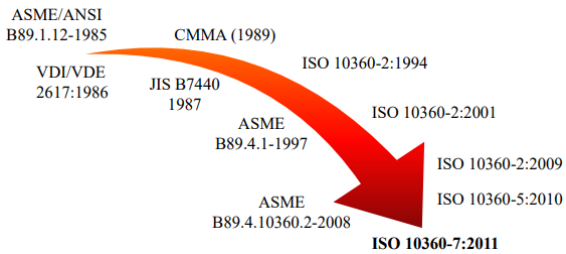

Figure 1. Evolution of CMM Performance Testing Standards [7].

ISO 10360-7 does not define universal tolerance values for measurement errors; instead, it specifies how machine performance should be tested so that results can be directly compared with the manufacturer's declared accuracy. This ensures transparency, reproducibility, and traceability to the SI unit of length. The manufacturer remains responsible for the declared specifications (e.g., maximum permissible errors), while the standard provides the framework for their verification [1].

The terminology used in ISO 10360-7 is partly inherited from tactile CMM standards. As a result, terms such as probing errors appear even though no physical contact occurs in optical systems. This wording has been retained for continuity and is well understood within the expert community [2,8].

The main aims of ISO 10360-7 are to verify display errors when measuring calibrated lengths with imaging probing systems, to evaluate characteristic errors of the imaging system, and to ensure traceability of measurement results to the metre. The standard also offers two testing approaches—the composite and the component approach—allowing either a holistic evaluation or a more detailed separation of error sources [4].

2.1. Bidirectional versus Unidirectional measurements

One important distinction between ISO 10360-2 and ISO 10360-7 lies in the permitted type of length measurement. ISO 10360-2, intended for tactile CMMs, requires strictly bidirectional probing, where opposite sides of a feature—such as edges of a gage block or a calibrated circle—must be measured to represent its true size [4]. ISO 10360-7 extends this concept by allowing both bidirectional (EB) and unidirectional (EU) measurements, reflecting the greater flexibility needed for imaging probing systems [4]. The standard does not mandate which variant must be used; the choice is left to the manufacturer, who selects the option best suited to the instrument's design and application [9]. The conceptual difference between unidirectional and bidirectional measurements is schematically illustrated in **Figure 2**.

Bidirectional measurements remain essential for features defined by opposing edges, such as widths or diameters [10]. Unidirectional measurements, in contrast, rely on repeated probing from the same direction and are suitable for features such as linescale pitch or center-to-center spacing of holes [11]. The ability to use either approach increases

the adaptability of ISO 10360-7, although the selection of EB or EU can influence result interpretation and comparability across systems [5].

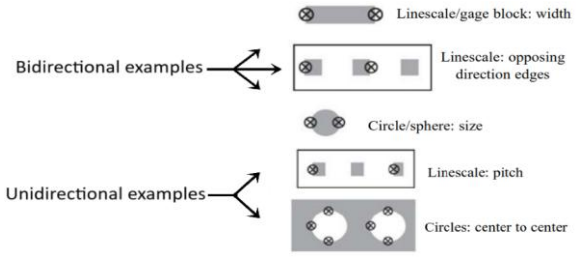

Figure 2. Unidirectional versus Bidirectional measurement [7].

The flexibility of allowing both bidirectional and unidirectional measurements makes ISO 10360-7 more adaptable than its tactile counterpart. Many artifacts, such as linescales, can be calibrated for both types of use, and manufacturers can therefore choose the most appropriate method depending on the application. However, it should be noted that the choice between EB and EU can affect the interpretation of results and their comparability across systems [5].

2.2. Composite approach in ISO 10360-7

The composite approach evaluates overall system performance through the E0 length test, inherited from ISO 10360-2 for tactile CMMs [4,6]. A calibrated step gauge or similar artefact is measured along seven lines—three axis-parallel and four diagonals—with five lengths per line repeated three times. The resulting 105 measurements are compared with the manufacturer's EB,MPE or EU,MPE specification to confirm conformity [9].

ISO 10360-7 extends the tactile methodology by allowing either bidirectional or unidirectional testing, offering flexibility for different imaging probe designs and application needs [11]. The approach is efficient, easy to interpret, and consistent with established CMM verification practices [5]. Its key limitation is that it provides only a single global error indicator, without identifying the source of deviations. This limitation motivates the more detailed component approach, which separates individual error contributions [12,13].

2.3. Component approach in ISO 10360-7

The component approach first evaluates length-measurement errors in the XY plane using a calibrated linescale measured in four orientations: parallel to the X-axis, parallel to the Y-axis and along both diagonals. This setup enables detection of distortions across the entire field of view, not only in its central region. In each orientation, five lengths are measured and repeated three times, yielding 60 values from which deviations from the reference are calculated. The resulting parameters EUXY or EBXY express the system's capability to measure planar dimensions reliably [7–9,12].

Length measurements along the Z-axis are assessed using standard artefacts such as gauge blocks or stair-step gauges. Five lengths are measured with three repetitions (15 values), following procedures analogous to tactile CMM testing according to ISO 10360-2 [14]. The parameters EUZ or EBZ quantify vertical accuracy and allow verification of performance outside the optical field of view [9].

Vertical performance is further linked to the squareness test ESQ, which determines the perpendicularity of the Z-axis to the XY plane using a precision square measured in the XZ and YZ planes. While squareness specifications were historically less formalized for tactile CMMs, ISO 10360-7 incorporates this parameter to ensure geometric integrity of optical systems. Even minor deviations from orthogonality can cause significant errors

in applications involving combined planar and vertical movements ("2½-D measurements"). When higher reliability is required, auxiliary indicators or electronic gauges may be used [4,7].

The approach also includes the probing performance test PF2D, derived from probing verification procedures in the ISO 10360 series [15]. A circular artefact with a diameter of 10–30% of the shortest field-of-view side is measured by acquiring 25 evenly distributed points along its circumference. A Gaussian circle fits the data, and the probing error is defined as the radial distance difference between the maximum and minimum measured values. The PF2D parameter thus characterizes the repeatability and stability of the optical probing system despite the absence of physical contact [1]. An example of a permissible test pattern used for evaluating the PF2D probing error according to ISO 10360-7 is shown in **Figure 3**.

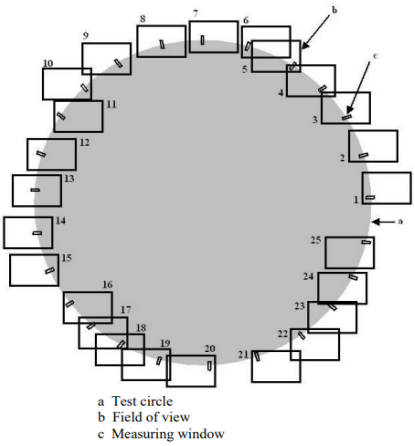

Figure 3. Example of an allowable test pattern for measuring PF2D [7,9].

In addition to the mandatory component tests, ISO 10360-7 introduces optional field-of-view tests, namely the length test EUV or EBV and the probing test PFV2D. Their principles correspond to the EUXY/EBXY and PF2D tests, but all measurements are performed entirely within the imaging window, without any CMM axis movement. For EUV/EBV, all measurement lines remain fully contained within the field of view, while PFV2D employs a smaller circular artefact that can be captured in a single image. The standard does not specify maximum permissible errors for these tests, leaving this decision to manufacturers, who may use them to emphasise strengths of their systems. These optional procedures are especially useful when measurements are carried out exclusively within the optical field of view and stage motion is not required [4,16,17].

Overall, the component approach of ISO 10360-7 provides a comprehensive and modular framework for characterising the performance of optical coordinate measuring machines. By independently assessing XY measurement accuracy, Z-axis performance, squareness, and probing repeatability, it enables not only verification but also diagnosis of which aspects of the system may limit measurement quality in industrial and research applications.

3. Reference Standards and Calibration Artefacts for ISO 10360-7

The verification procedures defined in ISO 10360-7 require the use of reliable calibration artefacts that serve as references for determining measurement accuracy. These artefacts, often referred to as etalons, must be precisely manufactured, stable, and traceable to higher-order standards to guarantee that the test results reflect the true performance of the measuring system rather than imperfections of the reference itself. In practice, several types of artefacts are used, each of them suitable for a specific class of tests defined by the standard. For length measurement in the XY plane, calibrated linescales and grid patterns

are most frequently applied. Typical examples of glass-based calibration artefacts used for planar length verification, such as stage micrometers, are shown in **Figure 4**.

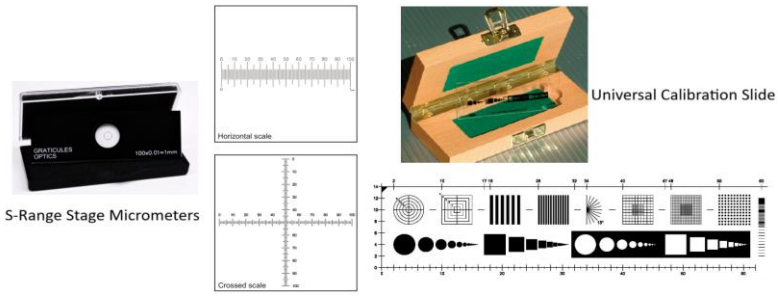

Figure 4. Examples of stage micrometers [18].

These artefacts typically consist of fine chrome patterns deposited on glass substrates, such as the stage micrometers and calibration slides offered by Graticules Optics [18]. Glass is advantageous due to its thermal stability, low expansion, and favorable optical properties, which are crucial when observed through microscope objectives. The high precision of the deposited structures enables reliable detection of systematic errors, including scaling deviations and image distortion. Such artefacts are therefore well suited for the EUXY and EBXY length tests defined in ISO 10360-7.

For Z-axis measurements, artefacts with defined vertical steps or gauge blocks are required. As described by Steger et al. [19], these height-reference artefacts verify the accuracy of focus-based displacement or vertical scanning. They provide known height differences against which the system is tested, supporting the evaluation of EUZ and EBZ error parameters. Examples of artefacts used for Z-axis verification, including a step gauge built on an optical flat and gauge blocks, are presented in **Figure 5**.

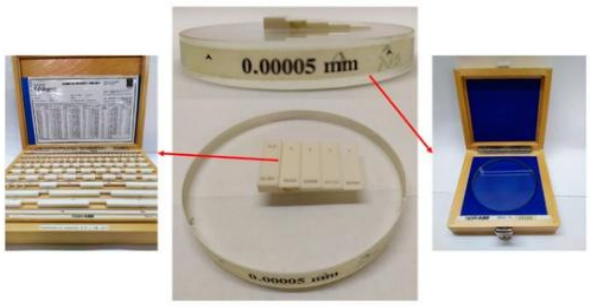

Figure 5. A step gauge built on an optical flat and a set of gauge blocks [19].

The verification of squareness, or ESQ, requires the use of precision squares, which serve as references for the perpendicularity between the vertical and horizontal axes of the measuring machine. The test is performed in both the XZ and YZ planes, using artefacts that are manufactured with minimal deviation from 90°. Such measurements are especially relevant for combined planar and vertical tasks, sometimes referred to as 2½-D measurements, where any loss of orthogonality between axes can directly propagate into systematic dimensional errors. An example of squareness artefacts and procedures can be found in industrial studies such as those by Lai et al., which demonstrate the potential of precision squares to separate geometric misalignments from other error sources [16].

Another important class of artefacts are circular standards, which are employed in probing error tests such as PF2D and its field-of-view variant PFV2D. In these tests, a circle of defined diameter, usually between 10 and 30% of the shortest field dimension, is measured at 25 evenly distributed points. From these data, a Gaussian circle is fitted, and deviations of the measured points from the ideal form are calculated. The PTB report on calibration of photomasks for optical coordinate metrology discusses the use of circular

artefacts for similar purposes, emphasising the importance of roundness calibration of the circle itself before it is used as a test standard [18,20]. A representative circular artefact used for checking the PF2D probing performance is illustrated in **Figure 6**.

Figure 6. Test artifact for checking PF2D [7].

In addition to these functional groups, there are commercial artefacts designed by major metrology companies, such as Zeiss, which provide reference scales intended for high-precision length verification. These artefacts can be used not only for basic length tests but also for assessing the linearity of imaging systems across the field of view [21]. Their robustness and certified traceability make them particularly suitable for industrial calibration laboratories where reproducibility and compliance with international standards are critical. A commercial example of a multifunctional calibration artefact designed for industrial verification tasks is shown in **Figure 7**.

Figure 7. ZEISS O-SELECT Check artefact [21].

A notable trend in practice is the increasing use of glass-based artefacts as universal standards. Their versatility comes from the ability to integrate multiple patterns—lines, grids, circles—on a single substrate, enabling one artefact to support length, probing, distortion, and field-of-view tests. This multi-functionality is especially valuable in optical metrology, where high dimensional stability and good optical properties are essential. However, their fragility and sensitivity to contamination require careful handling and storage. Despite these limitations, their optical performance and broad applicability make them among the most widely used artefacts for ISO 10360-7 verification.

In essence, the choice of calibration artefacts depends on the specific ISO 10360-7 test: line and grid scales for planar length, vertical step artefacts for Z-axis calibration, precision squares for squareness, and circular standards for probing performance. Although dedicated artefacts exist for each task, glass-based universal standards remain the most common industrial solution due to their stability, versatility, and compatibility with optical systems.

4. Discussion

The review of ISO 10360-7 shows that although originally intended for vision-based CMMs, the standard offers a practical framework for evaluating optical measuring microscopes. Its two verification strategies—the composite and component approaches—provide complementary information: the composite method is efficient and comparable to tactile CMM testing but cannot isolate individual error sources, while the component method separates planar, vertical, squareness, and probing performance at the cost of increased effort.

A persistent issue is the terminology inherited from tactile CMM standards, which can appear inconsistent for optical systems. Despite this, the underlying principles remain applicable, particularly when suitable reference artefacts are used. Glass-based artefacts stand out for their stability and capacity to integrate multiple calibration patterns, though their fragility limits industrial use.

The discussion also highlights the need to harmonize calibration procedures across laboratories. Current variations in methods and artefacts hinder comparability and traceability, reducing confidence in results. Developing universal artefacts and adapted ISO procedures would substantially improve the reliability of optical coordinate metrology.

Future work should focus on refining existing procedures, establishing universally accepted standards, and promoting artefact designs that combine robustness with versatility.

Acknowledgments: The authors would like to thank the Slovak Grant Agency - project VEGA 1/0191/24 and KEGA 004TUKE-4/2024.

Conflicts of Interest: The authors declare no conflict of interest.

References

1. Mínguez Martínez, A., Gómez Pérez, C., Pérez-Caballero, D. C., Carcedo Cerezo, L., & de Vicente y Oliva, J. (2020). Design of industrial standards for the calibration of optical microscopes. Materials, 14(01), 29.
2. Gill, C., Haynes, A., Justham, L., Dobrzanski, J., Buswell, R., Lohse, N., & Kinnell, P. (2025). A novel robot-assisted calibration procedure for Optical Coordinate Measuring Systems. Precision Engineering.
3. Yin, Y., Peng, X., Liu, X., Li, A., & Qu, X. (2012). Calibration strategy of optical measurement network for large-scale and shell-like objects. Optics Communications, 285(8), 2048-2056.
4. ISO 10360-7:2011 — Geometrical product specifications (GPS) — Acceptance and reverification tests for coordinate measuring machines (CMMs) equipped with imaging probing systems.
5. ASME B89.1.12M. Methods for Performance Evaluation of Optical Coordinate Measuring Systems. American Society of Mechanical Engineers.
6. VDI/VDE 2617 series. Accuracy of coordinate measuring machines. Verein Deutscher Ingenieure, Düsseldorf.
7. Mitutoyo America Corporation. (2016). Testing vision CMMs and the international standard, ISO 10360-7: Education – A technical presentation from the leading manufacturer of metrology instruments (Bulletin No. 2183, EDU-14004A-H). Mitutoyo.
8. Copeland, C. R., McGray, C. D., Ilic, B. R., Geist, J., & Stavis, S. M. (2021). Accurate localization microscopy by intrinsic aberration calibration. Nature Communications, 12(1), 3925.
9. Salsbury, J. G. (2016). Testing vision CMMs and the international standard, ISO 10360-7: Education: A technical paper from the leading manufacturer of metrology instruments [Tech. paper]. Mitutoyo America Corporation. Prezentované na NCSL International Workshop and Symposium, Sacramento, CA.
10. Zeiss Industrielle Messtechnik GmbH. (n.d.). ISO 10360-7: Guaranteeing precision for quality measurements [White paper]. Quality Magazine.
11. Schwarz-Müller, F., Marshall, R., Summerskill, S., & Poredda, C. (2021). Measuring the efficacy of positioning aids for capturing 3D data in different clothing configurations and postures with a high-resolution whole-body scanner. Measurement, 169, 108519.
12. Zhou, S., Xu, J., Lei, T., Yu, Y., & Ni, Y. (2019, December). An experimental evaluation method for the performance of multiple probes on coordinate measuring system. In AOPC 2019: Optical Sensing and Imaging Technology (Vol. 11338, pp. 183-189). SPIE.
13. Calvo, R., D'Amato, R., Gómez, E., & Domingo, R. (2016). Integration of error compensation of coordinate measuring machines into feature measurement: Part I—model development. Sensors, 16(10), 1610.
14. ISO 10360-2:2009. Geometrical product specifications (GPS) — Acceptance and reverification tests for coordinate measuring machines (CMMs) — Part 2: CMMs used for measuring linear dimensions. International Organization for Standardization, Geneva.
15. ISO 10360-5:2010. Geometrical product specifications (GPS) — Acceptance and reverification tests for coordinate measuring machines (CMMs) — Part 5: CMMs using single and multiple stylus contacting probing systems. International Organization for Standardization, Geneva.
16. Lai, T., Peng, X., Tie, G., Liu, J., & Guo, M. (2017). High accurate squareness measurement squareness method for ultra-precision machine based on error separation. Precision Engineering, 49, 15-23.
17. Rodriguez-Ibanez, D., Alonso, J., & Quiroga, J. A. (2013). Squareness error calibration of a CMM for quality control of ophthalmic lenses. The International Journal of Advanced Manufacturing Technology, 68(1), 487-493.
18. Graticules Optics. (n.d.). Scales and Calibration Standards: Brochure Graticules Optics [PDF].

19. Mínguez Martínez, A., & de Vicente y Oliva, J. (2019). Industrial calibration procedure for confocal microscopes. Materials, 12(24), 4137.
20. Meli, M., Paulus, A., & Christen, T. (n.d.). Calibration of Photomasks for Optical Coordinate Metrology.
21. Zeiss Metrology (2023). Calibration Reference Standards.

TECHNICAL UNIVERSITY OF KOŠICE
Faculty of Mechanical Engineering

Communication Layer Compatibility in Cross-Generation ROS Systems

Marek Málik [1,*], Rudolf Jánoš [1]

[1] Technical University of Košice, Department of Production Technology and Robotics, Park Komenského 8, 042 00 Košice; marek.malik@tuke.sk; rudolf.janos@tuke.sk
* Correspondence: marek.malik@tuke.sk

Abstract: The migration from ROS 1 to ROS 2 presents a significant challenge for many robotic platforms, especially when direct version compatibility is not officially supported. This study investigates the feasibility of establishing bidirectional communication between ROS 1 Melodic and ROS 2 Humble using the ros1_bridge tool in a non-standard configuration. The experimental setup involved the JetAuto mobile robot, originally operating under ROS 1, and its virtual twin in Gazebo under ROS 2. Due to the lack of official support for the Melodic–Humble pair, ROS 1 Noetic was employed as a compatible runtime layer to align message definitions and communication interfaces. Our methodology focused on custom-compiling ros1_bridge against both ROS 2 Humble and the adjusted ROS 1 Noetic environment, followed by rigorous verification of message-type consistency. The results demonstrate that core sensor and control topics with identical data structures—such as laser scans and velocity commands—were successfully bridged. However, complex or custom message types remained incompatible without manual conversion. The study also identified configuration-related limitations, such as private namespaces restricting data visibility.These findings confirm that a structured, interface-first approach can enable functional interoperability between non-standard ROS versions, providing a practical pathway for incremental system migration.

Keywords: ROS 1, ROS 2, ros1_bridge, Mobile robotics, JetAuto

1. Introduction

Migration from ROS 1 to ROS 2 currently represents one of the key research topics in the field of robotic software architectures. ROS 2 was designed as a modernized platform that addresses the limitations of ROS 1, particularly in the areas of scalability, real-time processing, and distributed robotic systems. Its core is the transition to the Data Distribution Service (DDS), which introduces support for QoS profiles, reliable communication, and robust deployment in multi-robot environments [1]. Despite these advantages, ROS 1 Noetic remains dominant in many industrial and research applications, and a full migration is often complicated due to dependencies on legacy packages, missing software ports, and the risks associated with rewriting existing systems [2]. One of the most widely used methods for incremental migration is ros1_bridge, a tool enabling bidirectional communication between ROS 1 and ROS 2 systems [6]. The bridge functions as a dynamic message translator, automatically mapping messages of the same type in both versions. However, the literature highlights its limitations – particularly differences in message type definitions, increased latency, hardware requirements, and the lack of support for certain specialized ROS 1 packages [7–9]. Furthermore, ros1_bridge officially supports only specific, well-defined version combinations of ROS 1 and ROS 2, which limits its usability in heterogeneous systems.

In this study, we focus on experimentally bridging ROS 1 Melodic and ROS 2 Humble Hawksbill on the JetAuto mobile platform. Since Melodic and Humble do not represent

an officially supported combination, it was necessary to use a modified version of ROS 1 Noetic compatible with the communication mechanisms of ROS 2 Humble. This minimized type differences and enabled successful bridging of foundational topics.

The experiment was implemented on the physical JetAuto platform (ROS 1) and its virtual twin in Gazebo (ROS 2), allowing for the analysis of topic transmission, visibility, and consistency in both real and simulated environments.

The objective of this paper is to verify the practical feasibility of such a non-standard bridge, identify its limitations, and discuss the suitability of this method for the incremental migration of mobile robotic systems.

2. Materials and Methods

In this work, we used the JetAuto mobile robotic platform as the primary experimental system. JetAuto is a compact differential-drive robot equipped with a robust set of sensors and computing hardware, making it suitable for research in autonomous navigation, SLAM, and robot–sensor integration. The platform features a Slamtec A1 2D LiDAR, which provides laser scans for localization and mapping, and an Orbbec FHD-1080P Astra Pro Plus depth camera capable of delivering both RGB images and 3D point clouds. The sensing hardware enables reliable perception of the surrounding environment and supports the evaluation of multimodal SLAM algorithms.

JetAuto utilizes a four-wheel differential chassis powered by two motor units on each side, allowing precise control of linear and angular motion in both simulated and real-world conditions. As the main computing unit, the platform integrates an NVIDIA Jetson Orin 4 GB module, optimized for parallel processing and real-time execution of ROS-based robotic pipelines. This hardware configuration allows us to run ROS 1 and ROS 2 nodes concurrently, which is essential for testing interoperability and communication between both middleware versions.

A virtual model of the platform was also deployed in the Gazebo simulator, providing an identical configuration of sensors and kinematics. The availability of both real and simulated environments makes JetAuto a suitable platform for evaluating hybrid ROS 1/ROS 2 communication, validating algorithm behavior, and analyzing differences between simulated and physical robot performance. [10]

Figure 1. Hiwonder JetAuto.

2.1.Softwer

In the experiment, three robotic software systems were used—ROS 1 Melodic (the robot's native environment), ROS 1 Noetic (employed as a compatible intermediate environment for establishing the bridge), and ROS 2 Humble. The primary objective was to verify the connectivity possibilities between ROS 1 and ROS 2 using the ros1_bridge tool in a configuration that is not officially supported for ROS 2 Humble.

ROS 2 Humble

ROS 2 Humble Hawksbill is a long-term supported (LTS) version based on the Data Distribution Service (DDS) architecture with the ROS Middleware (RMW) layer. This version provides mechanisms for QoS profiles, reliable discovery, multi-robot systems, and better modularity compared to ROS 1. Within the ROS 2 environment, a simulation JetAuto stack was created in Gazebo, and ROS 2 packages were migrated to serve as a test platform for validating hybrid communication between ROS 1 and ROS 2.

ROS 1 Noetic as a Bridge-Compatible Runtime

The JetAuto platform originally operates under ROS 1 Melodic. A direct bridge between ROS 1 Melodic and ROS 2 Humble using ros1_bridge is not feasible due to significant disparities in their underlying communication libraries and core message definitions. The official ros1_bridge is compiled and validated only for specific version pairs (e.g., Noetic–Foxy, Noetic–Galactic) [8-9].

Our approach is inspired by the fundamental requirement of ros1_bridge: to function, it requires type-identical message definitions on both the ROS 1 and ROS 2 sides [9]. Since ROS 1 Noetic is the final release of ROS 1 and shares a more modern codebase and message definition lineage with ROS 2 Humble (compared to Melodic), it was selected as a bridge-compatible runtime. The hypothesis was that by using Noetic's communication stack and aligning its build environment with Humble, we could create a compatible interface layer. This method aligns with the incremental migration paradigm suggested in literature, where creating a unified interface layer is a critical step [2-5]. It is important to note that the Noetic–Humble pair is not officially validated, making this an experimental verification of compatibility under non-standard conditions.

ros1_bridge Configuration and Compilation

The ros1_bridge tool enables dynamic, bidirectional message conversion between ROS 1 and ROS 2. It automatically generates bridges for topics and services, but only if:

- The message definitions are byte-for-byte identical in both environments,
- The bridge is compiled against both specific ROS 1 and ROS 2 distributions simultaneously [8].

Given the absence of an official Melodic–Humble bridge, our procedure was as follows:

1. Environment Setup: A unified workspace was prepared containing both ROS 1 Noetic and ROS 2 Humble installations.
2. Source Alignment: Both ROS distributions were sourced, and ros1_bridge was compiled against ROS 2 Humble and the adjusted ROS 1 Noetic environment, ensuring the same set of common message packages (std_msgs, geometry_msgs, sensor_msgs, etc.) were available and identical.
3. Type Verification: Message definition consistency was rigorously checked using rosmsg show (ROS 1) and ros2 interface show (ROS 2) for all core message types used by the JetAuto platform.
4. Bridge Deployment & Testing: The compiled bridge node was launched, creating a proxy that translated messages between the ROS 1 Noetic runtime (which itself communicated with the native ROS 1 Melodic robot nodes) and the ROS 2 Humble ecosystem.

This method created a functional, albeit indirect, communication channel: ROS 1 Melodic (Robot) ↔ ROS 1 Noetic (Bridge Runtime) ↔ ROS 2 Humble (Development/Simulation). This setup allowed us to test the practical limits of cross-version interoperability where direct, official tooling is unavailable.

3. Results

The experiment verified which data flows could be successfully bridged between ROS 1 Noetic and ROS 2 Humble using the compiled ros1_bridge and which remained incompatible without additional conversion. Testing was performed both in simulation and on the physical JetAuto platform, focusing on three topic groups: sensors, motion control, and odometry data.

3.1. Network Setup and Bridge Initialization

Following the environment preparation described in Section 2.1, the first step was to establish a network connection between the ROS 2 Humble workstation and the JetAuto unit running ROS 1 Melodic via the Noetic bridge runtime. The internal platform network was used, requiring proper permission configuration on the workstation to access ROS 1 services.

Initial attempts to compile and run ros1_bridge within a Docker container failed due to workspace incompatibility and issues with sourcing both ROS versions. Therefore, a direct compilation on the host system was performed, using a ROS 1 Noetic runtime compatible with ROS 2 Humble. This allowed successful initialization of the bridge on both ends and configuration for mutual communication over the shared network.

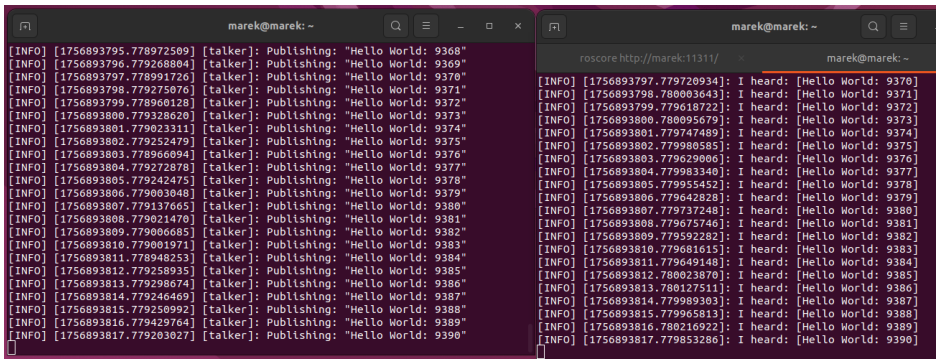

Figure 2. Network connectivity test between the ROS 2 workstation and the JetAuto platform.

3.2. Topic Discovery and Bridging

After successfully launching the bridge, all available ROS 1 topics published by the JetAuto platform became visible from the ROS 2 workstation. A manual check confirmed that the majority of foundational topics (e.g., /scan, /odom, /cmd_vel) were correctly listed and bridged, as shown in Figure 3.

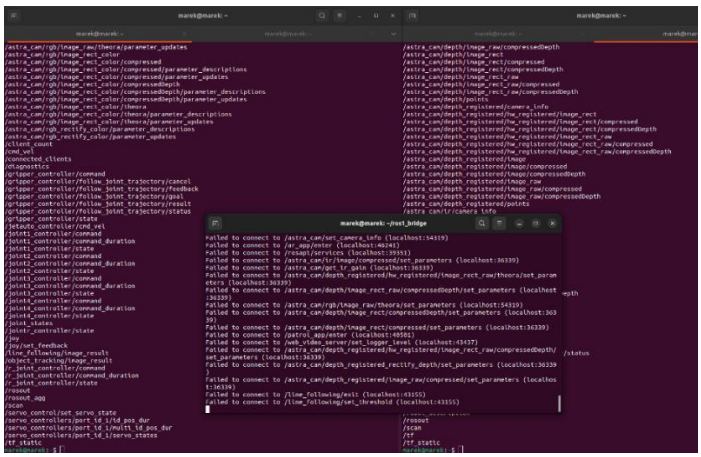

Figure 3. Topic list successfully transferred from ROS 1 Noetic to ROS 2 Humble via ros1_bridge.

The specific output of dynamica, showing autogenerated bridge topics for successfully matched message types, is best illustrated in Figure 4. This output confirms the ability of the translation layer for those messages that met the type identity condition.

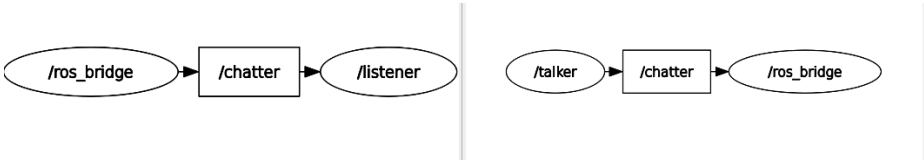

Figure 4. Output of a running ros1_bridge node, showing automatically created bridges for compatible themes.

More complex topics with different message definitions (e.g. some camera-related topics or custom messages) were not dynamically bridged, which is consistent with known limitations of ros1_bridge and are missing from this listing. In a few cases, the topics were visible, but the data being transferred was empty - likely due to the use of private namespaces or limited publishing settings in the JetAuto ROS 1 configuration.

4. Discussion

The experimental results confirm that bidirectional communication between ROS 1 and ROS 2 using ros1_bridge is feasible even for a non-official distribution pair such as ROS 1 Noetic and ROS 2 Humble. This work demonstrates that with careful environment configuration—particularly the use of a compatible ROS 1 runtime—core topics can be successfully bridged, enabling functional interoperability during a transitional migration phase.

The observed compatibility was primarily achieved for standard message types with identical definitions in both ROS versions, such as LaserScan and Twist. This aligns with the fundamental design of ros1_bridge, which relies on type equality for dynamic bridge generation [9]. Conversely, more complex or custom message types—particularly those involving multi-array structures, transformed timestamps, or non-standard QoS settings—were not bridged automatically. This limitation is consistent with findings from other migration studies, which note that ros1_bridge alone is insufficient for translating semantically rich or middleware-specific data flows [5, 8]. In such cases, manual conversion nodes or intermediate repackaging of messages would be required.

An important methodological insight from this study is the viability of using ROS 1 Noetic as a bridge-compatible runtime for platforms originally built on older ROS 1 distributions like Melodic. Although not officially supported, this approach effectively unified the communication interface enough to allow bridging with ROS 2 Humble. This suggests that in incremental migration scenarios, runtime alignment can be a practical alternative to full package porting, especially when legacy systems cannot be immediately upgraded.

Furthermore, the experiment revealed that certain topics, though visible in the ROS graph, transmitted empty data when bridged. This is likely attributable to the use of private namespaces or restricted publication settings within the original JetAuto ROS 1 driver—a configuration not uncommon in production robotic systems [2]. Such behavior underscores the importance of not only message-level compatibility but also node-level publication policies when designing hybrid ROS 1/ROS 2 architectures.

From a systems perspective, the study supports the view that ros1_bridge can serve as a useful transitional tool in a phased migration strategy, allowing newer ROS 2 modules to coexist and interact with stable ROS 1 components. However, its limitations must be accounted for in planning: teams should anticipate additional development effort for custom message translation and node adaptation, particularly for perception, transformation, or real-time control topics.

Finally, the current work is qualitative and focused on connectivity verification. Planned quantitative analysis—especially latency measurements across the bridge—will provide deeper insight into the performance trade-offs introduced by this interoperability layer and help determine its suitability for time-sensitive applications.

In summary, this experiment reinforces that migration from ROS 1 to ROS 2 is not merely a software upgrade but a systems integration challenge. Successful bridging depends on message definition alignment, runtime configuration, and node-level communication behavior. The approach taken here offers a pragmatic pathway for platforms like JetAuto to gradually adopt ROS 2 without requiring a full and immediate rewrite of existing functional stacks.

5. Conclusions

This contribution presented the initial phase of ongoing work focused on enabling ROS 2-based control and simulation for the Hiwonder JetAuto mobile robot platform, originally designed for ROS 1 Noetic. By analyzing the communication interfaces and unifying message definitions, we established a bridgeable and specification-consistent foundation that allows ROS 2 Humble nodes to interact with the original ROS 1 functionality. The migration of core interface packages and the preparation of a mock SDK enabled early-stage integration with Gazebo simulation, providing a hardware-independent environment for further development.

The results indicate that a structured migration approach—starting with interface extraction, protocol alignment, and simulation-ready drivers—can significantly reduce the complexity typically associated with ROS 1 to ROS 2 transitions. Future work will focus on completing the migration of the full JetAuto driver, implementing SLAM and navigation pipelines in ROS 2, and validating the full robotic stack both in simulation and on the physical platform.

Acknowledgments: This research was supported by project VEGA 1/0215/23 Research and development of robotic workplaces equipped with industrial and collaborative robots, KEGA 043TUKE-4/2024 - Creation of prospective educational tools for the field of additive manufacturing with the implementation of progressive elements of virtual reality.

References

1. Maruyama, Yuya & Kato, Shinpei & Azumi, Takuya. (2016). Exploring the performance of ROS2. 1-10. 10.1145/2968478.2968502.
2. Yoon, Y.; Kim, H.; Lee, D. Evaluation of Real-Time Performance in ROS 2 for Industrial Applications. In Proceedings of the 18th International Conference on Control, Automation and Systems (ICCAS), Jeju, South Korea, 17–20 October 2018; IEEE: Jeju, South Korea, 2018
3. Macenski, S.; Martín, F.; White, R.; Ginés, J. The New Generation of ROS: Why ROS 2? *IEEE Robotics & Automation Magazine*, 2022
4. Cruz, P.; Monteiro, D.; Almeida, L.; Fonseca, P. Latency and Overhead Analysis of ROS 1 and ROS 2 in Distributed Systems. *Journal of Open Source Software*, accepted.
5. Ekumen Labs. Practical Considerations in ROS 1 to ROS 2 Migration. Personal communication, 2021
6. Quigley, M.; Gerkey, B.; Smart, W.D. ROS: An Open-Source Robot Operating System. In *Proceedings of the ICRA Workshop on Open Source Software*, Kobe, Japan
7. eProsima. DDS Middleware Architecture and Its Integration in ROS 2. Available online: https://www.eprosima.com (accessed on 1 December 2025).
8. Open Robotics. ros1_bridge Documentation. Available online: https://docs.ros.org (accessed on 1 December 2025).
9. GitHub Organization: ROS 2. ros1_bridge — Known Limitations and Type Compatibility. Available online: https://github.com/ros2/ros1_bridge (accessed on 1 December 2025).
10. Hiwonder. **JetAuto Mobile Robot Platform**. Available online: https://www.hiwonder.com/products/jetauto (accessed on 1 December 2025).

TECHNICAL UNIVERSITY OF KOŠICE
Faculty of Mechanical Engineering

Sound Generator Selection for Musical Tesla Coils

Damian Pytka [1], Maksymilian Maślanka [1,*] and Mateusz Waluszek [1]

[1] University of Bielsko-Biała; dpytka@ubb.edu.pl; mmaslanka@ubb.edu.pl; mwaluszek@ubb.edu.pl
* Correspondence: mmaslanka@ubb.edu.pl;

Abstract: The study evaluates audio-generation techniques for a solid-state Tesla coil driven by aClass-E amplifier. A compact coil was designed, validated using JavaTC and made using 3D printed components. A dedicated ATmega328P-based synthesizer replaced the traditional line input interrupter to improve sound loudness and clarity. Three methods were tested: PWM modulated audio input, wavetable synthesis and direct phase- and frequency-correct PWM. Carrier-based modulation and amplitude scaling reduced arc conduction time, producing weak output dominated by spark noise. Wavetable synthesis suffered from insufficient interrupt throughput, causing waveform distortion and unstable arc formation. The direct PWM method delivered the strongest performance. By maintaining continuous conduction without an ultrasonic carrier, it produced a longer and more stable arc, resulting in significantly louder and clearer sound despite being limited to monophonic square waves. Results indicate that audio quality in Tesla-coil systems is constrained primarily by arc physics rather than waveform complexity. Effective sound production depends on sustaining a stable, energetic discharge rather than reproducing detailed digital timbres. The system, housed in a Faraday cage, also serves as a platform for future RF-interference studies and planned multi-coil experiments targeting broader resonance-range evaluation.

Keywords: Tesla coil, Class-E driver, MIDI synthesizer, wavetable synthesis, PWM audio

1. Introduction

The Tesla coil is an air-cored resonant transformer designed to produce electric currents through electromagnetic induction. Patented and first built by Nikola Tesla in 1891, it remains one of his most iconic inventions. Tesla coils generate high-frequency, high-voltage alternating currents, reaching frequencies of up to 12 million hertz and voltages as high as 20 megavolts [1, 2].

In our implementation, the primary of the transformer is driven using solid-state electronics. We selected a Class-E RF power amplifier due to its simplicity and low component count. Unlike feedback-based oscillator designs, this type of Tesla coil driver requires manual tuning to match the coil's resonant frequency. The absence of feedback also allows multiple coils to operate near one another without interference. The circuit includes an enable signal that can pulse the coil in sync with an audio input, allowing sound to be produced directly from the high-voltage discharge [3,4].

The standard method for playing music through a Tesla coil involves a line-input interrupter. Similar to a Class-D amplifier, it converts the audio signal into a PWM waveform with an ultrasonic carrier, which then modulates the coil's spark output [5-7].

This paper explores the selection of an audio generator tailored specifically for musical Tesla coil applications. Instead of a line-input interrupter, we introduce a dedicated sound synthesizer. Our research concentrated on improving loudness and sound fidelity for a single coil and driver design. The resulting system integrates a synthesizer with the coil, offering compatibility with the widely used electronic music protocol, MIDI.

2. Materials and Methods

An ATmega328P microcontroller was selected as the development platform for the synthesizer. The primary reasons for this choice were the ease of initial prototyping within the Arduino ecosystem and the low cost of producing later hardware revisions.

Communication between the host and the synthesizer is handled via the MIDI protocol, which operates over a UART interface at the hardware level (see **Figure 1)**. MIDI was chosen for its straightforward implementation and its broad compatibility with existing music software and hardware. Standard MIDI files, which store musical information such as note sequences, can be readily adapted for playback on the synthesizer.

Figure 1. Simplified block diagram of musical circuitry.

The first audio-generation technique implemented is wavetable synthesis. This method uses two hardware timers to create the output waveform. One timer provides a PWM signal at an ultrasonic frequency, while the second timer issues periodic interrupts according to the following interval:

$$t = \frac{1}{s \cdot f} \tag{1}$$

Where:

- t – time interval,
- s – sample rate,
- f – frequency of the desired output wave.

Sample rate of 32 samples per period was chosen as a compromise between sound fidelity and range of possible frequencies that can be achieved.

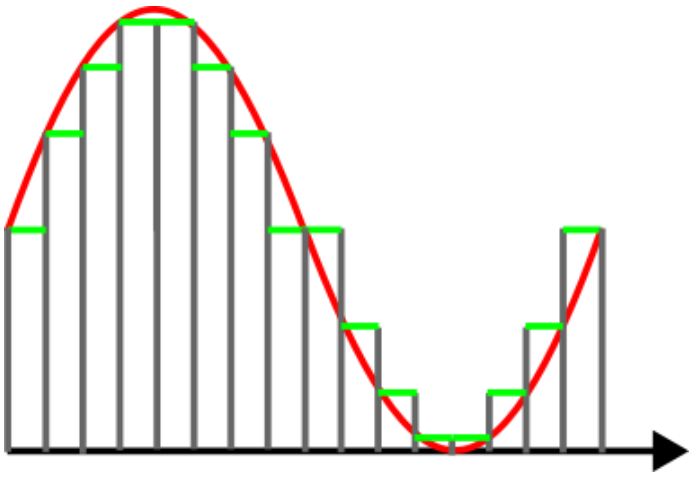

Figure 2. Sine wave represented as 16 samples.

A sample rate of 32 samples per waveform cycle was selected as a balance between sound quality and the frequency range achievable by the system. This approach resembles conventional audio generation techniques that rely on an ultrasonic carrier signal. With wavetable synthesis, any arbitrary waveform can be represented, and output volume can be adjusted by scaling the waveform amplitude within the table.

The second audio-generation method uses a hardware timer configured in phase- and frequency-correct PWM mode. By modifying the timer's compare registers, both the

output frequency and pulse width can be controlled. This technique produces only square waves, with timbre determined exclusively by the pulse-width parameter. Because it does not require periodic interrupts, more processing time is available for communication tasks and signal modulation. In this mode, the audio level can be adjusted only by varying the input voltage supplied to the driver circuit.

As part of this project a compact Tesla coil was constructed. All structural components were designed and fabricated using 3D-printing technology. The toroidal topload was additionally wrapped with conductive aluminum tape and installed to reduce the resonant frequency of the secondary coil winding. The technical parameters of the coil are summarized in the table below.

Table 1. Tesla coil technical parameters.

Parameter	Value
Primary winding diameter	89 mm
Primary winding turns	4
Secondary winding diameter	41.25 mm
Secondary winding height	155 mm
Secondary winding turns	775
Torus major diameter	100 mm
Torus minor diameter	30 mm
Calculated resonant frequency	814 kHz

Additionally, the design was validated prior to fabrication using the free JavaTC software (see **Figure 3**), which computes the electrical parameters of Tesla coils. This tool enabled verification of the expected resonant behavior and ensured that the constructed system would operate within the intended frequency range.

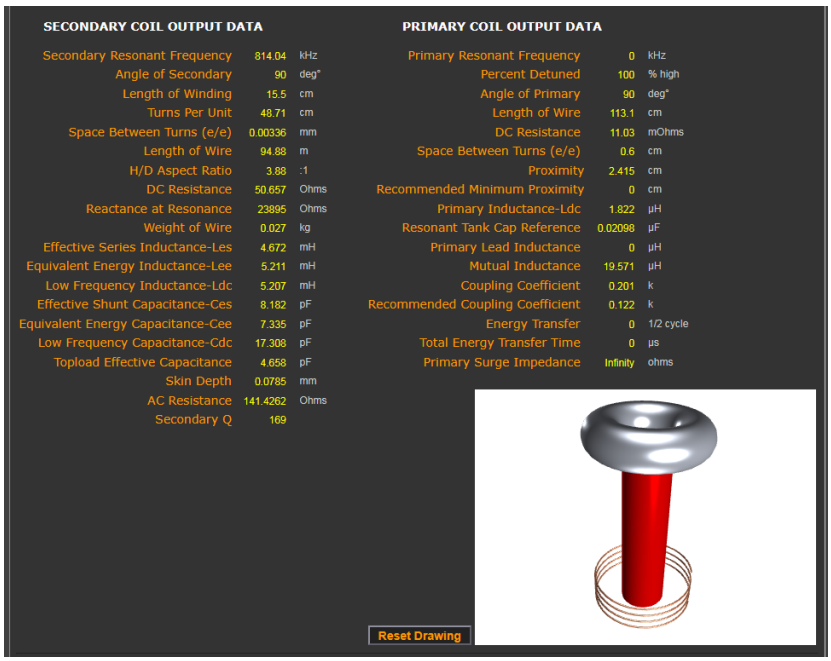

Figure 3. Tesla coil parameters calculated in JavaTC program.

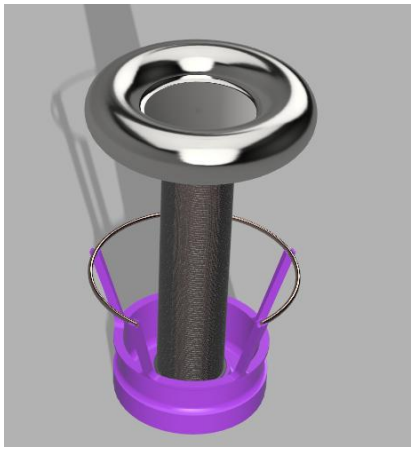

Figure 4. Render of final model of Tesla coil.

3. Results

In practice, the conventional line-input interrupter method produced low-fidelity audio and relatively quiet output. Musical content was often masked by the inherent sizzle of the Tesla coil's spark. Although simple waveforms such as sine waves were somewhat more audible, they remained weak. Further improvement of this method may be possible through the use of dedicated Class-D amplifier integrated circuits.

The wavetable-based waveform generation approach exhibited many of the same shortcomings. Non-square waveforms were noticeably distorted and lacked clarity, and achieving acceptable fidelity would require a faster microcontroller to support higher sample rates. Additionally, the volume-control capability provided by this method proved ineffective in practice: reducing the signal amplitude below roughly 70% caused the coil to produce only a sizzle rather than a stable audible tone, as the spark was interrupted too rapidly to generate sound.

The final method yielded the strongest performance among all approaches tested. By eliminating the ultrasonic carrier that interrupts the signal, the spark duration increased, resulting in significantly improved sound output. Although this technique produces less varied, monophonic audio, its expressiveness can be enhanced by incorporating features such as arpeggiation and smooth note transitions into the synthesizer.

4. Discussion

The experimental results demonstrate that audio generation for Tesla coil systems is constrained primarily by the physical mechanisms of arc formation rather than by the digital synthesis method itself. Each technique used to drive the primary circuit directly influences the arc's duration, stability, and effective energy transfer, which collectively determine the loudness and perceptual clarity of the produced sound. The line-input interrupter approach illustrates the limitations of carrier-based modulation. Introducing an ultrasonic switching frequency reduces the average conduction time of the primary switch, resulting in an arc that is too short and unstable to produce a strong acoustic output. Although the waveform is modulated correctly from an electrical standpoint, the acoustic response is dominated by the reduced energy delivered per cycle rather than by the fidelity of the digital signal. The same limitation is evident in the wavetable-based method. Even when the waveform is accurately synthesized, the ATmega328P does not provide sufficient interrupt throughput to sustain high sample rates without degrading system stability. Consequently, the non-square waveforms become distorted, and the reduced average drive level leads to weak or inconsistent arc formation.

In contrast, the phase- and frequency-correct PWM method maintains continuous conduction during tone generation. By eliminating the ultrasonic carrier, the driver sus-

tains a longer and more stable discharge, which directly increases acoustic output. Although this method inherently restricts the synthesizer to square-wave timbres and monophonic operation, it affords significantly better energy transfer and avoids the processing overhead associated with timed interrupt-driven synthesis. The improvement in loudness arises not from superior digital representation but from more efficient coupling of electrical power into the plasma channel.

From an instrumentation perspective, the superior performance of the pure square-wave technique therefore stems from fundamental physical constraints. In musical Tesla coils, the primary determinant of sound quality is the duration and stability of the arc, not the harmonic complexity of the synthesized waveform. Any method that reduces conduction time—whether through high interrupt load, amplitude scaling, or high-frequency modulation—inevitably diminishes acoustic output.

Future improvements in synthesis fidelity would require either a substantially faster microcontroller or a power stage capable of maintaining continuous arc formation under high-rate modulation. Within the limits of the present hardware, the PWM-based approach without an ultrasonic carrier provides the most effective balance of volume, stability, and implementation simplicity.

5. Conclusions

Selecting a phase- and frequency-accurate PWM audio generator produced the highest audio quality for our specific Tesla coil setup. Although dedicated timbre control was limited, we compensated using additional pulse-width adjustments. The monophonic output was enriched through fast arpeggiation and fluid note transitions, which can be enabled or disabled via the MIDI protocol.

The constructed Tesla-coil test platform enclosed within a Faraday cage is intended not only for audio demonstrations but also for controlled RF disturbance studies. The enclosure will provide an isolated electromagnetic environment, enabling repeatable measurements of radiated interference and its effects on electronic devices placed inside the cage.

In future work, multiple coils with different resonant frequencies are planned for integration into the system. Operating coils at distinct resonance points will allow targeted exploration of RF susceptibility across a wider spectral range. By selecting coils with appropriately spaced resonances, the test bench can evaluate how specific frequency bands influence the behavior, stability, and failure modes of sensitive electronic circuits. This modular approach will extend the platform from a single-application demonstrator into a versatile tool for examining RF coupling mechanisms, immunity characteristics, and interference pathways in controlled laboratory conditions.

Conflicts of Interest: The authors declare no conflict of interest.

References

1. S. Skok, L. Havaš, T. Horvat, and A. Šumiga, “TESLA COIL – CONSTRUCTION PROJECT – EDUCATIONAL APPLICATION,” in EDULEARN22 Proceedings, in 14th International Conference on Education and New Learning Technologies. Palma, Spain: IATED, Jul. 2022, pp. 6504–6510. doi: 10.21125/edulearn.2022.1538.
2. N. Tesla, Colorado Springs Notes, 1899–1900, Beograd, Yugoslavia: Nolit / Zavod za udžbenike i nastavna sredstva, 1978/1999. ISBN: 0-913022-26-8.
3. N. O. Sokal, “Class-E RF power amplifiers,” Qex, vol. 204, no. 1, pp. 9–20, 2001.
4. N. O. Sokal and A. D. Sokal, "Class E-A new class of high-efficiency tuned single-ended switching power amplifiers," in *IEEE Journal of Solid-State Circuits*, vol. 10, no. 3, pp. 168-176, June 1975, doi: 10.1109/JSSC.1975.1050582.
5. N. Tanwar, M. R. Kumar, and R. C. Naidu, “Design of Solid State Tesla Coil With Music Playback Functionality,” IEEE Access, vol. 12, pp. 14285–14297, 2024, doi: 10.1109/ACCESS.2024.3357534.
6. N. Teraguchi and M. Minami, “Development of musical solid-state Tesla coil based on pulse repetition frequency method,” Electronics and Communications in Japan, vol. 102, no. 8, pp. 11–16, 2019, doi: https://doi.org/10.1002/ecj.12196.
7. P. Horowitz and W. Hill, The Art of Electronics, 3rd ed. Cambridge, U.K.: Cambridge University Press, 2015.

TECHNICAL UNIVERSITY OF KOŠICE
Faculty of Mechanical Engineering

Methodology of Design and Simulation Verification of the Air Force TUKE Pneumatic Drive

Jaroslav Melko [1,*], Rudolf Jánoš [1], Dušan Mlinarček [1], Jakub Brna [1]

[1] Technical University of Košice, Department of Production Technology and Robotics, Park Komenského 8, 042 00 Košice; jaroslav.melko@tuke.sk; rudolf.janos@tuke.sk; dusan.mlinarcek@tuke.sk; jakub.brna@tuke.sk
* Correspondence: jaroslav.melko@tuke.sk

Abstract: The paper presents a methodology for the design and simulation verification of an innovative pneumatic drive developed within the Air Force TUKE project. The main objective of the research is the transformation of theoretical thermodynamic principles into a comprehensive dynamic model in the MATLAB/Simulink environment, serving as a digital twin of a competition Pneumobil vehicle. The contribution of the paper lies in the systematic integration of nonlinear gas flow dynamics, polytropic expansion, and mechanical resistances in the form of inertia and friction. The proposed model, implemented using the Simscape Fluids library, enables accurate prediction of the behavior of the power unit with linear actuators and a rack-and-pinion transmission at an operating pressure of 0.6 MPa. Simulation results confirm the stability of pressure control and provide key data for optimizing the valve timing strategy in order to maximize energy efficiency and vehicle range. The presented methodology represents an effective engineering tool that reduces the time and economic demands of the mechatronic system development cycle.

Keywords: Pneumobil, compressed air, MATLAB/Simulink, digital twin, Air Force TUKE, CAE simulation

1. Introduction

The current trend in mobility is strongly determined by efforts toward transport decarbonization and the search for alternative ecological propulsion systems. Alongside dominant electromobility, technologies utilizing compressed air as a low-emission energy carrier are gaining attention. Vehicles powered by compressed air are primarily developed in academic environments within international engineering competitions and represent an ideal platform for researching the efficiency of transforming pressure energy into mechanical work under strict technical constraints.

The main challenge in designing such vehicles is the low energy density of compressed air, which requires an extremely precise approach to powertrain design. Traditional solutions based on modified internal combustion engines often exhibit low efficiency due to improper timing and mechanical losses of the crank mechanism. Therefore, this paper focuses on describing a design methodology that combines an unconventional mechanical configuration (rack-and-pinion transmission) with advanced system simulation in a CAE environment.

The main contribution of the work lies in the implementation of the Digital Twin method into the design process. This approach allows for exact prediction of the dynamic behavior of the power unit even before its physical implementation. The methodology integrates nonlinear gas flow dynamics, thermodynamic changes in the actuator cham-

bers, and kinematic couplings of motion transformation. The aim of the paper is to demonstrate that by using the proposed methodology, it is possible to significantly optimize the consumption of the working medium and increase the vehicle range while maintaining the required dynamics.

2. Materials and Methods

The issue of pneumatic drives is closely related to the thermodynamics of expansion processes. In real operation, air expansion occurs between isothermal and adiabatic states, which we classify as a polytropic process. The effectiveness of this process is limited in practice by "dead volumes " in the distribution and the timing of valve opening.

Previous design solutions have shown the potential of using rectilinear cylinders, but there was no comprehensive methodology for connecting the mathematical model with real driving cycles. In the article, the author builds on these foundations and extends them with his own simulation algorithms in the MATLAB/Simulink environment, which allow independent control of the filling and exhaust of both chambers of a double-acting cylinder. This approach is key to achieving the energy balance of the system at a limited pressure of 0.6 MPa (6 bar), which is the standard for competition conditions [2].

The proposed methodological approach to the design of the power unit is based on the "Top-Down" principle, where the parameters of individual components are optimized based on the dynamic requirements of the entire system. The core of the proposed methodology is a mathematical model that considers compressed air as a real gas subject to polytropic changes in both closed and open systems.

For accurate simulation of piston motion, the equation of motion is implemented in the model, which takes into account the imbalance of forces acting on the piston surfaces and the effect of friction:

$$m_{red} \cdot \ddot{x} = (p_1 S_1 - p_2 S_2) - F_t - F_z \tag{1}$$

where m_{red} represents the reduced mass of the moving parts (piston, piston rod, rack),, p_1,p_2 are instantaneous pressures in the chambers, F_t represents the nonlinear friction component defined using the Stribeck curve, and F_z is the load force.

The benefit of this model is the inclusion of dynamic changes in chamber volume, which directly affects the pressure gradient.

The pressure change in the actuator chambers is not modeled as a static increase, but as a differential equation based on the first law of thermodynamics. The actual contribution in this area lies in the precise definition of the flow coefficients of the valves, which limit the maximum piston speed:

$$\frac{d_p}{d_t} = \frac{\kappa}{V}\left(R \cdot T \cdot \dot{m} - p \cdot \dot{V}\right) \tag{2}$$

where:
κ- adiabatic exponent
V- chamber volume
R - gas constant of air
T - air temperature

This relationship allows simulating the phenomenon of engine "choking" at high switching frequencies, when the flow cross-sections of the valves are unable to fill or empty the actuator chambers.

In the first phase, geometric parameters are defined based on a static calculation for peak load. Subsequently, a dynamic simulation is performed, where air consumption is monitored depending on the valve timing strategy. The modification of the control logic of the 5/3 valve in the model allows the simulation of three states: filling, expansion and exhaust. It is the introduction of the expansion phase (closing both chambers before the

end of the stroke) that represents a significant contribution to saving the working medium, which is demonstrated in the following chapters of the article through comparative simulations.

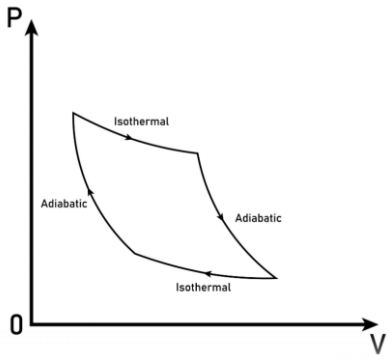

Figure 1. P-V diagram of compressed air expansion.

3. Simulation Model Description

The key benefit of the presented methodology is the creation of a connection between the nonlinear pneumatic part and the dynamic mechanical load. In the Simscape Fluids environment, we used multi-domain modeling, where energy transfer occurs between the gaseous medium and the solid body through the actuator interface.

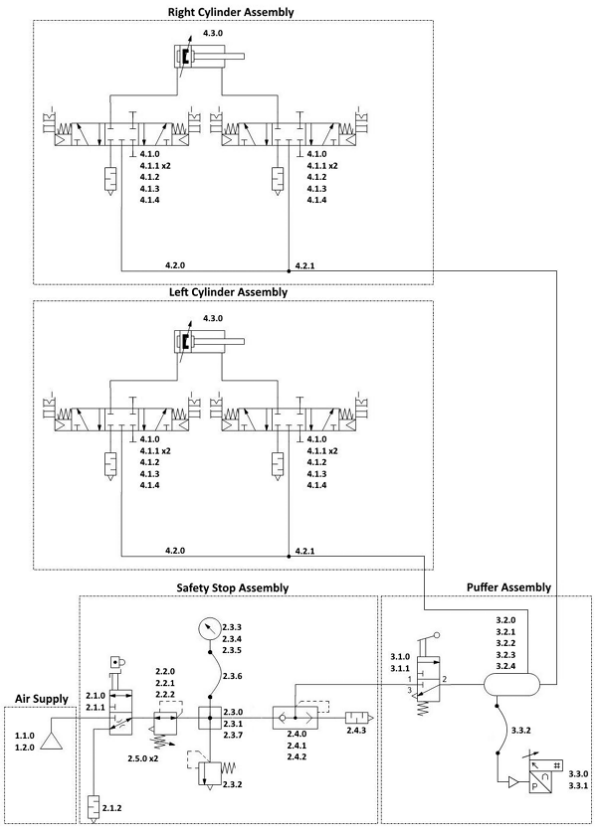

Figure 2. Diagram of the pneumatic circuit of the airmobile engine.

After building the simulation model in the MATLAB/Simulink environment (Fig. 3), a dynamic analysis with a solver time step was launched. Simulink itself needed further extensions, namely Simscape and Simscape Fluids, the blocks of which were used to create the simulated scheme. The model was divided into four parts, identically to the pneumatic

scheme in Fig. 2. The scheme solves the logic of controlling a 4/3 valve. A block with four gas ports (P, A, B and T) and flow paths between P–A and A–T and between P–B and B–T. The valve starts in the middle position. An input port S for the control signal is located on its block. If we apply ,,1, to the input, the valve will open the paths P-A and B-T, if we apply ,,-1, to the input, it will open the paths P-B and A-T. The drive itself has an output signal about its current position, so we built the logic on comparing the output position signal with constants that represent the end positions with hysteresis. If the comparison condition was met, the logic unit opened the switch and released the constant 1 or -1. The input signal to the switch was additionally treated by the Set – Reset block. And at the end of the logic circuit there was a Unit Delay block that held the signal and prevented the formation of an algebraic loop.

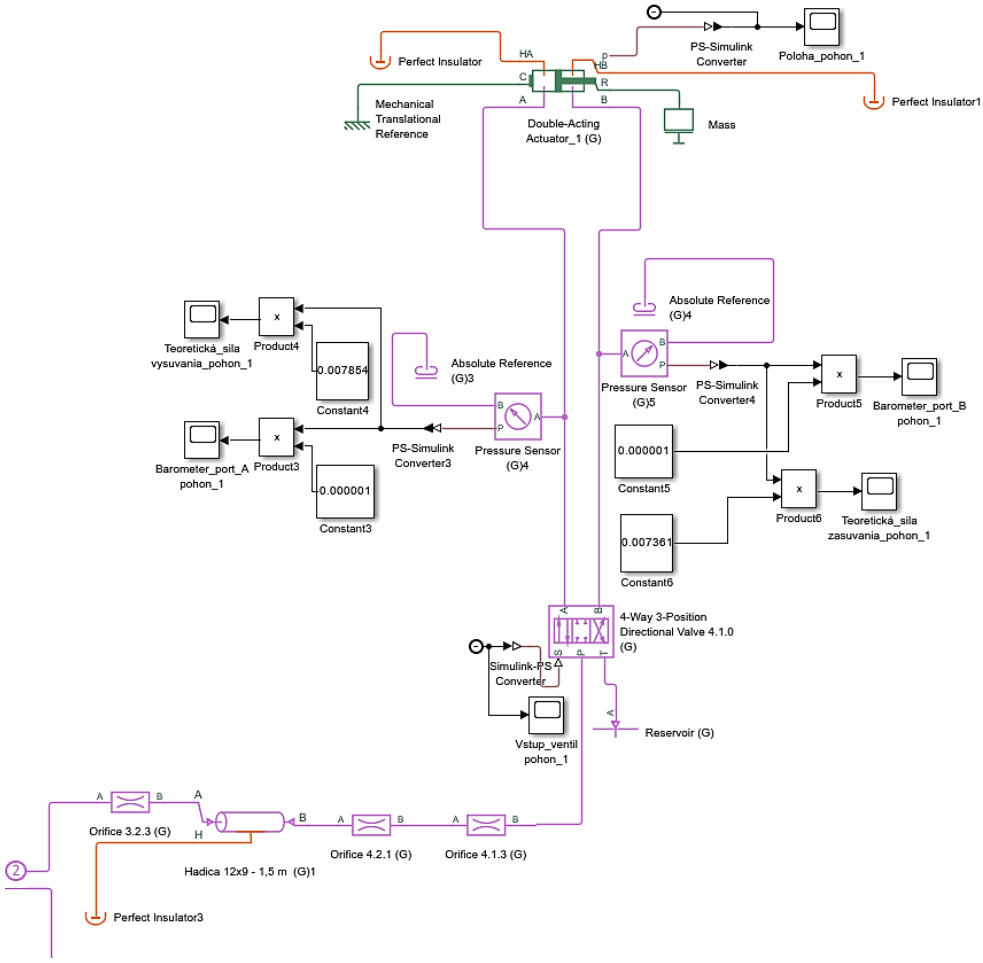

Figure 3. Simulink diagram of the drive.

Main components used in the model:

- Orifice (G) - Blocks expressing proportional cross-sections of components with identical code
- Pipe (G) – Pneumatic hose
- Perfect Insulator - Insulation or closure of thermal input
- 4-Way 3-Position Directional Valve (G)
- Reservoir (G) – Block with infinite volume and atmospheric pressure
- Pressure Sensor (G) – Barometer that measures the pressure between the valve and the actuator [MPa]
- Absolute Reference (G) – A reference expressing zero pressure
- Constant - Mathematical constant block

- Product - Mathematical product block
- Scope - A block that plots graphs from a signal
- Mechanical Translation Reference – Plug connected to input C (Actuator casing)
- Mass – The mass on the actuator piston rod (rack + piston rod) to the R (Actua-tor piston) input
- Double-Acting Actuator (G) – Double-acting linear

4. Results

After the blocks were assembled, the parameters and individual connections between the blocks were defined, several test simulations were run. The final simulation was set to a time of 60 s, of all the waveforms that were its outputs, we present the most important ones systematically in sequence with respect to the entire scheme. The first waveforms monitored were the pressure in the main tank and its decrease with respect to time, with the pressure behind the regulator rising to a value of 0.6 MPa and the total flow rate suddenly increased by pressurizing the entire circuit and slowly stabilized to a uniform value over time. The graphs, figure 4. depict the total drive force during both extension and retraction, then the output torque on the differential calculated through all the torques of the pneumobil, from which the driving force on the wheel and the value of maximum accel-eration are derived. The drive position output allowed us to calculate the revolutions up to the output shaft. From this data, we obtained the total revolutions on the differential shaft and the total distance traveled by the vehicle.

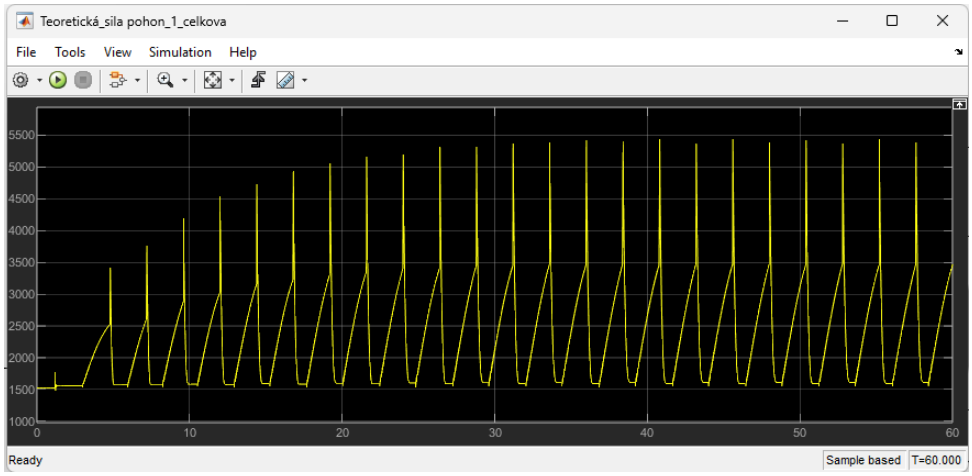

Figure 4. Graph of the drive force [N] versus time [s].

The simulation results demonstrated the functionality of the proposed methodology. Time courses of pressure in the main tank and behind the regulator confirmed the correctness of the dimensioning of the reducing elements to maintain a stable working pressure of 0.6 MPa. Dynamic analysis showed that the proposed rack mechanism is able to generate a smooth torque and provide the required driving force on the wheel, which was verified by acceleration and distance graphs. The simulation also revealed the influence of pressure losses in the pipes and the importance of optimizing dead volumes to maximize the range.

5. Conclusions

The article presents the methodology for the design and simulation verification of the power unit for the Air Force TUKE 2019 competition vehicle. The research conducted confirmed the effectiveness of the methodological approach based on the transformation of analytical relationships into a digital twin in the MATLAB/Simulink environment. By

integrating nonlinear phenomena such as polytropic expansion and mechanical resistances, a high degree of agreement of the model with the expected physical behavior of the system was achieved.

Dynamic analysis verified the ability of the combination of linear actuators and rack transmission to generate stable driving force for smooth vehicle acceleration. Simulation verified the functionality of the control elements at a working pressure of 0.6 MPa and the obtained data were used to optimize the timing strategy of the distributors in order to increase energy efficiency. The created robust simulation tool eliminated the trial and error method, which significantly shortened the development cycle of mechatronic systems. In the follow-up research, experimental validation of the results on a real vehicle prototype is planned.

Acknowledgments: This research was supported by project VEGA: 1/0215/23 *Research and development of robot-ic workplaces equipped with industrial and collaborative robots*

References

1. BUCKLEY, R. J. The Mékarski system of compressed air propulsion. [online]. Tramway Information, © 2003 [cit. 2024-05-22]. Dostupné na: https://www.tramwayinfo.com/tramways/Articles/Compair8.htm
2. TULEJA, P., JÁNOŠ, R., SEMJON, J., MARCINKO, P. Základy pneumatických mechanizmov III. Pneumatické výkonové členy. Košice : Technická univerzita v Košiciach , 2020. ISBN 978-80-553-3714-2
3. SOLÁRIK, Róbert. Návrh motora pre pneumobil 2019. Košice: Technická univerzita v Košiciach, 2019. Vedúci bakalárskej práce Ing. Rudolf Jánoš, PhD.
4. BRNA, Jakub. Analýza technických možností pre realizáciu pneumatickej pohonovej jednotky s nízkou spotrebou vzduchu 2025. Košice: Technická univerzita v Košiciach, 2025. Vedúci bakalárskej práce Ing. Peter Tuleja, PhD.
5. Xavier, Matheus & Fleming, Andrew & Yong, Yuen Kuan. (2020). Modelling and Simulation of Pneumatic Sources for Soft Robotic Applications. 916-921. 10.1109/AIM43001.2020.9158802. [online] Dostupné na internete: <https://www.researchgate.net/publication/343466100_Modelling_and_Simulation_of_Pneumatic_Sources_for_Soft_Robotic_Applications#pf4
6. Mathworks.com. Pneumatic Actuation Circuit [online] Dostupné na internete: https://www.mathworks.com/help/simscape/ug/pneumatic-actuation-circuit.html

TECHNICAL UNIVERSITY OF KOŠICE
Faculty of Mechanical Engineering

Segmental Dynamics and Thermo-Mechanical Response of PVC/TPU Blends Plasticized with a Bio-Based Plasticizer

Yitbarek Firew Minale [1,2], Ivan Gajdoš [3,*], Tamas Szabo [1], Annamaria Polyákné Kovács [1], Kálmán Marossy [1], and Andrea Ádámné Major [4]

[1] Institute of Energy, Ceramics, and Polymer technology, University of Miskolc, Hungary; minale.yitbarek@student.uni-miskolc.hu (Y.F.); polkal01@uni-miskolc.hu (K.M.)
[2] Department of Chemical Engineering, Bahir Dar Institute of Technology, Bahir Dar University, Ethiopia; minale.yitbarek@student.uni-miskolc.hu (Y.F.)
[3] Institute of Technology and Material Engineering, Faculty of Mechanical Engineering, Technical University of Košice, Slovakia; ivan.gajdos@tuke.sk (I.G.)
[4] Department of Innovative Vehicles and Materials, Johnvon Neumann University, Hungary; major.andrea@nje.hu (A.A.)
* Correspondence: ivan.gajdos@tuke.sk (I.G.)

Abstract: The thermo-mechanical behavior of polyvinyl chloride (PVC) can be tailored through blending and plasticization; however, achieving flexibility while maintaining thermal performance remains challenging, particularly when sustainable additives are employed. In this study, the segmental dynamics and thermo-mechanical response of PVC/thermoplastic polyurethane (TPU) systems plasticized with a bio-based plasticizer derived from waste cooking oil were investigated. Dynamic mechanical analysis (DMA) was used to evaluate temperature-dependent relaxation behavior, while Fourier transform infrared (FTIR) spectroscopy provided insight into molecular-level interactions among blend components. Representative binary and ternary formulations were examined to clarify the roles of TPU incorporation and bio-plasticization. The results show that plasticization strongly reduces the glass transition temperature of PVC and broadens relaxation behavior, whereas TPU incorporation leads to moderate mobility enhancement. In ternary PVC/TPU/bio-plasticizer systems, a single, broadened relaxation response is observed at substantially lower temperatures, indicating cooperative segmental dynamics across the blend. FTIR analysis confirms physical blending accompanied by weak intermolecular interactions that promote a more integrated molecular environment. These findings demonstrate that bio-based plasticization, combined with TPU blending, effectively modifies segmental dynamics and thermo-mechanical response, offering a sustainable pathway for designing flexible PVC-based materials.

Keywords: Polyvinyl chloride (PVC); Thermoplastic polyurethane (TPU); Sustainable plasticizer; Segmental dynamics; Thermo-mechanical response

1. Introduction

Polyvinyl chloride (PVC) is a widely used thermoplastic owing to its favorable balance of cost, chemical resistance, mechanical strength, and versatility across construction, automotive, medical, and consumer applications [1]. Despite these advantages, the thermo-mechanical behavior of PVC presents inherent limitations, particularly during processing, where elevated temperatures and mechanical shear are applied. Unlike many thermoplastics, PVC does not undergo simple melting but instead exhibits restricted segmental mobility associated with its polar backbone, necessitating careful formulation to achieve suitable processability and performance [2, 3].

Plasticization is commonly employed to enhance flexibility and reduce processing temperatures of PVC. Conventional plasticizers, particularly phthalates, have proven effective but raise concerns related to migration, environmental persistence, and potential toxicity [4, 5]. These concerns have motivated the development of alternative plasticizers derived from renewable or waste resources. Bio-based plasticizers offer the potential to reduce environmental impact while maintaining functional performance [6-8]; however, their influence on the thermo-mechanical behavior of PVC systems requires further clarification.

Blending PVC with thermoplastic polyurethane (TPU) represents an additional strategy to improve flexibility and toughness. TPU is a segmented polymer consisting of soft and hard domains, providing elasticity and resistance to mechanical deformation [9, 10]. While PVC/TPU blends have been explored for mechanical property enhancement [8, 11], their thermo-mechanical response depends strongly on segmental mobility, phase interactions, and the extent of molecular-level compatibility.

In this context, understanding how bio-based plasticizers and TPU jointly influence segmental dynamics is essential for effective formulation design. Rather than focusing on degradation kinetics, this work emphasizes the thermo-mechanical response of PVC/TPU systems, linking molecular interactions to relaxation behavior. Dynamic mechanical analysis (DMA) and Fourier transform infrared (FTIR) spectroscopy are employed to clarify how blending and plasticization modify segmental mobility and molecular environments in representative PVC-based systems. references.

2. Materials and Methods

2.1. Materials

Suspension-polymerized PVC (K-value 70) and a polyester-based TPU were used as the base polymers. A low-molecular-weight bio-based plasticizer, glycerol diacetate monolaurate, derived from waste cooking oil, was employed as a sustainable plasticizing agent. Standard PVC additives, including a CaZn stabilizer and an E-wax lubricant, were incorporated where required. All materials were used as received.

2.2. Blend Preparation

PVC, TPU, and the bio-based plasticizer were melt-blended using a laboratory-scale mixing and roll-milling process. Selected binary and ternary formulations were prepared to represent plasticized PVC, PVC/TPU blends, and PVC/TPU systems containing the bio-based plasticizer. The resulting sheets were compression molded to obtain specimens suitable for thermo-mechanical and spectroscopic analysis.

2.3. Dynamic Mechanical Analysis

Dynamic mechanical analysis was performed in tensile mode using rectangular specimens. Measurements were conducted over a temperature range of −80 to 120 °C at a constant heating rate, frequency, and displacement amplitude. The damping factor (tan δ) was recorded as a function of temperature, and the glass transition temperature (T_g) was determined from the tan δ maximum. The selected temperature range captures the relevant relaxation processes while avoiding temperature regions where no significant molecular transitions occur.

2.4. Fourier Transform Infrared Spectroscopy

FTIR spectra were recorded using an ATR-FTIR spectrometer over the range of 400–4000 cm^{-1}. Representative spectra of neat components and selected blends were analyzed to identify characteristic functional groups and assess changes in band shape or intensity associated with molecular interactions.

3. Results and Discussion

3.1. Thermo-Mechanical Response and Segmental Dynamics

Figure 1 presents the temperature dependence of the damping factor (tan δ) for selected PVC-based blends. Neat PVC exhibits a sharp relaxation peak at high temperature, reflecting its rigid amorphous structure and limited segmental mobility. Incorporation of the bio-based plasticizer leads to a pronounced shift of the tan δ peak toward lower temperatures, accompanied by significant peak broadening. This behavior indicates enhanced chain mobility and a wider distribution of relaxation times associated with plasticization.

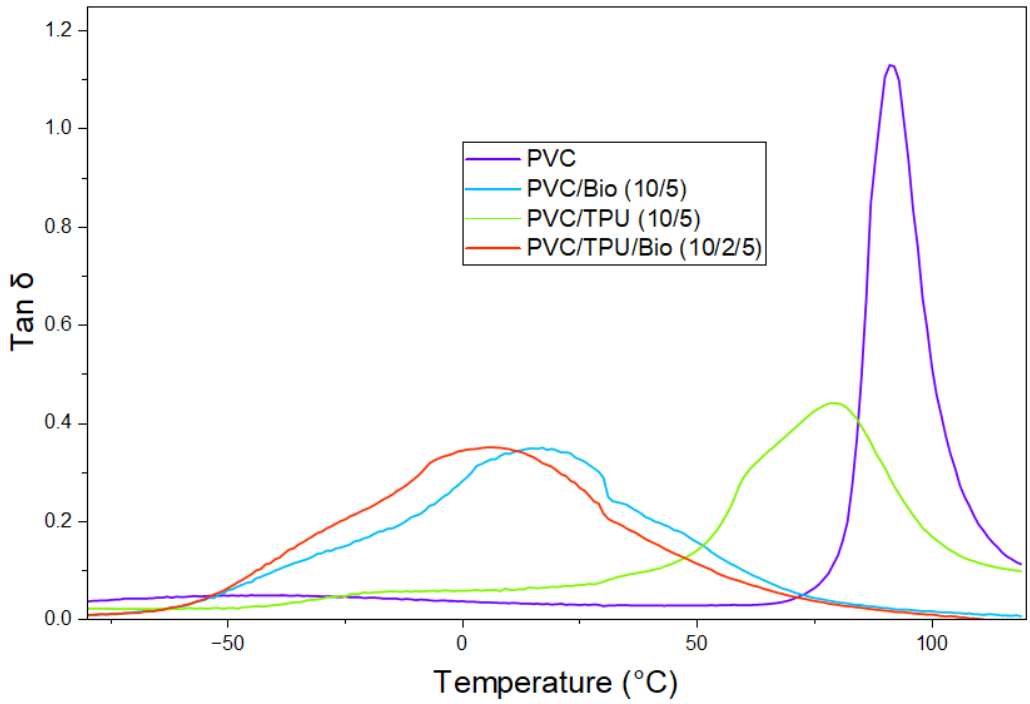

Figure 1. Dynamic mechanical tan δ curves illustrating segmental relaxation behavior of representative PVC-based blends.

The PVC/TPU binary blend displays a more moderate reduction in T_g relative to plasticized PVC. The dominant relaxation remains associated with the PVC phase, while TPU contributes to local mobility enhancement without fully disrupting the PVC glassy network. This observation suggests partial interaction between phases, consistent with physical blending rather than extensive molecular mixing.

In contrast, the ternary PVC/TPU/bio-plasticizer system exhibits a single, broad tan δ peak at substantially lower temperature. The disappearance of distinct PVC and TPU related relaxations indicates cooperative segmental dynamics across the blend. The combined presence of TPU and the bio-based plasticizer facilitates redistribution of mobility, leading to a more unified thermo-mechanical response.

3.2. FTIR Analysis of Intermolecular Interactions

FTIR spectra of neat PVC, TPU, and the ternary blend are shown in Figure 2. Neat PVC is characterized by aliphatic C–H stretching vibrations in the 3000–2800 cm^{-1} region and C–Cl absorptions below 700 cm^{-1}, while TPU exhibits characteristic urethane-related absorptions, including carbonyl (C=O) stretching vibrations in the 1700–1730 cm^{-1} region and N–H stretching vibrations around 3300–3400 cm^{-1}.

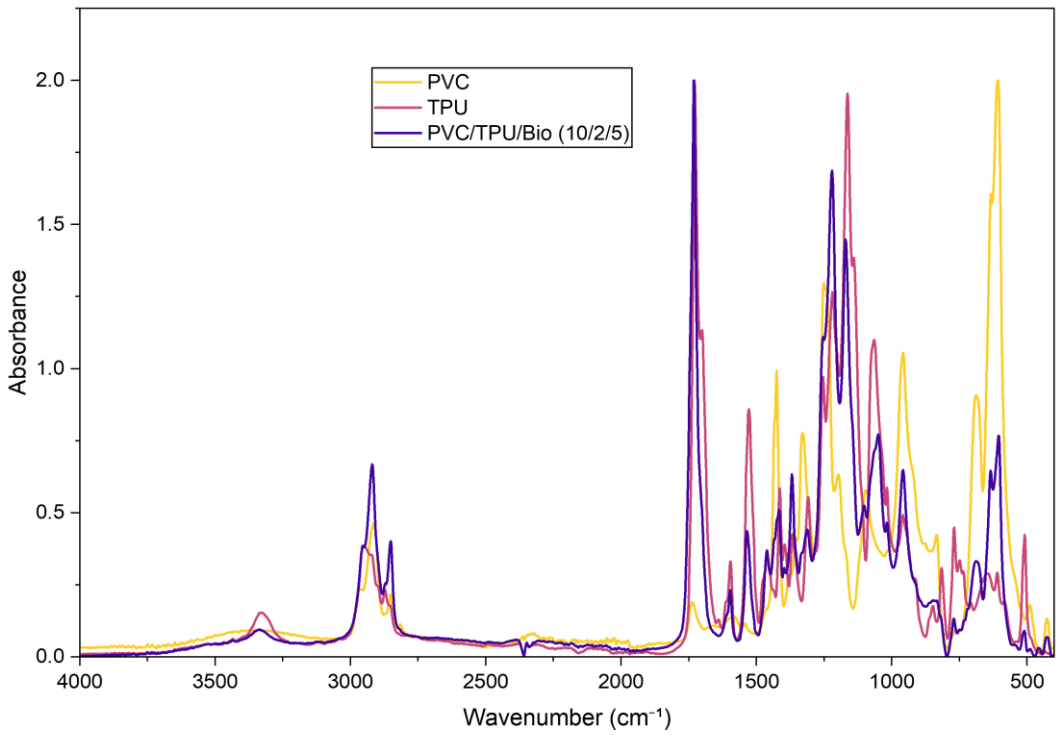

Figure 2. Infrared spectra of neat components and a ternary PVC/TPU/bio-plasticizer system illustrating intermolecular interactions.

In the ternary blend, characteristic bands from both PVC and TPU remain present, confirming the absence of chemical reactions during processing. However, subtle changes in band shape, particularly in the carbonyl region, indicate a distribution of local molecular environments. Slight broadening of the carbonyl absorption envelope suggests weak dipole–dipole interactions involving ester and urethane groups interacting with polar PVC segments.

These spectroscopic features support the DMA observations by indicating physical blending accompanied by weak intermolecular interactions. Such interactions are sufficient to promote cooperative segmental motion without forming new chemical species, consistent with the unified relaxation behavior observed in the ternary system.

3.3. Influence of Molecular Interactions on Thermo-Mechanical Response

The DMA and FTIR results demonstrate that segmental dynamics in PVC-based systems are governed not only by additive content but also by the molecular environment established through blending. Plasticization primarily increases free volume and mobility, while TPU contributes elastic domains that modify relaxation behavior. In ternary systems, the bio-based plasticizer mediates interactions between PVC and TPU, promoting a more integrated molecular environment and a balanced thermo-mechanical response.

4. Conclusions

This study demonstrates that the thermo-mechanical response of PVC can be effectively tailored through the combined use of TPU blending and bio-based plasticization. Dynamic mechanical analysis reveals that plasticization strongly enhances segmental mobility, while TPU incorporation provides moderate relaxation effects. In ternary PVC/TPU/bio-plasticizer systems, cooperative segmental dynamics emerge, resulting in a

single, broadened relaxation process at lower temperature. FTIR analysis confirms physical blending accompanied by weak intermolecular interactions that support this integrated behavior. These findings highlight the potential of bio-based plasticizers to enable sustainable formulation strategies for flexible PVC-based materials with tuned thermomechanical performance.

Acknowledgments: The authors acknowledge the support provided by the university research scholarship program of the ministry for culture and innovation from the source of the national research, development and innovation fund, Hungary, and National Scholarship Program of the Slovak Republic.

Conflicts of Interest: The authors declare no conflict of interest.

References

1. Lewandowski, K. Skórczewska, K., A brief review of poly (vinyl chloride)(PVC) recycling. *Polymers*. **2022**, *14*,(15): p. 3035. DOI: https://doi.org/10.3390/polym14153035
2. Bao, Y.-z.;Zhi-Ming, H.;Shen-Xing, L.Zhi-Xue, W., Thermal stability, smoke emission and mechanical properties of poly (vinyl chloride)/hydrotalcite nanocomposites. *Polymer degradation and Stability*. **2008**, *93*,(2): p. 448-455. DOI: https://doi.org/10.1016/j.polymdegradstab.2007.11.014
3. Liu, J.;Chen, G.Yang, J., Preparation and characterization of poly (vinyl chloride)/layered double hydroxide nanocomposites with enhanced thermal stability. *Polymer*. **2008**, *49*,(18): p. 3923-3927. DOI: https://doi.org/10.1016/j.polymer.2008.07.014
4. Zhang, Z.-M.;Zhang, H.-H.;Zou, Y.-W.Yang, G.-P., Distribution and ecotoxicological state of phthalate esters in the sea-surface microlayer, seawater and sediment of the Bohai Sea and the Yellow Sea. *Environmental pollution*. **2018**, *240*: p. 235-247. DOI: https://doi.org/10.1016/j.envpol.2018.04.056
5. Vieira, M.G.A.;Da Silva, M.A.;Dos Santos, L.O.Beppu, M.M., Natural-based plasticizers and biopolymer films: A review. *European polymer journal*. **2011**, *47*,(3): p. 254-263. DOI: https://doi.org/10.1016/j.eurpolymj.2010.12.011
6. Jia, P.;Zhang, M.;Hu, L.Zhou, Y., Green plasticizers derived from soybean oil for poly (vinyl chloride) as a renewable resource material. *Korean journal of chemical engineering*. **2016**, *33*,(3): p. 1080-1087. DOI: https://doi.org/10.1007/s11814-015-0213-9
7. Qadeer, A.;Kirsten, K.L.;Ajmal, Z.;Jiang, X.Zhao, X., Alternative plasticizers as emerging global environmental and health threat: another regrettable substitution? *Environmental science & technology*. **2022**, *56*,(3): p. 1482-1488. DOI: https://doi.org/10.1021/acs.est.1c08365
8. Minale, Y.F.;Gajdoš, I.;Štefčák, P.;Szabó, T.;Polyákné Kovács, A.;Ádámné Major, A.Marossy, K., Mechanical Properties of PVC/TPU Blends Enhanced with a Sustainable Bio-Plasticizer. *Sustainability (2071-1050)*. **2025**, *17*,(5). DOI: https://doi.org/10.3390/su17052033
9. Somdee, P.;Lassú-Kuknyó, T.;Konya, C.;Szabó, T.Marossy, K., Thermal analysis of polyurethane elastomers matrix with different chain extender contents for thermal conductive application. *Journal of Thermal Analysis and Calorimetry*. **2019**, *138*,(2): p. 1003-1010. DOI: http://dx.doi.org/10.1007/s10973-019-08183-y
10. Ebewele, R.O., Polymer science and technology, CRC press: **2000**. DOI: https://doi.org/10.1201/9781420057805
11. Pita, V.J.;Sampaio, E.Monteiro, E.E., Mechanical properties evaluation of PVC/plasticizers and PVC/thermoplastic polyurethane blends from extrusion processing. *Polymer Testing*. **2002**, *21*,(5): p. 545-550. DOI: https://doi.org/10.1016/S0142-9418(01)00122-2

TECHNICAL UNIVERSITY OF KOŠICE
Faculty of Mechanical Engineering

Design of engine modifications and construction for an experimental vehicle

Štefan Novotný [1,*], Maroš Palko [2]

[1] Department of Automotive production, faculty of mechanical engineering, technical university of Kosice; stefan.novotny@tuke.sk
[2] Prototype and innovation center of the faculty of mechanical engineering, technical university of Kosice; maros.palko@tuke.sk
* Correspondence: stefan.novotny@tuke.sk

Abstract: This paper addresses the mechanical design of a high-efficiency powertrain intended for the Shell Eco-marathon international competition, where fuel consumption minimization is the primary criterion. The objective of this work was to develop a single-cylinder spark-ignition engine that surpasses the limitations of commercially available engines regarding thermal efficiency and mechanical losses. The proposed solution utilizes CNC machining of high-strength aluminum alloys, enabling a modular construction with increased rigidity and optimized thermal management. Special attention was paid to the weight reduction of moving parts and the design of an OHC valve train with a timing belt to reduce passive resistance. The resulting CAD model, created in the Solidworks environment, demonstrates the feasibility of the thermally insulated cylinder concept and provides solid baseline platform for further experimental improvement.

Keywords: small-displacement; engine; efficiency; Shell eco marathon;

1. Introduction

The Shell Eco-marathon competition poses a unique engineering challenge requiring extreme optimization of the vehicle's energy balance. In the internal combustion engine prototype category, among many parameters, the decisive factor is the overall powertrain efficiency, defined as the product of thermal and mechanical efficiency. The necessity to develop a proprietary powertrain unit arose directly from the experimental experience of the team at the Faculty of Mechanical Engineering, Technical University of Kosice. The original propulsion concept, based on the modification of a commercially available Honda GX35 industrial engine, demonstrated during previous competitive seasons that its innovation potential had reached its limits. Further enhancement of thermodynamic efficiency was hindered by the geometric and material constraints, which disallowed the implementation of advanced modifications such as increasing the compression ratio beyond a critical threshold, redesigning intake and exhaust ports for improved fluid dynamics, or altering the combustion chamber shape. [1-6]

1.1. Current trends in Shell-Eco Marathon powertrains

The pursuit of maximum energy efficiency in the Shell Eco-marathon "Prototype" category has shifted focus from modifying stock industrial engines to developing custom power units. Commercial engines like the Honda GX35, while reliable, are constrained by mass-production compromises and lack the adaptability for extreme optimization. Contemporary research identifies three key areas for improvement: downsizing, thermal management, and friction reduction. Reducing displacement allows for operation at higher

load points, but requires a "downspeeding" strategy to minimize speed-dependent frictional losses. Standard air-cooled engines are ill-suited for this regime due to excessive heat dissipation through their monoblock construction. To approach a quasi-adiabatic cycle, heat must be retained within the cylinder, necessitating specialized thermal barriers rather than conductive cast-aluminum blocks. Furthermore, to mitigate significant parasitic losses, modern prototypes are abandoning splash lubrication in favor of "dry" architectures utilizing ceramic rolling bearings and timing belt systems. The engine proposed herein integrates these strategies through a modular billet construction and a thermally isolated cylinder design. [1-6]

Figure 1. Honda GX35 block [1].

2. Materials and Methods

The research and development methodology for the prototype powertrain unit was based on a systematic design process utilizing computer-aided engineering support. This chapter defines the software ecosystem employed, the theoretical foundations of the kinematic and thermodynamic analyses, and the specification of materials selected for key engine components.

2.1. Design Environment and Software Tools

The CAD modeling was realized in the SolidWorks 2025 environment. This software was utilized for the parametric modeling of individual parts, assembly creation, and collision control. To verify the mechanical integrity of critical components (crankcase, connecting rod), the Finite Element Analysis method (FEA) was employed using the SolidWorks Simulation module.

2.2. Material Characteristics

To precisely characterize the material limits of the reference powertrain, an elemental analysis was conducted using X-ray spectroscopy. The resulting spectrum (Figure 1) reveals a hypereutectic composition with a dominant Silicon content of 18.5% and Aluminum content of 76.4%.

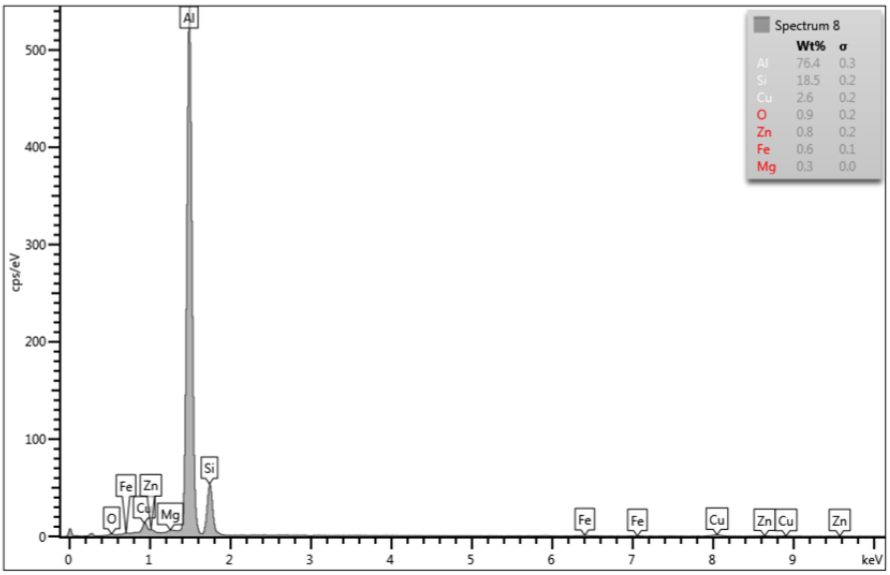

Figure 2. Material characteristics of Honda engine.

Based on this spectral analysis, the reference engine block material was identified as Japanese standard JIS ADC14, which is equivalent to EN AC-48100. This hypereutectic alloy utilizes primary silicon crystals for wear resistance, enabling a liner-less cylinder design. However, its heterogeneous structure limits its suitability for high-performance modifications. Consequently, the material selection for the prototype was strictly governed by the requirement for a high strength-to-density ratio. Unlike the conventional casting alloy found in the reference unit, the high-strength aluminum alloy EN AW-7075 T6 was selected for the main structural assemblies (engine block, cylinder head, connecting rod). The selection of EN AW-7075 T6 reflects the early prototyping phase, where low mass, machinability, and rapid design iteration are prioritized over long-term fatigue durability. The final material selection for highly loaded components such as the connecting rod will be subject to experimental validation and potential revision. As demonstrated in Table 1, the tensile strength of the proposed material (R_m= 570MPa) is more than double that of the reference cast material (R_m = 245 MPa), while maintaining a comparable density. This allows for a significant reduction in structural wall thickness and facilitates a modular design, albeit requiring the installation of a cast-iron liner EN-GJL-250 to ensure tribological compatibility. To further reduce friction losses, a critical factor in the Shell Eco-marathon competition, advanced surface treatments were specified. The piston pin and valve tappets are coated with DLC to reduce the coefficient of friction. The intake and exhaust valves are manufactured from Titanium alloy Ti-6Al-4V, reducing the moving mass of the valve train by 40% compared to steel equivalents. [1,5,6]

Table 1. Comparison of mechanical properties of utilized material.

Parameter	EN AW-7075 T6 (Proposed)	EN AC-48100 (spectral data)	Unit
Yield strength ($R_{p0,2}$)	505	140	MPa
Ultimate tensile strength (R_m)	570	245	MPa
Density (ϱ)	2810	2730	kg/m³
Young's modulus (E)	71.7	82	GPa

3. Results

The outcome of the design and simulation process is a complete digital twin of the combustion engine, optimized for the specific conditions of the Shell Eco-marathon competition. This chapter summarizes the final geometric characteristics of the proposed platform.

3.1. Geometric specification

Based on the thermodynamic requirements, the final engine geometry was defined as a long-stroke configuration. Table 2 presents a comparison between the reference commercial engine and the newly designed prototype.

Table 2. Comparison of technical parameters between the reference and the prototype engine [2].

Parameter	Honda GX35 (Reference)	FME P1 (Prototype)	Change
Bore × Stroke	39 × 30 mm	32,5 × 36 mm	S/B ratio: 0.77 to 1.11
Displacement (V_d)	35.8 cm^3	29.9 cm^3	-16,5%
Compression ratio (theoretical) [ε]	8.0: 1	12.5: 1	+56%
Weight	≈ 3,4 kg	≈ 2.6 kg (CAD)	-23.5 %

A key outcome of the geometric design is the alteration of the stroke-to-bore ratio to 1.11. This modification resulted in a more compact combustion chamber at top dead center, thereby achieving a reduction in the surface-to-volume ratio. Geometric analysis of the model confirms a 14% reduction in the heat transfer area of the combustion chamber compared to an oversquare concept, creating a prerequisite for reducing heat losses to the cylinder walls. The final structural design was validated in terms of easy assembly and part interchangeability. The split cylinder head concept and the separate cylinder block allow for variation of the compression ratio in the range of 10-14 by simply exchanging spacers or the piston, without the need for machining the block. Thus, the objective of creating a flexible hardware platform for future experimental optimization of the combustion process was achieved. [1,3]

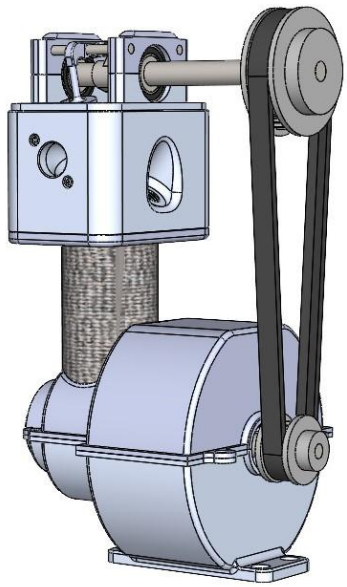

Figure 3. Isometric view of the engine prototype featuring a CNC-machined billet aluminum crankcase and external timing belt drive system with SOHC.

While the transition to an OHC layout with a toothed belt introduces greater complexity as the more common OHV layout in small engines, it offers better optimalization. The elimination of the oil bath for the valve train removes viscous drag, which is a significant parasitic loss factor in splash-lubricated engines. Furthermore, the separation of the lubrication domains allows for the use of minimal quantity lubrication (oil mist) for the crankshaft bearings, further reducing the hydrodynamic resistance that limits the efficiency of standard industrial engines. A critical aspect of the cylinder head design involved optimizing the internal flow paths and the combustion space. Unlike high-revving performance engines that prioritize maximum volumetric flow rate, the intake and exhaust ports of the prototype were designed to maintain high flow velocity at low-to-medium engine speeds. Furthermore, Figure 4 illustrates the resulting geometry of the combustion chamber. This highly compact design is a direct consequence of achieving the high target compression ratio within the reduced bore diameter of 32.5 mm. The minimal surface area of the chamber at top dead center (TDC) is intended to reduce heat transfer losses to the cylinder head walls, supporting the thermal management strategy.

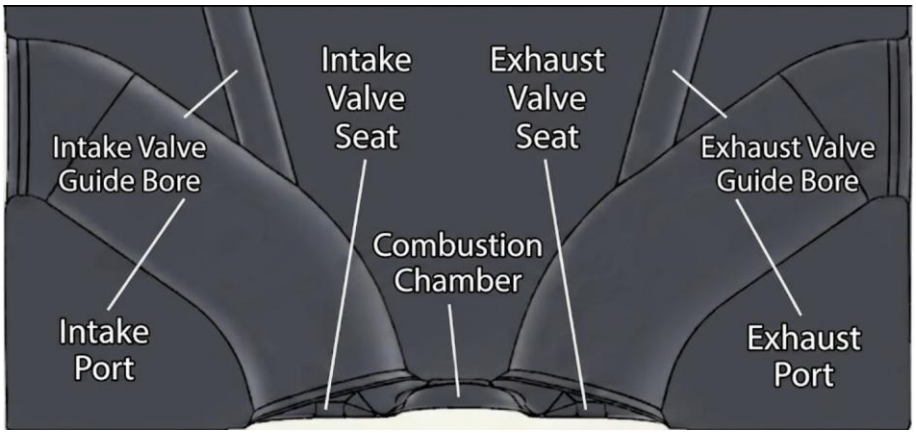

Figure 4. Cylinder head geometry detail.

4. Conclusions

The primary objective of this study was the design of a high-efficiency internal combustion engine prototype tailored for the specific requirements of the Shell Eco-marathon competition. The work focused on the early-stage development of a lightweight, mechanically efficient, and thermally optimized powertrain architecture, intended primarily as a flexible experimental basis rather than a finalized production-ready solution. A key achievement of the proposed geometric configuration is the successful implementation of a long-stroke architecture with a stroke-to-bore ratio of 1.11, and having block and head of the unit as separate parts. The presented prototype does not constitute a final product but rather a flexible hardware platform developed for further experimental optimization of the combustion process. It is important to note that the presented work is limited to the conceptual and geometric design stage. Structural durability, thermal behavior, friction losses, and overall efficiency improvements have not yet been experimentally verified and therefore are not quantified in this paper. These aspects will be addressed in subsequent phases of the project. The modular split-block design specifically allows for straightforward variation of the compression ratio within the range of 10 to 14 without the need for complex machining. Future work will focus on the physical realization of the prototype, followed by comprehensive test bench validation to verify the theoretical performance parameters and refine the engine's thermal management strategy. Future work will focus on the manufacturing of the proposed engine prototype, followed by comprehensive test bench experiments aimed at validating the theoretical assumptions, refining the thermal management strategy, and assessing the real-world efficiency potential of the proposed concept under Shell Eco-marathon operating conditions.

Acknowledgements: This research was supported by the Scientific Grant Agency VEGA under project No. 1/0597/23 "Possibilities of applying laser additive technologies in the restoration of functional surfaces" and by the Cultural and Educational Grant Agency KEGA under project No. 024TUKE-4/2025 "Hybrid education of students for the current needs of the automotive industry".

Conflicts of Interest: The authors declare no conflict of interest.

References

1. HEYWOOD, John B**.** *Internal Combustion Engine Fundamentals*. 2nd edition
2. HONDA ENGINES GX35 - 4 Stroke Engine. [Online]. Available: https://www.honda-engines-eu.com/en/products/power-units/gx35
3. WAHONO, Bambang, JWA, Kyeonghun and LIM, Ocktaeck. A Study on In-Cylinder Flow of Small Engine Using Steady-State Flow Benches. *Energy Procedia*. 2019, Vol. 158, pp. 1856-1862.
4. DUNERT, Fredrik. *Chalmers Ecomarathon Engine Design*. Gothenburg : Chalmers University of Technology, 2007.
5. DAHHAM, Rami Y., WEI, Haiqiao, PAN, Jiaying. Improving Thermal Efficiency of Internal Combustion Engines: Recent Progress and Remaining Challenges. *Energies*. 2022, Vol. 15, No. 17, p. 6222.
6. LI, Yapeng, HANIPAH, Mohd Razali, LIU, Feng. A Review of Advanced Camless Technologies for Engine Performance Enhancement. *Journal of Advanced Research in Applied Sciences and Engineering Technology*. 2025, Vol. 63, No. 4, pp. 105-120

TECHNICAL UNIVERSITY OF KOŠICE
Faculty of Mechanical Engineering

Construction of timetables in urban public transport from a metrological perspective

Peter Onderčo [1,*], Jan Rybář [1], Jozef Leja [2] and Stanislav Ďuriš [1]

[1] Institute of Automation, Informatization, and Measurement, Faculty of Mechanical Engineering, Slovak University of Technology in Bratislava, Nám. slobody 17, 812 31 Bratislava, Slovakia; peter.onderco@stuba.sk; jan.rybar@stuba.sk; stanislav.duris@stuba.sk
[2] Institute of Mathematics and Physics, Faculty of Mechanical Engineering, Slovak University of Technology in Bratislava, Nám. slobody 17, 812 31 Bratislava, Slovakia; jozef.leja@stuba.sk
* Correspondence: peter.onderco@stuba.sk; Tel.: +421 911 291 630

Abstract: This paper investigates the construction and optimization of urban public transport timetables, combining metrological and operational perspectives. Emphasis is placed on precise time measurement and synchronization as key factors for ensuring service reliability, punctuality, and operational efficiency. The study analyzes both objective factors—such as vehicle circulation, dwell times, distances, infrastructure capacity, traffic conditions, and technical capabilities—and subjective factors related to passenger perceptions, travel comfort, and behavioral variability. The research highlights metrological challenges in data acquisition, timekeeping standards, and performance evaluation, while demonstrating the importance of balancing objective and subjective considerations through adaptive, flexible timetabling. A case study of the extended tram line in Petržalka illustrates the practical application of these principles for improving urban transport planning and passenger satisfaction.

Keywords: Influencing factors, Metrology, Timetable optimization, Tram, Urban public transport

1. Introduction

Timetable planning in urban public transport is a key tool for ensuring reliable, efficient, and comfortable operation. From a metrological perspective, it involves the precise measurement and quantification of temporal and spatial parameters that affect the smoothness of connections, intervals between services, and the overall system capacity. This conference paper focuses on the construction of timetables with an emphasis on objective, measurable factors that enable operational optimization and enhance predictability and efficiency. At the same time, it addresses the relationships between metrological principles and the practical (subjective) requirements of passengers for reliable and comfortable transport.

2. Materials and Methods

Designing and optimizing efficient timetables for urban public transport is a complex process that requires consideration of a wide range of factors affecting service reliability, punctuality, and overall system performance. These factors can generally be divided into two main categories: objective (physical) and subjective (perceptual) factors. Objective factors are measurable and quantifiable. They often involve physical quantities such as time, distance, and speed—values defined metrologically. Examples include time intervals between connections, distances between stops, transport infrastructure capacity, traffic congestion, and the technical parameters of vehicles. These factors are largely predictable and can be effectively incorporated into timetable planning through mathematical models and simulations. Subjective factors, in contrast, relate to passenger perceptions, behavior, and

comfort, as well as elements of the traffic environment that cannot always be accurately predicted, such as delays or variability in travel times. Examples include passenger preferences for waiting times, adaptability to changing traffic conditions, perceived quality and comfort of travel, vehicle capacity and overload, maintenance and technical condition of vehicles, compliance with traffic regulations, the behavior of other road users, traffic light settings, and the occurrence of accidents or emergencies. Even the skills and experience of drivers can be considered a subjective factor influencing timetable adherence. Successful optimization of urban public transport timetables therefore requires balancing these objective and subjective factors. While objective factors can be modeled and planned, subjective factors are often more variable and dependent on human behavior and other dynamic elements of the transport system. [1] This paper aims to highlight approaches for integrating both types of factors into the creation and optimization of timetables and to demonstrate their influence on real operational conditions in urban public transport.

The research methodology includes an analysis of the current situation, including stops, distances, assumptions for line speed, working calculations, and predictions based on plans, regulations, and guidelines. It also considers traffic experience and the practical setting of timetables. Additionally, an analysis of both objective and subjective factors will be conducted as a prerequisite for designing a new timetable for the extended tram line. Based on the data collected, a comparative analysis will examine how objective factors, such as the physical and technical parameters of the route and its capacity, influence timetable compilation, and how subjective factors, such as passenger preferences and needs, can impact the efficiency and satisfaction with public transport. [1, 2, 3]

3. Results

In this conference paper, we present a proposed timetable for a new tram line in Bratislava. This line is an extension of the existing tram line number 3, running from the "Jungmannova" stop to the "Južné mesto" stop, with a total length of 3.9 kilometers in one direction. Trial operations commenced on the line in the summer of 2025, accompanied by a proposed timetable primarily based on objective factors and requirements. Following a period of operation, travel times will be optimized. [3, 4]

The proposed timetable currently considers only physical (objective) factors, with the primary parameter being the distance between stops. The operating speed is set at 50 km/h, although it is expected that in certain sections of the line, speeds of up to 60 km/h may be permitted after the trial period. Traffic lights along the route communicate with the tram, ensuring priority for public transport vehicles. It is important to note that while timetables at stops are given in minutes, tram drivers also rely on seconds within their information systems or the intelligent stop system. Furthermore, transfer nodes, where higher passenger volumes are expected, are not yet included. The preliminary physical timetable presented in Table 1 will therefore require optimization after testing and must also take into account subjective factors (Table 2) for the extended tram line number 3, connecting the Rača district with Petržalka and back. [3, 5]

When designing a new timetable, several key factors must be considered, such as allowing sufficient time between connections to prevent delays caused by unforeseen events, including traffic congestion or technical issues. It is also necessary to ensure the smooth flow of transport by effectively distributing intervals between services to maintain regularity and minimize passenger waiting times, including transfers to other modes of transport. Additionally, different peak and off-peak periods, transfer needs between connections, and local specifics such as important stops, transfer hubs, or areas with high passenger frequency must be taken into account.

Equally important is communication with the public to ensure that the new timetable is as well adapted as possible to passenger needs. For high-quality public transport, it is therefore essential to consider subjective factors, which may outweigh objective factors of

the timetable and thereby improve the quality of services provided. All of these factors must also respect safety and service quality for all participants in urban traffic.

Table 1. Draft timetable for a new section of tram line in Petržalka, a district of Bratislava. [6]

stop name ↓↑	~ distance from previous stop (meter)	net time needed to cover the section at a speed of 50 km/h, taking into account acceleration (seconds)	time correction to minutes (seconds)	timetable proposal, between stops, total travel time extension from the final stop "Rača" (minutes)
previous stop	---	---	---	---
Jungmannova*	482	44	+16	1 (33)
Gessayova	401	38	+22	1 (34)
Zrkadlový háj	496	45	+15	1 (35)
Pajštúnska	764	64	-4	1 (36)
Veľký Draždiak	618	53	+7	1.5 (37.5)
Lúčanka	564	49	+11	1.5 (39)
Južné mesto	597	52	+8	1 (40)

*This stop is considered, theoretically, the starting point for the timetable proposal.

After the opening of a new tram line, it is appropriate to carry out timetable optimisation, but first it is important to wait for a period when real operating conditions begin to stabilise. The best time for this optimisation is usually a few weeks to months after the start of operation, when sufficient data on real demand for transport, travel times, delays and line capacity have been obtained. The new section of the line and the individual stops are shown in Figure. 1.

Figure 1. Schematic extension of the line with proposed travel times in minutes. [6, 7], modified.

Table 2. Draft timetable for a new section of tram line in Petržalka, a district of Bratislava – prediction of subjective factors. [6, 7]

stop name ↓↑	it is a transfer hub with higher passenger traffic	model of subjective factors – church, supermarket, cultural amenities/leisure time, significant company, school, other restrictions	expected higher subjective factor
previous stop	---	---	---
Jungmannova*	yes	---	---
Gessayova	no	---	---
Zrkadlový háj	yes	supermarket	↑
Pajštúnska	yes	church	↑
Veľký Draždiak	no	leisure time	↑↑
Lúčanka	yes	supermarket, school	↑↑↑
Južné mesto	no	---	---

*This stop is considered, theoretically, the starting point for the timetable proposal. Legend: high ↑↑↑, medium ↑↑, low ↑.

Taking into account the known physical factors, we can predict and further assess the impact of subjective factors that are expected at busier stops from the perspective of transfer hubs (bus/tram), especially when we add civil amenities – large supermarkets, a church, a recreational area for water sports and leisure (Velký Draždiak), as well as shops and schools/daycares in the vicinity of the Lúčanka stop. Based on the model, higher consideration of subjective factors can be expected, which will be reflected in the tram timetable for line number 3. The above will be taken into account after a longer period of actual operation.

Before the optimisation itself, a detailed analysis should be carried out, which includes collecting real traffic data (number of passengers, arrival and departure times, average delays, time between connections and travel times), monitoring passenger behaviour (use of the new line), obtaining feedback from the public (questionnaires or surveys that can reveal passenger needs and preferences), assessing operational factors (technical problems, line maintenance). [8, 9]

Once all these factors have been taken into account, it is possible to adjust the timetable to better suit real conditions, optimise the intervals between connections and take into account operating costs and transport efficiency. Optimisation may include changes in departure times, interval lengths, adding or cancelling some connections, or adjusting vehicle capacity based on current demand.

4. Discussion

The analysis of the proposed extension of tram line number 3 in the Petržalka district highlights the complex interplay between objective and subjective factors in urban public transport scheduling. Objective elements, including stop spacing, speed constraints, and interactions with traffic signal priority systems, provide a necessary foundation for timetable design. However, these factors alone are insufficient to ensure an effective and passenger-oriented service. The study demonstrates that subjective factors—such as passenger demand patterns, comfort preferences, and driver responsiveness to real-time information—play a crucial role in shaping the overall performance and user satisfaction of the transport system [10, 11]. The findings suggest that a holistic approach, integrating both quantitative physical parameters and qualitative human-centric considerations, is essential to create timetables that are both efficient and adaptable to evolving urban mobility needs.

5. Conclusions

This research confirms that successful timetable planning for the new tram line in Petržalka requires careful consideration of both objective and subjective determinants. By combining operational parameters with passenger-focused insights, the proposed timetable can optimize travel times, vehicle capacity, and service frequency while responding to user expectations for comfort and reliability [12]. The study underscores the importance of iterative evaluation, including trial operations, to refine scheduling strategies and ensure sustainable urban transport solutions. Future research expanding to larger urban contexts and employing advanced real-time data analytics could further enhance the adaptability and responsiveness of public transport systems.

Acknowledgments: The authors would like to thank the Faculty of Mechanical Engineering of the Slovak University of Technology in Bratislava, urban transport company (Dopravný podnik Bratislava, a. s. /Bratislava Transport Company, Inc./) and, the grant agency KEGA project No. 028STU-4/2026 for their support in the preparation of this conference paper.

Conflicts of Interest: "The conference paper is not in any conflict of interest. The funders had no role in the design of the study; in the collection, analyses, or interpretation of data; in the writing of the manuscript, or in the decision to publish the results".

References

1. Šimeček, M. Preference uživatelů městské hromadné dopravy /Preferences of urban public transport users/. Perner's Contacts, 2022, 17(2). Available online: https://doi.org/10.46585/pc.2022.2.2381 (accessed on 12-11-2025).
2. Kampf, R. Požadavky uživatele dopravního systému /Transport system user requirements/. Perner's Contacts, 2009, 4(2), s. 47-51. Available online: https://aosp.upce.cz/index.php/perner/article/download/1120/949 (accessed on 10-12-2025).
3. Rybář, J., Onderčo, P., Bartalos, B., Ďuriš, S. (2022). Kalibrace času jízdy vozidel v městské hromadné dopravě /Calibration of vehicle travel time in urban public transport/. In Recenzovaný sborník příspěvků mezinárodní vědecké conference /Peer-reviewed proceedings of an international scientific conference/ MMK 2022. 1. vyd. Hradec Králové: Magnanimitas, 2022, S. 1063 - 1071. ISBN 978-80-87952-37-5.
4. DPB. Dopravný podnik Bratislava, a. s. /Bratislava Transport Company, Inc./. Available online: https://dpb.sk (accessed on 11-11-2025).
5. Chudý, V., Palenčár, R., Kureková, E., Halaj, M. Meranie technických veličín /Measurement of technical quantities/. Vydavateľstvo Bratislava: STU, 1999. 688 s. ISBN 80-227-1275-2.
6. Petržalská električka, (2025). Staviame električkovú trať v Petržalke /We are building a tram line in Petržalka/. 2025. Available online: https://petrzalskaelektricka.sk (accessed on 18-11-2025).
7. Imhd, (2025). Električky /trams/. Available online: https://imhd.sk/ba/mapa-schema/2844/Električky-29-3-2025 (accessed on 19-11-2025).
8. Niedzielski, M.A., Goliszek, S. & Górka, A. (2024). Signals, tracks, and trams: public transport signal priority impact on job accessibility over time. Sci Rep 14, 23459. Available online: https://doi.org/10.1038/s41598-024-74960-x (accessed on 22-11-2025).
9. Román, C., Martín, J. C., Espino, R. (2014). Using stated preferences to analyze the service quality of public transport. International Journal of Sustainable Transportation, 2014, 8(1), s. 28-46. Available online: https://www.econstor.eu/bitstream/10419/119910/1/ERSA2011_0086.pdf. (accessed on 30-11-2025).
10. Olivková, I. Metodika měření spokojenosti cestujících a hodnocení kvality MHD /Methodology for measuring passenger satisfaction and assessing the quality of public transport/. Perner´s Contacts, 2010, 5(3), s. 228-239. Available online: https://aosp.upce.cz/index.php/perner/article/download/1014/846 (accessed on 27-10-2025).
11. Široký, J. et al. Technologie dopravy /Transportation technology/. Pardubice: Univerzita Pardubice /University of Pardubice/. 2020.
12. Liu T., Ji W., Gkiotsalitis, K., Cats, O. (2023). Optimizing public transport transfers by integrating timetable coordination and vehicle scheduling, Computers & Industrial Engineering, 2023, Volume 184, ISSN 0360-8352, Available online: https://doi.org/10.1016/j.cie.2023.109577 (accessed on 02-12-2025).

TECHNICAL UNIVERSITY OF KOŠICE
Faculty of Mechanical Engineering

The Surface Roughness Standards

Katarína Paľová [1] and Tatiana Kelemenová [1,*]

[1] Technical University of Kosice, Faculty of Mechanical Engineering, Letná 9, Košice, Slovak Republic; katarina.palova@tuke.sk; tatiana.kelemenova@tuke.sk
* Correspondence: tatiana.kelemenova@tuke.sk

Abstract: The paper deals with the issue of standards or also called etalons for the calibration of stylus-based surface roughness profilometers. Surface roughness measurement is characterized by a large variability of the measurement result and thus the calibration of measuring instruments is a key activity associated with the measurement itself using these instruments. According to ISO 5436-1:2000, there are 5 basic groups of etalons for the calibration of profilometers. Type "D" Roughness measurement standard was used in this work. Using this etalon, the overall calibration of the used instrument was realized.

Keywords: surface roughness; surface texture; standard; stylus.

1. Introduction

Surface texture plays a crucial role in various applications, whether in the automotive industry, medical technology, or the optical industry. It affects the function, durability, and aesthetics of components and workpieces, influencing factors such as friction, sealing, adhesion, lifespan, and optical properties of a product. Surface roughness describes the microstructures and irregularities found on a surface, which can include grooves, scratches, or unevenness. The roughness depth indicates how deep the grooves or protrusions on the surface are. DIN EN ISO 21920 specifies how these parameters should be measured and indicated [1, 2, 3].

Surface roughness is a geometric property of the surface and there are no direct methods to measure it. Surface roughness has a decisive influence on the coefficient of friction of contacting surfaces, on adhesion between surfaces and various other properties and phenomena, while it also has direct effects on the material properties of components but also has a key role in other areas, where it significantly affects the function of various devices [4].

Profile curves are usually measured and appropriate characteristics and quantities are evaluated from them, which are considered criteria for assessing surface roughness. Surface roughness parameters and values are defined in standards EN ISO 4287 [5] and EN ISO 5436 [6]. These standards were later replaced by standards ISO 21920-1, ISO 21920-2, ISO 21920-3 [1, 2, 3].

Current engineering practice is characterized by an increase in requirements for precision and reproducibility of production in the period of production of sophisticated production. The optimal quality of the surface of the parts is one of the prerequisites for the correct function of products (machines, devices, tools) and significantly affects the service life of the parts and even the entire machines. The roughness of the surface represents a collection of irregularities with relatively small distances from a perfect and ideally smooth surface, while these irregularities arise as a result of the used pro-duction technology or wear due to use (ISO 4287, ISO 21920-1, ISO 21920-2, ISO 21920-3) [1, 2, 3, 5].

Every technology used in the realization of technical surfaces leaves inequalities that are of fundamental importance in the function of these surfaces. It is very difficult to assess

the irregularities on the surface, which represent a certain spatial formation. This problem of assessing irregularities (surface structure) is solved by reducing to the plane of the section a plane perpendicular to the surface of the part (Figure 1). The profile of the surface of the component, which is obtained in the plane of the section, is the basic source of information for assessing the structure of the surface of the component [4].

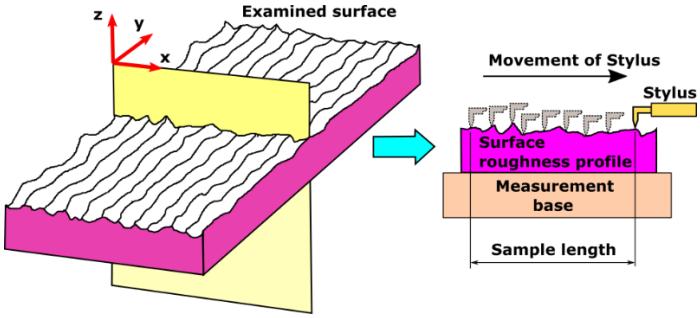

Figure 1. Part surface profile – as the intersection of the actual surface and the given plane [4].

For practical determination of surface roughness values there are two different methods known as surface roughness measurement which are contact-based and non-contact-based measurement. Contact based method is also referred to as Stylus-based surface roughness measurement. Stylus-based method uses a sharp tip that moves along the surface and allows to obtain information about its profile (Figure 2).

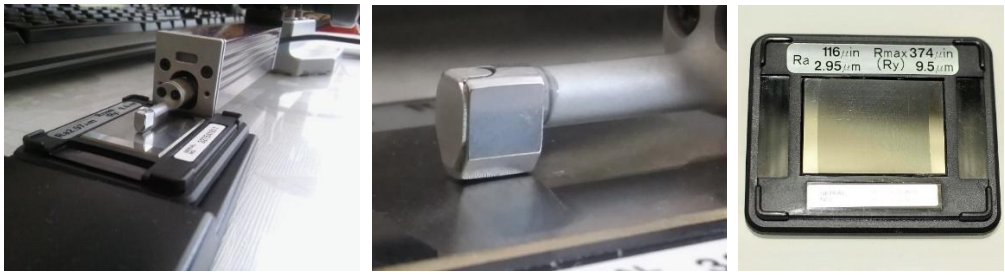

Figure 2. Stylus-based surface roughness measurement and calibration standard.

2. Calibration of stylus-based roughness testers

The basis for measuring surface roughness parameters and characteristics is the unit of length, defined in EN ISO standards and implemented by a set of micro-length etalons (line depth and line spacing), whose conventionally true value of line depth is measured by wavelength (on the device – interference microscopes), these etalons are for the area of surface roughness measurement - Primary Surface Roughness Standards.

Secondary Surface Roughness Standards also called etalons (Figure 2) are sets of standards that embody the values of roughness parameters – Ra, Rz, Ry and others. They are used to calibrate working gauges using the direct measurement method, where a measured standard of the same nominal value is directly calibrated using standard gauges.

Roughness standards (also called as Roughness etalons) are precision-made reference standards, essentially surface samples with known, highly accurate roughness values (like Ra, Rz), used to calibrate, check, and control surface roughness measuring instruments (profilometers) in laboratories, workshops, ensuring quality and accuracy in machining by comparing the tested part's texture to the standard's profile, often with traceable certificates.

For quick assessment of the surface quality of components, the Surface Roughness Standards Set – 30 Specimens made using various technologies is available on the market, which can be used to determine surface roughness by comparative methods, such as touch

or a comparative microscope (Figure 3). This set consists of 30 specimens 7/8" x 3/8" of electroformed solid nickel. Each type of surface finish, such as flat lapping, reaming, grinding, horizontal milling, vertical milling, and turning, is truly and consistently reproduced so as to give the operator or designer a realistic idea of the feel, appearance, and texture of the machined components [7].

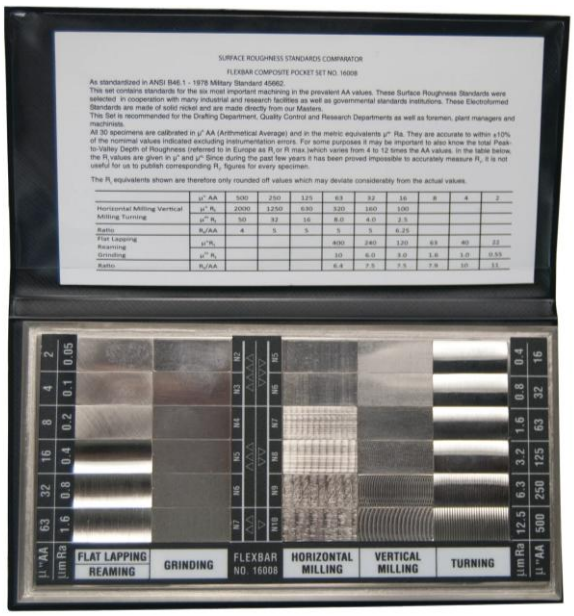

Figure 3. Surface Roughness Standards Set – 30 Specimens [7].

3. Secondary calibration standards

Surface roughness measuring instruments are calibrated using secondary calibration standards. ISO 5436-1:2000 defines 5 main types of standards (type A, type B, type C, type D, type E) [6, 8].

- **Type A**: Depth measurement standard - These measurement standards are for calibrating the vertical profile component of stylus instruments.

- Type A1 — Wide grooves with flat bottoms - These measurement standards have a wide calibrated groove with a flat bottom, a ridge with a flat top, or a number of such separated features of equal or increasing depth or height. Each feature is wide enough to be insensitive to the shape or condition of the stylus tip.

- Type A2 — Wide grooves with rounded bottoms - These measurement standards are similar to type A1, except that the grooves have rounded bottoms of sufficient radius to be insensitive to the shape or condition of the stylus tip.

- **Type B**: Tip condition measurement standard - These measurement standards are primarily for calibrating the condition of the stylus tip.

- Type B1 - These measurement standards have a narrow groove or a number of separated grooves proportioned to be increasingly sensitive to the dimensions of the stylus tip. The narrow grooves have rounded bottoms of sufficient radius to be sensitive to the shape or condition of the stylus tip.

- Type B2 - These measurement standards have a fine protruding edge. Uncoated razor blades, for example, have edge widths of approximately 0.1 μm or less. The stylus condition may be assessed by traversing such a specimen and recording the surface profile.

- **Type C**: Spacing measurement standard - These measurement standards are used primarily for calibrating vertical profile components. They may also be used for calibrating horizontal profile components if the spacing of the groves is held within limits acceptable for this purpose. The purpose of the series of measurement standards is to enable

the transmission characteristics to be checked for a number of spacings and amplitudes. They have a grid of repetitive grooves of simple shape (either sinusoidal, triangular or arcuate). An essential requirement of type C measurement standards is that standardized measurement standards of differing waveform are nevertheless compatible, in the sense that they will all lead to the same state of instrument calibration or verification, provided they are used correctly.

- **Type D**: Roughness measurement standard - These measurement standards are for overall calibration of instruments.

- Type D1 — Unidirectional irregular profile. These measurement standards have irregular profiles (for example as obtained by grinding) in the direction of traverse, but they have the convenience of an approximately constant cross-section perpendicular to the direction of traverse. The measurement standards simulate work pieces containing a wide range of crest spacings, but reduce the number of traverses needed to give a good average value. They provide, for reassurance, a final overall check on calibration.

- Type D2 — Circular irregular profile. These circular measurement standards have irregular profiles in the radial direction, but they have the convenience of an approximately constant cross-section along their circumference.

- **Type E**: Profile coordinate measurement standard - These measurement standards are intended for calibrating the profile co-ordinate system of the instrument.

- Type E1 — Precision sphere or hemisphere. These measurement standards consist of a sphere or hemisphere.

- Type E2 — Precision prism. These measurement standards consist of a prism with a trapezium cross-section. The base of the trapezium is the longer of the parallel surfaces. The top surface and the two surfaces generated by the sides of the trapezium are the measuring surfaces. The angles of the two side measuring surfaces are designed so that the stylus tip is in contact with the surface throughout the measuring instrument's range.

Each of these types of measuring standards may have a limited range of use according to their own characteristics and those of the instrument being calibrated. The validity of the instrument calibration will depend on the correct interrelation of these characteristics [6, 8].

4. Results

The surface tester used has an automatic calibration function using secondary surface roughness standards. A secondary standard meter for surface roughness testers is recommended for calibrating the meter, which is a calibration standard artifact with a unidirectional irregular profile type D1 (according to ISO 5436-1:2000) [6]. The value of Ra and Rz is defined for this artifact. In this work, this function is used and the calibration process is started before each batch of measurements and after the calibrations, a control measurement is always performed to verify the calibration process. Also, a control measurement is performed at the end of the measurement batch to verify the stability of the surface tester calibration (Figure 4).

To determine the measurement uncertainty for the used stylus-based profilometer, 100 control measurements were performed at the same location under the same measurement conditions on a secondary surface roughness standard (Figure 5).

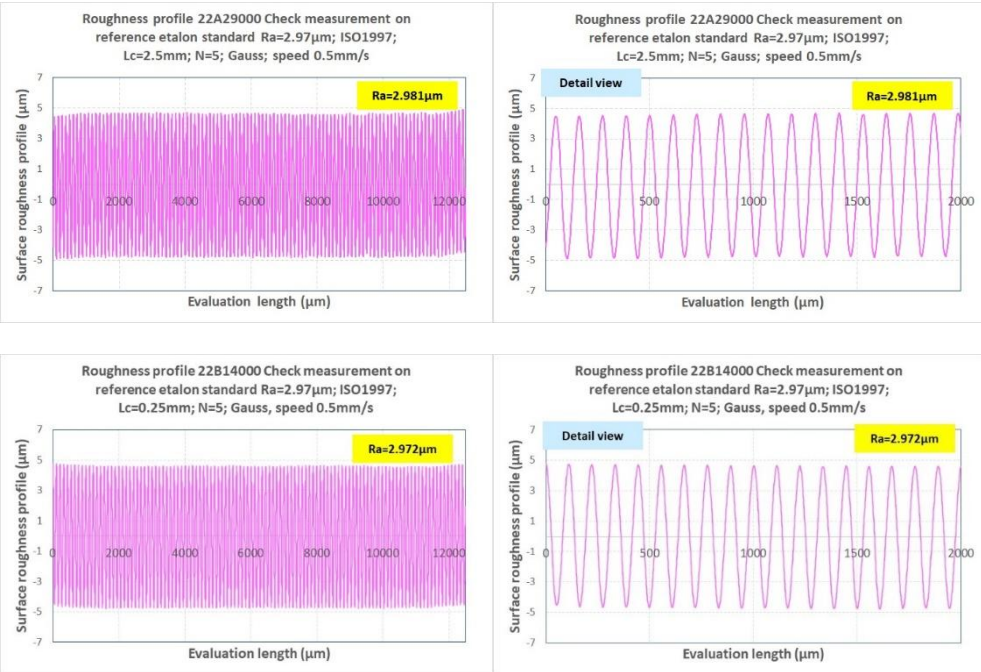

Figure 4. Control measurements after surface tester calibration.

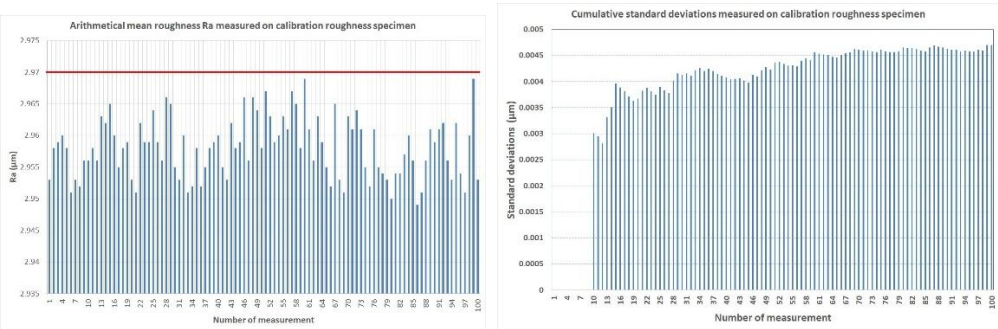

Figure 5. Arithmetical mean height of the roughness Ra values for 100 measurements at the same place under unchanged conditions (v=0.25 mm/s; Lc=0.8; X=5; Gauss). Cumulative standard deviations for 100 measurements at the same place under unchanged conditions.

5. Discussion

These measurements show a determining degree of variability (Figure 5 left) and the cumulative standard deviation was evaluated for these data (Figure 5 right). The cumulative standard deviation was determined by adding a new measured value to the dataset after each measurement and recalculating the standard deviation. This cumulative standard deviation thus also provides the development of the standard deviation with an increasing number of measurements. From this graph of the development of the cumulative standard deviation, it is possible to determine the maximum standard deviation of the measurement and at the same time it is possible to determine the required number of measurements. In this dataset, the optimal number of measurements is 30. By further increasing the number of measurements, the standard deviation worsens and further measurements are no longer necessary (Figure 5 right).

As a standard measurement uncertainty, we can consider the maximum value of the standard deviation of 0.005um (Figure 5 right).

6. Conclusions

The issue of determining surface roughness is quite complicated and with the development of available technologies, procedures and standards are also changing. In several

fields of science and technology, knowledge of surface roughness is a very important factor for identifying the manufacturing process and possible interaction with other parts of the device. This article addressed the calibration and estimation of the measurement uncertainty of a stylus based profilometer for determining surface roughness values. In further future research, the goal will be to obtain other types of standards and experimentally solve the problem of calibration and verification of these measuring devices.

Acknowledgments: The authors would like to thank the Slovak Grant Agency -project VEGA 1/0191/24, and project KEGA 004TUKE-4/2024.

Conflicts of Interest: The authors declare no conflict of interest.

References

1. ISO 21920-1:2021 Geometrical product specifications (GPS) — Surface texture: Profile — Part 1: Indication of surface texture. European Committee for Standardization. Brussels. December 2021.
2. ISO 21920-2:2021 Geometrical product specifications (GPS) — Surface texture: Profile — Part 2: Terms, definitions and surface texture parameters. European Committee for Standardization. Brussels. December 2021.
3. ISO 21920-3:2021 Geometrical product specifications (GPS) — Surface texture: Profile — Part 3: Specification operators. European Committee for Standardization. Brussels. December 2021.
4. Palová, K.; Kelemenová, T.; Kelemen, M. Measuring Procedures for Evaluating the Surface Roughness of Machined Parts. *Appl. Sci*. **2023**, *Volume 13*, 9385. https://doi.org/10.3390/app13169385.
5. ISO 4287:1997 Geometrical Product Specifications (GPS) – Surface texture: Profile method – Terms, definitions and surface texture parameters. First edition 1997-04-01. International Organization for Standardization. Geneve. Switzerland.
6. ISO 5436-1:2000 Geometrical Product Specifications (GPS) — Surface texture: Profile method; Measurement standards — Part 1: Material measures. European Committee for Standardization. Brussels. March 2000.
7. Surface Roughness Standards Set – 30 Specimens. Flexbar Machine Corporation. Available online: https://www.flexbar.com/products/surface-roughness-standards-sets (accessed on 7th dec 2025).
8. Leach, Richard. *The measurement of surface texture using stylus instruments*. Measurement Good Practice Guide No. 37. The National Physical Laboratory NPL. Teddington, Middlesex, United Kingdom, 2001, ISSN 1368-6550. 98 pages.
9. Semyon, G. Rabinovich. *Measurement Errors and Uncertainties*. Theory and Practice. Springer New York. 3rd ed. 2005, XII, 308 p. ISBN: 978-0-387-25358-9 (Print) 978-0-387-29143-7.
10. JCGM 100 – Evaluation of measurement data – Guide to the expression of uncertainty in measurement (ISO/IEC Guide 98-3). First edition September 2008. Available online: http://www.iso.org/sites/JCGM/GUM-JCGM100.htm.
11. JCGM 104 – Evaluation of measurement data – An introduction to the "Guide to the expression of uncertainty in measurement" (ISO/IEC Guide 98-1). First edition July 2009. Available online: http://www.bipm.org/en/publications/guides/gum_print.html.

TECHNICAL UNIVERSITY OF KOŠICE
Faculty of Mechanical Engineering

IMU-Based experimental verification of the stability of a specialized robotic locomotion system for pipeline environments

Patrik Pilát [1,*], Jozef Varga [1], and Ján Semjon [2] Filip Dominik [1], Kristián Takáč [2]

[1] Prototyping and Innovation centre, Faculty of Mechanical Engineering
[2] Department of Production Technology and Robotics
* Correspondence: patrik.pilat@tuke.sk; Tel.: +421908443216

Abstract: This paper presents an IMU-based experimental verification of the locomotion stability of a specialized mobile robot operating in a confined pipeline environment. The data was acquired using an Intel RealSense D435i sensor mounted on the robot chassis while moving inside the test channel, which forms the entrance section to the hot gas chamber of the KS-150 reactor. Two experiments with initial inclination angles of −20° and +20° were conducted. The recorded IMU data show that the robot motion reduces the inclination and stabilizes at a steady-state deviation of approximately 3–4 degrees. The results confirm that IMU-based sensing provides a suitable and practical method for stability assessment in confined environments where external measurement systems are not available.

Keywords: mobile robot, locomotion stability, IMU

1. Introduction

Robotic systems with capabilities for operation in pipeline and confined space environments are finding increased uses in areas such as industry inspection, maintenance, and nuclear decommissioning [1], [3], [9]. Pipeline environments and confined spaces represent geometrically constrained areas with limited visibility and a requirement for a high level of safety, all of which impose significant constraints on system design and control. In such environments, the stability of the mobility system becomes a critical factor.

Traditional validation of mobile robot stability often relies on external measurement systems or simplified laboratory setups [7]. However, in confined pipeline environments, external sensing is frequently infeasible. Inertial measurement units (IMUs) therefore represent a practical solution for monitoring of robot dynamics, as they provide direct measurements of linear acceleration and angular velocity independent of external references [7], [8].

This paper focuses on the experimental verification of locomotion stability using IMU data acquired during real robot motion inside a pipeline-like environment. The presented experiments build upon the mechanical design of a specialized service robot platform originally developed for nuclear decommissioning tasks [1], [9] and adapt it for systematic stability evaluation. The contribution of this work lies in the definition of an IMU-based experimental methodology, the implementation of a custom data-logging and visualization pipeline, and the interpretation of inertial data with respect to locomotion stability.

2. KS-150 Reactor and the hot gas chamber as the target operating environment

The real deployment environment motivating this research is the KS-150 reactor of the A1 nuclear power plant located in Jaslovské Bohunice, Slovakia. The A1 facility, commissioned in the early 1970s, employed a heavy-water moderated and carbon-dioxide-cooled reactor of unique design, which was permanently shut down following two serious

accidents in 1976 and 1977 [10], [11]. As a result, the reactor has been subject to long-term decommissioning activities involving high levels of radiological risk and extremely restricted human access.

From a robotics perspective, the hot gas chamber represents a challenging confined environment. Robotic systems operating in this space must reliably traverse the access pipeline, maintain stable contact with the inner surface, and perform precise operations without visual line-of-sight or external localization. These constraints directly motivate the need for experimental verification of locomotion stability under conditions representative of the KS-150 hot gas chamber environment [9], [10].

3. Robotic platform overview

The robotic platform used in this study is a specialized mobile service robot designed for operation in confined pipeline-like environments, specifically targeting the hot gas chamber of the KS-150 reactor at the A1 nuclear power plant in Jaslovské Bohunice. The platform architecture is derived from a service robot concept intended for nuclear decommissioning tasks, where restricted access, elevated radiation levels, and limited visibility prohibit direct human intervention [1], [9], [10].

The hot gas chamber is accessible through a straight cylindrical pipeline with an inner diameter of approximately 380 mm, which directly constrains the overall dimensions, wheel geometry, and stability requirements of the robotic platform. Consequently, the robot employs a wheeled locomotion system optimized for linear motion inside the pipeline, without the need for a steering axle.

The mobile platform consists of a driven front axle and a passive rear axle. The front axle provides traction and propulsion, while the rear axle ensures mechanical support and load distribution. To mitigate the risk of instability caused by shifts in the center of mass during manipulation tasks, an additional adjustable support wheel is integrated into the upper rear section of the robot. This design choice is particularly important during insertion and extraction of the cleaning robot from the hot gas chamber, when dynamic loading conditions are most pronounced.

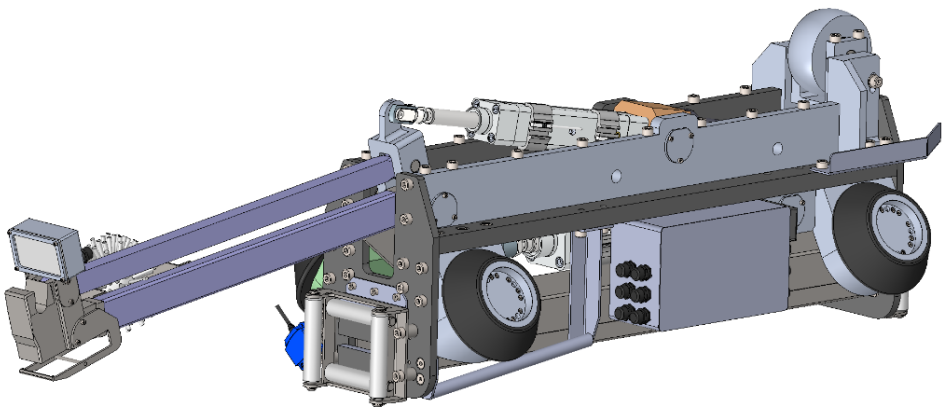

Figure 1. Service mobile robot.

Wheel geometry and surface treatment were selected to maximize contact stability with the inner surface of the pipeline. The wheels are shaped to conform to the cylindrical profile of the pipe and are coated with an elastomer layer to increase the coefficient of friction, thereby reducing slip and vibration during motion. Differential control of the driven wheels enables active compensation for minor deviations from the pipeline axis, which is essential for repeatable traversal of the access route [6].

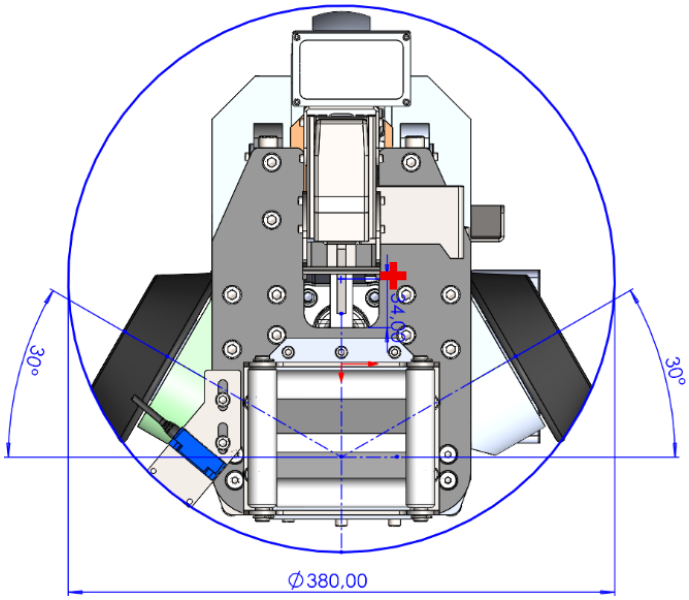

Figure 2. Position of the center of gravity of the mobile robot (front view), with the center of gravity marked by a red cross.

4. Overview Sensor System and IMU Integration

The experimental verification of locomotion stability presented in this study is fundamentally based on inertial sensing. For this purpose, an Intel RealSense D435i sensor was selected. In addition to its stereo vision capabilities, the D435i integrates a six-degree-of-freedom inertial measurement unit (IMU) consisting of a tri-axial accelerometer and a tri-axial gyroscope [5]. IMU-based sensing represents a well-established approach for analyzing the dynamic behavior of mobile robotic systems, particularly in confined or hazardous environments where external localization systems are unavailable or impractical [7], [8].

The IMU is rigidly mounted to the robot chassis to ensure that measured inertial signals directly reflect the dynamic behavior of the locomotion system. The sensor coordinate frame is aligned with the robot reference frame, with axes corresponding to the longitudinal, lateral, and vertical directions of motion inside the pipeline.

An inertial measurement unit (IMU) is a self-contained sensor system designed to measure the motion state of a rigid body by providing linear acceleration and angular velocity measurements. IMUs are widely used in mobile robotics for motion monitoring, stability assessment, and state estimation, especially in environments characterized by restricted geometry and limited accessibility [8], [9].

A conventional IMU consists of a tri-axial accelerometer and a tri-axial gyroscope, forming a six-degree-of-freedom sensing unit. Accelerometers measure specific force, which includes both linear acceleration and the gravitational component, while gyroscopes directly measure angular velocity. In the context of locomotion stability analysis, gyroscope measurements are of primary importance, as they capture rotational motion, vibrations, and transient disturbances of the robotic platform [7].

The gyroscope integrated in the Intel RealSense D435i belongs to the class of micro-electro-mechanical systems (MEMS) gyroscopes. MEMS gyroscopes are based on vibrating mechanical structures fabricated using micro- and nanoscale manufacturing techniques. Their compact size, low power consumption, and mechanical robustness make them suitable for embedded robotic applications [10], [11].

Figure 3. Left: 3-axis MEMS accelerometer layout; right: Intel RealSense D435i.

The operating principle of a MEMS gyroscope relies on the Coriolis effect. A microfabricated proof mass is driven to oscillate at a predefined resonance frequency (drive mode). When the sensor undergoes angular rotation, Coriolis forces induce a secondary vibration orthogonal to the drive motion (sense mode). The amplitude of this vibration is proportional to the applied angular rate and is detected using capacitive sensing elements [12], [13].

Modern MEMS gyroscopes, including those integrated into compact visual–inertial sensors such as the RealSense D435i, typically employ vibratory architectures such as tuning-fork or ring-type structures. These designs improve sensitivity, suppress common-mode disturbances, and reduce sensitivity to linear acceleration [11], [14].

According to the comprehensive review by Wang et al. [14], a typical vibratory MEMS gyroscope consists of a drive-mode resonator, a sense-mode resonator, electrostatic actuation electrodes, and capacitive sensing elements.

Figure 3 illustrates a representative MEMS gyroscope structure shown on the left. This architecture is directly applicable to the gyroscope technology employed in the Intel RealSense D435i (Fig. 3, right). The technical specifications of the Intel RealSense D435i camera are summarized in Table 1.

Table 1. Technical specifications of real sense D435i.

Parameter	hodnota	Parameter	hodnota
Depth Technology	Stereo depth with global shutter IR sensors	Dimensions	90 mm × 25 mm × 25 mm
RGB Camera Resolution	1920 × 1080 @ 30 FPS	Weight	72 g
Field of View (FOV)	87° × 58° (depth), 69° × 42° (RGB)	Gyroscope Type	MEMS, 3-axis
Depth Range	0.1 m to 10 m	Measured Axes	X, Y, Z (orthogonal)
Integrated IMU	Yes	Measurement Range (Full Scale)	±125, ±250, ±500, ±1000, ±2000 °/s
Illumination	Active IR projector with 850 nm wavelength	Minimum Detectable Angular Rate	0.02–0.05 °/s (after filtering)
Interface	USB 3.1 Type-C	Sampling Frequency	Up to 400 Hz
Power Consumption	~1.5 W	Angle Random Walk (ARW)	0.3–0.6 °/√h
Operating Temperature	0°C to 35°C		

5. Experimental setup

The experimental verification of the chassis stability was conducted on the robot entry device (Fig. 4- 2), designed for the hot gas chamber. This device enables controlled testing of the robot's (Fig. 4- 1), movement within a guide channel with an internal diameter of 380 mm. The channel has an approximate length of 2 m (Fig. 4- 4). Robot motion in both forward and backward directions was controlled via the robot's control panel. Before the start of the experiment, the robot was positioned inside the channel, and its nominal

orientation was defined using a spirit level, corresponding to a reference inclination of 0 degrees.

To record inertial data during the experimental verification of locomotion stability, a custom data acquisition script was developed using the Visual Studio Code environment. The script was implemented in Python and interfaces directly with the Intel RealSense SDK to access raw inertial measurements from the integrated IMU of the Intel RealSense D435i sensor.

The software enables real-time acquisition of tri-axial angular velocity and linear acceleration data at a predefined sampling rate. All IMU measurements are time-stamped using hardware-synchronized timestamps provided by the sensor, ensuring accurate temporal alignment of the recorded data with robot motion events.

During operation, inertial data are continuously streamed and logged into structured data files for subsequent offline analysis. Selected IMU signals are visualized in real time to allow immediate monitoring of the robot's dynamic behavior. Basic preprocessing, including offset handling and noise smoothing, is applied to improve signal quality while preserving stability-related dynamics.

Before the start of data acquisition, the camera was calibrated to establish the initial zero reference value.

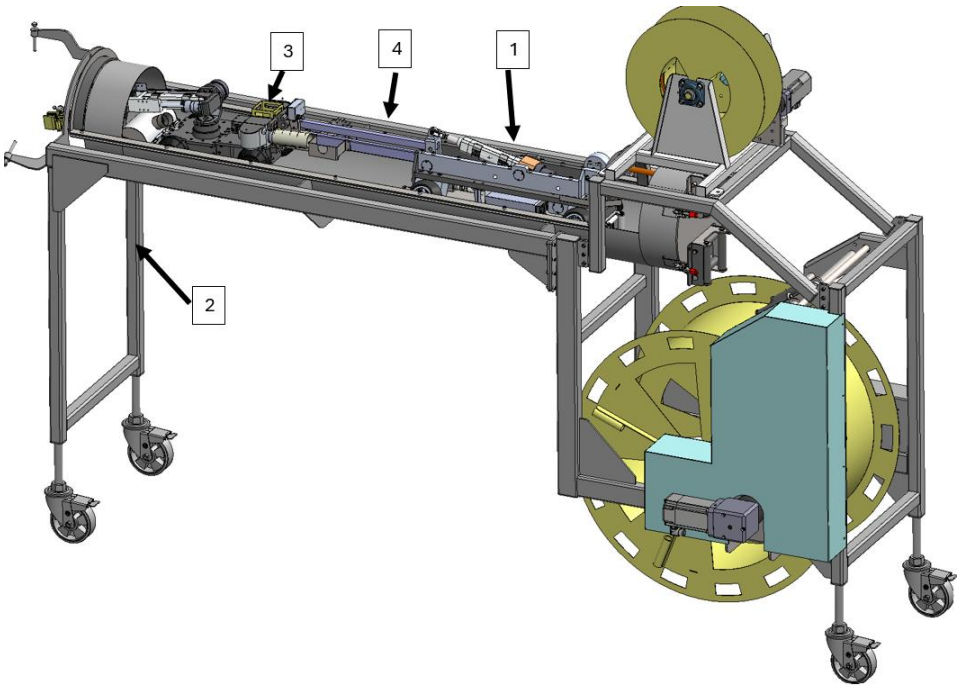

Figure 4. Entrance device with assistant service robot and cleaning robot.

Two experimental scenarios were considered. In the first case, the robot was initialized at an inclination angle of −20°, while in the second case, the initial inclination angle was +20°.

Experiment with −20° inclination: Following the definition of the nominal zero position, the mobile platform was intentionally inclined to −20°.

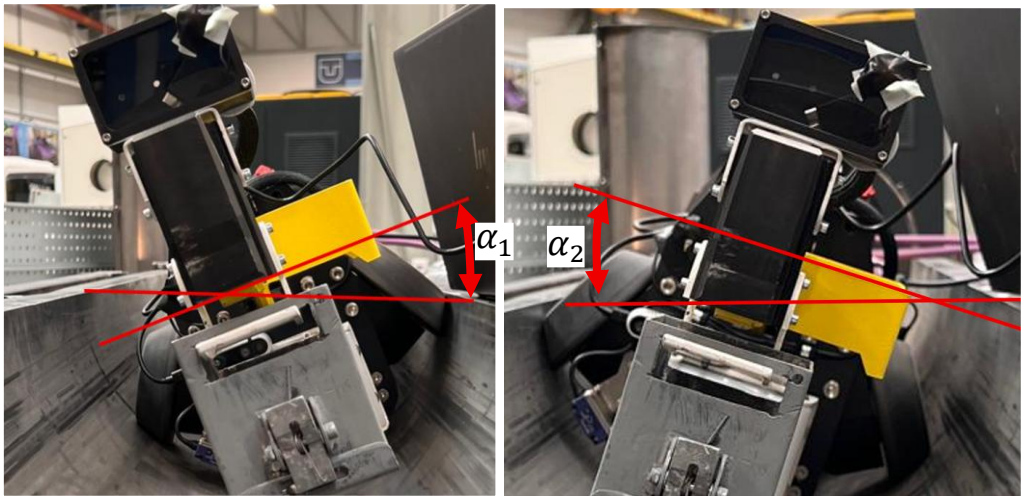

Figure 5. Left: Experiment 1 with an initial inclination of −20°. Right: Experiment 2 with an initial inclination of +20°.

After setting the mobile platform to an inclination angle of −20 degrees, the platform motion was initiated using the wheel-driven locomotion system. This inclination can be observed in the recorded data during the first 20 seconds of the graph. As the chassis rotation was performed manually, the resulting curve exhibits irregular behavior.

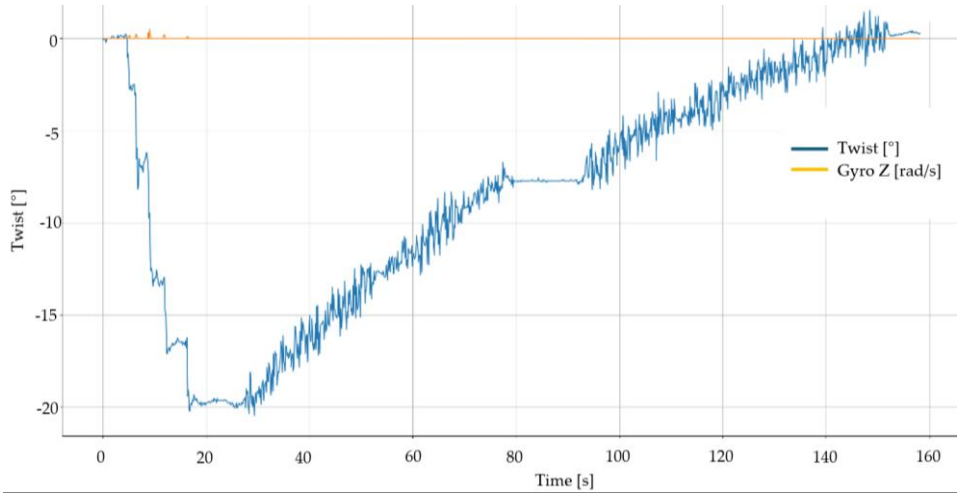

Figure 6. Recorded data from the first test.

From the recorded data, it can be observed that the robot's motion gradually reduces the inclination angle. The inclination value was measured with an uncertainty of ±3 degrees, which was caused by the dynamic motion of the wheeled chassis. The graph does not include the instantaneous distance traveled by the robot, as this parameter was not essential for the objectives of the experiment. Instead, only the total distance traveled during the experiment was recorded, amounting to 7 m.

Experiment with +20° inclination: In this experiment, after establishing the nominal zero position, the mobile platform was inclined to an angle of +20 degrees.

After setting the mobile platform to an inclination angle of +20 degrees, the platform motion was initiated using the wheel-driven locomotion system. As in the previous experiment, the chassis inclination was applied manually; therefore, the resulting curve exhibits irregular behavior.

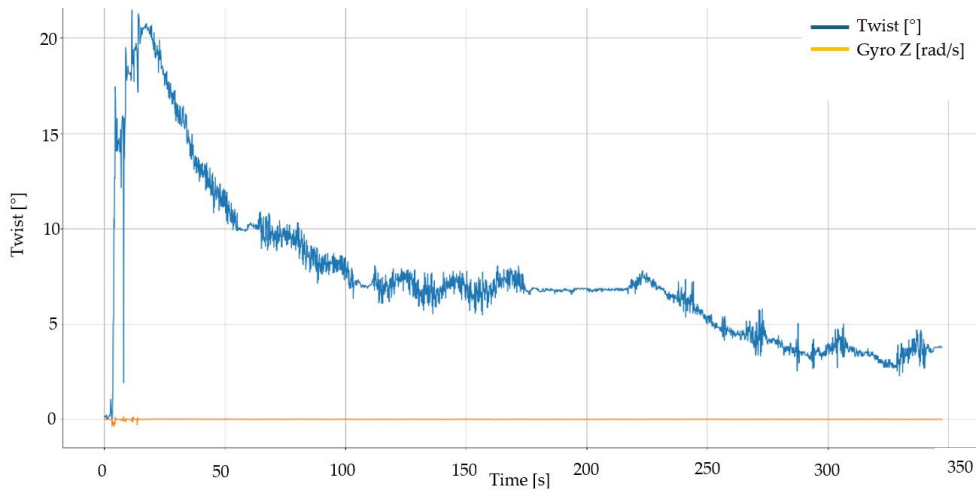

Figure 7. Recorded data from the second test.

From the recorded data, it can be observed that the robot's motion leads to a reduction of the inclination angle. The total distance traveled during this experiment was 8 m. The graph shows that the robot's inclination stabilizes at a value of approximately 3–4 degrees during motion and remains at this level for the remainder of the experiment.

Based on the experimental results, it was determined that the mobile platform stabilizes at an inclination angle of 3–4 degrees. This deviation from the expected behavior may be caused by the following factors:

- 3D model of the robot does not include the electrical enclosure and cable harnesses, which may cause a shift in the center of mass,
- supply cables were routed along one side of the guide channel, which may have contributed to lateral inclination of the platform,
- manufactured guide channel was formed by sequential bending and is therefore not perfectly circular; its geometry is not ideal. Consequently, if the experiment were performed in a channel with an ideal constant radius, the resulting values could differ.

An inclination of 3–4 degrees can be compensated by chassis steering correction. This correction is achieved by introducing a differential in the translational velocities of the right and left wheels. From the perspective of system functionality, an inclination of 3–4 degrees does not represent a limitation. Future experiments may focus on adjusting the center of gravity through the addition of weights to achieve full chassis alignment at zero inclination."

Figure 8. Mobile robot in the test channel.

6. Conclusions

An IMU-based experimental approach for verifying the locomotion stability of a mobile robotic platform was presented. Measurements performed under real operating conditions demonstrated that the robot stabilizes from initial inclinations to a steady-state deviation of approximately 3–4 degrees.

This deviation does not limit system functionality and can be compensated by differential wheel speed control. The proposed methodology offers a reliable tool for stability evaluation of robotic systems operating in confined and hazardous environments.

Conflicts of Interest: The authors do not declare any conflict of interest.

References

1. A. Iborra, J. A. Pastor, C. Fernandez, and J. M. F. Merono, "Robots in radioactive environments," *IEEE Robotics & Automation Magazine*, vol. 10, no. 4, pp. 12–21, 2003.
2. R. R. Murphy,"Humans and robots in off-normal applications and emergencies," in *Proceedings of the International Conference on Applied Human Factors and Ergonomics*, 2019.
3. M. Chiou, *Robot-Assisted Nuclear Disaster Response: Report and Insights from a Field Exercise*, 2021. Available online: https://www.osti.gov/biblio/1763665
4. E. J. L. Pulgarin and D. Hopper, "From traditional robotic deployments towards assisted robotic deployments in nuclear decommissioning," 2025. Available online: https://www.researchgate.net/publication/389119524
5. Intel Corporation, *Intel® RealSense™ Depth Camera D435i – Product Datasheet*, 2023. Available online: https://www.intelrealsense.com/depth-camera-d435i/
6. S. Hirose and H. Morishima,"Design and control of a mobile robot with articulated body for pipeline inspection," *IEEE Transactions on Robotics and Automation*, vol. 6, no. 1, pp. 36–44, 1990.
7. J. Borenstein and Y. Koren, "Gyro-based tracking of mobile robots," *IEEE Journal of Robotics and Automation*, vol. 4, no. 4, pp. 404–411, 1988.
8. H. Durrant-Whyte and T. Bailey, "Simultaneous localization and mapping: Part I," *IEEE Robotics & Automation Magazine*, vol. 13, no. 2, pp. 99–110, 2006.
9. International Atomic Energy Agency (IAEA), *Status, Barriers and Cost-Benefits of Robotic and Remote Systems Applications in Nuclear Decommissioning and Radioactive Waste Management*, Vienna, 2019. Available online: https://www.iaea.org/publications
10. S. Beeby, G. Ensell, M. Kraft, and N. White, *MEMS Mechanical Sensors*, Artech House, Boston, MA, USA, 2004.
11. C. Acar and A. M. Shkel, *MEMS Vibratory Gyroscopes: Structural Approaches to Improve Robustness*, Springer, New York, NY, USA, 2009.
12. D. Titterton and J. Weston, *Strapdown Inertial Navigation Technology*, 2nd ed., IET, London, UK, 2004.
13. O. J. Woodman, *An Introduction to Inertial Navigation*, University of Cambridge, Technical Report, 2007. Available online: https://www.cl.cam.ac.uk/techreports/UCAM-CL-TR-696.pdf
14. Y. Wang, Z. Zhao, X. Chen, and H. Luo, "A Review of MEMS Gyroscopes: Structure, Sensing Mechanism, and Error Sources," *Sensors*, vol. 21, no. 10, art. no. 3564, 2021.
Available online: https://www.mdpi.com/1424-8220/21/10/3564
15. VUJE Trnava Inc., *Decommissioning Project of A1 Bohunice Nuclear Power Plant*, Technical Report, Trnava, Slovakia, 2002.

TECHNICAL UNIVERSITY OF KOŠICE
Faculty of Mechanical Engineering

Assessment of the impact of noise on mental stress

Denisa Porubčanová [1,*], Tomáš Zábavský [1] and Michaela Balážiková [1]

[1] Technical University of Kosice, Faculty of Mechanical Engineering, Institute of Special Engineering Processologies, Department of Quality, Safety and Environment, Park Komenskeho 5, 042 00 Kosice-Sever, Slovakia; denisa.porubcanova@tuke.sk, tomas.zabavsky@tuke.sk, michaela.balazikova@tuke.sk.
* Correspondence: denisa.porubcanova@tuke.sk

Abstract: Noise is one of the factors in the working environment that is difficult to eliminate completely, so in practice we try to minimize it. The use of personal protective equipment is an appropriate means of protection against noise. Legislation sets maximum permissible noise levels in the working environment. It is well known that excessive noise in the workplace has a negative impact on hearing. However, noise itself can also have a negative impact on the mental well-being of employees, leading to increased psychological stress. This article deals with the assessment of the impact of noise in the workplace on the mental well-being of employees and the increase in mental stress during long-term exposure to noise. A GSR sensor was used to measure stress levels while noise measurements were also taken at the workplace.

Keywords: noise, workplace, psychical stress, risk assessment

1. Introduction

In recent years, psychological stress has become one of the most closely observed aspects of working life, mainly because stress-related illnesses and disorders are steadily rising. Human mental health is shaped by numerous influences encountered both in everyday life and in professional settings. Typical workplace factors include dust, elevated temperatures, unpleasant smells, and especially noise [1].

Noise represents one of the potential initiators of psychological difficulties. It can be characterized as a widespread environmental burden that primarily harms hearing, but research increasingly confirms its adverse effects on mental health as well. Long-term exposure to excessive noise functions as a psychological stressor and significantly increases the mental demands placed on employees. Even short-term exposure to extremely high noise levels may cause acute hearing damage, which can subsequently have negative psychological consequences [2].

2. Materials and Methods

2.1. Literature review

The harmful consequences of excessive noise on the human body have been thoroughly documented. Continuous or repeated exposure to sound levels exceeding 85 dBA is known to cause tinnitus, hearing impairment, and in severe cases complete hearing loss. Beyond auditory damage, noise also produces so-called extra-auditory effects, including cardiovascular disorders such as high blood pressure and heart rhythm disturbances, balance issues, sleep problems, and depressive symptoms. Some studies have also suggested a weaker and less consistent association between noise exposure and increased cholesterol levels. Moreover, workplace noise may directly influence employee performance and the quality of work, depending on the nature of the tasks performed [3, 4, 5].

While some authors question whether noise exposure can be considered a reliable predictor of mental health outcomes, other studies indicate a meaningful association between noise and psychological strain. Noise should not be viewed as the sole cause of mental distress; nevertheless, its contribution cannot be ignored [6].

Scientific findings demonstrate that noise not only damages hearing but also contributes to psychological discomfort, thereby increasing overall mental load at work. Numerous studies examining the relationship between noise and stress have shown that noisy environments can provoke irritability, fatigue, depressive moods, heightened sympathetic nervous activity, and gastrointestinal discomfort as manifestations of stress [4].

Further research has confirmed a link between noise exposure and physiological stress responses. The underlying biological mechanism involves increased physiological arousal triggered by activation of the endocrine and autonomic nervous systems, leading to elevated secretion of stress hormones [2].

This hormonal perspective is supported by additional studies that describe interactive stress models explaining how noise-related psychological stress raises the risk of cardiovascular, respiratory, and metabolic disorders. Recurrent stress responses disturb the body's internal balance and initiate a cascade of physiological reactions. Elevated levels of stress hormones have been consistently reported in investigations focusing on noise exposure [7].

Researchers in China have also examined the relationship between occupational noise and mental health, emphasizing the distinction between objectively measured noise and subjectively perceived noise. Perceived noise appears to exert a stronger negative effect on mental well-being than measured sound levels, highlighting individual differences in noise sensitivity. Factors such as age, gender, education, and occupation influence how noise is perceived and tolerated. Their findings indicate that higher perceived noise levels are associated with a greater risk of anxiety and depression [1].

To further substantiate the psychological effects of noise, a Malaysian research team monitored brain activity using electroencephalography while also measuring salivary alpha-amylase levels, a biomarker responsive to stress (figure 1). Participants performed identical tasks in both quiet and noisy environments. Results revealed increased alpha-amylase activity and reduced cognitive performance in noisy conditions, indicating heightened stress responses caused by noise [6].

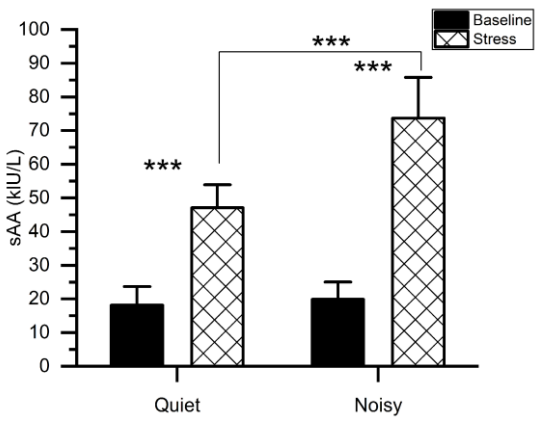

Figure 1. Comparison of salivary alpha amylase levels when working in a quiet environment (left) and in a noisy environment (right) [6].

The impact of noise on mental well-being has also been studied in open-plan office settings. Comparisons between open-plan offices and traditional, quieter office spaces showed reduced psychological well-being and increased stress in noisier, more crowded environments. Both subjective assessments and objective indicators, such as heart rate and skin conductance, confirmed higher stress levels in open-plan offices [8].

Similar conclusions were reached in studies comparing employees working in noisy production areas with those in quieter administrative departments. A clear relationship was identified between noise intensity and perceived work-related stress [9].

Simulation-based research further confirmed the association between noise levels and stress, emphasizing the effectiveness of hearing protection devices. Their use was shown to reduce perceived stress, again underscoring the link between occupational noise and psychological strain [10].

Other reviews addressing workplace conditions have likewise highlighted the combined negative effects of noise and unsuitable environments on overall human health [11].

2.2. Measurement

In order to assess the impact of noise on mental stress at work, an experiment was conducted to confirm the hypothesis that noise increases stress in the workplace. The measurements were taken on five subjects under the conditions specified in Table 1.

Table 1. Microclimate conditions at workplace.

Subject	Atmospheric pressure [hPa]	Humidity [%]	Temperature [°C]
1	1005	52	17
2	1010	51	18
3	1007	52	18
4	1001	54	17
5	1012	50	17

Noise was measured using a Bruel&Kjaer noise analyzer, model 2250-S. A GSR sensor was used to measure electrodermal activity, which is related to stress levels.

The measurement for each subject lasted 10 minutes and was performed in a natural working environment in a production hall, during a full range of work activities. The subject was informed in advance about the measurement procedure.

The measured data were then processed and evaluated.

3. Results

The measured values were used to calculate the average for each minute of measurement for each subject (table 2). These values were then used to create a graph and regression curve.

Table 2. Measured values of noise and stress.

Subject	Minute	1.	2.	3.	4.	5.	6.	7.	8.	9.	10.
Subject 1	Noise [dB]	74,5	77,2	79,9	75,3	78,8	79,2	80,5	77,5	81,1	78,8
	Stress [μS]	8,9	8,8	9,1	8,7	9,0	8,9	8,9	8,7	9,8	9,3
Subjec t 2	Noise [dB]	78,3	77,5	79,0	78,1	76,1	79,2	77,5	78,3	76,3	78,5

	Stress [μS]	8,6	8,4	8,6	8,2	8,0	8,5	7,9	8,5	8,4	8,8
Subject 3	Noise [dB]	76,4	79,5	77,8	75,3	77,9	75,3	78,6	80,7	79,5	80,5
	Stress [μS]	9,8	10,8	10,2	9,8	9,9	9,9	10,1	10,4	10,4	10,5
Subject 4	Noise [dB]	80,8	79,5	81,2	80,1	77,9	78,7	79,1	77,8	78,6	80,4
	Stress [μS]	8,2	8,3	8,5	8,3	7,9	8,2	8,2	8,0	7,9	8,1
Subject 5	Noise [dB]	77,2	78,7	79,9	80,1	77,7	79,6	80,4	76,9	78,1	76,8
	Stress [μS]	9,5	9,8	10,0	9,9	9,8	9,8	10,1	9,7	9,9	9,6

The data were processed into a mixed-effect model that highlights the relationship between noise levels and stress, taking into account the variability in physiological stress levels.

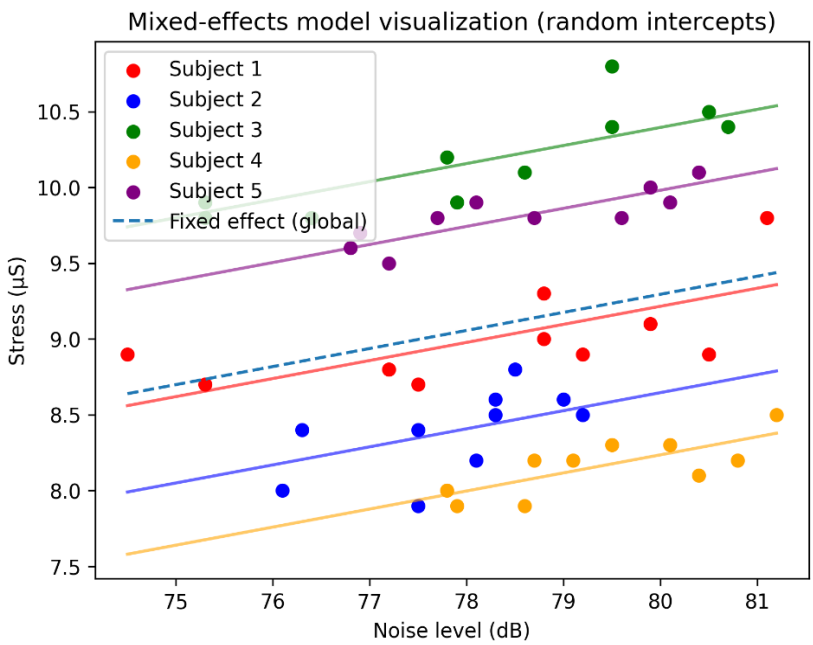

Figure 2. Relationship between noise level and stress illustrated in the Mixed-effect model visualization.

A linear mixed model with the subject as a random effect demonstrated a statistically significant positive relationship between noise and stress ($\beta = 0.119$, $p < 0.001$), with a 1 dB increase in noise leading to an increase in stress of approximately 0.12 μS. This result points to significant individual variability that was not captured by a simple correlation

analysis. The dashed line represents the fixed effect of noise, while the colored lines represent subject-specific intercepts. The results indicate a consistent positive relationship between noise and stress, with individual variability

4. Discussion

The experiment confirmed the hypothesis that noise has a negative impact on stress levels in the workplace. At the same time, however, it should be noted that stress is a complex problem caused by a large number of factors that cannot be completely separated. It can be said, however, that noise is one of the risk factors for psychological strain at work. Further measurements will be taken to examine the hypothesis in greater depth.

Acknowledgments: The research was prepared within the framework of the grant of KEGA Nr. 026TUKE-4/2023 Development Knowledge Support in the field of the quality management system requirements implementation in Aviation, Space and Defense Industry.

Conflicts of Interest: The authors declare no conflict of interest.

References

1. YANG, S., FU, Y., DONG, S., et all.: Association between perceived noise at work and mental health among employed adults in Southwest China. Journal of Affective Disorders, 2023, vol. 343, p.22-30. DOI: https://doi.org/10.1016/j.jad.2023.09.029
2. TAO, Y., CHAI, Y., KOU, L., KWAN, M.: Understanding noise exposure, noise annoyance, and psychological stress: Incorporating individual mobility and the temporality of the exposure-effect relationship. Applied Geography, 2020, vol. 125, art.102283. DOI: https://doi.org/10.1016/j.apgeog.2020.102283
3. THEMANN, C.L., MASTERSON, E.A.: Occupational noise exposure: A review of its effects, epidemiology, and impact with recommendations for reducing its burden. The Journal of the Acoustical Society of America, 2019, vol. 146, p.3879-3905. DOI: https://doi.org/10.1121/1.5134465
4. MOHAMED, A.O., PALEOLOGOS, E.K., HOWARI, F.M.: Chapter 19- Noise pollution and its impact on human health and the environment. Pollution Assessment for Sustainable Practices in Applied Science and Engineering, 2021, p.975-1026. DOI: https://doi.org/10.1016/B978-0-12-809582-9.00019-0
5. National Health Information Centre (NCZI). Occupational diseases or risk of occupational diseases. From https://data.nczisk.sk/statisticke_vystupy/choroby_povolania/Choroby_z_povolania_2022_Sprava_k_publikovanym_vystupom.pdf . Online: 2024-05-09
6. ALAYN, E., SAAD, N.M., KAMEL, N., et all: Frontal Electroencephalogram Alpha Asymmetry during Mental Stress Related to Workplace Noise. Sensors, 2021, vol. 21, i.6. DOI: https://doi.org/10.3390/s21061968
7. PRETZSCH, A., SEIDLER, A., HEGEWALD, J.: Health Effects of Occupational Noise. Noise Pollution, 2021, vol. 7, p. 344-358. DOI: https://doi.org/10.1007/s40726-021-00194-4
8. SANDER, E.J., MARQUES, C., BRIT, J., STEAD, M., BAUMANN, O.: Open-plan office noise is stressful: multimodal stress detection in a simulated work environment. Journal of Management & Organization, 2021, vol. 27 (6), p. 1021-1037. DOI: 10.1017/jmo.2021.17
9. ARDIYANSYAH, D., KAHAR, F., SURATMAN, et all.: The Relationship between Noise Level and Work Stress. International Journal of Medical Science and Clinical Research Studies, 2023, vol.3, p. 100-104. DOI: https://doi.org/10.47191/ijmscrs/v3-i1-20
10. MILAD, A., SAEID, Y., AHMAD, M., et all.: Noise Exposure and Job Stress – a Structural Equation Model in Textile Industries. BazTech, 2020, vol.45, no.4, p.601-611. DOI: 10.24425/aoa.2020.135248
11. KAMAL, E., REZA, T., TAYBEH, K., et all.: Evaluation of occupational noise exposure and general health of workers in industrial sites: A case study. Work, 2021, vol. 68, no.1, p. 115-121. DOI: 10.3233/WOR-203362

TECHNICAL UNIVERSITY OF KOŠICE
Faculty of Mechanical Engineering

Integration of Shape-Memory Alloy Actuator into a Scissor-Mechanism Gripper Design

Jaroslav Romančík [1,*], Marek Vagaš [1], Ondrej Majerčák [1]

[1] Technical University of Kosice, Faculty of Mechanical Engineering, Department of Industrial Automation and Mechatronics
* Correspondence: jaroslav.romancik@tuke.sk

Abstract: Miniaturization of actuators is essential for the development of lightweight and compact robotic systems. Shape memory alloys such as NiTi offer significant advantages due to their high-power density, silent operation, and inherent compliance. This paper presents the design, fabrication and testing of a scissor-type gripper actuated by a NiTi spring. The mechanism converts the thermal contraction of the NiTi element into a symmetric closing motion, assisted by an antagonistic return spring, while silicone fingers ensure better contact with objects. Gripping force was measured using a fixture with integrated strain gauges housed in a cylindrical enclosure. The experimental results confirm the feasibility of NiTi-based actuation for compact robotic end-effectors and highlight key considerations for their effective implementation.

Keywords: nitinol spring; shape memory alloy; scissor gripper

1. Introduction

Traditional actuators, such as electric motors, servomechanisms, or pneumatic cylinders, typically require complex mechanical transmissions, robust structural components, and extensive infrastructure for control. This leads to increased weight, size, and energy demands, which can significantly limit their use in compact, lightweight, and flexible robotic applications [1]. Intelligent materials offer an attractive alternative to these conventional technologies [2,3]. Among the most promising intelligent materials is NiTinol—a nickel–titanium alloy with shape-memory capabilities (SMA). This material combines low weight, high elasticity, fatigue resistance, and a unique ability to convert thermal energy directly into mechanical motion (Figure 1.) due to reversible transformation between austenite and martensite phases [4,5].

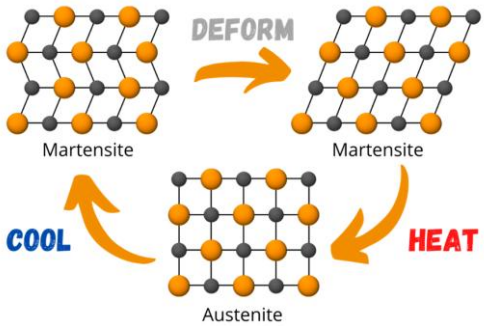

Figure 1. Diagram of the structural phase change between austenite and martensite.

As a result, NiTinol can function as an actuator without the need for bulky transmission mechanisms, simplifying the design and increasing the compactness of the entire device.

Integrating an SMA spring— which provides several times higher stroke compared to SMA wire—into a scissor mechanism represents a promising direction for developing end effectors, provided that high gripping speed is not required. Reaction speed is one of NiTinol's most significant limitations [6,7].

2. Materials and Methods

To model the behavior of the NiTinol spring, Brinson's mathematical model was used. This model makes it possible to calculate time-dependent changes in martensitic and austenitic fractions, the corresponding length deformation of the actuator, and the force generated depending on temperature and mechanical loading. For the dynamics of the SMA, the following applies [8]:

$$\xi_{eq}(T_w) = \frac{1}{1 + \exp\left(-\frac{T_w - T_{trans}}{dT}\right)} \tag{1}$$

$$\frac{d\xi}{dt} = \frac{\xi_{eq}(T_w) - \xi}{\tau_\xi}, \xi(t) \in [0, 1] \tag{2}$$

The thermal model of the SMA during cooling and heating is defined as [8]:

$$\frac{dT_w}{dt} = \begin{cases} \frac{T_{source} - T_w}{\tau_{heat}} \\ \frac{T_w - T_{initial}}{\tau_{cool}} \end{cases} \tag{3}$$

For SMA contraction and force generation, the following relations hold:

$$\Delta L(t) = \xi(t)\, p_{\mathrm{SMA}} \tag{4}$$

$$F_{\mathrm{SMA}}(t) = n_{\mathrm{wires}}\, T_{\mathrm{single}}\, \xi(t) \tag{5}$$

To connect the material model with the effector mechanics, a kinematic formulation of the scissor mechanism was developed. In the model, deformation of the SMA spring was transformed into a change in the finger opening angle of the effector, and subsequently into the output force at the tip of the arms, as follows:

$$\theta(t) = \theta_{\mathrm{open}} - \xi(t)(\theta_{\mathrm{open}} - \theta_{\mathrm{closed}}) \tag{6}$$

$$F_{\mathrm{tip}}(t) = \frac{F_{\mathrm{SMA}}(t)\, a_{\mathrm{SMA}} \cos\, \theta(t)}{b_{\mathrm{tip,lower}}} \tag{7}$$

These calculations provide the time-dependent response of the entire system, including the motion characteristics and force effects at the arm tips. This approach made it possible to analyze the gripping dynamics and to predict the geometry of the end-effector during opening and closing. The results serve as a basis for the design and optimization of an SMA-driven scissor actuator with an antagonistically coupled steel spring. The mathematical model was implemented in MATLAB (Figure 2.). Based on this model, simulations were performed, and their results enabled the design of the final physical prototype.

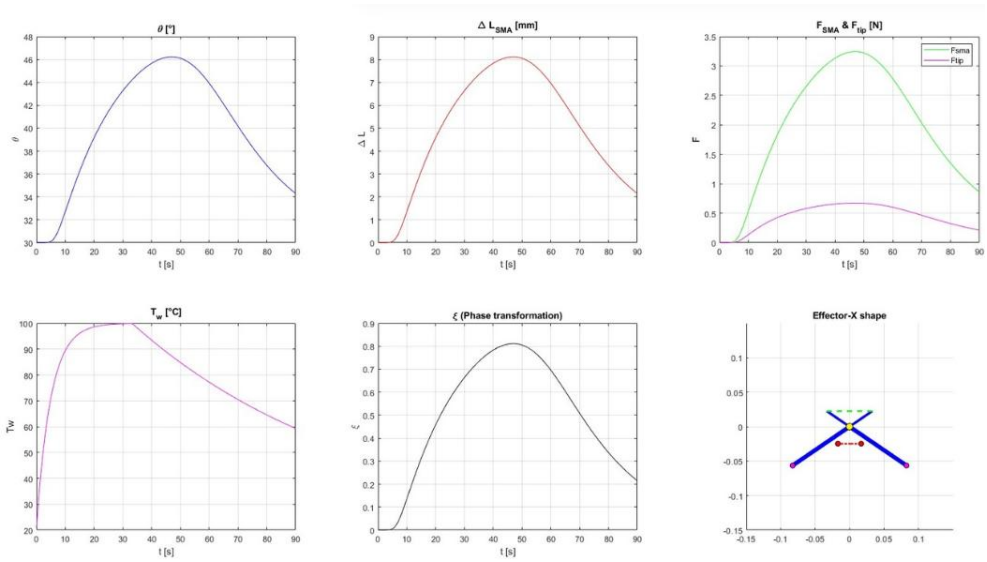

Figure 2. Graphical visualization of the simulation of the NiTi-actuated scissor gripper.

During the simulation of the effector's behavior, the length characteristics and placement of individual components were iteratively adjusted. Through this process, the following optimal configuration for our needs was determined:

- For a scissor gripper arm length of 100 mm, the pivot should be positioned at one-third of its length.
- The NiTi spring should be placed at one-half of the arm length and should connect both arms so that they are drawn together during actuation.
- The exact placement of the antagonistic spring is flexible, if it acts opposite to the NiTi force. The antagonistic effect can be tuned directly through the spring stiffness.

3. Real model actuator and experiment

For experimental validation, a fully functional physical prototype of the scissor effector was designed and manufactured, with dimensions derived from the simulations. The effector mechanism consists of two scissor arms that convert the longitudinal contraction of the NiTi spring into a symmetrical closing motion of the fingers (Figure 3.). An antagonistic return spring is mounted on the arms to generate the opposing motion. The end of the effector is equipped with two silicone fingers, which enhance gripping performance and provide a compliant contact surface with the object.

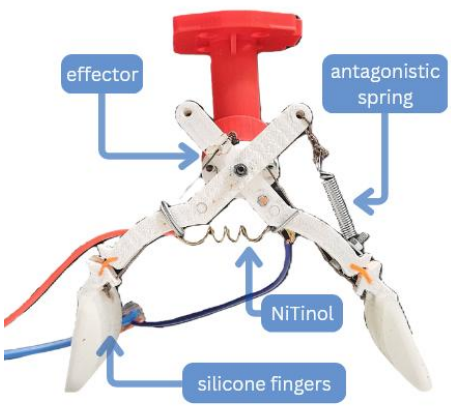

Figure 3. Gripper construction.

To measure gripping force, a force-measurement fixture was used, consisting of two strain gauges integrated into a cylindrical housing (Figure 4.). When the effector grasps the fixture at its central section, the forces are transmitted symmetrically to both strain-gauge elements. The mechanical deformation caused by gripping was converted into voltage changes, which were subsequently processed and interpreted as the resulting gripping force.

Figure 4. Force-measurement fixture.

Measurements were carried out on a laboratory test setup equipped with a programmable power supply and an oscilloscope (Figure 5.). These devices allowed precise control of the current flowing through the NiTi spring and simultaneous monitoring of the system's dynamic response, as the strain-gauge fixture was connected directly to the oscilloscope.

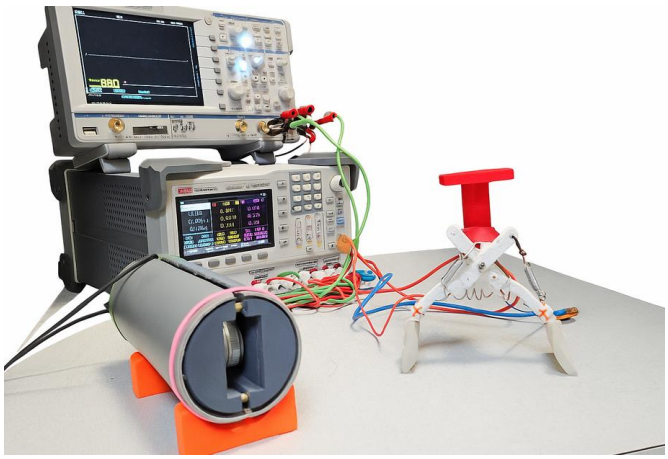

Figure 5. Test workstation for grip-force measurement.

After evaluating the collected oscilloscope data, we obtained a clear understanding of the gripping force produced by the designed effector. For improved data interpretation, filtered graphical representations were made (**Figure 6.**), yielding the following plot:

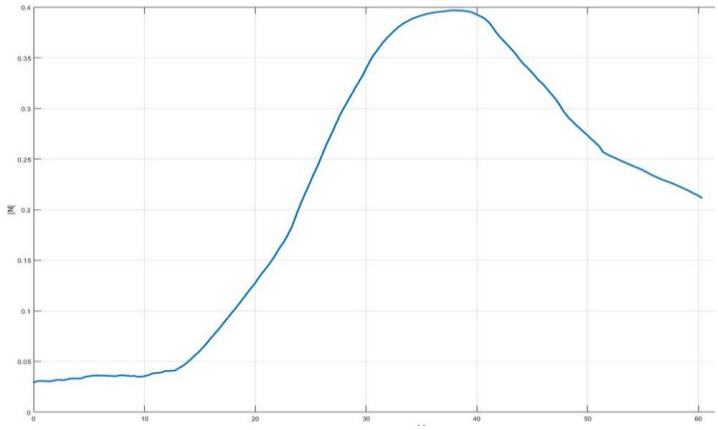

Figure 6. Graph of the gripping-force profile.

4. Discusion and evaluation of results

This article focuses on the design of an effector that generates a gripping force of 0.4 N. Although this value may seem low, the gripping efficiency is enhanced by silicone fingers, which improve grip stability through quasi-frictional interaction. Comparison of experimental results with the model confirms its functionality and provides a reliable basis for further mechanism evaluation, as well as for implementing parallel connections of Ni-Tinol elements to increase the generated force.

Acknowledgments: This work has been supported by the Slovak grant VEGA 1/0169/22 New methodics approaches to data from automated and robotized workplaces.

Conflicts of Interest: The authors declare no conflict of interest.

References

1. J.M. Jani, M. Leary, A. Subic, M.A. Gibson, A review of shape memory alloy research, applications and opportunities, Materials & Design (1980-2015), vol. 56, 2014, s. 1078-1113,ISSN 0261-3069.
2. M. S. Kim, J.-K. Heo, H. Rodrigue, H.-T. Lee, S. Pané, M.-W. Han, S.-H. Ahn, Shape Memory Alloy (SMA) Actuators: The Role of Material, Form, and Scaling Effects, Advanced Materials, vol. 35, no. 33, 2023, Article e2208517, doi:10.1002/adma.202208517.
3. K. Susmita, Introduction, Classification and Applications of Smart Materials: An Overview, American Journal of Applied Sciences 10 (8), Jul. 2013, ISSN:1546-9239
4. B. Zohuri, F. Behgounia, F. Behgouni, M. J. Moghaddam, Memory Metals or Shaping Alloys, Modern Approaches on Material Science, Feb. 2021, s. 415-423, ISSN: 2641-6921.
5. Qader I. N., Kök M., Dagdelen F., Aydoğdu Y., A review of smart materials: researches and applications, El-Cezerî Journal of Science and Engineering (ECJSE), vol. 6, no. 3, 2019, s. 755–788, ISSN 2148-3736.
6. C. Greco, "The evolution of mechanical actuation: from conventional actuators to artificial muscles," *International Materials Reviews*, 2022. doi:10.1080/09506608.2021.1971428
7. J. Romancik, M. Vagas, and O. Majercak, "Design, Implementation, and Testing of a 3D-Printed Gripper Actuated by Nitinol Springs," MM Science Journal, vol. 2024, pp. 7352–7356, 2024, doi: 10.17973/MMSJ.2024_06_2024009.
8. L. C. Brinson and M. S. Huang, "Simplifications and Comparisons of Shape Memory Alloy Constitutive Models," Journal of Intelligent Material Systems and Structures, vol. 7, no. 1, pp. 108–114, 1996, doi: 10.1177/1045389X9600700112.

TECHNICAL UNIVERSITY OF KOŠICE
Faculty of Mechanical Engineering

Influence of Rolling Mill Parameters on the Mechanical and Surface Properties of Thin Galvanized Sheets

František Ruda [1,*], Emil Spišák[1]

[1] Department of Technology, Materials and Computer-Aided Technology, Faculty of Mechanical Engineering, Technical University of Košice,04001 Košice, Slovakia; frantisek.ruda@student.tuke.sk; emil.spisak@tuke.sk
* Correspondence: frantisek.ruda@student.tuke.sk; Tel.: +421 910 947 185

Abstract The aim of this work is to analyze the influence of rolling process parameters, weld joint quality, and the condition of work rolls on the resulting surface micro-geometry of galvanized sheets. The study focuses on the role of chrome-plated work rolls, the control of thickness and mechanical properties in the weld area, and the identification of the most common defects occurring during skin-pass rolling. In the experimental part, surface roughness measurements (Ra, RPC) were performed on samples taken from a galvanized strip, complemented by visual flatness evaluation and imprint inspection. The results confirm that the stability of technological parameters, weld quality, and work-roll cleanliness are crucial for eliminating defects and ensuring the required surface quality.

Keywords: galvanized sheet, surface micro-geometry, skin-pass rolling, roughness Ra, weld joint, work rolls, imprints, flatness

1. Introduction

Rolling of galvanized sheets (Figure 1) represents a technologically demanding process in which precise parameter settings, work-roll quality, and the stability of the incoming material play key roles [12]. Modern rolling lines are designed to ensure high repeatability, accuracy, and surface quality; however, the presence of weld joints, material inhomogeneity, or insufficient roll maintenance can significantly affect the final product [4]. This chapter focuses on analyzing the factors influencing the quality of galvanized sheets, with emphasis on surface micro-geometry, weld behavior during rolling, and the formation of defects occurring in the skin-pass rolling process [2–3].

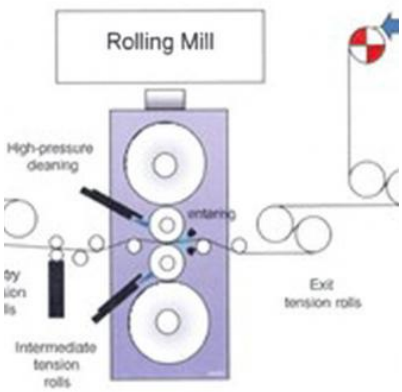

Figure 1. Skin-pass mill.

2. Important Conditions in the Production of Rolled Materials

2.1. Chrome-plated work rolls and their significance in the process

Chrome-plated work rolls (Figure 2) are currently the standard in the production of galvanized sheets, particularly in the automotive and electrical industries [5]. The chromium layer provides:

- increased surface hardness,
- higher resistance to abrasive wear,
- reduced susceptibility to imprint formation,
- longer roll service life,
- more stable rolling conditions.

Figure 2. Work rolls of the skin-pass mill: ground, chrome-plated.

Imprints on work rolls are among the most common causes of surface defects in galvanized sheets [5]. They occur under local overloading, which may be caused, for example, by non-uniform strip thickness, hard inclusions, weld joints with differing properties, surface contamination.

The chromium layer acts as a protective shield that reduces the risk of damage and thus the subsequent transfer of defects onto the strip surface, as illustrated in Figure 3.

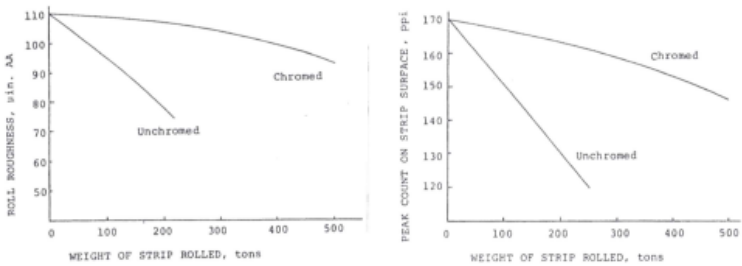

Figure 3. Defect rate on rolls with and without coating.

2.2. Rolling of welds under standard process parameters

Weld joints represent a critical section of the strip that can disrupt process stability [6]. To safely pass the weld through the rolling mill stand, it must meet strict requirements:

- the same thickness as the base material,
- the same strip width,
- the same mechanical properties,
- the same yield point,
- o visible surface irregularities.

If the weld behaves differently from the base material, this leads to uneven roll loading, local overloading, imprint formation, strip deformation, deterioration of flatness.

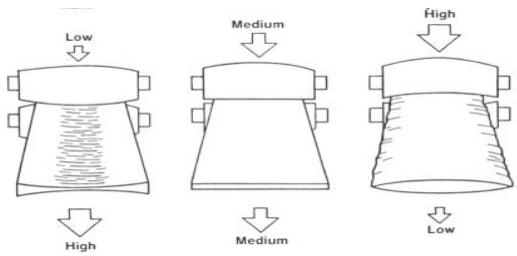

Figure 4. During weld passage, improper SPM settings can lead to defects.

From a technological standpoint, it is therefore essential to ensure that the weld is rolled under standard parameters without the need for process intervention [4]. Modern lines are equipped with automatic weld-detection systems that enable timely roll opening and prevent contact between the weld and the work rolls [2–4].

2.3. Thickness and mechanical-property inspection in the weld area

Changes in thickness or mechanical properties in the weld area can lead to significant technological issues [15]. The most common problems include:

- increased weld thickness,
- harder weld metal,
- unsatisfactory microstructure,
- local strength variations.

These deviations cause uneven force distribution during rolling, which may lead to roll damage [9]. Therefore, it is necessary to perform:

- thickness measurement before and after the weld,
- hardness inspection,
- metallographic analysis,
- flatness measurement,
- automatic weld detection.

The most effective solution is to avoid rolling welds entirely, which is achieved by automatic roll opening upon weld detection [16].

3. Surface Microgeometry of Galvanized Sheets

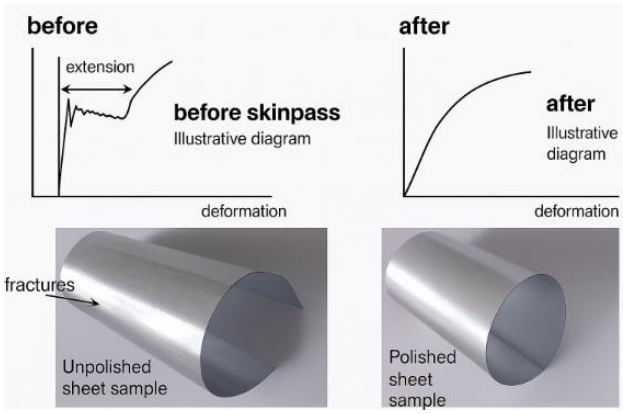

Figure 5. Comparison of surface finishing before and after SPM.

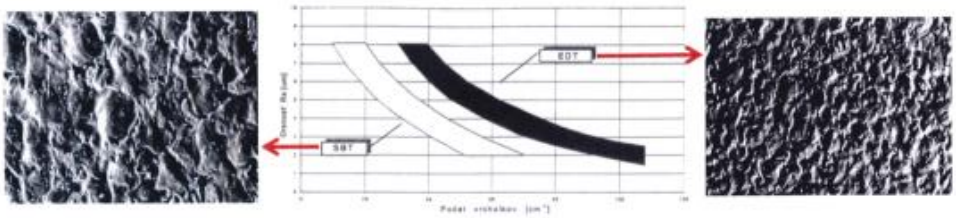

Figure 6. Differences in rolling with uncoated rolls and chromium-coated rolls.

3.1. Importance of surface roughness for subsequent processing

Surface roughness is one of the most important parameters determining the quality of galvanized sheets [18]. It represents a set of fine irregularities formed during rolling, galvanizing, and subsequent skin-pass rolling [4]. It is influenced by:

- formability during stamping,
- friction between the sheet and the tool,
- uniformity of paint application,
- aesthetic appearance after painting,
- adhesion of surface layers.

For customers, key values include Ra (average roughness) and RPC (peak count per unit length) [8]. These parameters must remain stable throughout the entire coil, as even small deviations can lead to issues during stamping or painting [7].

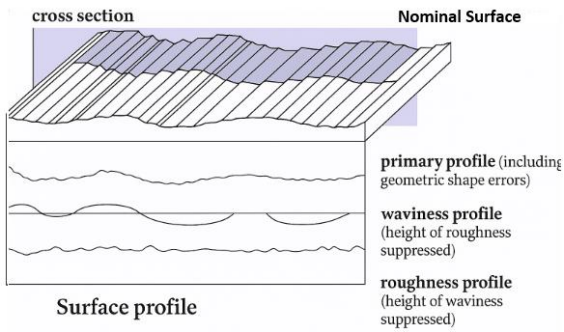

Figure 7. Perpendicular section of the nominal surface.

3.2. Methodology of Surface-Roughness Measurement

Roughness measurements are carried out on samples taken from the galvanized strip [4]. To ensure accurate results, it is necessary to follow these requirements:

- cleanliness of the measured surface,
- degreasing and removal of contaminants,
- measurement perpendicular to the rolling direction,
- measurement on both sides of the sheet,
- sampling 10 cm from the strip edge,
- three measurements: edge 1 – center – edge 2.

The results are averaged and compared with customer requirements or internal standards [3].

Figure 8. Surface-roughness meters.

4. Defects of skin-pass rolling

Skin-pass rolling is a process that improves strip flatness, surface microgeometry, and mechanical properties [4–5]. Nevertheless, defects may occur that negatively affect product quality [9].

4.1. The Most Common Defects After Rolling on the SPM:

- Strip flatness (edge or center waviness) Occurs due to non-homogeneous stresses or improper roll settings.
- **Strip marking** Appears as longitudinal streaks caused by contamination or damaged rolls. Illustrated in Figure 10.
- **Indentations on galvanized sheet** Occur when the strip comes into contact with a damaged work roll or during rolling over weld seams. Illustrated in Figure 9.
- **Build-ups on rolls** Caused by zinc or lubricant residues; prevention includes high-pressure cleaning and the use of detergents.
- **Non-conforming mechanical properties** Deviations in tensile strength or yield strength may cause issues during stamping.
- **Poor surface micro-geometry** Incorrect skin-pass mill settings lead to excessively low or high surface roughness.
- **Non-uniform surface appearance** May be caused by inhomogeneous zinc coating composition or surface contamination.
- **Under-rolled edges** Occur due to incorrect roll width adjustment or uneven roll pressure.

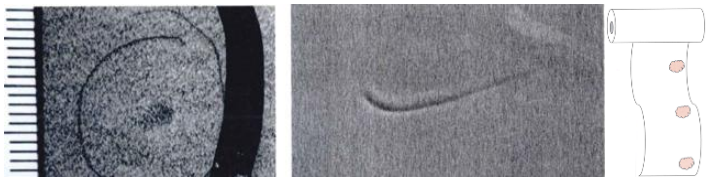

Figure 9. Roll indentations.

Figure 10. Strip marking and under-rolled edge.

5. Conclusion

The quality of galvanized sheets is the result of a complex interaction between the condition of the work rolls, the rolling parameters, and the surface micro-geometry. Chromium-plated rolls, properly adjusted technological parameters, and thorough inspection of weld joints represent key factors in preventing defects. Equally important is precise control of surface roughness, which influences both the processability and the aesthetic properties of the final product. Identifying and eliminating skin-pass rolling defects is essential for ensuring stable quality and meeting customer requirements.

Acknowledgments: This work was supported by the project APVV-21-0418 and project KEGA 018TUKE-4/2025.

Conflicts of Interest: "The authors declare no conflict of interest."

References

1. Blaščík, F., Polák, K.: Teória tvárnenia. Alfa Bratislava 1985, s. 374.
2. Blaščík, F. et al.: Technológia tvárnenia, zlievarenstva a zvárania. ALFA Bratislava , 1988.
3. Blaščík, F., Kmec, J. Automatizácia technologických pracovísk v plošnom tvárnení. ALFA Bratislava 1990, s. 393, ISBN 80-05-00055-3
4. Spišák, E., Slota, J., Majerníková, J.: Anisotropy evaluation of tinplates. In. Pro-tech-ma ´07 : Progressive Technologies and Materials: International Scientific Conference: Rzeszów – Bezmiechowa, Poland, 28th June – 30th June 2007. Rzeszów . Politechnika Rzeszowska, 2007. ISBN 978-83-7199-443-2. p. 217-222
5. ANDERSOM, J.C. et al.: Materials Science. Stanley Thornes Cheltenham, 1990, p. 608, ISBN 0-7487-4077-5
6. ASHBY, M.F.: Materials Selection in Mechanical Design. Heinemann, Third edition 2005, ISBN 0-7506-6168-2
7. ŠIMČÁK,D., BILLÝ,J., ŠTEFAN,B., KRAJČÍ,J.: Hodnotenie lisovateľnosti plechov pre automobilový priemysel. Hutnícke listy, 1998, č.6
8. Billy, J.; Štefan, B.; Slávik, P.; Mikolaj, L.; Gašpar, V.: Oceľové plechy 3-4, 1993, s.21-27
9. CMB.: Specification of Single and Double Reduced Tinplate for the Manufacture of Can Bodies and Ends, CMB Packaging Technology, Metalurgy and Materias, March 1992
10. STACHOWICZ,F. - SPIŠÁK,E.: Sposoby oceny zdolności blach cienkich do kształtowania plastycznego na zimno. Rzeszów 1998, s.121, ISBN 83-7199-078-2
11. Evin, E., Spišák, E., Majerníková, J.: Predikcia lisovateľnosti vysokopevných oceľových plechov. In: Materiál v inžinierskej praxí 2008: 7. vedecko-technická konferencia, Herl'any. Košice: TU, 2008, s. 79, ISBN 978-80- 8073-945-4.
12. Blaščík, F., Polák, K.: Teória tvárnenia. Alfa Bratislava 1985, s. 374
13. Čech, J., Grutková, J., Kurian, J., Rodziňáková, O.: Náuka o kovoch, Návody na cvičenia. ALFA Bratislava, 1981
14. KOTTFER, Daniel – FERDINANDY, Milan: Tenké vrstvy. Košice: Strojnícka fakulta technickej univerzity, 2010. 100 s. ISBN 978-80-553-0359-8
15. Žárové nástřiky – moderní technologie povrchových úprav, nástřik plamenem [online]. [cit. 2023-12-05]. Dostupné na http://www.kmm.zcu.cz/CD/content/8_1.html.
16. ZRŮNEK, Miroslav: Úprava povrchu kovových konstrukcí. Praha: SNTL- Nakladatelství technické literatury, 1981. 120 s. ISBN 04-209-81.
17. ČÍHAL, Vladimír: Kovové povlaky při protikorozní ochraně se zřetelem na jejich fyzikálně – chemické vlastnosti. In: Progresívní a netradiční technologie povrchových úprav: VI. Medzinárodná výstava povrchových úprav Protech ´98, Praha: Fakulta strojní ČVUT, 1998. s. 38 – 44.
18. STACOWICZ,F.: Odksztalcaność graniczna blach mosieznych, Rzeszów 1989, s.118, ISSN 0209-2689
19. STN EN 10002-1 Kovové materiály. Skúška ťahaním I.časť. Skúška ťahaním pri teplote okolia I., 7/1997

TECHNICAL UNIVERSITY OF KOŠICE
Faculty of Mechanical Engineering

A Data-Driven Forward Kinematics Model for a Tendon-Driven Continuum Robot Using MLP-Based Regression

Dárius Rusiňák [1,*], Ivan Virgala [1]

[1] Department of Industrial Automation and Mechatronics, Faculty of Mechanical Engineering, Technical University of Košice, 042 00 Košice, Slovakia; darius.rusinak@tuke.sk (D.R.); ivan.virgala@tuke.sk (I.V.)
* Correspondence: darius.rusinak@tuke.sk

Abstract: Traditional mathematical approaches to modeling the forward kinematics of continuum robots often result in complex formulations that are not well suited for real-time applications. This article presents a data-driven approach to forward kinematic modeling of a single-segment tendon-driven continuum robot. Experimental data were collected using a motion capture system to establish a mapping between tendon lengths and the corresponding tip position of the robot. These data were used to train a multilayer perceptron regression model, whose architecture and hyperparameters were selected through random search–based hyperparameter optimization. The resulting model achieves high accuracy in estimating the robot's tip position across the evaluated workspace. The results demonstrate that multilayer perceptron regression can effectively capture the nonlinear behavior of tendon-driven continuum robots, indicating its suitability as an alternative to analytical models for forward kinematics.

Keywords: continuum robot; machine learning; forward kinematics

1. Introduction

Continuum robots are robotic systems that differ from conventional robots, consisting of rigid bodies, by effectively having an infinite number of degrees of freedom. Their behavior mimics biological structures such as elephant trunks [1], cephalopod arms [2], or snake bodies [3]. Features such as high flexibility and adaptability make continuum robots attractive research subjects in the fields of industrial maintenance [4] or minimally invasive surgery [5] (MIS), where they have the potential to replace commonly used rigid tools. However, these features inherent to the continuum robots also make the problems of their modeling and control much more complicated.

The goal of the forward kinematics model for continuum robots is to describe the relationship between the actuation, shape of the robot, and its Cartesian coordinates in space. Some of the most commonly used mathematical approaches to modeling of forward kinematics of continuum robots are rigid link [6], which describes the robot as a series of rigid bodies connected with joints; piecewise constant curvature [7], which assumes that the robot consists of a series of tangent curves with constant curvature; and variable curvature [8], which describes the position and orientation of the robot as a function of arc length and curvature along its backbone. Application of these approaches enables the formulation of accurate kinematic models; this, however, comes with the caveat that the more accurate models are described by more complex equations that require more computational power. These factors make the listed approaches less adequate for the real-time applications. Due to these reasons, concurrent research increasingly explores the application of learning-based solutions for solving the forward kinematics of continuum robots [9].

This article introduces a data-driven solution to the forward kinematics problem for a single-segment, tendon-driven continuum robot based on the experimental data gathered by the motion capture system. Utilizing this dataset, a multilayer perceptron (MLP) regression model that maps tendon lengths to the corresponding positions of the robot's tip was developed. The article further examines how variations in network architecture and hyperparameters affect the performance of the trained models.

2. Materials and Methods

2.1. Continuum Robot

This article proposes a forward kinematics model for the single-segment tendon-driven continuum robot developed for the purposes of MIS. The mechanical structure of the robot is described by the outer diameter of 12 mm and the total length of 110 mm. In addition, a tube with an outer diameter of 4 mm is installed inside of the robot, whose purpose is the transition of medical instruments. The robot's motion is achieved through deformations caused by the elongation and tightening of three tendons routed along its entire length.

2.2. Training Dataset

The motion capture system (mocap), consisting of six OptiTrack PrimeX 13 mocap cameras and Motive software, was used to gather the necessary data for the training of the forward kinematics model of the inspected continuum robot. The robot was mounted to the testing bench that contains three motor units with servomotors, whose role is the transformation of rotational motion of motors into linear motion of runners to which the control tendons are connected. Reflective markers were attached to the body of the robot, precisely three at the base of the robot and one at its tip, to determine the position of the base and the position of the tip. After the calibration, performed according to a standard wand-based protocol, the calibration error reported by Motive was between 0.1 mm and 0.5 mm, which is enough for our uses. The final dataset contains more than 30,000 combinations of cable lengths ranging from 0 mm to 10 mm with a step of 0.1 mm and the corresponding positions (x, y and z coordinates) of the tip of the robot in the 3D space, exported without additional filtering. For the purpose of model development, the dataset was partitioned into three subsections training (70%), validation (20%) and testing (10%).

2.3. Computational Setup

The experimental setup for the training of various MLP models consists of operating system (Ubuntu 22.04.5 LTS), processor (Intel® Core™ i7-12700H), and python version (3.10.12). The system also operates with 16.0 GB of DDR4 RAM and an NVIDIA GeForce RTX 4070 graphics card. All training procedures were carried out in the CPU.

2.4. MLP Regression

Artificial neural networks (ANN) represent mathematical models that take inspiration from the workings of biological neurons; these networks allow approximation of complex nonlinear relationships between inputs and outputs. Thanks to these properties, neural networks see wide use in the areas of machine learning and artificial intelligence to solve various classification and regression problems.

MLP is an ANN that belongs to the class of feedforward neural networks (FNN) with multiple layers of fully connected neurons. Figure 1 shows the topology of MLP. The first layer, also referred to as the input layer, contains a number of neurons corresponding to the number of input features. The subsequent layers are called hidden layers, and each of them can contain any number of neurons that receive input from every neuron in the previous layer. The final layer, called the output layer, produces the network's output, with the number of neurons depending on the nature of the task. Neurons from the neighboring layers are fully connected with each other by the weighted connections, whose values decide how strong each connection is. Adjustment of the weight values happens during the learning phase. Neurons in hidden and output layers usually use activation functions

such as sigmoid, tanh, or rectified linear unit (ReLU), through which nonlinearity is introduced into the network.

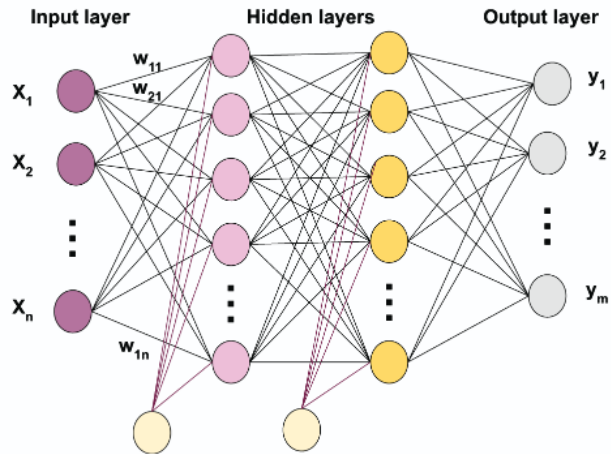

Figure 1. Topology of MLP [10].

During the learning phase, the backpropagation algorithm is used to compute the gradients of the loss function with respect to the network weights and biases. For regression problems, the mean squared error (MSE) is often adopted as the loss function. The updates of the network parameters are carried out by an optimization algorithm. In this article, the Adam optimizer is employed [11], and the weight parameter update rule is given by

$$w_{t+1} = w_t - \frac{\alpha \cdot \hat{m}_t}{\sqrt{\hat{v}_t} + \varepsilon}, \tag{1}$$

where α is the learning rate, $\hat{m}_t$ and $\hat{v}_t$ are the first and second bias corrected moment estimates respectively and ε is a small positive constant that ensures division by zero doesn't occur.

To evaluate the performance of the trained regression models, various metrics can be employed. Some of the most widely used performance metrics are mean absolute error (MAE), root mean square error (RMSE), and coefficient of determination (R^2). Both MAE and RMSE are measured in the same units as the target variable, making them easily interpretable.

Let p_i denote the actual position and $\hat{p}_i$ the predicted position for sample i, with n total samples. The mean of the actual position is denoted by $\bar{p}_i$.

MAE is then described as the absolute error between the predicted position and the actual position recorded in the dataset:

$$\text{MAE} = \frac{1}{n}\sum_{i=1}^{n} |\hat{p}_i - p_i| \,. \tag{2}$$

RMSE is also used to describe the error between the predicted position and the actual position, with this metric being more sensitive to outliers:

$$RMSE = \sqrt{\frac{1}{n}\sum_{i=1}^{n} (p_i - \hat{p}_i)^2} \,. \tag{3}$$

R^2 is used to measure the proportion of variance in the target variable explained by the model; its value can range from 0 to 1:

$$R^2 = 1 - \frac{\sum_{i=1}^{n}(p_i - \hat{p}_i)^2}{\sum_{i=1}^{n}(p_i - \bar{p}_i)^2} \,. \tag{4}$$

3. Hyperparameter Optimization

Hyperparameter optimization is a process that aims to increase overall model performance through the finding of optimal parameter configurations. To find the optimal parameters for the MLP regression model, the random search technique was employed through the W&B Sweeps platform. Random search is an iterative technique that selects random hyperparameter values from the given ranges and at the end presents the best combination.

To increase the performance of the MLP regression model, the following parameters were picked for optimization:

- Number of hidden layers: discrete values (2, 3, 4);
- Number of neurons per hidden layer: discrete values (32, 64, 128, 256, 512);
- Batch size: discrete values (16, 32, 64);
- Learning rate: continuous range (from 0.00005 to 0.01);
- Weight decay: binary values (true, false);
- Weight decay value: continuous range (from 0.000001 to 0.001).

The objective of the optimization algorithm was set to find the minimal value of the validation loss across the training runs (Figure 3). The optimization process was carried out over 50 iterations with the ReLU activation function and optimizer Adam as constant parameters of the model. A fixed seed was used to ensure that each iteration would face the same conditions and not be influenced by the random variations.

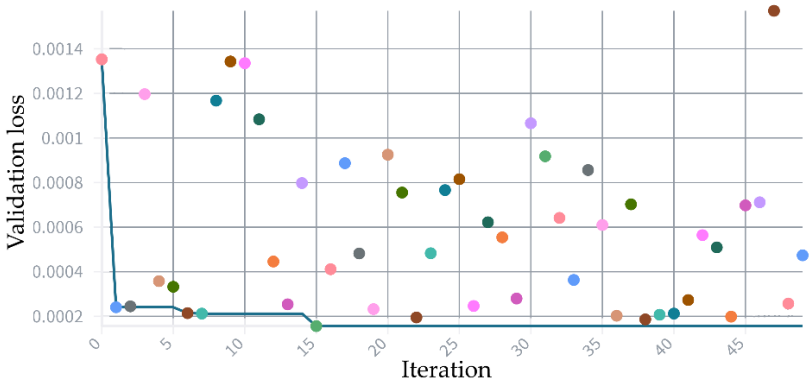

Figure 3. Hyperparameter optimization using random search.

Through this process the optimal parameters were determined, as seen in Table 1. The best-performing model shows a decrease of validation loss by 90.1% compared to the worst-performing one, highlighting the importance of carrying out hyperparameter optimization.

Table 1. Hyperparameter of MLP regression model.

Number of hidden layers	Number of neurons per hidden layer	Batch size	Learning rate	Weight decay	Weight decay value
2	256 – 128	64	0.0014	False	None

With the optimal hyperparameters established, the final MLP regression model describing the forward kinematics of the investigated continuum robot was trained for 300 epochs to ensure sufficient convergence and then tested on the unseen data.

4. Results

The performance of the proposed MLP regression forward kinematics model for the continuum robot is summarized in Table 2, which shows overall and per-axis evaluation.

All reported metrics are computed between the model-predicted tip position and the corresponding tip position recorded by the motion capture system used to construct the dataset.

Table 2. Performance evaluation of the proposed MLP regression forward kinematics model.

Performance metric	Overall	Per-axis		
		x	y	z
R^2	0.9999	0.99994767	0.9997419	0.9999512
MAE [mm]	0.1526	0.1679	0.1081	0.1819
RMSE [mm]	0.2223	0.2430	0.1826	0.2413

R^2 achieved an overall value of 0.9999 with similarly high values in each Cartesian axis. This indicates that the variance in the positions of the robot's tip is handled well by the proposed kinematics model. The veracity of this observation is further supported by the error-based metrics, as overall MAE and RMSE both recorded sub-millimeter values of 0.1526 and 0.2223 mm, respectively. Among the Cartesian directions, the y-axis demonstrates the lowest error values, while the x- and z-axes show slightly higher error magnitudes. Nevertheless, the per-axis distribution of error remains balanced and consistent, with no axes exhibiting significantly degraded performance. These results confirm the ability of MLP to represent the nonlinear behavior of the continuum robot.

5. Conclusions

This article presented a data-driven forward kinematics model for a single-segment, tendon-driven continuum robot based on MLP regression. An optimized network architecture and model parameters were derived through the random search hyperparameter optimization, after which the final model was trained.

The ability of the proposed model to capture nonlinear relationships between tendon actuation inputs and the robot's tip position is shown by its high coefficient of determination (R^2 = 0.9999 overall and above 0.9997 for all axes). In addition, it displays high agreement with the recorded mocap tip positions used as the reference in this study, as seen by the low MAE and RMSE (both under 0.25 mm). These results validate the suitability of MLP-based regression for forward kinematics modeling of tendon-driven continuum robots.

Future work will focus on extending this approach to multi-segment continuum robots and investigating the integration of data-driven kinematic models into real-time control and motion planning frameworks.

Acknowledgments: This project has received funding from the Slovak Grant Agency VEGA 1/0436/22, KEGA 008TUKE-4/2024 and VEGA 1/0409/25.

Conflicts of Interest: The authors declare no conflict of interest. The funders had no role in the design of the study; in the collection, analyses, or interpretation of data; in the writing of the manuscript; or in the decision to publish the results.

References

1. Walker, I. D.; Hannan, M. W. *A novel "elephant's trunk" robot*. In Proceedings of the IEEE/ASME International Conference on Advanced Intelligent Mechatronics, Atlanta, GA, USA, 1999; pp. 410–415. doi:10.1109/AIM.1999.803204.

2. Papadakis, E.; Tsakiris, D. P.; Sfakiotakis, M. *An octopus-inspired soft pneumatic robotic arm*. Biomimetics 2024, 9, 773. doi:10.3390/biomimetics9120773.
3. Buckingham, R. *Snake arm robots*. Ind. Robot 2002, 29, 242–245. doi:10.1108/01439910210425531.
4. Wang, Y.; et al. *An aero-engine inspection continuum robot with tactile sensor based on EIT for exploration and navigation in unknown environment*. In Proceedings of the IEEE/ASME International Conference on Advanced Intelligent Mechatronics, Hong Kong, China, 2019; pp. 1157–1162. doi:10.1109/AIM.2019.8868485.
5. Burgner-Kahrs, J.; Rucker, D. C.; Choset, H. *Continuum robots for medical applications: A survey*. IEEE Trans. Robot. 2015, 31, 1261–1280. doi:10.1109/TRO.2015.2489500.
6. Roesthuis, R. J.; Misra, S. Steering of multisegment continuum manipulators using rigid-link modeling and FBG-based shape sensing. IEEE Trans. Robot. 2016, 32, 372–382. doi:10.1109/TRO.2016.2527047.
7. Webster, R. J.; Jones, B. A. *Design and kinematic modeling of constant curvature continuum robots: A review*. Int. J. Robot. Res. 2010, 29, 1661–1683. doi:10.1177/0278364910368147.
8. Chirikjian, G. S.; Burdick, J. W. *The kinematics of hyper-redundant robot locomotion*. IEEE Trans. Robot. Autom. 1995, 11, 781–793. doi:10.1109/70.478426.
9. Mahamat Loutfi, I.; Bouyom Boutchouang, A. H.; Melingui, A.; Lakhal, O.; Biya Motto, F.; Merzouki, R. Learning-based approaches for forward kinematic modeling of continuum manipulators. IFAC-PapersOnLine 2020, 53, 9899–9904. doi:10.1016/j.ifacol.2020.12.2697.
10. Chan, K. Y.; Abu-Salih, B.; Qaddoura, R.; Al-Zoubi, A. M.; Palade, V.; Pham, D.-S.; Del Ser, J.; Muhammad, K. *Deep neural networks in the cloud: Review, applications, challenges and research directions*. Neurocomputing 2023, 545, 126327. doi:10.1016/j.neucom.2023.126327.
11. Kingma, D.; Ba, J. Adam: *A method for stochastic optimization*. In Proceedings of the 3rd International Conference on Learning Representations (ICLR 2015), 2015.

TECHNICAL UNIVERSITY OF KOŠICE
Faculty of Mechanical Engineering

Design and Testing of a Device for Measuring Flywheel Brake Rotation to Enhance Static Friction Coefficient Evaluation

Martin Bučko [1], Juraj Gerlici [1], Vladimír Samaš [1,*], Patrik Slušňák [1]

[1] University of Žilina, Faculty of Mechanical Engineering, Department of Transport and Handling Machines, Univerzitná 8215/1, 010 26 Žilina, Slovakia; martin.bucko@fstroj.uniza.sk; Juraj.Gerlici@fstroj.uniza.sk; vladimir.samas@fstroj.uniza.sk; patrik.slusnak@fstroj.uniza.sk
* Correspondence: vladimir.samas@fstroj.uniza.sk

Abstract: This paper addresses the design, implementation, and experimental validation of a measurement system for the precise determination of the flywheel brake state rotation angle during static friction coefficient testing used in rail vehicles. Two system variants are presented: the first, mechanically more complex, proved excessively complicated; the second, based on the LARM LS501 cable analog sensor, was fabricated and experimentally verified. The employed data acquisition system, utilizing an ATmega328P microcontroller and an ADS1115 A/D converter, enables high-resolution digitization of the analog signal and real-time processing in Excel, minimizing the microcontroller's load while ensuring accurate data capture during testing. Measurements of linear displacement demonstrated a smooth and continuous response without parasitic effects, confirming the system's high accuracy and reliability. The recorded acceleration profiles contained some noise, which can be nearly entirely eliminated through software smoothing. The presented solution provides a reliable tool for evaluating braking materials, offering high repeatability and accuracy acceptable to industry standards, and represents a significant contribution to experimental testing in the field of railway transportation.

Keywords: flywheel brake state, static friction, microcontroller, A/D converter, linear displacement, analog signal.

1. Introduction

The flywheel brake state is a specialized testing apparatus for evaluating brake lining materials in rail vehicles. It simulates real braking conditions to assess the performance, quality, and durability of both disc and block brake linings, which must undergo standardized tests before approval for railway use.

Testing follows technical standards, evaluating parameters such as friction coefficient versus speed, temperature, and force; stability during braking; wear; and behavior under extreme conditions. A key test is the static friction coefficient, conducted under quasi-static conditions with minimal relative motion between the brake element and friction surface. Designing a measurement system for this test requires a suitable position sensor, precise mechanical transmission, and software for continuous data acquisition, processing, and archiving. The resulting integrated unit guarantees high accuracy, reproducibility, and standards compliance. This paper presents two conceptual solutions for measuring the rotational angle, both using a common software platform.

Comparable sensing principles are widely implemented for distance measurement in various engineering domains. However, in flywheel brake rotational measurement systems, incremental rotary encoders are typically employed instead. These sensors generally provide lower resolution and reduced measurement fidelity compared to high-precision analog linear displacement sensors.

2. Definition of Boundary Conditions

In designing the measurement system, it is first essential to define the signal type—digital or analog—as it impacts the measurement chain, data processing, and achievable accuracy [2]. Given the need for precise detection of small angular changes, an analog signal was chosen, offering continuous variable representation and high-resolution measurements without complex sensor-level digitization. It also integrates easily into the existing control system.

In both system concepts, a potentiometer generates the analog signal. The first uses a standard 10 kΩ rotary potentiometer directly coupled to the device's rotation. The second employs a cable-based LARM 501 potentiometer, converting small angular motion into linear displacement, suitable for flexible mechanical arrangements.

According to UIC standards [1], the maximum speed is 23 mm·s^{-1}, with flywheel rotation limited to approximately 11.5°, requiring highly accurate angle measurement to ensure precise, repeatable, and comparable results.

During the 2–4 second test, the brake is gradually released, and the flywheel angle changes. Data are acquired at up to 100 Hz [3], yielding 200–400 measurements per cycle, sufficient for accurate analysis of the static friction coefficient.

3. Design of the Printed Circuit Board

The data acquisition system is implemented using a custom-designed printed circuit board (PCB). The board is equipped with an ATmega328P microcontroller [4] and a dedicated analog-to-digital converter (ADC), the Texas Instruments ADS1115 [5]. The use of an external ADC allows for higher measurement accuracy compared to the microcontroller's internal converter, as the ADS1115 provides 16-bit resolution. This means the measurement system has a total of:

$$2^{16} - 1 = 32{,}767 \text{ discrete steps} \tag{1}$$

Since the entire ADC measurement range is utilized for an angular displacement of 11.5°, the angular resolution per step can be calculated as follows:

$$\Delta\phi = \frac{11.5^\circ}{32{,}767} \approx 0.000351^\circ \tag{2}$$

Thus, the resulting angular resolution is approximately:

$$\Delta\phi \approx 0.00035^\circ \text{ per step} \tag{3}$$

The ATmega328P microcontroller is implemented within the Arduino Nano platform, facilitating simpler and more flexible system programming. This configuration also ensures easy replacement of the microcontroller in case of malfunction or hardware upgrade. Overall, this approach enhances the serviceability and practical usability of the proposed data acquisition system.

The article presents two PCB design variants. The first variant, shown in Figure 1, is powered via a 5 V DC USB interface, which supplies the ATmega328P microcontroller, the ADS1115 ADC, and the analog sensor. The second variant in Figure 2 incorporates an integrated voltage converter, enabling operation from a 12 V supply voltage. This variant additionally uses a TL431 voltage reference [6], which ensures a stable reference voltage for more accurate and long-term reliable measurements.

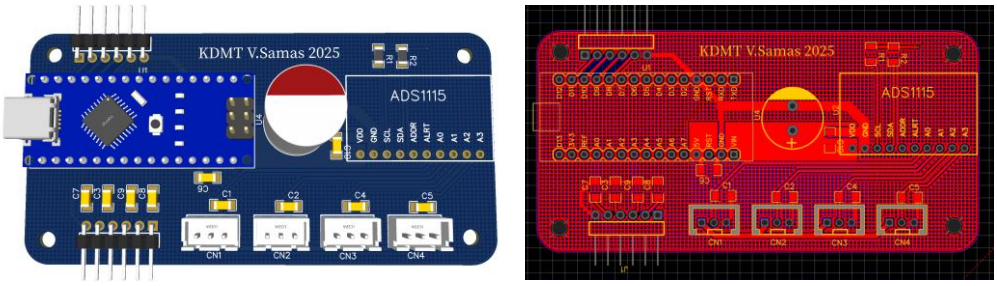

Figure 1. First variant of PCB.

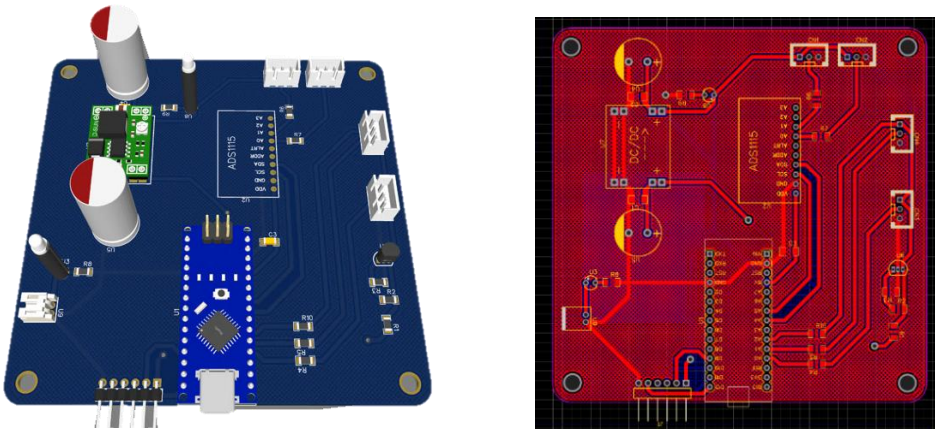

Figure 2. Second variant of PCB.

4. 3D Model of the First Variant

The first variant uses two rows of spur gears, each precisely engineered to minimize backlash and ensure high repeatable positioning accuracy. The gear assembly is mounted on an adjustable sliding support for precise alignment with the measured shaft. The frame, made of aluminum profiles, provides high stiffness with low weight and allows modular expansion. The system achieves a total gear ratio of 25, with two stages of 5:1 each. Mathematically:

$$i_{\text{total}} = i_1 \cdot i_2 = 5 \cdot 5 = 25 \tag{4}$$

The transmission mechanism is designed to map the full angular displacement of the flywheel—approximately 11.5°—onto the complete effective measurement range of the displacement sensor. In this configuration, the mechanical conversion ratio between rotational motion and linear displacement is selected such that the sensor operates across its entire calibrated stroke. As a result, the full digital resolution of the sensing system is utilized during operation.

By expanding the usable measurement span, the number of effective quantization increments increases, which directly enhances angular resolution. In practical terms, a larger portion of the sensor's dynamic range corresponds to a given angular displacement, thereby reducing the minimum detectable change in flywheel position. This improves not only instantaneous measurement accuracy but also the sensitivity of the system to small angular variations.

Figure 3 presents a 3D model of the first mechanical design variant, developed in Autodesk Inventor Professional 2025. The model illustrates the spatial configuration of the transmission components, their kinematic relationships, and the integration of the displacement sensing system within the experimental testing apparatus.

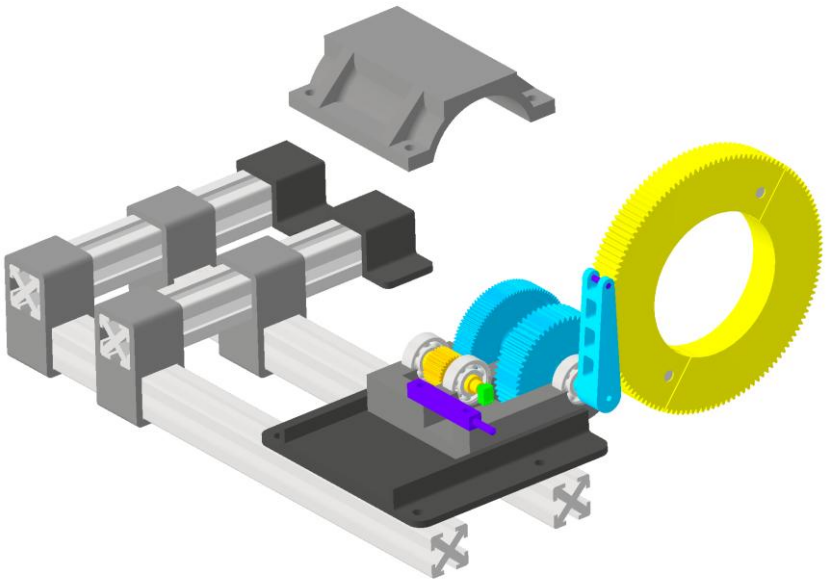

Figure 3. 3D model of the first variant.

5. 3D Model of the Second Variant

The second variant of the measurement system uses a LARM LS501 analog cable sensor [7], which produces a continuous output proportional to cable displacement over a 1 m range. To improve resolution, a pulley mechanism halves the effective range to approximately 500 mm, doubling linear displacement accuracy and enhancing angular measurement precision. The sensor and pulley are mounted on a 1 m arm integrated with the flywheel brake state. Flywheel rotation is converted via a lever into linear cable displacement, ensuring reproducible mapping between angular and linear motion. Figure 4 shows a 3D-printed guide designed to ensure precise cable attachment and secure installation of the transmission mechanism. The component was fabricated from PETG filament [8]. The figure also presents the final manufactured 3D-printed part after fabrication, installed directly on the pneumatic piston assembly.

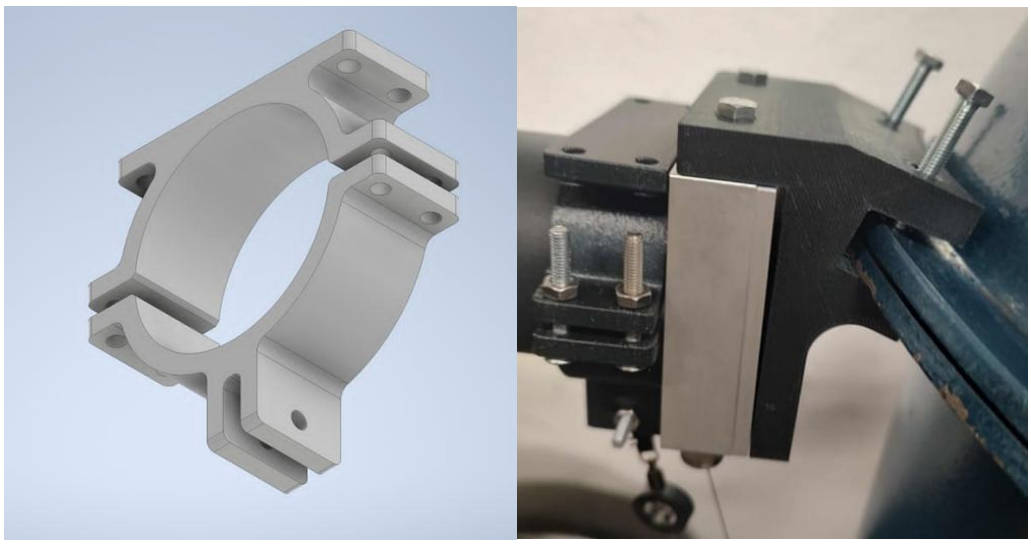

Figure 4. 3D model and fabricated version of the second variant.

6. Measurement Software

The ATmega328P microcontroller was programmed via the Arduino IDE to achieve rapid data acquisition at a stable 100 Hz sampling frequency, required for the static friction coefficient test. The code uses the Adafruit ADS1X15 library [9] to communicate with the ADS1115 analog-to-digital converter via I²C [10], allowing straightforward reading and transfer of digitized values to a host PC. Measurement monitoring and conversion to physical quantities are performed in real time on Microsoft Excel using a COM add-in, eliminating the need for post-test processing. Raw data are transmitted directly from the A/D converter, with scaling and conversion to angular displacement handled on the computer, enhancing acquisition stability and reliability. Excel records a single channel at a 10 ms sampling period (100 Hz), the software limit, though the hardware can support up to 860 Hz, the maximum capability of the ADS1115. Figure 5 shows the raw measured signal in binary form used for subsequent processing and evaluation. The measured values are encoded as a 15-bit digital count, i.e., in the range 0–32768, which corresponds linearly to a physical displacement range of 0–1000 mm.

For visualization and preliminary analysis, these binary counts were exported to Microsoft Excel, where they are plotted as shown in Figure 5. In the graph, the horizontal axis represents time, while the vertical axis represents the measured digital (analog-equivalent) value corresponding to the displacement signal.

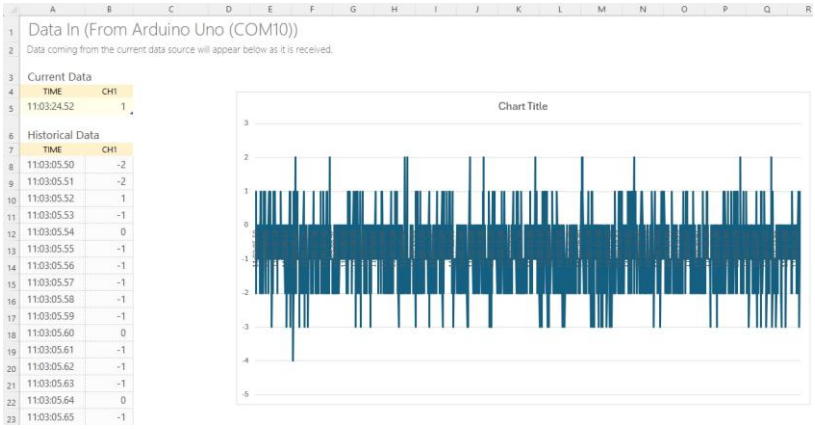

Figure 5. Raw signal in Excel.

7. Results

The measurement results were obtained exclusively using the second variant of the proposed system, as the first design variant had not been physically realized at the time the experiment was conducted. Consequently, the verification of the system's operational functionality, metrological performance, and practical applicability was carried out solely using the cable-based angle sensing mechanism. All evaluated parameters—including signal stability, resolution, repeatability, and dynamic response—therefore correspond to this mechanically implemented configuration.

The decision to experimentally validate only the second variant was driven by its higher level of technical maturity and readiness for integration into the flywheel brake test stand. In contrast to the first concept, the cable-based transmission allowed immediate mechanical coupling between the flywheel rotational motion and the linear displacement sensor, enabling full-scale testing under realistic operating conditions.

Figure 6 illustrates the complete measurement setup employed during the experiments. The figure documents the mechanical arrangement of the sensor, its attachment to the flywheel brake stand, and the associated data acquisition architecture. The data acquisition system consisted of a personal computer serving as the supervisory control and recording unit, powered independently from the flywheel brake stand. The measurement

chain included a USB-powered interface supplying an Arduino microcontroller and the ADS1115 analog-to-digital converter.

Importantly, the measurement system was electrically isolated from the primary power supply of the flywheel brake test stand. The Arduino and ADC module were powered exclusively via a stable USB power source. This separation minimized the influence of voltage fluctuations, electrical noise, and transient disturbances originating from the brake stand's drive system and power electronics. Such electrical decoupling significantly reduced the risk of ground loops, supply ripple interference, and measurement bias caused by dynamic load variations, thereby improving signal integrity and overall measurement reliability.

Figure 6. Real measurement setup.

Figure 7 shows linear displacement measurements under a 40 kN static load. The signal is smooth and continuous, free of parasitic effects or abrupt fluctuations, demonstrating the stability and isolation of the measurement system and its ability to detect very small positional changes—essential for accurate static friction coefficient evaluation.

Acceleration profiles exhibit some noise from external and electrical disturbances. Future improvements, such as adding a filtering capacitor, are expected to reduce this noise. For clarity, the recorded curves were smoothed and averaged in software, with the red curve in Figure 7 highlighting the overall acceleration trend without short-term fluctuations.

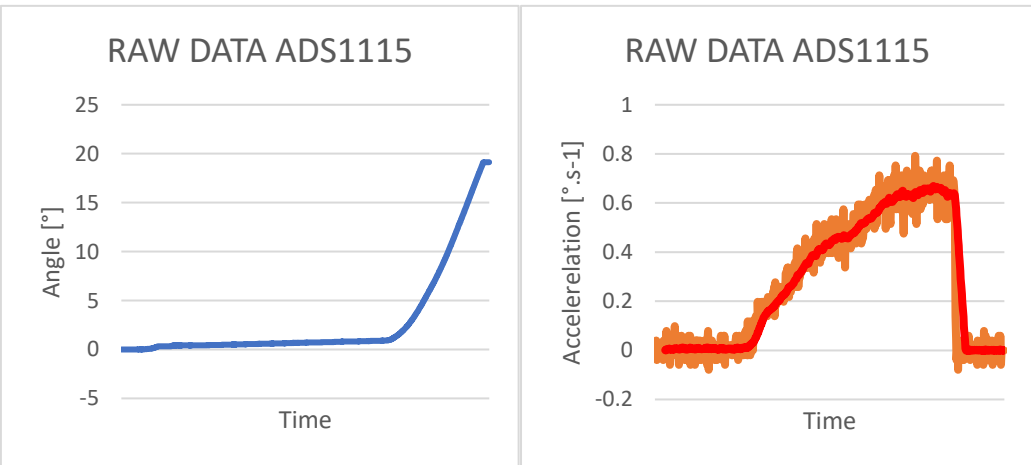

Figure 7. Displacement and acceleration figures.

8. Conclusions

The scientific contribution of this paper lies in the design and experimental verification of a measurement system for the precise determination of the flywheel brake state rotation angle during the static friction coefficient test. The paper presents a comprehensive approach to measuring small angular changes with high resolution, enabling reliable calibration and evaluation of braking materials used in railway transport.

The first variant of the measurement system proved to be excessively complex and practically unfeasible. Its mechanical and electronic design would have required unnecessarily demanding implementation without providing a corresponding improvement in measurement accuracy; therefore, it was not realized.

The second variant, based on the LARM LS501 cable analog sensor, was successfully fabricated, implemented, and experimentally verified. This variant enabled efficient and accurate detection of angular changes during the test and was fully compatible with the chosen data acquisition and software system.

Linear displacement measurement results exhibited a smooth and continuous profile without parasitic effects. Such a response provides high experimental significance and confirms the reliability of the measurement system in evaluating the static friction coefficient.

Acceleration measurement results still contain some noise; however, its impact can be substantially reduced through software smoothing and averaging. This approach allows near-complete elimination of short-term fluctuations and provides sufficiently accurate data for interpreting the dynamic behavior of the tested system.

Overall, the paper presents a functional and practically applicable measurement system that combines high accuracy, repeatability, and flexible implementation, with experimental results confirming its reliability for testing braking materials in railway applications.

Acknowledgments: This publication was supported by the UNIZA grant project No. 21107: Construction Design of a Device for Determining the Static Coefficient of Friction on an Inertia Brake Test Stand

References

1. International Union of Railways (UIC). Brakes—Performance requirements for freight wagons. UIC Code 544-1, International Union of Railways, Paris, France, 2016.
2. Ambardar, A. Analog and Digital Signal Processing. Michigan Technological University, Houghton, MI, USA.
3. Microsoft Corporation. Microsoft Excel. Version 365. Microsoft Corporation, Redmond, WA, USA, 2024.
4. Microchip Technology Inc. ATmega328P Automotive Microcontroller Datasheet. Document No. Atmel-7810, Microchip Technology Inc., Chandler, AZ, USA. Available online: https://ww1.microchip.com/downloads/en/DeviceDoc/Atmel-7810-Automotive-Microcontrollers-ATmega328P_Datasheet.pdf
5. Texas Instruments. ADS1115 16-Bit Analog-to-Digital Converter with I²C Interface. Texas Instruments Incorporated, Dallas, TX, USA. Available online: https://www.ti.com/lit/ds/symlink/ads1115.pdf
6. Texas Instruments. TL431 Precision Programmable Reference. Texas Instruments Incorporated, Dallas, TX, USA. Available online: https://www.ti.com/lit/ds/symlink/tl431.pdf
7. LARM. LS501 Sensor Datasheet. LARM, Czech Republic. Available online: https://www.larm.cz/templates/larm/data/130_ls501.pdf
8. Stecuła, B.; Sitko, J.; Stecuła, K.; Witkowski, M.; Orzeł, B. Comparison of the strength of popular thermoplastic materials used in 3D printing – PLA, ABS and PET-G. Combustion Engines 2024, 199, 97–103. https://doi.org/10.19206/CE-189386.
9. Adafruit. Adafruit ADS1X15 Arduino Library. Available online: https://github.com/adafruit/Adafruit_ADS1X15
10. Liu, C.; Meng, Q.; Liao, T.; Bao, X.; Xu, C. A Flexible Hardware Architecture for Slave Device of I2C Bus. In 2019 International Conference on Electronic Engineering and Informatics (EEI); IEEE: Nanjing, China, 2019; pp. 1–5. https://doi.org/10.1109/EEI48997.2019.00074.

TECHNICAL UNIVERSITY OF KOŠICE
Faculty of Mechanical Engineering

Advancing Early Cleft Care: The Role of Intraoral Scanning (IOS) in Neonatal Patients — A Case Report and Literature Review

Natália Savková [1,*], Branko Štefanovič [1], Eleonóra Ivančová [2], Marek Schnitzer [1], Jozef Živčák [1]

[1] Department of Biomedical Engineering and Measurement, Faculty of Mechanical Engineering, Technical University of Košice, Letná 1/9, 042 00, Košice, Slovakia, dr.nataliasavkova@gmail.com, branko.stefanovic@tuke.sk, marek.schnitzer@tuke.sk, jozef.zivcak@tuke.sk
[2] Clinic of dentistry and maxillofacial surgery, Faculty of Medicine, Pavel Jozef Šafárik University in Košice, Rastislavova 43, 040 11, Košice, Slovakia, eleonoraivancova@gmail.sk
* Correspondence: dr.nataliasavkova@gmail.com

Abstract: Cleft lip and palate (CLP) are among the most frequent congenital craniofacial anomalies, and early maxillary impressions are required for presurgical infant orthopedic treatment. Conventional impression techniques in newborns carry risks related to airway obstruction, tissue compression, and material distortion, which has led to increasing interest in digital alternatives. This study presents a clinical case evaluating the feasibility and accuracy of intraoral scanning in a newborn with CLP by comparing a 3D scan of a plaster cast derived from a conventional impression taken shortly after birth with a direct intraoral 3D scan obtained approximately two months later. The plaster cast was digitized using an optical 3D scanner, and both STL models were aligned using stable palatal landmarks; surface deviations were analyzed using an actual-to-nominal comparison method. Intraoral scanning was completed within approximately three minutes without respiratory compromise or infant distress. The comparison revealed localized surface deviations, predominantly along the cleft margins and anterior palate, while most areas showed agreement within approximately 2 mm. These differences reflect a combination of natural postnatal morphological changes and technical limitations of both methods. In conclusion, intraoral scanning is a safe and clinically feasible alternative to conventional impressions in newborns with CLP and enables objective three-dimensional monitoring of early palatal development to support presurgical treatment planning.

Keywords: intraoral scanning, cleft lip and palate, neonates, digital impression, nasoalveolar molding, airway safety.

1. Introduction

Cleft lip and palate (CLP) are among the most common congenital craniofacial anomalies, with incidence among newborns between 1:500 and 1:2000 with variations from region to region. [1,2] Early maxillary impressions are essential for fabricating nasoalveolar molding (NAM) appliances, also called presurgical infant orthopedics (PSIO), that guide presurgical orthopedic treatment. Traditionally, these impressions are taken with alginate or silicone materials, using customized trays to capture the infant's maxillary morphology. Most cleft centers use PSIO to improve the presurgical intraoral and extraoral situation, even though, since its appearance in 1950s, it has been quite controversial. [3–5]

However, conventional impression techniques in neonates carry significant risks, including airway obstruction, aspiration, gag reflex activation, and soft-tissue injury. Furthermore, residual impression material can cause inflammation in the cleft area.[6] Therefore, conventional impressions require additional safety measures and resources. [7]

In addition, the manual nature of alginate impressions may lead to dimensional inaccuracies and deformation upon removal or cast pouring. These limitations have prompted the exploration of safer, more precise alternatives.

Recent advances in digital intraoral scanning technology have introduced new possibilities for neonatal cleft care. Scanners capture surface anatomy using non-contact optical imaging, eliminating the need for impression materials. While intraoral scanners are widely used in adult and pediatric dentistry, their application in newborns remains emerging. The present study aims to illustrate the clinical advantages and feasibility of intraoral scanning for newborns with CLP, through a case report and review of current literature.

1.1. Digital impressions in cleft management

The first reports of digital scanning in cleft patients appeared in the early 2010s, demonstrating comparable accuracy to conventional techniques in older infants and children. [8,9] Modern scanners such as 3Shape TRIOS, iTero, and Medit i700 now offer faster acquisition times, compact wand sizes, and color rendering suitable for small oral cavities.

Team from University Hospital Tuebingen investigated intraoral scanning in 83 patients with craniofacial disorders. Their mean age was 137 days, and a median scanning duration was 138 seconds. Their conclusion is that IOS is a fast, safe and feasible procedure for neonates, small children and infants with craniofacial deformities. Only one patient, with unilateral CLP, required conventional impression taking, as the segments were too far apart with too many undercuts to be connected. [10]

The median scanning duration of a single patient with a bilateral CLP was in a Krey's study estimated to a less than 3 minutes, however this group included some breaks. [11]

Another study reported scanning time from 1.5 to 2 minutes with using Trios 3shape intraoral scanner, however this study was made on 4 patients only. [12]

A recent study from January 2025 compared conventional impression and IOS in 52 patients. Their conclusion was that no clinically relevant difference in accuracy was found between IOS and plaster casts. [13]

1.2. Advantages over conventional methods

The most significant difference between conventional impression and intraoral scanning is the safety. [13] The conventional impression presents a risk of aspiration and airway obstruction; therefore an anesthesiologist should be present in the room when taking the impression which limits this intervention to a hospital setting meanwhile with intraoral scanning, this risk is eliminated and therefore this procedure could be done in a dental office, potentially making the care of the CLP patient more accessible to a patient.

Okazaki's team compared the result of both impression methods in the same patient and found that a tissue is displaced due to a pressure applied when taking a conventional impression, therefore they concluded that shift to intraoral scanning would be advantageous.[14]

From a research perspective, intraoral scanning is superior to conventional impression techniques for evaluating inter- and intra-operator repeatability and reproducibility. Digital scans provide objective, measurable datasets, reduce operator-related variability, and avoid the material distortion and dimensional changes commonly associated with conventional impression techniques, making them far more suitable for longitudinal comparison.

In 2019, an early case report compared conventional impression-taking with intraoral 3D scanning in an infant with cleft lip and palate. A 3-month-old infant with bilateral CLP had undertaken a conventional alginate impression and a digital intraoral scan prior to primary lip repair. They found that digital scanning was found to be fast, accurate, and safe, when compared to a conventional alginate impression technique. [15]

1.3. Reported limitations

Challenges associated with intraoral scanning in neonates include the relatively large scanner tip size in relation to the small oral cavity, management of saliva and motion artifacts, and the requirement for experienced operators; however, clinically acceptable accuracy has been reported even in small oral cavities when appropriate stabilization techniques are applied. [16]

Intraoral scans were attempted in prematurely born neonates in Louis Pasteur University hospital; however, the scanner tip size was too large (Medit i700, Medit Corp, Seoul, South Korea) to perform an intraoral scan successfully.

1.4. Objectives of the study

The primary objective of this study was to evaluate the clinical feasibility and safety of intraoral scanning for recording maxillary anatomy in a newborn with cleft lip and palate. The secondary objectives were to compare a 3D-scanned plaster cast derived from a conventional impression with a direct intraoral 3D scan obtained during early postnatal development, to quantify surface deviations between the two models using three-dimensional deviation analysis, and to assess the potential contribution of digital monitoring to presurgical orthopedic treatment planning.

2. Materials and Methods

2.1. Case report

Conventional impression of a newborn with CLP was taken few days after birth according to standard procedure in Louis Pasteur University hospital, to fabricate a NAM passive plate.

For the same patient, 55 days later, intraoral scan was taken to fabricate a 3D printed plate. The infant was healthy, with stable vitals and no respiratory compromise. Parental consent was obtained for digital scanning and use of anonymized data for publication.

The infant was positioned on its back with the head facing the healthcare professional, without sedation or intubation in an adjustable child car seat that patient came into the clinic with. A Medit i700 (Medit Corp, Seoul, South Korea) intraoral scanner was used. (Figure 1. and Figure 2.) The operator began scanning from the unaffected alveolar ridge, gradually moving across the cleft margins and posterior palate in a smooth, continuous motion. The scan acquisition took approximately 3 minutes, with no interruption or distress noted.

Figure 1. Intraoral scanning of the patient with CLP.

Figure 2. Wireless Medit i700 (Medit Corp, Seoul, South Korea) was used to scan the patient.

2.2. 3D scans comparison methodology

In order to monitor the development of the oral cavity topography of a newborn with cleft palate, a methodology for comparing models of two 3D scans was proposed. The first 3D scan was created by scanning a plaster cast made from the conventional impression of the newborn's oral cavity, which was made few days after the birth (date of conventional impression: 5.3.2024). This 3D scan of the cast was subsequently compared with an intraoral 3D scan of the newborn made on 29.4.2024.

An optical 3D scanner Revopoint POP 2 (Revopoint 3D, Shenzhen, China) was used to scan the plaster cast with the scanning parameters written in the Table 1. The plaster cast was placed on an automatic turntable and the 3D scanner was placed to the model with a recommended distance of 200-300 mm from the scanned model. The ideal distance was checked in the 3D scanner software interface using the distance indicator (green color of the model = optimal distance). The exposure was then set so that the areas of the scanned model were not oversaturated. The scanning frequency was set to the highest allowed value of 10 fps (frames per second). The scanning itself took place without any complications or errors and took 60 seconds.

Table 1. 3D scanning parameters of the plaster casted model.

Optimal distance	200-300 mm
Turntable speed	1 RPM (≈ 6°/s)
Scanning frequency	10 fps

After successful scanning, a virtual 3D model of the scan was obtained (Figure 3A), processed by the algorithms of the 3D scanner software and exported in STL (Standard Triangle Language) format. This STL model was then compared with the STL model of the intraoral scan (Figure 3B) using the actual-to-nominal method in the freely downloadable CAD software Meshmixer (Autodesk Inc., San Rafael, USA). The goal was to obtain a color map of the maximum deviations of the actual model from the nominal one.

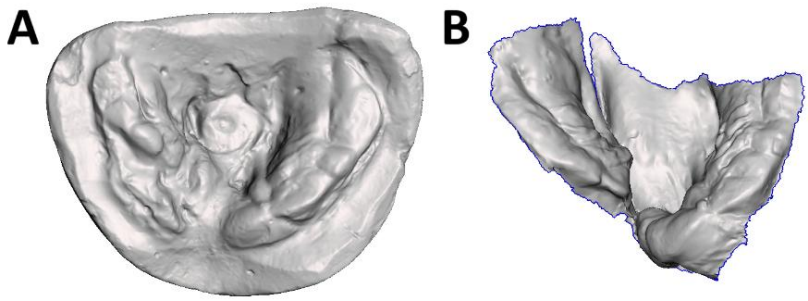

Figure 3. STL models of the 3D scan of the plaster cast(**A**) and the intraoral 3D scan (**B**).

In the first step, it was necessary to import both 3D models into the software interface (Figure 4.1) and to perform an initial manual alignment using the *Edit-Transform* tool (Figure 4.2). Subsequently, the 3D model of the plaster cast was selected as the nominal model, against which the current 3D model of the intraoral scan will be precisely aligned. For precise alignment, the *Select-Edit-Align to Target* function was used, where the surface of *palatal rugae* was located. (Figure 4.3) These palatal landmarks were selected as the surface against which the current 3D model would be aligned to. This surface was chosen because these landmarks are unique and relatively stable, present minimal displacement and have been validated in orthodontic growth studies [17,18]. The tolerance for the alignment error of 3D models was set as default 0.01 mm (Figure 4.4).

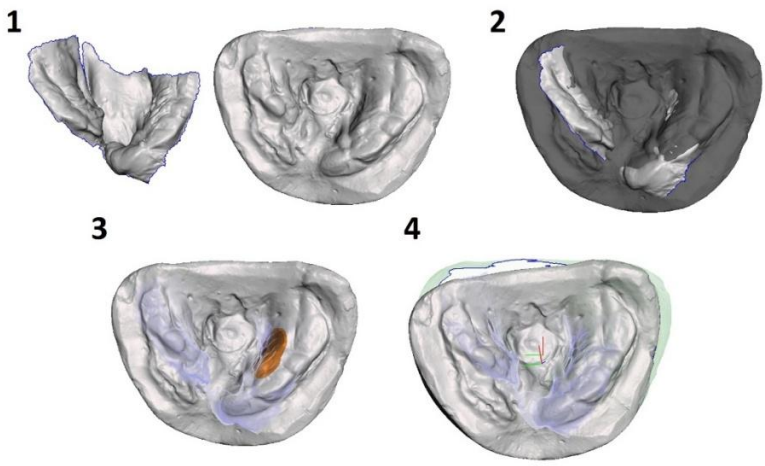

Figure 4. Methodology for 3D models alignment (1 – importing 3D models into the software interface, 2 – manually aligning 3D models, 3 – selecting the alignment surface, 4 – aligning 3D models).

After the 3D models' alignment, the *Analysis-Deviation* function was used to create color maps of surface deviations, where multiple values of the maximum permissible deviation were set to allow monitoring of the change in the color map depending on the change in a given value.

3. Results

Parameters such as safety, accuracy, patient comfort, time efficiency, data storage, integration and tissue deformation were evaluated in both groups, conventional impression and intraoral scanning. These results can be found in Table 2.

Table 2. Conventional impression versus intraoral scanning.

Parameter	**Conventional Impression**	**Intraoral Scanning**
Safety	Risk of aspiration and airway obstruction [10]	Little or no-contact, no obstruction
Accuracy	Material shrinkage, deformation, technique sensitive	High reproducibility, digital calibration
Patient comfort	Gag reflex, distress	Minimal discomfort
Time efficiency	Several minutes + setting time, no breaks possible	Real-time capture, possibility of making breaks if necessary
Data storage	Physical cast prone to damage	Digital file (STL/PLY) -reproducible
Integration	Manual workflows	Direct CAD/CAM and 3D printing
Tissue deformation	Tissue deformation due to pressure applied to the mucosa	No compression, little to no contact

A complete digital 3D model of the maxillary arch and cleft morphology was generated immediately. Surface integrity was visually verified, and no re-scans were required. During the procedure, no respiratory distress or cyanosis occurred. Parents reported less stress during the later process.

In Figure 5, the surface deviations between the plaster cast 3D model (highlighted in red) and the intraoral 3D scan (gray) are visualized at different maximum tolerances (0.5–3.0 mm). With increasing tolerance (Max. Deviation), the highlighted areas of deviation gradually decrease, confirming that the most differences are found in the range of 0.5–2.0 mm. The most pronounced deviations are repeatedly found:

- in the alveolar segments around the edges of the cleft,
- in the anterior segments of the palate,
- in the transition between the lateral segments and the premaxilla,
- locally and on surfaces that are more difficult to access for intraoral scanning.

At a tolerance of 0.5 mm, an extensive color map of deviations is visible, indicating subtle but widespread differences between the models. At a tolerance of 1.0–1.5 mm, deviations are still present, especially along the cleft line. At higher tolerances (2.0–3.0 mm), only isolated areas of larger differences remain, indicating that most of the model geometry matches within 2 mm. The deviations are therefore spatially localized and consistent – especially in places where both natural morphological changes happen over two months period and technical limitations of the intraoral scanning or conventional impression taking process may be evident.

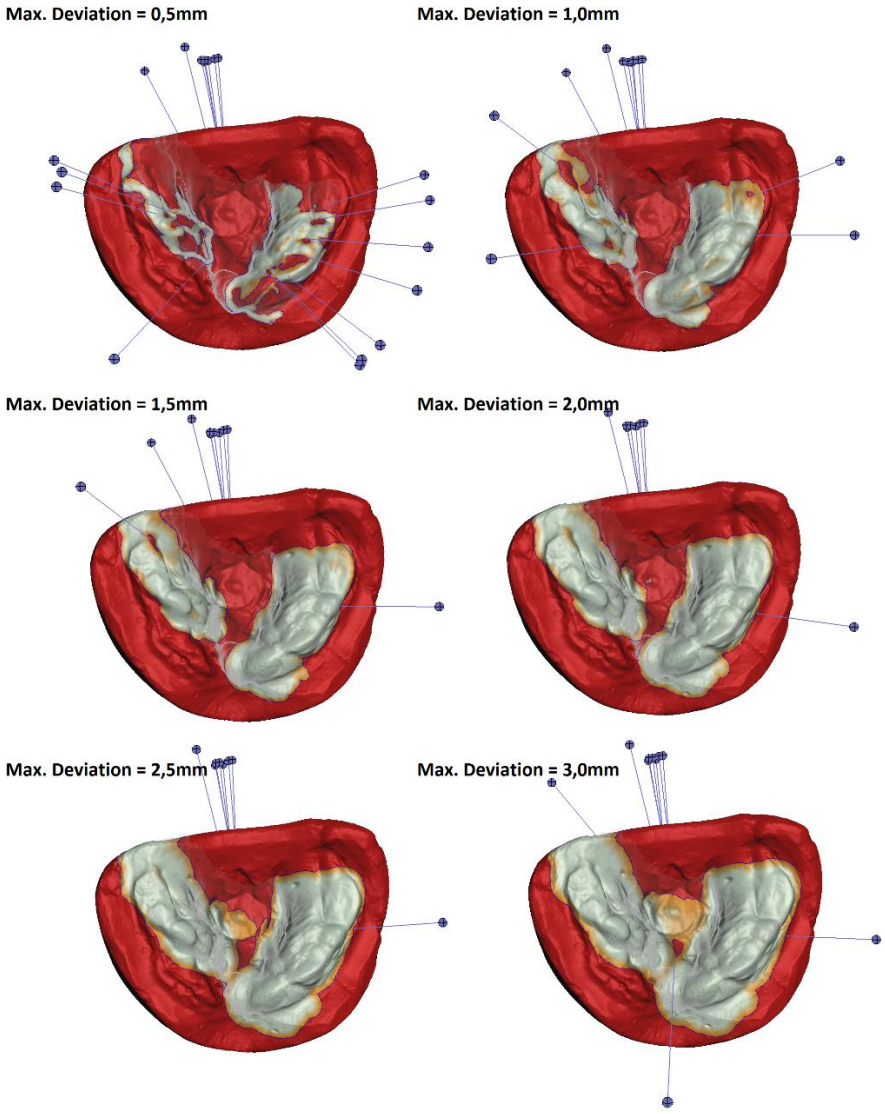

Figure 5. Surface deviations between the plaster 3D model and the intraoral 3D scan at different maximum tolerances (0.5–3.0 mm).

4. Discussion

This case demonstrates that intraoral scanning can be safely and effectively used to record maxillary anatomy in newborns with cleft deformities. The little or non-contact nature of scanning eliminates the airway risks associated with impression trays and materials. Furthermore, the digital workflow supports immediate appliance design and facilitates data sharing and therefore planning within multidisciplinary teams.

Clinical advantages include enhanced patient safety and comfort, improved precision and reproducibility, streamlined digital workflows for appliance fabrication and easy data archiving for follow-up comparisons in long-term care and research.

However, practical challenges remain. The scanner tip must be small enough for neonatal oral dimensions, and the operator must be trained to manage infant motion and saliva pooling. Device cost and access may also limit widespread implementation, especially in low-resource settings. Nonetheless, ongoing miniaturization of scanners and decreasing costs are making the technique more feasible.

The aim of this study was to compare a 3D-scanned plaster cast of a newborn's palate with cleft to an intraoral 3D scan obtained approximately two months after the conventional impression was taken. This time interval is clinically relevant, as the early postnatal

period is characterized by dynamic changes in the morphology of the oral cavity, particularly in the region of the cleft. The combination of a traditional impression technique and modern intraoral digital scanning therefore enables an objective assessment of the extent of these changes.

The alignment of both models and the subsequent surface deviation analysis performed in the freely available CAD software Meshmixer revealed clear differences in surface dimensions and geometry. These deviations can be interpreted on two levels. First, they reflect natural growth and palatal remodeling during the first weeks of life, which is consistent with current knowledge regarding the rapid postnatal maturation of both hard and soft tissues. Second, part of the observed discrepancies may be related to technical or methodological limitations of both procedures. The plaster cast model may be affected by infant's movement, the elasticity of the impression material, deformation during impression removal from the oral cavity or lab's manual workflow to create a positive plaster cast. The intraoral 3D scan, on the other hand, may be limited by restricted access of the scanner to deep anatomical areas, the presence of saliva, or the infant's reflexes. These factors may exert a minor influence on the accuracy of the comparison.

Despite these limitations, the comparison of the two models represents a valuable tool for clinical practice. The color deviation map enables the clinician to rapidly and visually identify areas of the most significant change and to accurately evaluate cleft development. Such feedback is useful in planning preoperative therapy, monitoring the effect of NAM devices, and determining the optimal timing of surgical intervention.

As digital technologies are increasingly accessible and gradually becoming standard procedures, their integration into the diagnostic process for cleft patients contributes to more precise, safer, and more reproducible anatomical assessments.

The results of this study support the implementation of regular 3D monitoring of newborns with cleft palate, which may significantly enhance the individualization of therapy. Future research should involve a larger patient cohort, apply statistical evaluation of deviations using professional metrological software, and compare different types of intraoral scanners. This would help strengthen the clinical validity of the method and better define the boundary between biological variability and technological limitations of measurement.

Overall, the findings confirm that 3D comparison of a plaster cast and an intraoral scan is a practical and informative approach for assessing the morphological development of the cleft in early life and can substantially complement current diagnostic protocols.

5. Conclusion

Intraoral scanning represents a safe, accurate, and efficient alternative to conventional impression techniques for newborns with cleft lip and palate. This approach reduces procedural risks, improves clinical outcomes, and supports a fully digital workflow for presurgical orthopedics. As technology advances, intraoral scanning is likely to become the new standard for early cleft management.

The comparison of the 3D-scanned plaster cast with the intraoral 3D scan of a newborn with a cleft confirmed the presence of localized and clinically relevant surface deviations between the two models. The most pronounced differences were found along the cleft margins and in anatomically complex regions of the palate, while most of the surface showed agreement within approximately 2 mm. These deviations reflect a combination of natural morphological changes occurring during early postnatal development and the technological limitations of the respective imaging methods. The analysis of color deviation maps thus represents an effective tool for objectifying the dynamics of palatal growth and the extent of the cleft and can substantially support clinical decision-making in preoperative treatment planning as well as in monitoring the effectiveness of NAM appliances. The findings of this study also highlight the potential of regular 3D monitoring as an integral part of the comprehensive management of patients with cleft palate.

Future research should focus on multicenter trials comparing long-term clinical outcomes, operator learning curves, and cost-benefit analyses to further validate its integration into cleft care protocols.

Acknowledgements: This research was supported by project KEGA 054TUKE-4/2025 Use of CAx systems in prosthetic and orthotic practice.

References

1. Tolarová MM, Cervenka J. Classification and birth prevalence of orofacial clefts. Am J Med Genet. 1998;75(2):126–37.
2. Mossey PA, Little J, Munger RG, Dixon MJ, Shaw WC. Cleft lip and palate. Lancet (London, England) [Internet]. 2009 [cited 2024 Mar 15];374(9703):1773–85. Available from: https://pubmed.ncbi.nlm.nih.gov/19747722/
3. Zarean P, Zarean P, Thieringer FM, Mueller AA, Kressmann S, Erismann M, et al. A Point-of-Care Digital Workflow for 3D Printed Passive Presurgical Orthopedic Plates in Cleft Care. Child (Basel, Switzerland) [Internet]. 2022 Aug 1 [cited 2023 Sep 17];9(8). Available from: https://pubmed.ncbi.nlm.nih.gov/36010151/
4. Prahl C, Kuijpers-Jagtman AM, Van 'T Hof MA, Prahl-Andersen B. A randomised prospective clinical trial into the effect of infant orthopaedics on maxillary arch dimensions in unilateral cleft lip and palate (Dutchcleft). Eur J Oral Sci [Internet]. 2001 Oct 1 [cited 2025 Dec 8];109(5):297–305. Available from: https://onlinelibrary.wiley.com/doi/full/10.1034/j.1600-0722.2001.00056.x
5. McNeil C. Orthodontic procedures in the treatment of congenital cleft palate. Dent Rec. 1950;70(5):126–32.
6. Xepapadeas AB, Weise C, Frank K, Spintzyk S, Poets CF, Wiechers C, et al. Technical note on introducing a digital workflow for newborns with craniofacial anomalies based on intraoral scans - Part I: 3D printed and milled palatal stimulation plate for trisomy 21. BMC Oral Health [Internet]. 2020 Jan 23 [cited 2023 Sep 18];20(1):1–8. Available from: https://bmcoralhealth.biomedcentral.com/articles/10.1186/s12903-020-1001-4
7. Benitez BK, Brudnicki A, Surowiec Z, Wieprzowski Ł, Rasadurai A, Nalabothu P, et al. Digital impressions from newborns to preschoolers with cleft lip and palate: A two-centers experience. J Plast Reconstr Aesthet Surg [Internet]. 2022 Nov 1 [cited 2024 May 18];75(11):4233–42. Available from: https://pubmed.ncbi.nlm.nih.gov/36154982/
8. Asquith JA, McIntyre GT. Dental arch relationships on three-dimensional digital study models and conventional plaster study models for patients with unilateral cleft lip and palate. Cleft Palate Craniofac J [Internet]. 2012 [cited 2025 Dec 8];49(5):530–4. Available from: https://pubmed.ncbi.nlm.nih.gov/21214319/
9. Chalmers E V., McIntyre GT, Wang W, Gillgrass T, Martin CB, Mossey PA. Intraoral 3D Scanning or Dental Impressions for the Assessment of Dental Arch Relationships in Cleft Care: Which is Superior? Cleft Palate Craniofac J [Internet]. 2016 [cited 2025 Dec 8];53(5):568–77. Available from: https://pubmed.ncbi.nlm.nih.gov/26623548/
10. Weise C, Frank K, Wiechers C, Weise H, Reinert S, Koos B, et al. Intraoral scanning of neonates and infants with craniofacial disorders: feasibility, scanning duration, and clinical experience. Eur J Orthod [Internet]. 2022 Jun 1 [cited 2024 May 18];44(3):279–86. Available from: https://pubmed.ncbi.nlm.nih.gov/34532733/
11. Krey, K.F., Ratzmann, A., Metelmann, P.H., Hartmann, M., Ruge S and, Kordaß B. Fully digital workflow for presurgical orthodontic plate in cleft lip and palate patients. Int J Comput Dent [Internet]. 2018;21:251–9. Available from: https://pubmed.ncbi.nlm.nih.gov/30264054/
12. Batra P, Gribel BF, Abhinav BA, Arora A, Raghavan S. OrthoAligner "NAM": A Case Series of Presurgical Infant Orthopedics (PSIO) Using Clear Aligners. Cleft Palate-Craniofacial J [Internet]. 2020 May 1 [cited 2023 Sep 11];57(5):646–55. Available from: https://journals.sagepub.com/doi/10.1177/1055665619889807?url_ver=Z39.88-2003&rfr_id=ori%3Arid%3Acrossref.org&rfr_dat=cr_pub++0pubmed
13. Keil C, Buckova M, Keil S, Hartmann L, Schlupp W, Zerjatke T, et al. Applicability of intraoral scans for presurgical orthopedic treatment of cleft lip and palate in infants: a prospective non-randomized comparative study. Clin Oral Investig [Internet]. 2025 Aug 1 [cited 2025 Dec 5];29(8):378-. Available from: https://link.springer.com/article/10.1007/s00784-025-06444-9
14. Okazaki T, Kawanabe H, Fukui K. Comparison of conventional impression making and intraoral scanning for the study of unilateral cleft lip and palate. Congenit Anom (Kyoto) [Internet]. 2023 Jan [cited 2024 Jul 15];63(1):16–22. Available from: https://pubmed.ncbi.nlm.nih.gov/36371642/
15. Patel J, Winters J, Walters M. Intraoral Digital Impression Technique for a Neonate With Bilateral Cleft Lip and Palate. Cleft Palate-Craniofacial J [Internet]. 2019 Sep 1 [cited 2025 Dec 4];56(8):1120–3. Available from: https://journals.sagepub.com/doi/10.1177/1055665619835082?url_ver=Z39.88-2003&rfr_id=ori%3Arid%3Acrossref.org&rfr_dat=cr_pub++0pubmed
16. Kuijpers MAR, Chiu Y-T, Nada RM, Carels CEL, Fudalej PS. Three-dimensional imaging methods for quantitative analysis of facial soft tissues and skeletal morphology in patients with orofacial clefts: a systematic review. PLoS One [Internet]. 2014; Available from: https://pubmed.ncbi.nlm.nih.gov/24710215/
17. Almeida MA, Phillips C, Kula K, Tulloch C. Stability of the palatal rugae as landmarks for analysis of dental casts. Angle Orthod [Internet]. 1995 Jan 1 [cited 2025 Dec 8];65(1):43–8. Available from: https://europepmc.org/article/med/7726462

18. Shukla Dr. D, Chowdhry A, Bablani D, Jain P, Thapar R. ESTABLISHING THE RELIABILITY OF PALATAL RUGAE PATTERN IN INDIVIDUAL IDENTIFICATION (FOLLOWING ORTHODONTIC TREATMENT). J Forensic Odontostomatol [Internet]. 2011 [cited 2025 Dec 8];29(1):20. Available from: https://pmc.ncbi.nlm.nih.gov/articles/PMC5734843/

TECHNICAL UNIVERSITY OF KOŠICE
Faculty of Mechanical Engineering

Overview of the Effects of Vibrations on Stem Cells

Veronika Sedláková [1,*], Radovan Hudák [1], Teodor Tóth[1] and Dominik Hakulin [2]

[1] Department of Biomedical engineering and measurement, Faculty of Mechanical Engineering, Technical university of Košice, Letná 9/B, 042 00 Košice, Slovakia; veronika.sedlakova@tuke.sk; radovan.hudak@tuke.sk; teodor.toth@gmail.com
[2] Datacomp s.r.o , Moldavská cesta 32, 040 11 Košice, Slovakia; hakulin.dominik@datacomp.sk
* Correspondence: veronika.sedlakova@tuke.sk ; Tel.: +421 556 022 745

Abstract: Mechanical vibrations have gained increasing attention as a non-invasive and physiologically relevant strategy for modulating mesenchymal stem cell (MSC) behavior in regenerative medicine. This review provides an overview of how vibrational stimulation influences MSC proliferation, survival, and lineage specification. Current evidence shows that both subtle low-frequency vibrations and high-frequency nanoscale cues can reorganize the cytoskeleton, modify cell adhesion dynamics, and activate key mechanotransduction pathways that govern differentiation. These mechanical inputs have been reported to support osteogenic and chondrogenic commitment while shaping signaling responses related to oxidative balance, inflammation, and extracellular matrix remodeling. Emerging nanoscale vibration platforms further highlight how controlled mechanical cues may mimic elements of the native microenvironment and enhance osteogenic outcomes. Despite encouraging results across various in vitro studies, challenges persist due to inconsistent stimulation protocols and an incomplete understanding of the molecular mechanisms underlying vibration-induced cellular responses. This review synthesizes current knowledge on vibration-based modulation of MSC biology and outlines its potential relevance for future regenerative strategies, particularly within bone and cartilage tissue engineering.

Keywords: mesenchymal stem cells; mechanical vibrations; tissue engineering; mechanotransduction; stem cell differentiation.

1. Introduction

Mesenchymal stem cells (MSCs) possess remarkable multipotent differentiation capacity, making them invaluable for regenerative medicine and tissue engineering applications [1,2]. The fate of MSCs can be directed toward various lineages including osteoblasts, chondrocytes, and adipocytes through biochemical and biophysical cues [3]. While biochemical factors such as growth factors and culture media supplements have been extensively studied, the role of mechanical stimulation in MSC differentiation has gained increasing attention in recent years [4].

Mechanical forces represent fundamental regulators of cellular behavior in physiological conditions. In the skeletal system, cells continuously experience various mechanical stimuli including compression, tension, fluid flow, and vibrations [5]. These mechanical signals are transduced into biochemical responses through mechanotransduction pathways, influencing gene expression, protein synthesis, and ultimately cell fate. Understanding and harnessing these mechanisms offers potential for developing more effective and physiologically relevant approaches to tissue engineering [6].

Vibration-based mechanical stimulation has emerged as a particularly promising modality due to its non-invasive nature and potential for clinical translation [7]. Low-magnitude high-frequency (LMHF) vibrations, typically characterized by frequencies

ranging from 20 to 100 Hz and accelerations below 1g, have demonstrated significant effects on MSC behavior [8,9]. Similarly, nanovibrations at higher frequencies (around 1000 Hz) with nanometer-scale amplitudes have shown remarkable osteoinductive properties [10].

Several studies have reported that specific vibration parameters can preferentially promote osteogenic differentiation while inhibiting adipogenic commitment, suggesting potential applications in treating osteoporosis and bone defects [11,12]. Other research has indicated that vibrations can enhance chondrogenic differentiation, offering possibilities for cartilage regeneration therapies. However, the optimal vibration parameters, underlying molecular mechanisms, and potential for clinical application remain areas of active investigation [13].

2. Effects of Vibrations on MSC

This section summarizes the effects of vibrations on MSC proliferation, Osteogenic Differentiation Enhancement, Chondrogenic Differentiation Modulation, and Key Mechanotransduction Mechanisms. Understanding how vibrational cues interact with the cellular microenvironment is essential for interpreting their biological effects and for designing physiologically relevant stimulation protocols. The following schematic summarizes the fundamental ways in which acoustic and vibrational stimuli act on cells cultured in vitro [19].

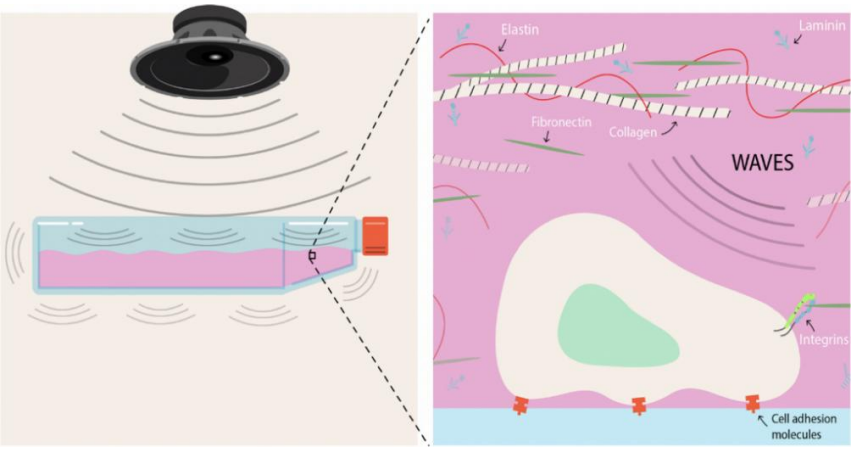

Figure 1. Schematic illustration showing how acoustic and vibrational cues interact with the culture system and influence the cellular microenvironment [19].

Schematic illustration of how acoustic and vibrational stimuli interact with a cell culture system. Mechanical waves transmit energy through the culture plate into the extracellular matrix and induce subtle substrate vibrations, altering cell–surface mechanics and influencing adhesion molecules. These changes modulate the cellular microenvironment and activate mechanosensitive signaling pathways [19].

2.1. Effects of Vibrations on MSC Proliferation

Multiple studies have examined the impact of mechanical vibrations on MSC proliferation with varying results depending on vibration parameters and cell types. Research on BMSCs exposed to 40 Hz vibrations showed that cell proliferation gradually increased over time in both vibrated and control groups [13]. While the vibration group showed rapid proliferation increase by day 3 ($p < 0.05$), the control group's significant increase occurred by day 7 ($p < 0.05$). Both groups peaked at day 7 and declined by day 14, with no statistical differences between groups at any time point.

In contrast, studies using hASCs demonstrated that vibrations at 25, 35, and 45 Hz significantly enhanced proliferation compared to controls [9]. Specifically, 25 Hz vibrations showed the most pronounced effects on cell morphology, ultrastructure, and proliferation rates. The proliferation factor, calculated as an arbitrary unit based on cell counts relative to controls, showed values above 1 for vibrated groups, indicating enhanced cell viability. Population doubling time was correspondingly reduced in stimulated groups, particularly at 25 Hz [9].

2.2. Osteogenic Differentiation Enhancement

Vibration-induced osteogenic differentiation has been extensively documented across multiple frequency ranges. Studies comparing 30 Hz and 100 Hz vibrations at different magnitudes (0.15g, 1g, 2g) demonstrated that mechanical vibrations contributed to mineralization and expression of osteogenic genes [14]. Low-intensity vibrations (LIV) below 1g have been shown to augment MSC proliferation and promote osteogenic pathways through multiple mechanisms [15].

Research on hASCs revealed that 25 Hz vibrations produced the greatest impact on osteogenic commitment. Stimulated cells exhibited formation of osteocyte-like structures and hydroxyapatite deposits, increased calcium and phosphorus deposition, and enhanced differentiation markers. These findings suggest that vibrations at this specific frequency optimally promote bone-forming phenotypes [9].

Nanovibration studies have provided additional insights into mechanotransduction mechanisms. A novel nanovibration bioreactor operating at 1000 Hz with 30 nm amplitude demonstrated remarkable osteoinductive properties [10]. The system utilizes reverse piezoelectric effect, where voltage mechanically expands piezoactive ceramics positioned between a large mass (aluminum block) and an iron top plate. This configuration generates precise nanometer-scale vibrations that induce therapeutic reactive oxygen species (ROS) and controlled inflammatory responses beneficial for three-dimensional bone tissue engineering [16].

2.3. Chondrogenic Differentiation Modulation

Vibrations have also shown significant effects on chondrogenic differentiation, though optimal parameters differ from those for osteogenesis. Studies examining 40 Hz vibrations at low amplitude demonstrated promotion of chondrogenic differentiation under appropriate conditions. A key marker of chondrogenic commitment is increased glycosaminoglycan (GAG) expression [13].

Research on BMSCs subjected to LMHF vibrations revealed that total GAG content in the vibration culture group significantly increased by 56.5% and 93.6% at days 7 and 14, respectively ($p < 0.0005$). Alcian blue staining of differentiated BMSCs at day 28 confirmed enhanced chondrogenic matrix production in vibrated samples com-pared to controls [13].

Investigations using hASCs examined the effects of 25, 35, and 45 Hz vibrations on chondrogenic potential. Results indicated that 35 Hz vibrations specifically promoted chondrogenic differentiation while significantly inhibiting adipogenic commitment. These findings suggest that frequency selection is critical for directing MSC fate toward desired lineages. The application of 35 Hz LFLM vibrations, combined with stem cell therapy, presents a promising approach for cartilage regenera-tion, particularly for treating degenerative joint diseases [17].

2.4. Mechanotransduction Mechanisms

Understanding the molecular mechanisms by which vibrations influence MSC behavior is crucial for optimizing protocols and predicting outcomes. Several mechanotransduction pathways have been implicated in vibration-induced differentiation.

Previous research identified altered cell adhesion and RhoA kinase (ROCK) activity in MSCs cultured in 2D nanovibration bioreactors [10]. Additionally, TRPV1 (transient receptor potential cation channel subfamily V member 1) was identified as participating in 3D nanovibra-tion-induced osteogenesis [18]. These findings suggest that mechanosensitive ion channels play important roles in translating mechanical stimuli into biochemical signals.

Studies have proposed that increasing nanovibration amplitude amplifies the underlying osteo-genic mechanism, allowing further dissection of MSC mechanotransduction pathways. Nanovibration stimulation induces therapeutic levels of reactive oxygen species and controlled inflammatory responses that promote osteogenic commitment in three-dimensional culture systems [16].

3. Discussion

Mechanical vibrations represent a promising biophysical cue for directing mesenchymal stem cell behavior, yet current findings highlight both clear opportunities and unresolved challenges. Evidence from low-frequency and nanovibration studies consistently shows that mechanical stimulation can enhance MSC proliferation and strongly promote osteogenic and, under specific conditions, chondrogenic differentiation. These outcomes appear to be mediated by cytoskeletal reorganization, altered adhesion dynamics, and activation of mechanosensitive pathways including ROCK signaling and ion channels such as TRPV1.

Despite these advances, several limitations remain. Experimental protocols vary widely in frequency, amplitude, duration, and exposure patterns, complicating direct comparison across studies and limiting reproducibility. Furthermore, the underlying molecular mechanisms particularly the interplay between ROS production, inflammatory signaling, and lineage commitment are not yet fully understood. Translation toward clinical settings is also constrained by the lack of standardized vibration platforms capable of delivering highly controlled and physiologically relevant stimuli.

An important perspective for future research lies in the integration of vibration-based stimulation with advanced biomaterials and three-dimensional (3D) scaffold systems. Combining mechanical cues with biomimetic scaffolds may better replicate the native cellular microenvironment, thereby enhancing cell adhesion, proliferation, and lineage-specific differentiation. In particular, the use of vibration-responsive or piezoelectric materials could enable more precise and localized delivery of mechanical stimuli within engineered tissues. Such approaches may significantly improve the effectiveness of tissue engineering strategies, especially in bone and cartilage regeneration, and represent a promising direction for clinical translation.

4. Conclusions

Mechanical vibrations, particularly in the low-magnitude high-frequency range (20-100 Hz) and nanovibration range (1000 Hz), represent effective tools for directing MSC differentiation toward osteogenic and chondrogenic lineages. Frequency specific effects enable selective promotion of desired cell fates, with 25-45 Hz optimal for bone formation and 35-40 Hz for cartilage development. Mechanotransduction mechanisms involve mechanosensitive ion channels, cytoskeletal remodeling, and controlled ROS signaling.

The non-invasive nature and physiological relevance of vibration stimulation make it particularly attractive for clinical translation in regenerative medicine. However, standardization of protocols, deeper mechanistic understanding, and validation in preclinical and clinical studies remain essential for realizing the full therapeutic potential of vibration-based MSC modulation.

Future research should focus on optimizing vibration parameters for specific applications, elucidating molecular mechanisms, developing standardized bioreactor systems, and conducting rigorous preclinical and clinical validation studies. Such efforts will help

establish vibration therapy as a mainstream approach in MSC-based regenerative medicine.

Acknowledgments: This scientific study was created thanks to support under the project KEGA Implementation of measurement systems of human physiological parameters in the educational process in the biomedical engineering program (025TUKE-4/2025).

References

1. Pittenger, M.F.; Discher, D.E.; Péault, B.M.; Phinney, D.G.; Hare, J.M.; Caplan, A.I. Mesenchymal stem cell perspective: cell biology to clinical progress. NPJ Regen. Med. 2019, 4, 22.
2. Uccelli, A.; Moretta, L.; Pistoia, V. Mesenchymal stem cells in health and disease. Nat. Rev. Immunol. 2008, 8, 726-736.
3. Kilian, K.A.; Bugarija, B.; Lahn, B.T.; Mrksich, M. Geometric cues for directing the differentiation of mesenchymal stem cells. Proc. Natl. Acad. Sci. USA 2010, 107, 4872-4877.
4. Chen, G.; Dong, C.; Yang, L.; Lv, Y. 3D scaffolds with different stiffness but the same microstructure for bone tissue engineering. ACS Appl. Mater. Interfaces 2015, 7, 15790-15802.
5. Thompson, W.R.; Rubin, C.T.; Rubin, J. Mechanical regulation of signaling pathways in bone. Gene 2012, 503, 179-193.
6. Jaalouk, D.E.; Lammerding, J. Mechanotransduction gone awry. Nat. Rev. Mol. Cell Biol. 2009, 10, 63-73.
7. Rubin, C.; Recker, R.; Cullen, D.; Ryaby, J.; McCabe, J.; McLeod, K. Prevention of postmenopausal bone loss by a low-magnitude, high-frequency mechanical stimulus: a clinical trial assessing compliance, efficacy, and safety. J. Bone Miner. Res. 2004, 19, 343-351.
8. Uzer, G.; Pongkitwitoon, S.; Ete Chan, M.; Judex, S. Vibration induced osteogenic commitment of mesenchymal stem cells is enhanced by cytoskeletal remodeling but not fluid shear. J. Biomech. 2013, 46, 2296-2302.
9. Paprocka, M.; Krawczenko, A.; Dus, D.; Joachimiak, R.; Głogowska-Szeląg, J.; Kraskiewicz, H. The Effect of Low-Magnitude Low-Frequency Vibrations (LMLF) on Osteogenic Differentiation Potential of Human Adipose Derived Mesenchymal Stem Cells. Cell. Mol. Bioeng. 2017, 10, 549-562. https://pmc.ncbi.nlm.nih.gov/articles/PMC5662672/
10. Henstock, J.R.; Rotherham, M.; Rashidi, H.; Shakesheff, K.M.; El Haj, A.J. Remotely Activated Mechanotransduction via Magnetic Nanoparticles Promotes Mineralization Synergistically With Bone Morphogenetic Protein 2: Applications for Injectable Cell Therapy. Stem Cells Transl. Med. 2014, 3, 1363-1374.
11. Garman, R.; Gaudette, G.; Donahue, L.R.; Rubin, C.; Judex, S. Low-level accelerations applied in the absence of weight bearing can enhance trabecular bone formation. J. Orthop. Res. 2007, 25, 732-740.
12. Sen, B.; Xie, Z.; Case, N.; Ma, M.; Rubin, C.; Rubin, J. Mechanical strain inhibits adipogenesis in mesenchymal stem cells by stimulating a durable β-catenin signal. Endocrinology 2008, 149, 6065-6075.
13. Zhou, Y.; Guan, X.; Liu, T.; Wang, X.; Yu, M.; Yang, G.; Wang, H. Low magnitude high frequency vibration promotes chondrogenic differentiation of bone marrow stem cells in collagen-based scaffolds. Arch. Biochem. Biophys. 2020, 690, 108449. https://www.sciencedirect.com/science/article/pii/S0003996920302387
14. Pongkitwitoon, S.; Uzer, G.; Rubin, J.; Judex, S. Cytoskeletal configuration modulates mechanically induced changes in mesenchymal stem cell osteogenesis, morphology, and stiffness. Sci. Rep. 2016, 6, 34791.
15. Nikukar, H.; Reid, S.; Tsimbouri, P.M.; Riehle, M.O.; Curtis, A.S.; Dalby, M.J. Osteogenesis of mesenchymal stem cells by nanoscale mechanotransduction. ACS Nano 2013, 7, 2758-2767. https://pubs.acs.org/doi/10.1021/nn400202j
16. Tsimbouri, P.M.; Murawski, K.; Kolomijska, G.; Alakpa, E.V.; Cusack, M.; Vassalli, M.; Keenan, G.; Oreffo, R.O.C.; Dalby, M.J.; Kantawong, F. Nanovibration Stimulation of Mesenchymal Stem Cells Induces Therapeutic Reactive Oxygen Species and Inflammation for Three-Dimensional Bone Tissue Engineering. ACS Nano 2020, 14, 9862-9876. https://pubs.acs.org/doi/full/10.1021/acsnano.0c03130
17. Fabre, H.; Ducret, M.; Degoul, O.; Rodriguez, J.; Perrier-Groult, E.; Aubert-Foucher, E.; Pasdeloup, M.; Marchand, M.; McGuckin, C.; Forraz, N.; Mallein-Gerin, F. Characterization of Different Sources of Human MSCs Expanded in Serum-Free Conditions with Quantification of Chondrogenic Induction in 3D. Stem Cells Int. 2019, 2019, 2186728.
18. Lyons, J.S.; Joca, H.C.; Law, R.A.; Williams, K.M.; Kerr, J.P.; Shi, G.; Khairallah, R.J.; Martin, S.S.; Konstantopoulos, K.; Ward, C.W.; Stains, J.P. Microtubules tune mechanotransduction through NOX2 and TRPV4 to decrease sclerostin abundance in osteocytes. Sci. Signal. 2017, 10, eaan5748.
19. DEL ROSARIO-GILABERT, D.; VALENZUELA-MIRALLES, Antonio; ESQUIVA, Gema. Advances in mechanotransduction and sonobiology: effects of audible acoustic waves and low-vibration stimulations on mammalian cells. *Biophysical Reviews*, 2024, 16.6: 783-812.

TECHNICAL UNIVERSITY OF KOŠICE
Faculty of Mechanical Engineering

Metamaterials for Smart and Sustainable Cities

Barbara Schürger [1,*], Peter Frankovský [1], Martina Hančinová [1], Erika Dubňanská [1] and Samuel Kerekeš [1]

[1] Technical University of Košice, Faculty of Mechanical Engineering, Department of Applied Mechanics and Mechanical Engineering, Letná 9, 042 00 Košice, Slovak Republic;
* Correspondence: barbara.schurger@tuke.sk; Tel.: +421910116236

Abstract: Metamaterials represent a new class of artificially engineered materials whose unusual properties originate from their geometry rather than their chemical composition. In recent years, the potential of metamaterials has extended far beyond physics and wave control, offering innovative opportunities to address environmental and urban challenges. This paper provides a concise review of optical, acoustic, and mechanical metamaterials and discusses their relevance for smart and sustainable cities. Optical metamaterials enable advanced environmental sensing and energy-efficient building envelopes; acoustic metamaterials contribute to noise reduction and improved urban soundscapes; and mechanical metamaterials enhance structural resilience, impact safety, and energy harvesting. By integrating these functions, metamaterials can help develop adaptive, energy-efficient, and resilient urban environments. The paper concludes by identifying challenges related to scalability, durability, and interdisciplinary integration, and outlines future research directions at the intersection of materials engineering, sustainability, and smart city design.

Keywords: metamaterials; smart cities; sustainable infrastructure; urban engineering

1. Introduction

Metamaterials are a new generation of artificially engineered materials whose properties stem primarily from their internal geometry rather than their chemical composition. Their unique ability to manipulate light, sound, and mechanical energy has opened new directions in materials science, architecture, and environmental engineering [1].

In recent years, the focus of metamaterial research has gradually shifted from fundamental demonstrations toward real-world applications that address key urban and environmental challenges. By controlling how energy and waves interact with matter, metamaterials enable solutions such as adaptive building façades for thermal regulation, lightweight noise barriers for transport corridors, and vibration-damping foundations for infrastructure protection [2]. These innovations directly contribute to the goals of smart and sustainable cities, where technology must harmonize with ecological responsibility and public well-being [3].

Traditional construction materials and infrastructures are typically static and resource-intensive, offering limited adaptability to dynamic environmental conditions. In contrast, metamaterials can be designed to respond actively to temperature, stress, or vibration, forming the basis for intelligent materials capable of self-regulation and multifunctional performance [4]. This adaptability makes them ideal candidates for integrating sustainability, resilience, and digital responsiveness into future urban systems.

2. Fundamentals of Metamaterials

Metamaterials derive their unusual properties from structural architecture rather than intrinsic material composition. Their repeating elements—known as unit cells—form periodic or quasi-periodic patterns that collectively behave as an effective medium with properties not found in nature. When the characteristic size of these units is much smaller

than the wavelength, the medium can be described by effective macroscopic parameters such as refractive index, density, or stiffness [5].

The theoretical groundwork was laid by Veselago [6], who predicted materials with simultaneously negative permittivity and permeability, leading to the concept of negative refraction. Decades later, Pendry [7] and Smith et al. [8] demonstrated the first experimental realizations, which triggered rapid advances across electromagnetic, acoustic, and mechanical domains.

Despite their variety, metamaterials share several universal principles:

- Effective-medium behavior: Subwavelength structures interact collectively, producing homogenized optical, acoustic, or mechanical properties that can be tuned geometrically [9].
- Local resonance: Designed cavities or inclusions create frequency-selective responses, enabling wave attenuation, reflection, or focusing at targeted bands [10].
- Geometry-induced effects: Architectures such as auxetic or chiral lattices exhibit negative Poisson's ratio, extreme deformability, or energy absorption under load [11].

These mechanisms make metamaterials inherently multifunctional and scalable. Advances in additive manufacturing, nanofabrication, and hybrid composite design now allow their production at both micro- and macro-scale levels [12].

In the context of smart cities, such physical foundations provide the basis for practical innovations—ranging from optical and thermal management systems [13] to acoustic insulation [14] and vibration mitigation [15]. By linking structural design with functionality, metamaterials bridge fundamental physics with the engineering of adaptive, efficient, and resilient urban environments.

3. Metamaterials for Smart City Applications

The practical potential of metamaterials extends beyond laboratory research into real-world applications that directly support the vision of smart and sustainable cities. Their ability to manipulate light, sound, and mechanical energy at multiple scales makes them ideal candidates for improving energy efficiency, environmental monitoring, and urban safety.

Depending on the type of wave or field they interact with, metamaterials can be broadly grouped into three functional categories: optical, acoustic, and mechanical.

The following sections summarize how these three classes of metamaterials can be integrated into modern city systems, outlining their principles, representative examples, and benefits for sustainable urban development.

3.1. Optical Metamaterials

Optical metamaterials are engineered to manipulate electromagnetic radiation in ways unattainable by conventional materials. By precisely shaping subwavelength structures, they achieve unusual properties such as negative refractive index, perfect absorption, and tunable reflection. These features allow light and thermal energy to be redirected, focused, or absorbed with exceptional control—opening possibilities for environmental sensing, imaging, and solar energy utilization [16].

From the perspective of smart cities, optical metamaterials have two major areas of relevance:

1. Environmental sensing and remote monitoring:

Optical metamaterials enable advanced environmental monitoring by combining high sensitivity with compact structural design. Their ability to manipulate electromagnetic waves at subwavelength scales allows precise detection of changes in humidity, pollutants, or electromagnetic radiation, making them suitable for distributed sensing networks in smart infrastructures [17].

At the same time, optical metasurfaces and flat lenses enhance remote imaging and data acquisition by enabling high-resolution focusing and spectral filtering across the visible and infrared ranges. These technologies support environmental mapping tasks such as vegetation health assessment, detection of urban heat islands, and hyperspectral water-quality monitoring [18].

By integrating sensing and imaging capabilities into lightweight and multifunctional platforms, optical metamaterials offer efficient tools for real-time environmental diagnostics, forming an essential component of next-generation smart city monitoring systems. Representative examples of metamaterial-based imaging systems used for environmental monitoring and sensing are shown in Figure 1.

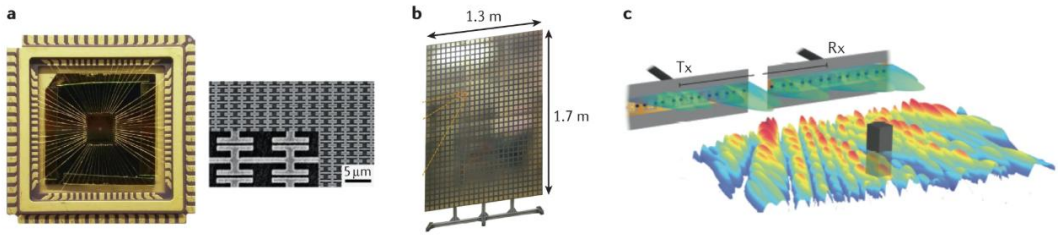

Figure 1. Examples of metamaterial-based imaging devices: (**a**) Graphene spatial light modulator for infrared imaging. (**b**) Metamaterial array for real-time microwave imaging. (**c**) Surface wave aperture enabling high-resolution imaging in the microwave band [18].

2. Energy management:

Metamaterial-based absorbers and coatings can significantly improve how urban structures capture and utilize solar energy. Carefully engineered nanostructures achieve over 90% absorption of incoming radiation while minimizing heat losses. When integrated into façades, rooftops, or solar panels, they enhance the efficiency of heating and cooling systems and reduce overall energy demand in buildings [19].

Overall, optical metamaterials provide a powerful toolset for designing adaptive, energy-efficient, and environmentally responsive urban environments. By embedding such materials into buildings and infrastructures, smart cities can move closer to the goals of reduced carbon emissions, renewable energy integration, and improved environmental monitoring. An example of a high-efficiency metamaterial solar absorber and its nanostructured design is presented in Figure 2.

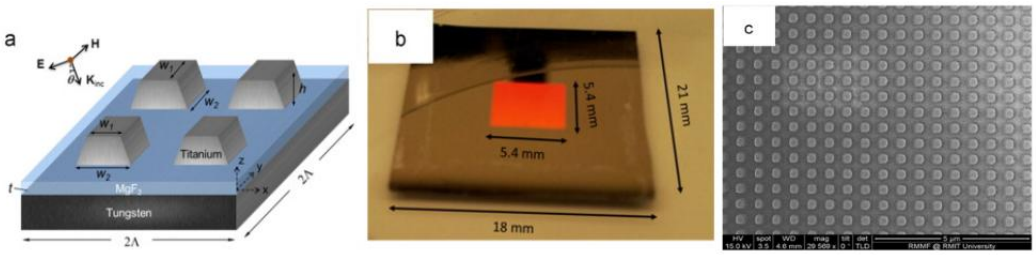

Figure 2. Metamaterial solar absorber: (**a**) Design schematic of the absorber structure. (**b**) Photograph of the fabricated sample. (**c**) SEM top-view of the nanostructured surface [19].

3.2. Acoustic Metamaterials

Acoustic metamaterials are engineered structures designed to control and attenuate sound in ways that conventional materials cannot. By incorporating local resonators, cavities, or periodic arrangements, they can open acoustic band gaps that selectively block or absorb unwanted frequencies with high efficiency and compact geometry [20]. Their ability to manipulate sound propagation beyond the diffraction limit makes them a promising solution for modern noise management in dense urban environments.

From a smart city perspective, acoustic metamaterials offer innovative strategies for reducing noise pollution and improving acoustic comfort:

1. Urban noise control:

One of the main challenges in cities is mitigating low-frequency noise from traffic and railways, where traditional concrete barriers are bulky and often ineffective. Metamaterial-based panels use resonant cavities and periodic microstructures to target these critical frequencies while remaining thinner and lighter. Bio-inspired designs and optimization algorithms have further improved their acoustic performance, making them an efficient and sustainable alternative for urban noise mitigation [20]. A schematic illustration of acoustic energy transmission and its application in urban noise barriers is shown in Figure 3.

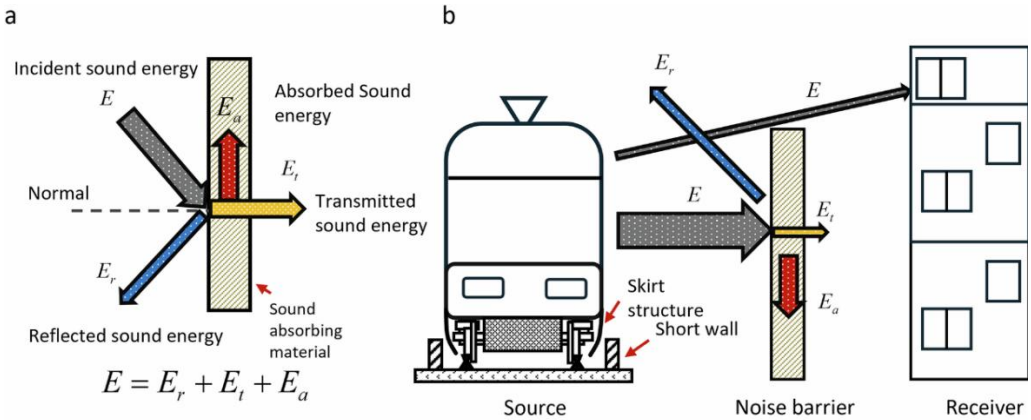

Figure 3. Acoustic metamaterials for noise control: (**a**) Principle of acoustic energy transmission, showing incident, absorbed, reflected, and transmitted sound. (**b**) Application of metamaterial noise barriers in transportation for reducing sound propagation from sources such as trains [20].

2. Building acoustics:

Indoors, low-frequency noise from HVAC systems, engines, or neighboring spaces significantly affects well-being. Hybrid acoustic metamaterials with resonant cavities or honeycomb cores enable strong absorption in the 100–500 Hz range, achieving quieter and healthier indoor environments. Integrated into façades or ceilings, such panels improve comfort without adding bulk [21]. A schematic representation of a compact double-negative acoustic metamaterial panel designed for low-frequency noise attenuation is shown in Figure 4.

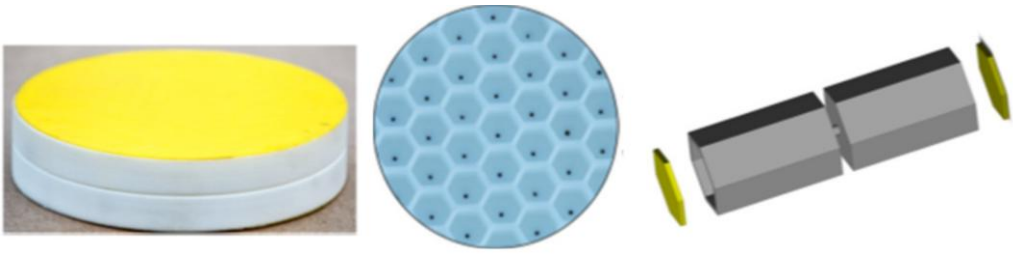

Figure 4. Schematic of a double-negative acoustic metamaterial, showing a compact panel structure with periodic cavities designed to attenuate low-frequency noise [21]

By enabling precise sound control through structural design, acoustic metamaterials support the creation of quieter, healthier, and more livable cities. Their lightweight, tunable, and sustainable nature makes them an essential component of next-generation urban infrastructure.

3.3. Mechanical Metamaterials

Mechanical metamaterials are architected structures designed to achieve unusual stress–strain responses, programmable stiffness, and exceptional energy absorption. Unlike conventional materials, their performance depends on geometry rather than chemical composition—using re-entrant, origami-inspired, or chiral patterns to realize effects such as negative Poisson's ratio, high damping, or tunable load-bearing capacity [22].

From the perspective of smart cities, mechanical metamaterials contribute mainly in three areas:

1. Infrastructure resilience:

Mechanical metamaterials can improve the resilience of buildings and civil infrastructure exposed to earthquakes, wind, or traffic vibrations. Their microstructured design enables frequency-selective vibration attenuation and energy dissipation. Seismic metamaterial barriers and layered foundations combining concrete with elastomeric elements have demonstrated reductions of transmitted vibrations by over 80%, improving safety and extending structural lifetime [22]. Examples of seismic metamaterial barriers and layered foundations for vibration mitigation are illustrated in Figure 5.

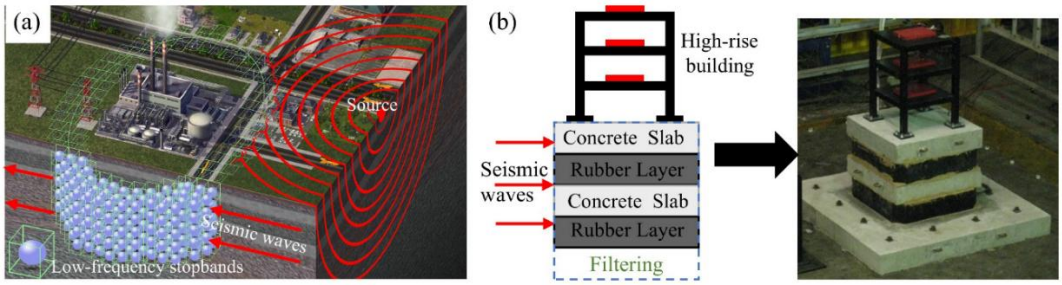

Figure 5. Seismic metamaterials for infrastructure protection: (a) Barrier deflecting low-frequency seismic waves. (b) Layered foundation of concrete and rubber with prototype for vibration filtering [22].

2. Urban safety:

For protecting people and vehicles in dense urban environments, lightweight auxetic or adaptive lattices provide efficient impact absorption. Recent advances include tunable lattices filled with granular particles that change stiffness through jamming transitions, reducing transmitted stress and enabling reuse after impact. Such materials could enhance safety in public transport systems, pedestrian zones, or protective equipment without adding bulk [23]. An example of an adaptive lattice structure utilizing a jamming transition for reusable impact protection is shown in Figure 6.

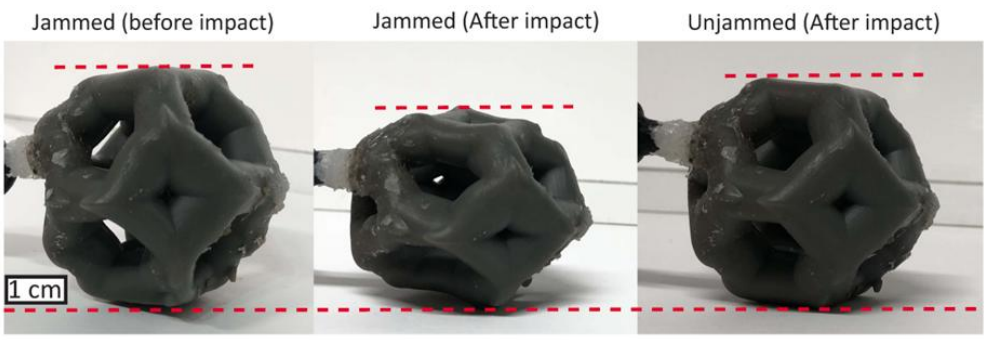

Figure 6. Adaptive lattice with jamming transition for reusable impact protection [23].

3. Energy harvesting:

Piezoelectric metastructures demonstrate how metamaterials can both harvest and mitigate vibrations—a dual functionality ideal for smart infrastructure. Periodic beams equipped with shunted piezoelectric patches convert traveling-wave energy into usable electricity while simultaneously reducing vibration transmission. Such self-powered systems can be embedded in bridges or roads to supply energy for sensors and IoT devices, aligning with the sustainability goals of future smart cities [24].

Mechanical metamaterials thus exemplify how geometry-driven design supports adaptive, safe, and energy-efficient infrastructures. Their integration into urban systems advances the transition toward resilient and self-sustaining city environments.

4. Discussion

The integration of metamaterials into urban environments demonstrates their potential to fundamentally transform how cities manage energy, comfort, and safety. By combining geometry-driven design with modern manufacturing, metamaterials can be precisely tailored for light control, noise mitigation, and vibration reduction—functions that are increasingly important in sustainable urban development.

Their multifunctionality makes them particularly attractive for smart city applications. A single engineered structure can simultaneously absorb vibrations, control sound, or optimize thermal radiation, offering compact and efficient solutions compared to conventional materials. However, several challenges remain before wide implementation can occur. Scalable and cost-effective fabrication processes are required to move from laboratory prototypes to industrial production.

Future progress will rely on strong interdisciplinary collaboration between materials engineers, architects, and data scientists. The combination of metamaterials with digital technologies—such as Internet of Things (IoT) networks, artificial intelligence, and digital twins—could enable self-monitoring and adaptive infrastructures that continuously optimize their performance. These developments would mark an essential step toward intelligent, resilient, and environmentally responsible cities.

5. Conclusions

Metamaterials represent a rapidly advancing field at the intersection of materials science, physics, and engineering, offering unprecedented control over the interaction between structure and external stimuli. Their geometry-driven nature enables functionalities—such as negative refraction, selective absorption, and tunable stiffness—that cannot be achieved with conventional materials.

Optical metamaterials provide efficient platforms for environmental sensing and adaptive energy management, reducing urban energy consumption and supporting the integration of renewable systems. Acoustic metamaterials contribute to healthier urban environments by mitigating noise pollution, while mechanical metamaterials improve structural resilience and enable vibration-based energy harvesting for self-powered monitoring systems. Together, these classes form a unified material toolkit that connects microscopic design principles with macroscopic urban performance.

The continued evolution of metamaterials will depend on advances in fabrication scalability, environmental durability, and interdisciplinary cooperation between materials scientists, civil engineers, and urban planners. As these challenges are addressed, metamaterials are expected to transition from laboratory prototypes to mainstream engineering solutions, enabling cities that are not only more intelligent and energy-efficient but also more resilient, adaptive, and human-centered.

Acknowledgments: The work was supported by the grant project VEGA No. 1/0152/24, KEGA 039TUKE-4/2024, APVV-23-0461.

Conflicts of Interest: The authors declare no conflict of interest.

References

1. Jiao, P.; Mueller, J.; Raney, J.R. et al. Mechanical metamaterials and beyond. *Nat Commun* **2023**, 14, 6004. https://doi.org/10.1038/s41467-023-41679-8
2. Cummer, S.; Christensen, J.; Alù, A. Controlling sound with acoustic metamaterials. *Nat Rev Mater* **2016**, 1, 16001. https://doi.org/10.1038/natrevmats.2016.1
3. Góra, P.; Lopato, P. Metamaterials' Application in Sustainable Technologies and an Introduction to Their Influence on Energy Harvesting Devices. *Applied Sciences* **2023**, 13. https://doi.org/10.3390/app13137742
4. Sun, J.; Zhou, J. Metamaterials: The Art in Materials Science. *Engineering* **2025**, 44, 145-161. https://doi.org/10.1016/j.eng.2024.12.011.
5. Buriak, I.; Zhurba, V.; Vorobjov, G. et al. Metamaterials: Theory, Classification and Application Strategies (Review). *Journal of Nano- and Electronic Physics* **2016**. 8. 04088-1.
6. Veselago, V. G. The electrodynamics of substances with simultaneously negative values of ε and μ. *Soviet Physics Uspekhi* **1968**, 10, 4, 509–514.
7. Pendry, J. B. Magnetism from conductors and enhanced nonlinear phenomena. *IEEE Transactions on Microwave Theory and Techniques* **1999**, 47, 11, 2075–2084.
8. Smith, D. R. et al. Composite medium with simultaneously negative permeability and permittivity. *Physical Review Letters* **2000**, 84, 18, 4184–4187.
9. Ruks, L.; Ballantine, K.E.; Ruostekoski, J. Negative refraction of light in an atomic medium. *Nat Commun* **2025**, 16, 1433. https://doi.org/10.1038/s41467-025-56250-w
10. Wang, K.; Zhou, J.; Tan, D. et al. A brief review of metamaterials for opening low-frequency band gaps. *Appl. Math. Mech.-Engl. Ed.* **2022,** 43, 1125–1144. https://doi.org/10.1007/s10483-022-2870-9.
11. Zhang, L.; Yan, S.; Liu, W. Mechanical metamaterials with negative Poisson's ratio: A review. *Engineering Structures* **2025**, 329, 119838. https://doi.org/10.1016/j.engstruct.2025.119838.
12. Bertoldi, K.; Vitelli, V.; Christensen, J.; Van Hecke, M. Flexible mechanical metamaterials. *Nature Reviews Materials* **2017**, 2, 11, 17066.
13. Huang, G. et al. Radiative cooling and indoor light management enabled by a transparent and self-cleaning polymer-based metamaterial. *Nature Communications* **2024**, 15, 1, 48150.
14. Lu, H.; Ding, Y. Bio-inspired acoustic metamaterials for traffic noise control. *Communications Engineering* **2025**, 4, 1, 70.
15. Wang, W. H. et al. Engineering metamaterials for civil infrastructure. *Materials* **2025**, 18, 17, 4032.
16. Kumar, R.; Kumar, M.; Chohan, J.S.; Kumar, S. Overview on metamaterial: History, types and applications, *Materials Today: Proceedings* **2022**, 56, 5, 3016-3024. https://doi.org/10.1016/j.matpr.2021.11.423.
17. Zhang, T.; Li, D.; Yang, Z. A multi-materials 3D-printed continuous conductive fibre-based metamaterial for broadband microwave absorption. *Virtual and Physical Prototyping* **2023**, 19, 1. https://doi.org/10.1080/17452759.2023.2285417
18. Padilla, W.; Averitt, R. Imaging with metamaterials. *Nature Reviews Physics* **2021**. 4. https://doi.org/10.1038/s42254-021-00394-3.
19. Wang, H.; Sivan, P.V. et al. Highly efficient selective metamaterial absorber for high-temperature solar thermal energy harvesting. *Solar Energy Materials and Solar Cells* **2015**, 137, 235-242. https://doi.org/10.1016/j.solmat.2015.02.019.
20. Lu, JH.; Ding, S.; Ni, YQ. et al. Bio-inspired acoustic metamaterials for traffic noise control: bridging the gap with machine learning. *Commun Eng* **2025** 4, 136. https://doi.org/10.1038/s44172-025-00470-x.
21. Kumar, S.; Lee, H.P. The Present and Future Role of Acoustic Metamaterials for Architectural and Urban Noise Mitigations. *Acoustics* **2019**, 1, 590-607. https://doi.org/10.3390/acoustics1030035
22. Wang, H.; Zhao, S.; Xu, C.; Sun, K.; Fan, R. Engineering Metamaterials for Civil Infrastructure: From Acoustic Performance to Programmable Mechanical Responses. *Materials* **2025**, 18, 4032. https://doi.org/10.3390/ma18174032
23. Wang, Y.; Krishnan, G.; Bertoldi, K.; Johnson, S. E. Architected lattices with adaptive energy absorption. *ArXiv preprint* **2019**. https://doi.org/10.48550/arXiv.1909.05231
24. Lin, T.; Al Ba'ba'a, H.; Tol, S. Piezoelectric metastructures for simultaneous broadband energy harvesting and vibration suppression of traveling waves. *AirXiv preprint arXiv* **2021**, 2104.00188. https://doi.org/10.48550/arXiv.2104.00188

TECHNICAL UNIVERSITY OF KOŠICE
Faculty of Mechanical Engineering

The use of digital calibration certificates in healthcare

Gregor Starinský [1,*], Jan Rybář [1], Peter Onderčo [1], Adam Benčat [2], Jana Gerneschová [3] and Andrej Smetánka [1]

[1] Institute of Automation, Informatization, and Measurement, Faculty of Mechanical Engineering, Slovak University of Technology in Bratislava, Nám. slobody 17, 812 31 Bratislava, Slovakia; gregor.starinsky@stuba.sk; jan.rybar@stuba.sk; peter.onderco@stuba.sk; andrej.smetanka@stuba.sk
[2] Institute of Energy Machinery, Faculty of Mechanical Engineering, Slovak University of Technology in Bratislava, Nám. slobody 17, 812 31 Bratislava, Slovakia; adam.bencat@stuba.sk
[3] Institute of Automation, Informatization, and Measurement, Faculty of Mechanical Engineering, Slovak University of Technology in Bratislava, Nám. slobody 17, 812 31 Bratislava, Slovakia & Laboratory for Fundamental Metrology, Czech Metrology Institute, V Botanice 1504/4, 150 72 Praha, Czech Republic; jana.gerneschova@stuba.sk & jana.gerneschova@cmi.gov.cz
* Correspondence: gregor.starinsky@stuba.sk; Tel.: +421 950 677 712

Abstract: This conference paper addresses the enhancement of measurement processes in healthcare through innovative management of measuring instruments. Accurate and reliable measurements are essential, as they directly impact patient safety and care quality. The growing number and variety of medical devices increase the complexity of instrument tracking and maintaining metrological traceability. The paper discusses current practices in laboratory and clinical settings, highlighting the adoption of digital calibration certificates as a modern solution to improve the management of metrological documentation. Digital certificates increase process transparency, reduce errors from manual handling, and enhance the reliability and efficiency of metrological operations in healthcare institutions.

Keywords: Digital calibration certificates, Healthcare, Medical metrology, Traceability

1. Introduction

Accurate and reliable measurements are essential in healthcare, as even small deviations can directly affect patient safety and the quality of care. Medical devices, ranging from diagnostic instruments to therapeutic equipment, require regular calibration to ensure measurement precision and consistency. With the growing number and variety of medical devices, managing and tracking these instruments has become increasingly complex, placing higher demands on healthcare metrology [1]. Traditionally, calibration records have been maintained in paper-based formats, which are time-consuming to manage, prone to human error, and difficult to update or share across departments.

The introduction of digital calibration certificates (DCCs) provides a modern solution to these challenges. Implementing DCCs allows healthcare institutions to efficiently manage metrological data in both laboratory and clinical practice, ensuring timely updates and easier access to calibration records. Digital calibration certificates enhance process transparency, reduce errors from manual handling, and improve the reliability and efficiency of metrological operations. Medical metrology, which ensures the accuracy and traceability of measuring instruments, is therefore essential for safe and high-quality healthcare, enabling correct diagnoses and effective patient treatment. This paper examines the implementation and benefits of digital calibration certificates in healthcare, emphasizing their role in accurate instrument tracking, maintaining metrological traceability, and supporting compliance with regulatory and accreditation requirements. [2]

2. Materials and Methods

The following section outlines the environment, instruments, and procedures considered in this study to evaluate the implementation of digital calibration certificates in a healthcare setting.

Study Setting

The study was conducted in a medium-sized healthcare institution comprising both laboratory and clinical departments, where a variety of medical devices, including diagnostic analyzers, monitoring equipment, and therapeutic instruments, are routinely used. The institution maintains an internal metrology system to ensure that all measuring instruments comply with regulatory requirements and maintain traceability to national and international standards. [2]

Data Collection

Data were collected on the current practices for calibration management, including the frequency of calibrations, record-keeping methods, and accessibility of calibration documentation. Information was obtained from institutional metrology records, maintenance logs, and interviews with laboratory and clinical personnel responsible for instrument management. [2]

Digital Calibration Certificates Implementation

The study focused on the implementation of digital calibration certificates DCCs as a replacement for traditional paper-based records. A DCC system was selected based on its compatibility with existing instrument management software and its ability to provide secure, time-stamped, and easily shareable calibration records. The implementation process included:

1. Digitization of existing calibration records.
2. Integration of DCCs into the laboratory and clinical workflow.
3. Training of personnel in using the DCC system.

Evaluation Metrics

The effectiveness of DCCs was evaluated using the following metrics:

- Accessibility and timeliness of calibration records.
- Reduction in errors related to manual record handling.
- Improvement in traceability and compliance with metrological and regulatory standards.
- User satisfaction and workflow efficiency among laboratory and clinical staff.

The collected data were analyzed quantitatively, comparing performance indicators before and after DCC implementation, and qualitatively through user feedback to assess the practical benefits and challenges of the digital system. [2]

3. Results

An example of the use of Digital Calibration Certificates DCCs is blood pressure measurement using sphygmomanometers, which are essential for the diagnosis and treatment of cardiovascular diseases. Every automatic or semi-automatic blood pressure monitor requires regular calibration to ensure that its measurements remain accurate and reliable. In some countries, these devices are even legally recognized measuring instruments, subject to mandatory verification procedures under national metrological regulations. [2; 3; 4]

When implementing DCCs, calibration is performed according to established metrological procedures, and the results (Table 1) are recorded directly in a digital system. The certificate contains all necessary information, including device identification, calibration date and results, deviations from reference values, and the validity period of the calibration.

The digital record is securely stored and accessible at any time to physicians, nurses, or biomedical technicians, thereby simplifying device management. For example, before use in an intensive care unit, medical personnel can verify the validity of the DCC and

ensure that the blood pressure monitor is operating within specified accuracy limits [3]. The system can automatically notify the responsible biomedical technician of a scheduled recalibration, minimizing the risk of using an inaccurate device. [2]

Benefits include increased measurement reliability, reduced errors from manual data entry, simplified management of multiple devices, and improved documentation for audits and regulatory authorities. From a biomedical engineering perspective, DCCs enhance medical metrology processes by ensuring robust metrological traceability, taking into account clinical testing and the device's measurement history, thereby contributing to patient safety and effective healthcare delivery. [2; 4; 5]

Table 1. Blood Pressure Measurement Device: Calibration Results. Source: Own, adapted from [3; 4; 5].

Parameter	Details/Values
Device Identification	Model: XXXX Serial Number: XXX/2026
Calibration Date	DD.MM.YYYY
Calibrated Function	Measurement of systolic, diastolic, and pulse pressure
Reference Values	100/60 mmHg, 120/80 mmHg, 140/90 mmHg, 160/100 mmHg
Measured Values	100/61 mmHg, 121/80 mmHg, 139/89 mmHg, 161/101 mmHg
Deviation from Reference	+1 mmHg, 0 mmHg, -1 mmHg, +1 mmHg
Calibration Methodology	Comparison with a reference manometer according to ISO 81060-2
Accuracy Requirement	±3 mmHg (systolic/diastolic), ±5% (pulse)
Result	Compliant / Calibration Successful
Calibration Validity	Until DD.MM.YYYY
Responsible Person / Technician	First Name Last Name, Biomedical Technician

The table provides a clear and systematic presentation of the calibration results of an automatic blood pressure monitor. It includes all key information, such as device identification, calibrated functions, reference and measured values, deviations, calibration methodology, required accuracy, calibration result, and validity period. This format allows for straightforward verification of the measurement device's accuracy, ensures transparent documentation for audits and regulatory authorities, and facilitates device management in a clinical setting. Overall, the table ensures transparency, metrological reliability, and contributes to patient safety. [6]

In practice, the digitalization of calibration certificates can be implemented in several ways. Certificates can be stored as PDFs with a digital signature, ensuring the authenticity of the document, or supplemented with a QR code or barcode that links to a digital record in a database, enabling rapid verification of validity. Another approach is the use of structured data files such as XML, JSON, or CSV, which are machine-readable and allow integration with hospital information systems. Certificates can also be stored in cloud-based systems with centrally managed calibration histories and automatic reminders for recalibration, or made accessible through mobile applications that enable on-site device verification. In this way, digitalization enhances transparency, metrological reliability, and patient safety. [1; 2; 6]

4. Discussion and Conclusions

The implementation of digital calibration certificates DCCs in healthcare institutions, encompassing both laboratory and clinical practice, represents a significant advancement in the management of medical measuring instruments. By replacing traditional paper-based records, DCCs improve the accessibility, accuracy, and timeliness of calibration

documentation, directly supporting patient safety and the quality of care. The growing number and diversity of medical devices increase the complexity of instrument tracking and maintaining metrological traceability, which DCCs address through centralized, secure, and easily shareable records. Integration into laboratory and clinical workflows enhances operational efficiency, minimizes errors associated with manual data handling, and ensures compliance with regulatory and accreditation standards.

While challenges such as initial investment, staff training, and interoperability with existing systems remain, the benefits in terms of transparency, reliability, and process efficiency are substantial. Digital certificates also enable continuous monitoring and maintenance of instruments, allowing institutions to respond proactively to calibration needs and regulatory requirements. Overall, DCCs provide a robust framework for modern healthcare metrology, supporting both daily operations and long-term quality assurance [6]. This conference paper demonstrates that digital calibration certificates not only streamline administrative tasks but also strengthen the overall safety, reliability, and efficiency of medical instrument management, underscoring their essential role in enhancing metrological practices and advancing patient care quality in contemporary healthcare settings.

Acknowledgments: The authors would like to thank the Faculty of Mechanical Engineering of the Slovak University of Technology in Bratislava and the KEGA projects No. 025STU-4/2024 and No. 028STU-4/2026 for their support in the preparation of this conference paper. This conference output was also supported by the Competition for the Academic Čabelka Award No. CAC-01-26 (within the project call supporting young researchers). We would like to thank all of the above for their support.

Conflicts of Interest: "The conference paper is not in any conflict of interest. The funders had no role in the design of the study; in the collection, analyses, or interpretation of data; in the writing of the manuscript, or in the decision to publish the results".

References

1. Mustapää, T.; Nummiluikki, J. and Viitala, R. Digitalization of Calibration Data Management in Pharmaceutical Industry Using a Multitenant Platform, Applied Sciences, 12, 7531, https://doi.org/10.3390/app12157531, 2022.
2. Nummiluikki, J.; Mustapää, T.; Hietala, K. and Viitala, R. Benefits of network effects and interoperability for the digital calibration certificate management, 2021 IEEE International Workshop on Metrology for Industry 4.0 & IoT (MetroInd4.0&IoT), Rome, Italy, 3–5 June 2020, IEEE, 352–357, https://doi.org/10.1109/MetroInd4.0IoT51437.2021.9488562, 2021.
3. Sedlák, V.; Pražák, D. and Rybář, J. Metrologie tlaku ve zdravotnictví /Pressure metrology in healthcare/. In Metrologie /Metrology/. Roč. 30, č. 3 (2021), s. 22 – 26 / Vol. 30, No. 3 (2021), pp. 22–26/. ISSN 1210-3543.
4. Sedlák, V. Novel advanced methods of blood pressure standards traceability. [Dissertation thesis]. Slovak University of Technology in Bratislava. Faculty of Mechanical Engineering. Thesis supervisor: doc. RNDr. Jiří Tesař, PhD. Bratislava: FME STU BA, 2023. 88s.
5. Rybář, J. Selected topics from medical metrology. [Habilitation thesis]. Slovak University of Technology in Bratislava, Faculty of Mechanical Engineering. Institute of automation, informatization, and measurement. Bratislava: FME STU BA, 2022. 78 p.
6. Bruns, T.; Nordholz, J.; Röske, D. and Schrader, T. A demonstrator for measurement workflows using digital calibration certificates (DCCs), Measurement: Sensors, 18, 100208, https://doi.org/10.1016/j.measen.2021.100208, 2021.

TECHNICAL UNIVERSITY OF KOŠICE
Faculty of Mechanical Engineering

Trends in the Use of Artificial Intelligence in Enterprises in Slovakia and the EU and Their Relationship to Performance Indicators

Dominika Sukopová [1,*], Milan Fiľo [1], Jaroslava Kádárová [1] and Lenka Leščinská [1]

[1] Department of Business Management and Economics, Faculty of Mechanical Engineering, Technical University of Kosice, 040 01 Košice, Slovakia; milan.filo@ecoinvest.sk (M.F.); Jaroslava.kadarova@tuke.sk (J.K.); lenka.vyrostkova@tuke.sk (L.V.)
* Correspondence: dominika.sukopova@tuke.sk

Abstract: The aim of this paper is to provide a simple overview of how the use of artificial intelligence (AI) has developed in enterprises in Slovakia compared with the European Union, and to discuss whether differences in adoption may be related to short-term economic performance. The analysis is based on selected Eurostat data for the years 2021–2024. The results show that the share of Slovak companies using AI has increased across all size categories, although the pace of growth remains slower than in the EU27. When comparing these developments with trends in labour productivity, no direct or stable relationship can be observed. The findings highlight that the benefits of AI depend not only on the implementation of digital tools but also on the development of digital skills and organisational changes within enterprises.

Keywords: Artificial intelligence; digitalisation; enterprise adoption; economic performance; productivity trends

1. Introduction

Technologies based on artificial intelligence are becoming an integral part of the digital transformation taking place in European enterprises. Their applications range from the automation of routine tasks to supporting more complex decision-making processes. Although digitalisation is progressing across all EU Member States, the speed and intensity of AI adoption vary considerably from country to country.

In Slovakia, the uptake of AI is gradually increasing, yet the pace of digital transformation differs across enterprise size groups. Smaller firms, in particular, face a number of barriers linked to investment costs, access to technical specialists, and overall organisational preparedness. For this reason, it is important to monitor not only the general level of digital adoption but also its broader connections to economic performance and the dynamics of the national economy.

2. Materials and Methods

The analysis in this paper is based on publicly accessible data retrieved from Eurostat, focusing on two indicators relevant to the digital transformation of enterprises: the share of companies using at least one artificial intelligence (AI) technology and the year-to-year change in labour productivity per hour worked. Data were collected for Slovakia and the EU27 for the years 2021–2024, which represent the most recent period for which AI adoption statistics are available. Since the dataset covers only a small number of observation years, the study adopts a descriptive approach aimed at providing an overview rather than drawing causal conclusions.

To compare the level of AI adoption between Slovakia and the EU27, a simple difference indicator was calculated for each year using:

$$G_t = A_t^{EU} - A_t^{SK} \tag{1}$$

where A_t^{EU} denotes the EU27 average and A_t^{SK} the corresponding value for Slovakia. To assess changes over time, a basic rate-of-change formula was applied:

$$\Delta X_t = \frac{X_t - X_{t-1}}{X_{t-1}} * 100 \tag{2}$$

with X representing either AI adoption or productivity. Labour productivity trends were examined alongside AI adoption to determine whether movements in one indicator appeared to coincide with developments in the other. No statistical modelling was conducted, as the short time horizon does not permit robust inference.

This methodological approach offers a clear and accessible overview suitable for a conference contribution. The analysis relies entirely on aggregated Eurostat data and primarily highlights visible differences and broader patterns in Slovakia's digital transformation.

3. Results

The comparison of AI adoption levels shows a gradual increase in Slovak enterprises between 2021 and 2024. Although the trend is positive, Slovakia consistently remained below the EU27 average across the entire period. Medium-sized and large firms displayed the widest gap when compared with their European counterparts.

Labour productivity in Slovakia followed a more uneven pattern, with a decline in 2022 and moderate improvements in 2023 and 2024. By contrast, productivity in the EU27 developed in a more stable manner with fewer fluctuations.

To provide a concise overview of these developments, Table 1 summarises the main qualitative trends.

Table 1. Overview of AI Adoption and Productivity Trends in Slovakia and the EU27 (2021–2024).

Year	AI Adoption (Slovakia)	AI Adoption (EU27)	Productivity Trend (Slovakia)	Productivity Trend (EU27)
2021	Low but rising	Moderately higher	Positive growth	Slight increase
2022	Continued increase	Stable increase	Decline	Stable
2023	Further growth	Continued growth	Mild improvement	Stable
2024	Highest observed level	EU remains ahead	Moderate improvement	Slight positive trend

Table 1 summarises the main qualitative patterns without reporting numerical values, offering a simplified comparison suitable for conference-level evaluation.

4. Discussion

The results presented in Table 1 show that Slovakia is progressing in the adoption of artificial intelligence, although at a noticeably slower pace than the EU27. The persistent gap between Slovakia and the EU suggests structural limitations that influence the ability of enterprises—particularly medium-sized and large ones—to adopt advanced digital technologies at a competitive rate.

The absence of a visible short-term alignment between AI adoption and labour productivity is consistent with international findings. Many studies emphasise that AI-driven productivity benefits tend to materialise gradually, as firms require time to reorganise internal processes, integrate new workflows, and build the necessary digital and

data-related competencies. In the Slovak context, these prerequisites often develop more slowly due to factors such as limited availability of specialised professionals, lower innovation capacity among SMEs, and uneven access to technological infrastructure.

Overall, the findings indicate that technology adoption alone is not sufficient to generate immediate improvements in productivity. Complementary investments in organisational change, workforce development, and digital readiness remain essential for ensuring that AI contributes to long-term economic performance.

5. Conclusions

This paper provided a concise comparison of AI adoption trends and labour productivity development in Slovakia and the EU27 for the period 2021–2024. Although the use of artificial intelligence has increased in Slovak enterprises, the country continues to lag behind the EU average. Productivity trends do not reflect these increases, suggesting that short-term economic outcomes are influenced more strongly by broader macroeconomic factors than by digital uptake alone.

The findings highlight the need for policies that strengthen digital skills, support innovation in small and medium-sized enterprises, and enhance organisational capacity to integrate advanced technologies. Such measures are crucial for ensuring that the long-term potential of artificial intelligence translates into meaningful and sustainable productivity growth.

Acknowledgments: In This paper was developed within the implementation of the project KEGA 019TUKE-4/2025 "Individualization of approaches in the process of acquiring digital skills of students as part of a comprehensive competency profile of graduates".

Conflicts of Interest: The authors declare no conflict of interest.

References

1. European Commission. Coordinated Plan on Artificial Intelligence 2021 Review. Publications Office of the European Union, Luxembourg, 2021.
2. European Commission. Digital Economy and Society Index (DESI) – Overview Report 2022. Publications Office of the European Union, Luxembourg, 2022.
3. OECD. Digital Transformation in SMEs. OECD Publishing: Paris, France, 2021.
4. Eurostat. Artificial Intelligence Use in Enterprises (isoc_eb_ai). Available online: https://ec.europa.eu/eurostat (accessed January 2025).
5. Eurostat. Labour Productivity per Hour Worked (tipsna70). Available online: https://ec.europa.eu/eurostat (accessed January 2025).
6. Eurostat. Real GDP Growth Rate (tec00115). Available online: https://ec.europa.eu/eurostat (accessed January 2025).
7. European Commission. Shaping Europe's Digital Future. Publications Office of the European Union, Luxembourg, 2020.
8. UNCTAD. Digital Economy Report 2021: Cross-Border Data Flows and Development. United Nations, New York, 2021.

TECHNICAL UNIVERSITY OF KOŠICE
Faculty of Mechanical Engineering

Use of simulation methods in production machines using virtual and augmented reality

Daniel Szászi [1,*], Ján Kráľ [1]

[1] Technical University of Košice, Faculty of Mechanical Engineering, Department of Manufacturing Technologies and Robotics, Slovakia; daniel.szaszi@student.tuke.sk; jan.kral.2@tuke.sk
* Correspondence: daniel.szaszi@student.tuke.sk

Abstract: This paper explores how simulation methods using virtual and augmented reality (VR, AR) can support the production of sheet metal working machines and define the possibilities for further applications and concepts. One of the main focus is the flexible and responsive layout planning in manufacturing by placing full-scale 3D models directly into real environments. AR enabling accurate spatial checks helps teams conceptualize workstations, staging areas, and equipment placement. In addition, the paper maps the current landscape of plant simulation tools, examines how AR can be integrated into these systems, and considers lightweight visualization software as an alternative to full simulation for certain layout tasks. These comparisons highlight practical trade-offs in accuracy, usability, and implementation effort. Beyond improving internal planning processes, AR also strengthens customer engagement by enabling pre-installation checks at client sites, allowing buyers to visualize machinery footprints and assess spatial fit before committing to a purchase. The paper concludes by identifying several directions for future exploration, including the development of hybrid workflows, the examination of organizational adoption barriers, and the investigation of how artificial intelligence (AI) could be incorporated into AR-based layout planning solutions.

Keywords: Manufacturing, Simulation; Augmented Reality; Visualization

1. Introduction

Manufacturing environments characterized by low production volumes and a high mix of product variants face persistent challenges in layout planning. Large metal-forming equipment - such as punch presses or laser cutting machines - is often built to order, and frequent model changes driven by sales requirements and product development force production areas to adapt quickly to new equipment footprints.

Although the overall layout is primarily determined by the working envelope of the machine itself, the introduction of automation adds another layer of complexity. Production engineering teams must ensure that the complete system fits within the available shop-floor space while maintaining adequate clearance for equipment, testing units, tools, and operator access. These systems may include automated loading and unloading units, warehouse modules, or integrated machine cells where sheet-metal processing machines operate alongside robots and auxiliary equipment.

Ensuring that a proposed layout does not interfere with the existing manufacturing environment is not only a concern during final assembly. It is also a critical part of the sales preparation process. Customers expect confirmation before committing to a purchase, that the machine's design and automation features will not conflict with the spatial constraints of their facility.

Integrating the machine's 3D model into an augmented reality environment can significantly accelerate the preparation of both phases. AR enables both manufacturers and

customers to visualize the equipment directly within its intended real-world setting, providing a precise and intuitive understanding of how the system will occupy space. This capability enhances decision-making during the sales process and supports more efficient planning during manufacturing preparation.

This work examines whether the current practices represent the most effective method for conducting layout validations, or whether faster, simpler, and more easily integrated alternatives exist. To address this question, the study will explore additional opportunities beyond traditional Digital Twin–based validation. These include lightweight AR applications that enable rapid, on-site spatial checks; the potential development of a dedicated Oculus-based VR application to support immersive layout evaluation; and the integration of AI to automate aspects of model placement, collision detection, and layout optimization. Together, these avenues may offer more accessible and scalable solutions for both manufacturing engineers and sales teams involved in early-stage planning.

2. Materials and Methods

A strong foundation for this research comes from bringing together what is already known about simulation in the manufacturing [1, 2, 6] as well as Digital Twins [3,4,5] and the application of Virtual Reality and Augmented Reality in different industries [6, 7, 8, 9] from several credible sources. Peer-reviewed academic studies offer rigorous evidence and theoretical grounding, while industry reports from consulting firms and technology providers highlight current market trends, adoption patterns, and strategic considerations [10]. Real-world case studies from manufacturing companies add practical insight into how AR performs in operational settings, including successes and challenges. Technical documentation from AR platforms and hardware manufacturers rounds out the picture by clarifying system capabilities, limitations, and integration requirements. Taken together, these sources create a well-rounded understanding of the AR landscape and help guide the direction of the research.

Before augmented reality (AR) reached a level of maturity that enabled its use in industrial layout planning, traditional approaches were - and in many cases still are - the primary methods. These range from manual measurements to computer-aided methods using CAD software and Digital Twins (DT) simulations.

The terminology surrounding Digital Twins has evolved over the years, but the core idea has remained largely unchanged since the concept was introduced in 2002. The Digital Twin refers to a digital representation of a physical system that exists as an independent yet connected entity. This virtual counterpart mirrors the information contained within the physical system and remains linked to it throughout the system's entire lifecycle. [3]

Today, the application range of Digital Twins is extensive. A study by Enders and Hoßbach identifies major industrial sectors adopting DT technologies, including aerospace, manufacturing, healthcare, energy, automotive, petroleum, the public sector, mining, marine, and agriculture [4]. While their work emphasizes simulation, monitoring, and control purposes, Singh, Srivastava, Fuenmayor, Kuts, Qiao, Murray, and Devin highlight additional use cases such as design, validation, customization, optimization, prediction, and maintenance [5].

Ivanov, Amelin, and Haidabrus provide a comprehensive and structured comparative analysis of modern software tools for manufacturing process simulation. Their evaluation spans technical, analytical, organizational, economic, and educational criteria [6]

From the perspective of this study, understanding the capabilities of 3D modeling and visualization tools is essential. Trebuňa, Pekarčíková, Duda, and Svantner contribute further insight by examining the integration of virtual reality (VR) into discrete-event simulation for production and assembly processes, demonstrating how immersive environments can enhance simulation-based decision-making [7].

Creating a Digital Twin (DT) of a manufacturing facility provides valuable spatial insight, yet it often falls short when layouts must be verified and repeatedly adjusted directly on the shop floor. These iterations can become time-consuming and require significant expertise from the personnel involved, especially when frequent reconfiguration is driven by changing production needs or equipment variations. The opportunity of the integration of Artificial Intelligence (AI) is becoming more and more feasibly as described in the study of Sajadieh and Noh [11].

3. Overview of VR/AR in manufacturing simulation

3.1. Current Simulation softwares with VR and AR integration

There are several platforms that enables VR and AR use to improve manufacturing processes, creating work instructions and visualization of products. The overview in Table.1 shows the most common software packages with their primary use.

Table 1. Overview of platforms with VR/AR integration.

Platform	Primariy Use
PTC Vuforia	Layout planning Assembly guidance Remote assistance
Siemens Teamcenter (Tecnomatix)	Factory layout planning Digital twin visualization Process simulation
Dassault Systemes Delmia Augmented Experience	Assembly guidance Inspection Maintenance
LightGuide AR	Work instructions Quality Control Projected AR

3.1.1. PTC Vuforia

PTC Vuforia brings together CAD models, IoT data, computer vision, and low-code tools into one flexible, enterprise-ready AR platform. Because of this modular setup, it scales well and adapts to a wide range of industrial needs. The result is a system that helps teams work more efficiently, make fewer mistakes, and move their digital transformation efforts forward. [12] The core components of PTC Vuforia are summarized in Table.2.

Table 2. Core components of PTC Vuforia.

Modul	Use with AR
Vuforia Engine	platform for mobile and wearables
Vuforia Studio	CAD import IoT data integration
Vuforia Expert Capture	Capturing workflows and converting them to AR instructions
Vuforia Chalk	Real-time video annotations Remote troubleshooting
Vuforia Instruct	Inspection guidance CAD overlays

Figure 1. Quality control with PTC Vuforia [12].

3.1.2. Siemens Teamcenter (Tecnomatix)

The Siemens Teamcenter is a Product Lifecycle Management system (PLM). Tecnomatix is this system's integrated digital manufacturing suite. Tecnomatix relies heavily on Teamcenter as its backbone for data and process management, enabling a digital thread from product design to manufacturing operations. The core components of this package includes 10 modules. While five of them (Plant simulation, RobotExpert, FactoryCAD, FactoryFLOW, Mechatronics Concept Designer) are usable for VR presentations, the following five modules summarized in Table.3 have meaningful AR integrations..[13]

Table 3. Siemens Tecnomatix with AR integration.

Modul	Use with AR
Process Simulate	AR work instructions and AR based validation
Process Designer	AR visualization of processes and AR step-by-step instructions
Jack / Human Simulation	AR guidance for ergonomics and task execution
EasyPlan	Generating work instructions That can be transformed to AR
TeamCenter Manufacturing Integration	PLM backbone for AR

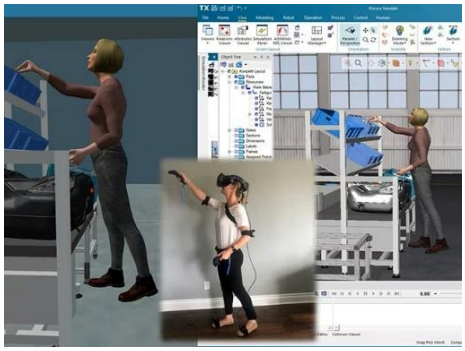

Figure 2. Process and human simulation with Siemens Tecnomatix [13].

3.1.3. Dassault Systèmes DELMIA

Dassault Systèmes provides manufacturing simulation through the DELMIA suite on the 3DEXPERIENCE platform. DELMIA enables companies to model, simulate, optimize, and execute manufacturing operations using their digital twin, while DELMIA Augmented Experience (DAE) is an industrial augmented reality (AR) solution that brings the digital twin directly onto the shop floor. It overlays 3D instructions, inspection criteria, and real time guidance onto physical products to improve assembly, inspection, and maintenance operations. [14]

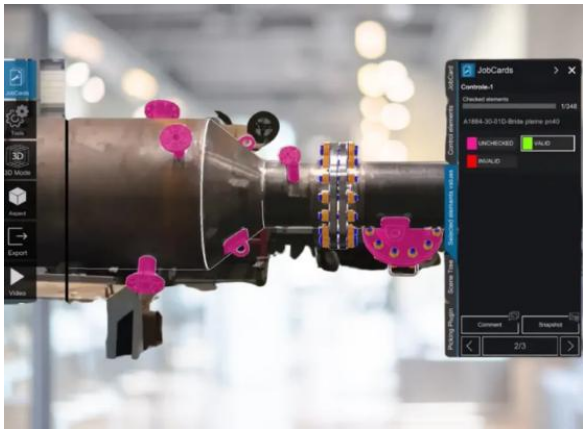

Figure 3. AR overlay in Dassault Systèmes DELMIA [14].

3.1.4. Augment

Augment is an AR platform designed to enable real time visualization of 3D digital assets in physical environments using mobile devices. The system integrates computer vision, 3D rendering, cloud based asset management, and mobile sensor fusion to support industrial, retail, and R&D use cases.

Its primary value proposition lies in reducing prototyping costs, accelerating design cycles, and improving customer decision making through scale accurate, context aware AR simulations. [15]

3.2 Simulation methods in manufacturing using VR/AR

Together, VR and AR create a powerful closed-loop system. VR helps teams design and validate processes before they reach the shop floor, while AR ensures that those processes are executed correctly and consistently in the real world. This combination strengthens digital continuity, improves operator performance, and accelerates the transition from virtual planning to physical production. Table.4. shows an overview of current applications.

Simulation Method	Purpose
Assembly Simulation	Validate and guide manufacturing process and training
Ergonomics simulation	Simulate human factors and safety
Robotics simulation	Path validation and commissioning
Factory layout simulation	Spatial planning and validation
Material flow simulation	Throughput and logistics optimization
Maintenance simulation	Service and diagnostics
Product simulation	Quality control and design review

3.3. Devices Used in VR/AR simulations in manufacturing

As technology continues to advance, new and increasingly capable devices enter the market every year. These tools can handle larger data and deliver more detailed visual experiences than ever before. In practice, the choice of device depends on the specific task, the type of simulation being performed, and the available budget. In manufacturing, the most used options include head-mounted displays, tablets, smartphones, and various projection-based systems.

4. Discussion

One of the major challenges in VR/AR-based simulations is the level of technical skill and experience required from personnel. Another significant factor is the substantial preparation time needed to create simulations that provide real added value, particularly when developing a Digital Twin as the foundation for a VR environment.

With the introduction of AR, however, new opportunities have emerged for developing manufacturing applications that allow real-time interaction with the physical environment without extensive preparation. For example, an AR-based tool can place a 3D model of a machine directly into the real workspace that opens plenty of room for different applications.

Once such a mixed-reality environment is established and the 3D models of products and required equipment are loaded from a cloud-based database it can be used to verify assembly progress, identify missing components, access the bill of materials on site, and even receive suggestions through an integrated AI module. The same tool could also support the definition of safety zones around machines and assist in designing safety fences and light-curtain placements.

As the AR industry continues to evolve rapidly, there is still plenty of room to explore new ways this technology can create added value in manufacturing. Many of these innovations can also be leveraged in the sales process, making AR a versatile tool across multiple stages of the product lifecycle.

As AR becomes increasingly accessible through advancements in the commercial and gaming industries, new development platforms are emerging that allow manufacturers to create applications tailored directly to their specific needs. One of the more easily accessible devices is the Meta Quest 3, which can be programmed using several different development platforms.

Acknowledgments: This work was supported by the grant project KEGA 040TUKE-4/2025.

References

1. William de Paula Ferreira, Fabiano Armellini, Luis Antonio De Santa-Eulalia, Simulation in industry 4.0: A state-of-the-art review, Computers & Industrial Engineering, Volume 149, 2020, 106868, ISSN 0360-8352, https://doi.org/10.1016/j.cie.2020.106868.
2. Alquraish, M. (2022). Modeling and simulation of manufacturing processes and systems: Overview of tools, challenges, and future opportunities. Engineering, Technology & Applied Science Research, 12(6), 9163–9169
3. Grieves, Michael. (2016). Origins of the Digital Twin Concept. 10.13140/RG.2.2.26367.61609.
4. Enders, Martin Robert, and Nadja Hoßbach. "Dimensions of Digital Twin Applications – A Literature Review." AMCIS 2019 Proceedings, 2019, Cancun, Mexico.
5. Singh, M.; Srivastava, R.; Fuenmayor, E.; Kuts, V.; Qiao, Y.; Murray, N.; Devine, D. Applications of Digital Twin across Industries: A Review. Appl. Sci. 2022, 12, 5727. https://doi.org/10.3390/app12115727
6. Ivanov, V., Amelin, M. & Haidabrus, B. Simulation software for smart manufacturing: a review. *Discov Appl Sci* **8**, 95 (2026). https://doi.org/10.1007/s42452-025-08012-y
7. Trebuna P, Pekarcikova M, Duda R, Svantner T. Virtual reality in discrete event simulation for production–assembly processes. Appl Sci. 2023;13(9):5469. https://doi.org/10.3390/APP13095469.
8. Al-Jundi, H. A., & Tanbour, E. Y. (2022). Design and evaluation of a high-fidelity virtual reality manufacturing planning system. Virtual Reality. https://doi.org/10.1007/s10055-022-00683-x
9. Husár, J., Knapčíková, L. Implementation of Augmented Reality in Smart Engineering Manufacturing: Literature Review. *Mobile Netw Appl* **29**, 119–132 (2024). https://doi.org/10.1007/s11036-023-02121-x
10. Deloitte. (2020). Augmented reality: On the threshold of a new future. Deloitte Insights. Published by Cognitive Market Research.
11. Sajadieh, S.M.M., Noh, S.D. From Simulation to Autonomy: Reviews of the Integration of Artificial Intelligence and Digital Twins. Int. J. of Precis. Eng. and Manuf.-Green Tech. 12, 1597–1628 (2025). https://doi.org/10.1007/s40684-025-00750-z
12. PTC. (n.d.). Vuforia. https://www.ptc.com/en/products/vuforia (accessed on 10.9.2025)
13. Siemens. (n.d.). Tecnomatix. https://plm.sw.siemens.com/en-US/tecnomatix/ (accessed on 15.9.2025)
14. Dassault Systèmes. (n.d.). *DELMIA Augmented Experience.* https://www.3ds.com/products/delmia/augmented-experience (accessed on 20.9.2025)
15. Augment. (n.d.). Augment – 3D & augmented reality platform. https://www.augment.com/ (accessed on 10.16.2025)

TECHNICAL UNIVERSITY OF KOŠICE
Faculty of Mechanical Engineering

Analysis of the Effect of Surface Treatment of Shearing Tools on the Accuracy and Quality of Roll-Bonded Sheet Cutting

Radovan Šiška [1,*], Ján Slota [1]

[1] Department of Technology, Materials and Computer- Aided Production, Faculty of Mechanical Engineering, Technical University of Kosice, Slovak republic; radovan.siska@tuke.sk; jan.slota@tuke.sk
* Correspondence: radovan.siska@tuke.sk; Tel.: +421950672212

Abstract: The quality of sheared edges and the durability of cutting tools are critical factors in high-volume production of aluminum sheet components. This study investigates the influence of surface treatment of shearing tools on cutting accuracy, edge quality, and tool wear during the blanking of roll-bonded aluminum sheets. The tested material consisted of roll-bonded EN AW-1050 and EN AW-3003 aluminum alloys. Two different PVD-based tool surface treatments supplied by voestalpine eifeler were compared: a polished DLC-based CARBON-X coating and a CrN-RB coating. Industrial production tests were performed on a mechanical press using a cutting die with approximately 5% cutting clearance. Each tool variant was evaluated during a production series of 20,000 parts, with one intermediate cleaning of the cutting elements after 10,000 strokes. Tool surface roughness, visual cut edge quality, and burr formation were monitored as a function of the number of cuts. The results demonstrate that the CARBON-X coated tools significantly outperformed the CrN-RB coated tools in terms of wear resistance, burr growth suppression, and stability of cut edge quality. The findings confirm the suitability of low-friction DLC coatings for cutting roll-bonded aluminum sheets and provide practical guidance for industrial tooling design.

Keywords: blanking; rollboding; DLC coating; aluminium sheet; tool wear

1. Introduction

Sheet metal blanking is a key manufacturing process in many industrial sectors, where cut edge quality directly affects dimensional accuracy, functional performance, and the need for secondary finishing operations. In high-volume production, tool wear and burr formation are critical limiting factors, particularly when processing ductile materials such as aluminum alloys [1,2].

The increasing use of aluminum in lightweight structures has intensified research into wear mechanisms during cutting operations. Aluminum is prone to adhesive wear and galling, which leads to rapid degradation of cutting edges and progressive burr growth [3–5]. Burr height is therefore widely used as an indicator of tool wear and cutting quality in blanking processes [6].

Roll-bonded aluminum sheets, composed of two metallurgically bonded alloys, are increasingly applied in thermal and structural components due to their combined material properties [7]. While their forming behavior has been studied, investigations focusing on their blanking and cutting performance remain limited. The presence of dissimilar bonded layers may influence stress distribution during shearing and accelerate tool wear, yet this effect is not well documented.

Tool surface engineering is commonly applied to improve wear resistance in aluminum cutting. Conventional hard PVD coatings such as CrN provide high hardness but show mixed effectiveness in suppressing aluminum adhesion, leading to divergent con-

clusions in the literature regarding their suitability for aluminum blanking [8–10]. In contrast, diamond-like carbon (DLC) coatings exhibit low friction and strong anti-adhesive behavior and have been shown to significantly reduce galling and burr formation in aluminum sheet cutting [11–13]. However, most reported studies focus on monolithic aluminum sheets and laboratory-scale tests.

The present study addresses this gap by experimentally evaluating the effect of two industrial tool coatings—a polished DLC-based CARBON-X coating and a CrN-RB coating—on the cutting accuracy and edge quality of roll-bonded EN AW-1050/EN AW-3003 sheets. Production-scale blanking tests comprising 20,000 parts were performed. The results demonstrate that the DLC-based coating provides superior wear resistance and more stable cut edge quality, highlighting the importance of friction reduction in cutting roll-bonded aluminum materials.

2. Materials and Methods

The investigated material was a roll-bonded aluminum sheet composed of EN AW-1050 and EN AW-3003 alloys. The roll bonding process creates a solid-state metallurgical bond between the layers, resulting in a composite sheet with combined mechanical and thermal properties. AW-1050 provides high ductility, while AW-3003 offers increased strength due to manganese alloying.

Blanking was performed using a hydraulic press equipped with a cutting die consisting of upper and lower cutting knives. The cutting clearance was set to approximately 5% of the total sheet thickness, which is commonly recommended for aluminum alloys to ensure low burr height and acceptable tool life. The process represents a conventional industrial shearing operation under dry conditions.

Two variants of cutting tools were tested:

- CARBON-X (polished): a DLC-based coating characterized by high hardness and very low friction coefficient, optimized for cutting and forming of non-ferrous metals.
- CrN-RB: a chromium nitride-based PVD coating designed for wear resistance in roll-bonded material processing.

Each tool variant was tested during a production series of 20,000 blanking cycles. A single cleaning of the cutting elements was performed after 10,000 cuts to remove adhered aluminum material.

The following parameters were evaluated:

- Surface roughness (Ra) of the cutting edge in the cutting zone
- Visual quality of the cut edge on the blanks
- Burr formation as a function of the number of cuts

3. Results

At the beginning of the production test, both tool variants exhibited smooth cutting edges with no visible defects. The initial surface roughness measured in the cutting zone was low for both coatings, with the polished DLC-based CARBON-X coating showing slightly lower Ra values than the CrN-RB coating.

After 10,000 cutting cycles, differences in surface condition became evident. The CrN-RB coated tools showed localized aluminum adhesion and an increase in surface roughness in the cutting edge region. In contrast, the CARBON-X coated tools exhibited only

minor changes in surface topography, with no significant material transfer observed. Following cleaning of the cutting elements at 10,000 cuts, aluminum deposits were removed from both tools; however, traces of surface degradation remained visible on the CrN-RB coated tools.

After 20,000 cutting cycles, the CrN-RB coated cutting edges showed pronounced wear marks and a further increase in surface roughness. The CARBON-X coated tools retained a comparatively smooth cutting edge, with only limited signs of wear.

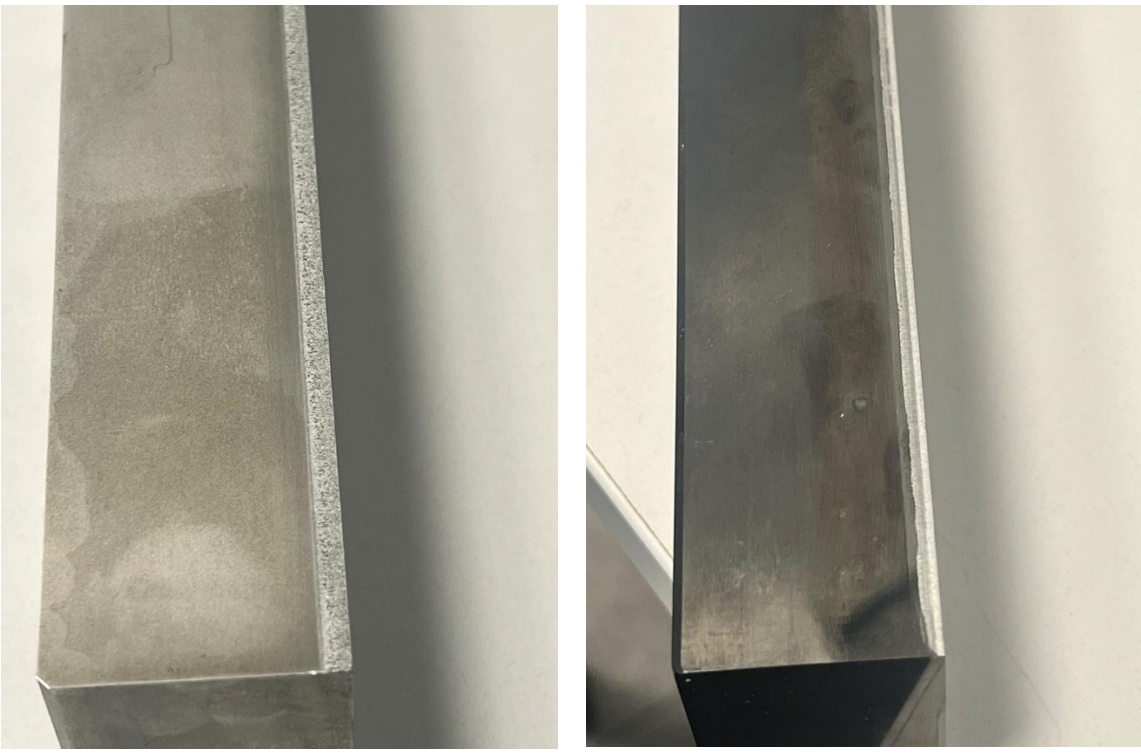

(**a**) (**b**)

Figure 1. Difference of the cutting surface of cutting element cut. **(a)** showing Pondruff CrN-RB with increased roughness in the area of cut. (b) showing Eifeler Carbon-X with visible difference in the area of cut, roughness is way less.

The cut edges of blanks produced at the beginning of the test exhibited a uniform burnished zone and a small fracture zone for both tool variants. Burr height was minimal and visually comparable for both coatings.

With increasing number of cuts, differences in edge quality developed. Blanks cut using the CrN-RB coated tools showed progressive deterioration of edge quality, characterized by an increase in burr height and irregularities in the fracture zone. These effects became noticeable before the intermediate cleaning at 10,000 cuts.

Blanks produced with the CARBON-X coated tools maintained a stable cut edge appearance throughout the test. The burr height increased only slightly with the number of cuts and remained visually uniform even after 20,000 cycles.

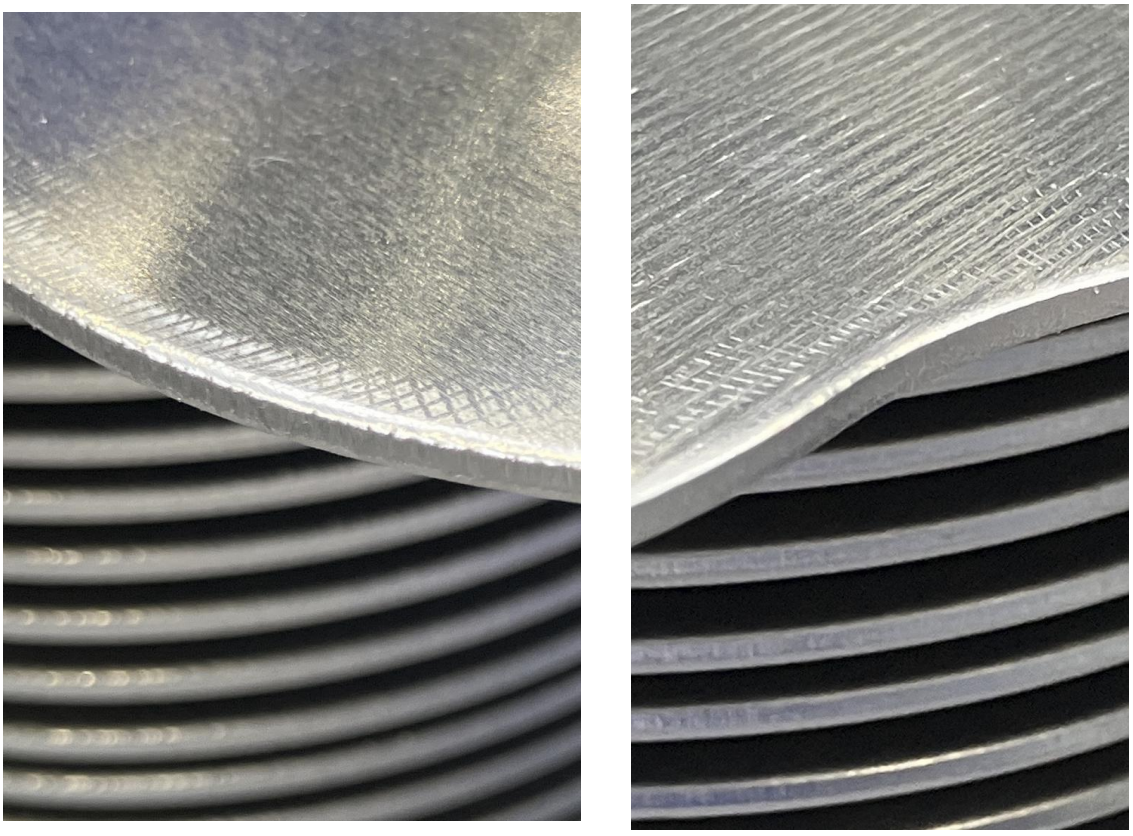

(**a**) (**b**)

Figure 2. Difference of the edge surface quality after the cut. **(a)** Showing Pondruff CrN-RB with increased burr in the area of cut. (b) Showing Eifeler Carbon-X with visible visual difference in the area of cut. The edge is more smooth, with less burrs.

4. Discussion

The blanking process of aluminum sheets typically produces a cut edge consisting of rollover, burnished zone, fracture zone, and burr. Burr formation is strongly influenced by tool wear, cutting clearance, and material ductility. In ductile materials such as aluminum, burr height generally increases with the number of cuts due to progressive degradation of the cutting edge.

The experimental results showed a clear difference in wear behavior between the two tested surface treatments. The CrN-RB coated tools exhibited increasing aluminum adhesion and surface roughening of the cutting edge during production. This adhesive wear accelerated burr growth and degraded cut edge quality, even after intermediate cleaning.

In contrast, the CARBON-X DLC coating significantly reduced material adhesion and maintained a smooth cutting edge throughout the test. The low friction coefficient and anti-adhesive nature of the DLC coating effectively suppressed galling, resulting in slower burr growth and more consistent edge quality.

The roll-bonded nature of the material did not cause delamination during cutting; however, the presence of two bonded alloys likely intensified adhesive wear mechanisms, further highlighting the importance of low-friction tool surfaces. The superior performance of the DLC-coated tools confirms findings reported in literature for monolithic aluminum sheets and extends them to roll-bonded aluminum materials.

5. Conclusions

This study demonstrates that surface treatment of shearing tools plays a decisive role in maintaining cutting accuracy and edge quality during blanking of roll-bonded aluminum sheets. Based on industrial-scale testing of 20,000 parts, the following conclusions can be drawn:

- The DLC-based CARBON-X coating provided significantly better resistance to wear and aluminum adhesion compared to the CrN-RB coating.
- Tools coated with CARBON-X exhibited lower burr formation and more stable cut edge quality throughout the production series.
- Intermediate cleaning was more effective for the DLC-coated tools, while CrN-coated tools rapidly redeveloped adhesive wear.
- Roll-bonded AW-1050/AW-3003 sheets can be successfully cut using conventional shearing dies, provided that appropriate low-friction tool coatings are applied.

The results confirm that DLC coatings are a highly effective solution for improving tool life and product quality in high-volume cutting of roll-bonded aluminum sheets.

Acknowledgments: This work was supported by the grant project VEGA 1/0539/23 – "Research into hybrid sandwich structures with customized properties" and project SK-PL-25-0118. The authors also gratefully acknowledge support for the experimental work provided under grant KEGA 035TUKE-4/2026.

References

1. Mucha, J., Tutak, J., *Influence of blanking clearance on burr formation and tool wear*, **Materials**, 12(8), 2019.
2. Alpas, A.T., Bhowmick, S., *Galling behavior in punching of aluminum alloys with DLC-coated tools*, **Journal of Manufacturing Processes**, 85, 2023.
3. Badaluddin, A. et al., *Effect of tool coatings on burr height in blanking operations*, **Journal of Tribology**, 2024.
4. Ionbond, *Low-friction DLC coatings for aluminum forming and trimming*, Technical Report, 2021.
5. AHSS Application Guidelines, *Cutting, blanking, shearing and trimming*, WorldAutoSteel, 2021.
6. Voestalpine Eifeler, *CARBON-X® coating technical datasheet*, 2025.
7. KLS Clad Metals, *Roll bonding of aluminum alloys for industrial applications*, Industry Publication, 2022.

TECHNICAL UNIVERSITY OF KOŠICE
Faculty of Mechanical Engineering

Abdominopelvic Vascular Compression Syndromes: Pathophysiological Mechanisms and Connective Tissue Links

Silvia Šišková[1,2,*], Jozef Živčák[1], Talal Ali[1,3], Lukáš Vincze[3], Diana Deáková[3], Marta Ščipáková[4]

[1] Technical University of Košice, Faculty of Mechanical Engineering, Department of Biomedical Engineering, Letná 1/9 | 042 00 Košice-Sever, Slovakia
[2] Asociácia Vaskulárnych Kompresívnych Syndrómov a Ehlers-Danlos, o.z., Balkánska 110/108, 851 10 Bratislava, Slovakia
[3] National Institute of Cardiovascular Diseases, Pod Krásnou hôrkou 1/7185, 833 48 Bratislava; dr.talal.ali8@gmail.com, lukas.vincze@nusch.sk, diana.deakova@nusch.sk
[4] Alexander Winter Hospital, Winterova Street 66, 921 63 Piešťany, Slovakia, tulium@centrum.cz
* Correspondence: silvia.siskova@student.tuke.sk

Abstract: Abdominopelvic vascular compression syndromes (AVCS) are rare conditions caused by mechanical vessel compression in the abdominal and pelvic regions, leading to impaired blood flow and organ dysfunction. This review focuses on the biomechanical processes underlying major AVCS: Median Arcuate Ligament Syndrome (MALS), Nutcracker Syndrome (NCS), Superior Mesenteric Artery Syndrome (SMAS), May-Thurner Syndrome (MTS), and Pelvic Congestion Syndrome (PCS), and how anatomical variations, posture, and reduced retroperitoneal fat promote vascular compression. It also examines links between AVCS and heritable connective tissue disorders, particularly Ehlers-Danlos Syndrome (EDS) and Hypermobility Spectrum Disorders (HSD), where collagen defects, ligamentous laxity, and tissue fragility may predispose to AVCS through altered anatomy and Visceroptosis. Understanding these interconnected biomechanical mechanisms is essential for comprehensive patient management.

Keywords: vascular compression syndromes; biomechanics; hypermobility; Ehlers-Danlos syndrome; connective tissue disorders

1. Introduction

Abdominopelvic vascular compression syndromes (AVCS) constitute a heterogeneous group of rare conditions in which blood vessels within the abdominal and pelvic cavities are compressed by adjacent anatomical structures, resulting in disrupted venous return, compromised arterial perfusion, or impaired organ function [1], [2], [3]. These syndromes include Median Arcuate Ligament Syndrome (MALS), Nutcracker Syndrome (NCS), Superior Mesenteric Artery Syndrome (SMAS), May-Thurner Syndrome (MTS), and Pelvic Congestion Syndrome (PCS) [4]. While each syndrome exhibits distinct anatomical compression points, they share common biomechanical principles underlying their pathophysiology.

The clinical presentation of AVCS encompasses a wide spectrum of symptoms, including abdominal pain, nausea, weight loss, pelvic discomfort, and lower extremity swelling. Importantly, patients frequently present with multiple concurrent compression syndromes, particularly those with underlying connective tissue disorders such as Ehlers-Danlos Syndrome (EDS) and Hypermobility Spectrum Disorders (HSD)[5], [6]. This review focuses on the biomechanical mechanisms driving the pathophysiology of individual AVCS and explores the emerging link to connective tissue fragility.

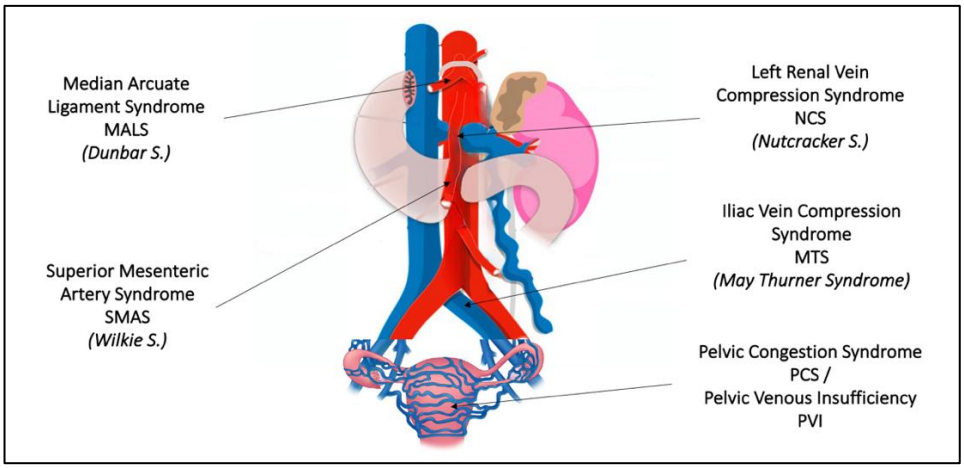

Figure 1. Graphical overview of all AVCS [7].

2. Biomechanical mechanisms of Vascular compression syndromes

2.1. Median Arcuate Ligament Syndrome (MALS / Dunbar Syndrome)

MALS arises from compression of the celiac artery by the median arcuate ligament near the T12–L1 level. The key biomechanical factors are a high-origin celiac artery or low diaphragmatic insertion, often exacerbated by spinal deformities such as kyphosis, scoliosis, or lordosis in connective tissue disorders [1], [6]. During expiration, upward diaphragm movement stretches the crura and intensifies celiac axis compression. In addition to vascular compression, the celiac plexus surrounding the celiac trunk is frequently entrapped and generates neuropathic pain. Typical symptoms are postprandial epigastric and post-exertional pain, tight or left-sided subcostal pain, nausea, vomiting, early satiety, weight loss, diarrhea, constipation, and autonomic complaints such as dizziness, palpitations, dyspnea, and syncope [1], [2], [6].

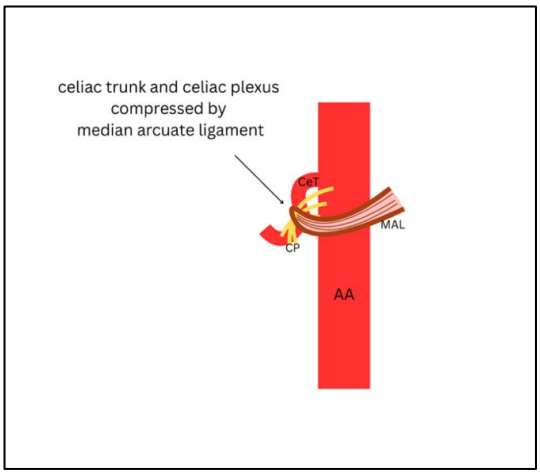

Figure 2. Graphical representation of MALS seen on CTA in sagittal view (own source)
AA - abdominal aorta, MAL - median arcuate ligament syndrome, CeT - celiac trunk, CP - celiac plexus.

2.2. Nutcracker Syndrome (NCS / Left Renal Vein Compression Syndrome)

NCS is compression of the left renal vein within the aortomesenteric space, either between the aorta and superior mesenteric artery (anterior NCS) or between the aorta and spine (posterior NCS). Pathologically reduced aortomesenteric angle and distance, and presence of clinical symptoms constitute the diagnosis [1], [2], [8]. The main biomechanical mechanism is loss of retroperitoneal fat which normally separates the aorta and SMA, with contributing factors such as low body weight, rapid weight loss, exaggerated lumbar

lordosis, visceroptosis, abdominal wall laxity, and abnormal SMA origin causing sharp angulation [8], [9]. Resulting venous hypertension elevates norepinephrine and angiotensin II, alters glomerular microcirculation, and may injure the kidney. It produces left flank pain, hematuria, orthostatic proteinuria, pelvic and abdominal pain, and collateral-related conditions such as varicocele and pelvic congestion [1], [2], [8].

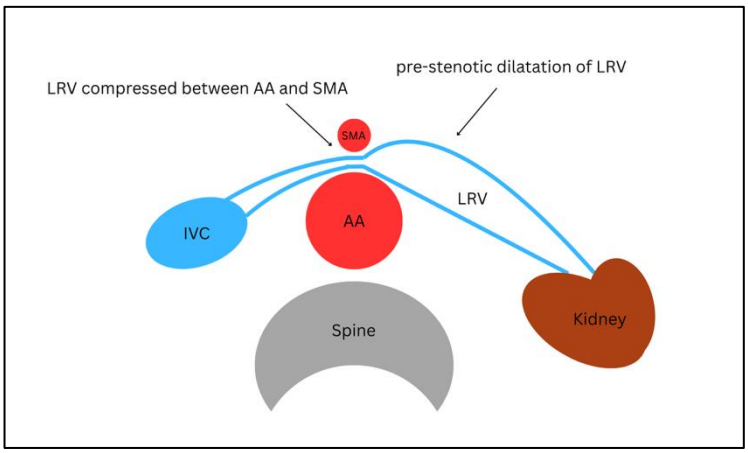

Figure 3. Graphical representation of anterior type of NCS seen on CTA in axial view (own source)
AA - abdominal aorta, SMA - superior mesenteric artery, IVC - inferior vena cava, LRV - left renal vein.

2.3. Superior Mesenteric Artery Syndrome (SMAS / Wilkie Syndrome)

In SMAS the third portion of the duodenum is compressed within the aortomesenteric clamp, similarly as in previously described NCS [10]. The principal biomechanical mechanisms are therefore the same. Predispositions include thin body habitus, rapid severe weight loss, catabolic states, prolonged supine positioning, spinal abnormalities including scoliosis and exaggerated lumbar lordosis, visceroptosis and and ligament laxity due to an underlying connective tissue disorder. A low takeoff of the SMA from the aorta or high insertion of the ligament of Treitz may also contribute [5], [8], [9]. The resulting duodenal compression leads to proximal dilation, impaired gastric emptying, and a vicious cycle of malnutrition perpetuating further weight loss. Clinical manifestations include postprandial epigastric pain, early satiety, nausea, bilious vomiting, abdominal distension, bloating, and significant unintentional weight loss potentially leading to malnutrition and dehydration [1], [2], [10].

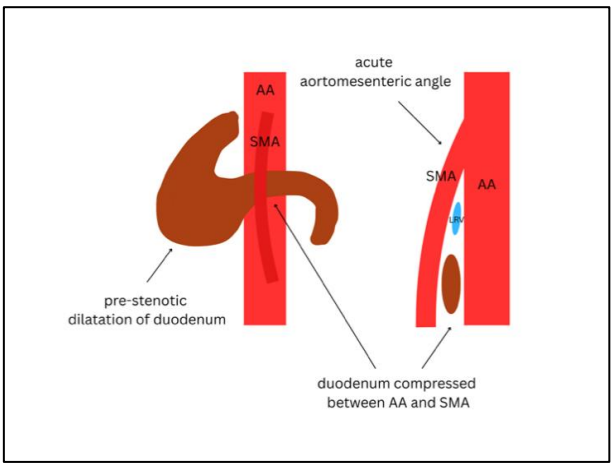

Figure 4. Graphical representation of SMAS seen on CTA in coronal and sagittal view (own source)
AA - abdominal aorta, SMA - superior mesenteric artery, IVC - inferior vena cava, LRV - left renal vein.

2.4. May-Thurner Syndrome (MTS / Left Common Iliac Vein Compression)

MTS arises from compression of the left common iliac vein between the right common iliac artery and the fifth lumbar vertebra, where chronic arterial pulsation causes endothelial injury and intraluminal fibrous spurs that promote venous obstruction. The vein's course posterior to the right iliac artery and anterior to the vertebral body promotes repetitive arterial contact, progressive luminal narrowing, venous stasis, and heightened thrombotic risk [1], [5]. Clinical manifestations include left lower extremity pain, swelling, heaviness, numbness, secondary varicose veins and pelvic pain, and recurrent or non-thrombotic symptoms [1], [2], [6].

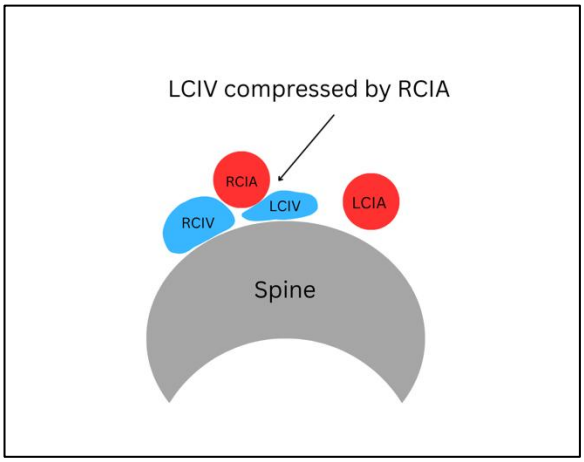

Figure 5. Graphical representation of the most common type of MTS seen on CTA in axial view (own source)
LCIA – left common iliac artery, RCIA – right common iliac artery, LCIV – left common iliac vein, RCIV – right common iliac vein.

2.5. Pelvic Congestion Syndrome (PCS) / Pelvic Venous Insufficiency (PVI)

Pelvic venous insufficiency (PVI) is characterized by dilation and reflux within the ovarian and pelvic veins. The biomechanical pathogenesis is multifactorial, involving dysfunctional venous valves, genetic predisposition, hormonal influences, and venous wall damage [1], [5]. Notably, PCS frequently occurs secondary to upstream venous compression from NCS or MTS. When left renal vein or iliac vein drainage is impaired, increased venous pressure propagates to the ovarian veins, causing progressive dilation and valve incompetence. The left ovarian vein is particularly susceptible due to its greater length and drainage into the left renal vein [1]. Clinical manifestations include chronic pelvic pain (burning, stabbing, or dull), dysmenorrhea, dyspareunia, pelvic heaviness, vulvar varicosities, and urinary symptoms [1], [2], [6].

Table 1. Overview of biomechanics in AVCS.

Syndrome	Biomechanics
Median Arcuate Ligament Syndrome (MALS)	***Vascular MALS (vMALS)*** **-** median arcuate ligament compresses celiac artery, resulting in a stenosis of the celiac trunk caused by an outer force. Blood flow in celiac trunk is compromised. ***Neurogenic MALS (nMALS)*** **-** celiac plexus compressed and irritated by the median arcuate ligament. The two types often coexist together.
Nutcracker Syndrome (NCS)	***Posterior NCS*** - Left renal vein is compressed between spine and abdominal aorta. ***Anterior NCS*** - Left renal vein is compressed between abdominal aorta and SMA. Other mechanisms: Left renal vein is stretched around aorta due to the pressure from lordosis. Left renal vein is stretched and pulled by nephroptosis. Left renal vein is compressed by other surrounding structures. Blood flow from left kidney is compromised in all cases.

Wilkie Syndrome (SMAS)	The third part of the duodenum is compressed between abdominal aorta and superior mesenteric artery. Visceroptosis of the bowel caused by connective tissue laxity stretches the vascular structures in a downward manner further pronouncing compressions. Food passage through the upper GI tract is hindered.
May-Thurner Syndrome (MTS)	Most commonly, left common iliac vein is compressed by right common iliac artery. However, compression may be bilateral. It is not uncommon to see multiple compression points bilaterally.
Pelvic Congestion Syndrome (PCS)	**Primary** – venous insufficiency. **Secondary** – as a result of primary NCS and MTS

3. The Connective Tissue Disorder Connection

3.1 Ehlers-Danlos Syndrome and Hypermobility Spectrum Disorders

Ehlers-Danlos Syndromes (EDS) encompass a group of heritable connective tissue disorders characterized by joint hypermobility, skin hyperextensibility, and tissue fragility [11]. Currently, 14 EDS types are recognized, with hypermobile EDS (hEDS) being most common yet lacking a defined genetic marker. Hypermobility Spectrum Disorders (HSD) share significant clinical overlap with hEDS [12].

3.2 Biomechanical Link Between Connective Tissue Disorders and AVCS

The association between EDS/HSD and AVCS is increasingly recognized, with patients frequently presenting with multiple concurrent compression syndromes [5], [13]. Several biomechanical mechanisms underlie this connection:

Connective tissue laxity and visceroptosis: In EDS, abnormal collagen affects the tensile strength of ligaments and supporting structures throughout the body [11]. This laxity can lead to Visceroptosis, downward displacement of abdominal organs, which alters anatomical relationships and may narrow the aortomesenteric angle, predisposing to NCS and SMAS [9]. Reduced support for vascular structures increases susceptibility to positional compression.

Vascular wall fragility: Defective collagen synthesis, particularly type III collagen in vEDS, weakens vessel walls, making them more susceptible to compression by adjacent structures. The hypermobility and hyperelasticity of blood vessels in hEDS allow greater mobility and displacement, increasing compression vulnerability [11], [13].

Ligamentous abnormalities: The median arcuate ligament, composed of fibrous connective tissue, may exhibit abnormal laxity or displacement in EDS, contributing to dynamic compression of the celiac axis during respiration. Structural vulnerability of arterial walls due to collagen dysfunction further increases susceptibility to compression [5], [13].

Postural abnormalities: Patients with EDS frequently exhibit postural deviations including lumbar hyperlordosis and scoliosis, which can narrow the aortomesenteric space and exacerbate vascular compression [8].

3.3 Clinical Implications

The clinical symptoms of AVCS substantially overlap with manifestations of EDS-related comorbidities, including dysautonomia (particularly Postural Orthostatic Tachycardia Syndrome), Mast Cell Activation Syndrome, and gastrointestinal dysmotility [4], [6]. This overlap complicates differential diagnosis and necessitates a comprehensive, multidisciplinary approach. Patients with EDS and HSD frequently require evaluation for multiple AVCS simultaneously, as the connective tissue abnormalities predispose to coexistent compressions [13].

4. Conclusions

Abdominopelvic vascular compression syndromes arise from specific biomechanical interactions between vessels and surrounding anatomical structures. The loss of protec-

tive fat pad, narrowed vascular angles, chronic pulsatile trauma, and ligamentous compression represent the primary mechanisms driving pathology in NCS, SMAS, MTS, PCS, and MALS. The emerging association between these syndromes and heritable connective tissue disorders, particularly Ehlers-Danlos Syndrome and Hypermobility Spectrum Disorders, highlights how connective tissue laxity, collagen defects, and visceroptosis may biomechanically predispose individuals to vascular compressions. Recognition of these interconnected mechanisms is essential for comprehensive diagnostic evaluation and individualized patient management.

Acknowledgments: This paper was written with the financial support from the KEGA granting agency within the project solutions No. 050TUKE-4/2022 and No. 021TUKE-4/2022, and with financial support from the APVV granting agency within the project solutions No. APVV-20-0068 and No. SK-CZ-RD-21-0056.

Conflicts of Interest: The authors declare no conflict of interest.

References

1. M. D'Oria *et al.*, "International Union of angiology consensus document on vascular compression syndromes," *International Angiology*, vol. 42, no. 4, pp. 282–309, Aug. 2023, doi: 10.23736/S0392-9590.23.05100-3.
2. Spanish Society of Vascular Compresion Syndromes, "Spanish Society of Vascular Compresion Syndromes," *Angiologia*, vol. 77, no. 2, pp. 142–144, Mar. 2025, doi: 10.20960/angiologia.00742.
3. J. Živčák, T. Tóth, and M. Trebuňová, *Meranie intraabdominálneho tlaku*. Košice: Technická univerzita, Košice, 2013.
4. S. Šišková, J. Živčák, R. Gil Sánchez, and T. Ali, "The Biomechanisms and Links between Abdomino-Pelvic Vascular Compression Syndromes and Symptomatic Joint Hypermobility Syndromes," *Novus Scientia 2024*, pp. 369–374, 2024, [Online]. Available: http://www.sjf.tuke.sk/NovusScientia/index.html
5. W. Sandmann, T. Scholbach, and K. Verginis, "Surgical treatment of abdominal compression syndromes: The significance of hypermobility-related disorders," *Am J Med Genet C Semin Med Genet*, vol. 187, no. 4, pp. 570–578, Dec. 2021, doi: 10.1002/ajmg.c.31949.
6. Lukáš Vincze, Silvia Šišková, Jozef Živčák, and Talal Ali, "Abdomino-Pelvic Vascular Compression Syndromes in the Abdominal Cavity," in *13. Slovenská konferencia o zriedkavých chorobách*, Nov. 2024.
7. Asociácia Vaskulárnych Kompresívnych Syndrómov a Ehlers-Danlos, "Ehlers-Danlos a Vaskulárne kompresívne syndrómy." Accessed: Nov. 30, 2025. [Online]. Available: https://avks.sk/ehlers-danlos
8. T. Scholbach and W. Sandmann, "Under false flag—the so-called nutcracker syndrome: An extract from 30 years of personal experience," Feb. 01, 2022, *Springer Medizin*. doi: 10.1007/s00772-021-00856-z.
9. S. Kucera and S. Sullivan, "Visceroptosis and the Ehlers-Danlos Syndrome," *Cureus*, Nov. 2017, doi: 10.7759/cureus.1828.
10. T. Ali, J. Tomka, I. Bakirli, and I. Bakirov, "Surgical Treatment of Wilkie's Syndrome by Vascular Transposition," *Cureus*, Apr. 2022, doi: 10.7759/cureus.24251.
11. F. Malfait *et al.*, "The 2017 international classification of the Ehlers–Danlos syndromes," *Am J Med Genet C Semin Med Genet*, vol. 175, no. 1, pp. 8–26, Mar. 2017, doi: 10.1002/ajmg.c.31552.
12. C. Gensemer, R. Burks, S. Kautz, D. P. Judge, M. Lavallee, and R. A. Norris, "Hypermobile Ehlers-Danlos syndromes: Complex phenotypes, challenging diagnoses, and poorly understood causes," *Developmental Dynamics*, vol. 250, no. 3, pp. 318–344, Mar. 2021, doi: 10.1002/dvdy.220.
13. A. Hakim, "Hypermobile Ehlers-Danlos Syndrome: Synonyms: Ehlers-Danlos Syndrome Hypermobility Type, Ehlers-Danlos Syndrome Type III, hEDS," in *GeneReviews*, M. P. Adam, J. Feldman, G. M. Mirzaa, R. A. Pagon, S. E. Wallace, and A. Amemiya, Eds., Seattle, 2024. Accessed: Mar. 07, 2025. [Online]. Available: https://www.ncbi.nlm.nih.gov/books/

TECHNICAL UNIVERSITY OF KOŠICE
Faculty of Mechanical Engineering

Effect of Laser Shock Peening on Additively Manufactured Components

Peter Spuro [1,*], Andrej Czan [1], Michal Sajgalik [1], Mario Drbul [1], Jaromir Markovic [1], Andrej Scotka[1]

[1] Faculty of Mechanical Engineering, University of Zilina, Univerzitna 8215/1, 010 26 Zilina, Slovakia
* Correspondence: peter.spuro@fstroj.uniza.sk

Abstract: Additive manufacturing of metal components represents a modern approach to producing complex geometrical structures with a high degree of material efficiency. Despite these advantages, such parts are often affected by undesirable residual stresses that arise from rapid thermal cycles during the layer-by-layer deposition process. These stresses may negatively influence fatigue performance and overall product reliability. The present study investigates the effect of Laser Shock Peening (LSP) on the character and distribution of residual stresses in metal specimens produced by the Atomic Diffusion Additive Manufacturing (ADAM) process. LSP is a non-contact surface strengthening technique that utilizes high-intensity laser pulses to induce plastic deformation and modify the residual stress state within the surface layers of a material. Experimental results indicate that the application of LSP significantly reduced the magnitude of the initial tensile residual stresses; however, a complete transformation to a compressive stress state was not achieved in all specimens. This outcome can be attributed primarily to limitations related to the applied process parameters and the available laser power, as well as to the specimen clamping conditions during processing, which influenced the intensity of the generated shock waves and the resulting redistribution of residual stresses in the near-surface region.This work contributes to a deeper understanding of the interaction between additive manufacturing and subsequent surface treatment, highlighting the necessity of process optimization for specific material-geometry combinations.

Keywords: Additive manufacturing, Laser shock peening, Ressidual stress

1. Introduction

Metal additive manufacturing (MAM) is a modern production method in which metallic components are fabricated directly from a digital model through layer-by-layer material deposition [1]. This field is undergoing rapid development, with critical reviews focusing on methods, modeling, and manufacturing applications [2], including product development for specialized sectors [3] and biomedical applications [4]. The quality of AM metal parts is the subject of extensive research, particularly concerning the anisotropy and heterogeneity of microstructure and mechanical properties [5].

Atomic Diffusion Additive Manufacturing (ADAM), developed by Markforged, is a hybrid technique combining polymer-based extrusion with subsequent metallurgical sintering. In ADAM, a composite filament of metal particles in a polymer binder is extruded, producing a “green part” [6]. Following debinding and sintering, which are crucial for obtaining dense parts with controlled microstructure [7], the metal particles fuse via atomic diffusion. ADAM has garnered attention for producing near-net-shape metallic parts. Galati and Minetola [8] reported that 17-4 PH stainless steel parts achieve approximately 90% density, exhibit higher surface roughness compared to powder-bed fusion, and possess dimensional accuracy within ISO IT12–IT13. Mechanical performance is influenced by layer orientation, affecting tensile behavior and stiffness [9]).

Residual stresses are internal stresses remaining after external loads or thermal gradients are removed. Beneficial compressive residual stresses are often introduced through surface treatments, such as Laser Shock Peening (LSP) [10], which has been shown to be highly effective compared to traditional shot peening and ultrasonic impact peening [11]. Studies confirm that LSP can mitigate the susceptibility to Stress Corrosion Cracking (SCC) in stainless steels [12, 13]. The development of LSP technology has also been demonstrated on specialized alloys for steam turbine applications [14]. Numerical models are critical for predicting the distribution and magnitude of residual stress induced by LSP [15], which is generated by stress waves originating from the laser pulse [16]. These stresses can be tensile or compressive and significantly affect fatigue resistance, corrosion, and dimensional stability [17].

2. Materials and Methods

For the printing process, the material selected was 17-4 PH stainless steel, a precipitation-hardened steel known for its high strength and excellent corrosion resistance. This material is well suited for applications requiring a combination of mechanical performance, durability, and environmental resistance. The chemical composition of the alloy is presented in Table 1.

Table 1. Chemical composition of Markforged 17-4 PH stainless steel [18].

Element	Cr	Ni	Mo	Si	Mn	N	C	Cu	S
% of Weight	16.5	4.03	0.01	0.36	0.15	0.52	1.71	3.77	0.05

2.1. Test Specimen Design and Additive Manufacturing Parameters

The test specimens were designed as solid cylindrical rods with a diameter of Ø5 mm and a length of 100 mm. This geometry was chosen to comply with widely recognized standards for assessing the geometry and surface quality of metallic components, while also allowing evaluation of specimens produced using the ADAM technology.

During the printing process, a layer height of 125 micrometers (μm) was set. This value was selected as a compromise between surface quality and printing time, enabling adequate detail resolution while maintaining production efficiency. The printing speed was set to 25 cubic centimeters per hour (cm^3/h). A lower printing speed ensures precise material deposition, minimizing defects and improving the quality of the final product. Five specimens were printed exclusively in a horizontal orientation (Figure 1).

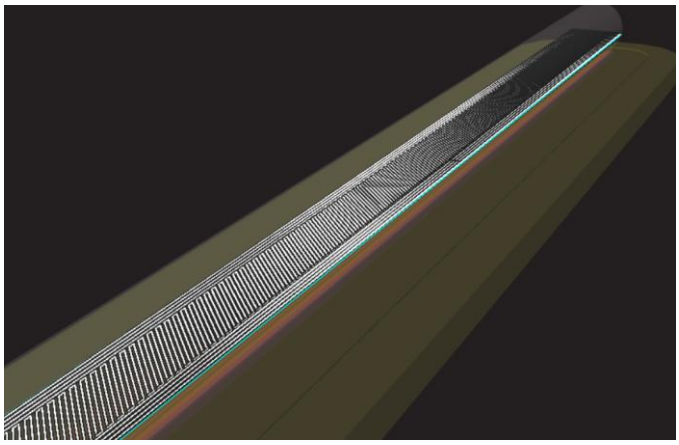

Figure 1. Layers deposited horizontally along the cylinder.

2.2. Laser Shock Peening: Experimental Setup

Experiments were conducted using the high-power diode-pumped solid-state laser system Bivoj, developed at the HiLASE Centre (Institute of Physics, Czech Academy of Sciences, Dolní Břežany).

For the experiments, a Litron IR laser was employed with a pulse energy of 1.0 J, a pulse duration of 17 ns, and a repetition rate of 1 Hz. The laser spot size (diameter) was 1.15 mm, the lens position was set to 18.1 mm, and the distance between the laser and the specimen was 950 mm. Pulse overlap in both the Y and Z directions was set to 50%, while sequence overlap was 0%. The process was carried out in a single layer with one sequence per layer, resulting in a power density of 5.67 GW/cm².

Previous studies conducted at LALP (Laboratoire d'Application des Lasers de Puissance, Arcueil Cedex) and LULI (Laboratoire pour l'Utilisation des Lasers Intenses, École Polytechnique, Palaiseau Cedex) further explored the industrial applicability of the LSP process. Laser Shock Peening (LSP) is a mechanical cold-working process in which high-energy laser pulses impinge on the surface, generating shock waves. These waves plastically deform the surface, and compressive stresses are transferred into subsurface layers. The induced dynamic stresses are highest at the surface and decrease with depth into the material).

2.3. Measurement of ressidual stress

Residual stress measurements were performed using a ProtoiXRD system, which employs MnKα radiation with an irradiated area of 1 mm². Residual stresses were measured in both the axial and tangential directions, with diffraction data obtained from the {311} plane at a diffraction angle of 152.80°. The $\sin^2\psi$ method was applied, with a ψ tilt range of ±39°. The X-ray tube was operated at 20.00 kV and 4.00 mA. Intensity correction was applied using the P/G(s) function. During the measurements, a β-oscillation of 3.00° was used, without rotation along the φ, X, or Y axes. Peak shifts were analyzed as absolute shifts of the maxima.

To ensure the reliability of residual stress data, a combined methodology of local averaging and directional rotation was applied at the measurement locations. Within each directional orientation, the residual stress was measured at three proximate, perpendicular points ; these three recorded values were averaged to obtain a single, stable stress value for that specific direction. The measurement process was subsequently repeated after rotating the measuring block by 120° and 240° from the initial position (Figure 2). This procedure yielded three independent, locally averaged residual stress values, representing the state of stress in the 0°, 120°, and 240° orientations.

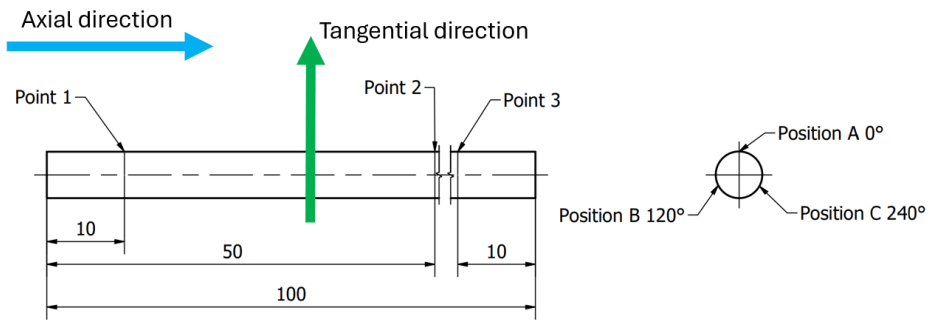

Figure 2. Schematic representation of the residual stress measurement points on the specimen.

3. Results and Discussion

The graph illustrates the normal stress values at a 0° angle for specimens produced using the ADAM (Atomic Diffusion Additive Manufacturing) technology with a Markforged Metal X system from 17-4 PH stainless steel. In all cases, tensile residual stresses predominated. After the application of Laser Shock Peening (LSP), compressive residual stress values were lower; however, they did not exhibit the same level of compressive residual stresses typically generated by LSP, which induces plastic deformation and increases compressive residual stress. The labels ADAM01 to ADAM05 correspond to individual specimens (Figure 3). Measurements were performed at three different angular positions of the specimens (0°, 120°, and 240°) relative to the build direction to assess potential anisotropy in mechanical properties. Two groups of results are compared: PRINT (blue bars): normal stress in specimens after additive manufacturing (post-sintering), LSP (orange bars): normal stress in specimens after Laser Shock Peening, which is intended to enhance surface resistance to fatigue and mechanical loading. The graph shows that: In all specimens (ADAM01–ADAM05), normal stress values after LSP (orange bars) decreased compared to the as-printed condition (PRINT, blue bars). This trend was consistently observed in all measured orientations (0°, 120°, 240°). The scatter of values (indicated by error bars) is generally higher for PRINT than for LSP, suggesting stabilization of residual stresses following laser shock peening. These results indicate that LSP can significantly modify residual stresses in the surface layers of ADAM-manufactured components, contributing to improved stability of mechanical properties regardless of the measured angular orientation.

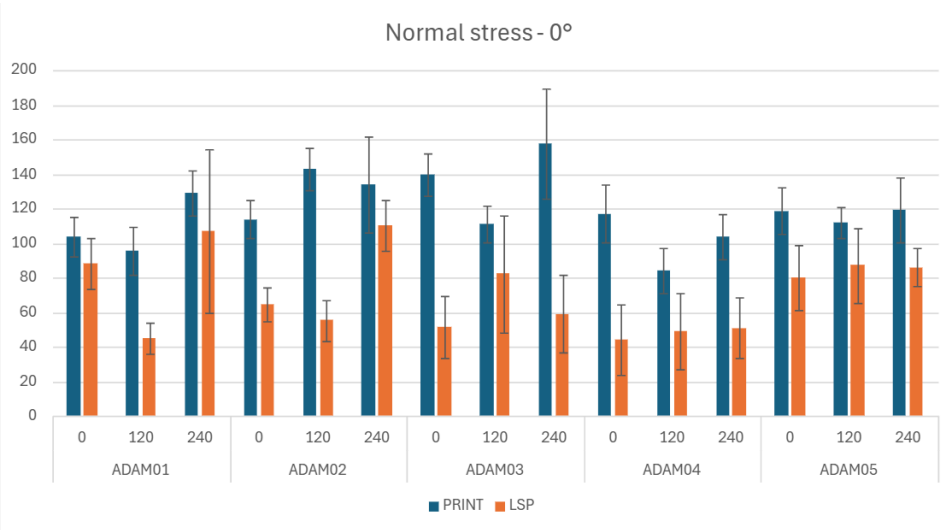

Figure 3. Residual Stress Distribution in the Axial Direction.

The graph shows the normal stress measured at a 90° orientation relative to the additive manufacturing direction (i.e., perpendicular to the material layering) for five specimens produced using ADAM (Atomic Diffusion Additive Manufacturing) technology from 17-4 PH stainless steel on a Markforged Metal X system (Figure 4). As in the previous case, measurements were performed at three angular positions of the specimens: 0°, 120°, and 240°, comparing two conditions: PRINT (blue bars): as-printed and sintered state, LSP (orange bars): after Laser Shock Peening (LSP). Key observations: Compared to the 0° results (from the previous graph), normal stress values are significantly lower in most specimens, particularly in the PRINT condition, indicating anisotropic material behavior. For specimens ADAM01 to ADAM04, stress values in the LSP condition decreased markedly compared to PRINT, confirming the effectiveness of LSP in relieving or redistributing residual stresses. Specimen ADAM05 exhibits specific behavior: some values after LSP are

even negative, which may indicate the development of compressive residual stresses typical for LSP. The pronounced scatter of values (error bars), especially in the PRINT condition, points to higher instability and variability of stresses without LSP treatment.

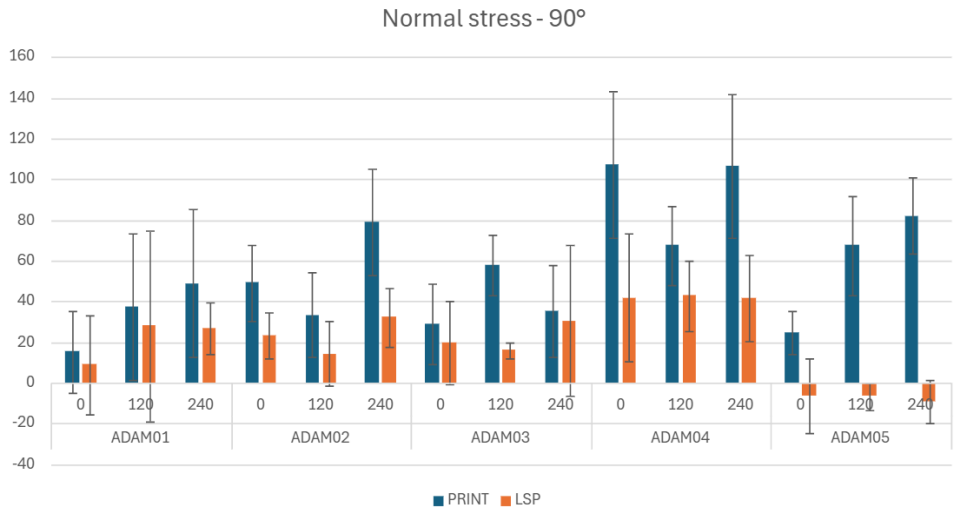

Figure 4. Residual Stress Distribution in the Tangential Direction.

Residual stress measurements performed after Laser Shock Peening (LSP) on 17-4 PH stainless steel specimens manufactured by the ADAM process showed only a reduction of the initial tensile stresses, without a complete shift into the compressive region. The effectiveness of LSP in generating deeper compressive stresses may have been limited by the applied process parameters and the available laser power, which affected the intensity of the induced shock waves and the depth of plastic deformation.

A similar mechanism was reported by Duan et al. [19] for DED-produced 316L, where LSP also reduced surface tensile stresses and improved fatigue performance, while the formation of compressive residual stresses strongly depended on pulse intensity, spot overlap, and material behavior. Reviews of LSP applied to additively manufactured materials consistently emphasize that achieving significant compressive stresses requires carefully optimized processing parameters, including sufficient laser fluence, energy density, and beam overlap.

Additionally, due to the small diameter of the specimens, slight bending occurred during LSP irradiation. The thin rods partially deflected under the laser pulses, limiting the development of sufficient plastic deformation and, consequently, the formation of compressive residual stresses. Increasing the laser pulse energy and improving specimen clamping could enhance process effectiveness.

In future work, this issue will be addressed through an improved fixturing system designed to suppress lateral deflection during irradiation. The spatial distribution and stability of the laser beam profile will also be investigated in detail. Furthermore, comprehensive microstructural characterization, including SEM analysis, will be conducted to better understand the mechanisms of plastic deformation and residual stress distribution.

4. Conclusions

- LSP reduced the initial tensile stresses in ADAM 17-4 PH specimens but did not fully shift them into the compressive region.
- Measurements at different orientations (0° and 90°) show variations in stress values, indicating anisotropy of residual stresses in ADAM components.
- LSP significantly reduced residual stresses in specimens ADAM01–ADAM04, while some negative stress values in ADAM05 suggest localized compressive stress formation.

- The small specimen diameter caused bending during LSP, reducing plastic deformation and limiting the development of compressive stresses.

Acknowledgement: APVV-20-0561: „Research into the implementation of new measuring methods for the calibration of measuring systems for industrial metrological practice“, APVV-20-0216: „Research on the Implementation of High-Impact Surface Technologies for Precision Automotive Structural Components“, VEGA 1/0722/25: „Research on additive technologies with a focus on their application in the design and construction of cutting tools“, 09I05-03-V02-00080 DigiDent (Research on the Digitalization of Dental Implant Components for the Creation of Personalized 3D Models for the Manufacturing Process)“ and by the grant scheme UNIZA 21068: “Research on the Mechanical Properties of Materials in Additive Manufacturing”.

Referenes

1. Zhang, Y.; Wu, L.; Guo, X. et al. Additive Manufacturing of Metallic Materials: A Review. J. of Materi Eng and Perform 2018, 27, 1–13.
2. Bikas, H.; Stavropoulos, P.; Chryssolouris, G. Additive manufacturing methods and modelling approaches: a critical review. Int J Adv Manuf Technol 2016, 83, 389–405.
3. Badiru, A.B.; Valencia, V.V.; Liu, D. (Eds.). Additive Manufacturing Handbook: Product Development for the Defense Industry, 1st ed.; CRC Press, 2017.
4. Jamróz, W.; Szafraniec, J.; Kurek, M. et al. 3D Printing in Pharmaceutical and Medical Applications – Recent Achievements and Challenges. Pharm Res 2018, 35, 176.
5. Kok, Y.; Tan, X.P.; Wang, P.; Nai, M.L.S.; Loh, N.H.; Liu, E.; Tor, S.B. Anisotropy and heterogeneity of microstructure and mechanical properties in metal additive manufacturing: A critical review. Mater. Des. 2018, 139, 565–586.
6. Watson, A.; Belding, J.; Ellis, B.D. Characterization of 17-4 PH Processed via Bound Metal Deposition (BMD). In TMS 2020 149th Annual Meeting & Exhibition Supplemental Proceedings, Proceedings of the TMS 2020 149th Annual Meeting & Exhibition; The Minerals, Metals & Materials Series; Springer: Cham, 2020.
7. Banerjee, S.; Joens, C.J. Debinding and sintering of metal injection molding (MIM) components. In Handbook of Metal Injection Molding; Heaney, D.F., Ed.; Woodhead Publishing, 2012; pp. 133–180.
8. Galati, M.; Minetola, P. Analysis of Density, Roughness, and Accuracy of the Atomic Diffusion Additive Manufacturing (ADAM) Process for Metal Parts. Materials 2019, 12, 4122.
9. Henry, T.C.; Morales, M.A.; Cole, D.P. et al. Mechanical behavior of 17-4 PH stainless steel processed by atomic diffusion additive manufacturing. Int J Adv Manuf Technol 2021, 114, 2103–2114.
10. R, S.; P, G.; Gupta, R.K. et al. Laser Shock Peening and its Applications: A Review. Lasers Manuf. Mater. Process. 2019, 6, 424–463.
11. Gujba, A.K.; Medraj, M. Laser Peening Process and Its Impact on Materials Properties in Comparison with Shot Peening and Ultrasonic Impact Peening. Materials 2014, 7, 7925–7974.
12. Gupta, R.K.; Sundar, R.; Kumar, B.S. et al. A Hybrid Laser Surface Treatment for Refurbishment of Stress Corrosion Cracking Damaged 304L Stainless Steel. J. of Materi Eng and Perform 2015, 24, 2569–2576.
13. Sundar, R.; Ganesh, P.; Kumar, B.S. et al. Mitigation of Stress Corrosion Cracking Susceptibility of Machined 304L Stainless Steel Through Laser Peening. J. of Materi Eng and Perform 2016, 25, 3710–3724.
14. Pant, B.K.; Sundar, R.; Kumar, H.; Kaul, R.; Pavan, A.H.V.; Ranganathan, K.; Bindra, K.S.; Oak, S.M.; Kukreja, L.M.; Prakash, R.V.; Kamaraj, M. Studies towards development of laser peening technology for martensitic stainless steel and titanium alloys for steam turbine applications. Mater. Sci. Eng., A 2013, 587, 352–358.
15. Wei, X.L.; Ling, X. Numerical modeling of residual stress induced by laser shock processing. Appl. Surf. Sci. 2014, 301, 557–563.
16. Masse, J.-E.; Barreau, G. Laser generation of stress waves in metal. Surf. Coat. Technol. 1995, 70, 231–234.
17. Withers, P.J.; Turski, M.; Edwards, L.; Bouchard, P.J.; Buttle, D.J. Recent advances in residual stress measurement. Int. J. Press. Vessels Piping 2008, 85, 118–127.
18. ASTM International. (2021). ASTM A564/A564M – Standard Specification for Hot-Rolled and Cold-Finished Age-Hardening Stainless Steel Bars and Shapes. ASTM International.
19. Duan, C.; Shang, D.; Luo, X.; Hao, X.; Cao, X. Effects of Residual Stress Induced by Laser Shock Peening on Fatigue Crack Propagation Behavior in Directed Energy Deposition Stainless Steel. Steel Research Int. 2024, 95, 2300328. https://doi.org/10.1002/srin.202300328

TECHNICAL UNIVERSITY OF KOŠICE
Faculty of Mechanical Engineering

Definition and application of process tools for rib structure design in Large-scale additive manufacturing

Pavol Štefčák [1], Ivan Gajdoš [1,*], Łukasz Sobaszek [2], Yitbarek Firew Minale [3,4]

[1] Department of Technology, Materials and CAx, Faculty of Mechanical Engineering, Technical University of Košice,04001 Košice, Slovakia; ivan.gajdos@tuke.sk (I.G.); pavol.stefcak@tuke.sk (P.Š.);
[2] Department of Information Technology, Faculty of Mathematics and Information Technology,Lublin University of Technology, 20-618 Lublin, Poland
[3] Institute of Energy, Ceramics and Polymer Technology, University of Miskolc, 3515 Mis-kolc-Egyetemváros, Hungary
[4] Department of Chemical Engineering, Bahir Dar Institute of Technology, Bahir Dar University, Bahir Dar 6000, Ethiopia
* Correspondence: ivan.gajdos@tuke.sk

Abstract: This paper introduces an innovative approach to large-format robotic additive manufacturing (LFRAM) by implementing a parametric point array patterning (PAP) method within Rhino Grasshopper. Unlike conventional slicing algorithms that convert 3D models into layers, the proposed solution generates toolpath sequences directly from parametric models. The method-ology leverages integrated Grasshopper components to create customizable ribbed structures with adjustable dimensions and spacing, offering enhanced flexibility for large-scale applications. Experimental validation was performed using a FANUC M-20iB/25 industrial robot equipped with a pellet extruder, with PETG selected for manufacturing a structural component measuring 1500 × 100 × 60 mm. Several calibration samples confirmed the feasibility of the PAP method and its scalability for complex geometries. The results demonstrate validity of proposed method and critically highlight the challenges ahead. However, further refinement is required to address issues such as material overlap at rib intersections and building plate adhesion. This research highlights the potential of parametric modeling and robotic AM in advancing additive manufacturing for industrial-scale applications.

Keywords: LFRAM, Grasshopper, slicing, parametric design, visual scripting

1. Introduction

Currently, 3D printers are being utilized for prototyping and developing new products. The appeal of this solution mostly stems from its capability to facilitate the additive manufacturing (AM) of three-dimensional items featuring intricate geometries [1].

A crucial step in the AM process is the division of the model into layers, commonly referred to as slicing [2]. However, the well-known solutions in this area are mainly dedicated to classic 3D printers and their manufacturing specifications, therefore do not fully support the process of large format robotic additive manufacturing (LFRAM) [3–5] which brings challenges to overcome in the form of technological requirements for material processing that must be considered. The challenges lie not only in the requirement to produce large components, where conventional 3D printers reach their limits in terms of printing space and flexibility, but also in optimizing current manufacturing processes in order to speed them up, reduce their costs and gain full control over the entire process. One of those challenges is tool path movement control. With the large amount of material that the print head needs to process, it is sometimes difficult to ensure proper retraction or suspension of material extrusion for infill strategies offered by classic slicer software and

therefore, the only way to optimize such production is to properly design and control tool path movement so that such retractions or suspensions are not necessary at all [6-8].

In order to demonstrate such approach, a script in Rhino software within Grasshopper plugin (RGP) was created that demonstrates how such tool path movement can be designed for example, for the purpose of creating building or facade structures where conventional infill strategies are replaced with ribbed ones that could be quickly edited with possibility to generate customized unconventional infills instructions, where no Computer aided design (CAD) model is needed and additionally one continual tool path movement is generated. In response to the challenges noted, a novel solution is presented which employs a parametric model of the prototyped and manufactured component to directly generate control code ready to postprocess for LFRAM. Methodologies related to LFRAM are discussed in section 2, with a specific focus on the slicing stage of the process where new point array patterning method is presented. Section 3 presents a description and the assumptions of the proposed solution, dedicated to experimental verification of developed system.

2. Materials and Methods

To generate such movement a grasshopper script capable of the point array patterning (PAP) method was created and used. Instead of a common slicing algorithm that transforms 3D objects into individual layers, the grasshopper script allows to create sequences of points which represent positions and orientations of the tool center point (TCP) directly. The Grasshopper PAP script (fig. 1) was developed to generate G-code for a simple ribbed structure to verify functionality of this approach. To achieve this, several integrated function blocks and special position obtaining blocks of Rhino Grasshopper software were used.

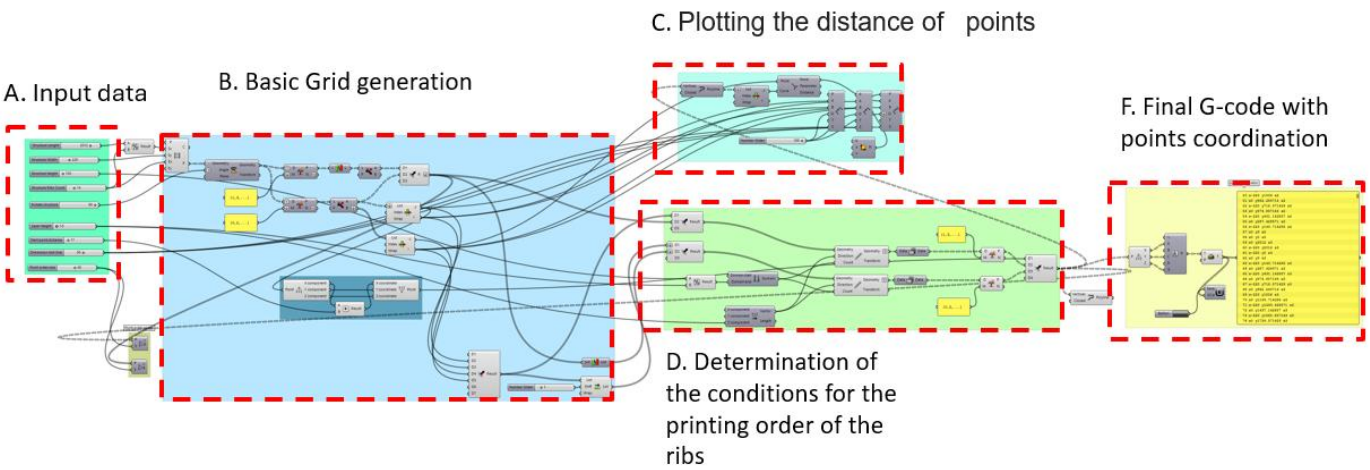

Figure 1. Grasshopper PAP script.

The Grasshopper PAP script consists of 5 sections, which are parametrically connected and convert Input data into printable G code. Section A (fig. 1) collects input data as general dimensions of structure, layer height, number of ribs, ribs spacing, and more. Section B (fig. 1) is generating and patterning points in a simplified 2D grid block function where the sequence of the points are specified. Plotting of the distance of the points (Section C.) serves as an aid for the user to verify the final dimensions and can be deactivated for a detailed view of the structure layers. In section D (fig. 1), points and layers are generated, and the condition of the layer printing order is specified. The curves created by connecting patterned points serve as layer indicators and are displayed in Figure 2.

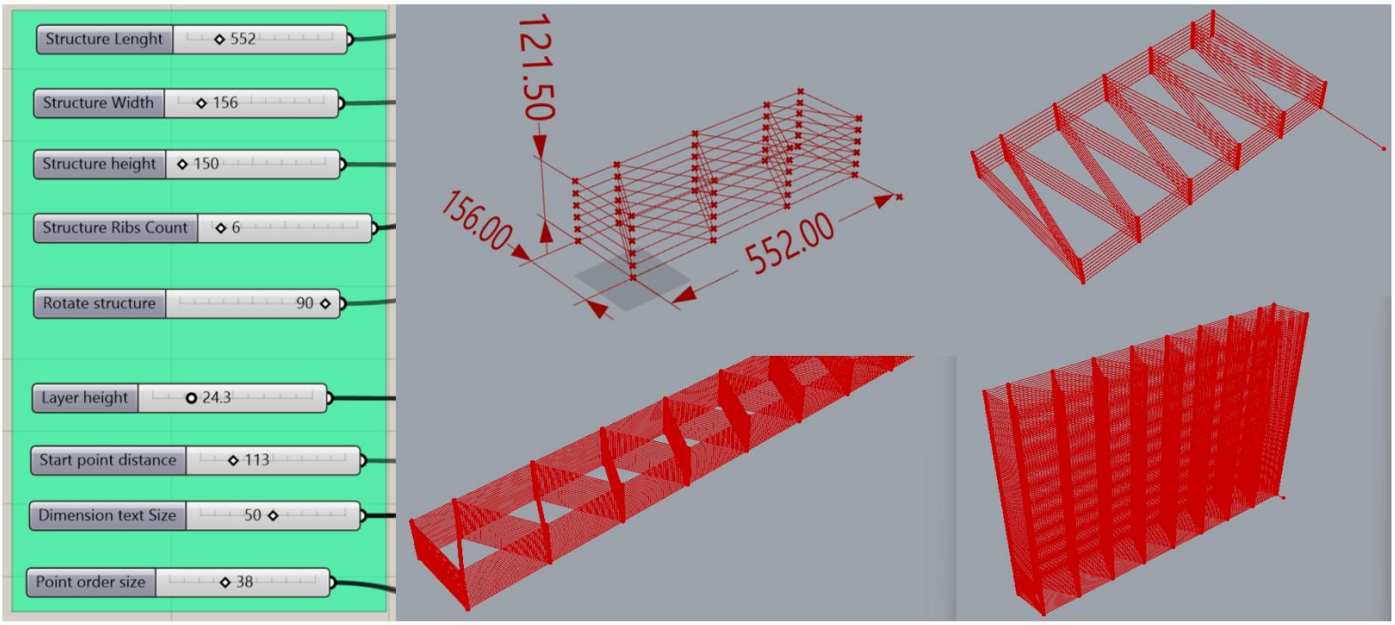

Figure 2. Graphical preview of PAP script with different input data combinations.

Final points coordination representing the tool path movement order is obtained in section D. The results of the grasshopper script (Section D) can then be exported in G-code format. Once the G-code has been generated, it must be uploaded into the robot simulating software RoboDK. This is where the robot's movement is programmed and the G-code is translated into the robot's movement language. The final steps of the preprocessing of robotics 3D printing include setting up start/end procedures, final checking for possible collisions, and uploading the program to the robot. The experiment was conducted on a FANUC M-20iB/25 robot equipped with an MDPH2 pellet extruder.

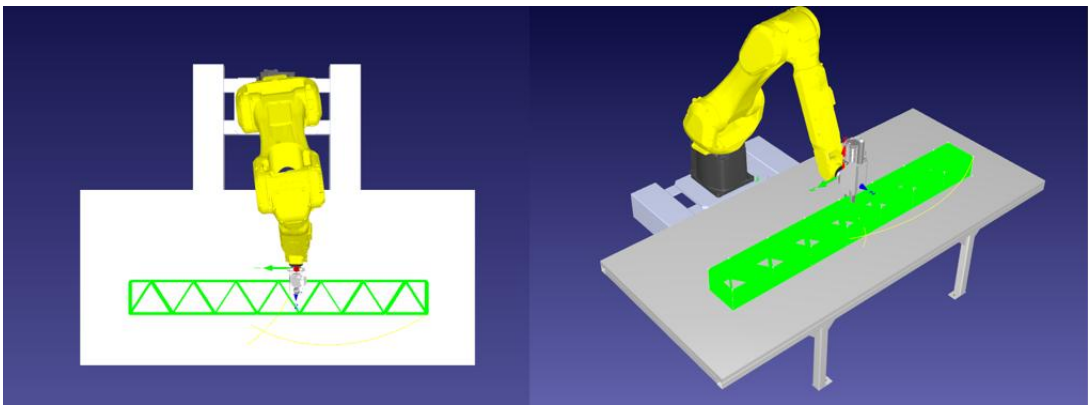

Figure 3. Simulation of PAP script in RoboDK CAM software.

3. Results

Offline programming and simulation of the robot's movements was done in specialized RoboDK software for industrial robots with 3D printing plugin. Translated robot language was transferred to the control system of the robot and then executed. The script tests the PAP method as approach to design unique structures in the field of large-scale additive manufacturing. Several samples were printed for validation of method functionality.

Table 1. Material and input data combination for calibration samples.

Sample	Material	Printing speed [mm/s]	Layer height [mm]	Nozzle temperature [C°]
A	PETG	25	2	215
B	ABS	20	1,5	230
C	PP	20	1,5	200

Different materials as PETG, ABS and PP where used in combination of input data setting which were tested to find proper combination settings to ensure material extrusion and overall manufacturing process stability. Samples A, B and C were printed with overall dimension of 250 x 50x 30 mm

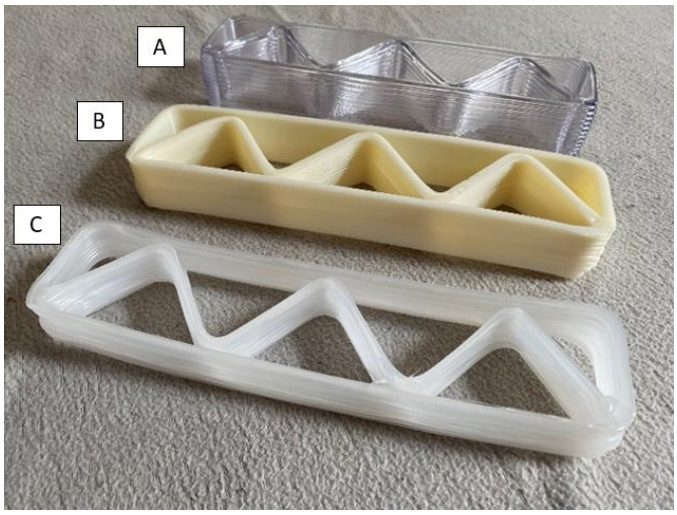

Figure 4. Calibration samples.

After initial calibration of input data and materials, PETG material was chosen for the manufacturing of a large structural part of overall dimensions 1500 x 100 x 60 mm. In figure 5 where shape warpage, are presented and detailed in section A and B.

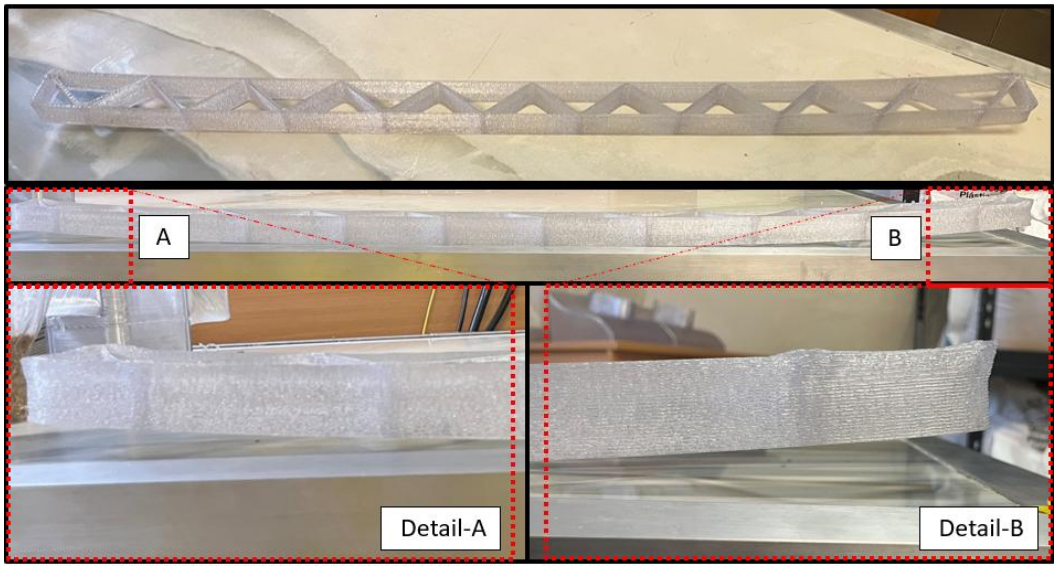

Figure 5. Large Scale ribbed structure.

4. Conclusions

The printed samples proved that the designed script works. Calibration samples were printed to determine input manufacturing data for chosen materials. The use of the Rhi-noceros Grasshopper software extends the possibilities of designing the toolpath to create unique ribbed structures with customized dimension and ribs spacing options. Manufac-turing large scale ribbed structure verified the scalability of the created PAP script however, further optimization is necessary to prevent material layer overlapping in areas where ribs are connected. Also Build plate adhesion must be improved by redesign-ing build plate to be able to physically anchor parts to prevent warping.

Acknowledgments: This research was funded by the European Union's programme for research and in-novation Horizon Europe under the Marie Skłodowska-Curie Action grant agreement No 101129698–PROMATAI– Horizon–MSCA–2022–SE–01. Views and opinions expressed are however those of the author(s) only and do not necessarily reflect those of the European Union or European Research Executive Agency. Neither the European Union nor the granting authority can be held responsible for them.

References

1. Referenc Fortunato, G. M., Nicoletta, M., Batoni, E., Vozzi, G., & De Maria, C. (2023). A fully automatic non-planar slicing algorithm for the additive manufacturing of complex geometries. Additive Manufacturing, 69, 103541. https://doi.org/10.1016/j.addma.2023.103541
2. Tamir, T. S., Xiong, G., Shen, Z., Leng, J., Fang, Q., Yang, Y., Jiang, J., Lodhi, E., Wang, F. Y., & The Authors. (n.d.). 3D printing in materials manufacturing industry: A realm of Industry 4.0. In Heliyon. https://doi.org/10.1016/j.heliyon.2023.e19689
3. Pelzer, L., & Hopmann, C. (2020). Additive manufacturing of non-planar layers with variable layer height. Additive Manufac-turing, 37, 101697. https://doi.org/10.1016/j.addma.2020.101697
4. Rodriguez-Padilla, C., Cuan-Urquizo, E., Roman-Flores, A., Gordillo, J. L., & Vázquez-Hurtado, C. (2021). Algorithm for the conformal 3D printing on non-planar tessellated surfaces: applicability in patterns and lattices. Applied Sciences, 11(16), 7509. https://doi.org/10.3390/app11167509
5. Lee, T. (n.d.). Hand motion based 3D printing slicer.
6. Reich, M.J., Woern, A.L., Tanikella, N.G., Pearce, J.M.: Mechanical properties and applications of recycled polycarbonate particle material extrusion-based additive manufacturing. Materials 12(10), 1642 (2019) [ONLINE].[cit. 2022.12.04] dostupné na internete: https://www.mdpi.com/1996-1944/12/10/1642/htm
7. Greg Costantino, Covestro Additive Manufacturing, and Zac DiVencenzo, JuggerBot: 3D Printing with Fused Filament Fabri-cation and Fused Granulate Fabrication (Pellet Printing) [ONLINE].[cit. 2022.05.05] available on the internet:
8. https://am.covestro.com/en_US/insights/blog/3d-printing-with-fused-filamentfabrication-and-fused-granulate-fabrica-tion.html
9. Next generation of 3D printing- robot guided additive manufacturing. [ONLINE].[cit.2022.12.04] available on the internet: https://zal.aero/en/news/next-generation-3dprinting-robot-guided-additive-manufacturing/?cookie-statechange=1648994679559

TECHNICAL UNIVERSITY OF KOŠICE
Faculty of Mechanical Engineering

Manufacturing possibilities of steel sheets with organic coatings, their testing and damage in practice

Vanda Tomková [1,*], Ján Slota [2]

[1] USSE Research and Development, U.S. Steel Košice s.r.o., Vstupný Areál U.S. Steel, 044 54 Košice, Slovakia; vandatomkova@sk.uss.com (V.T.)
[2] Institute of Technology and Materials Engineering, Faculty of Mechanical Engineering, Technical University of Košice, Mäsiarska 74, 040 01 Košice, Slovakia; jan.slota@tuke.sk (J.S.)
* Correspondence: vandatomkova@sk.uss.com (V.T.); Tel.: +421-55-673-0221

Abstract: The presented article focuses on the typical characteristics and general possibilities of producing color coating sheets. It describes in more detail the standard production flow on color coated lines, also points out the basic tests of color coated sheets. The article mentions studies in the field of poor adhesion of paint layers caused by the absence of a conversion layer. In Cr-free technology on coil coating lines, a several times higher amount of passivation is as inappropriate as its lack, because it also has a negative effect on the proper adhesion of organic paints, which is also confirmed by research devoted to this issue. This fact was also verified by laboratory tests and real production. Last but not least, it elaborates on the defects that can occur on steel sheets with organic coatings due to unprofessional handling.

Keywords: steel sheets with organic coatings, conversion and organic coatings, tests of optical, physical and corrosion properties, sheet damage

1. Introduction

One of the modern materials used mainly in the construction industry for more than 60 years is steel sheet with organic coatings, so-called color-coated sheet (CC). In the construction industry, it is used for both exterior and interior applications. Its use is also increasing in the automotive industry and in the production of white goods. CC sheets have recently been frequently used in the production of furniture and lamps. A standard painted sheet consists of a steel substrate, which may or may not have a Zn layer. Subsequently, a chemical pretreatment (conversion layer) is applied to it, which initiates the metal surface for the final application of organic layers. The most common combination is a 3-layer system, where a primer and topcoat are applied to the top side of the steel sheet and a backcoat to the bottom side, Figure 1a. In addition, there are also 2-layer and 4-layer systems, Figure 1b, c.

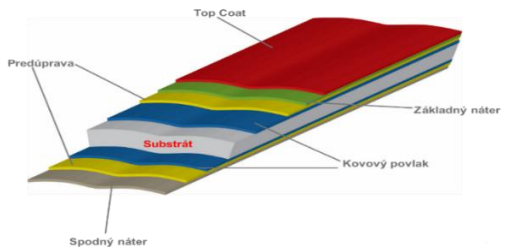

Figure 1a. Cross-section of CC material with standard 3-layer system.

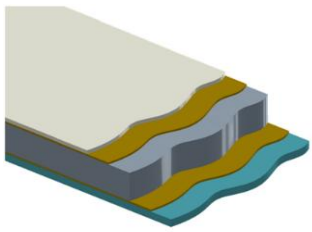

Figure 1b. Cross-section of CC material with 2-layer system.

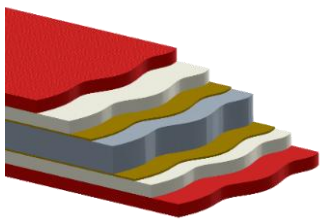

Figure 1c. Cross-section of CC material with 4-layer system.

2. Substrate for Color coated Sheet

The main substrates for CC lines are **steel and aluminum**. Steel is the general name given to a large group of alloys of iron with carbon and several other elements. Small differences in the composition of steel can have a dramatic effect on its properties. The properties of steel can also be modified by different mechanical and thermal treatments. For continuous painting with organic coatings on CC lines, the following can be used:

- *Cold-rolled steel (CR)* – it is the so-called bare (uncoated) sheet metal, and if it is left unprotected (exposed) in the air for some time - it will corrode.
- *Hot-dip galvanized steel (HDG) with a standard Zn layer.* Hot-dip galvanized steel is the main type of substrate for painted steel, mainly for structural applications and roofing. Hot-dip galvanizing is the most widely used method of protecting steel from corrosion.
- *Hot-dip galvanized steel with a ZnAlMg layer (1-3.5% Mg and 0.5-3.5% Al).* These are modern coatings with high corrosion resistance with half the thickness of the ZnAlMg layer compared to classic Zn coatings.
- *Other options* may be electrolytic galvanizing, Galvalume (55% Al / Zn), Galfan (5% Al / Zn), stainless steel (> 4% Cr), aluminum steel.

3. Technological production process

The production of CC sheets is a continuous process that takes place on coil coating lines. A standard coil coating line consists of several technological sections, Figure 2.

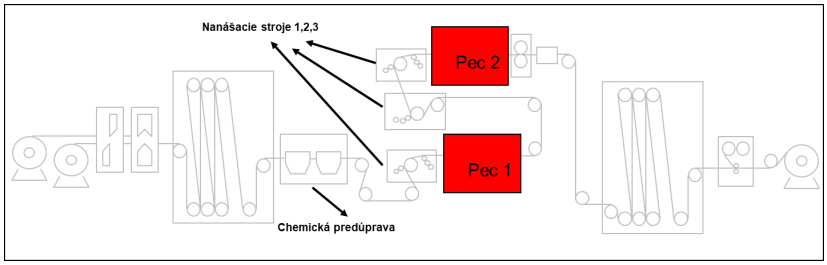

Figure 2. Illustrative picture of a coil coating line.

In order to achieve a continuous steel strip in the production process, the coils are connected to each other at the input section, i.e. the front end of the coil is connected to the end of the previous coil. To achieve maximum adhesion and corrosion resistance of the organic coating, the chemical pretreatment section is very important, including a cleaning section that serves to remove small parts or oils from the metal surface. This is followed by rinsing with demineralized water, which serves to remove contaminated cleaner from the steel sheet surface. This is followed by the application of the chemical pretreatment itself. Its main task is to serve as an anchoring intermediate layer between metal and paint, thereby improving the anti-corrosion properties of sheets with organic coatings. The most effective is application with rollers, i.e. chemcoater, Figure 3a., which applies a precisely defined amount of passivation agent to the strip surface. The coating that is formed is formed by a reaction in which part of the base metal converts to one of the coating components. This reaction makes the coating an integral part of the surface – so-called conversion coatings are formed, Figure 3b. It is usually applied in a thickness of up to 1 μm. Since 2017, Cr-free pretreatments have been used, most often Ti or Zr-based.

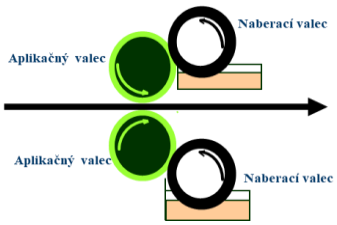

Figure 3a. Application of conversion layer by a chemcoater.

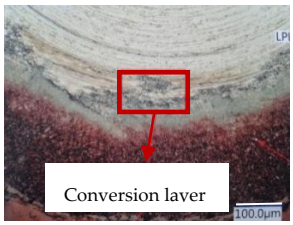

Figure 3b. Picture of the conversion layer of CC material.

After drying and cooling, the strip goes to the paint application section. The paints are applied with a roller, so-called coater. For continuously painted sheets, a two-layer coating on the top side (primer + topcoat) is standardly used. The primer is applied directly to the pre-treated metal surface, contains anti-corrosion pigments, the task of which is to protect the metal substrate from corrosion. The second layer - the topcoat provides the color and appearance of the final painted product and plays a major role in the mechanical properties of the final painted product and weather conditions. The thickness of the primer ranges from 5 - 35µm, the thickness of the topcoat 15 - 200µm. The thickness is determined by the type and quality of the selected paint.

Once the liquid paint is applied to the strip, it enters the oven, where the paint is:

1. *dried* - volatile substances (e.g. solvents) are removed
2. *fired* at high temperatures.

The firing must be carefully adapted to the type of paint and to allow the solvent to be removed without creating surface defects. If the heating is too fast, the paint will start to harden before the solvent has had time to evaporate. This results in a blistered surface on the finished coating, Figure 5. In the case of thick coatings such as plastisol, PVDF, the coating itself is not completely baked, but the drying process is done, patterning (embossing) can be applied to them before curing while the film is relatively soft.

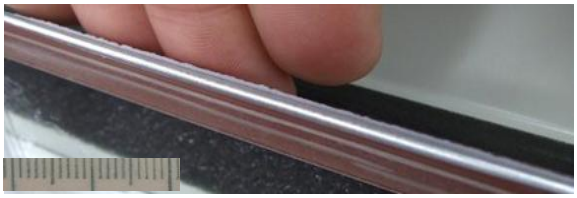

Figure 4. Picture of peeling of the organic layer of CC material without a conversion layer.

Figure 5. Illustrative photo of the blistered surface of CC sheet metal.

Once the coating is fully cured and cooled, the strip moves to the exit section. In some cases, a protective film may be applied to the strip surface to help protect the paint surface during the customer's forming operations. Some lines have a marker in the exit section that marks the back of the strip for future inspection. The coil is then securely packaged and shipped to the customer.

4. Tests of color coated steel sheets

Since the coated sheet metal is a complex material, where there is a unique combination of metallic and non-metallic elements and their properties, in order to obtain information about the behavior or suitability of the sheet metal for a specific area, it is necessary to perform a number of complex tests. The main properties of CC sheets can be divided into several groups:

- *Key properties:* formability, flexibility, corrosion resistance, resistance to UV radiation
- *Specific properties:* chemical resistance, reflectivity / emissivity
- *Special properties:* Reducing the energy consumption of buildings: cool roof varnishes, anti-graffiti paints, anti-dirt (self-cleaning) paints.

These properties are evaluated by various types of tests. Select test are described below.

4.1. Evaluating of the optical properties

- *Change in color shade:* It is most comprehensively assessed using a spectrophotometer. It is an optical instrument that can very easily and quickly convert any shade into three numbers (L, a, b) and numerically express the differences between shades (ΔE), Figure 6a.
- *Gloss:* The gloss of organic coatings is determined by measuring the specular reflection using a device - a glossmeter. Measurement at an angle of 60° is suitable for almost all organic coatings with a standard appearance. The principle of gloss measurement lies in the angle of incidence and the angle of reflection, Figure 6b.

Figure 6a. Principle of measuring color change.

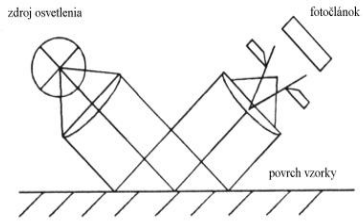

Figure 6b. Principle of measuring specular gloss.

4.2. Evaluating of the physical properties

Physical property tests of CC sheets generally determine the resistance of the organic coating to external influences (various stresses on the sheet, chemicals, etc.). Among others, these include:

- *Bending resistance: T-bend:* This test describes the resistance of the organic coating to cracking when a sheet sample is bent between 135°- 180°, Figure 7.
- *Cross-cut test:* This method is used to evaluate the resistance of coatings to separation from the metal substrate when the coating is cut through to the metal substrate using a grid with a rectangular pattern.
- *Erichsen test:* This is a test simulating slow deformation using the Erichsen device. The resistance to cracking of the coating during indentation at a given speed of indentation of the hemispherical indenter is evaluated, Figure 8.
- *Impact test:* This is a test simulating rapid deformation using the Impact tester. The resistance to cracking of the coating in the area of the hemispherical bulge is evaluated when a weight with a hemispherical end falls from a certain given height onto the tested sample, Figure 9.
- *Clemen test (scratch test):* describes the procedure for determining the resistance of an organic coating to scratching with a needle - up to a metal substrate. The result is the weight of the weight in g required to scratch the coating.
- *Abrasion resistance:* Describes resistance to abrasion and wear of an organic coating with sandpaper, which is attached to the grinding wheels. During the test, the grinding wheels are loaded with specified weights, Figure 10.

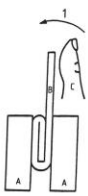

Figure 7. T-bend.

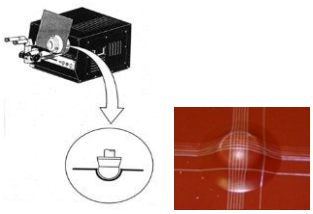

Figure 8. Erichsen tester, slow deformation.

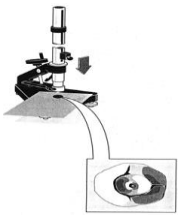

Figure 9. Impact tester, rapid deformation.

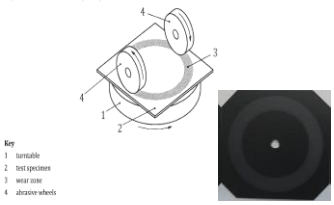

Figure 10. Abrasion resistance test.

4.3. Evaluating of the corrosion resistance

Corrosion resistance tests can be performed in a laboratory environment, so-called accelerated tests, and tests in atmospheric conditions, so-called long-term tests. Accelerated tests in laboratory conditions last hundreds of hours, while atmospheric tests last years. Corrosion tests include:

- *Neutral salt spray test (NSS test):* The principle of the test is to determine the resistance of an organic coating to the aggressive environment of neutral salt spray when the organic coating is deliberately damaged. The test itself is carried out in a corrosion chamber, Figure 11a.
- *Humidity test:* The principle of the test is to determine the resistance of an organic coating to long-term moisture that can enter the coating through pores in the paint. The test is carried out in a condensation corrosion chamber, Figure 11b.
- *Cyclic tests:* In most modern cyclic corrosion chambers, it is possible to simulate various corrosion test cycles - either according to international standards or according to customer requirements. The tests combine humidity, salt spray, drying - in different ratios and durations.
- *Corrosion test in external atmospheric conditions:* An atmospheric test is considered a long-term test, lasting at least 2 years. There are designated places on Earth for this type of test where tests can be carried out and they are divided according to areas - industrial, coastal, sunny/dry, ...

Figure 11a. Corrosion chamber (Salt spray test).

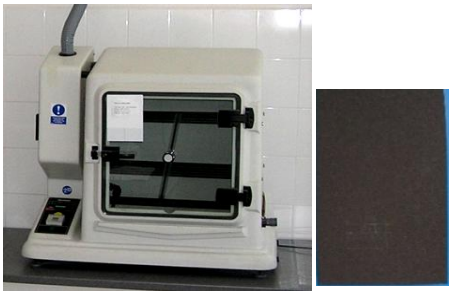

Figure 11b. Condensation chamber test.

4.4. Evaluating of the formability

Like all the previously mentioned tests, formability tests for steel sheets with organic coatings are used to evaluate the adhesion of organic coatings to the substrate. These include:

- *Cup test:* Simulates the deep drawing process. In the forming process, the material is subjected to a difficult transformation from a simple planar blank into a spatial 3D object, Figure 12a.
- *Stretch test:* Simulates forming in 2-axial tension. The influence of biaxial stress on the material with a tightly clamped pressing tool will reveal any imperfections in the adhesion of the applied coating to the base material, Figure 12b.

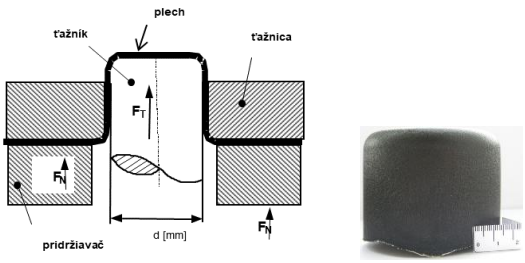

Figure 12a. Cup test.

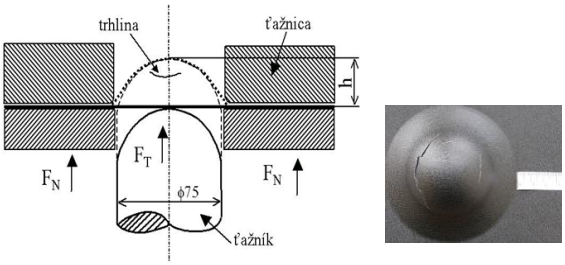

Figure 12b. Stretch test.

5. Verification of the theory of poor adhesion of organic coatings to the substrate

In the absence of a conversion layer, insufficient, weak adhesion of paints to the substrate occurs. Area loss of adhesion of an organic coating is almost always a consequence of insufficient surface cleaning, failure of the conversion coating or incompatibility of individual layers of the coating system. [6] This fact is supported by the scientific research "Mechanism of delamination at the metal-polymer interface", where the authors refer to the absence of a conversion layer, when corrosion under the paint spreads uncontrolled. The authors prove in the article that without chemical passivation, there is a loss of adhesion of the paint at the interface with the metal. [7] Similar cases have been addressed in case studies by the European Coated Sheet Association (ECCA) [8], as well as in the research project: "Study on the influence of pre-treatment on the adhesion of organic coatings", which discusses that although the initial dry adhesion may be similar for the samples, after exposure to humidity (in a condensation chamber) the samples without a conversion layer show 100% delamination of the paint. The conversion layer is defined as crucial for eliminating the formation of zinc hydroxides, which are the main cause of adhesion loss. [9]

Comparable experiences also occur among LP sheet metal manufacturers and their customers during the actual processing of the sheets. Also in connection with the transition of chemical pretreatment to a Cr-free Ti-based preparation, on prepainted sheets there is sporadically a weak, sometimes insufficient adhesion of the paints to the galvanized substrate. There is either extensive cracking or even massive peeling of the paint layers, Figure 13a. This fact tends to appear only after processing, or profiling of prepainted sheets. In Cr-free technology on the coil coating line, a several times higher amount of passivation is as inappropriate as its lack, because it also has a negative effect on the proper adhesion of organic paints, Figure 13b, which is described by the aforementioned authors and has also been confirmed by laboratory tests and production practice. [10, 11]

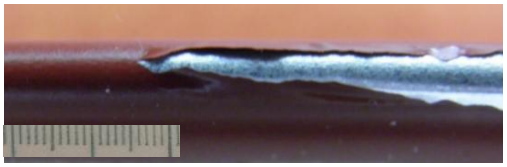

Figure 13a. Peeling of the organic layer of CC material without a conversion layer.

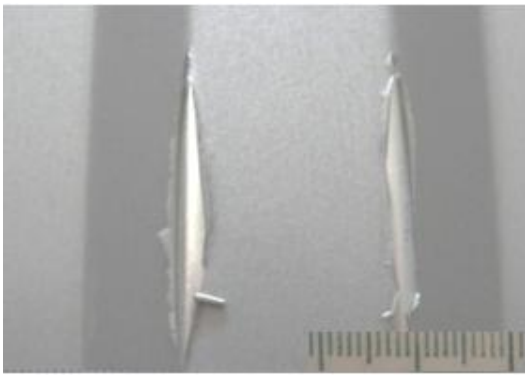

Figure 13b. Area with locally peeling organic coating - even after removal of organic coating.

6. Damage to CC sheets in practice

Color coated sheet is a material composed of several layers of varied materials - it combines a metal and a non-metal component. Therefore, such a material must be handled carefully, because damage to the surface - organic layer can occur relatively quickly and easily. Its disruption can result in corrosion, subsequent peeling of the paint layers, and thus degradation of the entire material. Such material no longer meets the original required parameters. Damage to CC sheets can be divided into several areas:

- *Improper storage:* Figure 14a, b.
- *Incorrect handling and installation:* Figure 15.
- *Other damage (dirt):* Figure 16a, b, c.

Figure 14a. Example of incorrect placement of CC sheets.

Figure 14b. Total failure – separation of the topcoat from the primer.

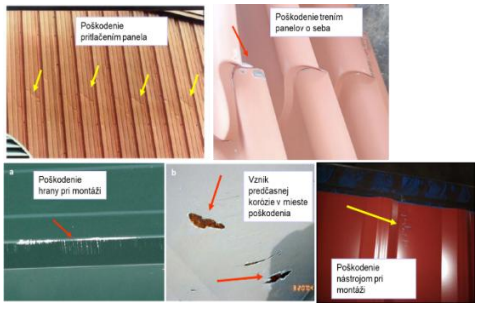

Figure 15. Examples of improper handling of CC material - mechanical damage.

Figure 16a. Soiling of CC panels with handprints, footprints.

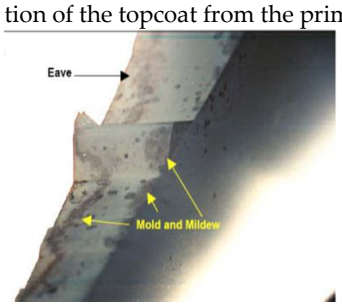

Figure 16b. Mold and fungus growth.

Figure 16c. Forgotten construction waste on the roof.

7. Conclusion

The article points to one of the modern materials - sheets with organic coatings, so-called color-coated steel sheets, deals with a general overview, standard production flow and the substrate used. It also introduces selected testing methods, which are characterized in more detail in the article. The article also dealt with studies in the area of the absence of a conversion layer and the subsequent poor adhesion of paint layers. In Cr-free technology on coil coating lines, a several times higher amount of passivation is as inappropriate as its lack, because it also has a negative effect on the proper adhesion of organic paints, which is also confirmed by research devoted to this issue. This fact was also verified by laboratory tests and supported by real production. Last but not least, it emphasizes the damage that can occur when this material is handled improperly in practice.

Conflicts of Interest: "The authors declare no conflict of interest.".

Acknowledgments: This work was supported by the grant project VEGA 1/0539/23 – "Research into hybrid sandwich structures with customized properties" and project SK-PL-25-0118. The authors also gratefully acknowledge support for the experimental work provided under grant KEGA 035TUKE-4/2026.

References

1. ECCA - European coil coating association, Academy 2015. [online] [2015-04-25] Available on the Internet: <https://prepainted-metal.eu>
2. STN EN 13523: Coil coated metals – Test methods. (parts 2, 3, 5, 6, 7, 8, 12, 16, 19, 25)
3. EN 10169:2022, Continuously organic coated (coil coated) steel flat products
4. Brezinová, J. - Liptáková, T. - Guzanová, A. - Draganovská, D. - Kottfer, D.: Corrosion of materials and special surface treatment technologies. 1st edition, Kosice: TU, Kosice, 2020, 308 s., ISBN 978-80-553-3454-7
5. STN EN ISO 6270-2: 2025, Paints and varnishes – Determination of resistance to humidity – Part 2: Candensation (in-cabinet exposure with heated water reservoir)
6. Prošek, T.: Mechanismy degradace organických povlaků, Technopark Kralupy VŠCHT Praha
7. Vaidya Uday K.: Mechanisms of interfacial adhesion in metal–polymer composites – Effect of chemical treatment, Carol Ochoa-Putman, , Composites Part A: Applied Science and Manufacturing, Volume 42, Issue 8, August 2011, Pages 906-915
8. *European Coil Coating Association (ECCA)* – white papers and case studies.
9. Bajat, J.B. - Mišković-Stanković, V.B. - Bibić, N. - Dražić, D.M.: The influence of zinc surface pretreatment on the adhesion of epoxy coating electrodeposited on hot-dip galvanized steel, Progress in Organic Coatings, Volume 58, Issue 4, 1 March 2007, Pages 323-330

10. Németh, S. – Tomková, V. – Kundracík, V. – Hollý, F. – Filipovská, I. – Tomáš, M.: Posudzovanie priľnavosti lakoplastovaných plechov k pozinkovanému substrátu a možnosti ich skúšania, Transfer inovácií 51/2025, s. 22-32, ISSN 1337 – 7094
11. Vayeda, R. – Wang, J.: Adhesion of coatings to sheet metal under plastic deformation. Int J Adhes Adhes 2007; 27:480–92. https://doi.org/10.1016/j.ijadhadh.2006.08.003.

TECHNICAL UNIVERSITY OF KOŠICE
Faculty of Mechanical Engineering

Implementation of Realistic Physical Interactions for Maintenance Tools in Unity3D

Erik Varjú[1,*] and Juraj Kováč[1]

[1] Department of industrial and digital engineering, Technical University of Košice, Park Komenského 9, 04001 Košice; erik.varju@tuke.sk; juraj.kovac@tuke.sk
* Correspondence: erik.varju@tuke.sk

Abstract: The effectiveness of Virtual Reality (VR) for industrial maintenance training is often limited by the lack of realistic physical interaction with tools, which breaks immersion and hinders skill acquisition. This paper tackles this challenge by proposing a robust framework for simulating the nuanced mechanics of two essential tools: the torque wrench and the screwdriver. We detail a technical implementation in Unity3D, utilizing its NVIDIA PhysX physics engine to simulate torque, rotational states, and associated haptic cues. Key to our approach is the use of Configurable Joints for tool articulation and a state-machine model for discrete screwdriving phases. Given the significant performance cost of complex physics interactions, we also outline critical optimization techniques, such as collision layer management and simplified colliders, to ensure a fluid simulation. The outcome is a practical and efficient foundation for creating highly immersive and mechanically authentic VR training experiences that closely mimic real-world tactile feedback.

Keywords: virtual reality, Unity3D, physics simulation, haptic feedback, maintenance training

1. Introduction

The adoption of Virtual Reality (VR) technology has seen significant growth across various industrial sectors, particularly in training and simulation. Its ability to create safe, controlled, and repeatable environments makes it an ideal platform for training personnel in complex, dangerous, or costly procedures. This is especially true for industrial maintenance, where trainees can learn and practice intricate assembly and disassembly sequences, fault diagnosis, and equipment handling without the risks associated with real-world machinery or production downtime. The potential for standardized assessment and remote training further amplifies VR's value as a powerful pedagogical tool [1].

Despite these advantages, the full potential of VR for procedural skill transfer often remains untapped due to a critical shortcoming: the lack of realistic physical interaction. While modern VR systems deliver high-fidelity visuals and spatial audio, the tactile and kinesthetic feedback—the sense of touch and force—is frequently underdeveloped. In the context of maintenance training, this translates to a fundamental disconnect when a user interacts with a tool. Picking up a virtual wrench is trivial; however, simulating the precise resistance when turning a bolt, the distinct "click" of a torque wrench reaching its specified value, or the gradual release of a screw from its threads remains a complex challenge. This break in physical realism can shatter immersion, lead to the development of incorrect muscle memory, and ultimately reduce the training's effectiveness and credibility [2].

This paper addresses this gap by focusing on the implementation of high-fidelity physical interactions for two fundamental maintenance tools: the torque wrench and the screwdriver. Our primary objective is to present a robust and practical framework within the Unity3D game engine that moves beyond simple object manipulation to simulate the

nuanced mechanics and haptic cues essential for authentic training. The core contributions of this work are threefold:

1. A detailed methodology for simulating torque-based tool interactions, including the haptic and auditory feedback for a torque wrench's "click" mechanism.
2. A state-machine model for screwdriver interactions that accurately represents the discrete phases of the screwing process (tight, loose, removed) with corresponding visual and haptic feedback.
3. A discussion of the significant performance overhead associated with complex physics simulations in VR and a set of proven optimization strategies to maintain a stable and comfortable frame rate [3].

By leveraging the capabilities of Unity's underlying NVIDIA PhysX engine, specifically through the use of Rigidbodies, Colliders, and Configurable Joints, we demonstrate that it is feasible to create mechanically convincing and performant tool interactions. The proposed approach provides a foundational blueprint for developers aiming to enhance the realism and training efficacy of their VR maintenance simulations [4].

2. Materials and Methods

This section outlines the core components, software environment, and specific methodologies employed to develop realistic tool interactions. The implementation was built within the Unity3D game engine (version 6000.0.62f1), utilizing its built-in physics engine and scripting API to create the desired behaviors. This specific version, being part of the Unity 6 development cycle, provided access to the latest performance improvements and stability fixes for the physics and XR subsystems [5].

2.1 Software and Hardware Setup

The development environment consisted of the Unity3D engine (6000.0.62f1) with the OpenXR plugin for VR device management. The primary VR hardware used for testing and interaction was the Meta Quest 3 headset, operated in both standalone and PC-link modes. The physics simulation was handled by the integrated NVIDIA PhysX engine. All interaction logic was programmed in C# using the Visual Studio ID [6].

2.2 Core Physics Components

The foundation of all physical interactions in Unity rests on three key components:

- Rigidbody: this component grants an object physical properties, allowing it to react to forces, gravity, and collisions. Both tools (wrench, screwdriver) and their targets (nuts, screws) were equipped with Rigidbodies. Critical parameters such as Mass and Drag were carefully tuned to prevent unrealistic "floaty" behavior and to simulate the weight of metal tools.
- Colliders: for complex tools like the wrench, we used Convex Mesh Colliders. The 'Convex' property is critical: it instructs the PhysX engine to generate a simplified, volumetric hull that encloses the original mesh. This process fills in complex concavities, creating a collision shape that is vastly more performant than a full, non-convex mesh collider. The dramatic difference in complexity between these collider types is visualized in Fig. 1 (center vs. bottom). A key optimization in our work was the use of custom, low-poly meshes designed to create a good convex approximation, while retaining a separate, high-poly mesh for visuals.
- Configurable Joint: this powerful component was instrumental in creating articulated tool movements. It allows for defining constraints on the linear and angular motion between two Rigidbodies. We utilized it extensively to create the pivoting head of a socket wrench, locking all linear movement and all but one axis of angular rotation to create a natural hinge-like motion [7].

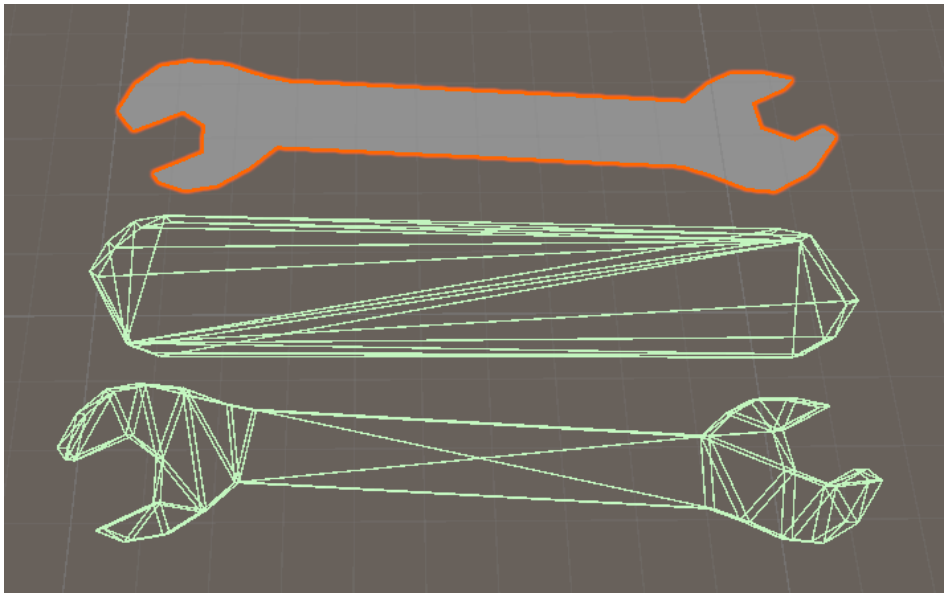

Figure 1. Comparison of visual and collision models for the wrench.

2.3 Torque Wrench and Nut Assembly

The simulation of a torque wrench involves both continuous mechanics and a discrete feedback event. The implementation follows a multi-stage process, as illustrated in Fig. 2.

1. Attachment & Alignment: A trigger collider on the wrench socket detects proximity to a nut. Upon a user grip input, the wrench is kinematically "snapped" into place, aligning its rotation axis with the nut's. The wrench and nut are logically linked, often through parenting in the Unity hierarchy.
2. Torque Calculation: The applied torque is calculated in real-time based on the user's hand movement. The formula Torque = LeverArm x AppliedForce is used, where:
    - LeverArm is the vector from the nut's center (the pivot point) to the controller's position.
    - AppliedForce is a vector representing the controller's rotational velocity.
3. The "Click" Feedback Mechanism: A target torque value is defined for the specific nut. A C# script continuously monitors the calculated torque. Upon reaching the threshold:
    - Haptics: A strong, short-duration haptic pulse is triggered on the VR controller.
    - Audio: A pre-recorded "click" sound is played spatially from the wrench.
    - Visual/Mechanical Cue: The kinematic link between the wrench and nut is temporarily broken, causing the wrench to "slip" slightly, providing a clear visual and mechanical confirmation of the achieved torque [8].

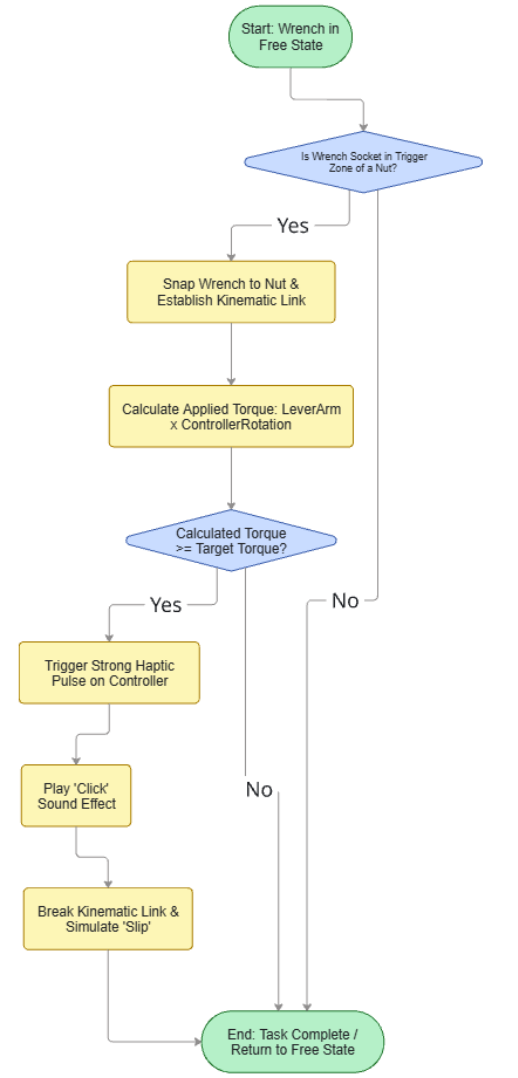

Figure 2. Torque Wrench Interaction Workflow.

2.4 Screwdriver State-Based Interaction

To simulate the non-linear, discrete nature of screwing, we implemented a Finite-State Machine (FSM) with three distinct states (Fig. 3):

- Tight State: The screw is fully seated. Rotation requires overcoming simulated static friction, translated into strong, high-frequency haptic resistance. The screw does not move linearly.
- Loose State: Triggered after the screw has been rotated a predefined number of times (simulating thread travel). In this state, rotation is easy and is coupled with linear motion along the screw's axis (Transform.Translate). Haptic feedback is a weaker, continuous rumble.
- Removed State: Once the screw's linear travel is complete, it transitions to this state. The physical connection to the base object is removed, and the screw becomes a separate, grabbable object.

A C# script on the screw manages this FSM, tracking rotation counts and updating the screw's position and physical behavior accordingly [9].

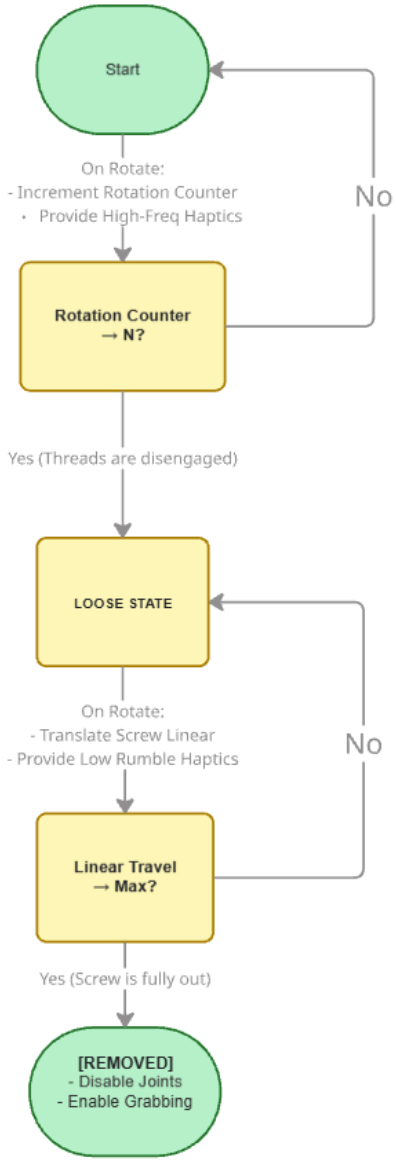

Figure 3. Screwdriver Finite-State Machine.

2.5. Performance Optimization Strategies

To maintain the critical 90 FPS required for VR comfort, we implemented several key optimizations:

- Simplified Collision Geometries: As shown in Fig. 1, we consistently used primitive or convex colliders instead of complex mesh colliders.
- Layer-Based Collision Matrix: We organized objects into dedicated Unity layers (e.g., Tools, Interactables, Environment) and configured the Physics collision matrix so that only necessary layers interact (e.g., Tools collide with Interactables, but not with other Tools). This drastically reduces the number of collision checks per frame.
- Object Pooling: For scenarios with multiple identical tools or parts, we pre-instantiated a pool of objects at load time and reused them, avoiding performance-heavy runtime instantiation and garbage collection [10].

3. Results

The implementation of the proposed physical interaction methods was tested within a focused technical demonstration scene in Unity3D. This section presents a functional validation of the core interaction mechanics for the wrench and screwdriver, demonstrating that the described approach successfully translates theoretical concepts into working, interactive behaviors. [11].

3.1. Realistic Torque Wrench Interaction Sequence

The simulation of the torque wrench demonstrates a complete physical interaction loop, from detection to force feedback. As illustrated in Fig. 4, 5 and 6, this process is broken down into three distinct phases:

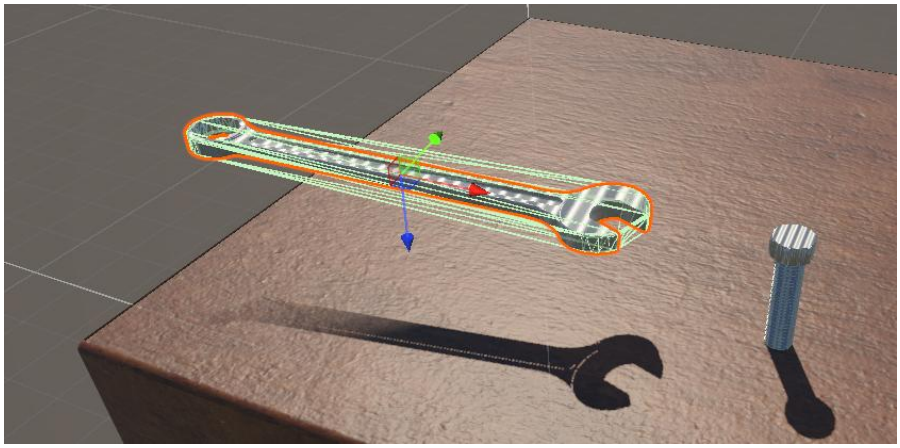

Figure 4. Collision Detection and Initial Engagement.

Phase 1: The wrench, equipped with a simplified convex mesh collider for performance, approaches the screw. The Unity Physics engine continuously checks for overlaps between the wrench's trigger collider and the screw's collider. At this stage, no interaction logic is active.

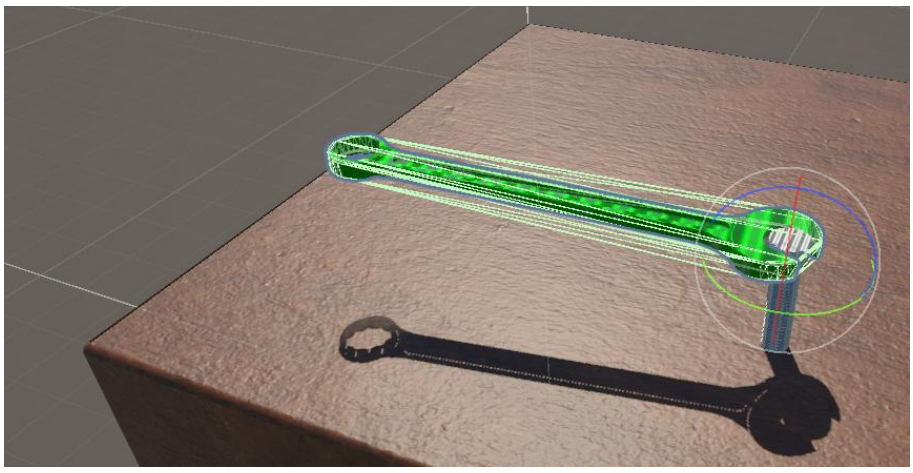

Figure 5. Tool Engagement and Kinematic Linking.

Phase 2: Upon a collision overlap, the OnTriggerEnter event is invoked, executing the EngageWithScrew() method in the WrenchController script. This method performs two critical actions: (1) it establishes a kinematic link between the wrench and screw, aligning their rotational axes, and (2) provides immediate user feedback by changing the wrench's material color to green. This visual cue confirms the successful "snap" of the tool onto the fastener, a crucial step for user confidence in VR.

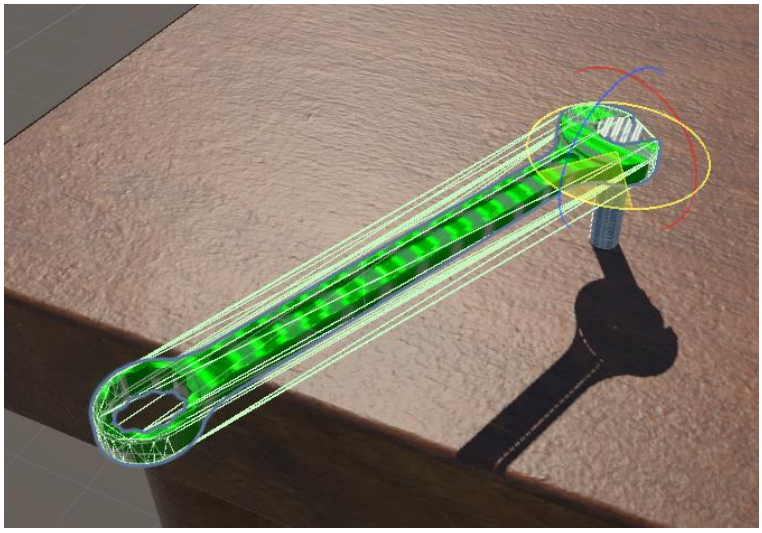

Figure 6. Torque Application and State Tracking.

Phase 3: With the link established, the user's rotational input is translated into simulated torque. The applied torque (τ) is calculated in real-time using the relation $\tau = r \times F$, where r is the lever arm vector from the screw's pivot point to the controller position, and F is a force vector derived from the controller's rotational velocity. The system tracks the accumulated angular displacement, which is the primary driver for the screw's state-based behavior.

The logic governing the screw's behavior is encapsulated in a Finite-State Machine (FSM), implemented in the ScrewController script (Fig. 7). The code excerpt below shows the Screw State Configuration() method, which evaluates the accumulated rotation count against predefined thresholds to manage transitions between the REMOVED, LOOSE, and TIGHT states. Each state transition triggers corresponding multi-sensory feedback.

Assembly-CSharp ScrewController_VisualDemo

```
using UnityEngine;
using System;

/// <summary>
/// State Machine Controller for realistic screwdriver interaction.
/// Simulates the three distinct states of a screw: REMOVED, LOOSE, and TIGHT.
/// Provides appropriate haptic and audio feedback for each state transition.
/// </summary>
Unity Script (1 asset reference) | 0 references
public class ScrewController_VisualDemo : MonoBehaviour
{
    // ===== SCREW STATE CONFIGURATION =====
    [Header("State Thresholds")]
    [Tooltip("Complete removal - screw is fully out")]
    [SerializeField] private const float REMOVED_THRESHOLD = 0.0f;

    [Tooltip("Screw threads are engaged but not tight")]
    [SerializeField] private const float LOOSE_THRESHOLD_MIN = 0.1f;

    [Tooltip("Screw is fully tightened")]
    [SerializeField] private const float TIGHT_THRESHOLD = 5.0f;

    [Header("Current State")]
    [SerializeField] private ScrewState currentState = ScrewState.REMOVED;
    [SerializeField] private float currentRotations = 0.0f;

    // ===== FEEDBACK SYSTEMS =====
    [Header("Haptic Feedback")]
    [SerializeField] private float tightHapticStrength = 0.8f;
    [SerializeField] private float looseHapticStrength = 0.3f;
    [SerializeField] private float clickHapticDuration = 0.1f;

    [Header("Audio Feedback")]
    [SerializeField] private AudioClip tightStateSound;
    [SerializeField] private AudioClip looseStateSound;
    [SerializeField] private AudioClip clickSound;
    [SerializeField] private AudioSource audioSource;

    [Header("Visual Feedback")]
    [SerializeField] private ParticleSystem tightParticles;
    [SerializeField] private ParticleSystem looseParticles;
```

Figure 7. Code screenshot for ScrewStateController.cs.

4. Conclusions

This paper detailed a concrete implementation methodology for achieving realistic physical interactions with maintenance tools in Unity3D, addressing a critical gap in VR training immersion. By providing a deep dive into the practical use of Unity's physics components—specifically convex Mesh Colliders for performance, Configurable Joints for articulated tool movement, and trigger-based collision detection for initiating interactions—we have demonstrated that standard Unity features are sufficient to simulate complex mechanical behaviors.

The presented workflow for the torque wrench, centered around real-time torque calculation and threshold-based multi-sensory feedback, alongside the finite-state machine model for the screwdriver, provides a reusable blueprint. These patterns can be directly adapted to simulate a wide range of tools (pliers, ratchets, hammers) within industrial training scenarios. Furthermore, the discussed optimization strategies are not mere suggestions but essential practices; they transform a proof-of-concept into a performant application capable of maintaining the 90 FPS required for comfortable VR.

The primary contribution of this work is therefore twofold: it raises the bar for tactile realism in procedural VR training by moving beyond visual mimicry to simulated mechanics, and it provides a validated, practical technical guide for developers. Implementing such interactions is no longer a question of feasibility but of applied engineering, paving the way for more convincing and effective virtual training simulations across the industry.

Acknowledgments: This paper was supported by the projects APVV-17-0258, APVV-19-0418, VEGA 1/0508/22, VEGA 1/0383/25, KEGA 020TUKE-4/2023, KEGA 003TUKE-4/2024.

Conflicts of Interest: The authors declare no conflict of interest. The funders had no role in the design of the study; in the collection, analyses, or interpretation of data; in the writing of the manuscript, or in the decision to publish the results.

References

1. Su, X. Virtual Reality Simulation of Equipment Training Based on Unity3D. IOP Conference Series: Materials Science and Engineering 2019, *562*, 012165. https://doi.org/10.1088/1757-899X/562/1/012165
2. Rouret, M.; et al. An efficient workflow for virtual reality simulation of maintenance tasks in IFMIF-DONES. Fusion Engineering and Design 2023, *190*, 113116. https://doi.org/10.1016/j.fusengdes.2023.113116
3. Radchenko, V.; et al. The Use of Virtual Reality in the Simulator of Maintenance and Repair Technical Components. AIP Conference Proceedings 2022, *2467*, 040008. https://doi.org/10.1063/5.0104094
4. Işık, B.; et al. A Unity 3D educational game of compressed air system training. Procedia Computer Science 2025, *215*, 148–157. https://doi.org/10.1016/j.procs.2025.01.014
5. Va, H.; et al. Efficient Simulation of Volumetric Deformable Objects in Unity3D: GPU-Accelerated Position-Based Dynamics. Electronics 2023, *12*(10), 2229. https://doi.org/10.3390/electronics12102229
6. Huo, A.; et al. Design and Implementation of Drilling Engineering Simulation System Based on Unity3D. Journal of Physics: Conference Series 2021, *1894*, 012043. https://doi.org/10.1088/1742-6596/1894/1/012043
7. Wang, J.; et al. Simulation and visualization of industrial processes in Unity. Proceedings of the 2015 Winter Simulation Conference 2015, 492–503. https://doi.org/10.1109/WSC.2015.7408189
8. Berg, L.P.; Vance, J.M. Industry use of virtual reality in product design and manufacturing: a survey. *Virtual Reality* **2017**, *21*, 1–17.
9. Gavish, N.; Gutiérrez, T.; Webel, S.; Rodríguez, J.; Peveri, M.; Bockholt, U.; Tecchia, F. Evaluating virtual reality and augmented reality training for industrial maintenance and assembly tasks. *Interact. Learn. Environ.* **2015**, *23*, 778–798.
10. NVIDIA. *PhysX SDK Documentation*; NVIDIA Corporation: Santa Clara, CA, USA, 2023
11. Unity Technologies. *Unity User Manual (2022.3 LTS)*; Unity Technologies: San Francisco, CA, USA, 2023.

TECHNICAL UNIVERSITY OF KOŠICE
Faculty of Mechanical Engineering

Follicular cyst removal and stabilization with 3D planned splint - case report

Jakub Viľcha [1,*], Ferko Ján [1], Jozef Živčák [2]

[1] Department of Head and Neck Surgery, maxillofacial surgery, FNsP J.A.Reimana Prešov, Jána Hollého 14, 08001, Prešov, Slovakia, mddr.vilcha@gmail.com (J.V); janferko93@gmail.com (J.F)
[2] Department of Biomedical Engineering and Measurement, Faculty of Mechanical Engineering, Technical University of Košice, 042 00 Košice, Slovakia; jozef.zivcak@tuke.sk (J.Ž.)
* Correspondence: mddr.vilcha@gmail.com

Abstract: We present the case of a 20-year-old male referred for evaluation of a tumorous lesion in the right mandibular region. Radiologic imaging (CT, MRI, OPG) revealed a well-defined multilocular cystic lesion measuring 37×19×53 mm in the right mandibular body and ramus, associated with an impacted lower third molar (tooth 48). Histological evaluation suggested a dentigerous follicular cyst. Initial management included marsupialization and placement of a drain to reduce lesion size. Definitive treatment was surgical enucleation (cystectomy) followed by reconstruction of the defect using a custom-made titanium plate.

Keywords: Dentigerous cyst, Marsupialization, Titanium plate, Cystectomy, Odontogenic lesions

1. Introduction

Odontogenic cysts are benign lesions that arise from the remnants of the dental epithelium. Among these, dentigerous cysts—also referred to as follicular cysts—are the second most frequent type and are typically associated with the crown of an unerupted or impacted tooth, most commonly the mandibular third molars. They are usually asymptomatic and discovered incidentally on routine radiographs; however, larger lesions can cause swelling, facial asymmetry, displacement of adjacent teeth, or cortical bone expansion. [1]

Differentiating dentigerous cysts from other odontogenic lesions such as odontogenic keratocysts (OKC) is crucial, as the latter tends to be more aggressive and has a higher recurrence rate. Imaging studies such as orthopantomography (OPG), computed tomography (CT), and magnetic resonance imaging (MRI) play a vital role in diagnosis and surgical planning. Histopathological evaluation remains the gold standard for definitive diagnosis.

Various treatment modalities have been proposed for these lesions, including marsupialization, enucleation (cystectomy), or a combination of both. Marsupialization is often used in large lesions to decompress the cyst and minimize the extent of surgical resection. In selected cases, custom-made titanium plates can be used to reconstruct mandibular defects and restore both functional and aesthetic aspects of the jaw. [2]

In this report, we describe a rare case of a large mandibular cyst in a young adult male associated with an impacted third molar, initially managed with marsupialization and followed by surgical enucleation and titanium plate reconstruction. The clinical presentation, diagnostic process, treatment plan, and postoperative outcome are discussed in detail with reference to current literature.

2. Materials and Methods

The diagnosis was established based on clinical examination, orthopantomography (OPG), computed tomography (CT), magnetic resonance imaging (MRI), and histopathological analysis of the lesion. Marsupialization was initially performed to decompress the cyst and reduce its volume. After sufficient healing and radiographic follow-up, complete cystectomy was carried out under general anesthesia. A custom-made titanium plate was used for mandibular reconstruction to restore anatomical contour and stability.

3. Case Presentation

A 20-year-old male was referred to the maxillofacial surgery department with a suspected tumor-like lesion in the right mandibular region, initially identified by his general dentist. The patient reported a two-month history of asymptomatic swelling in the posterior mandible. He denied any relevant medical history except for a prior episode of mild myocarditis. No regular medications were used, and no significant allergies were reported.

Initial radiographic examination (orthopantomogram) revealed an impacted lower right third molar (tooth 48) and a well-defined radiolucent lesion in the area of the mandibular angle and ramus. MRI and CT imaging confirmed a multilobular cystic lesion measuring 37 × 19 × 53 mm, with irregular cortical margins, mild diffusion restriction, and no signs of adjacent soft tissue invasion.

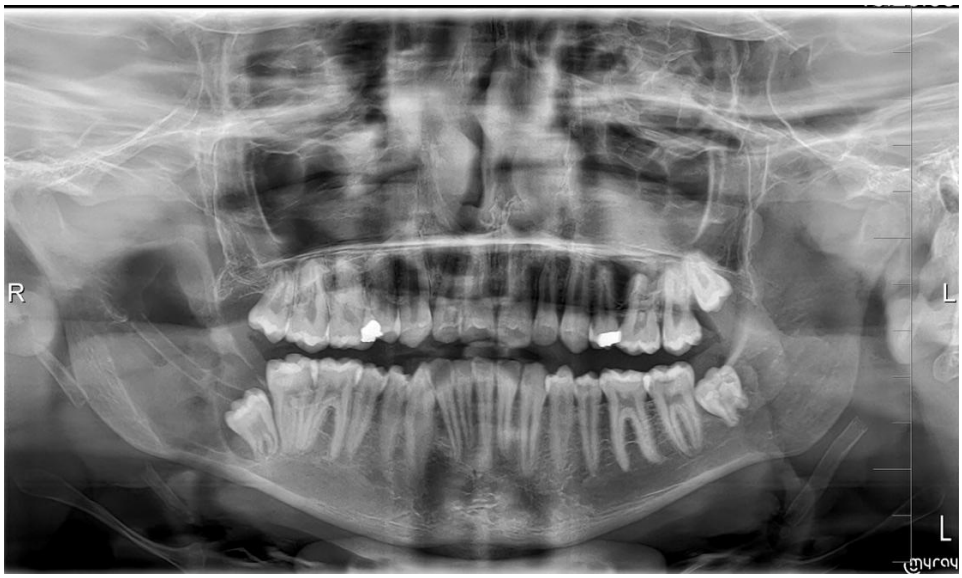

Figure 1. OPG showing a cystic lesion in the area of the mandibular angle and ramus.

Histopathological examination of a biopsy sample suggested a benign odontogenic cyst, likely a dentigerous follicular cyst.

As a first step, marsupialization was performed and a drain was placed to decompress the lesion. The patient was followed regularly. After reduction in cyst size and sufficient bone remodeling, he was admitted for definitive surgical management. Under general anesthesia, the cyst was completely enucleated (cystectomy) along with extraction of the associated impacted tooth. Reconstruction of the mandibular defect was achieved using a custom - made individual titanium plate. Made to specifically meet the needs of the patient based on the CT scan. There was no need to adjust the implant as it fitted perfectly in its place.

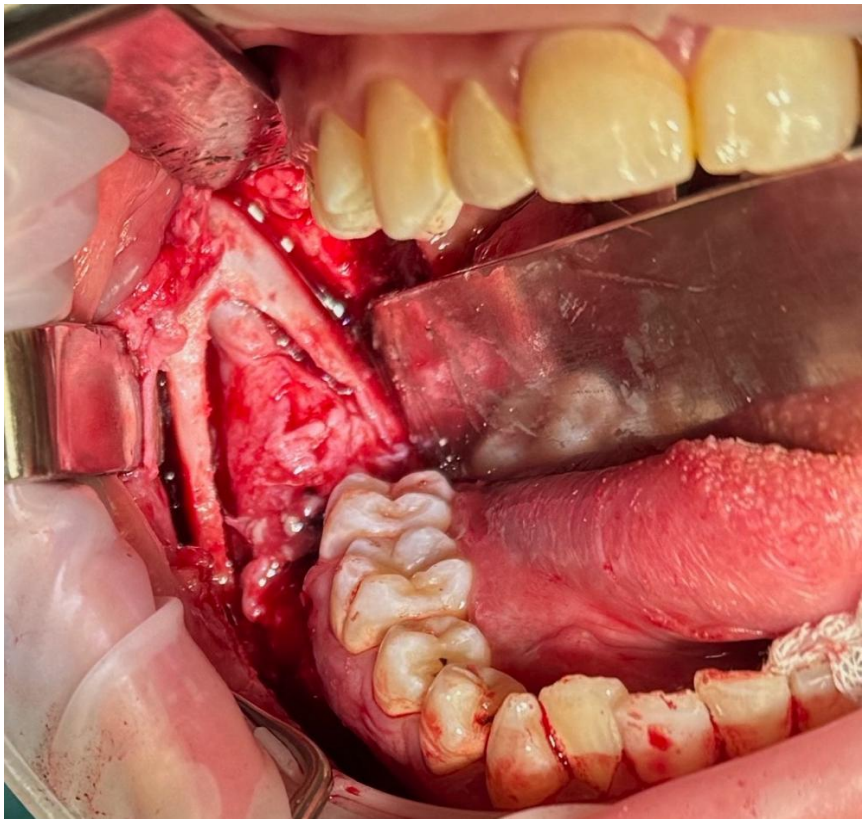

Figure 2. Peroperative photography showing the removal of the cystic lesion from the angle and ramus of the mandible.

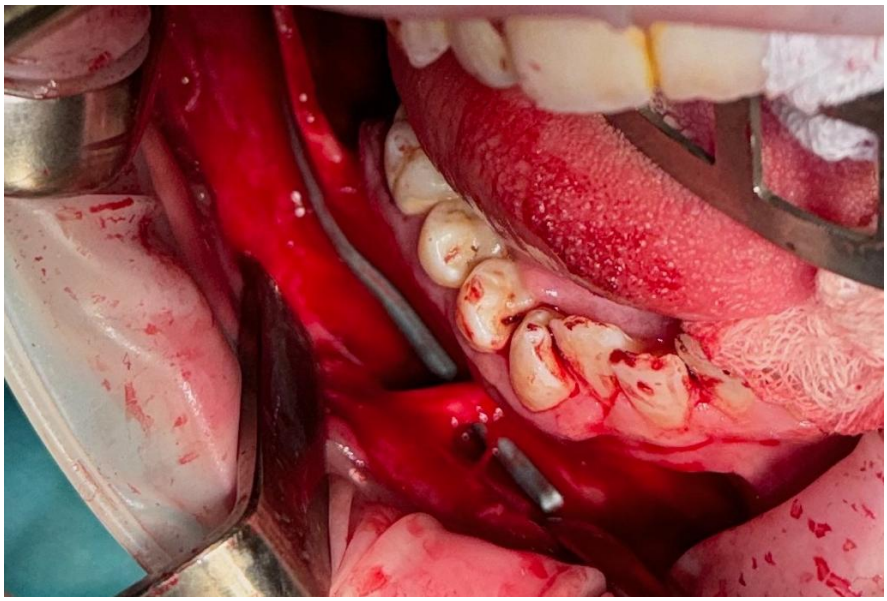

Figure 3. Peroperative photography showing the placement of the custom made implant, designed to aid the mandible in withstanding forces.

The patient recovered without complications. Follow-up visits confirmed stable wound healing and satisfactory functional outcome.

Figure 4. Custom made implant – made specifically to meet the needs of patient based on CT scan.

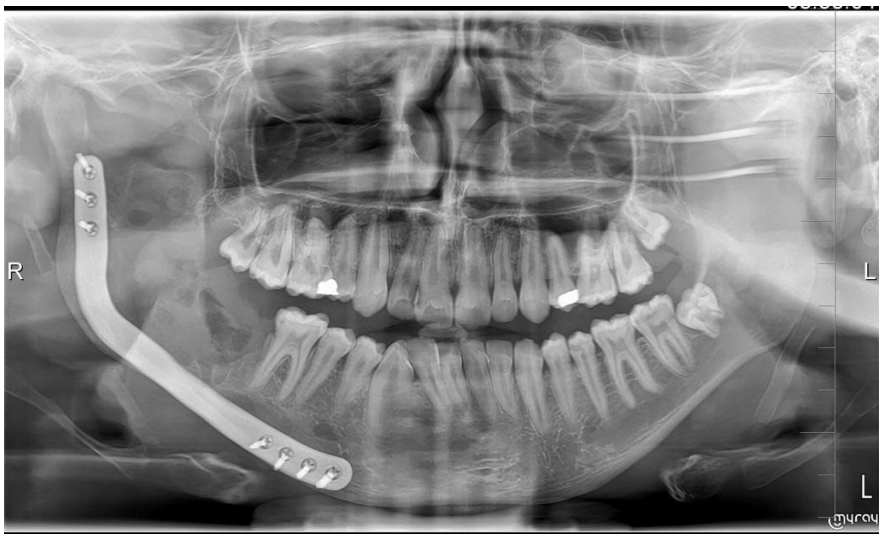

Figure 5. Postoperative imaging (OPG) showing the mandible splint in site.

4. Discussion

Dentigerous cysts are benign odontogenic lesions most commonly associated with unerupted mandibular third molars. Although typically asymptomatic, large lesions can lead to significant bone resorption and cortical thinning, posing a risk of pathological fracture or mandibular deformity.

In our case, the cyst measured over 5 cm in length and involved both the body and the ramus of the mandible. Given the size and location, there was a significant risk of postoperative mandibular instability following cyst enucleation. Therefore, preoperative planning included the fabrication of a custom-made titanium reconstruction plate, based on 3D imaging of the patient's mandible.

Titanium plates play a crucial role in restoring mandibular continuity and biomechanics after the resection of large cystic lesions. Their high strength-to-weight ratio, corrosion resistance, and excellent biocompatibility make them ideal for craniomaxillofacial reconstruction. Custom-fabricated plates, in particular, offer superior anatomical fit, reduced operative time, and minimized intraoperative bending or adjustments.

In young patients, preserving native bone and mandibular contour is essential not only for function but also for long-term aesthetic and developmental outcomes. The use of an individualized titanium plate in this case allowed for:

- Immediate structural support of the weakened mandible
- Maintenance of occlusion and jaw mobility
- Avoidance of segmental resection or bone grafting

Moreover, the staged surgical approach—beginning with marsupialization and followed by definitive cystectomy and plate reconstruction—enabled controlled decompression of the lesion, reduced surgical morbidity, and facilitated postoperative healing.

This case illustrates the value of integrating modern 3D planning and patient-specific implants in managing extensive mandibular defects caused by benign lesions. The approach preserved mandibular integrity and ensured optimal functional and cosmetic outcomes.

References

1. Kreidler, J. F., & Raubenheimer, E. J. (1993). A retrospective analysis of 367 cystic lesions of the jaw—the Ulm experience. *Journal of Cranio-Maxillofacial Surgery*, *21*(6), 273–276. https://repository.up.ac.za/bitstreams/bff62b7e-28bb-4c4c-b4ca-6f917b22bcb6/download#page=271
2. Goyal, R., Jhamb, A., & Kumar, R. (2020). Odontogenic keratocyst: Current concepts in management. *Journal of Oral Biology and Craniofacial Research*, *10*(2), 90–95. https://doi.org/10.1016/j.jobcr.2020.02.001
3. Jin, X., et al. (2022). Use of 3D-printed patient-specific titanium implants for mandibular reconstruction: A systematic review. *International Journal of Oral and Maxillofacial Surgery*, *51*(5), 636–644. https://doi.org/10.1016/j.ijom.2022.01.007
4. Neelakandan, R. S., et al. (2023). Patient-specific titanium implant for mandibular reconstruction: A case series. *Journal of Oral and Maxillofacial Surgery, Medicine, and Pathology*, *35*(3), 85–90. https://doi.org/10.1016/j.ajoms.2023.01.003

TECHNICAL UNIVERSITY OF KOŠICE
Faculty of Mechanical Engineering

Generative Design for Spur Gear Optimization

Matúš Virostko [1,*], Martin Mantič [1], Silvia Maláková [1], Ján Ivanecký [1]

[1] Technical University of Košice, Faculty of Mechanical Engineering, Department of Engineering for Design of Machines and Transport Equipment, matus.virostko@tuke.sk; martin.mantic@tuke.sk; silvia.malakova@tuke.sk; jan.ivanecky@tuke.sk
* Correspondence: matus.virostko@tuke.sk; Tel.: +421556022354

Abstract: This paper presents a simplified study on the application of generative design (GD) to reduce the weight of spur gears while maintaining the required tooth stiffness. Using the Fusion 360 CAD environment, multiple lightweighting design concepts were generated and compared for different manufacturing technologies. The results demonstrate that GD enables efficient material reduction and supports decision-making when selecting suitable manufacturing methods and materials for gear production.

Keywords: generative design, manufacturing, optimization, weight reduction

1. Introduction

The demand for lighter mechanical components has increased due to requirements for reduced energy consumption, higher efficiency, and more sustainable material use. Traditional gear design typically relies on ribs or lightening holes based on the designer's experience. Generative design (GD), however, enables intelligent geometry creation driven by input data and defined constraints, resulting in innovative shapes that improve the stiffness-to-weight ratio.

Spur gears are widely used in mechanical engineering, and even a small reduction in the weight of their bodies can lead to significant performance and cost benefits. This paper focuses on the application of GD for optimizing the internal structure of spur gears while preserving functional tooth engagement.

The aim of this study is to provide a concise overview of how GD can support the design and manufacturing of spur gears, highlight key considerations in load and constraint definition, and summarize the advantages and limitations of various production technologies. [1-5]

2. Methodology

Spur gear parameters (Figure. 1):

- Number of teeth: 71
- Module: 2,5 mm
- Spur gear width: 50 mm
- Inner bore diameter: 55 mm

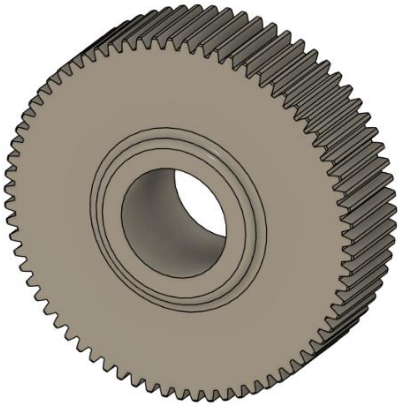

Figure 1. Initial spur gear model.

The complete spur gear model served as the baseline for evaluating volume reduction. Excessive material removal may decrease tooth stiffness and negatively affect the accuracy of gear meshing. Therefore, each lightweighting strategy must be validated through deformation or stiffness analysis. The gear geometry was required to meet standardized design criteria, particularly the minimum rim thickness beneath the teeth, to ensure sufficient stiffness during operation. A unit load of 1000 N was applied for the tooth deformation assessment.

GD always emphasizes realistic loading conditions. For spur gears, the operational loads can be defined in several ways:

1. A force applied sequentially to each tooth.
2. The total transmitted torque distributed across the meshing teeth.
3. A maximum force acting simultaneously on all teeth (Figure 2).

The third approach is the most conservative and often provides the most reliable outcomes for GD, since it ensures uniform loading of the entire gear body. [5]

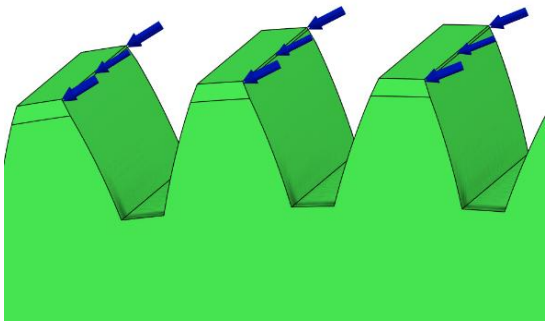

Figure 2. Illustrates how forces are applied to the spur gear.

2.1. Setup and Input Data for the GD Study

The GD workflow included the following steps:

- Preserved geometry (Figure. 3): hub region and the rim area beneath the teeth.
- Definition of the design space (Figure. 4): volume between the hub and the rim.
- Load definition: force applied to all teeth simultaneously (worst-case scenario).
- Geometric constraints: shaft mounting region and lightening hole boundaries.
- Manufacturing constraints: additive manufacturing, milling, and casting.

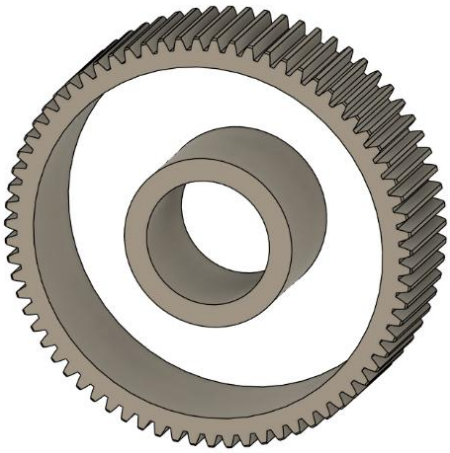

Figure 3. Input geometry of the spur gear study.

Two lightweighting concepts of the gear body were evaluated:

a) Variant with ten circular lightening holes
b) Variant without any additional preserved material around the holes.

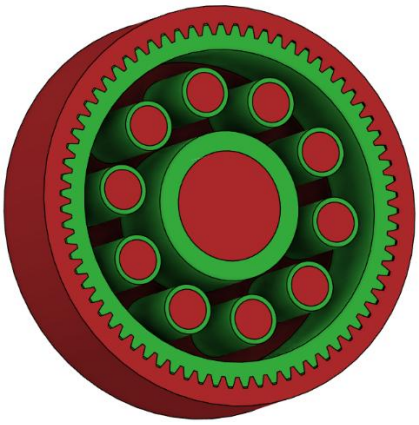

Figure 4. Definition of the design space and study constraints.

Lightweighting strategy conclusions:

- Removing material around the holes generally enabled more efficient optimization without causing excessive stiffness reduction.
- Preserving material around circular holes proved beneficial primarily for casting applications.

3. Results

3.1. Impact of Manufacturing Constraints

- Additive manufacturing enabled the creation of highly organic shapes with a significant volume reduction.
- 5-axis machining resulted in simpler geometries, closer to conventional rib-based designs.
- Casting produced less complex outcomes that required locally reinforced sections to maintain structural stability.

Table. 1. Overview of selected optimized gear variants.

Variant type	Manufacturing method		
	Additive manuf.	Milling	Casting
Variant a)			
Variant b)			

3.2. Comparison of volume and stiffness

Compared to the solid reference gear body:

- GD variants achieved a significant weight reduction while maintaining full functionality.
- Teeth located above hollow regions exhibited higher deformation, which is critical for stiffness evaluation.
- Some generated outcomes proved unsuitable for manufacturing when the input parameters were not properly defined (Figure 5).

Figure 5. Faulty results of GD spur gear design.

3.3. Identified optimal strategies

- Variants without preserved rings around the holes demonstrated better optimization performance.
- Versions with preserved material often provided a balanced compromise between weight reduction and stiffness
- The use of metallic materials increased stiffness, while polymers were mainly suitable for lightweight prototype applications.

Tooth stiffness was analyzed using FEM by applying a 1000 N force to the tooth tip (Figure 6). The stiffness was determined from the resulting deformation.

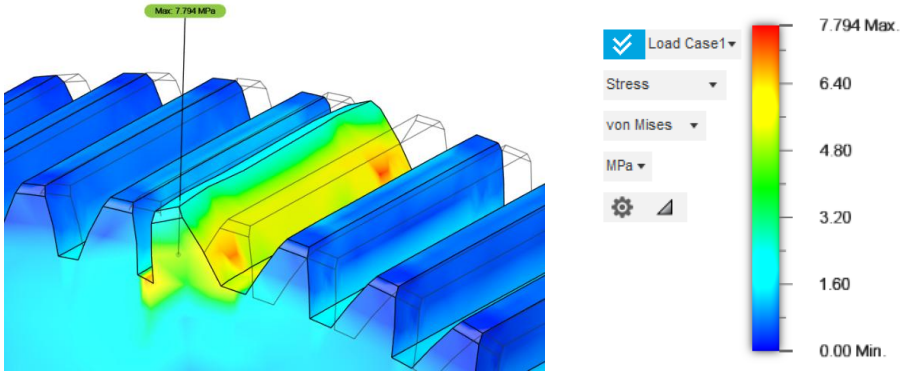

Figure 6. FEM analysis of a spur gear tooth.

4. Discussion

The effectiveness of generative design largely depends on defining realistic loading conditions and manufacturing constraints. The method identifies where material can be removed and where structural reinforcement must remain. Selecting an appropriate manufacturing technology early in the design process helps prevent the creation of shapes that cannot be produced. Generative design does not replace engineering judgment, but it significantly accelerates the evaluation of multiple design alternatives that would otherwise be time-consuming to model manually.

5. Conclusions

This study demonstrates that generative design is a powerful tool for optimizing components such as spur gear bodies across different manufacturing methods. Correct load definition plays a key role, with the simultaneous application of force to all teeth providing the most stable results. Avoiding preserved material around the lightening holes generally improves the optimization capability and leads to lighter structures. Additive manufacturing enables the greatest geometric freedom, while 5-axis machining and casting require more conventional shapes. The interaction between material properties, manufacturing constraints, and load definition has a significant influence on the final optimized geometry. Generative design thus offers engineers an efficient way to develop lightweight, high-performance, and manufacturable gear designs for modern engineering applications.

Acknowledgments: The contribution was created within the framework of the solution of the projects KEGA 044TUKE-4/2024, KEGA 037TUKE-4/2024 and Funded by the EU NextGenerationEU through the Recovery and Resilience Plan for Slovakia under the project No. 09I03-03-V05-00015.

Conflicts of Interest: The authors declare that they have no known competing financial interests or personal relationships that could have appeared to influence the work reported in this paper.

References

1. Sivam Krish. (2011) Computer-Aided Design, A practical generative design method, Volume 43, Issue 1, pp 88-100. doi.org/10.1016/j.cad.2010.09.009.
2. Autodesk. (2023) Fusion 360 Introduction to Generative design. Available online: https://www.autodesk.com/autodesk-university/article/Fusion-360-Introduction-Generative-Design (accessed on 20.11.2025)
3. Cad.Map. (2024) Cad - Fusion 360 Generative Design Extension. Available online: https://cad.map.sk/cad/fusion-360-generative-design-extension (accessed on 15.11.2025).
4. Zhang L, Li ZQ, Ying HQ. Lightweight design process combining generative design and topology optimization based on Fusion 360 and ANSYS: A case study of a biped robot's arch component. Int J Precis Eng Manuf 2025; Volume 26, Issue 7, pp 1775–1788. doi.org/10.1007/s12541-025-01226-5
5. Hodgyai, N.; Máté, M.; Oancea, G.; Dragoi, M.-V. Gear Hobs—Cutting Tools and Manufacturing Technologies for Spur Gears: The State of the Art. Materials 2024, Volume 17, pp 3219, doi:10.3390/ma17133219.

TECHNICAL UNIVERSITY OF KOŠICE
Faculty of Mechanical Engineering

Real-Time Machine Vision Inspection of Embedded Inserts on a Belt Feeder

Mateusz Waluszek [1,*], Maksymilian Maślanka [1] and Damian Pytka [1]

[1] University of Bielsko-Biała; dpytka@ubb.edu.pl; mmaslanka@ubb.edu.pl; mwaluszek@ubb.edu.pl
* Correspondence: mwaluszek@ubb.edu.pl;

Abstract: The study evaluates real-time machine vision system operating under dynamic feeding conditions. Research focuses on inspection of 3D-printed parts containing embedded threaded inserts, which constitute critical functional elements. Main objective was to assess influence of part motion on inspection quality, detection stability, and measurement feasibility. A belt feeder with continuous linear motion was used as primary experimental platform. Inspection tasks included verification of insert presence as well as attempts to measure insert size during part movement. Vision system was implemented using a smart camera platform and classical image processing tools. Experimental results obtained for different transport speeds indicate that insert presence detection can be reliably performed in real time on a belt feeder, whereas dimensional measurements are significantly affected by motion-induced image degradation.

Keywords: keyword machine vision; real-time inspection; belt feeder; rotary feeder; insert detection; industrial automation

1. Introduction

Machine vision systems are widely applied in industrial automation for quality control, inspection, and verification tasks. Main advantages include non-contact measurement, high repeatability, and ability to operate continuously without human intervention. In modern production environments, visual inspection is often required to be performed in real time on moving parts transported by feeding systems such as belt conveyors or rotary indexing tables.

In practical applications, inspection accuracy is determined not only by performance of image processing algorithms but also by dynamic factors related to part motion. Continuous linear motion may introduce image blur, synchronization errors, and variability in part positioning, negatively affecting detection reliability. Conversely, rotary feeders typically provide more controlled and repeatable motion at cost of reduced throughput.

This work addresses problem of real-time visual inspection under dynamic conditions by experimentally evaluating a vision system applied to a belt feeder. Particular attention is given to inspection of embedded threaded inserts, which require both presence verification and, in some cases, dimensional assessment. Motion blur and vibration effects are among the most common factors reducing detection accuracy in high-speed conveyor-based inspection systems, which makes proper camera configuration and illumination strategy essential. Vision-based inspection on conveyor systems has been widely studied in industrial quality control applications, where illumination design, exposure control, and robust detection algorithms play a critical role in maintaining reliable inspection performance.

2. Materials and Methods

Research was conducted with following objectives:

- evaluate feasibility of real-time detection of embedded inserts on a moving part,
- investigate influence of part transport speed on detection quality and system stability,
- to assess whether insert size or diameter can be measured during continuous motion,

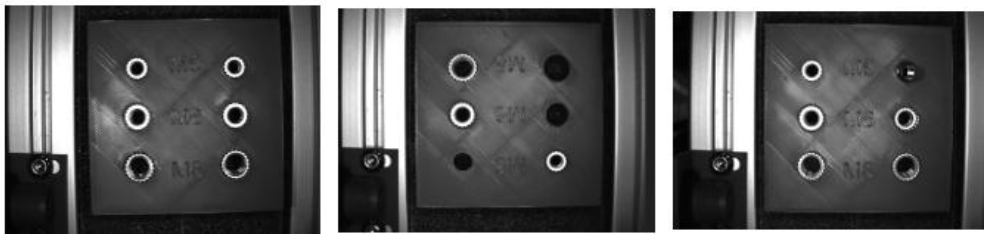

Figure 1. Examined details with embedded inserts (from the left: good detail, detail lacking inserts, detail with deffects).

Experimental inspection system was implemented using an industrial smart camera manufactured by Cognex, model In-Sight ISD902M, configured and programmed in In-Sight Explorer environment. Camera integrates image sensor, onboard processing unit, and communication interfaces, allowing inspection tasks to be executed directly on device without external computing hardware. Camera was mounted above belt feeder in a fixed position, providing a top-down view of inspected parts.

Image acquisition was performed using external triggering to ensure synchronization between part motion and image capture. Trigger signal was generated by an optical sensor positioned along conveyor belt, detecting leading edge of part and initiating image acquisition at a predefined inspection point. To ensure stable and repeatable image quality, camera was operated with integrated LED illumination system, set to 50% level. Two out of four available illumination zones were enabled to provide directional lighting conditions that improved contrast between threaded inserts and surrounding surface. This configuration reduced specular reflections and improved stability of blob-based detection used for insert verification. Illumination parameters, including intensity and exposure time, were experimentally adjusted to minimize influence of ambient lighting and reflections. Camera exposure time was set to 500ms in order to achieve sufficient image brightness while limiting motion blur at conveyor speeds up to 1.0m/s. Gain parameter was set to 60 to provide adequate signal amplification without introducing excessive image noise, while the offset parameter remained at 0 to ensure that the captured intensity range corresponded directly to the sensor output. Trigger delay was configured to 0, and debounce time was set to 500 μs to ensure stable processing of trigger signals generated by the optical sensor.

Preliminary tests showed that uncontrolled external light significantly affected image contrast and detection stability. Consequently, illumination was configured to dominate lighting conditions in inspection area, reducing sensitivity to environmental changes. Exposure time and gain were selected as a compromise between sufficient image brightness and motion-induced blur. This configuration was particularly critical at higher belt speeds, where excessive exposure times resulted in noticeable degradation of edge sharpness and reduced reliability of geometric measurements.

Belt feeder motion was monitored using an incremental rotary encoder mounted on drive system of conveyor motor. Encoder generated a fixed number of pulses per motor shaft revolution, acquired by a microcontroller-based measurement system built on Arduino platform. Arduino counted encoder pulses within a predefined sampling interval and calculated rotational speed of motor expressed in revolutions per minute (RPM). Cal-

culated motor speed was subsequently converted into linear velocity of conveyor belt using known mechanical parameters of drive system, including gearbox ratio and effective diameter of drive pulley. Resulting belt speed was expressed in meters per second (m/s) and used as a key variable in evaluation of motion influence on inspection performance.

Figure 2. View of the complete test stand.

3. Results

Experimental evaluation focused on influence of conveyor belt speed on quality of real-time visual inspection of embedded inserts. Inspection pipeline consisted of part localization using a trained pattern model and insert evaluation based on blob area analysis. Results were obtained for four discrete belt speeds: 0.25 m/s, 0.5 m/s, 0.75 m/s, and 1.0 m/s. For each speed level, multiple inspection cycles were performed, and detection quality values were averaged to ensure repeatability and reduce influence of random measurement noise.

Detection performance was evaluated using detection quality values obtained from the vision system together with qualitative assessment of false detections. During experiments, false positive detections were rarely observed, while occasional false negatives occurred primarily at the highest conveyor speed of 1.0 m/s, where motion blur reduced clarity of insert edges.

TrainPatMaxPattern tool was used to train a reference pattern based on characteristic geometric features of inspected part. Trained pattern enabled reliable localization of part position and orientation across all tested speeds. For correct parts, pattern matching score remained consistently high, exceeding 90% even at maximum tested speed. However, a gradual decrease in matching score was observed with increasing belt speed, indicating growing influence of motion-induced image degradation.

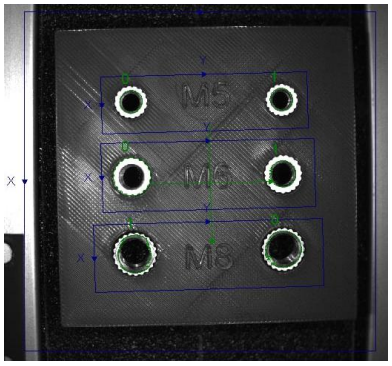

Figure 3. Example view of vision system operation during inspection.

At belt speed of 0.25 m/s, average pattern matching quality for correct parts reached 95.56%. As speed increased to 0.5 m/s and 0.75 m/s, quality decreased to 94.82% and 93.69%, respectively. At highest speed of 1.0 m/s, matching quality further dropped to 91.69%. Despite this decline, values remained within a range sufficient for stable part localization.

For parts with missing inserts, detection quality was significantly lower across all speeds. At 0.25 m/s, average detection quality reached 67.87%, increasing slightly to 68.96% at 0.5 m/s and remaining nearly constant at 0.75 m/s. A pronounced decrease was observed at 1.0 m/s, where detection quality dropped to 63.06%. This behavior indicates that absence of expected features reduces robustness of blob-based detection, particularly under increased motion blur.

Parts with improperly embedded inserts exhibited intermediate detection quality between correct and incomplete parts. At lower and moderate speeds, detection quality remained relatively stable, ranging from 73.55% at 0.25 m/s to 74.49% at 0.75 m/s. At highest speed of 1.0 m/s, detection quality decreased to 71.40%. This result suggests that geometric distortions caused by improper insert embedding become increasingly difficult to resolve as image quality degrades with speed.

Table 1. Comparison of detection quality for different conveyor belt speeds.

Speed	Good detail	Detail lacking inserts	Detail with deffects
0,25m/s	95,56%	67,86%	73,54%
0,5m/s	94,82%	68,96%	73,96%
0,75m/s	93,69%	68,71%	74,48%
1m/s	91,68%	63,06%	71,40%

4. Discussion

Results clearly demonstrate that conveyor belt speed is a critical factor influencing performance of real-time visual inspection systems. Although inspection pipeline based on pattern matching and blob area analysis proved effective under dynamic conditions, systematic degradation of detection quality was observed with increasing transport speed.

Pattern-based localization stage exhibited high robustness across entire tested speed range. Even at maximum belt speed of 1.0 m/s, TrainPatMaxPattern score for correct parts remained above 90%, indicating that global geometric features used for localization are relatively insensitive to moderate motion blur. This confirms that pattern matching can be reliably applied for part localization in continuous belt feeder systems, provided that triggering and illumination are properly configured.

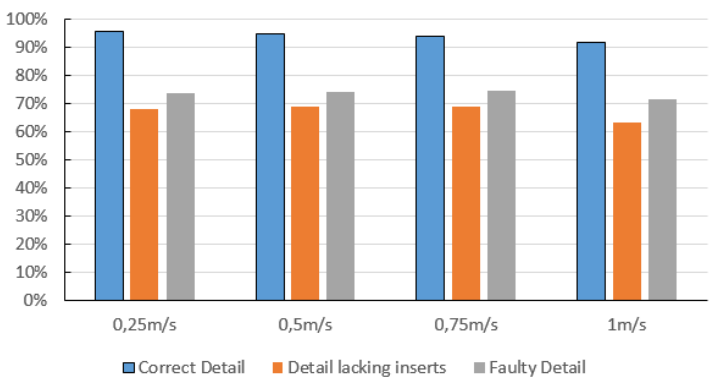

Figure 4. Comparison of detection quality as a function of conveyor belt speed.

Analysis of Table 1 and Figure 4 indicates that degradation trend is not strictly linear. For moderate speeds (0.25–0.75 m/s), detection quality remained relatively stable for most part categories. However, a clear threshold effect was observed at 1.0 m/s, where detection quality dropped significantly for defective parts. This suggests existence of a practical upper speed limit beyond which reliable inspection of non-ideal geometries becomes increasingly challenging without additional countermeasures such as increased illumination intensity, reduced exposure times, or motion compensation techniques.

Several technical approaches may be considered to mitigate motion blur in high-speed inspection systems. One solution is the use of shorter exposure times combined with higher illumination intensity. Another commonly applied approach involves stroboscopic lighting synchronized with the camera trigger signal, which effectively freezes the motion of inspected objects. Alternatively, encoder-synchronized image acquisition or line-scan camera systems may be used in conveyor-based inspection tasks to eliminate motion-induced blur.

Observed results also explain why dimensional measurements of inserts during continuous motion are more difficult than presence verification. Presence detection relies on coarse feature identification, whereas dimensional assessment requires precise edge localization, which is highly sensitive to blur and contrast reduction. As a result, even when presence detection remains acceptable, geometric measurement accuracy deteriorates rapidly with increasing speed.

Overall, discussion confirms that belt feeder–based inspection systems are well suited for high-throughput presence verification tasks but exhibit inherent limitations when applied to detailed geometric measurements under high-speed conditions.

5. Conclusions

This study evaluated performance of a real-time machine vision system operating on a belt feeder under dynamic transport conditions. Inspection focused on 3D-printed parts with embedded threaded inserts and addressed both presence detection and feasibility of dimensional assessment during motion.

- Based on experimental results, it can be concluded that:
- reliable insert presence detection can be achieved in real time over a wide range of conveyor belt speeds,
- increasing transport speed leads to gradual reduction in detection quality, with strongest impact observed for defective parts,
- pattern-based part localization remains robust even at higher speeds, whereas blob-based insert detection is more sensitive to motion-induced image degradation,
- dimensional measurements of inserts during continuous motion are significantly limited by image blur and reduced edge clarity.

Findings indicate that belt feeder systems are suitable for high-throughput inspection tasks focused on completeness and presence verification. Applications requiring precise geometric measurements may benefit from alternative feeding concepts or reduced transport speeds. Presented results provide practical guidelines for selection and tuning of machine vision inspection systems in industrial environments requiring real-time operation.

References

1. D. Jancarczyk, J. Rysiński and J. Worek, "Comparative Analysis of Measurement Tools in the Cognex D900 Vision System," Applied Sciences, vol. 14, no. 18, p. 8296, 2024, doi: 10.3390/app14188296.
2. J. Han, T. Fang, W. Liu, C. Zhang, M. Zhu and J. Xu, "Applications of Machine Vision Technology for Conveyor Belt Monitoring: A Comprehensive Review," Journal of Conveyor Technology and Real-Time Monitoring, 2025.
3. M. Zhang, "A Computer Vision Based Conveyor Deviation Detection System," Applied Sciences, vol. 10, no. 7, p. 2402, 2020.
4. M. Dziubek, "Exploring the ViDiDetect Tool for Automated Defect Detection in Manufacturing," Applied Sciences, vol. 13, no. 19, p. 11098, 2023.

5. R. Rajagounder, "A Machine Vision System for Inspecting Mechanical Parts," International Journal of Machine Vision and Industrial Inspection, 2025.
6. Y. Yang, C. Miao, X. Li and X. Mei, "On-line conveyor belts inspection based on machine vision," Optik, vol. 125, no. 19, pp. 5803–5807, 2014.
7. C. Steger, M. Ulrich and C. Wiedemann, Machine Vision Algorithms and Applications, Wiley-VCH, 2018.
8. E. R. Davies, Machine Vision: Theory, Algorithms and Practicalities, Academic Press, 2012.
9. E. Malamas, E. Petrakis, M. Zervakis, L. Petit and J. Legat, "A survey on industrial vision systems, applications and tools," Image and Vision Computing, vol. 21, no. 2, pp. 171–188, 2003.

TECHNICAL UNIVERSITY OF KOŠICE
Faculty of Mechanical Engineering

Assessment of the productivity of a robotic dental production cell design using simulation tool

Maryna Yeromina [1,*], Ján Duplák [1] and Samuel Mikuláško [1]

[1] Technical university of Kosice, Faculty of Manufacturing technologies with a seat in Presov, Bayerova 1, 080 01 Presov; Email: maryna.yeromina@tuke.sk, jan.duplak@tuke.sk, samuel.mikulasko@tuke.sk.
* Correspondence: maryna.yeromina@tuke.sk.

Abstract: This paper presents an assessment of the productivity and operational efficiency of a proposed robotic workplace for dental production, using the FlexSim simulation software tool. The robotic elements of the workplace consisted of two handling robots ensuring the manipulation of components and inter-operational transport of material, while the main production process was carried out by machining using CNC equipment. The created simulation model was used to monitor the dynamics of production cycles, equipment status modes, the time structure of operations and the available system performance. Based on the simulation results, quantitative indicators of operational behavior were evaluated. It was found that the utilization of the CNC production equipment was approximately 50% of working time, while the utilization of handling robots reached 50% (Robot1) and 39.77% (Robot2). The system throughput was determined to be 5 inputs and 4 processed outputs, which was equivalent to approximately 80% material processing efficiency. Time characteristics of the CNC´s work cycles were defined by the dominant occurrence of the processing state with a cycle length of 11 minutes. Based on the analysis, it was identified that there were unproductive periods in the system caused by robots waiting in idle and waiting states. These facts pointed to the presence of a bottleneck in the processor service area and an uneven distribution of inter-operational operations. The results obtained can be implemented in diagnostic operations to identify operational limitations and potential for improving production flow, reducing downtime and increasing the performance of the robotic workplace.

Keywords: productivity, dental production, robotic cell, simulation.

1. Introduction

Current research on the application of industrial robots in machining and material handling focuses mainly on improving productivity, operational flexibility, and reducing manual labor. Barosz, Gołda, and Kamp [1] demonstrated through simulation and industrial implementation that robotic handling can significantly improve production flow and reduce downtime. However, their study evaluates primarily operational performance indicators and does not address machining accuracy, economic efficiency, or the broader integration of robotic systems within complex production environments. The issue of machining accuracy is examined in detail by Iglesias Sánchez et al. [2], who showed that robot configuration and workpiece orientation strongly influence tool-path precision. While their findings highlight important kinematic factors affecting machining accuracy, the study does not consider overall production productivity or material flow within the robotic cell.

A broader theoretical perspective is provided by Makulavičius et al. [3], who discuss the advantages and limitations of robotic machining systems, emphasizing the trade-off between high flexibility and lower structural rigidity compared with conventional machine tools. This reduced rigidity can lead to vibration sensitivity and reduced machining

stability, although the study remains largely conceptual and does not evaluate productivity impacts in integrated robotic workplaces. The importance of digital simulation in robotic cell design is highlighted by Souflas et al. [4], who demonstrated that simulation tools enable trajectory optimization, identification of singularities, and improved process accuracy. Nevertheless, their research focuses mainly on kinematic analysis and does not address production flow, equipment utilization, or throughput of the manufacturing cell.

Practical applications of robotic handling systems are presented by Galande et al. [5], who implemented an automated material-handling system using a six-axis Kawasaki robot. Their results confirm several operational benefits, including reduced downtime, improved safety, and stabilized production flow in industrial environments. However, the study lacks detailed simulation analysis and does not evaluate machining accuracy or overall productivity parameters. Similarly, Trinh et al. [6] investigated robotic machining accuracy using a grey-box modeling approach combining physical models and data-driven optimization. While this method improves tool-path precision, the study does not analyze material flow or overall system productivity. Makulavičius et al. [7] further emphasize the role of monitoring and control in robotic workplaces using industrial vision and sensor systems, although their work does not explicitly evaluate equipment utilization or production flow. Busch and Zaeh [8] focus on robot dynamics modeling and vibration prediction using multi-level information fusion, contributing to theoretical understanding of robot machining but without assessing the robotic workplace as an integrated production system.

Recent studies have increasingly explored the integration of digital technologies, collaborative robotics, and intelligent manufacturing systems. Singh et al. [9] investigated the use of Unity and ROS as a digital communication layer within a digital twin framework for robotic manufacturing cells, demonstrating improved monitoring and system visualization. However, their work focuses mainly on system architecture and digital connectivity rather than on evaluating productivity or material flow efficiency. Mathew et al. [10] examined the introduction of mobile collaborative robots into bioprocessing environments, highlighting their flexibility and adaptability in controlled production systems. Despite these advantages, the study focuses mainly on system integration and safety aspects rather than on quantitative productivity evaluation.

Digital manufacturing workflows in the dental sector are discussed by Wang, Chen, and Lin [11], who proposed a collaborative system for producing dental components using additive manufacturing technologies. While their work demonstrates the benefits of digital integration in dental manufacturing, it does not analyze robotic production cell productivity or interactions between manufacturing equipment. Ahmad et al. [12] provides a broader overview of dental robotics, emphasizing the potential of robotic systems to improve precision, repeatability, and automation in dental procedures. However, the study remains largely conceptual and lacks quantitative evaluation of robotic systems in production environments.

Further research on robotic cell design is presented by Miatliuk et al. [13], who developed a robotic work cell using a hierarchical systems approach and the Visual Components simulation environment. Their work demonstrates how digital simulation can support the design and configuration of robotic workstations, enabling verification of robot trajectories before real implementation. Nevertheless, the study focuses mainly on system design and structural modeling rather than on productivity or equipment utilization analysis. Baptista et al. [14] explored a human–robot collaborative manufacturing cell with learning-based interaction capabilities, highlighting adaptive cooperation between human operators and robots. However, the focus remains on interaction mechanisms rather than comprehensive evaluation of manufacturing performance indicators such as throughput or productivity.

Overall, existing studies tend to focus on isolated aspects of robotic manufacturing systems, including machining accuracy, robot dynamics, digital integration, or collabora-

tive interaction. Comprehensive analyses that simultaneously evaluate machining processes, material handling, and production flow within an integrated robotic manufacturing cell remain relatively limited. This gap highlights the need for further research employing simulation-based approaches capable of assessing the productivity and operational performance of robotic production cells as complex manufacturing systems.

2. Materials and Methods

As part of the practical section of the article, a three-dimensional model of robotic cell for the production of dental implants was developed using the FlexSim simulation program (see Figure 1). This workstation was created in accordance with the EN ISO 10218-1 and consists of two industrial robots (manipulators), a milling machine for thread machining, an input point (labeled Source), and an output point (labeled Drain). The entire cell is enclosed within a protective safety fence, which separates the workspace from the surrounding environment.

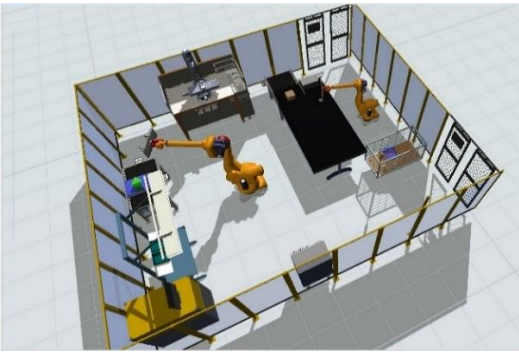

Figure 1. Designed robotic cell.

The operation of the cell is as follows: Robot 1 takes a semi-finished product from the input tray (Source) and places it into the milling machine, where the implant thread is machined. After completing this process, Robot 1 removes the workpiece from the machine and transfers it to the worktable designated for inspection. Robot 2 then performs a visual inspection of the workpiece and subsequently places it into the output storage (Drain).

The proposed model enables the simulation of smooth material flow, the analysis of robot cooperation, monitoring of the load on individual devices, and verification of the production cycle time. The workplace thus serves as a suitable basis for further evaluation of the efficiency and optimization of automated dental implant production.

3. Results

In this section, the results obtained from the analysis of the graphs generated during the simulation in the software environment are presented and discussed. The performance of the robotic workplace was evaluated based on simulation experiments conducted over three different time intervals: 1 minute, 10 minutes and 100 minutes. These time scales allow for the assessment of both short-term dynamic behavior and long-term operational stability of the system.

The State Graphs (see Figure 2 a), b) and c)) show the percentage distribution of the operating states of individual workplace devices at different simulation time intervals. In all cases, Processor1 shows a low but stable share of active processing (approximately 16.7–18.5%), with the rest of the time dominated by the waiting state. Robot1 achieves the highest utilization rate in all scenarios (81.5–83.3%), confirming its dominant role in handling workpieces, including transfers with and without load. The utilization of Robot2 varies depending on the length of the simulation – in a short time interval (State c), its activity is minimal (6.51%), while in the medium- and long-term evaluations (State b and

State a), it reaches more stable values (27.32–29.40%), reflecting its supporting role in the process of visual inspection and transfer of finished parts. A comparison of the graphs confirms that with increasing time intervals, the utilization of the equipment stabilizes, and the workplace exhibits consistent behaviour, with Robot1 remaining the main bearer of the workload, Processor1 ensuring the technological process, and Robot2 performing a supplementary control task.

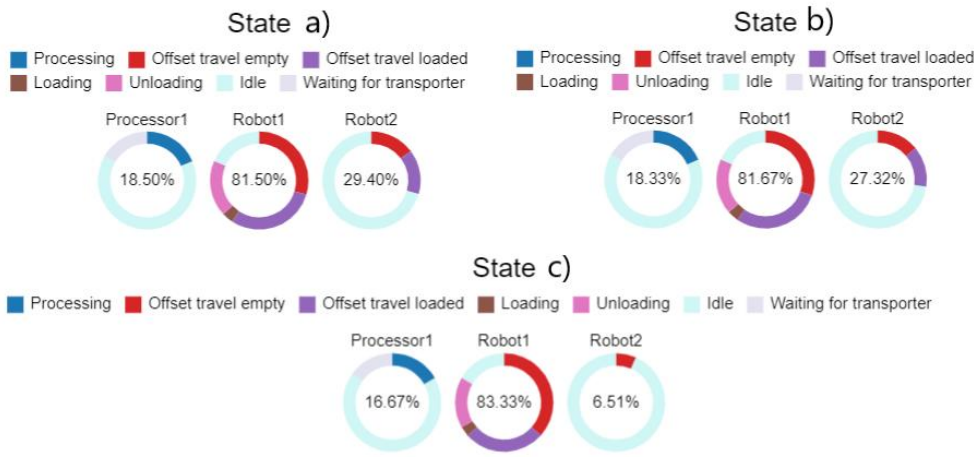

Figure 2. State Graphs – Status of individual devices; a) 100 minutes, b) 10 minutes, 1 minute.

The Staytime Graphs (see Figure 3 a), b) and c)) show the dwell time of individual devices (Processor1, Robot1 and Robot2) in active state at different simulation lengths. In graph a), the regular cyclical behavior of all devices is visible, with Processor1 achieving the highest dwell time, Robot1 slightly lower, and Robot2 the lowest, reflecting a stable and repeatable production cycle. Graph b) shows a short time period in which the activity of the devices is only manifested in individual significant peaks – especially for Robot1 and Processor1 – which is a result of the limited number of operations performed in a short simulation interval. Graph c) represents a long-term simulation, where the curves are very regular and evenly distributed over time, confirming stable system operation without fluctuations or interruptions. Processor1 maintains the highest activity time in the long term, Robot1 shows consistent values corresponding to handling operations, and Robot2 achieves lower but stable values related to control and transfer tasks. A comparison of all three graphs confirms that as the simulation time interval increases, the behavior of the system stabilizes, and the workplace operates in a regular, balanced, and repeatable mode.

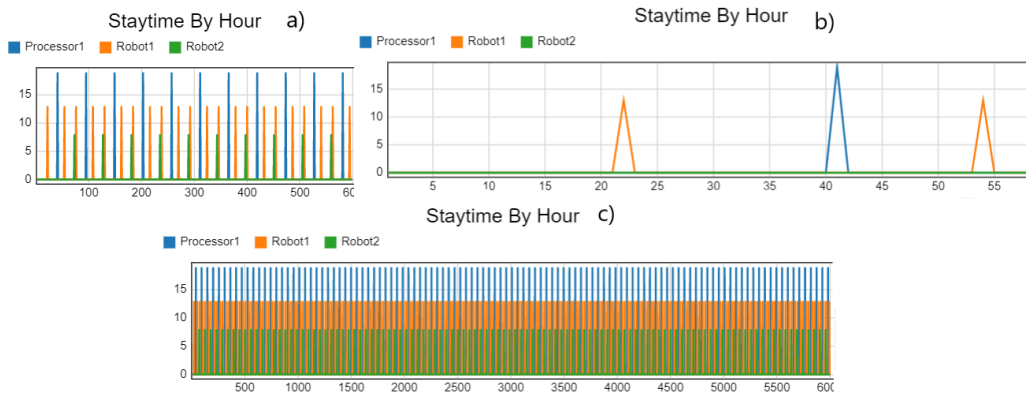

Figure 3. Staytime by Hour Graphs – Time spent in the system; a) 10 minutes, b) 1 minute, c) 100 minutes.

The Gantt Charts (see Figure 4 a), b) and c)) show the time course of the individual operating states of the Processor1, Robot1 and Robot2 devices at different simulation lengths. In all cases, it is clear that Processor1 is predominantly in the Idle state, with the actual processing taking place in short, regularly repeating intervals, which corresponds to the technological nature of the machining process. Robot1 exhibits a clearly defined sequence of activities consisting of unloading, moving without load, and subsequent handling of the workpiece, ensuring a smooth flow of material between the machine and the control point. Robot2 enters the process with a time delay after the completion of Robot1's operations, and its activity consists mainly of transfers and waiting phases related to visual inspection and storage of finished parts. In the short-term interval (graph a)), the individual operations are less significant in terms of time, while in the medium-term and long-term intervals (graphs b) and c)), a stable, repeatable cycle structure without collisions, blockages, or inefficient downtime is evident. Gantt charts thus confirm the correct time coordination of all equipment and the smooth operation of the robotic cell throughout the simulation.

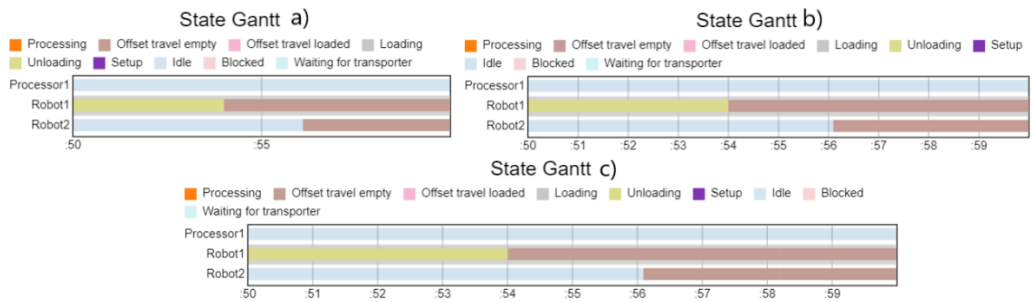

Figure 4. Gantt Charts – Time course of states; a)10 minutes , b) 100 minutes, c) 1 minute.

The Throughput Graphs (see Figure 5 a), b) and c)) show the number of pieces processed by individual system elements at different simulation time intervals. In graph a), which represents a short-term interval, the throughput is very low – Source1 and Processor1 processed one piece each, while Robot1 performed two handling operations, which corresponds to the initial phase of production. Graph b) represents a medium-term time interval, in which a more stable production flow is already evident: Source1 and Processor1 reached a value of 11 pieces, Robot2 processed 10 pieces, and Robot1 performed 22 grips, as it manipulates each part multiple times. Graph c) shows a long-term simulation where a linear increase in production is evident – Source1 and Processor1 processed 111 pieces each, Robot2 processed 110 pieces, and Robot1 performed 222 handling operations. This ratio confirms a consistent and smooth flow of material without accumulation or blockages, while emphasizing the dominant role of Robot1 in handling activities. A comparison of all three graphs clearly shows that as the simulation time increases, total production grows linearly and the workplace maintains stable and efficient operation.

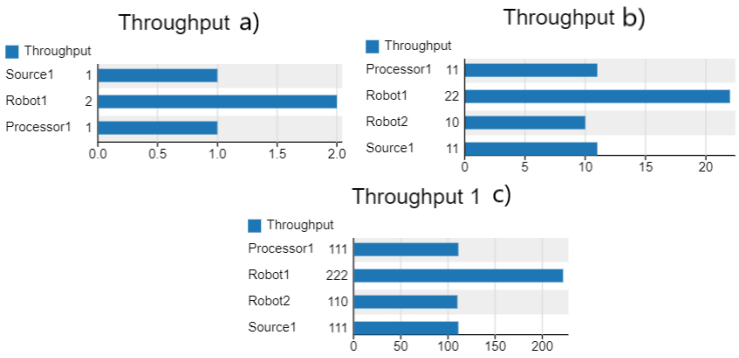

Figure 5. Throughput Graphs – System output; a) 1 minute, b) 10 minutes, c) 100 minutes.

4. Discussion

Table 1 summarizes the results of the robotic workplace simulation for three-time intervals (1 minute, 10 minutes, and 100 minutes) and provides an overview of the utilization of individual robots and the system's production indicators. The results show that the utilization of Robot1 remains stable during all time intervals and ranges from approximately 16.7% to 18.5%, while Robot2 achieves a long-term high and stable utilization of 81.5% to 83.3%. The proportion of processed pieces in the system increases linearly with increasing simulation time, which is particularly evident in Source1 and Processor1, where the number of manufactured parts increases from 1 to 11 and then to 111 pieces. A similar trend is observed for Robot2 and Robot1, with Robot1 performing twice as many grips due to repeated handling of each part. Overall, the table confirms stable workplace operation, uniform material flow, and linear production growth with no signs of bottlenecks or inefficient downtime, indicating appropriate logic and coordination settings for robotic cells.

Table 1. Comparison of system performance parameters for 10-Minute and 100-Minute Simulations.

Parameters	1 minute	10 minutes	100 minutes	Evaluation
Utilization Robot1	16.67%	18.33%	18.50%	Stable
Utilization Robot2	83.33%	81.67%	81.50%	Stably high
Number of parts-Source1	6.51%	27.32%	29.40%	Slight increase
Number of parts-Processor1	1	11	111	Linear growth
Number of parts-Robot2	1	11	111	Stable production
Number of parts-Robot1	1	10	110	Proportional growth
Number of grips	2	22	222	Linear growth

The graph (see Figure 6) compares key production indicators of the robotic workplace for simulation times of 1, 10, and 100 minutes. It shows a proportional increase in the number of processed parts and gripping operations as the simulation time increases. While the 1-minute simulation verifies basic system functionality, the 10- and 100-minute simulations confirm stable material flow and linear production growth. The results also highlight the dominant handling role of Robot1, which performs the highest number of gripping operations. Overall, the graph confirms long-term system stability without bottlenecks.

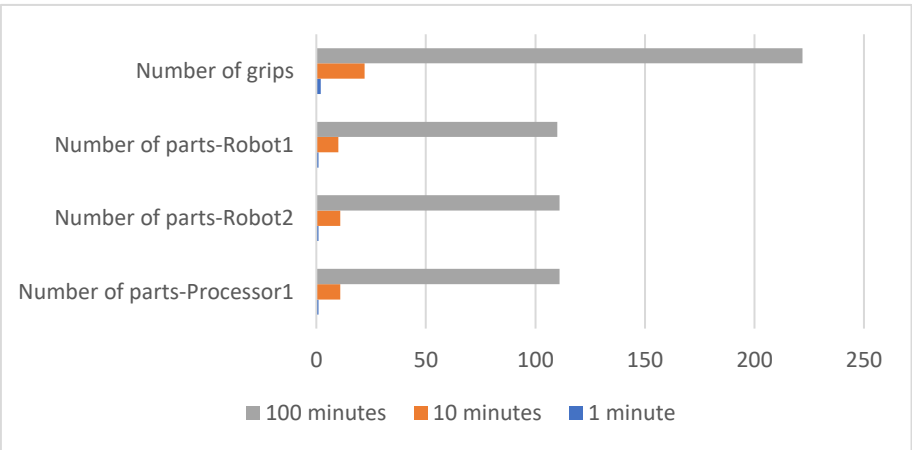

Figure 6. Comparison of Production Output and Handling Operations at Different Simulation Times.

5. Conclusions

The results of the simulation experiments confirmed the stable functionality of the designed robotic workstation without collisions, blockages, or significant material flow disruptions. Simulations were analyzed for time intervals of 1, 10, and 100 minutes, allowing both short-term and long-term system behavior to be evaluated. The comparison of these intervals showed that the system maintains a steady material flow and linear production growth even during extended operation. The characteristics of the selected graphs confirm the regularity of production cycles and the smooth continuity of individual operations. In terms of utilization, Robot1 is the dominant element throughout all simulation intervals, performing the main handling operations and achieving the highest activity values. Processor 1 shows stable but lower utilization, corresponding to the technological machining time, while Robot2 performs a supporting role in visual inspection and storage of finished products in the output warehouse. The results clearly confirm the correct configuration of the workplace logic and its suitability for automated dental implant production.

Acknowledgments: This work was supported by the Slovak Research and Development Agency under contract No. APVV-21-0293, also it was supported by research grant VEGA 1/0258/24.

Conflicts of Interest: The authors declare no conflict of interest.

References

1. Barosz, P.; Gołda, G.; Kampa, A. Efficiency Analysis of Manufacturing Line with Industrial Robots and Human Operators. *Appl. Sci.* **2020**, 10, 2862. https://doi.org/10.3390/app10082862
2. Iglesias Sánchez, I.; Ares, J.E.; González Gaya, C.; Rosales Prieto, V. A New Approach to the Consideration and Analysis of Critical Factors in Robotic Machining. *Appl. Sci.* **2020**, *10*, 8885. https://doi.org/10.3390/app10248885
3. Makulavičius, M.; Petkevičius, S.; Rožėnė, J.; Dzedzickis, A.; Bučinskas, V. Industrial Robots in Mechanical Machining: Perspectives and Limitations. *Robotics* **2023**, *12*, 160. https://doi.org/10.3390/robotics12060160
4. Souflas, T.; Gerontas, C.; Bikas, H.; Stavropoulos, P. On the Optimization of Robot Machining: A Simulation-Based Process Planning Approach. *Machines* **2024**, *12*, 521. https://doi.org/10.3390/machines12080521
5. Galande, V.G.; Ahire, N.; Pangavhane, K.; Avhad, A. Automatic material handling for machining process using 6 DOF of robot. *Int. J. Adv. Res. Comput. Commun. Eng.* **2025**, *14*(2), 1–6. https://doi.org/10.17148/IJARCCE.2025.14203
6. Trinh, M.; Königs, M.; Gründel, L.; Beier, M.; Petrovic, O.; Brecher, C. Accuracy Optimization of Robotic Machining Using Grey-Box Modeling and Simulation Planning Assistance. *J. Manuf. Mater. Process.* **2025**, *9*, 126. https://doi.org/10.3390/jmmp9040126
7. Makulavičius, M.; Petronienė, J.J.; Šutinys, E.; Bučinskas, V.; Dzedzickis, A. Industrial Robotic Setups: Tools and Technologies for Tracking and Analysis in Industrial Processes. *Appl. Sci.* **2025**, *15*, 10249. https://doi.org/10.3390/app151810249
8. Busch, M.; Zaeh, M.F. Multi-Fidelity Information Fusion to Model the Position-Dependent Modal Properties of Milling Robots. *Robotics* **2022**, *11*, 17. https://doi.org/10.3390/robotics11010017
9. Singh, M.; Kapukotuwa, J.; Gouveia, E.L.S.; Fuenmayor, E.; Qiao, Y.; Murry, N.; Devine, D. Unity and ROS as a Digital and Communication Layer for Digital Twin Application: Case Study of Robotic Arm in a Smart Manufacturing Cell. *Sensors* **2024**, *24*, 5680. https://doi.org/10.3390/s24175680
10. Mathew, R.; McGee, R.; Roche, K.; Warreth, S.; Papakostas, N. Introducing Mobile Collaborative Robots into Bioprocessing Environments: Personalised Drug Manufacturing and Environmental Monitoring. *Appl. Sci.* **2022**, *12*, 10895. https://doi.org/10.3390/app122110895
11. Wang, Y.-C.; Chen, T.; Lin, Y.-C. A Collaborative and Ubiquitous System for Fabricating Dental Parts Using 3D Printing Technologies. *Healthcare* **2019**, *7*, 103. https://doi.org/10.3390/healthcare7030103
12. Ahmad, P.; Alam, M.K.; Aldajani, A.; Alahmari, A.; Alanazi, A.; Stoddart, M.; Sghaireen, M.G. Dental Robotics: A Disruptive Technology. *Sensors* **2021**, *21*, 3308. https://doi.org/10.3390/s21103308
13. Miatliuk, K.; Koc, K.; Eliacik, A.; Miyagi, P.E.; Pessoa, M.A.O. Design of a Robotic Work Cell Using Hierarchical Systems Approach and Visual Components Software. *Appl. Sci.* **2025**, *15*, 4744. https://doi.org/10.3390/app15094744
14. Baptista, J.; Castro, A.; Gomes, M.; Amaral, P.; Santos, V.; Silva, F.; Oliveira, M. Human–Robot Collaborative Manufacturing Cell with Learning-Based Interaction Abilities. *Robotics* **2024**, *13*, 107. https://doi.org/10.3390/robotics13070107

Poznámky

Poznámky

Novus Scientia 2026

Zborník príspevkov z XXIII. Medzinárodnej vedeckej konferencie doktorandov strojníckych fakúlt technických univerzít a vysokých škôl

Názov:	Novus Scientia 2026
Editor:	© prof. Ing. Ján Slota, PhD.
	© Ing. Erika Dubňanská
	© Ing. Martina Hančinová
	© Ing. Barbara Schürger
Vydavateľ:	Technická univerzita v Košiciach,
	Strojnícka fakulta,
	Letná 1/9, 042 00 Košice-Sever
Rok:	2026
Náklad:	75 výtlačkov
Rozsah:	374 strán
Miesto konania:	Strojnícka fakulta, Technická univerzita v Košiciach
Dátum konania:	29.01.2026

ISBN 978-80-553-5042-4